All aTwitter over an Internet study *p. 686*

The extragalactic background's uneven glow *pp. 696 & 732*

A cellular target for human norovirus *pp. 700 & 755*

Science

$10
7 NOVEMBER 2014
sciencemag.org

AAAS

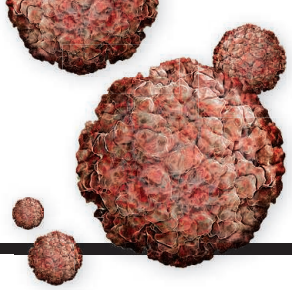


Insect phylogeny resolved

Molecular insights into insect origins and evolution

p. 763

CONTENTS



700 & 755
Bacteria make norovirus more infectious

7 NOVEMBER 2014 • VOLUME 346 • ISSUE 6210

NEWS

IN BRIEF

680 Roundup of the week's news



IN DEPTH

683 **PLAN TO PROTECT GREAT BARRIER REEF UNDER FIRE**
Continuing degradation threatens reef's World Heritage Site status *By D. Normile and L. Dayton*

684 **DELAYS HINDER EBOLA GENOMICS**
For months, no sequences from the virus have been released *By G. Vogel*

685 **WHAT'S KILLING THE REINDEER?**
Conservationists and herders in Norway differ about whether to blame predators or overpopulation *By E. Kintisch*

686 **AN INTERNET RESEARCH PROJECT DRAWS CONSERVATIVE IRE**
Truthy project at Indiana University analyzes Twitter traffic to understand patterns of political discourse
By J. Mervis

687 **GENETICS MAY FOSTER BUGS THAT KEEP YOU THIN**
Twin study shows genes influence gut microbiome *By E. Pennisi*

FEATURES

688 **A GLIMPSE OF COSMIC DAWN**
Astronomers are attempting to look back to when the first stars and galaxies lit up and changed the universe forever
By D. Clery

692 **RARE EARTH**
Soil scientists are tracking down rare and endangered soils in a quest to document—and preserve—"pedodiversity" *By M. Tennesen*

INSIGHTS

PERSPECTIVES

696 **THE OTHER HALF OF THE UNIVERSE?**
A large previously unknown population of stars inhabits intergalactic space
By S. H. Moseley
▸ REPORT P. 732

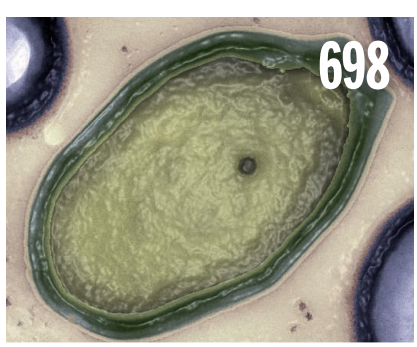
698 **SEARCHING FOR NEW BRANCHES ON THE TREE OF LIFE**
Is there undiscovered life that differs fundamentally from that in the three known domains?
By T. Woyke and E. M. Rubin

700 **LEAPING THE NOROVIRUS HURDLE**
Bacteria and B cells solve the problem of culturing human norovirus in the laboratory
By C. M. Robinson and J. K. Pfeiffer
▸ REPORT P. 755

701 **LOCAL SYNTHESIS AND DISPOSAL**
New experimental strategies reveal spatial and temporal features of protein synthesis and degradation in cells
By S. Shao and R. S. Hegde
▸ RESEARCH ARTICLE 716; REPORTS PP. 748 & 751

703 **COPING WITH LOW OCEAN SULFATE**
Did sulfate-reducing microbes exist in the Archean ocean? *By Y. Ueno*
▸ REPORTS PP. 735, 739, & 742

704 **SIMULATIONS PROVIDE A RARE LOOK AT REAL MELTING**
Advanced computational methods allow sampling of rare events and reveal multiple pathways in melting of metals
By A. van de Walle
▸ REPORT P. 729





706 **BRAZIL'S ENVIRONMENTAL LEADERSHIP AT RISK**
Mining and dams threaten protected areas *By J. Ferreira* et al.

BOOKS *ET AL.*

709 **THE THEORY OF EVERYTHING**
J. Marsh, director; reviewed by V. Thompson

709 **WHAT IF?**
By R. Munroe

LETTERS

710 **HIDDEN EFFECTS OF MOUSE CHOW**
By L. Augenlicht

710 **EARTHSHAKING ENERGY DEVELOPMENT PLANS**
By H. Yang et al.

710 **ONLINE BUZZ: CLINICAL TRIALS**

711 **GIVE YOUNG SCIENTISTS A LEVEL PLAYING FIELD**
By P. C. Jordan

DEPARTMENTS

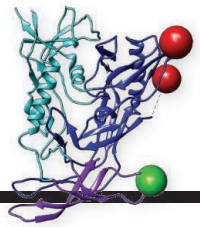
679 **EDITORIAL**
Journals unite for reproducibility
By Marcia McNutt

782 **WORKING LIFE**
Reflections of a woman pioneer
By Vijaysree Venkatraman

Science Staff 676
New Products 768
Science Careers 770

Published by AAAS

CONTENTS



759
Structure of the HIV-1 envelope protein subunit gp120

7 NOVEMBER 2014 • VOLUME 346 • ISSUE 6210

RESEARCH

IN BRIEF

712 From *Science* and other journals

REVIEW

715 **ECONOMICS**
Economics in the age of big data
L. Einav and J. Levin
REVIEW SUMMARY; FOR FULL TEXT:
dx.doi.org/10.1126/science.1243089

RESEARCH ARTICLES

716 **LOCAL TRANSLATION**
Principles of ER cotranslational translocation revealed by proximity-specific ribosome profiling
C. H. Jan et al.
RESEARCH ARTICLE SUMMARY; FOR FULL TEXT:
dx.doi.org/10.1126/science.1257521
▸ PERSPECTIVE P. 701; REPORT P. 748

717 **NANOMATERIALS**
Casting inorganic structures with DNA molds *W. Sun* et al.
RESEARCH ARTICLE SUMMARY; FOR FULL TEXT:
dx.doi.org/10.1126/science.1258361

718 **THE RIBOSOME**
Structure of the large ribosomal subunit from human mitochondria
A. Brown et al.

REPORTS

722 **QUANTUM SPIN LIQUIDS**
Coherent transmutation of electrons into fractionalized anyons
M. Barkeshli et al.

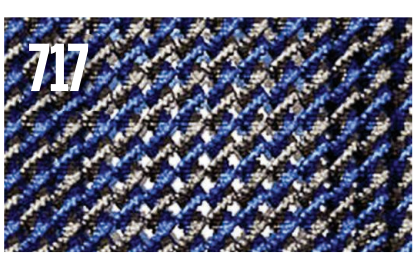
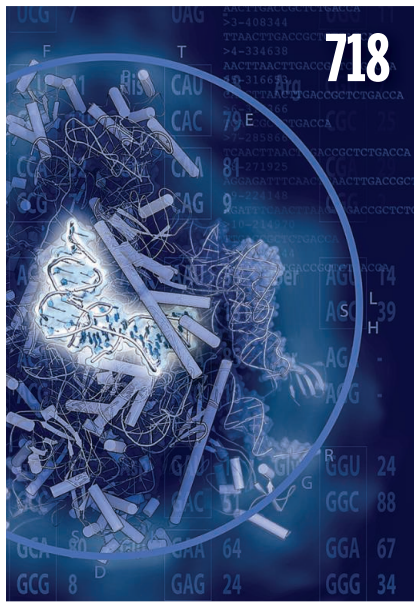


IMAGE: (MIDDLE) ALEXEY AMUNTS/LESLEY MCKEANE



725 **PHOTOCHEMISTRY**
Reduction of aryl halides by consecutive visible light-induced electron transfer processes *I. Ghosh* et al.

729 **PHASE TRANSFORMATION**
Microscopic mechanisms of equilibrium melting of a solid *A. Samanta* et al.
▸ PERSPECTIVE P. 704

732 **EARLY UNIVERSE**
On the origin of near-infrared extragalactic background light anisotropy *M. Zemcov* et al.
▸ PERSPECTIVE P. 696

EARLY EARTH

735 Sulfate was a trace constituent of Archean seawater *S. A. Crowe* et al.

739 Neoarchean carbonate–associated sulfate records positive $\Delta^{33}S$ anomalies *G. Paris* et al.

742 Large sulfur isotope fractionations associated with Neoarchean microbial sulfate reduction *I. Zhelezinskaia* et al.
▸ PERSPECTIVE P. 703

745 **ANIMAL BEHAVIOR**
Bats jamming bats: Food competition through sonar interference
A. J. Corcoran and W. E. Conner

748 **LOCAL TRANSLATION**
Targeting and plasticity of mitochondrial proteins revealed by proximity-specific ribosome profiling
C. C. Williams et al.
▸ PERSPECTIVE P. 701;
RESEARCH ARTICLE P. 716

751 **QUALITY CONTROL**
Quality control of inner nuclear membrane proteins by the Asi complex
O. Foresti et al.
▸ PERSPECTIVE P. 701

755 **NOROVIRUS**
Enteric bacteria promote human and mouse norovirus infection of B cells
M. K. Jones et al.
▸ PERSPECTIVE P. 700; PODCAST

759 **HIV ENTRY**
Conformational dynamics of single HIV-1 envelope trimers on the surface of native virions *J. B. Munro* et al.

763 **INSECT PHYLOGENOMICS**
Phylogenomics resolves the timing and pattern of insect evolution
B. Misof et al.

ON THE COVER



A composite image of individually photographed insects illustrates a small fraction of their enigmatic diversity. Scientists from the 1KITE project used a data set of 1478 protein-coding genes from 144 insect species to provide reliable estimates on controversial dates of origin and relationships of all major insect groups. See page 763. *Image: Hans Pohl, Friedrich-Schiller-Universität Jena, Germany*

SCIENCE (ISSN 0036-8075) is published weekly on Friday, except the last week in December, by the American Association for the Advancement of Science, 1200 New York Avenue, NW, Washington, DC 20005. Periodicals mail postage (publication No. 484460) paid at Washington, DC, and additional mailing offices. Copyright © 2014 by the American Association for the Advancement of Science. The title SCIENCE is a registered trademark of the AAAS. Domestic individual membership and subscription (51 issues): $153 ($74 allocated to subscription). Domestic institutional subscription (51 issues): $1282; Foreign postage extra: Mexico, Caribbean (surface mail) $55; other countries (air assist delivery) $85. First class, airmail, student, and emeritus rates on request. Canadian rates with GST available upon request, GST #1254 88122. Publications Mail Agreement Number 1069624. **Printed in the U.S.A.**
Change of address: Allow 4 weeks, giving old and new addresses and 8-digit account number. **Postmaster:** Send change of address to AAAS, P.O. Box 96178, Washington, DC 20090–6178. **Single-copy sales:** $10.00 current issue, $15.00 back issue prepaid includes surface postage; bulk rates on request. **Authorization to photocopy** material for internal or personal use under circumstances not falling within the fair use provisions of the Copyright Act is granted by AAAS to libraries and other users registered with the Copyright Clearance Center (CCC) Transactional Reporting Service, provided that $30.00 per article is paid directly to CCC, 222 Rosewood Drive, Danvers, MA 01923. The identification code for *Science* is 0036-8075. *Science* is indexed in the *Reader's Guide to Periodical Literature* and in several specialized indexes.

Published by AAAS

Science
AAAS
1200 New York Avenue, NW, Washington, DC 20005
Bateman House, 82-88 Hills Road, Cambridge, UK CB2 1LQ

Editor-in-Chief Marcia McNutt
Executive Editor Monica M. Bradford **News Editor** Tim Appenzeller
Managing Editor, Research Journals Katrina L. Kelner
Deputy Editors Barbara R. Jasny, Andrew M. Sugden(UK), Valda J. Vinson, Jake S. Yeston

Research and Insights

SR. EDITORS Caroline Ash(UK), Gilbert J. Chin, Lisa D. Chong, Maria Cruz(UK), Julia Fahrenkamp-Uppenbrink(UK), Pamela J. Hines, Stella M. Hurtley(UK), Paula A. Kiberstis, Marc S. Lavine(Canada), Kristen L. Mueller, Ian S. Osborne(UK), Beverly A. Purnell, L. Bryan Ray, Guy Riddihough, H. Jesse Smith, Jelena Stajic, Peter Stern(UK), Phillip D. Szuromi, Brad Wible, Nicholas S. Wigginton, Laura M. Zahn **ASSOCIATE EDITORS** Brent Grocholski, Melissa R. McCartney, Margaret M. Moerchen, Sacha Vignieri **ASSOCIATE BOOK REVIEW EDITOR** Valerie B. Thompson **ASSOCIATE LETTERS EDITOR** Jennifer Sills **CHIEF CONTENT PRODUCTION EDITOR** Cara Tate **SR. CONTENT PRODUCTION EDITORS** Harry Jach, Trista Wagoner **CONTENT PRODUCTION EDITORS** Jeffrey E. Cook, Chris Filiatreau, Cynthia Howe, Lauren Kmec, Barbara P. Ordway **SR. EDITORIAL COORDINATORS** Carolyn Kyle, Beverly Shields **EDITORIAL COORDINATORS** Ramatoulaye Diop, Joi S. Granger, Lisa Johnson, Anita Wynn **PUBLICATIONS ASSISTANTS** Aneera Dobbins, Jeffrey Hearn, Dona Mathieu, Le-Toya Mayne Flood, Shannon McMahon, Scott Miller, Jerry Richardson, Rachel Roberts(UK), Alice Whaley(UK), Brian White **EXECUTIVE ASSISTANT** Anna Bashkirova **ADMINISTRATIVE SUPPORT** Janet Clements(UK), Michael Crabtree(UK, Intern), Lizanne Newton(UK), Maryrose Madrid, John Wood(UK)

News

NEWS MANAGING EDITOR John Travis **INTERNATIONAL EDITOR** Richard Stone **DEPUTY NEWS EDITORS** Daniel Clery(UK), Robert Coontz, Elizabeth Culotta, David Grimm, David Malakoff, Leslie Roberts **CONTRIBUING EDITORS** Martin Enserink(Europe), Mara Hvistendahl (Asia) **SR. CORRESPONDENTS** Jeffrey Mervis, Elizabeth Pennisi **NEWS WRITERS** Adrian Cho, Jon Cohen, Jennifer Couzin-Frankel, Carolyn Gramling, Eric Hand, Jocelyn Kaiser, Kelly Servick, Robert F. Service, Erik Stokstad, Emily Underwood **INTERNS** David Shultz, Jia You **CONTRIBUTING CORRESPONDENTS** Pallava Bagla(South Asia), Michael Balter(Paris), John Bohannon, Ann Gibbons, Sam Kean, Richard A. Kerr, Eli Kintisch, Kai Kupferschmidt(Berlin), Andrew Lawler, Christina Larson(Beijing), Mitch Leslie, Charles C. Mann, Eliot Marshall, Virginia Morell, Dennis Normile(Tokyo), Heather Pringle, Tania Rabesandratana(Brussels), Gretchen Vogel(Berlin), Lizzie Wade(Mexico City) **CAREERS** Jim Austin(Editor), Donisha Adams **COPY EDITORS** Kara Estelle, Nora Kelly, Jennifer Levin **ADMINISTRATIVE SUPPORT** Scherraine Mack

Executive Publisher Alan I. Leshner
Publisher Kent R. Anderson **Chief Digital Media Officer** Rob Covey

BUSINESS OPERATIONS AND ADMINISTRATION DIRECTOR Deborah Rivera-Wienhold **BUSINESS SYSTEMS AND FINANCIAL ANALYSIS DIRECTOR** Randy Yi **MANAGER OF FULFILLMENT SYSTEMS** Neal Hawkins **SYSTEMS ANALYST** Nicole Mehmedovich **ASSISTANT DIRECTOR, BUSINESS OPERATIONS** Eric Knott **MANAGER, BUSINESS OPERATIONS** Jessica Tierney **BUSINESS ANALYSTS** Cory Lipman, Cooper Tilton, Celeste Troxler **FINANCIAL ANALYST** Jeremy Clay **RIGHTS AND PERMISSIONS ASSISTANT DIRECTOR** Emilie David **PERMISSIONS ASSOCIATE** Elizabeth Sandler **RIGHTS, CONTRACTS, AND LICENSING ASSOCIATE** Lili Kiser

MARKETING DIRECTOR Ian King **MARKETING MANAGER** Julianne Wielga **MARKETING ASSOCIATE** Elizabeth Sattler **SR. MARKETING EXECUTIVE** Jennifer Reeves **SR. ART ASSOCIATE, PROJECT MANAGER** Tzeitel Sorrosa **ART ASSOCIATE** Seil Lee **ASSISTANT COMMERCIAL EDITOR** Selby Frame **MARKETING PROJECT MANAGER** Angelissa McArthur **SR. WRITER** Bill Zimmer **PROGRAM DIRECTOR, AAAS MEMBER CENTRAL** Peggy Mihelich **FULFILLMENT SYSTEMS AND OPERATIONS** membership@aaas.org **MANAGER, MEMBER SERVICES** Pat Butler **SPECIALISTS** LaToya Casteel, Javia Flemmings, Latasha Russell **MANAGER, DATA ENTRY** Mickie Napoleoni **DATA ENTRY SPECIALISTS** JJ Regan, Jaimee Wise, Fiona Giblin

DIRECTOR, SITE LICENSING Tom Ryan **DIRECTOR, CORPORATE RELATIONS** Eileen Bernadette Moran **SR. PUBLISHER RELATIONS SPECIALIST** Kiki Forsythe **PUBLISHER RELATIONS MANAGER** Catherine Holland **PUBLISHER RELATIONS, EASTERN REGION** Keith Layson **PUBLISHER RELATIONS, WESTERN REGION** Ryan Rexroth **MANAGER, SITE LICENSE OPERATIONS** Iquo Edim **FULFILLMENT ANALYST** Lana Guz **ASSOCIATE DIRECTOR, MARKETING** Christina Schlecht **MARKETING ASSOCIATES** Thomas Landreth, Minah Kim

DIRECTOR OF WEB TECHNOLOGIES Ahmed Khadr **SR. DEVELOPER** Chris Coleman **DEVELOPERS** Dan Berger, Jimmy Marks **SR. PROJECT MANAGER** Trista Smith **SYSTEMS ENGINEER** Luke Johnson **PRODUCT MANAGER** Walter Jones

CREATIVE DIRECTOR, MULTIMEDIA Martyn Green **DIRECTOR OF ANALYTICS** Enrique Gonzales **SR. WEB PRODUCER** Sarah Crespi **WEB PRODUCER** Alison Crawford **VIDEO PRODUCER** Nguyen Nguyen **SOCIAL MEDIA PRODUCER** Meghna Sachdev

DIRECTOR OF OPERATIONS PRINT AND ONLINE Lizabeth Harman **PRINT PRODUCTION DIRECTOR** Wendy K. Shank **PREFLIGHT MANAGER** Marcus Spiegler **ASSISTANT MANAGER ONLINE** Lisa Stanford **ASSISTANT MANAGER PRINT** Rebecca Doshi **SR SPECIALISTS** Steve Forrester, Jason Hillman, Antoinette Hodal, Tara Kelly, Anthony Rosen **SPECIALISTS** Jacob Hedrick, Nichele Johnston, Lori Murphy, Kimberley Oster

DESIGN DIRECTOR Beth Rakouskas **ASSOCIATE ART DIRECTOR** Laura Creveling **SR. ILLUSTRATORS** Chris Bickel, Katharine Sutliff **ILLUSTRATOR** Valerie Altounian **SR. ART ASSOCIATES** Holly Bishop, Preston Huey **ART ASSOCIATES** Kay Engman, Garvin Grullón, Chrystal Smith **SR. PHOTO EDITOR** William Douthitt **PHOTO EDITOR** Leslie Blizard

DIRECTOR, GLOBAL COLLABORATION, CUSTOM PUBLICATIONS, ADVERTISING Bill Moran **EDITOR, CUSTOM PUBLISHING** Sean Sanders: 202-326-6430 **ASSISTANT EDITOR, CUSTOM PUBLISHING** Tianna Hicklin: 202-326-6463 **ADVERTISING MARKETING MANAGER** Justin Sawyers: 202-326-7061 science_advertising@aaas.org **ADVERTISING MARKETING ASSOCIATE** Javia Flemmings **ADVERTISING SUPPORT MANAGER** Karen Foote: 202-326-6740 **ADVERTISING PRODUCTION OPERATIONS MANAGER** Deborah Tompkins **SR. PRODUCTION SPECIALIST/GRAPHIC DESIGNER** Amy Hardcastle **PRODUCTION SPECIALIST** Yuse Lajiminmuhip **SR. TRAFFIC ASSOCIATE** Christine Hall **SALES COORDINATOR** Shirley Young **ASSOCIATE DIRECTOR, COLLABORATION, CUSTOM PUBLICATIONS/CHINA/TAIWAN/KOREA/SINGAPORE** Ruolei Wu: +86-186 0822 9345, rwu@aaas.org **COLLABORATION/CUSTOM PUBLICATIONS/JAPAN** Adarsh Sandhu + 81532-81-5142 asandhu@aaas.org **EAST COAST/E. CANADA** Laurie Faraday: 508-747-9395, FAX 617-507-8189 **WEST COAST/W. CANADA** Lynne Stickrod: 415-931-9782, FAX 415-520-6940 **MIDWEST** Jeffrey Dembksi: 847-498-4520 x3005, Steven Loerch: 847-498-4520 x3006 **UK EUROPE/ASIA** Roger Goncalves: TEL/FAX +41 43 243 1358 **JAPAN** Katsuyoshi Fukamizu(Tokyo): +81-3-3219-5777 kfukamizu@aaas.org **CHINA/TAIWAN** Ruolei Wu: +186-0082-9345

WORLDWIDE ASSOCIATE DIRECTOR OF SCIENCE CAREERS Tracy Holmes: +44 (0) 1223 326525, FAX +44 (0) 1223 326532 tholmes@science-int.co.uk **CLASSIFIED** advertise@sciencecareers.org **U.S. SALES** Tina Burks: 202-326-6577, Nancy Toema: 202-326-6578 **SALES ADMINISTRATOR** Marci Gallun **EUROPE/ROW SALES** Axel Gesatzki, Sarah Lelarge **SALES ASSISTANT** Kelly Grace **JAPAN** Hiroyuki Mashiki(Kyoto): +81-75-823-1109 hmashiki@aaas.org **CHINA/TAIWAN** Ruolei Wu: +86-186 0082 9345 rwu@aaas.org **MARKETING MANAGER** Allison Pritchard **MARKETING ASSOCIATE** Aimee Aponte

AAAS BOARD OF DIRECTORS RETIRING PRESIDENT, CHAIR Phillip A. Sharp **PRESIDENT** Gerald R. Fink **PRESIDENT-ELECT** Geraldine (Geri) Richmond **TREASURER** David Evans Shaw **CHIEF EXECUTIVE OFFICER** Alan I. Leshner **BOARD** Bonnie L. Bassler, May R. Berenbaum, Carlos J. Bustamante, Claire M. Fraser, Laura H. Greene, Elizabeth Loftus, Raymond Orbach, Inder M. Verma

SUBSCRIPTION SERVICES For change of address, missing issues, new orders and renewals, and payment questions: 866-434-AAAS (2227) or 202-326-6417, FAX 202-842-1065. Mailing addresses: AAAS, P.O. Box 96178, Washington, DC 20090-6178 or AAAS Member Services, 1200 New York Avenue, NW, Washington, DC 20005

INSTITUTIONAL SITE LICENSES 202-326-6755 **REPRINTS:** Author Inquiries 800-635-7181 **COMMERCIAL INQUIRIES** 803-359-4578 **PERMISSIONS** 202-326-6765, permissions@aaas.org **AAAS Member Services** 202-326-6417 or http://membercentral.aaas.org/discounts

Science serves as a forum for discussion of important issues related to the advancement of science by publishing material on which a consensus has been reached as well as including the presentation of minority of conflicting points of view. Accordingly, all articles published in *Science*—including editorials, news and comment, and books reviews—are signed and reflect the individual views of the authors and not official points of view adopted by AAAS or the institutions with which the authors are affiliated.

INFORMATION FOR AUTHORS See pages 680 and 681 of the 7 February 2014 issue or access www.sciencemag.org/about/authors

SENIOR EDITORIAL BOARD
A. Paul Alivisatos, *Lawrence Berkeley Nat'l. Laboratory,* **Ernst Fehr,** *U. of Zürich*
Susan M. Rosenberg, *Baylor College of Medicine,* **Michael S. Turner,** *U. of Chicago*

BOARD OF REVIEWING EDITORS (Statistics board members indicated with **(S)**)
Adriano Aguzzi, *U. Hospital Zürich*
Takuzo Aida, *U. of Tokyo*
Leslie Aiello, *Wenner-Gren Foundation*
Judith Allen, *U. of Edinburgh*
Sonia Altizer, *U. of Georgia*
Virginia Armbrust, *U. of Washington*
Sebastian Amigorena, *Institut Curie*
Kathryn Anderson, *Memorial Sloan-Kettering Cancer Center*
Peter Andolfatto, *Princeton U.*
Meinrat O. Andreae, *Max-Planck Inst. Mainz*
Paola Arlotta, *Harvard U.*
Johan Auwerx, *EPFL*
David Awschalom, *U. of Chicago*
Jordi Bascompte, *Estación Biológica de Doñana CSIC*
Facundo Batista, *London Research Inst.*
Ray H. Baughman, *U. of Texas, Dallas*
David Baum, *U. of Wisconsin*
Kamran Behnia, *ESPCI-ParisTech*
Yasmine Belkaid, *NIAID, NIH*
Philip Benfey, *Duke U.*
Stephen J. Benkovic, *Penn State U.*
Carlo Beenakker, *Leiden U.*
Gabriele Bergers, *U. of California, San Francisco*
Christophe Bernard, *Aix-Marseille U.*
Bradley Bernstein, *Massachusettes General Hospital*
Peer Bork, *EMBL*
Bernard Bourdon, *Ecole Normale Supérieure de Lyon*
Chris Bowler, *École Normale Supérieure*
Ian Boyd, *U. of St. Andrews*
Emily Brodsky, *U. of California, Santa Cruz*
Ron Brookmeyer, *U. of California Los Angeles* **(S)**
Christian Büchel, *U. Hamburg-Eppendorf*
Joseph A. Burns, *Cornell U.*
Gyorgy Buzsaki, *New York U. School of Medicine*
Blanche Capel, *Duke U.*
Mats Carlsson, *U. of Oslo*
David Clapham, *Children's Hospital Boston*
David Clary, *U. of Oxford*
Joel Cohen, *Rockefeller U., Columbia U.*
Jonathan D. Cohen, *Princeton U.*
James Collins, *Boston U.*
Robert Cook-Deegan, *Duke U.*
Alan Cowman, *Walter & Eliza Hall Inst.*
Robert H. Crabtree, *Yale U.*
Roberta Croce, *Vrije Universiteit*
Janet Currie, *Princeton U.*
Jeff L. Dangl, *U. of North Carolina*
Tom Daniel, *U. of Washington*
Frans de Waal, *Emory U.*
Stanislas Dehaene, *Collège de France*
Robert Desimone, *MIT*
Claude Desplan, *New York U.*
Ap Dijksterhuis, *Radboud U. of Nijmegen*
Dennis Discher, *U. of Pennsylvania*
Gerald W. Dorn II, *Washington U. School of Medicine*
Jennifer A. Doudna, *U. of California, Berkeley*
Bruce Dunn, *U. of California, Los Angeles*
Christopher Dye, *WHO*
Todd Ehlers, *U. of Tuebingen*
David Ehrhardt, *Carnegie Inst. of Washington*
Tim Elston, *U. of North Carolina at Chapel Hill*
Gerhard Ertl, *Fritz-Haber-Institut, Berlin*
Barry Everitt, *U. of Cambridge*
Ernst Fehr, *U. of Zurich*
Anne C. Ferguson-Smith, *U. of Cambridge*
Michael Feuer, *The George Washington U.*
Kate Fitzgerald, *U. of Massachusetts*
Peter Fratzl, *Max-Planck Inst.*
Elaine Fuchs, *Rockefeller U.*
Daniel Geschwind, *UCLA*
Andrew Gewirth, *U. of Illinois*
Karl-Heinz Glassmeier, *TU Braunschweig*
Ramon Gonzalez, *Rice U.*
Julia R. Greer, *Caltech*
Elizabeth Grove, *U. of Chicago*
Kip Guy, *St. Jude's Children's Research Hospital*
Taekjip Ha, *U. of Illinois at Urbana-Champaign*
Christian Haass, *Ludwig Maximilians U.*
Steven Hahn, *Fred Hutchinson Cancer Research Center*
Michael Hasselmo, *Boston U.*
Martin Heimann, *Max-Planck Inst. Jena*
Yka Helariutta, *U. of Cambridge*
James A. Hendler, *Rensselaer Polytechnic Inst.*
Janet G. Hering, *Swiss Fed. Inst. of Aquatic Science & Technology*
Michael E. Himmel, *National Renewable Energy Lab.*
Kai-Uwe Hinrichs, *U. of Bremen*
Kei Hirose, *Tokyo Inst. of Technology*
David Hodell, *U. of Cambridge*
David Holden, *Imperial College*
Lora Hooper, *UT Southwestern Medical Ctr. at Dallas*
Raymond Huey, *U. of Washington*
Steven Jacobsen, *U. of California, Los Angeles*
Kai Johnsson, *EPFL Lausanne*
Peter Jonas, *Inst. of Science & Technology (IST) Austria*
Matt Kaeberlein, *U. of Washington*
William Kaelin Jr., *Dana-Farber Cancer Inst.*
Daniel Kahne, *Harvard U.*
Daniel Kammen, *U. of California, Berkeley*
Masashi Kawasaki, *U. of Tokyo*
Joel Kingsolver, *U. of North Carolina at Chapel Hill*
Robert Kingston, *Harvard Medical School*
Eitonne Koechlin, *Ecole Normale Suprieure*
Alexander Kolodkin, *Johns Hopkins U.*
Roberto Kolter, *Harvard Medical School*
Alberto R. Kornblihtt, *U. of Buenos Aires*
Leonid Kruglyak, *UCLA*
Thomas Langer, *U. of Cologne*
Mitchell A. Lazar, *U. of Pennsylvania*
David Lazer, *Harvard U.*
Thomas Lecuit, *IBDM*
Virginia Lee, *U. of Pennsylvania*
Stanley Lemon, *U. of North Carolina at Chapel Hill*
Ottoline Leyser, *Cambridge U.*
Marcia C. Linn, *U. of California, Berkeley*
Jianguo Liu, *Michigan State U.*
Luis Liz-Marzan, *CIC biomaGUNE*
Jonathan Losos, *Harvard U.*
Ke Lu, *Chinese Acad. of Sciences*
Christian Lüscher, *U. of Geneva*
Laura Machesky, *CRUK Beatson Inst. for Cancer Research*
Anne Magurran, *U. of St. Andrews*
Oscar Marin, *CSIC & U. Miguel Hernández*
Charles Marshall, *U. of California, Berkeley*
C. Robertson McClung, *Dartmouth College*
Graham Medley, *U. of Warwick*
Yasushi Miyashita, *U. of Tokyo*
Richard Morris, *U. of Edinburgh*
Alison Motsinger-Reif, *NC State U.* **(S)**
Sean Munro, *MRC Lab. of Molecular Biology*
Thomas Murray, *The Hastings Center*
James Nelson, *Stanford U. School of Med.*
Karen Nelson, *J. Craig Venter Institute*
Daniel Neumark, *U. of California, Berkeley*
Timothy W. Nilsen, *Case Western Reserve U.*
Pär Nordlund, *Karolinska Inst.*
Helga Nowotny, *European Research Advisory Board*
Ben Olken, *MIT*
Joe Orenstein, *U. of California Berkeley & Lawrence Berkeley National Lab*
Harry Orr, *U. of Minnesota*
Andrew Oswald, *U. of Warwick*
Steve Palumbi, *Stanford U.*
Jane Parker, *Max-Planck Inst. of Plant Breeding Research*
Giovanni Parmigiani, *Dana-Farber Cancer Inst.* **(S)**
Donald R. Paul, *U. of Texas, Austin*
John H. J. Petrini, *Memorial Sloan-Kettering Cancer Center*
Joshua Plotkin, *U. of Pennsylvania*
Albert Polman, *FOM Institute AMOLF*
Philippe Poulin, *CNRS*
David Randall, *Colorado State U.*
Colin Renfrew, *U. of Cambridge*
Felix Rey, *Institut Pasteur*
Trevor Robbins, *U. of Cambridge*
Jim Roberts, *Fred Hutchinson Cancer Research Ctr.*
Barbara A. Romanowicz, *U. of California, Berkeley*
Jens Rostrup-Nielsen, *Haldor Topsoe*
Mike Ryan, *U. of Texas, Austin*
Mitinori Saitou, *Kyoto U.*
Shimon Sakaguchi, *Kyoto U.*
Miquel Salmeron, *Lawrence Berkeley National Lab*
Jürgen Sandkühler, *Medical U. of Vienna*
Alexander Schier, *Harvard U.*
Randy Seeley, *U. of Cincinnati*
Vladimir Shalaev, *Purdue U.*
Robert Siliciano, *Johns Hopkins School of Medicine*
Joseph Silk, *Institut d'Astrophysique de Paris*
Denis Simon, *Arizona State U.*
Alison Smith, *John Innes Centre*
Richard Smith, *U. of North Carolina* **(S)**
John Speakman, *U. of Aberdeen*
Allan C. Spradling, *Carnegie Institution of Washington*
Jonathan Sprent, *Garvan Inst. of Medical Research*
Eric Steig, *U. of Washington*
Paula Stephan, *Georgia State U. and National Bureau of Economic Research*
Molly Stevens, *Imperial College London*
V. S. Subrahmanian, *U. of Maryland*
Ira Tabas, *Columbia U.*
Sarah Teichmann, *Cambridge U.*
John Thomas, *North Carolina State U.*
Shubha Tole, *Tata Institute of Fundamental Research*
Christopher Tyler-Smith, *The Wellcome Trust Sanger Inst.*
Herbert Virgin, *Washington U.*
Bert Vogelstein, *Johns Hopkins U.*
Cynthia Volkert, *U. of Göttingen*
Douglas Wallace, *Dalhousie U.*
David Wallach, *Weizmann Inst. of Science*
Ian Walmsley, *U. of Oxford*
David A. Wardle, *Swedish U. of Agric. Sciences*
David Waxman, *Fudan U.*
Jonathan Weissman, *U. of California, San Francisco*
Chris Wikle, *U. of Missouri* **(S)**
Ian A. Wilson, *The Scripps Res. Inst.* **(S)**
Timothy D. Wilson, *U. of Virginia*
Rosemary Wyse, *Johns Hopkins U.*
Jan Zaanen, *Leiden U.*
Kenneth Zaret, *U. of Pennsylvania School of Medicine*
Jonathan Zehr, *U. of California, Santa Cruz*
Len Zon, *Children's Hospital Boston*
Maria Zuber, *MIT*

BOOK REVIEW BOARD
David Bloom, *Harvard U.,* **Samuel Bowring,** *MIT,* **Angela Creager,** *Princeton U.,*
Richard Shweder, *U. of Chicago,* **Ed Wasserman,** *DuPont*

Published by AAAS

EDITORIAL

Journals unite for reproducibility



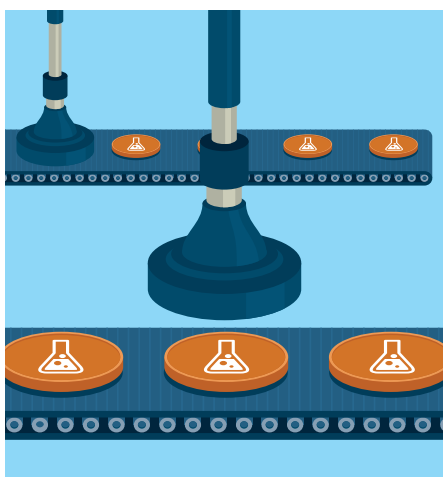
Marcia McNutt
Editor-in-Chief
Science *Journals*

Reproducibility, rigor, transparency, and independent verification are cornerstones of the scientific method. Of course, just because a result is reproducible does not necessarily make it right, and just because it is not reproducible does not necessarily make it wrong. A transparent and rigorous approach, however, can almost always shine a light on issues of reproducibility. This light ensures that science moves forward, through independent verifications as well as the course corrections that come from refutations and the objective examination of the resulting data.

It was with the goal of strengthening such approaches in the biomedical sciences that a group of editors representing over 30 major journals, representatives from funding agencies, and scientific leaders assembled at the AAAS headquarters in June of 2014 to discuss principles and guidelines for preclinical biomedical research. The gathering was convened by the U.S. National Institutes of Health, *Nature*,* and *Science*.

The discussion ranged from what journals were already doing to address reproducibility and the effectiveness of those measures, to the magnitude of the problem and the cost of solutions. The attendees agreed on a common set of Principles and Guidelines in Reporting Preclinical Research (www.nih.gov/about/reporting-preclinical-research.htm) that list proposed journal policies and author reporting requirements to promote transparency and reproducibility.

The new guidelines suggest that journals include in their information for authors their policies for statistical analysis and how they review the statistical accuracy of work under consideration. Any imposed page limits should not discourage reproducibility. The guidelines encourage using a checklist to ensure the reporting of important experimental parameters, such as standards used, number and type of replicates, statistics, method of randomization, whether experimenters were blind to the conduct of the experiment, how the sample size was determined, and what criteria were used to include or exclude any data. Journals should recommend the deposition of data in public repositories where available and link data bidirectionally to the published paper. Journals should strongly encourage, as appropriate, that all materials used in the experiment be shared with those who wish to replicate the experiment. Once a journal publishes a paper, it assumes the obligation to consider publication of a refutation of that paper, subject to its usual standards of quality.



"...scientific journals are standing together in their conviction that reproducibility and transparency are important..."

The more open-ended portion of the guidelines suggests that journals establish best practices for image-based data (such as screening for manipulation and storing full-resolution archival versions) and how to describe experiments more completely. An example for animal experiments is reporting the source, species, strain, sex, age, husbandry, inbred and strain characteristics, or transgenic animals, etc. For cell lines, one might report the source, authentication, and mycoplasma contamination status. The existence of these guidelines does not obviate the need for replication or independent verification of research results, but should make it easier to perform such replication.

Some of the journals at the meeting already had implemented all or most of these principles and guidelines. But the important point is that a large number of scientific journals are standing together in their conviction that reproducibility and transparency are important issues.† As partners to the research enterprise in the communication and dissemination of research results, journals want to do their part to raise the standards for the benefit of all scientists and the benefit of society. The hope is that that these guidelines will not be viewed as onerous, but as part of the quality control that justifies the public trust in science.

– Marcia McNutt

*See www.nature.com/news/1.16259. † A list of all journals and publishers signatory to the principles and guidelines is at www.nih.gov/about/reporting-preclinical-research.htm.

10.1126/science.aaa1724

IMAGES: (INSET) SORBETTO/ISTOCKPHOTO.COM; (RIGHT) STACEY PENTLAND PHOTOGRAPHY

Downloaded from www.sciencemag.org on November 6, 2014

Published by AAAS

NEWS

> “Africa has … become powerless, confused, disoriented, and totally helpless, resorting to international aid, begging for everything.”
>
> **Nigerian Academy of Science President Oyewale Tomori**, criticizing Africa’s response to Ebola at an emerging diseases meeting in Vienna last week. **http://scim.ag/Tomori**

IN BRIEF



In the last spiral of an embryonic python, paired penises are forming.

One penis, or two?

Ever wonder why men have one penis while snakes have two? The genetic instructions specifying the organ’s development are essentially the same in reptiles and mammals. So to understand the differences, Harvard University developmental biologist Patrick Tschopp and colleagues traced penis development in mouse and snake embryos. Signals from the cloaca, a cavity destined to become the lower gut, initiate penis formation in both animals—but in snakes, the penis arises from what would have been the beginnings of the rear legs, whereas in mice, cells destined to become the tail take on that task, the team reported this week in *Nature*. As in real estate, location is everything: The rodent cloaca is by the solo tail-to-be and taps some of those cells for the penis—while the snake cloaca is by where two limbs used to form, so it gets two penises instead of just one. Thus, penis formation is an example of “deep homology”: Instead of a common cellular ancestry, the same organ in different species has a common molecular ancestry. **http://scim.ag/penisev**

CREDITS: (TOP TO BOTTOM) PATRICK TSCHOPP/HARVARD MEDICAL SCHOOL/DEPARTMENT OF GENETICS; JO SCOTT, LIZ ALLEN, AMY BRAND *ET AL.*/BIOMED CENTRAL DESIGN TEAM

AROUND THE WORLD

Ebola fears hamper U.S. meetings

NEW ORLEANS, LOUISIANA | Fears of the Ebola virus are barring researchers from two scientific meetings in New Orleans. Several scientists—including representatives of the World Health Organization and the Centers for Disease Control and Prevention—had to cancel their trip to the annual meeting of the American Society of Tropical Medicine and Hygiene this week after the state of Louisiana barred attendees who had treated Ebola patients or been in Guinea, Sierra Leone, or Liberia in the previous 3 weeks. The same rules will affect the annual convention of the American Public Health Association (APHA), held in New Orleans from 15 to 19 November, says APHA Executive Director Georges Benjamin. Meanwhile, two infectious diseases meetings in Europe went ahead as planned this week because no Ebola travel restrictions applied in their host cities, Vienna and Stockholm. **http://scim.ag/Ebolamtgban, http://scim.ag/EbolaEur**

Germans boost research funding

BERLIN | After months of deadlock, German politicians agreed on 30 October to a €25.3 billion ($31.6 billion) funding package for universities and research institutes through 2020. The bulk of the new money, €19.3 billion, will go to universities. Nonuniversity research organizations like the DFG funding agency, the Max Planck Society, and the Leibniz Association will receive 3% annual budget increases from 2016 through 2020, down from recent 5% yearly increases. Funding for overhead costs—a long-simmering issue—will rise from 20% to 22%. The country’s Excellence Initiative, a competition between universities for extra funding, will also continue, though details won’t be worked out until after an evaluation of the program is finished in early 2016.

Badges clarify co-authors’ roles

LONDON | A collection of science, publishing, and software groups is developing a solution to the problem of how to identify the contributions of each of a



Downloaded from www.sciencemag.org on November 6, 2014

Published by AAAS

paper's authors: digital "badges"—such as "computation," "investigation," and "data visualization"—that detail what each author did for the work. Authors can link the badges to their profiles elsewhere on the Web. The collaboration, which includes BioMed Central, the Public Library of Science, Mozilla Science Lab, and ORCID (an effort to assign researchers digital identifiers), presented the project at the Mozilla Festival in London late last month. Early prototypes are scheduled to launch next year, according to Amye Kenall, journal development manager of open data initiatives and journals at BioMed Central.
http://scim.ag/_digitalbadges

Science's memory deepens

BOSTON | Today's scientists are standing on the shoulders of giants, relying on the work of their predecessors—to whom they give a nod by citing their papers. But is the work of those predecessors becoming obsolete, as scientists choose to cite more recent work? In a paper posted on arXiv, the team behind Google Scholar weighed in this week with a study of their own massive data set. The team analyzed papers published between 1990 and 2013 and compared the publication dates of citations listed in them. The results should give older scientists reason to cheer: The fraction of citations that are at least 10 years older than the paper citing them has increased steadily, from 28% in 1990 to 36% in 2013, the team reports.
http://scim.ag/papercites

Climate report sounds alarm

COPENHAGEN | Climate change is taking hold and will bring worrying impacts—but there is still time to limit the damage. That is the message delivered by the Intergovernmental Panel on Climate Change's (IPCC's) Synthesis Report, released this week, which caps work on three massive studies issued by IPCC over the past year, comprising the group's fifth assessment of climate science and mitigation since 1990. "The core message from the IPCC is the growing urgency of action," said Bob Perciasepe, president of the Arlington, Virginia–based Center for Climate and Energy Solutions, in a statement. "The scientists have done their job. Now it's up to governments to do theirs."

New research chief touts dowsing

SYDNEY, AUSTRALIA | Larry Marshall, the next CEO of Australia's leading research agency, the Commonwealth Scientific and Industrial Research Organisation (CSIRO), is in hot water after suggesting in a recent radio interview with the Australian Broadcasting Corporation (ABC) that CSIRO investigate water divining, or dowsing. Although it is "a little out there," he told ABC, it's the agency's job to "push the envelope." CSIRO scientists are keeping their heads down in the wake of a 5.45% (AU$111.4 million) budget cut that will see up to 420 jobs eliminated by June 2015, along with the closure of eight research facilities. But experts outside the agency decried the interest in dowsing expressed by a Silicon Valley venture capitalist with a doctorate in physics. "I'm appalled," says John Williams of the Wentworth Group of Concerned Scientists and former chief of CSIRO Land and Water.
http://scim.ag/CSIROdowsing

Experiments lost in rocket explosion

Six seconds after liftoff, on 28 October an unmanned Antares rocket commissioned by NASA and bound for the International Space Station (ISS) exploded just over the launch pad at Wallops Island, Virginia. The explosion of the rocket, built by Orbital Sciences Corp., incinerated numerous scientific experiments on board as well as 748 kg of supplies for the six astronauts on the ISS. Among the losses were 18 experiments by students from across the United States and Canada; a high-resolution camera developed by the Southwest Research Institute in San Antonio, Texas, to observe the chemical composition of meteors entering Earth's atmosphere; and an experiment to test materials for their suitability as solar sails, which use radiation pressures from stars to propel spacecraft without burning fuel.
http://scim.ag/Antaresrocket



An unmanned rocket bound for the ISS exploded shortly after its launch 28 October.

PHOTO: JOEL KOWSKY/NASA/SIPA

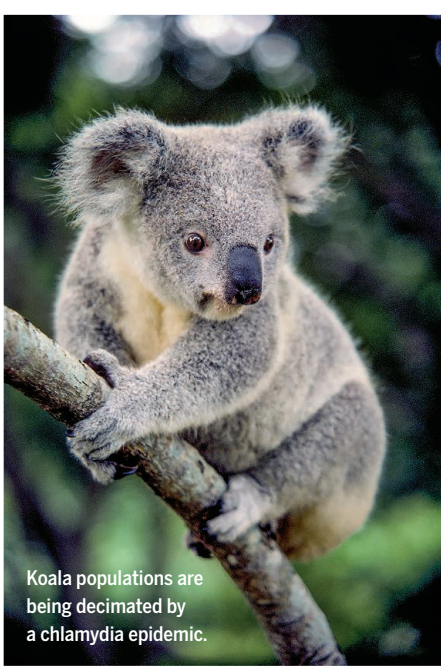
Published by AAAS



Plant biologist Uma Nagendra's aerial dance was the overall winner.

The trees and the tornado: Winner of 'Dance Your Ph.D.'

A circus extravaganza by plant biologist-cum-aerialist Uma Nagendra depicting plant-soil interactions in the aftermath of a tornado is the overall winner of this year's "Dance Your Ph.D." contest, co-sponsored by *Science*. Nagendra, a Ph.D. student at the University of Georgia, Athens, demonstrates how tornadoes' destruction can offer tree seedlings a respite from parasitic soil fungi. Nagendra, also the biology category winner, will receive $1000 and a trip to Stanford University in May 2015, where her video will be screened. The three other category winners, each of whom will receive $500, include: Hans Rinderknecht of the Massachusetts Institute of Technology in Cambridge, who explained how he uses light to trigger nuclear fusion; Saioa Alvarez of the University of the Basque Country in Leioa, Spain, for her dance explaining the chemistry of emulsions like mayonnaise; and David Manzano Cosano of the Complutense University of Madrid, who danced about the history of technology and colonialism in the Pacific. **http://scim.ag/DancePhD2014**



Koala populations are being decimated by a chlamydia epidemic.

Vaccine may slow koalas' decline

QUEENSLAND, AUSTRALIA | Help may be on the way for koalas, whose numbers have declined from millions in the 1700s to as few as 43,000 today. In addition to urbanization, which has decimated the eucalyptus forest koalas live in, and deaths due to cars and dogs, a chlamydia epidemic is ravaging the marsupial's populations, causing blindness, infertility, and death. But last week, microbiologists at the University of the Sunshine Coast in Queensland, Australia, announced that a vaccine helps stem the course of disease. Peter Timms and his colleagues examined and put radio collars on 60 koalas, vaccinating half of them. Of that half, uninfected koalas were protected, koalas already infected did not get sicker, and their eye infections improved, they said. They hope to get more funding to extend the vaccination program.

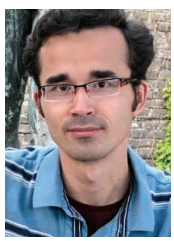
BY THE NUMBERS

$193 billion

China's record-high research and development expenditures in 2013, according to the National Bureau of Statistics, the Ministry of Science and Technology, and the Ministry of Finance.

NEWSMAKERS

Petition for jailed student



An open letter signed by 31 Nobel laureates that calls for the release of jailed Iranian physics Ph.D. student **Omid Kokabee** was delivered to the Iranian mission to the United Nations last week, along with earlier petitions signed by more than 14,000 people. Kokabee, 32, has been in prison since January 2011 (http://scim.ag/Kokabeetrial). He was studying the interaction of lasers and plasma at the University of Texas, Austin, when he was arrested and was later condemned to 10 years for espionage. In April 2013, Kokabee claimed in an open letter that he was jailed for refusing to cooperate with a military research project. In early October, Iran's supreme court accepted Kokabee's lawyer's appeal and ordered a retrial. Kokabee was also awarded the AAAS Scientific Freedom and Responsibility prize last week. (AAAS publishes *Science*.)

Italian physicist to lead CERN

Fabiola Gianotti will be the next director-general of CERN, the European particle physics laboratory near Geneva, Switzerland, which is home to the world's biggest atom smasher, the Large Hadron Collider (LHC). A staff member at CERN, Gianotti, 52, served from March 2009 to February 2013 as spokeswoman for the 3000 researchers working with ATLAS, one of four gargantuan particle detectors fed by the LHC. In that position, she participated in the biggest event in particle physics in decades: On 4 July 2012, she and the representative for rival detector CMS reported that the two teams had independently discovered the long-sought Higgs boson. Gianotti will take over from Rolf-Dieter Heuer on 1 January 2016.

PHOTOS: (CLOCKWISE FROM TOP) UMA NAGENDRA; COURTESY OF OMID KOKABEE; © MICHELE AND TOM GRIMM/ALAMY

Published by AAAS



Though well-managed, Australia's Great Barrier Reef is deteriorating.

PHOTO: DAVID DOUBILET/GETTY IMAGES

CONSERVATION

Plan to protect Great Barrier Reef under fire

Continuing degradation threatens reef's World Heritage Site status

By **Dennis Normile** *and* **Leigh Dayton**

Australia's Great Barrier Reef is under assault from fishers, agricultural runoff, and coastal development, and now climate change looms as a threat. But it was the prospect of humiliation—a threat by the World Heritage Committee to list the reef as "in danger"—that finally spurred the Australian government to act. It has crafted what it calls a comprehensive strategy to protect the reef's "values" while allowing "sustainable development and use." Scientists who have reviewed the draft plan are not impressed.

The plan "fails to effectively address" any of the pressures the reef is facing, according to a statement last week from the Australian Academy of Science, which argued that "much bolder action is required" to prevent further degradation. Scientists hope the government will considerably strengthen the Reef 2050 Long-Term Sustainability Plan before submitting it to the World Heritage Committee early next year.

Australia created the 344,400-square-kilometer Great Barrier Reef Marine Park off the state of Queensland in 1975, along with a Marine Park Authority to protect it. Conservation efforts were bolstered in 1981, after the reef was designated a World Heritage Site in recognition of its "outstanding universal value."

Yet conditions at the reef have deteriorated. In a 2012 report in the *Proceedings of the National Academy of Sciences*, Glenn De'ath of the Australian Institute of Marine Science in Townsville and colleagues reported that the reef's coral cover shrunk by half between 1985 and 2012. The culprits, De'ath's group found, were cyclones, predation by crown-of-thorns starfish, and bleaching—loss of the coral's photosynthetic organisms when the water gets too warm. "Without intervention," the team warned, "the GBR may lose the biodiversity and ecological integrity for which it was listed as a World Heritage Area."

The Great Barrier Reef's decline has alarmed scientists around the world. "The fact that a very well managed reef system is still showing substantial deterioration should be cause for general concern, because it reveals how pervasive our impacts are and how serious the consequences are for coral reefs," says Peter Sale, a reef ecologist and professor emeritus at the University of Windsor in Canada. It has also alarmed the World Heritage Committee, which warned last summer that in the absence of a long-term plan by early next year, it would consider listing the reef as "in danger." That "would be such a public shame for Australia," says Selina Ward, a reef ecologist at the University of Queensland, St. Lucia.

The draft 2050 plan acknowledges that more work is needed to address threats to the reef and calls for targets on water quality, biodiversity, ecosystem health, and economic and community benefits. But the academy points out that "many important targets are not quantified, nor are they connected to any mechanisms through which they can be achieved." The Australian Coral Reef Society adds that the plan anticipates port expansion and dredging and sets an objective of completing such work with "no detrimental impact on the health and resilience of the Great Barrier Reef." However, states the society, "There is no indication of the method to achieve this ambitious objective." Nor, states the Australian Museum, does the plan address "the long term viability of fisheries and endangered species."

For a long-term conservation strategy, the plan pays little attention to climate change, says Terry Hughes, director of the ARC Centre of Excellence for Coral Reef Studies in Townsville. It notes that climate change will lead to more frequent bleaching and extreme weather events. But it doesn't offer any solutions, Hughes says. Earlier this year, the Australian government repealed the nation's carbon tax and is promoting the development of coal deposits for export from Queensland.

The Australian government says it is listening to critics, but hasn't tipped its hand on how it may revise the plan. "We appreciate community engagement in how we can better manage the reef," wrote an environment ministry representative in an e-mail to *Science*. He did note that "the plan acknowledges that climate change is a global problem which requires global action, and is being addressed by the government through other policies."

"We hope that the government will improve the plan, and we'd like to help with that," Hughes says. A final plan must be submitted to the World Heritage Committee by 1 February, after which an advisory panel will review it and present a recommendation at the committee's annual meeting in Bonn in June. At a 2 October press conference, Environment Minister Greg Hunt said he's "optimistic" the committee will maintain the reef's current status. ■

Downloaded from www.sciencemag.org on November 6, 2014

Published by AAAS

INFECTIOUS DISEASES

Delays hinder Ebola genomics

For months, no sequences from the virus have been released

By **Gretchen Vogel**

As the Ebola epidemic sweeps through West Africa, scientists lack key genetic data to answer a question that has provoked much worried speculation: Is the virus becoming more transmissible or more deadly, or acquiring changes that would let it evade diagnostic tests or vaccines? Thousands of blood samples from Ebola patients have been sitting in refrigerators in Africa and Europe, untouched. And, as *Science* went to press, the few groups that have new sequence data have not made them public.

Researchers are eager for a close-up look at how the virus may be evolving. Besides answering questions about its virulence, genomic data could reveal details about the epidemic, including hotspots of transmission and how often the virus has escaped from its animal reservoir to humans, says Andrew Rambaut, an evolutionary biologist who studies infectious diseases at the University of Edinburgh in the United Kingdom. "If it can be done on a timely basis, you can really get insight into what is going on." But faced with the all-consuming public health response to the epidemic, bureaucratic obstacles, and chaotic record keeping, scientists have had to wait.

In August, the world got its closest molecular look at the virus so far, when researchers published 99 genomes of viruses from 78 patients who were infected in or around Kenema, Sierra Leone, from late May to mid-June. That analysis, published online on 28 August in *Science*, included more than half of the known cases in Sierra Leone at the time.

The sequence data, which the researchers deposited in public databases as soon as they were generated, showed how the virus changed as it passed from person to person at the start of the Sierra Leone outbreak, with one variant disappearing as another gained prominence among later cases. Since then, the outbreak has exploded into an epidemic—it has now sickened more than 13,000 and killed 5000—but the team, led by Pardis Sabeti and Stephen Gire at the Broad Institute in Cambridge, Massachusetts, has been unable to import any new samples from Sierra Leone. Other groups have been similarly stymied.

Several researchers say that getting export approval from beleaguered health ministries has been tough. "I can only assume that the system is so overwhelmed that processing samples beyond simple diagnostic tests is not high priority," says Rambaut, who was a co-author on the August sequence paper.

Stephan Günther, a virologist at the Bernhard Nocht Institute for Tropical Medicine (BNI) in Hamburg, Germany, and coordinator of the European Mobile Laboratory (EMLab) consortium, says they have been unable to export samples from Nigeria or Liberia. But BNI has been receiving samples from the EMLab mission in Guinea since March and now has close to 3000, he says. (BNI is storing them in its high-security lab on behalf of the Guinean government, which still owns them.)

> ***"We are all busy with fieldwork ... personnel is a bit of a problem."***
>
> **Stephan Günther**, Bernhard Nocht Institute for Tropical Medicine

Günther and his colleagues have not yet sequenced any of the samples, because consortium staff members have been busy supporting diagnostic centers in affected countries. "We are all busy with fieldwork," Günther says. "Personnel is a bit of a problem." That should ease, he says, with a new €1.7 million ($2.1 million) award from the European Union to EMLab for Ebola research.

In France, the Institut Pasteur, where early samples from Guinea were first identified as Ebola, also experienced delays exporting samples from West Africa but plans to start sequencing new viral genomes soon. The institute's lab in Dakar recently received samples from Guinea, says Felix Rey, who is coordinating the institute's Ebola task force in Paris. The Dakar lab will extract RNA and send it to Paris for high-throughput sequencing. "We hope to have sequenced viruses from a couple of hundred samples in the next month or so," Rey says.

Sabeti and her colleagues should soon get their Sierra Leone samples, which finally were cleared for export and arrived in the United States last week, says Robert Garry of Tulane University in New Orleans, Louisiana, who collaborates with Sabeti. But to speed the research, she and her colleagues are trying to secure funding to send sequencing machines to West Africa. "If we can't get the samples here, we will get the sequencers there," she says. The effort will build on the researchers' ongoing work with the African Centre of Excellence for Genomics of Infectious Diseases, a consor-

A changeable foe

The proteins that enable the Ebola virus to spread and cause disease are encoded by seven protein-sheathed genes. Mutations in the gene for the glycoprotein could affect the efficacy of antibody-based treatments. Other genes, such as those for polymerase and transcription factor VP30, can affect how quickly the virus replicates.

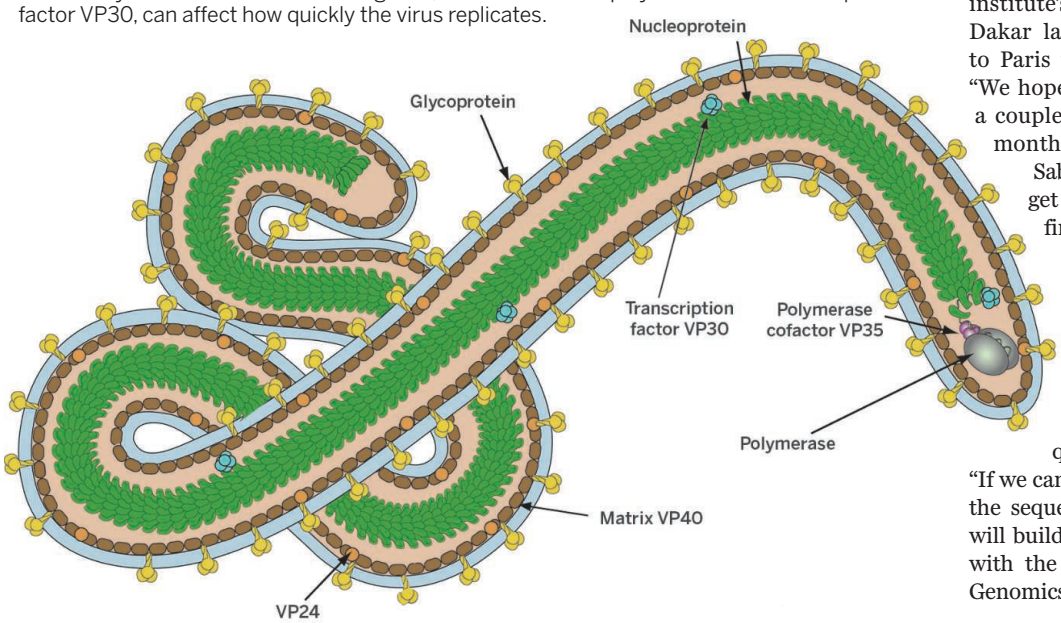


ILLUSTRATION: VIRALZONE/SIB SWISS INSTITUTE OF BIOINFORMATICS

Downloaded from www.sciencemag.org on November 6, 2014

Published by AAAS

tium of universities and research institutes in the United States, Nigeria, Sierra Leone, and Senegal, which for several years has been training African researchers in the use of genomics tools.

Blood samples alone aren't enough for genomic studies. Investigators need to know at least where each patient was from; ideally they will also have clinical information such as whether he or she survived. "Only when you have those pieces of information can you come up with useful information from the sequences," Günther says—and because of spotty record keeping, that information is often missing. He and his colleagues are working with Doctors Without Borders and the World Health Organization to match samples with relevant information, but setting up a database is time- and labor-intensive, he says.

Meanwhile, the few Ebola virus sequences that have been generated since that initial batch from Sierra Leone have not been made public. The U.S. Centers for Disease Control and Prevention (CDC) announced in August that it had sequenced Ebola virus samples from patients treated in the United States. But the data have not been placed in any public sequence repositories. That's unfortunate, Rambaut says. "As the U.S. cases are from Liberia and we have zero sequences from there so far, even one genome would be interesting and potentially useful," he says. Duncan MacCannell, a bioinformatics specialist at CDC in Atlanta, told *Science* that the sequences had been "actively shared and discussed with the public health community." He says CDC is working to submit the sequences to a public database.

New sequences probably won't show that the virus is finding new ways to attack or spread, Rambaut says. Instead, the prize is a clearer picture of the outbreak. A cluster of closely related viruses might point to a hotspot of transmission, he says, while unexpectedly diverse sequences would suggest that many cases were going undetected. Sequence data could also help researchers tell whether there has been more than one animal-to-human introduction.

Earlier sequence data did suggest that the virus was undergoing rapid changes, but that is not necessarily a sign that it is becoming more dangerous, Rambaut says. "Most RNA viruses mutate quickly, but adaptation and functional change is a much slower process." Measles mutates nearly as quickly as Ebola virus, but it has never evolved to escape the lifelong immunity of previously infected or vaccinated individuals. Even in an outbreak this big, Rambaut says, "I see no reason to suspect the virus will radically change its life cycle or its mode of transmission." ■



Sami herder Per Anders Eira wrangles a reindeer calf in northern Norway.

PHOTO: KNUT LANGELAND

ECOLOGY

What's killing the reindeer?

Conservationists and herders in Norway differ about whether to blame predators or overpopulation

By **Eli Kintisch**, *in Nordkapp, Norway*

An ecologist's study of reindeer has touched off a firestorm in this land of ice, tundra, and Sami herders, who tend vast numbers of the semi-domesticated animals. Each year, the herders file compensation claims for tens of thousands of reindeer deaths that they blame on carnivores, primarily lynx and wolverines. Ecologist Torkild Tveraa, however, pins the blame on overpopulation: The land simply cannot support the herds, which number roughly 180,000 here in Finnmark, Norway's most northern region.

Tveraa, who is with the Norwegian Institute for Nature Research in Tromsø, first presented his case in a government-funded report last year, and he added new analysis in a study published in the October issue of the *Journal of Applied Ecology*. The government has pointed to the findings as exonerating the threatened lynx and wolverines, which are already protected by strict hunting limits. To the Sami, however, the study threatens an economic lifeline.

To receive compensation, a herder must prove that a dead reindeer was killed by a lynx or wolverine. That's hard when herders find remains of only 5% to 10% of the reindeer that they lose. The government approved just a quarter of more than 60,000 such applications in 2011. The claims nonetheless are lucrative: That year, Sami herders in Norway received $11 million in predator payments, or two-thirds of what they received from meat sales.

To find out how much damage the predators really do, Tveraa's team combined their own data on reindeer health since 2000 with herd sizes reported by herders, observations of lynx and wolverines, and satellite data on grazing areas. They found that as a factor in reindeer mortality, food scarcity was two to three times more significant than lynx, and more than 20 times more significant than wolverines.

"Tveraa has a very solid basis for these findings—a very large data set collected over a very long time series," says Terje Bø, head of wildlife management in the Norwegian government's environment division in Trondheim. In the global canon of human-carnivore conflict research, Tveraa's "robust" study, says Matt Hayward, an ecologist at Bangor University in the United Kingdom, "goes against the grain of papers saying, 'It's the predators' fault.' " Other experts agree that the findings are plausible. "It's sort of official: We have too many reindeer," says Emil Halvorsrud, a wildlife official in Lakselv. Large herds are becoming less sustainable, he says, as a warming subarctic climate results in more slush and rain in winter, leaving pastures covered in ice.

Ellinor Jåma, with the Sami Reindeer Herders' Association of Norway in Karasjok, agrees that overpopulation is a factor in some deaths. "We may have too many reindeer in some areas of Finnmark," she concedes. "But in the middle of the country, reindeer health is good—and we still have heavy losses," which she blames on predation.

Bø hopes Tveraa's findings will show how ecological data could underpin a new compensation system the government has proposed to launch in 2017. Tveraa underscores that he doesn't take sides in the debate. "We hear: 'Oh, since your research is paid for by the government, you are only there to protect the carnivores,' " he says. That's not so, he insists: "The data speak for themselves." ■

Published by AAAS



Protesters in Istanbul's Taksim Gezi Park in 2013 used social media to spread their message.

SOCIAL SCIENCE

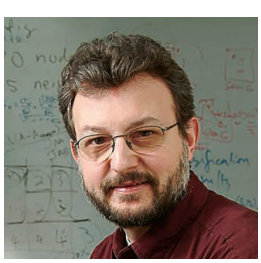
An Internet research project draws conservative ire

Truthy project at Indiana University analyzes Twitter traffic to understand patterns of political discourse

By **Jeffrey Mervis**

The truth about Truthy has become a scarce commodity.

Truthy is a 4-year-old academic study of how information spreads on Twitter. The work, by researchers at Indiana University (IU), Bloomington, has been cited favorably in mainstream media reports about the broader phenomenon of online memes—messages about ideas, issues, and events—and the role they can play in everything from shaping protest movements to signaling outbreaks of disease. But recently the Indiana project fell afoul of another Internet phenomenon—how some messages can spread even if they are not correct.



"The headlines are saying something that is completely false and fabricated."

Filippo Menczer, Indiana University

In the past few months, Truthy has become the target of withering attacks from conservative bloggers and politicians. In particular, they have characterized a 4-year, $920,000 grant the scientists received in 2011 from the National Science Foundation (NSF) as an attempt by the U.S. government to monitor and restrict free speech. The attacks are "not simply a misunderstanding of our research," says computer scientist Filippo Menczer, the principal investigator on the NSF grant. They are "a deliberate attempt to distort what we have done."

Menczer's work, which is also supported by the military's Defense Advanced Research Projects Agency and by the private James S. McDonnell Foundation, is rooted in the growing field of complex, nonlinear feedback systems. "It has become a very hot topic of research," notes Menczer, who is the director of IU's Center for Complex Networks and Systems Research. The field includes studies of natural systems such as planetary orbits and climate—and also social ones, such as the spread of information on Twitter. Twitter itself has begun awarding grants to academics who want to study its daily torrent of more than half a billion tweets.

Under the NSF grant, Menczer and his colleagues have studied Twitter messages to shed light on the nature of social discourse. Some of their early work on U.S. political debate, for example, found evidence of a growing polarization, in which people communicate mostly with those who hold similar views on any particular issue rather than trying to engage those who disagree with them. More recently, the researchers' examination of the 2013 protests against the Turkish government found that the movement became more democratic over time, with a growing number of people shaping the direction of the protest. The researchers also hope to learn how to differentiate memes spread by real people from those broadcast by automated software, a technique used by some businesses and advocacy groups to create the illusion of a groundswell of public interest in an issue.

This summer, Truthy itself fell under scrutiny, starting with a 25 August piece in *The Washington Free Beacon*, a conservative online news website. Its headline proclaimed that the U.S. government is "Creating [a] Database to Track 'Hate Speech' on Twitter." Within days, several conservative commentators jumped on the anti-Truthy bandwagon. "So some bureaucrat decides whether you are being hateful or misinforming people—what could possibly go wrong?" a reporter for Fox News asked sarcastically.

Elizabeth Harrington, who wrote the *Free Beacon* story, says she was just doing her job. "One of the areas that I cover is how government is spending taxpayers' money, and I found this grant interesting," she explains. "The whole premise of the project struck me as questionable, and I hadn't seen any other coverage of this aspect of the research."

Many of the critical stories quote selectively from a Truthy grant abstract on NSF's website to argue that the research is an example of the Obama administration's targeting of conservatives. The *Free Beacon* story, for example, says NSF "is financing the creation of a web service that will monitor 'suspicious memes' and what it considers 'false and misleading ideas,' with a major focus on political activity online." But those phrases actually apply to an online platform that the researchers created to give the public a chance to comment on anything being tweeted. The scientists weren't deciding which tweets were "suspicious," nor targeting any particular ideological position.

PHOTOS: (TOP TO BOTTOM) OZAN KOSE/AFP/GETTY IMAGES; COURTESY OF INDIANA UNIVERSITY

Downloaded from www.sciencemag.org on November 6, 2014

Published by AAAS

"The headlines are saying something that is completely false and fabricated," Menczer told the *Columbia Journalism Review*, which covered the flap in September. "We are not defining hate speech. We are not tracking people. We don't have a database." New findings are posted regularly on the project's website and written up in regular academic journals, he explained, and nothing is being secretly funneled to a government agency for some nefarious purpose.

Even so, conservative commenters have continued to pillory the work. A 17 October op-ed in *The Washington Post* by Ajit Pai, one of two Republicans on the five-member Federal Communications Commission, called the project an attempt "to squint for and squelch" political comments. "The federal government has no business spending your hard-earned money on a project to monitor political speech on Twitter," Pai asserted.

Senior Republican lawmakers are also suspicious of Truthy. Representative Lamar Smith (R–TX), the chair of the science committee in the U.S. House of Representatives, said he's adding the grant to his list of questionable research projects that NSF has funded over the years (*Science*, 10 October, p. 152). "[T]his one appears to be worse than a simple misuse of public funds," Smith said in a 21 October press release.

Truthy takes its name from "truthiness," a word satirist Stephen Colbert invented for his television show, *The Colbert Report*. In a 2006 interview, Colbert explained why he coined the word. "It used to be, everyone was entitled to their own opinion, but not their own facts," Colbert noted. "But that's not the case anymore. Facts matter not at all. Perception is everything. It's certainty [that counts]."

Ironically, the NSF solicitation for the program that is funding Menczer's team notes that the growth of social media may aggravate social conflict because it offers a common platform to "parties who may not know or trust each other." Those conflicts can easily snowball online, the program solicitation noted.

NSF officials warned Menczer that attempting to defend himself could backfire, he notes. "They said, 'Be very careful. You don't want to talk about politics. That's not what you do.' " Even so, the Truthy researchers have posted a running rebuttal on their website, including what the project is and isn't, and Menczer says he's willing to speak with those he views as "bona fide reporters who want to know about my work."

The team's current NSF grant ends next summer, and Menczer isn't sure if he'll submit a new proposal to the agency. But if he does, he predicts that "we will probably stay away from anything to do with politics." ■

PHOTO: LELAND BOBBE/GETTY IMAGES

MICROBIOLOGY

Genetics may foster bugs that keep you thin

Twin study shows genes influence gut microbiome

By **Elizabeth Pennisi**

Gut microbes are soldiers in the battle of the bulge, researchers have learned in the past few years, with some organisms seeming to promote thinness and others triggering weight gain. The makeup of such microbes is known to be influenced by a person's diet and environment. Now, a study of twins shows that genetics can also provide an edge in the microbial battle. Researchers identified a microbe that appears to keep waistlines trim—and found that genes influence its abundance. "It's the first really strong evidence that human gut microbiology is genetically controlled," says geneticist Oluf Pedersen of the University of Copenhagen, who wasn't involved in the study.



Identical twins are likely to carry similar kinds of microbes in their guts, making them likely to have similar weights.

The work, published in the 6 November issue of *Cell*, raises hopes for microbial treatments for obesity. But microbial ecologist Ruth Ley of Cornell University and her colleagues originally wanted to answer a more basic question: Do genes affect the makeup of the gut microbiome? Like many researchers trying to distinguish environmental from inherited influences, they turned to twins. Working with colleagues running a large-scale project called TwinsUK, the team collected more than 1000 stool samples from 171 identical and 245 fraternal pairs of twins, as well as 173 samples from unrelated individuals. Among these people, 322 were overweight and 183 were obese.

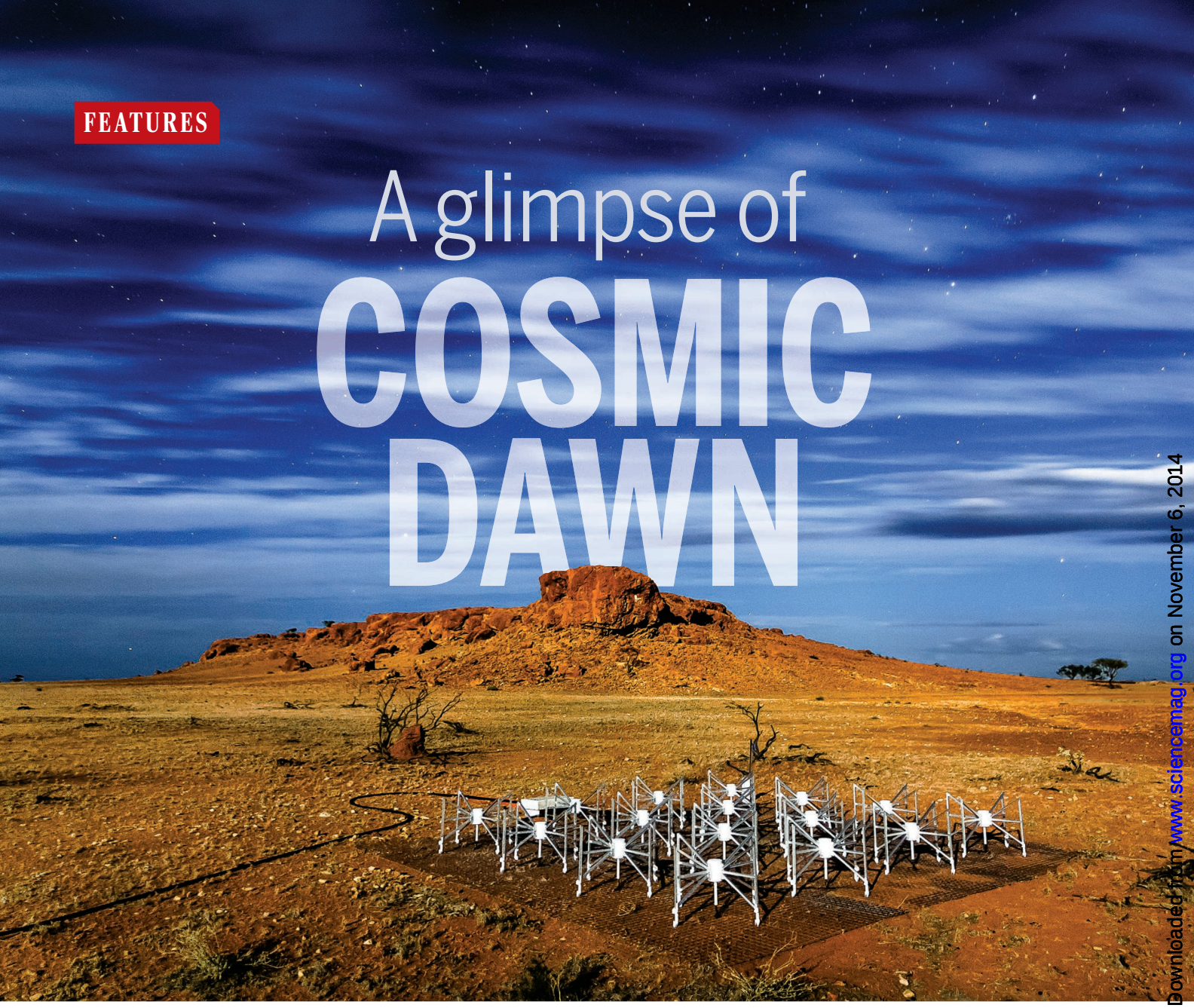
Previous twin studies had failed to identify a genetic connection to microbiome diversity and abundance, but those studies looked at the microbiome as a whole. The new study instead takes a species-by-species approach. By sequencing and analyzing DNA from the fecal samples, Cornell graduate student Julia Goodrich and her colleagues found more than 9600 genetically distinct microbial "species." Most microbes varied according to environmental factors, but some were apparently influenced by genetics, because they were more similar in identical twins than in fraternal twins. The genetic makeup of these twins may affect gut physiology or biochemistry in a way that favors the growth of some microbes over others, the researchers suggest.

The microbes most strongly affected by genes belong to a recently discovered, rather obscure family of bacteria called Christensenellaceae. To the researchers' surprise, this family was most abundant in lean twins and rare in obese ones. To see how the microbes might influence weight, Ley and her team transferred fecal material from lean and obese twins into germ-free mice. The weight gain in the mice mirrored that of the humans donating the feces. And when Goodrich supplemented feces from obese twins with one of the microbes, *Christensenella minuta*, and gave them to mice, the mice stayed lean. The microbe "has some aspect of being able to influence weight," says Cornell geneticist and co-author Andrew Clark.

"We want to see if [the microbe] can be developed as a probiotic for helping people maintain their weight once they've lost it," Ley says. But she and her colleagues first need to figure out how *C. minuta* exerts its effects and whether such a treatment would work only in people genetically disposed to supporting it. At this point, says Nita Salzman, a pathologist at the Medical College of Wisconsin in Milwaukee, to think about a probiotic "is almost certainly an oversimplification." ■

Published by AAAS

A glimpse of COSMIC DAWN



Downloaded from www.sciencemag.org on November 6, 2014

Astronomers are attempting to look back to when the first stars and galaxies lit up and changed the universe forever

By **Daniel Clery**

They may be the strangest telescopes on Earth. They have no domes, no giant mirrors, no steerable radio dishes—just scattered arrays of simple antennas, some on poles as tall as a person, others resembling robot spiders or bizarre garden furniture. These antenna arrays—one in Northern Europe, one in South Africa, a third in Australia—can't point at particular heavenly targets. Instead, they passively take in whatever signals come their way and feed them to distant supercomputers where the real work of detection is done.

The otherworldly instruments have an otherworldly target. They are probing a time so far back in the universe's history that there was very little to see: just a few of the very earliest stars and galaxies. And their quarry is not the scattered points of light at that early epoch, but the diffuse ocean of gas between them, where a profound change was taking place.

By some 400,000 years after the big bang, the expansion of the universe had cooled the maelstrom of particles and energy formed in the instant of creation. The result was a dark fog of gas, mostly hydrogen. The universe's "dark ages" had begun. It took many millions of years for the gas, which was cool and electrically neutral, to slowly swirl together to form stars and galaxies—and when it did, the gas itself was transformed.

The most distant galaxies astronomers can now see, about a billion years after the

PHOTO: © PETE WHEELER

Published by AAAS

The Murchison Widefield Array in Australia is using 2000 simple spiderlike antennas and massive computer power to detect the faint signal of the ionization of the universe.

big bang, live in a universe full of ionized hydrogen—bare protons with their electrons stripped away. Just as the lights came on, something must have ionized all the universe's hydrogen. The most likely culprits are the early stars and galaxies themselves, but to do this they would have had to be very different from the stars and galaxies we can see today: bigger, more violent, more exotic. Astronomers are desperate to know more—but not much can be gleaned from scattered lights in a fog more than 13 billion light-years away.

In 1997, however, British astronomer Martin Rees and colleagues Piero Madau and Avery Meiksin suggested that astronomers look for a signal from the early neutral hydrogen itself. In a hydrogen atom, the central proton and the orbiting electron normally have opposite magnetic orientations. When some energy source flips them into the same orientation, the atom quickly relaxes back into its ground state and emits a microwave photon, at a wavelength of 21 centimeters.

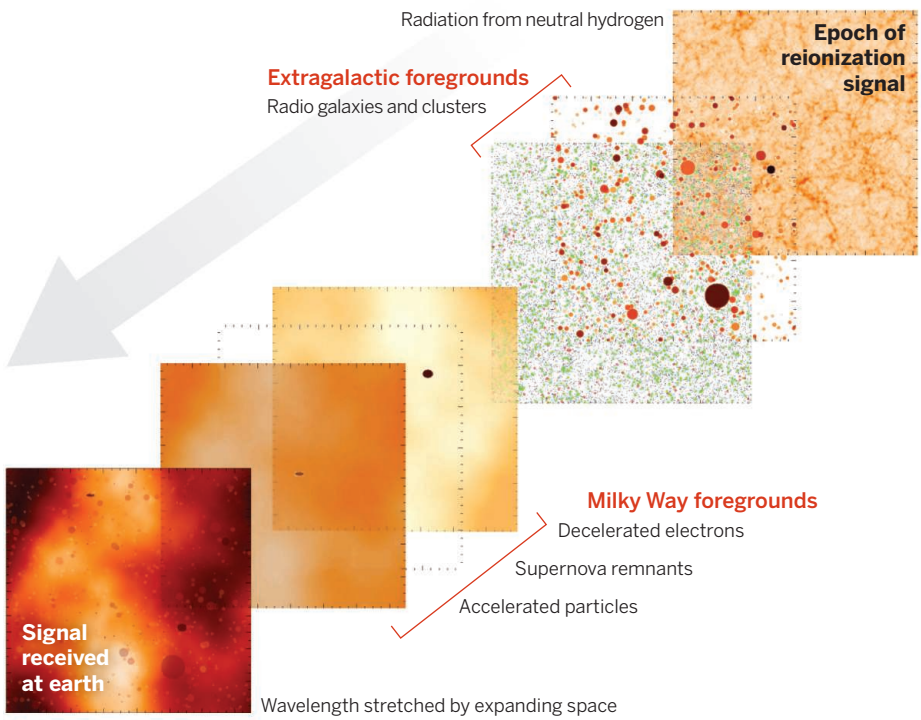
Unlike the neutral gas, ionized hydrogen emits no such radiation. Rees *et al.* suggested that if astronomers could detect the 21-centimeter radiation from the so-called epoch of reionization (EoR), they might see radiation-free "bubbles" of ionized hydrogen around whatever was ionizing the gas. The size and distribution of those bubbles could provide information about the nature of the sources and the timing of reionization.

Astronomers began thinking about what it would take to detect such a signal. As 21-cm radiation from the EoR travels across the universe, cosmic expansion stretches its wavelength to about 2 meters. Conventional radio telescopes are mostly blind to such long wavelengths, and a purpose-built dish would be impractically large. But there was another way: an array of simple antennas and some heavy-duty number crunching. As astrophysicist Don Backer of the University of California (UC), Berkeley, said at the time: "All you need is paperclips and a supercomputer."

Now, several of these paperclips-and-supercomputer telescopes are in hot pursuit of the first detection of the EoR signal. They hope to glimpse something within the next year or two—and the stakes could be enormous. Scientists say the 21-cm radiation could open up a floodgate of information about the astrophysics and cosmology of this unstudied part of the universe's history, perhaps comparable to the discoveries that have flowed from studying the cosmic microwave background left over from the big bang. But detecting the primordial radio signal amid the cacophony of other radio sources, earthbound and astronomical, is akin to hearing a whisper amid a crowd of cheering sports fans. "We're learning all the lessons," says Judd Bowman of Arizona State University, Tempe, chief scientist of one of the new instruments, the Murchison Widefield Array (MWA) in Australia. "We're hopeful and eager."

Signal and noise

The faint radio signal coming from the epoch of reionization is almost drowned out by the "foreground" noise from sources in deep space, our own galaxy, and closer to home.



The largest of the telescopes in the hunt—the Low Frequency Array, or LOFAR—bristles in the middle of a peat bog in the northern Netherlands. One of its creators, co–principal investigator (PI) Michiel Brentjens of ASTRON, the Netherlands Institute for Radio Astronomy, in Dwingeloo, calls it "the most unimpressive radio telescope in the world." He's right: It's just a thicket of hundreds of white plastic poles about the height of a person, braced by guy ropes. The guys are the antennas, no different in principle from a rooftop TV antenna. Large low boxes under tarpaulin covers contain more, smaller antennas. A few scattered electrical cabinets hum ominously.

LOFAR is an interferometer, a device that combines signals from widely spaced detectors to extract information from the differences between them. The core of the array in and around the peat bog at Exloo has 24 clusters, each containing more than 850 antennas, spanning a 4-kilometer-wide area; another 14 clusters are scattered around the Netherlands, plus another five in Germany and one each in France, Sweden, and the United Kingdom. (More are under construction in Germany and Poland.) Widely spaced stations give the interferometer finer resolution, enabling it to zoom in on smaller patches of sky.

But the location of LOFAR is far from ideal. The Dutch government provided €53 million to build the array so long as its core was sited in the north of the country to help build up high-tech infrastructure there. Besides the boggy terrain, LOFAR has to contend with interference from nearby radio sources, including the 88-to-108 megahertz band of FM broadcasts, which are slap in the middle of the frequencies LOFAR is trying to detect. "The signals from all the radio and TV transmitters in [the FM] band are just phenomenal," says LOFAR PI Ger de Bruyn of ASTRON. "They're a million times brighter [than the EoR signal], so you can't observe there." Fortunately, the team found that the main hunting ground for EoR signals, about 150 MHz, "seemed to be very quiet," he says.

The other main arrays are sensibly situated in remote radio-quiet areas. The

CREDIT: ADAPTED FROM V. JELIĆ/ASTRON/LOFAR

Published by AAAS



Precision Array for Probing the Epoch of Reionization (PAPER)—Backer's brainchild—is in the semidesert Karoo region of South Africa. Its garden chair–like antennas have been growing in number since 2009 and have now reached 128. The third instrument, MWA, sits on the semiarid plains of Western Australia, a few hundred kilometers north of Perth. MWA was instigated by a group of U.S. institutions that were originally part of the LOFAR project. They parted company with the Dutch over the issue of building LOFAR in the noisy environment of the Netherlands and set out to build their own array, teaming up with researchers in Australia, New Zealand, and India. The resulting telescope has 2048 spider-like antennas arranged in 128 four-by-four tiles. "It's in good shape and running well," Bowman says.

But building the arrays is, in a sense, the easy part. The antennas are "old technology," says theorist Saleem Zaroubi of the University of Groningen in the Netherlands, a co-PI on LOFAR. They have no moving parts and so cannot focus on a particular spot—they simply pick up everything coming from the sky. It falls to distant supercomputers to make sense of the signals, processing them to calibrate the instrument, focus on a part of the sky, and separate the signal from the noise. Such "software telescopes" offer the advantage of becoming more powerful as computers do, even without changes to the antennas on the ground.

The biggest challenge the arrays face is picking out the extremely feeble EoR signal from all the other radio sources at the same frequency. In our Milky Way galaxy, radio waves at those frequencies come from sources including supernova remnants, charged particles accelerated by the galaxy's own magnetic field, and radiation from electrons colliding with ions inside hydrogen clouds. Outside the Milky Way, countless radio galaxies and galaxy clusters also broadcast their own signals. Models of the EoR signal suggest that these other radio sources are between 1000 and 100,000 times brighter—which means astronomers must identify them and strip them out.

> ***"To do what we do, you have to be hopelessly optimistic, but also brutally realistic."***
>
> **Saleem Zaroubi**, University of Groningen

No images or catalogs of sources exist for this poorly studied part of the spectrum; the teams must map it out themselves before they can discount it from their data. "After subtracting all the foregrounds, the signal-to-noise ratio is still one-tenth. You have to understand the noise [and] find out ways to quantify it," says ASTRON's Brentjens.

Once that's done, investigators will be rewarded not with an image of the neutral hydrogen at the EoR, but rather a power spectrum: a statistical analysis of how the radio signal varies across the sky. It will reveal whether the biggest variations occur over small distances or large ones—whether the bubbles of ionized gas were small, the handiwork of individual stars, or galaxy-sized cavities. The teams should also be able to watch reionization unfold over time. The EoR may have lasted millions of years; 21-cm radiation from earlier in its history will have traveled farther and thus will be stretched out to a longer wavelength and a lower frequency than later radiation. So a signal detected at 140 MHz will be from an earlier time than one at 160 MHz.

As interferometers are sensitive to differences, the middle of the EoR—when half the universe is neutral and half ionized—will produce the strongest signal. So the teams will be scanning the frequencies for a signal that has a peak and then drops off farther into the past (when more of the universe was neutral) and farther toward the present (when more of the universe was ionized). "These telescopes hope to learn two basic things: when the EoR happened and how long it lasted," Bowman says. "That should be easy to read when they detect a signal."

All three teams are optimistic that they will soon get their first glimpse of the EoR. "We're getting pretty close to what theorists predict the signal level is, and we expect to do two or three times better with the data that is coming in right now," De Bruyn says. He hopes LOFAR will get a "first-order re-

CREDIT: © SKA ORGANISATION/SWINBURNE ASTRONOMY PRODUCTIONS

Published by AAAS





The Square Kilometre Array (*left*, in an artist's conception) will use dishes and static antennas to pick up different radio frequencies. LOFAR (*above*) mingles low-frequency antennas (brown specks) with higher frequency ones (inside dark tiles).

PHOTO: © TOP-FOTO, ASSEN

sult" by next year. The PAPER and MWA teams are similarly hopeful. But MWA's Bowman adds that those projections are all based on theoretical models of the EoR signal. "If there is no detection by 2020," he acknowledges, "that will be a disappointment for the community."

Because of the amount of signal processing required and the many different assumptions that underlie the calculations, "there'll be no eureka moment. It'll be hard to convince ourselves [of the detection]," Brentjens says. Even harder will be convincing the rival teams. "I worry about this a lot," says Aaron Parsons of UC Berkeley, who is head of PAPER. "I hope journal editors are very careful. It's very important that papers are reviewed by people who are really knowledgeable. And we have to be very careful not to overstate claims."

A confirmed and reliable signal from the time of reionization could amount to what some researchers are calling "a COBE moment" for astrophysics. COBE was the NASA satellite that, in 1992, revealed the size of fluctuations in the microwave background and opened a floodgate of results in cosmology. A glimpse of the EoR would give astrophysicists their own origins story and a starting point for studying the very first things to shine.

Knocking out an electron and ionizing hydrogen takes quite a lot of energy, so any potential ionizing source needs to produce a lot of photons at high energies—ultraviolet or higher. It's expected that the first stars to form in the universe were unlike any that exist now because they were made of almost pure hydrogen, without any of the heavier elements that were forged inside stars as the universe aged. Pure hydrogen stars, known as population III stars, should grow to enormous size before their internal furnaces ignite—hundreds or even thousands of times as massive as our sun. Big stars burn bright, hot, and fast, making them a perfect source of ionizing radiation. But do they form in isolation, or does dark matter draw the hydrogen into galaxies first? Or were bigger, more powerful sources such as quasars—hugely luminous galactic nuclei centered on supermassive black holes—the engine of reionization? Theorists speculating about the EoR have also invoked more exotic drivers, including decaying dark matter and cosmic strings. "We're shooting in the dark. We have no idea what they are," Zaroubi says.

The existing arrays probably won't be able to answer all of these questions. "To really understand how the first stars form and what early galaxies were like needs the next generation of instrument," Parsons says.

The LOFAR team hopes to build up its array with more stations and faster computing. But the PAPER and MWA teams are joining forces to build a new, more powerful instrument called HERA, the Hydrogen Epoch of Reionization Array. HERA's antennas will be static wire-mesh dishes pointing straight up. The joint team has won $2 million to build a test array of 37 dishes in the Karoo, using PAPER's infrastructure. This alone will have up to three times the sensitivity of PAPER, Parsons says. Then the team will seek up to $20 million to build an array of 350 dishes by 2019. "We'll turn the tables on theorists and really start to drive theory, really advance our understanding," he says.

Looming on the horizon is the next generation: the Square Kilometre Array (SKA). This enormous international project will be built mostly in South Africa, starting in 2018, and will target everything from galaxy evolution to signals from extraterrestrial intelligence. But part of the array, to be sited at the Murchison Radio-astronomy Observatory, home of MWA, will collect low-frequency radiation with a quarter of a million antennas spread over 100 kilometers. With its huge collecting capacity, SKA will be able to move beyond statistical observations and produce images. "We'll see the structures themselves directly. That's a huge step," Zaroubi says.

But first the rival teams need to catch that first glimpse of early light. They will have to overcome radio interference, computing challenges, and the deafening noise—and they must hope that theoretical models of the EoR signal are correct. Says Zaroubi: "To do what we do, you have to be hopelessly optimistic, but also brutally realistic. You need both sides." ■

Published by AAAS



Downloaded from www.sciencemag.org on November 6, 2014

RARE EARTH

Soil scientists are tracking down rare and endangered soils in a quest to document—and preserve—"pedodiversity"

By **Michael Tennesen**

In a verdant woodland on the Calhoun Experimental Forest in South Carolina, soil scientist Daniel Richter peers into a gash in the ground. It's a kind of earthen operating room, where researchers have sliced open the soil to examine its subterranean profile. In the layers of sand and clay, Richter sees telltale signs of past ecological trauma. Nearly all the thick, yellow-brown topsoil that once capped this layered soil, named the Cecil, has been eroded away. "It's decapitated," says Richter, a professor at Duke University in Durham, North Carolina. "We are looking at a natural soilscape that 150 years of cotton, corn, wheat, and tobacco farming have all but destroyed."

The Calhoun isn't the only place where the Cecil's head has gone missing. The soil covers some 40,000 square kilometers of the southeastern United States and is a regional icon, with North Carolina naming it the official state soil. But in many places, Richter says, intact Cecil is now "endangered, and may be nearly extinct."

Endangered dirt? Not that long ago, few researchers would have talked up the idea. But in recent years, efforts to identify the world's rare and endangered soils have been gaining momentum. Aided by increasingly powerful geographic information systems and Earth-observing sensors, researchers have begun mapping "pedodiversity"—the distribution and extent of different soils. This past summer, for example, Chinese researchers released the first-ever pedodiversity survey of that huge nation, identifying nearly 90 endangered soils—as well as at least two dozen that have already gone extinct. Similar surveys suggest unique dirt is also in danger in the United States, Europe, and Russia, the victim of agriculture and development.

Soil extinction carries potentially weighty implications, researchers say. Healthy, diverse soils are not only key to food production, but they also sustain a diversity of species and ecosystems—and can serve as helpful guides to restoring ravaged soilscapes. "We bury our people in it, walk on it, and yet too easily forget it," says soil scientist James Bockheim of the University of Wisconsin, Madison, a co-editor of *Pedodiversity*, the first major scholarly book on

PHOTO: USDA FOREST SERVICE

Published by AAAS



In a South Carolina forest, soil scientist Daniel Richter dissects a soil profile that, by the 1950s (*opposite page*), had been severely damaged by more than a century of farming.

PHOTO: JARED LAZARUS/© DUKE PHOTOGRAPHY

the topic, published last year. "Why not protect soils as we do plants and animals?"

Some researchers are urging governments to do just that, by creating reserves for rare and endangered soils that bar destructive agricultural practices and development. Before a rare soil can be protected, however, it has to be identified and mapped, an effort still hampered by sparse data, competing classification schemes, and technical debates over concepts and methods. Some help could come from new technologies that have the potential to cut survey costs by more than 80%. But creating trustworthy maps "still takes an element of groundtruthing," says soil researcher Alex McBratney of the University of Sydney in Australia. "Which means getting out there with a shovel."

HUMANS HAVE BEEN CHARACTERIZING and mapping soils for at least 3000 years. The ancient Egyptians identified at least two types, which helped determine land prices. In feudal China, officials recognized at least nine classes based on color, texture, and moisture content. Today, nations have adopted an array of classification schemes based on numerous soil characteristics, including its geological and climatic setting, parent rock, age, texture, moisture content, color, and chemical signature. The U.S. government's system recognizes some 20,000 soil series, typically named after places. Like life forms, they are classified in a hierarchy: a dozen orders comprising thousands of smaller groups and families. The order Gelisol, for instance, includes polar soils typified by permafrost, while Histosols are sodden soils found in wetlands.

88
Number of endangered soil types in China

24
Number of extinct soil types in China

The Cecil is an Ultisol, which are typically leached, acid forest soils found in humid areas. It was first mapped in 1899 at a site in Cecil County, Maryland, and usually has granular, yellowish topsoil up to 20 cm thick, underlain by sticky red clays flecked with mica, a shiny mineral.

In the late 1980s and early 1990s, as the concept of biodiversity was becoming a buzzword in biological circles, soil scientists began to discuss how they, too, could measure and protect diversity. By then, the problem of soil loss from erosion, farming, and development was well-understood. But just how many soils were rare or confined to small areas wasn't clear. In 1992, McBratney argued for efforts to fill that gap in a paper that is believed to mark the first use of the word "pedodiversity" (although another soil scientist, Juan José Ibáñez of Spain's National Research Council in Madrid, the other co-editor of *Pedodiversity*, was writing extensively in Spanish about similar concepts at the time).

Tallying pedodiversity turns out to be a complicated endeavor. Like biologists measuring biodiversity, soil scientists confront conceptual and technical dilemmas, such as when to lump or split soil "species," and how best to calculate single numbers, or index scores, that reflect an area's diversity and allow easier comparisons between regions. Soil nomenclature can be confusing, too. Different nations often use different names for the same soils, for instance, or the same name for different soils. In Russia, some

Published by AAAS







Ground assault. California made the San Joaquin soil the state's official dirt in 1997, but stopped short of protecting it from farmers who break up its hard subsoil with explosives (*top*, in 1916) and machines in order to plant crops.

soils still carry folk names originally coined by peasants.

STILL, soil researchers have begun to reveal the magnitude of the threat to rare soils. In 2003, a team led by Ronald Amundson of the University of California (UC), Berkeley, published a pair of milestone studies documenting pedodiversity in the United States. Analyzing government data that detailed the distribution of some 13,000 soil series, the researchers identified more than 4500 "rare" soils that each covered fewer than 1000 hectares, often the product of unique geological and ecological histories. They also found 508 "endangered" soils—ones disturbed by farming, urbanization, or other human activities across at least half their historic range. An additional 31 soils were essentially "extinct," they reported in *Ecosystems*—disturbed across more than 90% of their historic range. In six heavily farmed midwestern states, more than half of each state's known soil species were at risk.

California was another hot spot, with 104 of its 1755 soil series rated as endangered. Ironically, Amundson notes, one of those threatened soils is the San Joaquin—named California's official soil in 1997. The San Joaquin is famous for a tough, impermeable layer of silica-rich subsoil that creates seasonal ponds called vernal pools, a key habitat for an array of rare plants and animals. But the soil also sits in the middle of prime agricultural land, and farmers have routinely used explosives and machinery to rip out the hardpan. And when lawmakers gave the San Joaquin state soil honors, they also insisted that the soil get no special legal protection.

While Amundson's team took a national perspective, other U.S. researchers are zooming in on smaller regions, in part to study how often rare soils coincide with rare plant communities and ecosystems. Last year, Bockheim and Sarah Schliemann of the Metropolitan State University of Denver took a close look at an ecological transition zone that cuts diagonally across Wisconsin, where southern prairies meet northern forests. Although this transition zone covered just 13% of Wisconsin, it held 40% of the state's unique, "endemic" soils, the researchers reported in *Catena*. That's likely a result of the region's history of intense glaciation and a confluence of climatic factors. But the rare soils had little statistical association with some 100 en-

PHOTOS: (TOP TO BOTTOM) POP LAVAL FOUNDATION; © STEVEN C. WILSON; © ED DARACK/SCIENCE FACTION/CORBIS

demic plants, they found, which tended be more affected by topography than soil type.

The study also revealed that half of the 159 endemic soils covered relatively small areas, fewer than 4900 hectares. That puts them at greater risk of being lost to plows or pavement, Bockheim says, adding that "I don't know if you could ever restore them."

OTHER NATIONS ARE ALSO MOVING to find rare soils. In 2009, Russian soil scientists published a mammoth Red Data Book of Russian Soils, and this past August another team published the new study of China's pedodiversity. One goal, says coauthor Peng Gong of UC Berkeley, who also worked on the 2003 U.S. survey, was to examine how massive land use change, including rapid urbanization and farm abandonment, is affecting China's soils.

Completing the survey required a mammoth treasure hunt, with researchers scouring hundreds of regional offices to unearth more than 8900 soil surveys, which were combined with a larger national survey. The end result, published in *The Scientific World Journal*, is relatively broad-brush, Gong says: The mapping scale is coarser than the U.S. study, for instance, and there is little or no information on some regions.

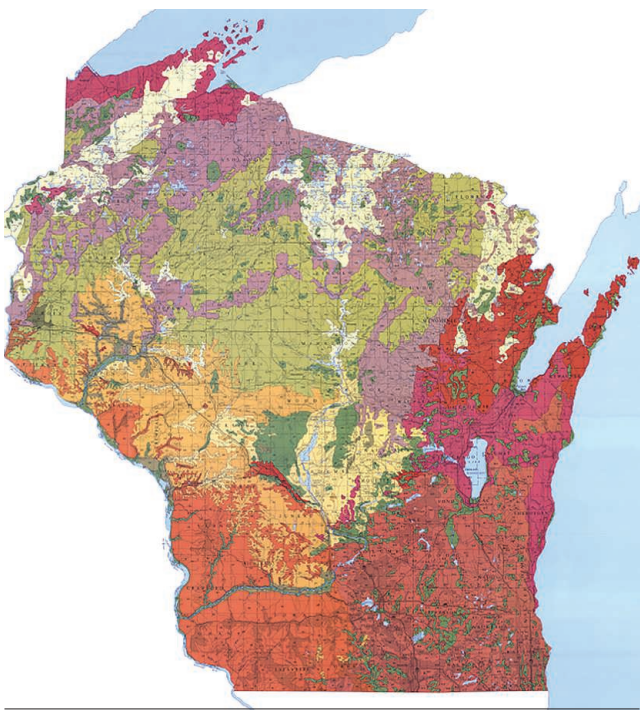
Still, the results are revealing. Most of China's soils are limited to just five or fewer provinces, and 332 are rated rare or unique. There are also at least 231 kinds of "new" soils essentially created by humans, the product of centuries of plowing, sifting, and fertilizing; they have replaced natural soils over 12% of China's land area. And farming continues to threaten more soils: Eighty-eight "endangered" soils and 17 "extinct" soils are mostly found in intensely cultivated northern regions. In contrast, urbanization threatens just six soils, the researchers estimate.

The China study also took a new step, analyzing how many endangered soils already enjoy some level of protection, such as being within a park. The answer was worrying, the researchers say: Just 11% of endangered soil series, and 16% of the area they cover, are protected. Safeguarding soils "should be a high priority in the creation of future nature reserves," the authors urge.

SOIL RESERVES may be a ways off, but some nations are already taking tentative steps. In Russia, soil scientists helped persuade the government in 2001 to adopt a soil protection policy, but subsequent action has been limited. More recently, environmental agencies in the United Kingdom have issued formal guidance on taking soil diversity into account when planning reserves, but farm groups have generally resisted rules that might restrict agriculture. In the European Union, Ibáñez and other researchers have pushed officials to formally integrate pedodiversity into conservation policies and have even proposed a network of "PanEuropean Soil Reserves." So far, however, "these issues do not seem to interest anyone," Ibáñez says.

Wisconsin's dirty secret

America's Dairyland is home to at least 119 "endemic" soils found only in the state, according to a 2013 study that linked soil diversity to past glaciation and other factors. Map shows major soil groups.



MAP: WISCONSIN GEOLOGICAL AND NATURAL HISTORY SURVEY

One obstacle is the relatively high cost of the soil surveys needed to guide conservation decisions. In the United States, traditional large-scale soil surveys cost about $10 per hectare in 2010, according to one estimate. But prices could come down as new technologies come into use, including air- and space-based sensors that can detect soil chemical signatures and physical characteristics, and computer models that can use climate, geological, and other data to help predict soil types. Some teams have been able to drive the cost down to just $0.20 or $0.30 per hectare. Still, reliable surveys will still require boots on the ground—and spades in the earth.

Many researchers argue that the cost of soil mapping is meager, however, compared with the value of the "ecological services" that dirt provides, such as storing carbon or filtering water. That idea could get a boost next year, as the United Nations launches its International Year of Soils. It will culminate in December 2015 with the release of a major report on the status of soils worldwide.

IN THE MEANTIME, SOUTH CAROLINA'S Cecil suggests the costs of inaction, Richter says. In the early 1900s, when soil mappers first began surveying the lands around the U.S. Forest Service's Calhoun research station, the damage from erosion was so severe that they initially labeled the territory as just "rough gullied land." Over the next few decades, however, improved farming and management practices restored a semblance of health as pine forests and wildlife returned.

But "if you lift up the green blanket and look at the soil underneath," you can see the damage done, Richter says. The absence of topsoil has exposed clays that choke local rivers with bright orange sediment after heavy rains. Also missing: much of the Cecil's stored carbon, which escaped into the atmosphere as a result of the mistreatment, reported Megan Mobley of the University of Wyoming in Laramie and colleagues including Richter this past September in *Global Change Biology*. The damaged soils also aren't absorbing much new carbon from the atmosphere, they found. That's bad news for climate scientists hoping the region's soils might help curb global warming.

The tale of the lost carbon suggests one more parallel between pedodiversity and biodiversity: fail to protect either, and it is gone for good. The Cecil's decapitation and slow regeneration, Richter says, provides a reminder that past damage can leave soils "compromised for centuries." ■

Michael Tennesen is a writer living near Joshua Tree National Park, California. He is the author of the forthcoming The Next Species: The Future of Evolution in the Aftermath of Man *(Simon and Schuster).*

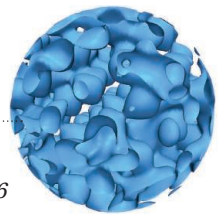
With reporting by David Malakoff.

Published by AAAS

INSIGHTS

Many pathways lead to melting *p. 704*

Threats to Brazil's environmental credibility *p. 706*



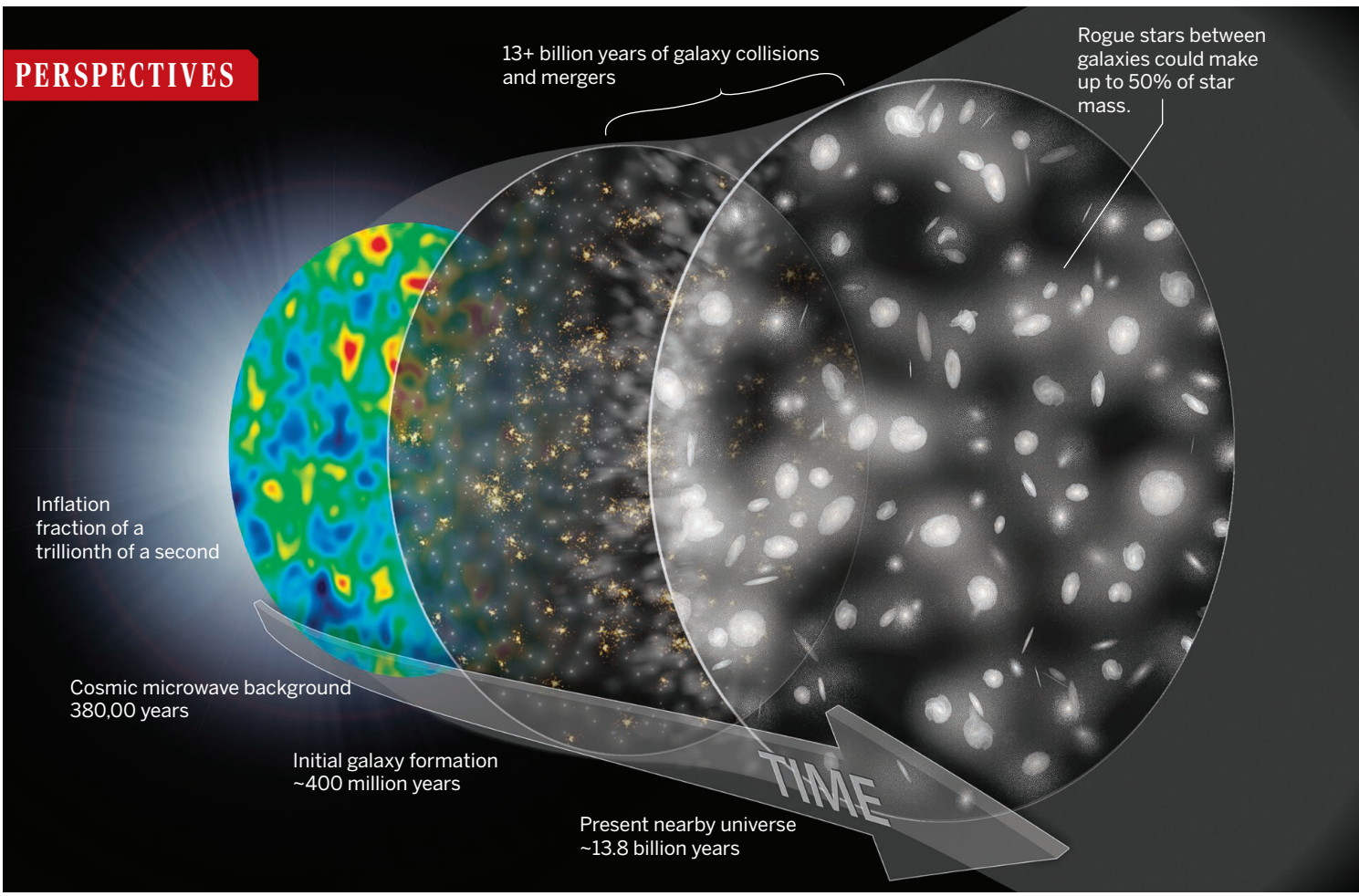


ILLUSTRATION: BRITT GRISWOLD/MASLOW MEDIA GROUP/NASA'S GODDARD SPACE FLIGHT CENTER

ASTRONOMY

The other half of the universe?

A large previously unknown population of stars inhabits intergalactic space

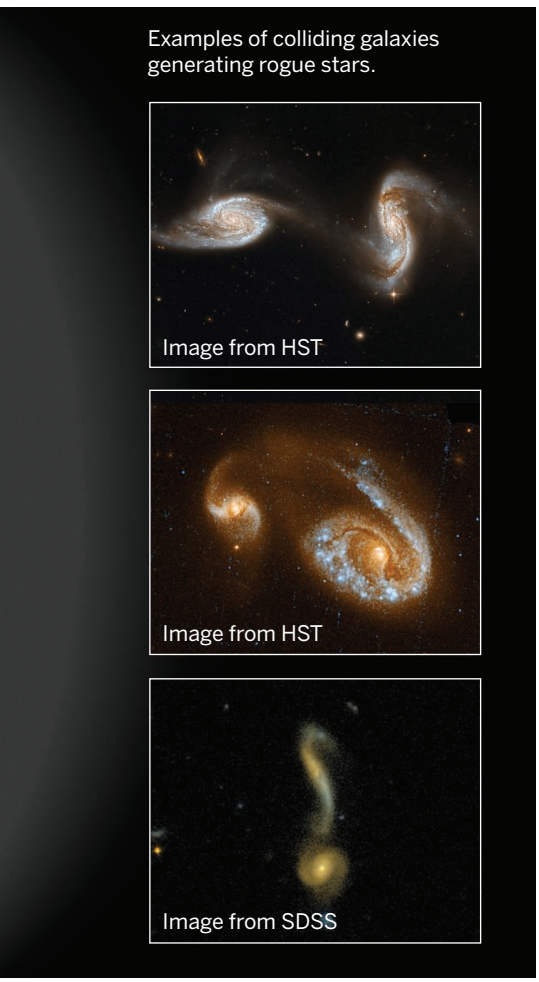
By **S. H. Moseley**

The history of astronomy has largely been concerned with the study of discrete objects: planets, stars, and galaxies. From such observations, we have discovered the nature and evolutionary histories of these objects. It is natural to ask whether these studies provide a comprehensive picture of the evolution of the universe, or whether large numbers of objects too faint to detect individually or intrinsically diffuse sources may be present. On page 732 of this issue, Zemcov *et al.* (*1*) present results from a study of near-infrared background light that reveal that as many as half of all stars have been stripped from galaxies in their many collisions and mergers over the history of the universe. At galactic distances, the stars are faint but can be detected in ensemble through the spatial variations in sky brightness caused by their spatial distributions. It is remarkable that such a major component of the universe could have been hiding in plain sight as an infrared background between the stars and galaxies.

Ancient observers saw the milky glow of our Galaxy and the smooth radiance of the zodiacal light. The development of telescopes resolved our Galaxy into a high density of faint stars. The zodiacal light, arising from light scattered from dust in our solar system, was found to be intrinsically diffuse. Other such backgrounds have been detected in the modern era: radio, x-ray, and, most famously, the cosmic microwave background (CMB). The radio and x-ray backgrounds have been resolved into faint sources that explain most of the sky brightness, but the CMB, the radiation from the surface of the

Published by AAAS

Messy mergers. Galaxies grew from small irregular objects (**left**) to much more massive systems (**right**) through interactions and mergers (examples shown at right), which may have resulted in the scattering of a large fraction of stars into the halos of the galaxies, creating a low surface brightness background. Zemkov *et al*. (*1*) use multi-wavelength observations to show that most NIR anisotropies arise from stars in galactic halos in the relatively nearby universe.



last scattering after the Big Bang, is an intrinsically diffuse source, in which much information about the early evolution of the universe is encoded.

The near-infrared spectral region has long been of particular interest because the ultraviolet and visible outputs of stars during the epoch of initial galaxy formation (see the figure) are redshifted into this spectral region. The detection of this infrared light has been an important observational objective, because it can provide direct information on the evolution of stars and galaxies in this important and largely unobservable stage of the universe. Measurements of this background were attempted from suborbital rockets and a first all-sky measurement was done by the Diffuse InfraRed Background Experiment (DIRBE) (*2*) on the Cosmic Background Explorer (COBE). These observations and subsequent work (*3*) have shown that detection of any residual radiation from this epoch is very difficult to make. Bright foreground emission from the zodiacal cloud, faint stars in our Galaxy, scattered light from galactic dust, and undetected faint galaxies must be removed in our search for radiation from the first stars and galaxies. Even with multispectral observations and full-sky coverage, removal of foregrounds ultimately limited the DIRBE and its successors in their search for the epoch of initial galaxy formation.

Given the difficulties of measuring the total power from the early universe, a promising approach was to search for the sources using their spatial correlation properties. The advantage that the sources making up the background signals are much fainter than most of the anticipated foreground sources. Thus, an observer can remove point sources, which will remove the shot noise in the image, the fluctuations caused by the random arrangement of brighter sources. As more and more point sources are removed, both the shot noise and the large-scale fluctuation power will drop. If the large-scale power ceases to decrease as we remove more point sources, it can be concluded that it is composed of sources appreciably fainter than those being removed and that the residual point sources make no further contribution to the large-scale power fluctuations.

An analysis of Spitzer near-infrared observations (*4*) showed that the large-scale power fluctuations that existed in the near infrared observations could not be related to any known populations of galaxies. The fluctuations were interpreted as arising from primordial galaxies (see the figure), and limits on early universe processes were made in the context of this assumption. Further work (*5*, *6*) confirmed the observational results and extended the measurements of the correlations to larger scales. It was then proposed that the observed large-scale fluctuations could arise from stars stripped from galaxies during their merger history (*7*) (see the figure). Because the stars are faint, they can produce robust large-scale correlations just as in the case of the putative high-redshift sources. The two models (primordial galaxies versus stripped stars) are expected to have different spectral distributions, because the light from high redshifted sources will be strongly attenuated by redshifted neutral hydrogen at wavelengths shorter than about 1 μm. The rogue stars from galaxy interactions should have colors typical of an older stellar population and characteristic of the time scale since they were stripped from their galaxy. The color of the fluctuations has been seen as the key to distinguishing between the two models.

Zemcov *et al*. have made large-spatial-scale observations from a suborbital rocket in the 0.8 to 1.6 μm spectral band, where the intrahalo light and early galaxies are expected to have different spectral shapes. Their observations show fluctuations rising steeply from 1.6 to 0.8 μm, a shape that is more consistent with the intrahalo light model. If confirmed, these observations reveal an unexpected stellar population, with as many as half the stars in the local universe being outside galaxies. Because these stars are to a great extent individually undetectable, observations of this kind are uniquely suited for their detection.

The existence of such a population of sources complicates the measurement of the fluctuations from the early universe. We are in some sense in the same situation as with total power measurement. A strong foreground is making the observation of the first stars difficult, and we need improved tools to separate them. One such tool is spatial correlation with other databases that are thought to trace the population of interest.

It should not be easy to hide half the stars in the universe! Now that we know to look, there may be other observations to explore the properties of this background. For example, if the stripped stars are similar to those in their host galaxies, we would expect to see supernova explosions not associated with galaxies. The ratio of core-collapse supernovae, arising from the death of luminous young stars, to type Ia supernovae, seen with a time delay, should allow us to estimate the age of the population.

The confirmation and characterization of this population is important and will require appreciable effort and perhaps new tools as we explore the newly revealed low-surface-brightness universe. ■

Laboratory for Observational Cosmology, Goddard Space Flight Center, Greenbelt, MD 20771, USA. E-mail: harvey.moseley@nasa.gov

REFERENCES AND NOTES

1. M. Zemcov *et al*., *Science* **346**, 732 (2014).
2. M. G. Hauser *et al*., *Astrophys. J.* **508**, 25 (1998).
3. T. Matsumoto *et al*., *Astrophys. J.* **626**, 31 (2005).
4. A. Kashlinsky *et al*., *Nature* **438**, 45 (2005).
5. A. Cooray *et al*., *Astrophys. Lett.* **659**, L91 (2007).
6. A. Kashlinsky *et al*., *Astrophys. Lett.* **654**, L5 (2007).
7. A. Cooray *et al*., *Nature* **490**, 514 (2012).

ACKNOWLEDGMENTS

I thank R. Arendt and J. Mather for their help, and R. Arendt for the idea of searching for supernovae from the diffuse population.

10.1126/science.aaa1077

Published by AAAS

EVOLUTION

Searching for new branches on the tree of life

Is there undiscovered life that differs fundamentally from that in the three known domains?

By **Tanja Woyke** *and* **Edward M. Rubin**

Ever since Woese's seminal work nearly 40 years ago (*1*), life has been divided into three domains: Archaea, Bacteria, and Eukaryota. But could there be life that does not fit into any of these domains? Novel techniques for exploring microbes that cannot readily be grown in the laboratory offer hope that scientists can discover such life, if it exists (see the first figure). These methods include metagenomics, which involves the sequencing of DNA extracted from environmental samples, and single-cell genomics, where individual microbial cells are isolated from the environment and their genomes amplified and sequenced.

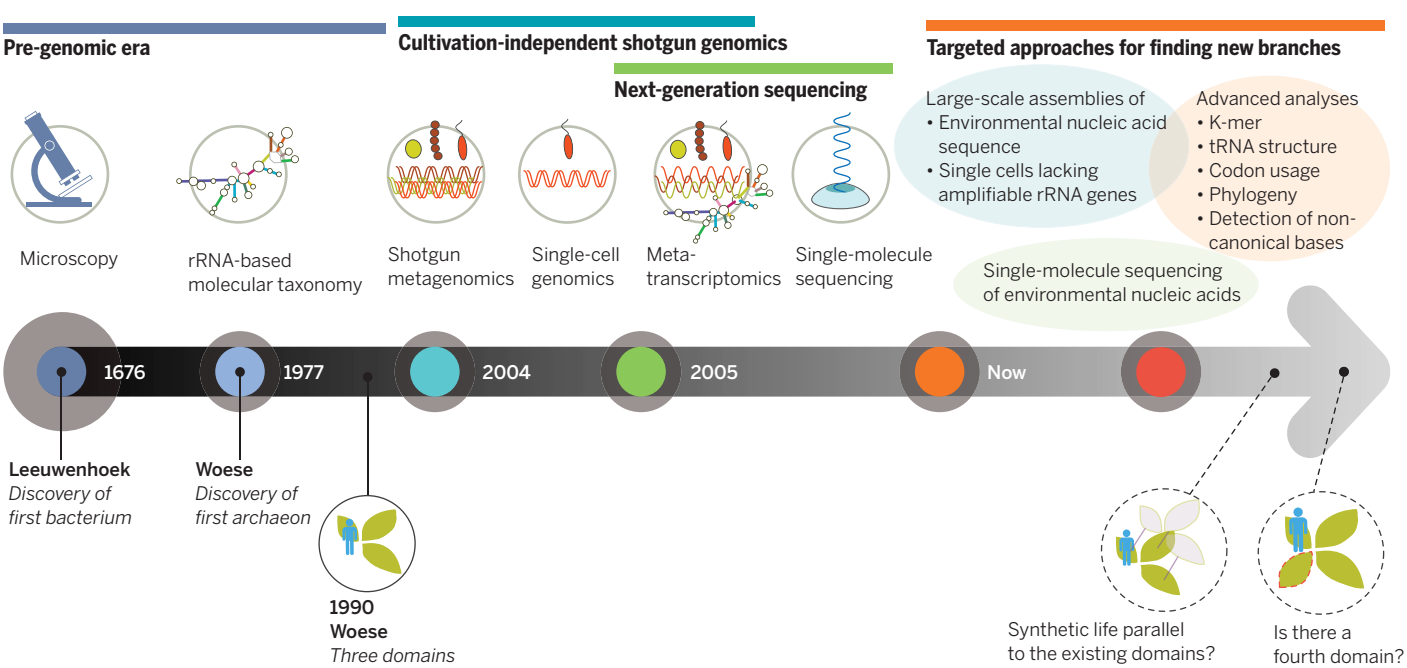
On the basis of these and other approaches, we propose that microbial life be operationally divided into three categories: explored, unexplored, and undiscovered. It is among the latter that potential signs of additional branches on the tree of life beyond the three known domains may be found.

EXPLORED, UNEXPLORED, UNDISCOVERED. The explored category encompasses microorganisms that can be cultivated in the laboratory. The unexplored category includes uncultivated organisms present in environmental samples, whose existence is known only through their molecular signatures and occasionally from partial genome assemblies obtained through metagenomics (*2*) and single-cell genomics studies (*3*). The sequence of the 16*S* ribosomal RNA (rRNA) gene, which can be amplified from environmental samples with a set of "universal" primers, has been extensively used as a molecular signature to assess the microbial diversity in a given sample, and to build phylogenetic trees. Taxa from the unexplored category dwarf the explored in both numbers and diversity (*4*). Beyond these organisms for which we have ribosomal barcodes or other molecular signatures resides the as yet undiscovered life—the putative organisms that have thus far eluded our detection.

Undiscovered life, if it exists, is either absent at the locations of existing environmental surveys or is missed by current approaches. There are reasons to believe that current approaches may indeed miss taxa, particularly if they are very different from those that have so far been characterized. The "universal" primers used to detect 16*S* rRNA genes from bacteria and archaea in environmental samples can miss major lineages because of primer mismatches (*5*). Similarly, the selection of specific single cells from environmental samples for genome sequencing has been based on rRNA gene identity, thus also relying on these universal primers. Organisms whose 16*S* rRNA genes are not recognized by the primers would not be detected using this approach. Past explorations of available metagenomic data sets have focused on the discovery of matches to the known genes and genomes—an analysis that is naturally biased against uncovering completely novel life. Finally, although we may soon have petabases of metagenomic sequence data, samples have been collected from only a minute fraction of Earth's countless different environments.

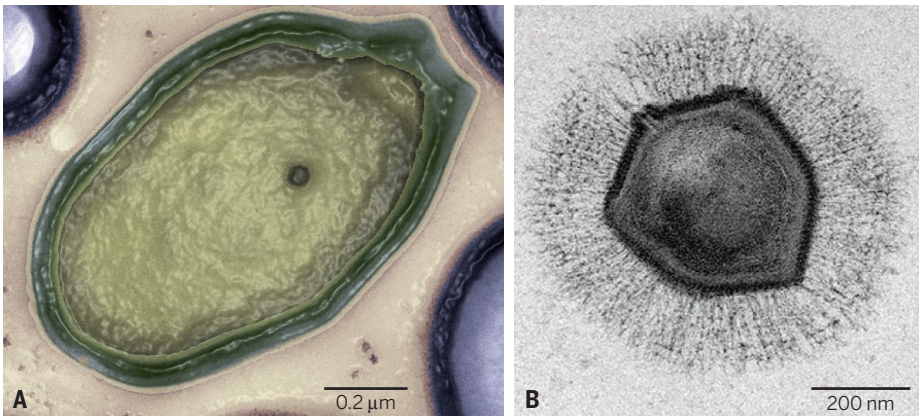
Recognizing these limitations, it is reasonable to speculate that undiscovered and highly divergent branches of life may exist, possibly represented by domains whose marker genes differ extensively from those of the bacterial and archaeal branches on the tree of life. Refined strategies, involving both the application of new approaches and access to previously unexplored habitats, will be required for their discovery.

THE SEARCH FOR UNDISCOVERED LIFE. Approaches to further explore the diversity of microbial life will need to include the expansion and optimization of methods used



The search for new major branches on the tree of life. Cultivation-independent methods, novel sequencing technologies, and analytical approaches can be directed toward the detection of life outside currently established domains.

Published by AAAS



Parasitic remnants of a fourth domain? Electron microscopy images of (**A**) pandoravirus dulcis particle and (**B**) acanthamoeba polyphaga mimivirus particle. These viruses may be remnants of a fourth domain. Cellular entities from this domain either went extinct or remain to be found.

to capture the genomes of unexplored (uncultivated) organisms (see the first figure). Single-cell sequencing with microfluidic and cell-sorting approaches, focused specifically on cells lacking amplifiable rRNA genes, is a high-throughput strategy to search for novel organisms. Massive-scale metagenomic sequencing of environmental DNA and RNA samples should, in principle, generate sequence data from any entity for which nucleic acids can be extracted. The analysis of such sequence data with novel computational methods focused specifically on discovering outliers to previously defined life is another powerful means to explore the unknown. Assembled contiguous stretches of sequence data generated from environmental samples can be mined for unusual features in nucleotide composition, transfer RNA structures, and codon usage, as well as phylogenetic placement of rRNA and other marker genes (*6*). This would facilitate the detection of biological outliers and genomic fragments with deep phylogenies.

Finally, the application of single-molecule sequencing technologies that can recognize modified or nonstandard bases is another approach for the detection of life that may differ from the life we know. Sequencing to date has mostly been limited to the detection of the canonical four bases. Emerging new techniques, such as single-molecule real-time DNA sequencing (*7*) and nanopore-based single-molecule sequencing (*8*), have the potential to allow the recognition and characterization of environmental organisms with base modifications and compositions distinct from the four standard bases and their currently described modifications.

Beyond a new set of technologies and methodologies, the choice of suitable environmental niches will be critical in cataloging the diversity of life. Although discoveries may be made by mining existing data sets from explored environments, future searches for deeply branching clades should include inhospitable and isolated environments. These sites would be expected to be preferred niches for early life, potentially sheltered from more modern microbial competitors. This would include hypoxic subsurface sites with environmental conditions predating the Great Oxidation Event that occurred about 2.3 billion years ago. Support for the idea that isolated hypoxic environments may be preferred niches for early life comes from observations that anaerobic niches deep within Earth's crust tend to harbor acetogens and methanogens; these species represent ancient branches of autotrophs in the bacterial and archaeal domains (*9*).

Using some of the aforementioned strategies, scientists are already speculating on the possible discovery of a "fourth domain." Phylogenetic analysis of marker genes from metagenomic data revealed the presence of deep, novel branches thought to be occupied by either a cellular entity or novel viruses (*6*). Extremely large and unusual DNA viruses such as mimivirus and pandoravirus (see the second figure) (*10*) have also been shown to contain marker genes with deep phylogenetic roots between the archaeal and eukaryal domains (*11*). One interpretation of these findings is that there was an ancestral, cellular lineage that gave rise to these viruses but went extinct as a cellular entity, and that its genome now only is present as a so-called parasitic fourth domain (*11*). It is possible, however, that this cellular precursor has simply not yet been detected and still exists awaiting discovery. Even more speculative is the idea that an RNA world still exists in a niche of favorable conditions. A recent survey on the distribution of viruses among the domains of life found RNA viruses to be solely associated with bacteria and eukaryotes; the authors hypothesize that these viruses are remnants of an RNA world (*12*). Under the appropriate conditions, cellular entities with RNA genomes may still persist.

A BRAVE NEW WORLD. While the search for new life is focused on organisms that exist in nature, a parallel effort is under way to create fundamentally new organisms in the laboratory. Organisms with an expanded genetic alphabet of six nucleotides (*13*) and with noncanonical codon usage (*14*) have already been built, representing human-designed variations of existing branches. This quest of synthetic biologists to build radically novel organisms also offers possible models for unusual varieties of life that may be sought in nature. A recent computational analysis of a global metagenomic data set revealed an unexpected abundance of environmental organisms with diverse noncanonical codon usage in nature (*15*)—a feature that has been targeted for creation in the laboratory through genome engineering (*14*).

An advanced toolkit of powerful genomic technologies is now poised to generate and mine increasingly large data sets for hints of life that differs strikingly from the life cataloged thus far. The discovery of new building blocks and organisms from a new domain would likely have major implications for biotechnology, agriculture, human health, and synthetic biology efforts. It might also elucidate the early evolution of the domains and their divergence from the last universal common ancestor. Irrespective of the depth at which newly discovered branches may be anchored in the tree of life, the quest to find them will likely reveal unexpected and valuable insights about the fruits of more than 3 billion years of biological tinkering. ■

DOE Joint Genome Institute, Walnut Creek, CA 94598, USA, and Lawrence Berkeley National Laboratory, Berkeley, CA 94720, USA. E-mail: emrubin@lbl.gov

IMAGES: (PANEL A) REPRINTED FROM (*10*); (PANEL B) REPRINTED FROM E. GHIGO *ET AL.*, *PLOS PATHOG.* **4**, E1000087 (2008)

REFERENCES AND NOTES

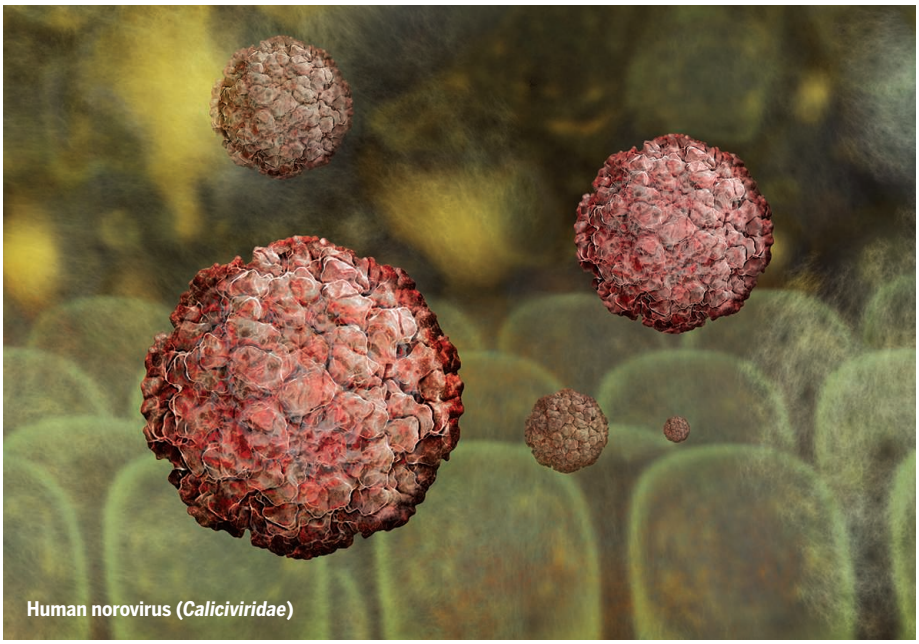
1. C. R. Woese, G. E. Fox, *Proc. Natl. Acad. Sci. U.S.A.* **74**, 5088 (1977).
2. K. C. Wrighton *et al.*, *Science* **337**, 1661 (2012).
3. C. Rinke *et al.*, *Nature* **499**, 431 (2013).
4. N. R. Pace, *Science* **276**, 734 (1997).
5. B. J. Baker *et al.*, *Science* **314**, 1933 (2006).
6. D. Wu *et al.*, *PLOS ONE* **6**, e18011 (2011).
7. J. Eid *et al.*, *Science* **323**, 133 (2009).
8. G. F. Schneider, C. Dekker, *Nat. Biotechnol.* **30**, 326 (2012).
9. W. F. Martin, *FEBS Lett.* **586**, 485 (2012).
10. N. Philippe *et al.*, *Science* **341**, 281 (2013).
11. J. M. Claverie, *Commun. Integr. Biol.* **6**, e25685 (2013).
12. A. Nasir, P. Forterre *et al.*, *Front. Microbiol.* **5**, 194 (2014).
13. D. A. Malyshev *et al.*, *Nature* **509**, 385 (2014).
14. M. J. Lajoie *et al.*, *Science* **342**, 357 (2013).
15. N. N. Ivanova *et al.*, *Science* **344**, 909 (2014).

ACKNOWLEDGMENTS

Supported by the U.S. Department of Energy Joint Genome Institute, a DOE Office of Science User Facility, under contract no. DE-AC02-05CH11231. We thank N. Kyrpides, N. Ivanova, and A. Visel for critical feedback.

10.1126/science.1258871

Published by AAAS



Human norovirus (*Caliciviridae*)

VIROLOGY

Leaping the norovirus hurdle

Bacteria and B cells solve the problem of culturing human norovirus in the laboratory

By **Christopher M. Robinson** *and* **Julie K. Pfeiffer**

Noroviruses are the leading cause of viral gastroenteritis worldwide with over 1 million hospitalizations and more than 200,000 deaths per year (*1*). Outbreaks have been on the rise, particularly in hospitals, dormatories, and cruise ships. A major hurdle to understanding norovirus biology is the inability to culture human strains in the laboratory since the first human norovirus was identified over 40 years ago (*2*). On page 755 of this issue, Jones *et al.* (*3*) solve this problem. In discovering that human norovirus can infect B cells in vitro, the authors find that bacteria promote viral replication and may have been the missing factor.

Human norovirus has been very difficult to study. The cellular tropism is unknown, it cannot be grown in culture, and there is no robust small-animal model. Much of our knowledge comes from human volunteer studies or experiments with individual viral components. The discovery of murine norovirus (*4*) provided a valuable tool because it replicates in mice and in cultured cells, but it is not known how closely murine norovirus mimics human norovirus.

The cellular targets of human noroviruses may include intestinal epithelial cells and immune cells, particularly B cells. For example, mice infected with murine norovirus have virus-positive cells in intestinal B cell zones, and mice lacking B cells have reduced viral titers (*5*–*7*).

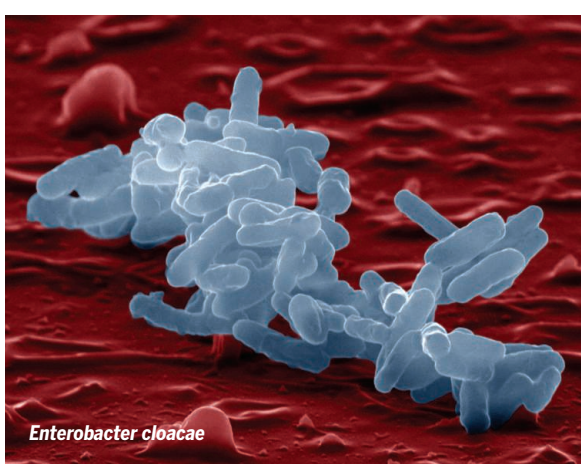
Because human norovirus cannot be cultured, virus is acquired from stool of infected individuals. Standard practice is to filter the stool samples using 0.2-μm membranes to remove contaminating bacteria. However, Jones *et al.* observed that unfiltered stool samples contained norovirus that could replicate in cultured human B cells.

A hint to the identity of the missing factor came from a finding that human norovirus binds to *Enterobacter cloacae* bacteria (*8*). Certain strains of *E. cloacae* express histo-blood group antigens on their surface. These antigens constitute a family of glycans that are used in blood typing and are found in body fluids and on the surface of red blood cells, and epithelial cells of the digestive, respiratory, and genitourinary tracts. Human noroviruses bind to certain histo-blood group antigens, an interaction proposed to facilitate viral attachment to cells (*9*). Indeed, individuals that lack certain histo-blood group antigens are resistant to human norovirus infection (*10*).

Jones *et al.* assessed whether the missing factor in filtered stool samples was bacteria expressing histo-blood group antigens. The authors demonstrate that human norovirus from filtered stool samples could infect B cells only when mixed with *E. cloacae* that express these antigens or synthetic H antigen, a specific histo-blood group antigen known to bind human noroviruses. Furthermore, exposure to *E. cloacae* or synthetic H antigen enhanced viral attachment to B cells, suggesting that bacteria expressing these antigens may promote viral replication by aiding attachment to host cells.

Comparing human norovirus and murine norovirus, Jones *et al.* examined whether bacteria promote murine norovirus infection in vivo and whether murine norovirus can infect B cells in vitro. They noted that murine norovirus replication was reduced in antibiotic-treated mice, suggesting that bacteria promote viral infection in vivo. Additionally, they found that murine norovirus infects B cells in vitro, although bacteria were not required.

The discovery of Jones *et al.* underscores the importance of bacteria for enteric virus infection. To date, enteric viruses from four different viral families rely on bacteria for replication and/or transmission. Mouse mammary tumor virus (*Retroviridae*) binds to bacterial lipopolysaccharide, inducing immune tolerance (*11*). Reovirus (*Reoviridae*) requires the presence of intestinal bacteria for viral replication and pathogenesis (*12*). Poliovirus (*Picornaviridae*) requires bacteria for optimal viral replication and transmission, potentially through viral binding of bac-



Enterobacter cloacae

Department of Microbiology, University of Texas Southwestern Medical Center, Dallas, TX 75390, USA. E-mail: julie.pfeiffer@utsouthwestern.edu

IMAGES: (TOP) CAROL AND MIKE WERNER/SCIENCE SOURCE. (BOTTOM) EYE OF SCIENCE/SCIENCE SOURCE

Published by AAAS

terial surface polysaccharides such as lipopolysaccharide and peptidoglycan (*12*, *13*). Thus, Jones *et al*. have added noroviruses (*Caliciviridae*) to this list of enteric viruses that benefit from bacteria. Validation of this promising new cell culture model for human norovirus infection will pave the way for studies that have been impossible for decades.

A common theme is emerging: Enteric viruses bind to bacterial surface glycans, which directly or indirectly promotes viral replication. There are several questions that emerge from the findings of Jones *et al*. relevant to this theme. It is not clear how bacterial histo-blood group antigens enhance human norovirus attachment to B cells. Studies on poliovirus suggest that bacterial surface glycans enhance the binding of virions to the viral receptor protein (*13*). Perhaps histo-blood group antigen-bound noroviruses have enhanced attachment to host cell glycans or another cellular cofactor. There is also the question of whether additional human norovirus genotypes infect B cells, and whether bacterial histo-blood group antigens are required. There are more than 25 highly variable human norovirus genotypes. The binding site for histo-blood group antigens on viral particles is hypervariable and it is reasonable to expect differences in antigen-binding affinity.

Do bacteria promote norovirus infections in humans? If so, how prevalent are bacteria that express histo-blood group antigens in the human intestine, and do some of those strains promote human norovirus infection more than others? Microbial communities vary from person to person. It is possible that some individuals harbor more bacterial strains that promote human norovirus infection than others.

We are only beginning to understand the roles of commensal bacteria in the human gut for viral pathogenesis and/or transmission. Future work in this area may yield novel strategies for treating enteric virus infection and limiting transmission.

REFERENCES

1. M. M. Patel *et al*., *Emerg. Infect. Dis.* **14**, 1224 (2008).
2. E. Duizer *et al*., *J. Gen. Virol.* **85**, 79 (2004).
3. M. K. Jones *et al*., *Science* **346**, 755 (2014).
4. S. M. Karst, C. E. Wobus, M. Lay, J. Davidson, H. W. Virgin, 4th, *Science* **299**, 1575 (2003).
5. S. M. Mumphrey *et al*., *J. Virol.* **81**, 3251 (2007).
6. M. Basic *et al*., *Inflamm. Bowel Dis.* **20**, 431 (2014).
7. S. Zhu *et al*., *PLOS Pathog.* **9**, e1003592 (2013).
8. T. Miura *et al*., *J. Virol.* **87**, 9441 (2013).
9. S. Marionneau *et al*., *Gastroenterology* **122**, 1967 (2002).
10. A. M. Hutson, R. L. Atmar, D. Y. Graham, M. K. Estes, *J. Infect. Dis.* **185**, 1335 (2002).
11. M. Kane *et al*., *Science* **334**, 245 (2011).
12. S. K. Kuss *et al*., *Science* **334**, 249 (2011).
13. C. M. Robinson, P. R. Jesudhasan, J. K. Pfeiffer, *Cell Host Microbe* **15**, 36 (2014).

10.1126/science.aaa0607

CELL BIOLOGY

Local synthesis and disposal

New experimental strategies reveal spatial and temporal features of protein synthesis and degradation in cells

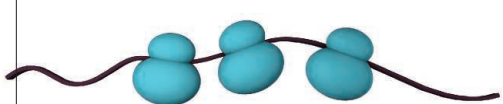
By **Sichen Shao** *and* **Ramanujan S. Hegde**

Most cells in our body have functionally specialized regions containing distinct sets of proteins. The evolution of this complexity from prokaryotic ancestors relied on the capacity to generate, sustain, and regulate subcellular compartments. At least part of this specialization exploited the ability to synthesize and degrade subsets of proteins in restricted areas of the cell. For example, neurons change the responsiveness of individual synapses during learning by controlling local protein production and degradation (*1*). Discovering and analyzing such local pathways amid parallel general pathways has posed a substantial challenge. On pages 751, 716, and 748 of this issue, Foresti *et al*. (*2*), Jan *et al*. (*3*), and Williams *et al*. (*4*), respectively, make progress toward this aim by applying powerful whole-proteome analyses in a yeast model, discovering a new pathway for localized protein degradation (*2*) and providing unprecedented views of all protein synthesis occurring at particular organelles (*3*, *4*). The findings may guide the study of region-specific reactions in morphologically complex metazoan organisms.

Foresti *et al*. and Jan *et al*. focus on the endoplasmic reticulum (ER), an expansive and functionally diverse eukaryotic organelle. This is the site of maturation for nearly all secreted and integral membrane proteins, collectively representing ~20% of all genes in a typical eukaryotic genome. Proteins that fail to assemble properly are destroyed by ER-associated protein degradation (ERAD). The diversity of clients transiting through the ER means that biosynthesis and degradation must be remarkably pliant. Hence, neither process occurs through a unifying pathway; rather, multiple routes, differing in their clientele, collectively handle this diversity (*5*, *6*). These pathways have been characterized for a handful of proteins, but the overall flux through each pathway has been difficult to infer without broader analyses.

Foresti *et al*. exploit proteome-wide tracking of protein abundances to detect a new degradation pathway. In yeast, ERAD was thought to comprise two pathways defined by ubiquitin ligases (Hrd1 and Doa10) that polyubiquitinate proteins for degradation (*6*). These ligases use ubiquitin supplied by the factor Ubc7. Using a quantitative proteomics method (*7*), the authors identified substrates whose degradation requires Ubc7 but neither ligase. Following up one substrate, Erg11, led to the discovery of a new ERAD pathway that uses the Asi ubiquitin ligase complex (see the figure). The Asi complex localizes to the inner nuclear membrane, a restricted subdomain of the ER that was not previously appreciated to have membrane protein quality control. The amount of Erg11 protein, an enzyme for sterol synthesis, could perhaps be regulated by controlling its trafficking to the inner membrane.

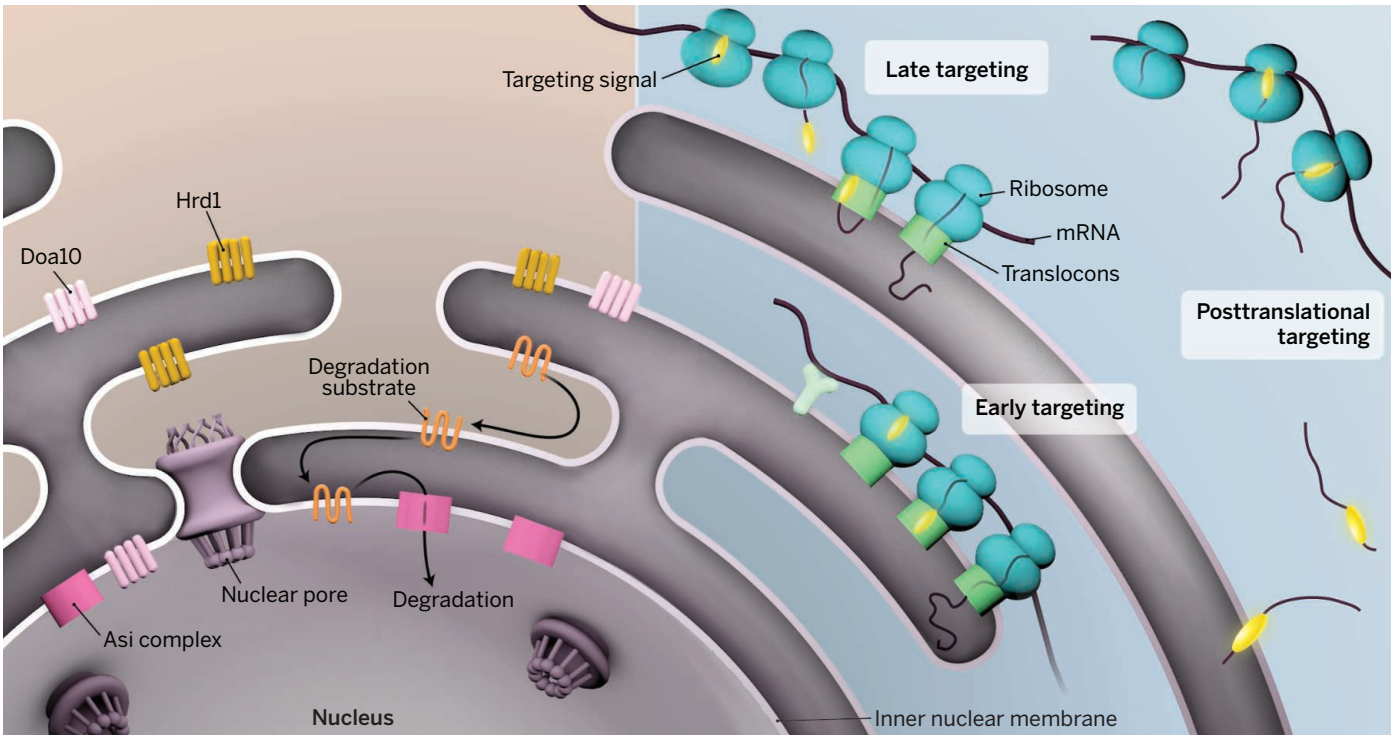
Although sequence homologs of the Asi complex are not apparent outside fungi, the findings of Foresti *et al*. will stimulate a search for the analogous pathway in other organisms. It is noteworthy that, unlike the traditional strategy of using a model protein to drive pathway discovery, a global search for clients that do not fit into existing frameworks pointed the way to both a new pathway and an ideal model substrate for its analysis.



The power of quantitative proteomics may well shift how new biological pathways are uncovered in future studies.

This is why the study by Jan *et al*., describing strategies to obtain global views of localized protein synthesis, is an important conceptual and technical advance. Ribosome profiling was previously described as a means to quantitatively identify ribosomal footprints on all cellular mRNAs—snapshots of the global translational program—under different conditions (*8*). Jan *et al*. sought to refine ribosome profiling by analyzing a localized subset of ribosomes. The authors pursued an orthogonal tagging strategy (*9*) in which a peptide acceptor sequence becomes biotinylated when it encounters the biotin ligase BirA. Such tagging has been used to infer protein-protein interactions (*10*) and protein exposure to specific cellular compartments (*11*). Thus, incorporating the biotin acceptor site into a ribosomal protein and localizing BirA to a specific cellular area allows tagging of only those ribosomes in proximity to BirA. Tagged ribosomes can then be purified and analyzed to determine

Published by AAAS



Spatial specialization. (**Left**) Different degradation machineries in the ER membrane have distinct localizations. The Asi complex, which tags proteins destined for destruction with ubiquitin, is restricted to the inner nuclear membrane. Its substrates must first enter the nucleus. (**Right**) The timing of ribosome engagement with ER translocons is highly variable.

their position along individual mRNAs.

Jan *et al.* develop this strategy for the ER membrane. Many secretory and integral membrane proteins are coordinately translated and inserted into the ER at translocons, conduits across or into the membrane. Ribosomes translating these proteins were preferentially biotinylated by ER-tethered BirA, whereas BirA tethered at mitochondria labeled ribosomes translating mitochondrial proteins. Ribosomes translating tail-anchored proteins, which target to the ER after translation (*12*), were not tagged by ER-localized BirA. Thus, proximity-based ribosome profiling is a minimally perturbing method for identifying all proteins produced at a specific location, permitting Jan *et al.* to define putative secretory proteins not predicted by bioinformatics alone.

The same strategy was applied by Williams *et al.* to define proteins imported into mitochondria, clarifying numerous ambiguous bioinformatic annotations. Curiously, the fumarate reductase Osm1 seemed to be synthesized at both mitochondrial and ER membranes. By analyzing the ribosomal start site footprints, they identified alternative translation initiation as the mechanism of this dual localization. Williams *et al.* noticed that enrichment of most mitochondrial clients was only seen when translation was stalled for several minutes prior to analysis, indicating that they are ordinarily synthesized on cytosolic ribosomes and translocated after translation. Thus, manipulating translation elongation allowed Williams *et al.* to discriminate between posttranslational and cotranslational routes, revealing that mitochondrial inner membrane proteins preferentially use the latter.

Proximity-specific ribosome profiling also allows analysis of how individual substrates engage their translocon. In yeast, ribosomes can use one of two homologous ER translocons built around either Sec61 or Ssh1; the former can also associate with the Sec63 complex to mediate posttranslational translocation (*5*). By fusing BirA to either Sec63 or Ssh1, Jan *et al.* aimed to identify their respective clientele. Although most clients promiscuously engage both proteins, the respective profiles of ribosome footprints obtained with Ssh1- and Sec63-tethered BirA showed some curious differences. In general, the time of ribosome arrival at a translocon, marked by where mRNA footprints are first seen, occurs just as the signal for targeting to the translocon emerges from the ribosome. However, some Sec63-marked clients arrive at the translocon earlier, perhaps indicating that the respective mRNAs were pre-tethered to the ER membrane. By contrast, some Ssh1-marked clients arrive later, possibly reflecting a need for extra nascent chain length for productive insertion into the translocon. Although the basis of these observations is speculative, they highlight the timing of ribosome targeting as a variable that merits future investigation.

Tuning the promiscuity of BirA (*10*), adapting it to use biotin analogs (*13*), and developing variants that can be activated and inactivated will provide greater spatial and temporal control of the proximity-specific tagging method, a likely prerequisite for its adaptation to more complex organisms. Combining this with genome editing and the increasing ability to produce diverse cell types in culture should provide opportunities to explore spatially regulated protein dynamics in numerous physiological contexts. ■

MRC Laboratory of Molecular Biology, Cambridge, CB2 0QH, UK. E-mail: rhegde@mrc-lmb.cam.ac.uk

REFERENCES

1. O. Steward, E. M. Schuman, *Neuron* **40**, 347 (2003).
2. O. Foresti *et al.*, *Science* **346**, 751 (2014).
3. C. H. Jan *et al.*, *Science* **346**, 1257521 (2014).
4. C. C. Williams *et al.*, *Science* **346**, 748 (2014).
5. E. Park, T. A. Rapoport, *Annu. Rev. Biophys.* **41**, 21 (2012).
6. A. Ruggiano *et al.*, *J. Cell Biol.* **204**, 869 (2014).
7. S.-E. Ong *et al.*, *Mol. Cell. Proteomics* **1**, 376 (2002).
8. N. T. Ingolia *et al.*, *Science* **324**, 218 (2009).
9. P. J. Schatz, *Biotechnology* **11**, 1138 (1993).
10. M. Fernández-Suárez *et al.*, *J. Am. Chem. Soc.* **130**, 9251 (2008).
11. A. B. Emerman *et al.*, *Mol. Biol. Cell* **21**, 4325 (2010).
12. R. S. Hegde, R. J. Keenan, *Nat. Rev. Mol. Cell Biol.* **12**, 787 (2011).
13. W.-C. Lu *et al.*, *Biotechnol. Bioeng.* **111**, 1071 (2014).

10.1126/science.1261602

ILLUSTRATION: V. ALTOUNIAN/*SCIENCE*

Published by AAAS

EARTH SCIENCE

Coping with low ocean sulfate

Did sulfate-reducing microbes exist in the Archean ocean?

By **Yuichiro Ueno**[1,2,3]

Sulfate (SO_4^{2-}) is the second-most abundant anion after chloride in the modern ocean. It serves as an easily accessible energy source for sulfate-reducing prokaryotes (SRPs), which are commonly found in organic-rich sediments and play an important role in the decomposition of organic matter. Were these microbes major players in ecosystems during the Archean (before 2.5 billion years ago), when molecular oxygen was virtually absent from both the atmosphere and oceans? Whether this was the case depends on how much sulfate there was in the Archean ocean. Three articles in this issue (*1*–*3*) use precise measurements of stable sulfur isotope ratios to investigate how much sulfate there was in the Archean ocean and where that sulfate originated.

Scientists use the ratio between two stable sulfur isotopes, ^{34}S and ^{32}S, to trace SRP activity in ancient sedimentary rocks. In sediments, the microbes preferentially reduce $^{32}SO_4^{2-}$ compared to $^{34}SO_4^{2-}$, producing iron sulfide minerals that are depleted in ^{34}S (a process called mass-dependent isotopic fractionation). ^{34}S depletion recorded in pyrite (FeS_2) minerals is thus a good indicator of SRP activity. Large ^{34}S depletions are seen in the geological records starting about 2.3 billion years ago, but not before (*4*). One possible interpretation of these data is that there was little SRP activity in the Archean. Another possibility is that these microbes appeared much earlier, but that the Archean sulfate levels were too low for them to selectively reduce $^{32}SO_4^{2-}$; low sulfate levels are known to reduce the degree of isotopic fractionation (*5*).

Some early Archean hydrothermal deposits (*6*) and oceanic basalts (*7*) contain moderately ^{34}S-depleted pyrites that may suggest local SRP activity. On page 742 of this issue, Zhelezinskaia *et al.* (*1*) report very large ^{34}S depletion and widely varying $^{34}S/^{32}S$ ratios in pyrites in 2.5-billion-year-old carbonates from Brazil. These observations strongly support the presence of SRPs in the late Archean ocean. The authors calibrate the data using the relationship between sulfate concentration and microbial isotopic fractionation in laboratory experiments (*5*). They estimate that the sulfate concentration in the late Archean ocean was less than 1% of that in modern seawater (28 mM).

Findings from a modern analog suggest that Archean sulfate levels may have been even lower. On page 735, Crowe *et al.* (*2*) investigate microbial sulfate reduction in Lake Matano, Indonesia, where the bottom waters are free from oxygen and rich in iron, providing an analog to the Archean ocean. They find that in this iron-rich environment, the microbial fractionation is larger than previously thought even when the sulfate concentration is below 20 μM. Thus, the threshold sulfate level below which isotopic fractionation by SRPs is reduced may be lower than previously believed. Based on these results, the authors interpret the observed small isotopic fractionation in the Archean geological record to mean that sulfate levels were below 0.01% of their concentrations in modern seawater. The study also shows that SRPs could have survived and been active in such a low-sulfate environment.

Further evidence for Archean SRP activity comes from the less abundant sulfur isotopes ^{33}S and ^{36}S. Precise measurements of these minor species provide information not only on microbial activity but also on where the sulfur came from. Most chemical processes such as precipitation, evaporation, and microbial sulfate reduction depend on isotope mass, resulting in mass-dependent

[1]Department of Earth and Planetary Sciences, Tokyo Institute of Technology, Meguro Tokyo, 152-8551, Japan. [2]Earth-Life Science Institute (WPI-ELSI), Tokyo Institute of Technology, Meguro Tokyo, 152-8551, Japan. [3]Precambrian Ecosystem Laboratory, Japan Agency for Marine-Earth Science and Technology, Yokosuka 237-0061, Japan. E-mail: ueno.y.ac@m.titech.ac.jp

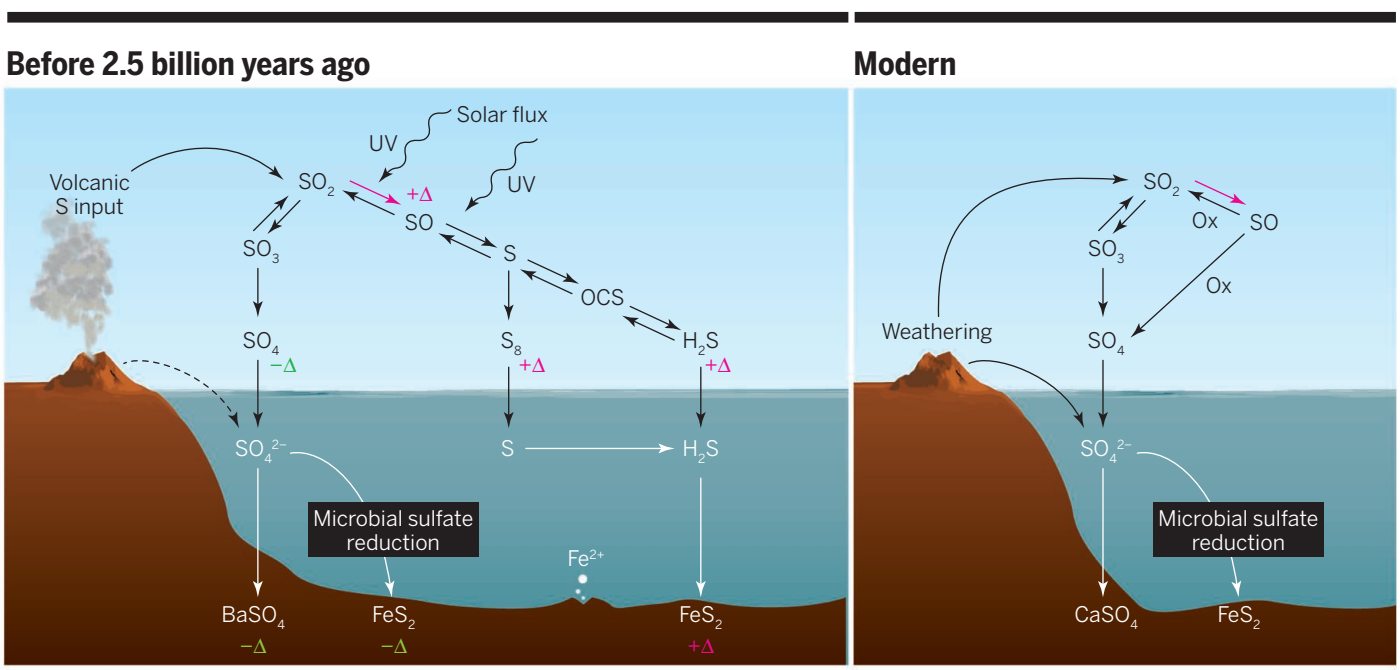


ILLUSTRATION: ADAPTED BY P. HUEY/*SCIENCE*

Modern and Archean sulfur cycling. The Archean ocean contained much less sulfate than today's ocean. Three studies in this issue (*1*–*3*) aim to determine the sulfate concentration and sources in the Archean ocean and the implications for sulfate-reducing prokaryotes. A key factor in this process is the mass-independent fractionation of ^{33}S, which is indicative of photochemical reactions in the ancient atmosphere. The ^{33}S fractionation signal, shown here as −Δ and +Δ, helps to determine the origin of the sulfate used by SRPs.

Published by AAAS

fractionation (*8*). However, photochemical reactions such as that of SO_2 driven by ultraviolet (UV) light in the atmosphere do not depend on isotope mass. Thus, sulfate derived from the anoxic atmosphere should have an anomalous isotopic ratio that does not obey the normal mass-dependent relationship. Indeed, all known Archean sulfate deposits show a negative ^{33}S anomaly, implying that Archean seawater sulfate was depleted in ^{33}S as a result of sulfate input from the anoxic atmosphere (*9*).

The late Archean ^{34}S-depleted pyrites analyzed by Zhelezinskaia *et al.* also show a negative ^{33}S anomaly, a clear sign that the pyrites were produced from seawater sulfate at that time. This view, however, is challenged by the microscopic analysis reported by Paris *et al.* on page 739 (*3*). The authors report that trace sulfate preserved in late Archean carbonate rocks from South Africa was anomalously rich in ^{33}S.

Why are the results from Brazilian (*1*) and South African (*3*) rocks of similar ages so different? One possibility is that sulfate levels in the coastal evaporitic basin, where the carbonates studied by Zhelezinskaia *et al.* were deposited may have been higher than in the open ocean. In such a basin, elevated sulfate levels may have facilitated local SRP activity; the isotopic signal could have been controlled by local sulfate input and may not necessarily represent the entire Archean ocean. Alternatively, late Archean sulfur cycling may have been more dynamic than previously thought (*10*). Furthermore, the ages of the two sets of rocks are not exactly the same. Seawater isotopic compositions could have fluctuated on much shorter time scales than they do today. In this case, the change in the sulfur isotopic anomaly may reflect a substantial perturbation of atmospheric chemistry (*10*, *11*). A definitive explanation will require better understanding of primary photochemical processes and how the chemical and physical state of the atmosphere influences the sulfur isotopic fractionation (*12*). ■

REFERENCES

1. I. Zhelezinskaia *et al.*, *Science* **346**, 742 (2014).
2. S. A. Crowe *et al.*, *Science* **346**, 735 (2014).
3. G. Paris *et al.*, *Science* **346**, 739 (2014).
4. J. E. Johnson *et al.*, *Proc. Natl. Acad. Sci. U.S.A.* **110**, 11238 (2013).
5. K. S. Habicht *et al.*, *Science* **298**, 2372 (2002).
6. Y. Ueno *et al.*, *Geochim. Cosmochim. Acta* **72**, 5675 (2008).
7. N. McLoughlin *et al.*, *Geology* **40**, 1031 (2012).
8. J. Farquhar, B. A. Wing, *Earth Planet. Sci. Lett.* **213**, 1 (2003).
9. S. Ono *et al.*, *Earth Planet. Sci. Lett.* **213**, 15 (2003).
10. A. L. Zerkle *et al.*, *Nat. Geosci.* **5**, 359 (2012).
11. Y. Ueno *et al.*, *Proc. Natl. Acad. Sci. U.S.A.* **106**, 14784 (2009).
12. S. O. Danielache *et al.*, *J. Geophys. Res.* **117**, D24 (2012).

10.1126/science.1261676

MELTING MECHANISMS

Simulations provide a rare look at real melting

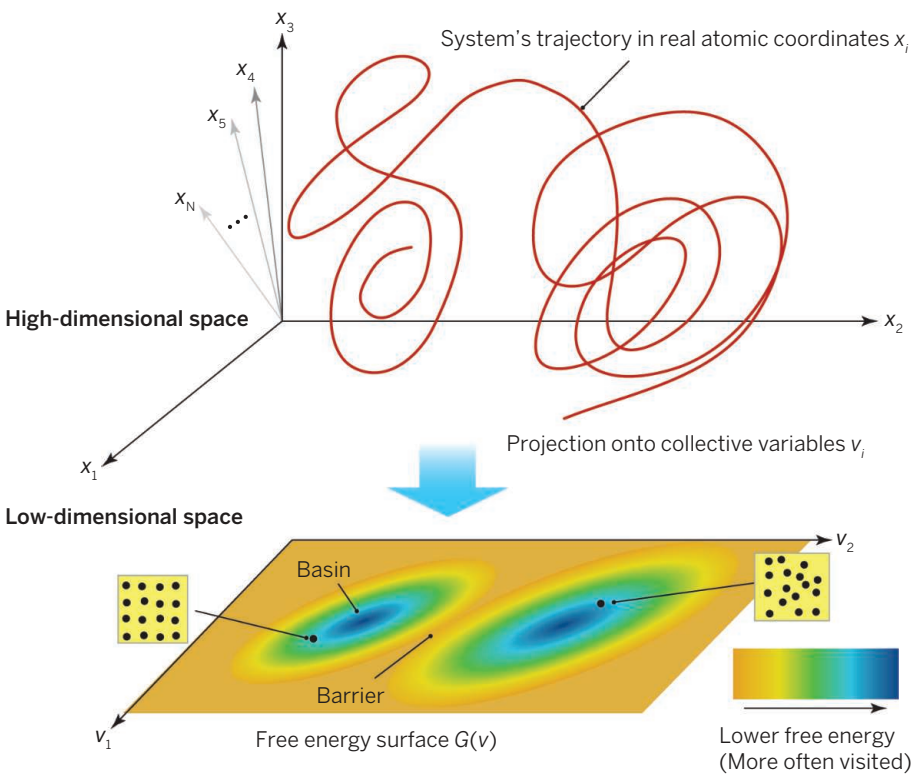
Advanced computational methods allow sampling of rare events and reveal multiple pathways in melting of metals

By **Axel van de Walle**

Melting is perhaps one of the most familiar phase transformations. Yet, surprisingly, the complex mechanisms leading to melting have just recently been clarified. On page 729 of this issue, Samanta *et al.* (*1*) report a large-scale atomistic computational investigation that offers an exceptionally detailed look at the underlying mechanisms for melting of metals under near-equilibrium conditions.

The traditional description of melting is based on classical nucleation theory. It involves the formation, via random thermal fluctuations, of a small liquid nucleus, which then irreversibly grows once it exceeds a certain critical size. Crossing this critical size is the sole barrier in the "reaction path" toward melting. However, this simple picture is being drastically revisited. The study of Samanta *et al.* reveals that the path to melting can vary with temperature and with the nature of preexisting defects.

As is often the case in computational studies, an idealized system is studied initially, and more realistic features are added one by one to see their effects. The limiting case of equilibrium melting of a perfect defect-free crystal is not accessible experimentally, both because defects (such as surfaces) are



Cutting the problem down to size. The high-dimensional space containing the system's real dynamic trajectory, in terms of all atomic coordinates (top panel), can be projected onto a low-dimensional space (bottom panel) that preserves only a few collective variables (CVs) that summarize the state of the system (e.g., its degree of crystallinity). Each point in the low-dimensional representation is assigned a free energy that reflects how often a point with a particular value of the CV is visited by the real trajectory in the high-dimensional space. Insets show typical atomic configurations associated with selected values of the CV. The resulting free-energy surface can be interpreted as a landscape of basins and barriers that the system traverses as it undergoes melting, powered by its thermal energy.

Published by AAAS

unavoidable and because equilibrium melting without defects would take longer than the age of the universe. However, simulations can readily handle this ideal case, and the results indicate that the melting transition in this case consists of multiple barrier crossings that involve the formation and coalescence of various localized defects in the crystalline solid, onto which the liquid then nucleates. These phenomena occur over very different time and length scales.

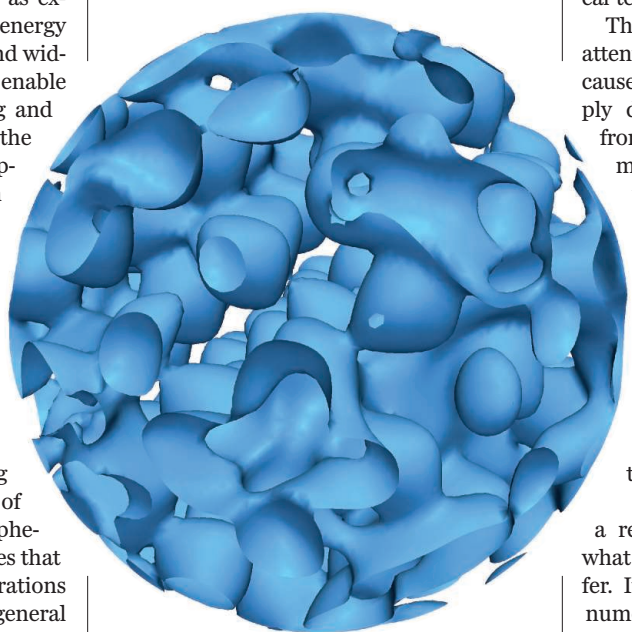
Adding various preexisting defects not only drastically reduces the barriers, as expected, but also modifies the system's energy landscape, eliminating some basins and widening others. The calculations also enable a study of the effect of superheating and identify a temperature above which the barrier toward melting entirely disappears. This finding ties in nicely with the recent investigations of the kinetics of homogeneous melting under superheated conditions (*2*).

The computational approaches used are perhaps as interesting as the findings themselves. The work by Samanta *et al.* is part of a broader effort within the computational materials, chemistry, and physics communities aimed at overcoming the well-known time-scale limitation of standard molecular dynamics. Most phenomena of interest occur on time scales that far exceed the period of atomic vibrations (about 10^{-14} s), which determines the general time scale accessible.

Beyond the time-scale issue, traditional molecular dynamics generates an oversupply of data that does not provide an intuitive picture of the mechanisms at work. The key to simultaneously solving both problems is to "project" the very high-dimensional space of all possible atomic configurations onto a low-dimensional space comprising only a few easy-to-understand coordinates that capture the progress the system is making toward melting (see the first figure). These so-called "collective variables" quantify properties such as the system's state of order (crystalline or amorphous) or its average density. The system's behavior is then summarized by assigning, to each value of these collective variables, a free energy. The resulting free-energy surface can be readily interpreted as a set of barriers that the system must overcome with its available thermal energy. Sampling of rarely visited regions (with a high free energy) can be enhanced by artificially assigning a higher temperature to "slow" degrees of freedom, a trick only computer simulations can accomplish.

School of Engineering, Brown University, Providence, RI 02912, USA. E-mail: avdw@brown.edu

Although this approach is especially adapted to the question studied here, a vast array of alternative rare-event sampling methods is available. The key concepts of collective variables and free-energy surface have close ties to metadynamics (*3*, *4*). Sophisticated methods can autonomously detect when the system gets trapped in some set of states, and in effect repel the system from "boring" repetitive dynamics in favor of rare but more interesting events. More generally, the concept of coarse-graining



Aluminum dynamics. Snapshot of a molecular-dynamics simulation of liquid aluminum based on quantum-mechanical calculations that solve for the electronic distribution (represented as a surface of constant electronic density) at each time step.

(i.e., reducing the number of degrees of freedom) underlies most multiscale methods (*5*).

Often, it is desirable to decouple the acceleration goal from the data reduction goal to avoid specifying a priori what the interesting coordinates are. Examples of methods achieving this abound (*6*–*8*). Hyperdynamics modifies the system's potential energy to make the basins, which trap the system for extended time, less deep. Temperature-accelerated dynamics runs the simulation at an artificially high temperature to increase the rate of transition events. Saddle-point search-based methods identify the possible reaction pathways by numerical optimization. Other methods initiate trajectories specifically from the outer rim of the system's potential energy basins to avoid trapping.

In developing these methods, specific algorithms had to be devised to ensure that the acceleration procedure preserves the correct relative rates of occurrence for different transition events. Typically, transition state theory (*9*) is used to estimate the true rate of barrier-crossing events based on the height of the actual free-energy barriers. Attention is currently being devoted to a related challenge, that of keeping an accurate record of the transition events' absolute rates (*8*, *10*). The difficulties lie in limitations of transition state theory itself and in the exponential dependence of rates on energy barriers, which places stringent demands on statistical techniques.

The study of melting continues to attract attention of the modeling community because many open issues remain. Even simply determining the melting temperature from state-of-the-art accurate quantum-mechanical electronic structure methods is challenging (see the second figure). Sophisticated schemes are continuously being devised to reach a useful accuracy within a tractable amount of computer time (*11*, *12*). Repeating the study of melting mechanisms for more complex molecular liquids, with quantum-mechanical energy models, or both would constitute a tremendous tour de force with current techniques.

The study by Samanta *et al.* provides a representative snapshot of the best of what current modeling techniques can offer. It is now possible to perform realistic numerical experiments that specifically test features of various theories underlying a given phenomenon. Simplifying assumptions need not be imposed a priori; instead, formal methods exist to properly project the high-dimensional numerical output of the simulations onto simple, easy-to-understand coordinates, while selectively blurring unimportant details. Who knows what complexity awaits us when studying, via similarly rigorous approaches, processes even slightly more intricate than melting? ■

REFERENCES

1. A. Samanta, M. E. Tuckerman, T.-Q. Yu, W. E, *Science* **346**, 729 (2014).
2. D. Alfè, C. Cazorla, M. J. Gillan, *J. Chem. Phys.* **135**, 024102 (2011).
3. A. Barducci, G. Bussi, M. Parrinello, *Phys. Rev. Lett.* **100**, 020603 (2008).
4. A. Laio, F. L. Gervasio, *Rep. Prog. Phys.* **71**, 126601 (2008).
5. S. Yip, Ed., *Handbook of Materials* Modeling (Springer, Dordrecht, Netherlands, 2005).
6. D. Perez, B. Uberuaga, Y. Shim, J. Amar, A. Voter, *Annu. Rep. Comput. Chem.* **5**, 79 (2009).
7. G. Henkelman, H. Jónsson, *J. Chem. Phys.* **115**, 9657 (2001).
8. P. Tiwary, A. van de Walle, *Phys. Rev. B* **87**, 094304 (2013).
9. G. H. Vineyard, *J. Phys. Chem. Solids* **3**, 121 (1957).
10. P. Tiwary, M. Parrinello, *Phys. Rev. Lett.* **111**, 230602 (2013).
11. D. Alfè, M. J. Gillan, G. D. Price, *Nature* **401**, 462 (1999).
12. Q. J. Hong, A. van de Walle, *J. Chem. Phys.* **139**, 094114 (2013).

10.1126/science.1259685

Published by AAAS

ENVIRONMENT AND DEVELOPMENT

Brazil's environmental leadership at risk

Mining and dams threaten protected areas

By **J. Ferreira*, L. E. O. C. Aragão, J. Barlow, P. Barreto, E. Berenguer, M. Bustamante, T. A. Gardner, A. C. Lees, A. Lima, J. Louzada, R. Pardini, L. Parry, C. A. Peres, P. S. Pompeu, M. Tabarelli, J. Zuanon**

POLICY

Over the past two decades, Brazil has emerged as an environmental leader, playing a prominent role in international fora such as the United Nations (UN) Conferences on Sustainable Development. The country has earned praise for the expansion of its protected area (PA) network and reductions in Amazon deforestation. Yet these successes are being compromised by development pressures and shifts in legislation. We highlight concerns for the newly elected government regarding development of major infrastructure and natural resource extraction projects in PAs and indigenous lands (ILs).

Brazil has the largest PA system of any country, covering nearly 2.2 Mkm^2 or 12.4% of the global total (*1*). This network helps conserve some of the most species-rich biomes on Earth and safeguard regionally and globally important ecosystem services [e.g., (*2*, *3*)]. Since 2008, Brazil has lost 12,400 km^2 of PAs due to degazetting and 31,700 km^2 due to downsizing, with an additional 21,000 km^2 threatened by proposals in the National Congress to downsize or degazette reserves in the Brazilian Amazon (*4*). Until now, unplanned agricultural expansion has been the greatest pressure on the environment, but new pressures are being exerted in response to rising demands for hydropower and mineral resources (see the chart). Hydropower accounts for 77% of Brazil's energy supply, while 70% of national potential, much of which is in the Amazon and Cerrado, remains untapped (*5*). The Brazilian government predicts that the majority of this latent capacity will need to be exploited by 2030 (*5*). Mining has grown from 1.6% of gross domestic product in 2000 to 4.1% in 2011; production is expected to further increase by a factor of 3 to 5 by 2030 (*6*).

Brazil has made concerted efforts to create a political and legislative framework supportive of mining and energy sectors. This includes strategic plans and draft legislation (PL 1610/96) to develop new mines in sustainable use reserves and ILs (*5*, *6*). Legislation being debated in the Congress (PL 3682/2012) calls for 10% of even strictly protected areas to open for mining concessions, and general prohibition of new PAs in areas of high mineral or hydropower potential.

Our analysis indicates that across Brazil there are 1.65 Mkm^2 of land with some form of registered mining interest; 1.01 Mkm^2 are in Amazonia (chart, A). While relatively few areas have been physically cleared for mining, at least 20% of all strictly protected areas and ILs overlap with areas registered as under consideration for mining (chart, B), demonstrating the potential for widespread effects if only a small fraction is authorized (chart, D and E). In the Amazon alone some 34,117 km^2 of strictly protected areas (8.3% of their total area) and 281,443 km^2 of ILs (28.4% of the total) lie in areas of registered interest for mining. Few PAs are free from the influence of large hydroelectric dams (chart, C).

This analysis raises four key issues. First, the existing PA network plays a critical role in conserving Brazil's ecosystems, counter to claims that PAs fail to serve their intended function. Second, there is potential for lasting environmental damage from direct, indirect, and cumulative effects associated with many large-scale development projects. Third, environmental mitigation policies are poorly conceived, fall short of international minimum standards for mitigation, and are unlikely to succeed. Finally, systematic inconsistencies and contradictions in the political process, if left unresolved, will undermine the credibility, effectiveness, and transparency of Brazil's PA system and ILs.

Brazil's new government should not squander the country's hard-won environmental leadership.

Politicians who support industrial development within PAs argue that many PAs only "lock away" mineral reserves and are nothing more than poorly managed "paper parks," often embroiled in chronic land tenure disputes. Many Brazilian PAs are understaffed, yet there is strong and growing evidence of their key role in conserving Brazilian ecosystems. For instance, the probability of deforestation is 7 to 10 times lower in Amazonian PAs than in surrounding areas (*7*).

Environmental effects of large-scale mining and hydropower within PAs are likely to be multiple and severe. Localized, direct effects can be particularly destructive within hyperfragmented Cerrado and Atlantic Forest biomes, where further loss or degradation of native vegetation could undermine opportunities to restore ecological connectivity and prevent extinctions (*8*). Yet direct local effects of development within PAs may be eclipsed by indirect environmental effects likely to ensue in surrounding regions over decadal time scales, such as increased deforestation, illegal logging, overhunting, and forest fires. Large-scale in-migration of labor and subsequent infrastructure and population growth in new development areas can open up "internal" deforestation frontiers in hitherto relatively undisturbed regions.

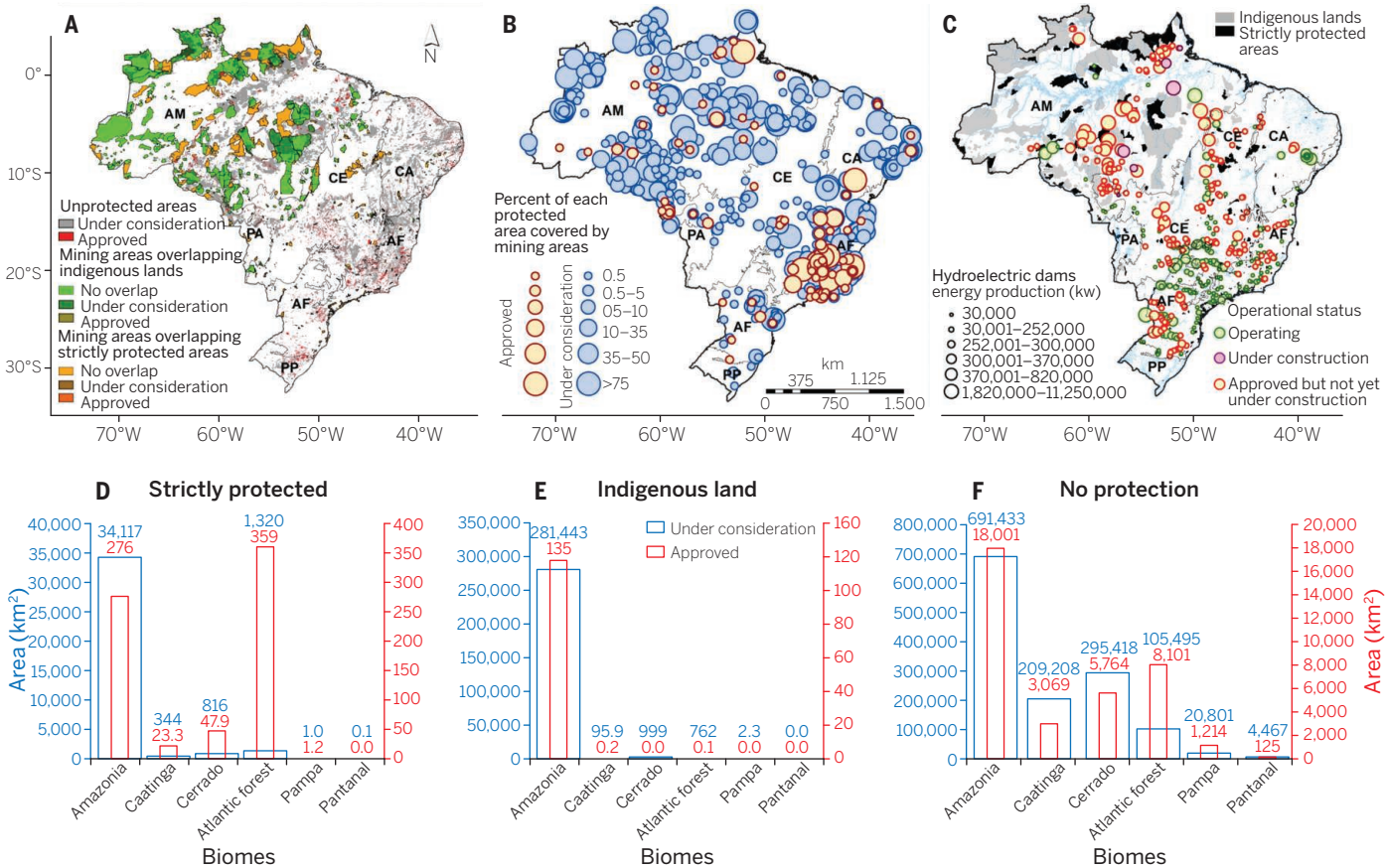
Current proposals (e.g., PL 3682/2012) for mitigating environmental damage caused by extractive activities within PAs are inadequate, poorly conceived, and fail to meet international best-practice standards prescribed by the basic mitigation hierarchy: avoid; minimize; mitigate; offset [for example, (*9*)]. In presuming that extraction can be authorized within PAs, the first mitigation option—avoid effects—is discarded. The assumption that there are no "no-go" areas for development could result in irreversible environmental damage.

Mitigation actions can provide substantial conservation benefits relative to a business-as-usual "no mitigation" development scenario (*10*). But mitigation actions for large development projects in Brazil are rarely designed before project approval and initiation and may never be implemented (*11*). Restoration is often viewed as a magic wand, yet there is little evidence that we can restore complex natural ecosystems after large-scale mining (*12*). Mitigation and restoration efforts rarely address indirect and cumulative effects. Recognizing that environmental effects cannot be fully mitigated on-site, proposed legislation to open up to 10% of strictly protected areas for mining recommends that offset areas be twice the size of affected areas (PL 3682/2012). Applying biodiversity offsets here is, at best, inappropriate. Although a case can be made to use offsets to enhance protection of threatened PAs to compensate

See the supplementary materials for author affiliations.
**E-mail: joice.ferreira@embrapa.br*

Published by AAAS

Downloaded from www.sciencemag.org on November 6, 2014



Distribution of municipal, state, and federal strictly protected areas, indigenous lands, approved mining concessions, areas of registered mining interest, and approved hydroelectric dams in Brazil (A and C). Areas officially approved as mining concessions and publicly registered as under consideration for extraction are compared against the distribution of all strictly protected areas (**D**), ILs (**E**), and unprotected areas (**F**), in addition to the percentage of overlap between all protected areas and approved mining concessions and areas of registered mining interest (**B**). See the supplementary materials for details.

for environmental damage elsewhere, it is counterintuitive to expect that protection elsewhere can compensate, on an ecological like-for-like basis, for effects on PAs. PAs established in part on criteria of vulnerability and irreplaceability may be too risky or impossible to offset (*13*), as is increasingly the case in the most deforested areas of Brazil.

Brazil's National System of Protected Areas was established in 2000 after more than a decade of debate in the Congress, building on public consultation across society and academia and representing a major contribution toward Brazil's international environmental commitments, including UN Conventions on Biological Diversity and Climate Change. In contrast, the process of dismantling PAs to allow industrial development has paid little regard to criticism from Brazilian society, exemplified by a recent campaign in defense of Brazilian PAs by the federal Public Prosecutor's Office. To be credible and fair, any attempt to change and downgrade this legislation should involve the same level of public consultation and democratic due process.

Beyond conservation and stewardship of its own biodiversity and environmental resources, Brazil has a vital role in motivating and supporting adoption of more sustainable development trajectories around the world. Yet, the integrity of Brazil's ecosystems and the credibility of its environmental leadership are jeopardized by recent shifts toward weaker and poorly negotiated environmental safeguards in the national PA system and ILs. This is consistent with recent changes in Brazil's Forest Code, which include an amnesty for large areas that were illegally deforested in the past (*14*). Although there are often strong economic and ethical arguments for development, Brazil should not squander its hard-won record of success and leadership in favor of fast-tracking short-lived development projects that leave a long legacy of environmental damage. We call on Brazil's newly elected government to ensure that individual development initiatives are subject to a comprehensive, socially inclusive, and long-term cost-benefit analysis that allows for any new proposal to be compared against possible alternatives and that takes full account of environmental and social effects, including rights of traditional and indigenous peoples. ■

REFERENCES

1. WDPA, 2012. World Database on Protected Areas. Database accessed in June 2014 from www.protectedplanet.net.
2. A. Veríssimo *et al.*, "Protected areas in the Brazilian Amazon: Challenges and Opportunities" (Imazon, Belém, Brazil; Instituto Socioambiental (ISA), Sao Paulo, Brazil, 2011)
3. D. V. Spracklen *et al.*, *Nature* **489**, 282 (2012).
4. E. Bernard *et al.*, *Conserv. Biol.* **28**, 939 (2014).
5. Brasil Ministério de Minas e Energia (MME), *Plano Nacional de Energia 2030* (MME, Rio de Janeiro, 2007).
6. Brasil Ministério de Minas e Energia (MME), *Plano Nacional de Mineração 2030* (MME, Rio de Janeiro, 2010).
7. T. H. Ricketts *et al.*, *PLOS Biol.* **8**, e1000331 (2010).
8. F. P. L. Melo *et al.*, *Trends Ecol. Evol.* **28**, 462 (2013).
9. Business and Biodiversity Offsets Programme (BBOP), *Guidance Notes to the Standard on Biodiversity Offsets* (BBOP, Forest Trends, Washington, DC, 2012).
10. A. Villarroya *et al.*, *PLOS ONE* **9**, e107144 (2014).
11. P. M. Fearnside, *Environ. Sci. Policy* **38**, 164 (2014).
12. M. Maron *et al.*, *Biol. Conserv.* **155**, 141 (2012).
13. J. D. Pilgrim *et al.*, *Conserv. Lett.* **6**, 376 (2013).
14. B. Soares-Filho *et al.*, *Science* **344**, 363 (2014).

ACKNOWLEDGMENTS

The following authors thank the following grants for support: L. E. O. C. A. (CNPq 304425/2013-3), T. A. G. (Formas 2013-1571), R. P. (CNPq 306715/2011-2), J. B. (CNPq 400640/2012-0), and E. B. (NE/K016431/1).

SUPPLEMENTARY MATERIALS

www.sciencemag.org/content/346/6210/706/suppl/DC1

10.1126/science.1260194

Published by AAAS

BOOKS *et al.*



FILM

A brief history of love

By **Valerie Thompson**

"It's American!" the woman exclaims with dismay, as her British husband demonstrates a speech synthesizer that will allow him to communicate after months of silence. With two words, Jane Hawking, portrayed by Felicity Jones, brings a moment of levity to a film that might easily have sunk under the weight of its own serious subject matter. Instead, *The Theory of Everything*, directed by James Marsh, masterfully weaves moments of humor and happiness throughout the dramatized retelling of the early life of renowned cosmologist Stephen Hawking.

Despite receiving a devastating diagnosis—motor neuron disease—at the age of 21, Stephen Hawking married Jane Wilde in the summer of 1965. Yet even as his health was rapidly deteriorating, his fame as a physicist was growing. The film gives equal consideration to the effects these factors had on the couple.

In a subtle performance, actor Eddie Redmayne conveys an almost palpable frustration as the progression of Stephen's affliction gradually makes everyday tasks difficult and then impossible. Not to be overshadowed, Jones's Jane is at once full of quiet grace and steely resolve.



The Theory of Everything
James Marsh, director
Working Title Films, 2014.
123 minutes.

Hawking has confirmed the general accuracy of the story, which is based on Jane's 2007 memoir (*1*), reportedly describing it as "broadly true" (*2*). In a more tacit endorsement, the film also features Hawking's own computer-generated voice.

Although the film only briefly touches on Hawking's many illustrious scientific contributions, it does a delightful job of introducing his complex theories to a lay audience. A potato and a pea, for example, become the framework for explaining quantum physics, while the properties of a black hole are illustrated with a beer poured on a pub table.

In a poignant homage to Hawking's contributions to our understanding of time, the film closes with a sweeping montage of scenes from the relationship's early days, as the couple, now divorced, reflects on their life together. In the end, we are left with a unique and intimate portrait of the personal struggles that accompanied Hawking's meteoric rise in the field of theoretical physics.

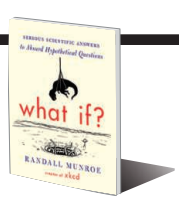
REFERENCES AND NOTES

1. J. Hawking, *Travelling to Infinity: My Life with Stephen* (Alma Books, London, 2007).
2. www.slate.com/blogs/quora/2014/10/07/theory_of_everything_stephen_hawking_how_difficult_was_it_to_make_a_movie.html.

10.1126/science.aaa0460

The reviewer is on staff at Science *magazine, AAAS, Washington, DC 20005, USA. E-mail: vthompso@aaas.org*

BOOKS IN BRIEF



What If? Serious Scientific Answers to Absurd Hypothetical Questions
By Randall Munroe
Houghton Mifflin Harcourt, 2014. 320 pp.

ARMED WITH AN INSATIABLE CURIOSITY, a penchant for wild extrapolation, and his signature stick-figure comics, Randall Munroe, a former NASA roboticist, presents meticulously researched answers to zany questions submitted by readers of his popular webcomic, xkcd.com. If you've ever wished for an evidence-based analysis of how many laser pointers it would take to light up the moon or wondered what would happen if you tried to hit a baseball pitched at 90 percent of the speed of light, Munroe has you covered.



CREDITS: (TOP) PHOTO: LIAM DANIEL/FOCUS FEATURES; (BOTTOM) ILLUSTRATION: RANDALL MUNROE/HOUGHTON MIFFLIN HARCOURT

Downloaded from www.sciencemag.org on November 6, 2014

Published by AAAS



Edited by **Jennifer Sills**

Hidden effects of mouse chow

IN HER 3 OCTOBER News Features "The littlest patient" (p. 24) and "Hope in a mouse" (p. 28), J. Couzin-Frankel discusses the utility of mouse genetic cancer models for testing the efficacy of chemotherapeutic drugs [also discussed in (*1*)]. She omits the importance of mouse diet.

Standard chow diets vary between batches in both macro and micro nutrients (*2*). These diets can elevate biochemically powerful phytoestrogens to mouse serum levels 50,000 times as high as those of endogenous estrogen (*3*). Standard chow diets also provide high levels of vitamin D3, a hormone with wide-ranging effects on genes and pathways affecting growth and differentiation in multiple tissues (*4*). As a result, vitamin D serum levels are elevated (*5*, *6*) to levels far exceeding the range in the U.S. human population (*7*). Yet, vitamin D signaling in the stroma profoundly influences chemotherapeutic efficacy for pancreatic cancer (*8*).

Many other nutrients also substantially alter tumor development and phenotype. It seems foolish to believe that even the most elegant mouse genetic models will be highly useful without paying attention to nutrient intake. Newmark and Lipkin conducted pioneering work on rodent diets that reflect nutrient intake common in populations at risk for tumor development (*9*–*11*). Unfortunately, these lessons and a tremendous body of literature in epidemiology, carcinogenesis, and chemoprevention are routinely ignored in high-profile work on the molecular biology and genetics of cancer.

Leonard Augenlicht

Albert Einstein Cancer Center, Montefiore Medical Center, Department of Medicine and Cell Biology, Bronx, NY 10467, USA.
E-mail: leonard.augenlicht@einstein.yu.edu

REFERENCES

1. S. Perrin, *Nature* **507**, 423 (2014).
2. H. Wang *et al.*, *Proc. Natl. Acad. Sci. U.S.A.* **102**, 9960 (2005).
3. N. M. Brown, K. D. Setchell, *Lab. Invest.* **81**, 735 (2001).
4. J. C. Fleet, M. DeSmet, R. Johnson, Y. Li, *Biochem. J.* **441**, 61 (2012).
5. C. Bolton, J. Gates, G. Giovannoni, *Inflamm. Res.* **62**, 659 (2013).
6. Y. Wang, S. J. Marling, J. G. Zhu, K. S. Severson, H. F. DeLuca, *Proc. Natl. Acad. Sci. U.S.A.* **109**, 8501 (2012).
7. Centers for Disease Control and Prevention, National Health and Nutrition Examination Survey (www.cdc.gov/nchs/nhanes/nhanes_products.htm).
8. M. H. Sherman *et al.*, *Cell* **159**, 80 (2014).
9. H. L. Newmark, *Carcinogenesis* **8**, 871 (1987).
10. K. Yang *et al.*, *Cancer Res.* **58**, 5713 (1998).
11. H. L. Newmark *et al.*, *Carcinogenesis* **22**, 1871 (2001).

Earthshaking energy development plans

PARTNERSHIPS BETWEEN scientists, engineers, legislators, and local communities can substantially enhance earthquake resilience ("'Epicenters' of resilience," M. L. Zoback, Editorial, 17 October, p. 283). Such resilience must not be compromised by energy development.

Reducing greenhouse gas emissions by developing low-carbon and renewable energy including hydropower, geothermal power, and natural gas is now a global priority. These options are not without risks. Changing reservoir water levels can induce shallow earthquakes, and water injection, common in the geothermal and gas industries, increases pore pressures, potentially inducing seismic events (*1*). There is a clear association between seismicity and active injection at the Geysers geothermal plant north of San Francisco (*1*). Injection of wastewater from unconventional gas fracking has been reported as the reason for the sharp increase in seismicity in Oklahoma (*2*).

Such enhanced seismicity is of particular concern in regions with poorly developed infrastructure and limited community resilience to earthquakes. China has the world's largest shale-gas reserves (about 36 trillion m^3), with many located near earthquake fault zones (*3*). The 12th Five-Year Plan (2011–2015) includes proposals to exploit these reserves, especially in

ONLINE BUZZ: CLINICAL TRIALS

Nonadherence takes its toll

IN HER IN DEPTH NEWS story "'Nonadherence': A bitter pill for drug trials" (17 October, p. 288), K. Servick explored a crucial confounding variable in drug trials: patients who stop taking the drug as prescribed. Readers added their own views about the causes and effects of nonadherence in the online comments section. Excerpts from their comments are below. Read the comments, and add your own, at http://comments.sciencemag.org/content/10.1126/science.346.6207.288.

A selection of your thoughts:

…This issue was less of a problem before clinical trials morphed into a business model as distinct from a clinical model. Patients who present through the clinical referral stream are less likely to be problematic concerning adherence. Pharma became impatient with the slowness of recruitment under the clinical model, and they traded speed for quality. Now they are reaping what they sowed.

Bernard Carroll

Another negative fallout from drug trials is the nature of the side effects that, once a drug makes it to market, must be described on the label or in the advertising. When we must sit through some of those drug ads, I've noted some of the side effects include those symptoms the drug is supposed to alleviate. Of course, some of these observations may be due to the fact that the drug did not work adequately for some patients, but it could also be fallout from abuses of the system described here.

Robert Buntrock

PHOTO: RAMA/WIKIMEDIA COMMONS

Downloaded from www.sciencemag.org on November 6, 2014

Published by AAAS

Sichuan and Chongqing (*4*). The population of these areas exceeds 110 million, and water injection has already induced 14 earthquakes of at least magnitude 4.0 in Chongqing's Rongchang conventional gas field (*5*, *6*). Furthermore, management actions for major hydropower dams, such as Three Gorges, need to be better informed so that seismic events can be better managed and risks minimized (*7*).

Earthquakes induced by the energy sectors are generally low in magnitude. However, effects could be deadly if they trigger release of accumulated tectonic strain in a large fault. Building partnerships based on the San Francisco model is necessary for all populous regions, and resilience enhancement is especially important where ground-source energy development is expanding rapidly.

Hong Yang,[1]* Julian R. Thompson,[2] Roger J. Flower[2]

[1]CEES, Department of Biosciences, University of Oslo, Blindern, 0316 Oslo, Norway. [2]Wetland Research Unit/Environmental Change Research Centre, UCL Department of Geography, University College London, London, WC1E 6BT, UK.

*Corresponding author.
E-mail: hongyanghy@gmail.com

REFERENCES

1. National Research Council, *Induced Seismicity Potential of Energy Technologies* (National Academies Press, Washington, DC, 2012).
2. K. M. Keranen, M. Weingarten, G. A. Abers, B. A. Bekins, S. Ge, *Science* **345**, 448 (2014).
3. C. Zou *et al.*, *Petrol. Explor. Devel.* **37**, 641 (2010).
4. China National Energy Administration, "China's shale gas development plan (2011–2015)" (2012).
5. X. Lei, G. Yu, S. Ma, X. Wen, Q. Wang, *J. Geophys. Res.-Sol. Ea.* **113**, 1 (2008).
6. H. Yang, J. R. Thompson, *Nature* **513**, 315 (2014).
7. R. Stone, *Science* **321**, 628 (2008).

Give young scientists a level playing field

AS A PH.D. STUDENT who has worked in multiple institutions, I have observed and experienced the disparity in rigor, pedagogy, and professional development in the training of new scientists. Candidacy standards, graduation benchmarks, and preparation for independent scientific careers were markedly different between universities. Public speaking skills preparation, visits from career counseling experts, and presentations on the options available to Ph.D.s besides research professorships also varied. This largely unrecognized disparity, driven by a decreasing funding rate for grants, is not sustainable if the United States is to remain globally competitive in the sciences.

Graduate students in the United States receive disparate levels of professional development, networking opportunities, and assessments of basic levels of competency depending on where and with whom they train. For example, industrial scientists may regularly present research and recruit at high-level institutions because a funded seminar series exists. Meanwhile, Ph.D. students at other institutions may never see an industrial scientist on their campus over an entire doctoral degree. This phenomenon is not new, but the standards expected from newly minted Ph.D.s have evolved as research has become increasingly competitive, globally collaborative (*1*), and fast paced. The inequality between institutions places a minority of new Ph.D.s on a track with the best toolbox and a majority to pick up the crumbs.

For the U.S. scientific output to sustain its current pace, funding agencies must invest in a strategic plan for the development of younger scientists. These investments should have priorities established by scientists-in-training. A multiregional steering committee should set structured goals and benchmarks to address the heterogeneity in educational and professional development between institutions.

Paul C. Jordan

Department of Chemistry, Indiana University, Bloomington, IN, 47405, USA.
E-mail: pcjordan@indiana.edu

REFERENCE

1. *Science* **346**, 47 (2014).

NEXTGEN VOICES

Missing classes: Last call

You have one more week to respond to the NextGen VOICES survey! Share your thoughts about this question:

What was missing from your science education? Name and describe a course that would have better prepared you for your science career.

Your course can be as serious ("Preventing Plagiarism 239") or as quirky ("Handwriting for Physicians 101") as you choose.

To submit, go to http://scim.ag/NG_13

Deadline for submissions is 14 November. A selection of the best responses will be published in the 2 January 2015 issue of *Science*. Submissions should be 100 words or less. Anonymous submissions will not be considered.

Published by AAAS

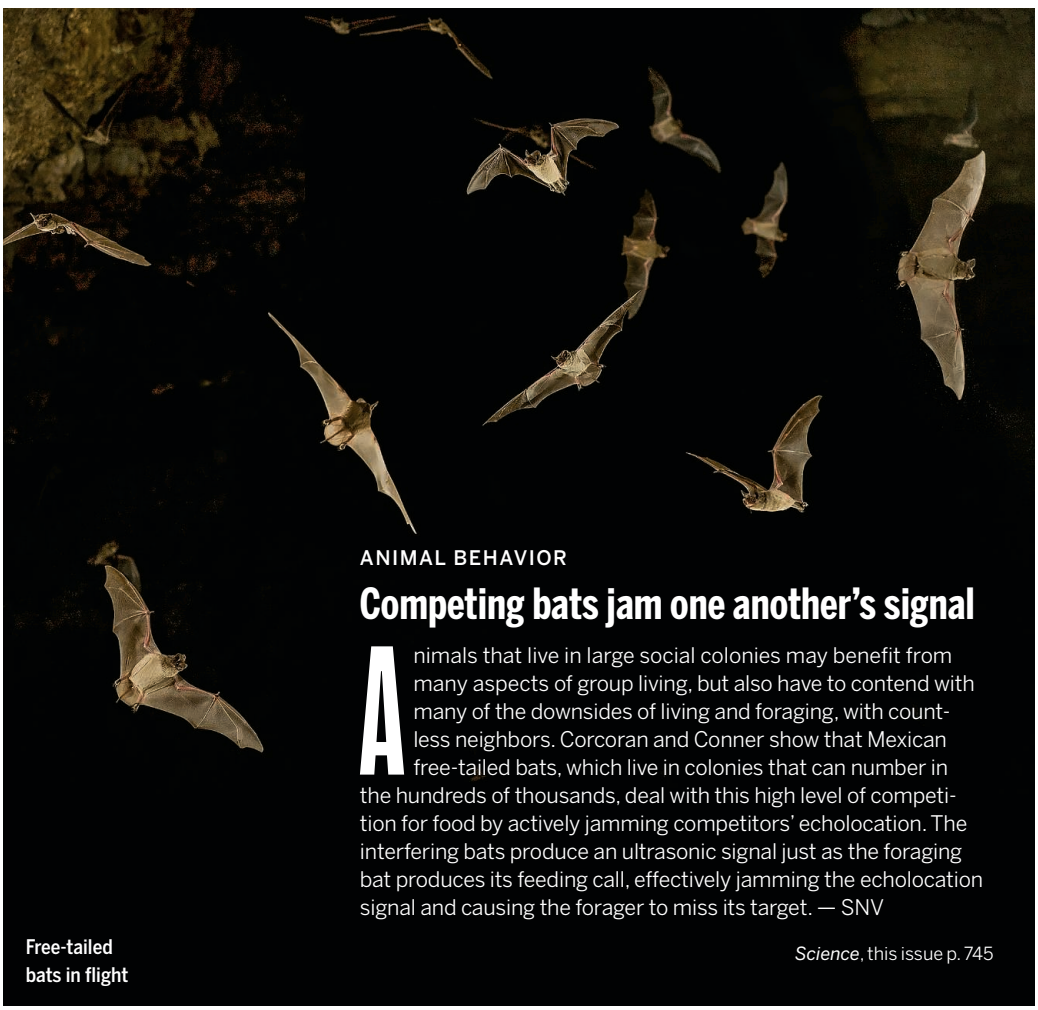
RESEARCH

Toward an insect evolution resolution
Misof et al., *p. 763*



IN *SCIENCE* JOURNALS

Edited by **Stella Hurtley**



Free-tailed bats in flight

ANIMAL BEHAVIOR

Competing bats jam one another's signal

Animals that live in large social colonies may benefit from many aspects of group living, but also have to contend with many of the downsides of living and foraging, with countless neighbors. Corcoran and Conner show that Mexican free-tailed bats, which live in colonies that can number in the hundreds of thousands, deal with this high level of competition for food by actively jamming competitors' echolocation. The interfering bats produce an ultrasonic signal just as the foraging bat produces its feeding call, effectively jamming the echolocation signal and causing the forager to miss its target. — SNV

Science, this issue p. 745

BIOCHEMISTRY

Protein folds as phosphorylation sites

Proteins fold into complex three-dimensional structures, yet most modification sites in proteins have been identified in short linear consensus motifs in the primary amino acid sequence. Duarte *et al.* found that kinases can recognize a consensus site that is formed by noncontiguous parts of the folded substrate protein. They characterized such a "structurally formed" consensus site in a substrate for the kinase PKC and identified structurally formed consensus sites in other substrates of PKC and of another kinase, PKA. Thus, researchers need to look at both the linear sequence and the three-dimensional structure to identify all the potential phosphorylation sites in a protein. — NRG

Sci. Signal. **7**, ra105 (2014).

THE RIBOSOME

Making mitochondrial hydrophobic proteins

Mitochondria produce chemical energy for the cell. Human mitochondria have their own specific ribosomes—mitoribosomes, which are distinct from cytoplasmic ribosomes. Mitoribosomes synthesize the mitochondrial membrane proteins that generate the chemical energy. Brown *et al.* used cryo–electron microscopy to determine the high-resolution structure of the large subunit of the human mitoribosome. The mitoribosome has a number of unique features, including an exit tunnel lined with hydrophobic amino acid residues. — GR

Science, this issue p. 718

PHOTOCHEMISTRY

Doubling up on optically driven catalysis

During photosynthesis, plants absorb light from the Sun four consecutive times before they accumulate enough energy to make oxygen from water. In contrast, when chemists harness light energy to promote reactivity, they tend to rely on single discrete absorption events. Ghosh *et al.* now show that a particular dye molecule can channel the combined energy from two absorbed photons to the reduction and subsequent coupling reactions of aryl halide molecules. The method expands the reach of photocatalysis to a broader range of compounds, such as chlorides, which are too stable to breach with a single photon. — JSY

Science, this issue p. 725

QUALITY CONTROL

Trashing misfolded membrane proteins

Proteins move to and from the inner nuclear membrane (INM) from the rest of the endoplasmic reticulum through the nuclear pores. This movement is tightly controlled. Consequently, the INM accumulates a specific

Downloaded from www.sciencemag.org on November 6, 2014

CREDITS: (TOP TO BOTTOM) 1KITE CONSORTIUM; © MICHAEL DURHAM/MINDEN PICTURES/CORBIS

Published by AAAS

set of proteins required for a variety of functions, including chromosome organization and transcriptional control. But when INM proteins misfold, how are they eliminated? Foresti *et al.* addressed this question in yeast and found that a previously elusive branch of the endo–plasmic reticulum–associated degradation system was key (see the Perspective by Shao and Hegde). — SMH

Science, this issue p. 751; see also p. 701

EARLY UNIVERSE

A diffuse cosmic glow is not primordial

A cumulative map of all photons ever emitted by any star or galaxy is a highly desirable historical record of the universe's evolution. For this reason, cosmologists have sought to measure this diffuse distribution of light: the extragalactic background light. Zemcov *et al.* sent up a rocket to measure the fluctuations in this faint background and found large-scale fluctuations greater than known galaxies alone should produce (see the Perspective by Moseley). Stars tidally stripped from their host galaxies are the most likely culprit, rather than unknown primordial galaxies. — MMM

Science, this issue p. 732; see also p. 696



Rocket launch June 2013

CREDITS: (LEFT TO RIGHT) TOSHIAKI ARAI; MEDICALRF/SCIENCE SOURCE

NOROVIRUS

Bacteria help norovirus infect B cells

Stomach ache, nausea, diarrhea—many people know the sort of gastrointestinal havoc norovirus can wreak. Despite this, norovirus biology remains unclear, because human norovirus cannot be grown in culture. Jones *et al*. now report that with the help of bacteria, human norovirus can infect cultured B cells (see the Perspective by Robinson and Pfeiffer). To infect B cells, human norovirus required the presence of gut bacteria that expressed proteins involved in determining blood type. Mouse norovirus also infected B cells, and the treatment of mice with antibiotics protected them from norovirus infection. — KLM

Science, this issue p. 755; see also p. 700

EARLY EARTH

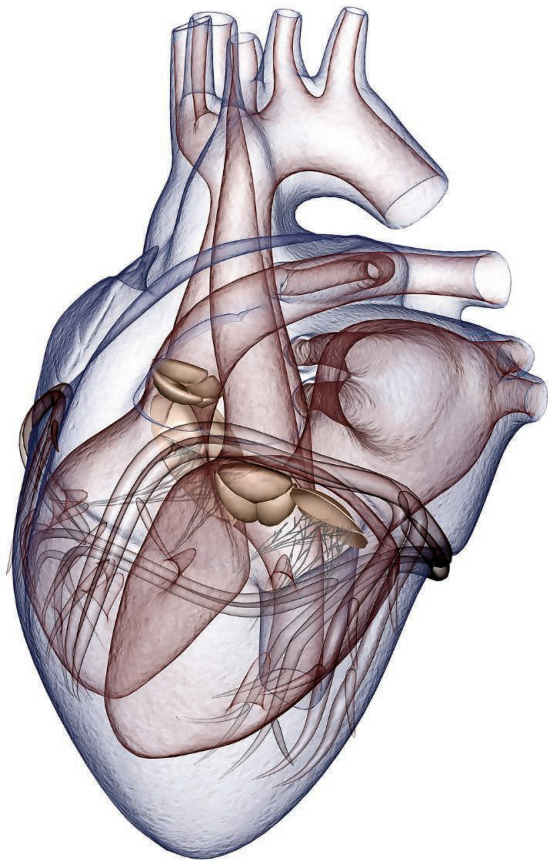
Dissecting ancient microbial sulfur cycling

Before the rise of oxygen, life on Earth depended on the marine sulfur cycle. The fractionation of different sulfur isotopes provides clues to which biogeochemical cycles were active long ago (see the Perspective by Ueno). Zhelezinskaia *et al.* found negative isotope anomalies in Archean rocks from Brazil and posit that metabolic fluxes from sulfate-reducing microorganisms influenced the global sulfur cycle, including sulfur in the atmosphere. In contrast, Paris *et al.* found positive isotope anomalies in Archean sediments from South Africa, implying that the marine sulfate pool was more disconnected from atmospheric sulfur. As an analog for the Archean ocean, Crowe *et al.* measured sulfur isotope signatures in modern Lake Matano, Indonesia, and suggest that low seawater sulfate concentrations restricted early microbial activity. — NW

Science, this issue p. 703, p. 742, p. 739; see also p. 735

IN OTHER JOURNALS

Edited by **Kristen Mueller** *and* **Jesse Smith**



BIOMEDICINE

Disease biomarkers: What's the risk?

With approximately 60% of cardiac events occurring in patients of low or moderate risk, doctors need new biomarkers to accurately predict which of their patients will develop disease. Antibodies targeting the protein apolipoprotein A-1 (apoA-1), which plays a role in lipid metabolism, are one such candidate. Some of these antibodies may confer more risk than others, depending where on apoA-1 they bind. Using serum samples from cardiac patients, Teixeira *et al.* identified the peptides within apoA-1 where antibodies bound. These finding may point toward new therapeutic opportunities and improved biomarkers for predicting the risk of cardiovascular disease. — MDC

J. Biol. Chem. 10.1074/jbc.M114.589002 (2014).

EDUCATION

One scoring rubric to rule them all

Evaluating the effectiveness of undergraduate STEM (science, technology, engineering, and mathematics) courses requires assessing teaching practices. This is largely done through student course evaluations, which often have not been administered or collected in a consistent manner. To standardize this process, Wieman and Gilbert developed a rubric that assigns points to each teaching practice for which there

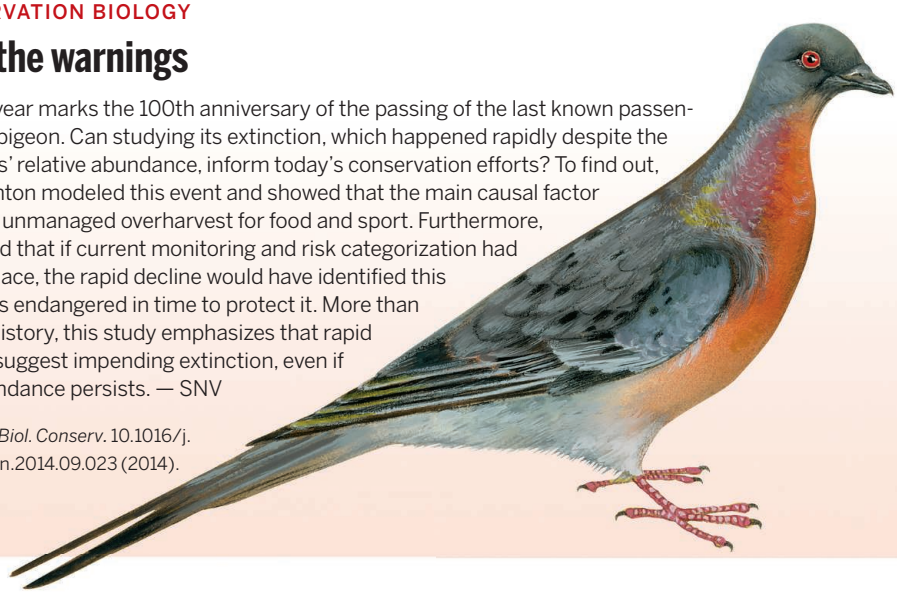
Published by AAAS

CONSERVATION BIOLOGY

Heed the warnings

This year marks the 100th anniversary of the passing of the last known passenger pigeon. Can studying its extinction, which happened rapidly despite the birds' relative abundance, inform today's conservation efforts? To find out, Stanton modeled this event and showed that the main causal factor was unmanaged overharvest for food and sport. Furthermore, they found that if current monitoring and risk categorization had been in place, the rapid decline would have identified this species as endangered in time to protect it. More than just sad history, this study emphasizes that rapid declines suggest impending extinction, even if local abundance persists. — SNV

Biol. Conserv. 10.1016/j.biocon.2014.09.023 (2014).



is research showing that the practice improves learning. Although a potentially valuable tool for improving undergraduate STEM teaching, it will need to be periodically updated in order to incorporate the latest developments in teaching and learning research. — MM

CBE Life Sci. Educ. **13**, 552 (2014).

NEUROBIOLOGY

Diversity generates complexity in the brain

Complexity in the brain derives not only from having a lot of neurons but also from the different ways neurons connect. Neurexin proteins help to establish these connections, but they themselves complicate the picture. Alternative splicing adds diversity to neurexins' protein coding regions by creating mRNAs with different combinations of exons. This diversity broadens the range of molecules bound by neurexins and modulates when and where neurons express them. To get a complete picture of neurexin diversity, Schreiner *et al*. sequenced the many neurexin transcripts produced adult mouse brains. Although two types of neurexins made good use of the diversity available to them, a third neurexin barely scratched the surface of its options. — PJH

Neuron **84**, 386 (2014).

SURFACE CHEMISTRY

Charge control of silicon chemistry

A site on an organic molecule often can be made more or less reactive by changing its neighboring functional groups so that they add or withdraw electronic charge from the site. Piva *et al.* show a similar effect for the reaction of dangling bond states on a hydrogen-terminated silicon surface with unsaturated organic molecules such as styrene. They modified the electronic properties of the surface by changing the surface concentration of arsenic dopants and used scanning tunneling microscopy to monitor product formation. Negatively charged doubly occupied dangling bonds, which were more prevalent on the highly doped surfaces, were less reactive than neutral singly occupied dangling bonds. These results are consistent with density functional theory calculations and help explain the heterogeneous reactivity of dangling bonds on silicon surfaces. — PDS

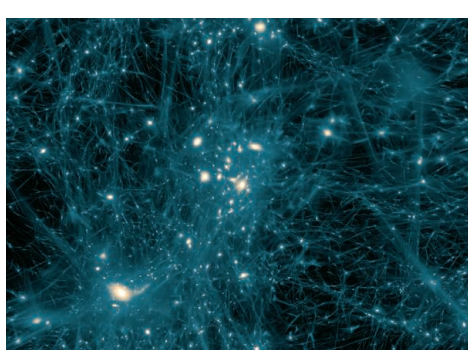
Phys. Rev. B **90**, 115422 (2014).

COSMOLOGY

Out with the WIMPs, in with the SIMPs?

Physicists seeking to identify dark matter—the stuff whose gravity may bind the galaxies—may have been stalking the wrong particle. The favorite candidate is the weakly interacting massive particle (WIMP), thought to have a mass between 1 and 1000 times that of a proton and interacting with each other and ordinary matter only through the weak nuclear force. But hypothetical strongly interacting massive particles (SIMPs) would do just as good a job at explaining the stuff, report Hochberg *et al*. They argue that dark matter could also consist of lighter particles that have a mass around one-10th of the proton and interact with one another very strongly, but with ordinary matter much more weakly than WIMPs. Strongly interacting dark matter would help resolve some differences between dark matter simulations and observed properties of galaxies. — AC

Phys. Rev. Lett. 10.1103/PhysRevLett.113.171301 (2014).



SIMPs would help reconcile observed properties of galaxies and models of dark matter distribution (shown).

GEOCHEMISTRY

Constructing geochemical geometry

Lavas erupted from oceanic hot spots have diverse chemistries that provide clues to the evolution of Earth's mantle. Jackson *et al.* develop a conceptual model of chemical variations within the mantle plume supplying the Samoan hot spot, by correlating geographic and geochemical variations in the erupted volcanic products. Lead and helium isotopes identify four distinct geochemical groups, all embedded in a common component that defines the mantle plume. The lens-like embedded materials appear to be isolated from one another, mixing only with the common component and creating compositionally distinct lavas in different spots along the Samoan hot spot track. — BG

Nature 10.1038/nature13794 (2014).

KIDNEY DISEASE

The dark side of protective genes

Aberrant antibody deposits in the kidney characterize immunoglobulin A nephropathy (IgAN), a disease most prevalent in East Asians. Kiryluk *et al*. studied the underlying genetics of IgAN and found that variants of genes with roles in maintaining the intestinal epithelial barrier or in the immune response to mucosal pathogens conferred an elevated risk of IgAN. People living in areas with the greatest diversity of helminthes showed the highest genetic risk for developing IgAN. This intriguing correlation suggests that the high incidence of IgAN in certain regions might be a consequence of protective adaptation to mucosal pathogens. — PAK

Nat. Genet. 10.1038/ng.3118 (2014).

CREDITS: (TOP TO BOTTOM) ENCYCLOPAEDIA BRITANNICA/UIG VIA GETTY IMAGES; RALF KAEHLER, OLIVER HAHN AND TOM ABEL/KAVLI INSTITUTE FOR PARTICLE ASTROPHYSICS AND COSMOLOGY

Published by AAAS

ALSO IN *SCIENCE* JOURNALS

Edited by **Stella Hurtley**

NANOMATERIALS

Casting gold and silver with DNA origami

Controlling the size and shape of nanoparticles synthesized in solution can be challenging, especially if the goal is to create less symmetric shapes for use in electronic and plasmonic applications. Sun *et al.* show that DNA "origami"—nanostructures in which the contacts between DNA strands are designed to assemble a particular shape—are sufficiently stiff to act as a mold for the growth of gold and silver nanostructures. The authors created shapes, including a gold particle with a rectangular cross section and a silver triangle with designed plasmonic properties. — PDS

Science, this issue p. 717

LOCAL TRANSLATION

The wheres and whys of protein translation

Localized protein synthesis is important for a broad range of biological activities, from specifying the animal body plan to coordinating entry into the secretory pathway. Few tools are available that can investigate translation at specific subcellular sites. Jan *et al.* present a flexible ribosome profiling–based methodology to enable precise characterization of localized protein synthesis (see the Perspective by Shao and Hegde). Proximity-specific ribosome profiling provides a high-precision tool for looking at the mechanism of localized protein targeting and synthesis in living cells. The approach yielded a high-resolution systems-level view of cotranslational translocation at the endoplasmic reticulum. Williams *et al.* applied the technique to look at localized mRNA translation at the mitochondrial outer membrane. — SMH

Science, this issue p. 716, p. 701; see also p. 748

QUANTUM SPIN LIQUIDS

Nailing down a quantum spin liquid

Quantum spin liquids (QSLs) possess magnetic interactions that, even at absolute zero temperature, remain in a disordered liquid-like spin state. It is very difficult to prove unambiguously that a material is a QSL, because there is always a possibility that it can become ordered below the lowest measured temperature. Barkeshli *et al.* used quantum field theory to propose a direct way to identify a QSL by placing it in contact with other exotic materials, such as superconductors or magnets. The theory predicted that, at such a boundary, electrons entering the QSL would turn into excitations lacking charge or lacking spin. Future experiments may be able to detect this transmutation. — JS

Science, this issue p. 722

PHASE TRANSFORMATION

Melting can follow many pathways

Melting involves the loss of order as additional kinetic energy is added to a system. Although simple models of this sort of phase transition exist, it can be very difficult to observe the initial stages either experimentally or using simulations. Samanta *et al.* developed a robust rare-event sampling technique that makes it possible to examine melting events without needing excessive computing time (see the Perspective by van de Walle). For both copper and aluminum, they observed the formation of defects that act as starting points for the melting process rather than the homogeneous loss of order assumed in classic nucleation theory. — MSL

Science, this issue p. 729

HIV ENTRY

HIV's shape-shifting envelope protein

HIV's envelope protein (Env) coats virus particles and allows HIV to enter host cells. HIV entry is highly dynamic. Env proteins work in groups of three (called trimers), which bind to the viral receptor and co-receptor, both expressed by host cells. Viral receptor binding causes a structural rearrangement in the trimer that allows for co-receptor binding and finally, viral entry. To visualize dynamic changes in Env conformation during viral entry, Munro *et al.* added differently colored fluorescent tags to two different regions of individual HIV trimers. Single-molecule

Published by AAAS

fluorescence resonance entry transfer revealed three distinct Env conformations before cell entry. Occupation of particular conformations depended on host receptor binding. — KLM

Science, this issue p. 759

INSECT PHYLOGENOMICS

Toward an insect evolution resolution

Insects are the most diverse group of animals, with the largest number of species. However, many of the evolutionary relationships between insect species have been controversial and difficult to resolve. Misof *et al.* performed a phylogenomic analysis of protein-coding genes from all major insect orders and close relatives, resolving the placement of taxa. The authors used this resolved phylogenetic tree together with fossil analysis to date the origin of insects to ~479 million years ago and to resolve long-controversial subjects in insect phylogeny. — LMZ

Science, this issue p. 763

EVOLUTION

On the hunt for a fourth domain of life

All known living organisms belong to one of three broad domains: archea, bacteria, and eukaryotes. But could there be life on Earth so different that it defines a novel fourth domain? In a Perspective, Woyke and Rubin explain that scientists may have missed signs of such unusual organisms. Powerful genomic technologies overcome the limitations of earlier searches and allow scientists to characterize microbes that cannot be grown in the laboratory. With these advanced tools, we may now be poised to discover fourth-domain organisms—if they exist. — JFU

Science, this issue p. 698

HEPATITIS C VIRUS

Toward an ounce of HCV prevention

Chronic hepatitis C virus (HCV) infection causes liver inflammation that can reduce liver function or even cause liver failure. Recent approval of antiviral drugs for HCV provides treatment options; however, these new therapies are expensive, with limited availability, leaving the door open for preventative approaches such as vaccines. Now, Swadling *et al.* report a preliminary trial of a prime-boost vaccine strategy for HCV in human patients. The strategy induced an immune T cell response similar to one that can control HCV in natural infection. — ACC

Sci. Transl. Med. **6**, 261ra153 (2014).

Published by AAAS

REVIEW SUMMARY

ECONOMICS

Economics in the age of big data

Liran Einav[1,2]* and Jonathan Levin[1,2]

BACKGROUND: Economic science has evolved over several decades toward greater emphasis on empirical work. The data revolution of the past decade is likely to have a further and profound effect on economic research. Increasingly, economists make use of newly available large-scale administrative data or private sector data that often are obtained through collaborations with private firms, giving rise to new opportunities and challenges.

ADVANCES: These new data are affecting economic research along several dimensions. Many fields have shifted from a reliance on relatively small-sample government surveys to administrative data with universal or near-universal population coverage. This shift is transformative, as it allows researchers to rigorously examine variation in wages, health, productivity, education, and other measures across different subpopulations; construct consistent long-run statistical indices; generate new quasi-experimental research designs; and track diverse outcomes from natural and controlled experiments.

Perhaps even more notable is the expansion of private sector data on economic activity. These data, sometimes available from public sources but other times obtained through data-sharing agreements with private firms, can help to create more granular and real-time measurement of aggregate economic statistics. The data also offer researchers a look inside the "black box" of firms and markets by providing meaningful statistics on economic behavior such as search and information gathering, communication, decision-making, and microlevel transactions. Collaborations with data-oriented firms also create new opportunities to conduct and evaluate randomized experiments.

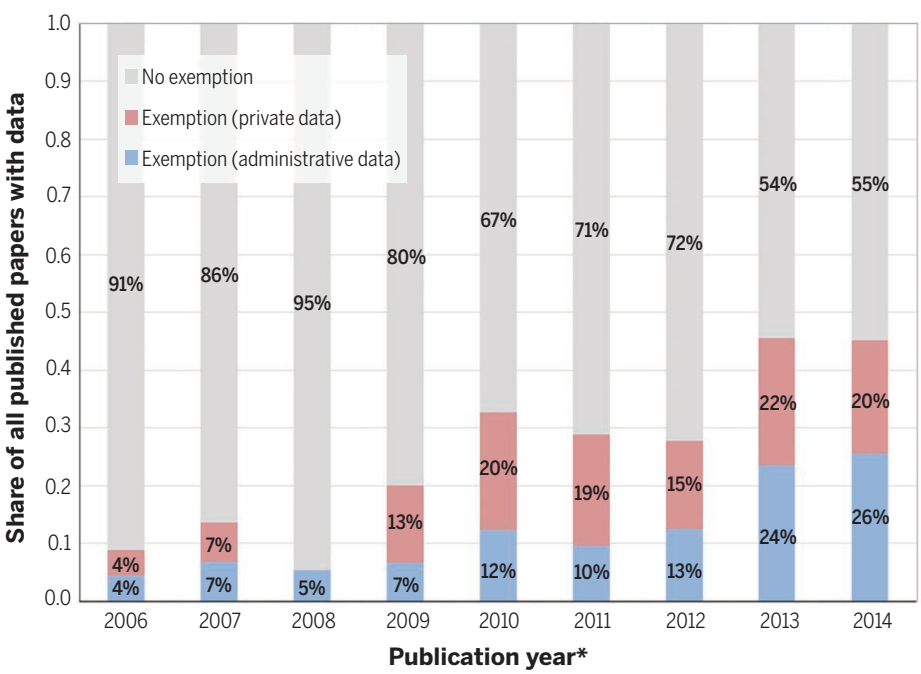
ON OUR WEB SITE

Read the full article at http://dx.doi.org/10.1126/science.1243089

Economic theory plays an important role in the analysis of large data sets with complex structure. It can be difficult to organize and study this type of data (or even to decide which variables to construct) without a simplifying conceptual framework, which is where economic models become useful. Better data also allow for sharper tests of existing models and tests of theories that had previously been difficult to assess.

OUTLOOK: The advent of big data is already allowing for better measurement of economic effects and outcomes and is enabling novel research designs across a range of topics. Over time, these data are likely to affect the types of questions economists pose, by allowing for more focus on population variation and the analysis of a broader range of economic activities and interactions. We also expect economists to increasingly adopt the large-data statistical methods that have been developed in neighboring fields and that often may complement traditional econometric techniques.

These data opportunities also raise some important challenges. Perhaps the primary one is developing methods for researchers to access and explore data in ways that respect privacy and confidentiality concerns. This is a major issue in working with both government administrative data and private sector firms. Other challenges include developing the appropriate data management and programming capabilities, as well as designing creative and scalable approaches to summarize, describe, and analyze large-scale and relatively unstructured data sets. These challenges notwithstanding, the next few decades are likely to be a very exciting time for economic research. ■



The rising use of non–publicly available data in economic research. Here we show the percentage of papers published in the *American Economic Review* (*AER*) that obtained an exemption from the *AER*'s data availability policy, as a share of all papers published by the *AER* that relied on any form of data (excluding simulations and laboratory experiments). Notes and comments, as well as *AER Papers and Proceedings* issues, are not included in the analysis. We obtained a record of exemptions directly from the *AER* administrative staff and coded each exemption manually to reflect public sector versus private data. Our check of nonexempt papers suggests that the *AER* records may possibly understate the percentage of papers that actually obtained exemptions. The asterisk indicates that data run from when the *AER* started collecting these data (December 2005 issue) to the September 2014 issue. To make full use of the data, we define year 2006 to cover October 2005 through September 2006, year 2007 to cover October 2006 through September 2007, and so on.

[1]Department of Economics, Stanford University, Stanford, CA 94305, USA. [2]National Bureau of Economic Research, 1050 Massachusetts Avenue, Cambridge, MA 02138, USA.
*Corresponding author. E-mail: leinav@stanford.edu
Cite this article as L. Einav, J. Levin, *Science* **346**, 1243089 (2014); DOI: 10.1126/science.1243089

Published by AAAS

REVIEW

ECONOMICS

Economics in the age of big data

Liran Einav[1,2]* and Jonathan Levin[1,2]

The quality and quantity of data on economic activity are expanding rapidly. Empirical research increasingly relies on newly available large-scale administrative data or private sector data that often is obtained through collaboration with private firms. Here we highlight some challenges in accessing and using these new data. We also discuss how new data sets may change the statistical methods used by economists and the types of questions posed in empirical research.

The expansion of data being collected on social and economic activity is likely to have profound effects on economic research. In this Review, we describe how newly available public and private sector data sets are being employed in economics. We also discuss how statistical methods in economics may adapt to take advantage of large-scale granular data, as well as some of the challenges and opportunities for future empirical research.

After providing some brief background in the next section, we divide the Review into three parts. We first discuss the shift from relatively small-sample government surveys to administrative data with universal or near-universal population coverage. These data have been used in Europe for some time but are just starting to be explored in the United States. We explain the transformative power of these data to shed light on variation across subpopulations, construct consistent long-run statistical indices, generate new quasi-experimental research designs, and track diverse outcomes from natural and controlled experiments.

The second part of the Review describes the marked expansion of private sector data on economic activity. We outline the potential of these data in creating aggregate economic statistics and some nascent attempts to do this. We then discuss the rise of collaborations between academics and data-rich companies. These relationships have some trade-offs in terms of maintaining data confidentiality and working with samples that have been collected for business rather than research purposes. But as we illustrate with examples from recent work, they also provide researchers with a look inside the "black box" of firms and markets and create new opportunities to conduct and evaluate randomized experiments.

The third part of this Review addresses statistical methods and the role of economic theory in the analysis of large-scale data sets. Today, economists routinely analyze large data sets with the same econometric methods used 15 or 20 years ago. We contrast these methods to some of the newer data mining approaches that have become popular in statistics and computer science. Economists, who tend to place a high premium on statistical inference and the identification of causal effects, have been skeptical about these methods, which put more emphasis on predictive fit and handling model uncertainty and on identifying low-dimensional structure in high-dimensional data. We argue that there are considerable gains from trade. We also stress the usefulness of economic theory in helping to organize complex and unstructured data.

We conclude by discussing a few challenges in making use of new data opportunities, in particular the need to incorporate data management skills into economics training, and the difficulties of data access and research transparency in the presence of privacy and confidentiality concerns.

[1]Department of Economics, Stanford University, Stanford, CA 94305, USA. [2]National Bureau of Economic Research, 1050 Massachusetts Avenue, Cambridge, MA 02138, USA.
*Corresponding author. E-mail: leinav@stanford.edu

The rise of empirical economics

Hamermesh (*1*) recently reviewed publications from 1963 to 2011 in top economics journals. Until the mid-1980s, the majority of papers were theoretical; the remainder relied mainly on "ready-made" data from government statistics or surveys. Since then, the share of empirical papers in top journals has climbed to more than 70%, and a substantial majority of these papers use data that have been assembled or obtained by the authors or generated through a controlled experiment.

This shift mirrors the expansion of available data. Even 15 or 20 years ago, interesting and unstudied data sets were a scarce resource. Gathering data on a specific industry could involve hunting through the library or manually extracting statistics from trade publications. Collaborations with companies were unusual, as were experiments, both in laboratory settings and in the field. Nowadays the situation is very different along all of these dimensions. Apart from simply having more observations and more recorded data in each observation, several features differentiate modern data sets from many used in earlier research.

The first feature is that data are now often available in real time. Government surveys and statistics are released with a lag of months or years. Of course, many research questions are naturally retrospective, and it is more important for data to be detailed and accurate rather than available immediately. However, administrative and private data that are continuously updated have great value for helping to guide economic policy. Below, we discuss some early attempts to use Internet data to make real-time forecasts of inflation, retail sales, and labor market activity and to create new tracking measures of the economy.

The second feature is that data are available on previously unmeasured activities. Much of the data now being recorded is on activities that were previously difficult to quantify: personal communications, social networks, search and information gathering, and geolocation data. These data may open the door to studying issues that economists have long viewed as important but did not have good ways to study empirically, such as the role of social connections and geographic proximity in shaping preferences, the transmission of information, consumer purchasing behavior, productivity, and job search.

Finally, data come with less structure. Economists are used to working with "rectangular" data, with N observations and $K << N$ variables per observation and a relatively simple dependence structure between the observations. New data sets often have higher dimensionality and less-clear structure. For example, Internet browsing histories contain a great deal of information about a person's interests and beliefs and how they evolve over time. But how can one extract this information? The data record a sequence of events that can be organized in an enormous number of ways, which may or may not be clearly linked and from which an almost unlimited number of variables can be created. Figuring out how to organize and reduce the dimensionality of large-scale, unstructured data is becoming a crucial challenge in empirical economic research.

Public sector data: Administrative records

In the course of administering the tax system, social programs, and regulation, the federal government collects highly detailed data on individuals and corporations. The same is true of state and local governments, albeit with less uniformity, in areas such as education, social insurance, and local government spending. As electronic versions of these data become available, they increasingly are the resource of choice for economists who work in fields such as labor economics, public finance, health, and education.

Administrative data offer several advantages over traditional survey data. Workhorse surveys—such as the Survey of Consumer Finances, the Current Population Survey, the Survey of Income and Program Participation, and the Panel Study on Income Dynamics—can suffer from substantial missing data issues, and the sample size may be limited in ways that preclude natural quasi-experimental research designs (*2*). The rich microlevel administrative data sets maintained by, among others, the Social Security Administration, the Internal Revenue Service, and the Centers for Medicare and Medicaid, often have

high data quality and a long-term panel structure. Sample selection and attrition, a common issue with survey panels, is not a primary concern (*3*).

These "universal" data sets are especially powerful for analyzing population variation. For instance, Piketty and Saez (*4*) have used tax records to calculate income and wealth shares for the very upper portion of the income distribution. These calculations are problematic for traditional surveys because of small sample sizes, underreporting of high incomes or asset levels, and the fact that surveys generally extend back only a few years or, at most, decades. In contrast, tax data allow for the creation of relatively homogeneous time series spanning many decades, or even centuries.

Administrative data have been similarly useful in documenting regional disparities in economic mobility (*5*) (Fig. 1) and health care spending (*6*), in discovering the wide variation in test-score value-added measures across public school teachers (*7*), and in identifying the sizable differences in wages and productivity across otherwise similar firms (*8*, *9*). In each case, researchers have used large-scale administrative data to measure and compare the relevant variable (e.g., income, spending, productivity, or wages) across small subpopulations of individuals or firms. These results have helped to guide policy discussions and define research agendas in multiple subfields of economics.

Recent work also highlights the value of using administrative data for causal inference and policy evaluation. For these purposes, administrative data can be valuable both because its coverage and detail allow for novel research designs and because of the possibility of linking records to track outcomes from an existing experiment or quasi-experiment. The last point is an important one. Matching a data set with a random survey of 1 million U.S. households will reduce the original sample to just 1% of its original size. Merging with administrative data may leave the sample virtually unchanged.

Akerman *et al.*'s (*10*) recent study of the effects of broadband Internet access is illustrative of how administrative data sets can be combined to perform a successful evaluation study. Their research design relies on the gradual expansion of broadband access in Norway into different geographic regions. The authors link this staggered rollout to administrative tax records to estimate how broadband adoption affected firm wages and productivity. By linking individual and firm-level administrative data sets, the authors can observe multiple outcome measures and assess the effect broadband access has on specific subpopulations—for example, broadband access turns out to have very different effects on workers of different education levels.

The same advantages of universal coverage apply when the experiment or quasi-experiment that forms the basis for the study's research design affects only a relatively small population. A recent example is Chetty *et al.*'s (*11*, *12*) study of the long-term effects of teacher quality. The authors use student-level test-score data from a specific city and identify a quasi-experiment in the way students are assigned to teachers that creates variation in teacher quality. The notable step comes when the authors link the student records to administrative tax data and are able to trace the effect of teacher quality on the students' subsequent wages, two decades later.

Several recent studies have also used administrative records in powerful fashion to track outcomes from truly randomized experiments. Chetty *et al.* (*13*) track the future earnings of students who were randomly assigned to classrooms during the Tennessee STAR (Student-Teacher Achievement Ratio) experiment conducted in the late 1980s. Taubman *et al.*'s (*14*) evaluation of the Oregon Medicaid expansion similarly uses a range of administrative data to track outcomes after an episode in which Oregon expanded its Medicaid program to a randomly selected subset of newly eligible individuals. The latter study links state administrative data, hospital admission records, private sector credit bureau records, and more targeted survey data to estimate the impact of Medicaid on health and financial measures.

The potential of administrative data for academic research is just starting to be realized, and

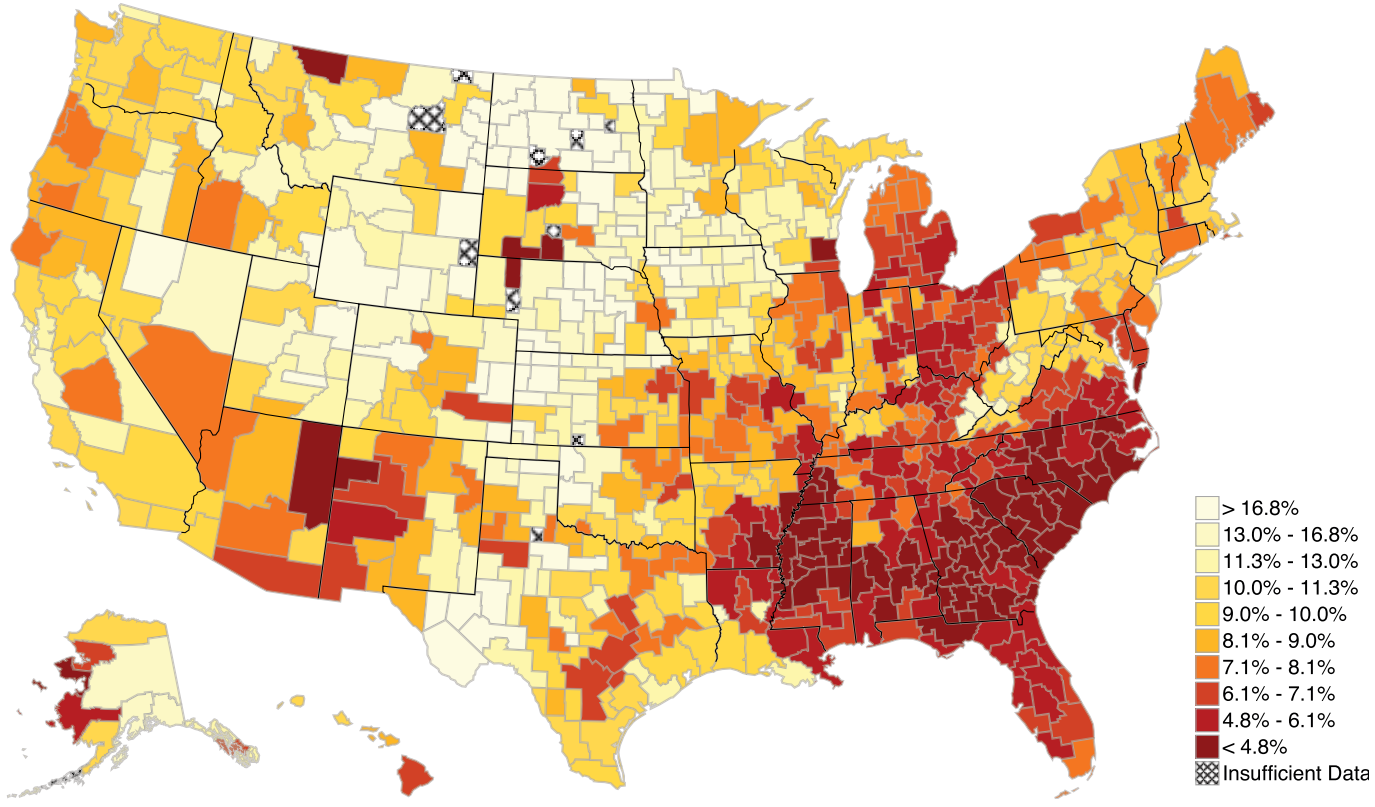


Fig. 1. Economic mobility across U.S. commuting zones. Heat map of upward income mobility using anonymous earnings records on all children in the 1980–1985 birth cohorts. Upward income mobility is measured by the probability that a child reaches the top quintile of the national family income distribution for children, conditional on having parents in the bottom quintile of the family income distribution for parents. Children are assigned to commuting zones based on the location of their parents (when the child was claimed as a dependent), irrespective of where they live as adults. [Reprint of appendix figure VIb in (*5*)]

substantial challenges remain (*15*, *16*). This is particularly true in the United States, where confidentiality and privacy concerns, as well as bureaucratic hurdles, have made accessing administrative data sets and linking records between these data sets relatively cumbersome. European countries such as Norway, Sweden, and Denmark have gone much farther to merge distinct administrative records and facilitate research. Card *et al.* (*3*) have articulated a set of principles for expanding access to administrative data, including competition for data access, transparency, and prevention of disclosure of individual records. We view these as useful guideposts. However, even with today's somewhat piecemeal access to administrative records, it seems clear that these data will play a defining role in economic research over the coming years.

Private sector data: Collection and collaborations

An even more dramatic change in data collection is occurring in the private sector. Whereas the popular press has focused on the vast amount of information collected by Internet companies such as Google, Amazon, and Facebook, firms in every sector of the economy now routinely collect and aggregate data on their customers and their internal businesses. Banks, credit card companies, and insurers collect detailed data on household and business financial interactions. Retailers such as Walmart and Target collect data on consumer spending, wholesale prices, and inventories. Private companies that specialize in data aggregation, such as credit bureaus or marketing companies such as Acxiom, are assembling rich individual-level data on virtually every household.

Although the primary purpose of all this data collection is for business use, there are also potential research applications in economics and other fields. These applications are just starting to be identified and explored, but recent research already provides some useful signals of value.

One potential application of private sector data is to create statistics on aggregate economic activity that can be used to track the economy or as inputs to other research. Already the payroll service company ADP publishes monthly employment statistics in advance of the Bureau of Labor Statistics, MasterCard makes available retail sales numbers, and Zillow generates house price indices at the county level. These data may be less definitive than the eventual government statistics, but in principle they can be provided faster and perhaps at a more granular level, making them useful complements to traditional economic statistics.

The Billion Prices Project (BPP) at the Massachusetts Institute of Technology is a related researcher-driven initiative. The BPP researchers coordinate with Internet retailers to download daily prices and detailed product attributes on hundreds of thousands of products (*17*). These data are used to produce a daily price index. Although the sample of products is, by design, skewed toward products stocked by online retailers, it can replicate quite closely the consumer price index (CPI) series generated by the Bureau of Labor Statistics, with the advantage that the standard consumer series is published monthly, with a lag of several weeks. More interestingly, the project generates price indices for countries in which government statistics are not regularly available or countries in which the published government statistics may be suspect for misreporting, as in Argentina (*18*) (Fig. 2).

Baker *et al.* (*19*) have adopted a similar data aggregation strategy by assembling the full texts of 10 leading newspapers to construct a daily index of economic policy uncertainty. In contrast to the BPP indices, their Economic Policy Uncertainty Index is a new measure of economic activity that does not have a parallel in any formal government report. However, it captures a concept that economists have argued may be important for understanding firm investment decisions and macroeconomic activity.

Recent work suggests that publicly available search query data or tweets on Twitter might be used to provide similar statistics on aggregate activity (*20*, *21*). As an example, Varian and coauthors (*22*, *23*) use Google search data to provide short-run forecasts of unemployment, consumer confidence, and retail sales. Their analysis has parallels to the well-known Google Flu Trends index, which used search query data to predict the Center for Disease Control's measure of flu infections. There is a cautionary note here as well, given that the Google Flu Trends index model broke down as Google changed its underlying search algorithm (*24*). It is likely that successful economic indices using private data will have to be maintained and updated carefully.

A second application of private data is to allow researchers to look "inside" specific firms or markets to study employee or consumer behavior or the operation of different industries. Recent work in this vein often relies on proprietary data obtained through collaborations with private firms. These agreements may take various forms, depending on the sensitivity of the data

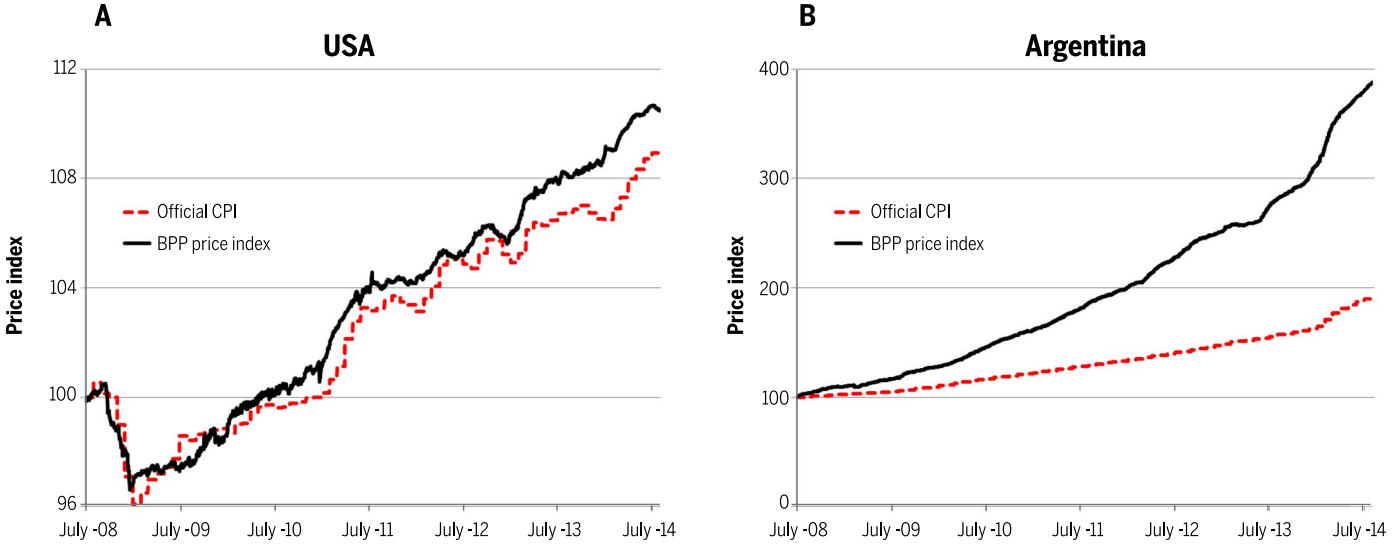


Fig. 2. BPP price index. Dashed red lines show the monthly series for the CPI in the United States (**A**) and Argentina (**B**), as published by the formal government statistics agencies. Solid black lines show the daily price index series, the "State Street's PriceStats Series" produced by the BPP, which uses scraped Internet data on thousands of retail items. All indices are normalized to 100 as of 1 July 2008. In the U.S. context, the two series track each other quite closely, although the BPP index is available in real time and at a more granular level (daily instead of monthly). In the plot for Argentina, the indices diverge considerably, with the BPP index growing at about twice the rate of the official CPI. [Updated version of figure 5 in (*18*), provided courtesy of Alberto Cavallo and Roberto Rigobon, principal investigators of the BPP]

from a privacy and business perspective. Researchers may have to agree to keep the underlying data confidential. In exchange, however, they often get to work with granular employee- or customer-level data that provide a window into the detailed operations of specific businesses or markets.

Relative to government surveys or administrative data, company data have some important differences. Sampling usually is not representative, and how well findings generalize must be evaluated case by case. Data collection emphasizes recency and relevance for business use, so variables and data collection may not be comparable and uniform over long periods. In short, the data are best viewed as "convenience" samples, albeit with potentially enormous scale. At the same time, private entities are not bound by some of the bureaucratic constraints that limit public agencies. The detail of private data can be much greater, the computing resources can be more powerful, and private companies can have far more flexibility to run experiments.

The detail and granularity of private data can offer novel opportunities to study a range of markets. For example, as part of collaboration with researchers at eBay, we recently used their marketplace data to study the effect of sales taxes on Internet shopping (*25*). One of our empirical strategies was to find instances in which multiple consumers clicked on a particular item and then compare consumers located in the same state as the seller (in which case the seller collected sales tax) to consumers located at a similar distance but across state lines (so that no sales tax was collected). The idea of the research design is to assess the sensitivity to sales taxes for otherwise similar consumers looking at the exact same product listing. This sort of analysis would not have been feasible without access to underlying browsing data that allowed us to sift through billions of browsing events to identify the right ones for our empirical strategy.

In two other recent studies (*26*, *27*), also undertaken in collaboration with eBay, we studied the effectiveness of different Internet pricing and sales strategies. To do this, we identified millions of instances in which an online seller listed the same item for sale multiple times with different pricing or shipping fees or using alternative sales mechanisms (e.g., by auction or by posted price) (Fig. 3). We then used the matched listings to estimate the demand response to different item prices and shipping fees, compare auctions with posted price selling, and study alternative sales mechanisms such as auctions with a "buy-now" option. This type of large-scale, microlevel study of market behavior is likely to become more and more common in coming years.

Similar to some of the research described above, a central theme in these papers is the use of highly granular data to find targeted variation that plausibly allows for causal estimates (in these examples, estimates of the effects of sales tax collection, pricing changes, and so forth). In the Internet case, this comes in moving from aggregated data on market prices and quantities to individual browsing data or seller listing data. Having granular data on a market with billions of transactions also provides a chance to analyze specific consumer or market segments: geographic variation, new and used goods, or experienced versus inexperienced sellers. In addition, having richer data can be useful in constructing more nuanced outcome measures. As an example, in studying the effects of sales taxes, we were able to examine not only whether facing a sales tax deterred buyers from purchasing but also whether they continued browsing and then purchased a similar untaxed item.

Large-scale granular data can also be particularly useful for assessing the robustness of identifying assumptions. Virtually every observational study in economics must deal with the critique that even after controlling for sources of confounding, the data do not approximate a controlled experiment. For example, in our work on Internet selling strategies, we aggregated many matched-listing episodes, hoping that each episode might approximate a pricing experiment conducted by the seller. But sometimes sellers may make pricing changes in response to consumer demand, complicating what one can infer from the price change. One way to check if this contaminates the results is to use narrower matching strategies that remove potential sources of confounding—for instance, focusing on cases in which sellers post two offers at the exact same time. This type of extra detective work is much easier with plentiful data.

Collaborations with private sector firms can also give rise to structured economic experiments. This type of research has accelerated

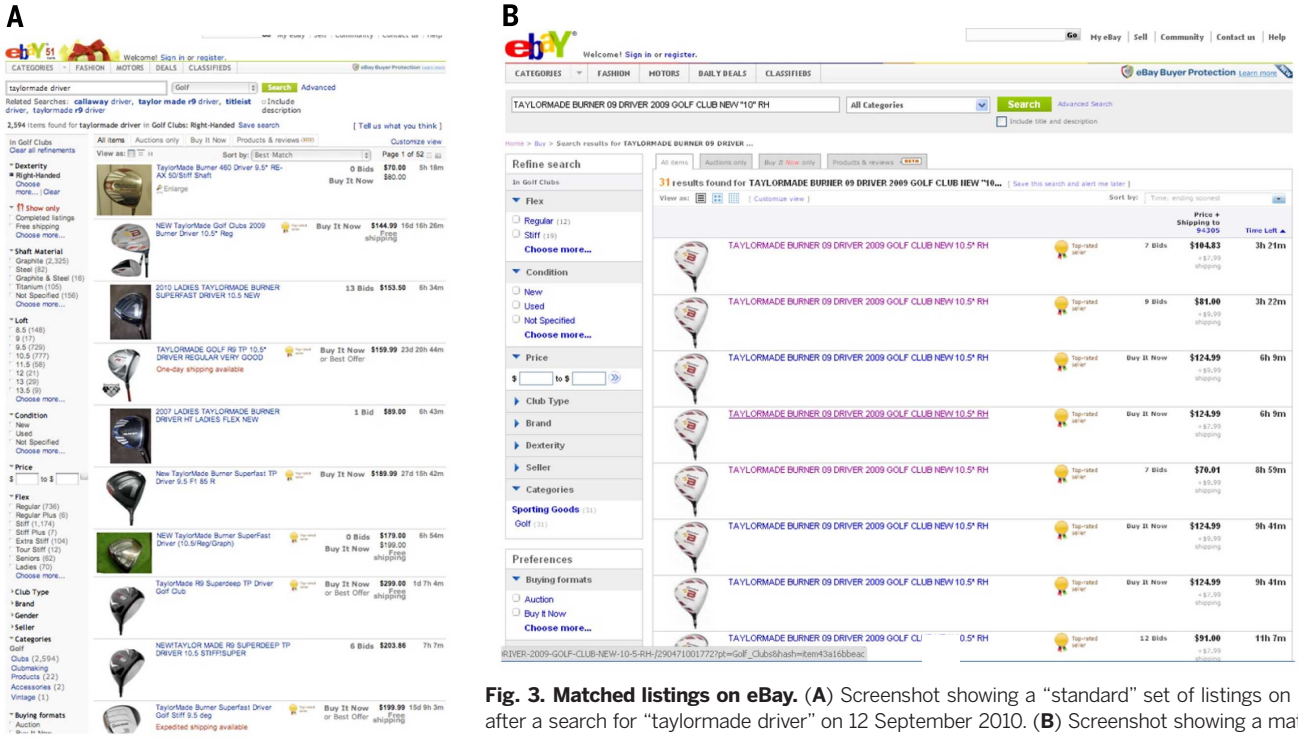


Fig. 3. Matched listings on eBay. (**A**) Screenshot showing a "standard" set of listings on eBay, after a search for "taylormade driver" on 12 September 2010. (**B**) Screenshot showing a matched set. It shows the first 8 out of 31 listings for the same golf driver by the same seller. All of the listings were active on 12 September 2010. Of the eight listings shown, four are offered at a fixed price of $124.99. The other four listings are auctions with slightly varying end times. The listings have different shipping fees (either $7.99 or $9.99). Such matched sets are ubiquitous on eBay and are useful as natural experiments in assessing the effects of changes to sale format and parameters. [Reprint of figure 1 in (*26*)]

and is particularly low-cost and scalable on the Internet, where experimentation is already a standard business practice (*28*, *29*). Recent examples include Ostrovsky and Schwarz (*30*), who worked with Yahoo! to test the use of different reserve prices in advertising auctions; Blake *et al.* (*31*), who worked with eBay to selectively shut down its Google search advertising and track the effect on eBay site visits and sales; and Horton (*32*), who worked with oDesk to provide recommendations to employers about who to hire (*33*).

As in the case of administrative data, economists working with private companies face some challenges, particularly regarding data access. Although companies may be willing to make small, nonsensitive data sets public, researchers usually have to agree to keep data confidential if they want to work directly with company records. As a result, opportunities for other researchers to replicate or extend studies may be limited. In addition, some collaborative research projects are part of broader consulting or employment relationships, raising issues regarding conflict of interest and selectivity in what results are pursued or submitted for publication.

These issues have only recently become a major topic of discussion in economics, as journals and research organizations have begun to adopt policies on transparency and disclosure. As companies capture increasing amounts of economic data, however, it seems almost certain that collaborations between academics and private sector firms will expand, so we hope that disclosure policies will prove effective and that companies will begin to establish open processes for allowing researchers access to data in ways that reasonably maintain privacy and confidentiality. The underlying issues around data privacy and acceptable types of research experiments are clearly sensitive ones that need to be handled with care and thoughtfulness (*34*).

Econometrics, machine learning, and economic theory

Recent economic research using large data sets has relied primarily on traditional econometric techniques. The estimated models usually focus on one or a few coefficients of interest, which often represent the causal effect of a particular policy or policies. Researchers put considerable thought and effort into controlling for heterogeneity or other confounding factors, often using a large set of fixed effects, and into obtaining carefully constructed standard errors for the main parameters of interest. Though studies often focus on a single preferred specification, frequently linear, it is typical to assess the robustness of the results by estimating a variety of alternative specifications and running placebo regressions to see if the preferred model generates false-positive findings.

This approach, both in conception and execution, stands in contrast to some of the data mining methods that have become popular for large-data applications in statistics and computer science [e.g., (*35*, *36*)]. These latter approaches put more emphasis on predictive fit, especially out-of-sample fit, and on the use of data-driven model selection to identify the most meaningful predictive variables (*37*). There often is less attention paid to statistical uncertainty and standard errors and considerably more to model uncertainty. The common techniques in this sort of data mining—classification and regression trees, lasso and methods to estimate sparse models, boosting, model averaging, and cross-validation—have not seen much use in economics (*38*).

There are some good reasons why empirical methods in economics look the way they do. Economists are often interested in assessing the results of a specific policy or testing theories that predict a particular causal relationship. So empirical research tends to place a high degree of importance on the identification of causal effects and on statistical inference to assess the significance of these effects. Having a model with an overall high degree of predictive fit is often viewed as secondary to finding a specification that cleanly identifies a causal effect.

Consider a concrete example: Suppose we set out to measure whether taking online classes improves a worker's earnings. An economist might hope to design an experiment or to find a natural experiment that induced some workers to take online classes for reasons unrelated to their productivity or current earnings (e.g., a change in the advertising or pricing of online classes). Absent an experimental design, however, she might consider estimating a model such as

$$y_i = \alpha + \beta x_i + \boldsymbol{z}_i'\gamma + \varepsilon_i \qquad (1)$$

where y_i is the outcome (an individual's earnings in a given year), x_i is the policy of interest (whether the worker has taken online classes before that year), β is the key parameter of interest (the effect of online education on earnings), α and γ are other parameters, $\boldsymbol{z}_i$ is a set of control variables, and ε_i is an error term.

The hope is that in a group of individuals with the same $\boldsymbol{z}_i$, whether or not an individual decides to take online classes is not related in a meaningful way to their earnings. Better data obviously help. With detailed individual data over time, the control variables might include a dummy variable for every individual in the sample and perhaps for every employer. Then the effect of online education would be estimated by comparing increases in worker earnings for those who take online classes to increases in earnings for those who do not, perhaps even making the comparison within a given firm. The focus of the analysis would be on the estimate of β, its precision, and on whether there were important omitted variables (e.g., a worker becoming more ambitious and deciding to take classes and work harder at the same time) that might confound a causal interpretation.

Given the same data, a machine learning approach might start with the question of exactly what variables predict earnings, given the vast set of possible predictors in the data, and the potential for building a model that predicts earnings well, both in-sample and out-of-sample. Ultimately, a researcher might estimate a model that provides a way to predict earnings for individuals who have and have not taken online classes, but the exact source of variation identifying this effect—in particular, whether it was appropriate to view the effect as causal—and inference on its statistical significance might be more difficult to assess.

This example may help to illustrate a few reasons economists have not immediately shifted to new statistical approaches, despite changes in data availability. An economist might argue that, short of an experimental approach, the first observational approach has the virtue of being transparent or interpretable in how the parameter of interest is identified, as well as conducive to statistical inference on that parameter. Yet a researcher who wanted to predict earnings accurately might view the first model as rather hopeless, particularly if it included a dummy variable for every individual and the researcher wanted to predict out-of-sample.

However, the two approaches are not necessarily in competition. For instance, if only a subset of control variables is truly predictive, an automated model-selection approach may be helpful to identify the relevant ones (*39*, *40*). Data mining methods may also be useful if there are important interaction effects (*41*) so that one cares about predicting effects for specific individuals rather than an average effect for the population. A potential benefit of large data sets is that they allow for more tailored predictions and estimates (e.g., a separate β depending on many specifics of the environment). Rather than estimate only average policy treatment effects, it is possible to build models that map individual characteristics into individual treatment effects and allow for an analysis of more tailored or customized policies.

The potential gains from trade go in the other direction as well. To the extent that machine learning approaches are used to assess the effect of specific policy variables and the estimates are given a causal interpretation, the economists' focus on causal identification is likely to be useful.

Economic theory also plays a crucial role in the analysis of large data sets, in large part because the complexity of many new data sets calls for simpler organizing frameworks. Economic models are useful for this purpose.

The connection between big data and economic theory can already be seen in some applied settings. Consider the design of online advertising auctions and exchanges. These markets—run by companies such as Google, Yahoo!, Facebook, and Microsoft—combine big data predictive models with sophisticated economic market mechanisms. The predictive models are used to assess the likelihood that a given user will click on a given ad. This might be enough for a company such as Google or Facebook, with enormous amounts of data, to figure out which ads to show. However, it does not necessarily tell them how much to charge, and given that each ad impression is arguably distinct, trying to experimentally set hundreds of millions of prices could be a challenge. Instead, these companies use (quite sophisticated) auction mechanisms to set prices.

The operation of the auction market depends on the interplay between the predictive modeling and the incentive properties of the auction. Therefore, making decisions about how to run this type of market requires a sophisticated understanding of both big data predictive modeling and economic theory. In this sense, it is no surprise that over the past several years many of the large e-commerce companies have built economics teams (in some cases, headed by high-profile academic researchers) or combined economists with statisticians and computer scientists or that computer science researchers interested in online marketplaces draw increasingly on economic theory.

More generally, we see some of the main contributions that economists can make in data-rich environments as coming from the organizing framework provided by economic theory. In the past century, most of the major advances in economics came in developing conceptual or mathematical models to study individual decisions, market interactions, or the macroeconomy. Frequently, the key step in successful modeling has been simplification: taking a complex environment and reducing it down to relationships between a few key variables. As data sets become richer and more complex and it is difficult to simply look at the data and visually identify patterns, it becomes increasingly valuable to have stripped-down models to organize one's thinking about what variables to create, what the relationships between them might be, and what hypotheses to test and experiments to run. Although the point is not usually emphasized, there is a sense that the richer the data, the more important it becomes to have an organizing theory to make any progress.

Outlook

This review has discussed the ways in which the data revolution is affecting economic and broader social science research. More granular and comprehensive data surely allow improved measurements of economic effects and outcomes, better answers to old questions, and help in posing new questions and enabling novel research designs. We also believe that new data may change the way economists approach empirical research, as well as the statistical tools they employ.

Several challenges confront economists wishing to take advantage of these large new data sets. These include gaining access to data; developing the data management and programming capabilities needed to work with large-scale data sets (*42*); and, most importantly, thinking of creative approaches to summarize, describe, and analyze the information contained in these data (*29*). Big data is not a substitute for common sense, economic theory, or the need for careful research designs. Nonetheless, there is little doubt in our own minds that it will change the landscape of economic research. Here we have outlined some of the vast opportunities. We look forward to seeing how they will be realized.

REFERENCES AND NOTES

1. D. S. Hamermesh, Six decades of top economics publishing: Who and how? *J. Econ. Lit.* **51**, 162–172 (2013). doi: 10.1257/jel.51.1.162
2. R. Chetty, "Time trends in the use of administrative data for empirical research," presentation slides (2012); http://obs.rc.fas.harvard.edu/chetty/admin_data_trends.pdf.
3. D. Card, R. Chetty, M. Feldstein, E. Saez, "Expanding access to administrative data for research in the United States," NSF SBE 2020 white paper ID 112 (2010); www.nsf.gov/sbe/sbe_2020/submission_detail.cfm?upld_id=112.
4. T. Piketty, E. Saez, Inequality in the long run. *Science* **344**, 838–843 (2014). doi: 10.1126/science.1251936; pmid: 24855258
5. R. Chetty, N. Hendren, P. Kline, E. Saez, Where is the land of opportunity? The geography of intergenerational mobility in the United States. *Q. J. Econ.* 10.1093/qje/qju022 (2014). doi: 10.1093/qje/qju022
6. Dartmouth Atlas of Health Care, www.dartmouthatlas.org.
7. S. G. Rivkin, E. A. Hanushek, J. F. Kain, Teachers, schools and academic achievement. *Econometrica* **73**, 417–458 (2005). doi: 10.1111/j.1468-0262.2005.00584.x
8. C. Syverson, What determines productivity? *J. Econ. Lit.* **49**, 326–365 (2011). doi: 10.1257/jel.49.2.326
9. J. M. Abowd, F. Kramarz, D. N. Margolis, High wage workers and high wage firms. *Econometrica* **67**, 251–333 (1999). doi: 10.1111/1468-0262.00020
10. A. Akerman, I. Gaarder, M. Mogstad, "The skill complementarity of broadband Internet," Institute for the Study of Labor (IZA) discussion paper no. 7762 (2013); http://ftp.iza.org/dp7762.pdf.
11. R. Chetty, J. Friedman, J. Rockoff, Measuring the impacts of teachers I: Evaluating bias in teacher value-added estimates. *Am. Econ. Rev.* **104**, 2593–2632 (2014). doi: 10.1257/aer.104.9.2593
12. R. Chetty, J. Friedman, J. Rockoff, Measuring the impacts of teachers II: Teacher value-added and student outcomes in adulthood. *Am. Econ. Rev.* **104**, 2633–2679 (2014). doi: 10.1257/aer.104.9.2633
13. R. Chetty *et al*., How does your kindergarten classroom affect your earnings? Evidence from Project Star. *Q. J. Econ.* **126**, 1593–1660 (2011). doi: 10.1093/qje/qjr041; pmid: 22256342
14. S. L. Taubman, H. L. Allen, B. J. Wright, K. Baicker, A. N. Finkelstein, Medicaid increases emergency-department use: Evidence from Oregon's health insurance experiment. *Science* **343**, 263–268 (2014). doi: 10.1126/science.1246183; pmid: 24385603
15. G. King, Ensuring the data-rich future of the social sciences. *Science* **331**, 719–721 (2011). doi: 10.1126/science.1197872; pmid: 21311013
16. H. C. Kum, S. Ahalt, T. M. Carsey, Dealing with data: Governments records. *Science* **332**, 1263 (2011). doi: 10.1126/science.332.6035.1263-a; pmid: 21659589
17. A. Cavallo, "Scraped data and sticky prices," Massachusetts Institute of Technology Sloan working paper no. 4976-12 (2012); www.mit.edu/~afc/papers/Cavallo-Scraped.pdf.
18. A. Cavallo, Online and official price indexes: Measuring Argentina's inflation. *J. Monet. Econ.* **60**, 152–165 (2012). doi: 10.1016/j.jmoneco.2012.10.002
19. S. Baker, N. Bloom, S. Davis, "Measuring economic policy uncertainty," Chicago Booth research paper no. 13-02 (2013); http://papers.ssrn.com/sol3/papers.cfm?abstract_id=2198490.
20. S. Goel, J. M. Hofman, S. Lahaie, D. M. Pennock, D. J. Watts, Predicting consumer behavior with Web search. *Proc. Natl. Acad. Sci. U.S.A.* **107**, 17486–17490 (2010). doi: 10.1073/pnas.1005962107; pmid: 20876140
21. D. Antenucci, M. Cafarella, M. Levenstein, C. Re, M. Shapiro, "Using social media to measure labor market flows," National Bureau of Economic Research (NBER) working paper no. 20010 (2014); www.nber.org/papers/w20010.
22. H. Choi, H. Varian, Predicting the present with Google trends. *Econ. Rec.* **88**, 2–9 (2012). doi: 10.1111/j.1475-4932.2012.00809.x
23. H. Varian, S. Scott, Predicting the present with Bayesian structural time series. *Int. J. Math. Model. Numer. Optim.* **5**, 4–23 (2014). doi: 10.1504/IJMMNO.2014.059942
24. D. Lazer, R. Kennedy, G. King, A. Vespignani, The parable of Google flu: Traps in big data analysis. *Science* **343**, 1203–1205 (2014). pmid: 24626916
25. L. Einav, D. Knoepfle, J. Levin, N. Sundaresan, Sales taxes and Internet commerce. *Am. Econ. Rev.* **104**, 1–26 (2014). doi: 10.1257/aer.104.1.1
26. L. Einav, T. Kuchler, J. Levin, N. Sundaresan, "Learning from seller experiments in online markets," NBER working paper no. 17385; www.nber.org/papers/w17385.
27. L. Einav, C. Farronato, J. Levin, N. Sundaresan, "Sales mechanisms in online markets: What happened to Internet auctions?" NBER working paper no. 19021 (2013); www.nber.org/papers/w19021.
28. R. Kohavi, R. Longbotham, D. Sommerfield, R. Henne, Controlled experiments on the Web: Survey and practical guide. *Data Min. Knowl. Discov.* **18**, 140–181 (2009). doi: 10.1007/s10618-008-0114-1
29. H. Varian, "Beyond big data," presented at the National Associate for Business Economics Annual Meeting, San Francisco, CA, 7 to 10 September 2013; http://people.ischool.berkeley.edu/~hal/Papers/2013/BeyondBigDataPaperFINAL.pdf.
30. M. Ostrovsky, M. Schwarz, "Reserve prices in Internet advertising auctions: A field experiment," Stanford University Graduate School of Business research paper no. 2054 (2009); http://papers.ssrn.com/sol3/papers.cfm?abstract_id=1573947.
31. T. Blake, C. Nosko, S. Tadelis, "Consumer heterogeneity and paid search effectiveness: A large scale field experiment." NBER working paper no. 20171; www.nber.org/papers/w20171.
32. J. J. Horton, "The effects of subsidizing employer search," New York University working paper (2013); http://papers.ssrn.com/sol3/papers.cfm?abstract_id=2346486.
33. Another example is Lewis and Reiley (*43*), who report on consumer advertising experiments done in conjunction with Yahoo!. These experiments have become common, although Lewis and Rao (*44*) have recently argued that extracting useful information from them may be more challenging than one might have hoped or expected.
34. The recent episode involving an experiment that manipulated Facebook's newsfeed (*45*) is a case in point.
35. T. Hastie, R. Tibshirani, J. Friedman, *The Elements of Statistical Learning: Data Mining, Inference and Prediction* (Springer, New York, 2009).
36. A. Rajaraman, J. D. Ullman, *Mining of Massive Datasets* (Cambridge Univ. Press, New York, 2011).
37. A. Vespignani, Predicting the behavior of techno-social systems. *Science* **325**, 425–428 (2009). doi: 10.1126/science.1171990; pmid: 19628859
38. This statement mainly applies to microeconomics; there is more work in time-series macroeconomics that uses such methods.
39. A. Belloni, D. Chen, V. Chernozhukov, C. Hansen, Sparse models and methods for optimal instruments with an application to eminent domain. *Econometrica* **80**, 2369–2429 (2012). doi: 10.3982/ECTA9626
40. A. Belloni, V. Chernozhukov, C. Hansen, "Inference on treatment effects after selection amongst high-dimensional controls," Cemmap working paper no. CWP10/12 (2012); http://arxiv.org/abs/1201.0224.
41. H. Varian, Machine learning: New tricks for econometrics. *J. Econ. Perspect.* **28**, 3–28 (2014). doi: 10.1257/jep.28.2.3
42. D. Lazer *et al*., Computational social science. *Science* **323**, 721–723 (2009). doi: 10.1126/science.1167742 pmid: 19197046
43. R. Lewis, D. Reiley, Online ads and offline sales: Measuring the effects of retail advertising via a controlled experiment on Yahoo! *Quant. Mark. Econ.* **12**, 235–266 (2014). doi: 10.1007/s11129-014-9146-6
44. R. A. Lewis, J. M. Rao, "The unfavorable economics of measuring the returns to advertising," working paper (2014); http://papers.ssrn.com/sol3/papers.cfm?abstract_id=2367103.
45. R. Albergotti, "Facebook experiments had few limits," *Wall Street Journal*, 2 July 2014, http://online.wsj.com/articles/facebook-experiments-had-few-limits-1404344378.
46. L. Einav, J. Levin, "The data revolution and economic analysis," in *Innovation Policy and the Economy*, J. Lerner, S. Stern, Eds. (Univ. of Chicago Press, Chicago, 2014), vol. 14, pp. 1–24.

ACKNOWLEDGMENTS

Parts of this Review draw on an earlier article (*46*). We have benefited from discussions with S. Athey, P. McAfee, and H. Varian. We acknowledge research support from the NSF, the Alfred P. Sloan Foundation, and the Toulouse Network on Information Technology.

10.1126/science.1243089

RESEARCH ARTICLE SUMMARY

LOCAL TRANSLATION

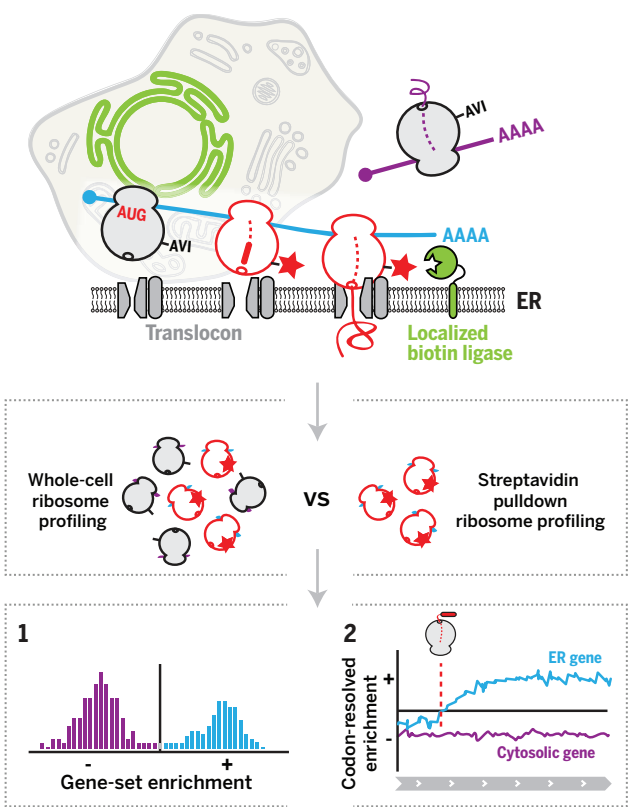
Principles of ER cotranslational translocation revealed by proximity-specific ribosome profiling

Calvin H. Jan, Christopher C. Williams, Jonathan S. Weissman*

INTRODUCTION: Localized protein synthesis plays a critical role in creating subcellular structures by allowing protein production at the site of action and in response to local cellular need. Local translation is involved in diverse processes, including developmental patterning, cellular motility, synaptic plasticity, and protein trafficking through the secretory pathway. Despite this broad importance, few gene expression tools are available that faithfully preserve spatial information. We developed a flexible deep sequencing–based methodology (termed proximity-specific ribosome profiling) that enables precise characterization of localized protein synthesis. We applied our method to analyze translation at the endoplasmic reticulum (ER) in yeast and mammalian cells.

RATIONALE: The basis of our approach is to biotinylate ribosomes in intact cells in a manner dependent on their subcellular location. This is accomplished through the coexpression of a spatially restricted biotin ligase (BirA) fusion protein together with ribosomes containing an AviTag, which makes them substrates for BirA. Controlled pulses of biotin are then provided to allow for spatiotemporal control of ribosome labeling. This in vivo biotinylation enables the recovery of ribosomes from defined locations, including those that cannot be purified by classical cell fractionation techniques. Combining this purification strategy with ribosome profiling, the deep sequencing of ribosome-protected mRNA fragments, provides subcodon resolution of which messages were translated at the site of interest.

RESULTS: We identified several principles used by cells to coordinate translation with ER targeting. Cotranslational targeting to the ER is pervasive and is principally determined by the location of the hydrophobic targeting sequence within the protein, rather than the mechanism of targeting or translocation. The position of this hydrophobic domain within the open reading frame determines the duration of time a targeted ribosome nascent-chain complex (RNC) can associate with the ER. Our data suggest a role for polysomes in retaining mRNAs at the ER, allowing for efficient targeting of RNCs for translocation.



Proximity-specific ribosome profiling provides spatiotemporal details of translation at the ER. Biotin ligase is localized to the ER as a fusion protein, where it biotinylates Avi-tagged ribosomes at the ER surface. Ribosome profiling is performed on streptavidin-purified ribosomes and compared to whole-cell profiling to resolve which genes are translated at the ER (1) and how much nascent chain was required to target the ribosome to the translocon (2).

Position-specific analyses revealed that distinct translocon complexes engage nascent chains at different points during synthesis. Most proteins engage the ER immediately after or even before the signal sequence or signal anchor emerges from the ribosome. These nascent chains typically undergo a conformational rearrangement within the translocon, the proteinaceous tunnel through which nascent proteins cross the ER membrane. This rearrangement results in a "looped" conformation of the nascent chains, with their N termini facing the cytosol. This conformation is required for signal sequence processing. However, we discovered a class of Sec66-dependent proteins that engage only when they are long enough to adopt the looped conformation.

Finally, we monitored the fate of ER-associated ribosomes after translation termination using pulsed-labeling experiments. These data demonstrated that ER-associated ribosomes readily exchanged into the cytosol after at most a few rounds of translation at the ER.

CONCLUSION: These results, together with those in an accompanying Report on translation at mitochondria, establish proximity-specific ribosome profiling as a robust and general tool. In principle, this method can be applied to any site that can be specified by a biotin-ligase fusion protein. Thus, our approach provides in vivo access to a broad spectrum of subpopulations of ribosomes defined either by their subcellular locations or through their interactions with specific factors, such as chaperones. ■

ON OUR WEB SITE

Read the full article at http://dx.doi.org/10.1126/science.1257521

RELATED ITEMS IN SCIENCE

C. C. Williams, C. H. Jan, J. S. Weissman, *Science* **346**, 1257522 (2014).
S. Shao, R. S. Hegde, *Science* **346**, 701–702 (2014).

Department of Cellular and Molecular Pharmacology, Howard Hughes Medical Institute, California Institute for Quantitative Biosciences, Center for RNA Systems Biology, University of California, San Francisco, San Francisco, CA 94158, USA.
*Corresponding author.
E-mail: jonathan.weissman@ucsf.edu
Cite this article as C. H. Jan, C. C. Williams, J. S. Weissman, *Science* **346**, 748–751 (2014).
DOI: 10.1126/science.1257521

Published by AAAS

RESEARCH ARTICLE

LOCAL TRANSLATION

Principles of ER cotranslational translocation revealed by proximity-specific ribosome profiling

Calvin H. Jan,* Christopher C. Williams,* Jonathan S. Weissman†

Localized protein synthesis is a fundamental mechanism for creating distinct subcellular environments. Here we developed a generalizable proximity-specific ribosome profiling strategy that enables global analysis of translation in defined subcellular locations. We applied this approach to the endoplasmic reticulum (ER) in yeast and mammals. We observed the large majority of secretory proteins to be cotranslationally translocated, including substrates capable of posttranslational insertion in vitro. Distinct translocon complexes engaged nascent chains at different points during synthesis. Whereas most proteins engaged the ER immediately after or even before signal sequence (SS) emergence, a class of Sec66-dependent proteins entered with a looped SS conformation. Finally, we observed rapid ribosome exchange into the cytosol after translation termination. These data provide insights into how distinct translocation mechanisms act in concert to promote efficient cotranslational recruitment.

Eukaryotic cells contain highly specialized subcellular environments, including both membrane- and nonmembrane-bound compartments. Localized protein synthesis can play a critical role in creating these subcellular structures by allowing protein production at the site of action and in response to local cellular need. Local translation is involved in diverse processes, including developmental patterning, cellular motility, synaptic plasticity, and protein trafficking through the secretory pathway (*1*). Dysfunctional RNA localization is linked to neurodevelopmental and neurodegenerative diseases (*2*). Numerous microscopy-based studies of individual mRNAs have demonstrated a breadth of subcellular localizations, and recent genome-wide mapping of transcript localization within cells and tissues has further emphasized the widespread spatial control of mRNA (*3*).

By contrast, global approaches for studying spatial control of protein synthesis are limited to bulk interrogations that cannot uniquely identify proteins—such as the RiboPuroMycylation (*4*) and FUNCAT (*5*) methods—or require careful biochemical fractionation of the compartment of interest (*6*), limiting both the location and resolution of analyses. These considerations motivated us to develop a generalizable strategy for enabling proximity-specific ribosome profiling that preserves in vivo spatiotemporal information about the site of synthesis. We employed a two-step approach wherein we (i) used a spatially restricted biotin ligase (BirA) to mark ribosomes containing a biotin acceptor peptide (AviTag) in live cells with all membranes and spatial relations intact (*7*) and (ii) read out the translational activity of purified biotinylated ribosomes with ribosome profiling (the deep sequencing of ribosome-protected fragments) (*8*) that quantitatively reports on genome-wide translation with subcodon resolution (Fig. 1A).

Here we used this proximity-specific ribosome profiling strategy to study protein synthesis at the endoplasmic reticulum (ER), a major site of localized protein synthesis where a diverse set of proteins enter the secretory pathway. Work spanning several decades has revealed multiple routes of targeting nascent proteins to the ER (*9*). These include the canonical signal recognition particle (SRP)–dependent pathway in which translation is halted upon binding of SRP to hydrophobic sequences, and resumes only when the ribosome engages the translocon. Additionally, there are several SRP-independent pathways, although these are generally considered to mediate posttranslational import (*9*). Extensive studies have also elucidated the core translocational machinery necessary for protein import across and into the ER membrane, and identified accessory translocon factors in yeast and metazoans thought to increase the efficiency of protein import or assist the translocation of specific proteins (*10*).

Despite our in-depth mechanistic and structural understanding of these steps, the broader cellular organization of these targeting routes in vivo has remained largely unexplored. Experimental limitations have prevented a systematic characterization of substrate flux through the various ER-targeting pathways in unperturbed cells. Similarly, our understanding of rough ER dynamics remains limited because of the difficulty in precisely measuring both the timing of ribosome-nascent chain (RNC) recruitment to the translocation machinery, as well as RNC fate following translation termination. Here we developed and applied proximity-specific ribosome profiling to address these fundamental questions.

A general approach for subcellular ribosome profiling: Development and application to the ER

To establish the proximity-specific ribosome profiling method, we implemented the following five steps: (i) introduction of a nonperturbing ribosome tag consisting of a tobacco etch virus (TEV) protease-cleavable AviTag; (ii) genetic targeting of BirA to a subcellular location of interest; (iii) temporal control of ribosome biotinylation in vivo; (iv) inhibition of postlysis biotinylation; and (v) selective isolation of biotinylated ribosomes and specific elution via TEV cleavage (Fig. 1A). We developed and validated these steps in the budding yeast *Saccharomyces cerevisiae*, as well as in the human embryonic kidney–293 (HEK-293) cell line.

Informed by a recent structure of the yeast 80*S* ribosome (*11*), we expressed Avi-tagged versions of several candidate ribosomal proteins with surface-accessible termini. We identified multiple subunits that when tagged and expressed from their endogenous loci, including the natural 3′ untranslated region (UTR), were incorporated into ribosomes and covered growth defects seen in deletion mutants. These included C-terminally tagged *RPL16* and *RPS2* [also called uL13 and uS5 (*12*)], which were used for subsequent experiments (Fig. 1B). N-terminally tagged *RPL10a* [uL1] was used for mammalian studies (*13*) (fig. S1A).

For our yeast studies, we constructed three different ER-localized BirA fusion proteins, as well as cytosolic and mitochondrial controls (Fig. 1C). To broadly capture the translational activity of all ER-associated ribosomes, we localized BirA to the ER using the C-terminal tail-anchor (TA) from *UBC6* (*14*). To more specifically examine translation at two known translocation entry points to the ER, we fused BirA to *SEC63*, a member of the SEC complex that specifically associates with the Sec61 translocon (*15*), and to *SSH1*, a paralog of the canonical Sec61 translocon that interacts with SRP but not the SEC complex (*16*). For the mitochondrial studies, we used a BirA-fusion to *OM45*, a major constituent of the mitochondrial outer membrane (MOM). Finally, the mammalian studies used a BirA fusion to Sec61β that uniformly labeled the ER (*17*). In all cases, the BirA fusion proteins showed the expected localization (Fig. 1C and fig. S1B).

Because of the potential cycling of ribosomes between different cellular locations, especially following translation termination, it was critical to be able to induce rapid ribosome biotinylation while also suppressing any constitutive background BirA activity. Although biotin is an essential

Department of Cellular and Molecular Pharmacology, Howard Hughes Medical Institute, California Institute for Quantitative Biosciences, Center for RNA Systems Biology, University of California, San Francisco, San Francisco, CA 94158, USA.
*These authors contributed equally to this work.
†Corresponding author. E-mail: jonathan.weissman@ucsf.edu

cofactor for both yeast and mammalian cells, titrating biotin levels in the growth media (7) suppressed BirA activity to undetectable levels without affecting cell growth (fig. S2). Brief biotin pulses were sufficient to give a robust biotinylation signal in live cells (Fig. 1E), and it was possible to prevent postlysis biotinylation by depleting lysates of biotin and adenosine 5′-triphosphate (ATP) (Fig. 1D and fig. S2). This procedure allowed us to achieve rapid (on the time scale of polypeptide synthesis) and efficient biotinylation of both our 40*S* and 60*S* Avi-tagged ribosomes using a cytosolic BirA. In marked contrast, ER-localized BirAs failed to label the 40*S* Avi-tagged ribosomal subunit but retained the ability to robustly label the 60*S* Avi-tagged subunit (Fig. 1E). Based on the length of our BirA tether, which is too short to allow biotinylation of the 40*S* subunit of a docked, translocating ribosome, this result demonstrates the specific biotinylation of oriented translocating ribosomes over those that passively encounter the ER membrane. Finally, we optimized the purification of biotinylated, ribonuclease-digested monosomes (fig. S3) (18).

Validation of proximity-specific ribosome profiling

We performed proximity-specific ribosome profiling in *S. cerevisiae* using the three different ER-localized BirA constructs, as well as the cytosolic and mitochondrially localized controls (Fig. 2A), and in mammalian HEK-293 cells using an ER-localized BirA fusion protein. For each experiment, brief treatment with the translation elongation inhibitor cycloheximide (CHX), which preserves the ribosome position along an mRNA, was followed by a biotin pulse. Subsequent to processing and sequencing, we determined an enrichment value for each gene by taking the $\log_2$ ratio of ribosome footprint densities in the matched streptavidin-pulldown versus input whole-cell ribosome profiling samples. Enrichment metrics obtained from the same BirA were highly reproducible between replicates (Fig. 2B; Ssh1 Pearson r = 0.97; Sec63 Pearson r = 0.98) and robust across expression levels (fig. S4)

Targeting of BirA to the cytosol yielded a narrow range of enrichment values (90% of genes fell within −0.2 to +0.2 $\log_2$ enrichment units), demonstrating that our protocol for isolating biotinylated monosomes introduced minimal bias. We detected a modest but significant ($P < 1 \times 10^{-15}$, Kolmogorov-Smirnov test) depletion of secreted genes, consistent with the expected lower accessibility of ER-docked ribosomes. By contrast, BirA targeted to mitochondria produced a clear bimodal distribution, enriching for genes annotated to localize to this cellular compartment (19). An in-depth analysis of translation at the mitochondrial outer membrane is presented in an accompanying Report (20). Targeting of BirA to the ER membrane inverted the mitochondrial enrichment pattern, cleanly separating secreted proteins from those synthesized in the cytosol or targeted to mitochondria. Ssh1, Sec63, and Ubc6 ER-localized BirA fusion

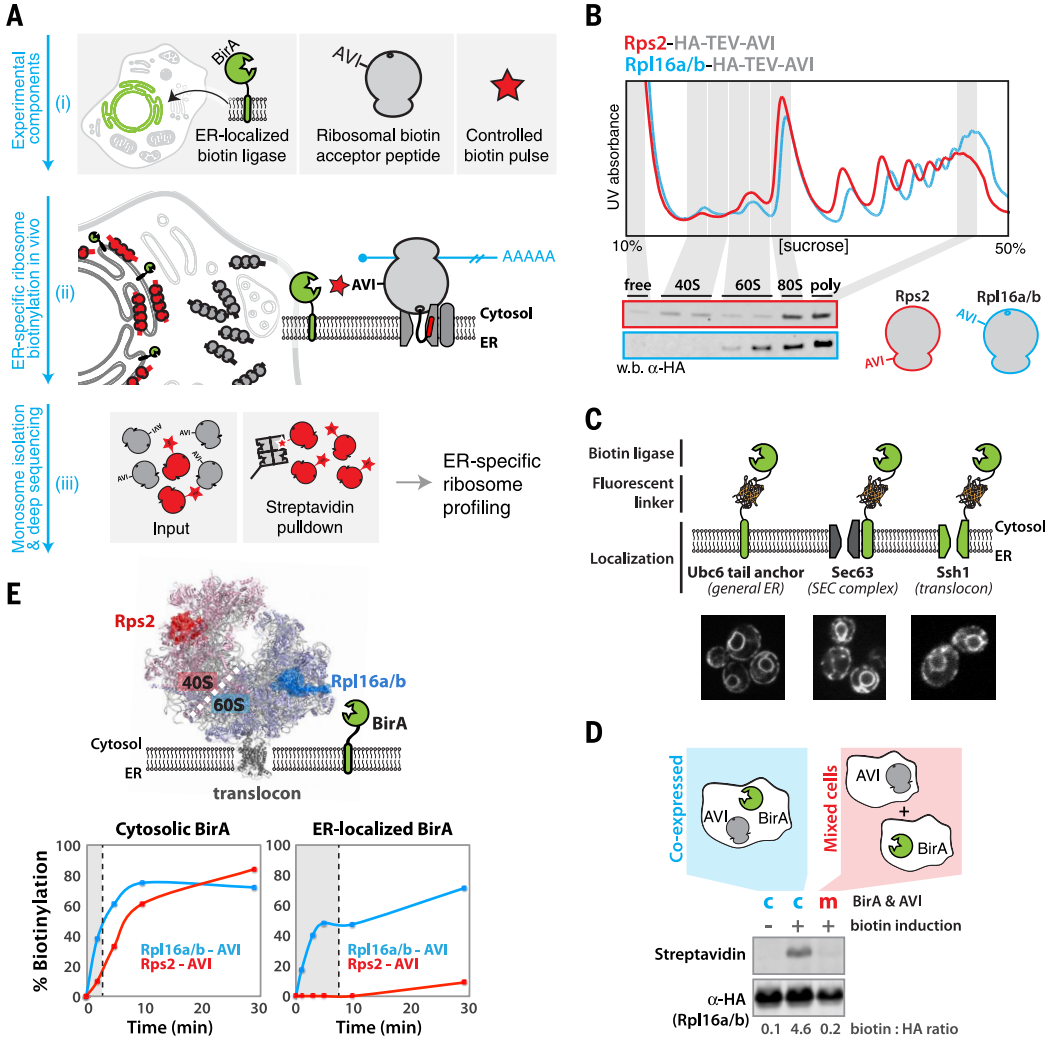


Fig. 1. A system for in vivo proximity-dependent ribosome biotinylation to monitor local protein synthesis at the ER. (**A**) Schematic for proximity-specific ribosome profiling. (i) The *Escherichia coli* biotin ligase BirA is localized to a subcellular site of interest in cells expressing an Avi-tagged ribosomal protein and grown in low-biotin conditions. (ii) A biotin pulse is applied, resulting in specific biotinylation of ribosomes in close physical proximity to the localized BirA. (iii) Ribosome profiling of paired input (gray and red) and isolated biotinylated (red) monosomes reveals codon-resolved translational enrichment specific to the BirA locale. (**B**) Fractionation of yeast lysates derived from strains containing scarless C-terminal Rps2 or Rpl16a/b hemagglutinin (HA)-TEV-AviTags on 10 to 50% sucrose gradients. Polysome traces demonstrate proper ribosomal assembly, and incorporation of tags into polysomes demonstrates their nonperturbative nature. (**C**) ER localization of BirA fusion proteins used in this study. BirA-mVenus-Ubc6, Sec63-mVenus-BirA, and BirA-mVenus-Ssh1 all localize to the perinuclear and cortical ER. (**D**) Western blot analysis demonstrates that biotinylation of ribosomal AviTags does not occur before the addition of excess biotin or postlysis in our assay. (**E**) Biotinylation kinetics of 40S and 60S AviTags by BirAs localized to the cytosol or ER (Sec63). Favorable kinetics were achieved independent of localization, and preferential 60S biotinylation demonstrates the specificity of the ER-localized ligase for oriented ER ribosomes. Shaded regions indicate biotinylation times used in subsequent sequencing experiments.

constructs labeled ribosomes translating similar sets of secretome genes [defined in (*21*)], though we observed pronounced differences in the point during translation at which RNCs interact with these BirA fusions (explored below). To determine whether other gene categories were significantly overrepresented in the enriched populations of our ER data sets, we performed gene ontology (GO-) term analysis on gene categories in yeast and mammalian cells that were enriched above a threshold derived from a receiver operator characteristic (ROC) analysis (Fig. 2, C and D, and fig. S5). In both yeast and HEK-293 cells, enriched gene sets were exclusively from the secretome (*18*). However, a substantial number of mammalian secretome transcripts predicted by Phobius (*22*) to encode secretory proteins were not enriched in our assay. This set of genes was enriched in GO-terms for nucleus and cytosol when compared to all secretome genes, arguing that these proteins represent potential false positives in the computationally predicted secretory gene set. This discrepancy serves to highlight both the sensitivity and utility of our approach for experimentally defining proteins that are targeted to specific cellular compartments.

We noted that peroxisomal proteins exhibited heterogeneous ER translational enrichment. The peroxisome is a highly conserved organelle responsible for lipid catabolism whose mechanism of biogenesis has been controversial. There is evidence for both de novo peroxisome generation from ER-derived vesicles, as well as for derivation from preexisting peroxisomes through growth and fission (*23*). Our data reveal that 16 of 54 yeast peroxisomal proteins showed clear cotranslational enrichment. Consistent with previous targeted studies in yeast (*24*), a unifying determinant for this ER targeting is the presence of one or more transmembrane domains (TMDs)—we found no evidence for the enrichment of peroxisomal matrix proteins (Fig. 2E). Notably, this partitioning was also seen in mammalian cells (fig. S6). Thus, peroxisomes appear to obtain transmembrane proteins from the ER and matrix proteins from the cytosol.

Cotranslational targeting of SRP-dependent and -independent substrates in vivo

Whereas a subset of proteins are strictly reliant on SRP for ER targeting, a process that is thought to be obligatorily cotranslational, import of other proteins occurs efficiently without SRP when measured both in vitro and in vivo (*21*, *25*). A recent in silico analysis revealed that ~40% of yeast secretome substrates use the less-studied SRP-independent pathway (*21*). SRP-independent translocation depends on translocon accessory factors, as well as the luminal chaperone Kar2/BiP, and in vitro can occur efficiently after translation (*26*, *27*) (Fig. 3A).

Notably, we found that the vast majority of secretory proteins undergo cotranslational targeting in vivo, irrespective of their dependence on SRP (Fig. 3B). This pattern held across all BirA fusions (fig. S7) for 162 genes experimentally validated as SRP-dependent or –independent (*21*, *25*), as well as for an additional 756 genes whose SRP dependence was predicted using a hydropathy-based analysis (*21*).

It was a formal possibility that the apparent cotranslational ER enrichment of these translating messages was a result of brief treatment with the translation elongation inhibitor (CHX) prior to biotinylation, because this provides extra time for the RNC complex to engage the translocon. We evaluated this possibility by omitting translation inhibitors and labeling with biotin

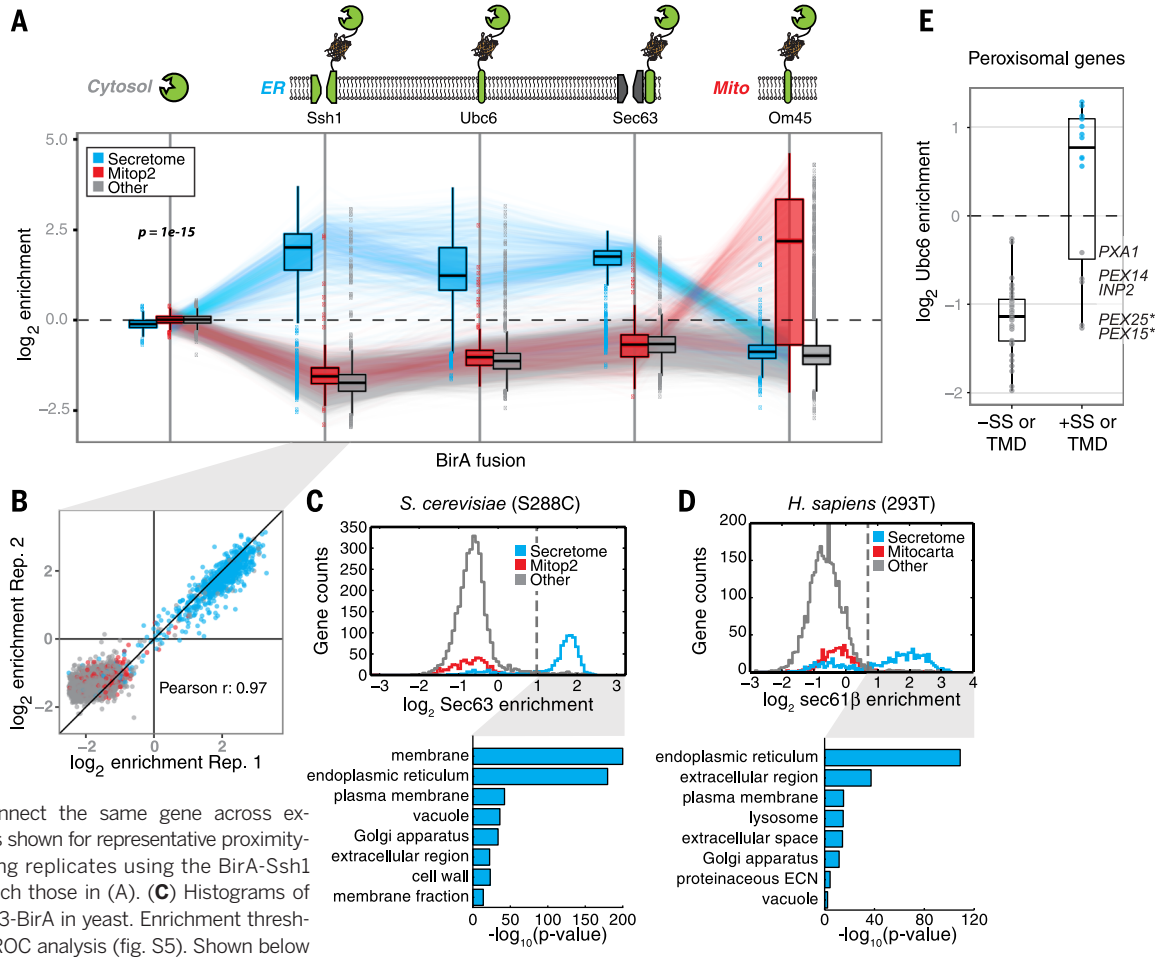


Fig. 2. Specificity of proximity-dependent ribosome profiling across multiple systems. (**A**) Boxplots of the $\log_2$ enrichment distributions for secretome (blue), curated mitochondrial (red), and all other (gray) gene categories obtained from proximity-specific ribosome profiling experiments in yeast using different BirA fusions. Biotinylation was carried out in the presence of CHX for 2 min (cytosolic, mitochondria) or 7 min (ER). Enrichments were computed for each reliably expressed gene as the $\log_2$ ratio of biotinylated footprint density (RPM) over the corresponding density from the matched input whole-cell ribosome profiling experiment. Where possible, lines connect the same gene across experiments. (**B**) Enrichments shown for representative proximity-specific ribosome profiling replicates using the BirA-Ssh1 fusion protein. Colors match those in (A). (**C**) Histograms of $\log_2$ enrichments for Sec63-BirA in yeast. Enrichment thresholds were determined by ROC analysis (fig. S5). Shown below are the corresponding enrichment analyses of GO-slim cellular components for robustly enriched genes versus expressed genes. Colors match those in (A). (**D**) As in (C) for BirA-Sec61β in HEK-293T cells. Additionally, GO-term analysis of dis-enriched secretome genes versus expressed secretome genes is shown. (**E**) Gene enrichments obtained with the general BirA-Ubc6 ER marker in yeast, for well-expressed CHX-independent peroxisomal genes. SS and TMD annotations were predicted by SignalP and TMHMM, respectively. * denotes necessarily posttranslational tail-anchor TMDs [see (*18*)].

for 1 min, a time scale comparable to that of a single round of polypeptide synthesis. For the large majority of SRP-dependent and -independent substrates, levels of translational enrichment were not dependent on CHX (Fig. 3B). Intriguingly, ribosomes translating a small minority of the SRP-independent proteins lost their enrichment, suggesting that in an unperturbed setting, these proteins translocate posttranslationally.

Thus, SRP independence is not synonymous with posttranslational translocation; import concurrent with protein synthesis is the principal route into the ER in vivo. By effectively coupling translation and translocation for the large majority of proteins entering the secretory pathway, the cell minimizes the dangers associated with having a cytosolic cohort of untranslocated, aggregation-prone proteins (*28*). Understanding how the cell achieves cotranslational translocation of SRP-independent messages remains unclear.

Comprehensive analysis of co- versus posttranslational translocation in vivo

Having uncoupled SRP independence from posttranslational translocation, we sought to better understand the determinants for partitioning between the co- and posttranslational import pathways. To classify genes on the basis of their ER translational enrichment, we systematically identified genes whose enrichments were dependent on CHX using a support vector machine (SVM) classifier trained to distinguish between ~140 proteins characterized empirically as being CHX-dependent or -independent (*18*). This SVM analysis enabled us to systematically characterize the import of proteins as being either cotranslational (CHX-independent), cotranslational translocation that is dependent upon (or enhanced by) treatment with a translation inhibitor (CHX-dependent), or obligatorily posttranslational (dis-enriched) (Fig. 3C). The enrichment of CHX-dependent proteins was greatest for Sec63-BirA, consistent with its role in co- and posttranslational translocation (fig. S8). These differences demonstrate the specificity of ribosome labeling by BirA fusion proteins and suggest that cotranslational insertion (CHX-independent) typically occurs through both translocons.

The SVM analysis indicated that the large majority (681 of 837) of Phobius-predicted secretory genes were translated at the ER independent of CHX. Of the remaining predicted secretory proteins, 63 were dependent on CHX for enrichment, whereas 93 were not enriched under any condition tested. The latter dis-enriched group contained nearly all of the roughly 50 annotated TA proteins whose C-terminal TMDs preclude cotranslational recognition and that are known to be targeted to the ER posttranslationally through the guided entry of TA proteins (GET) pathway (*29*, *30*).

What, then, accounts for the remaining proteins whose translocation is not strictly cotranslational? The position of an ER-targeting signal within a protein imposes restrictions on when during synthesis targeting may occur, and thus might be an important determinant. Indeed, robustly enriched CHX-independent secreted genes and dis-enriched TA genes fall on the opposite sides of this spectrum, with extreme N- and C-terminal ER-targeting signals, respectively (Fig. 3D). The targeting signals of proteins dependent on CHX for cotranslational targeting to the ER fall in between these two extremes, often present far downstream in relation to their overall gene length. Following cotranslational targeting to the ER, translation of long downstream regions leads to prolonged mRNA retention on the ER surface, which would be mediated by multiple translocating RNCs. In contrast, short downstream regions are unlikely to stably tether the mRNA to the ER following targeting (fig. S9). The CHX dependence of genes with short

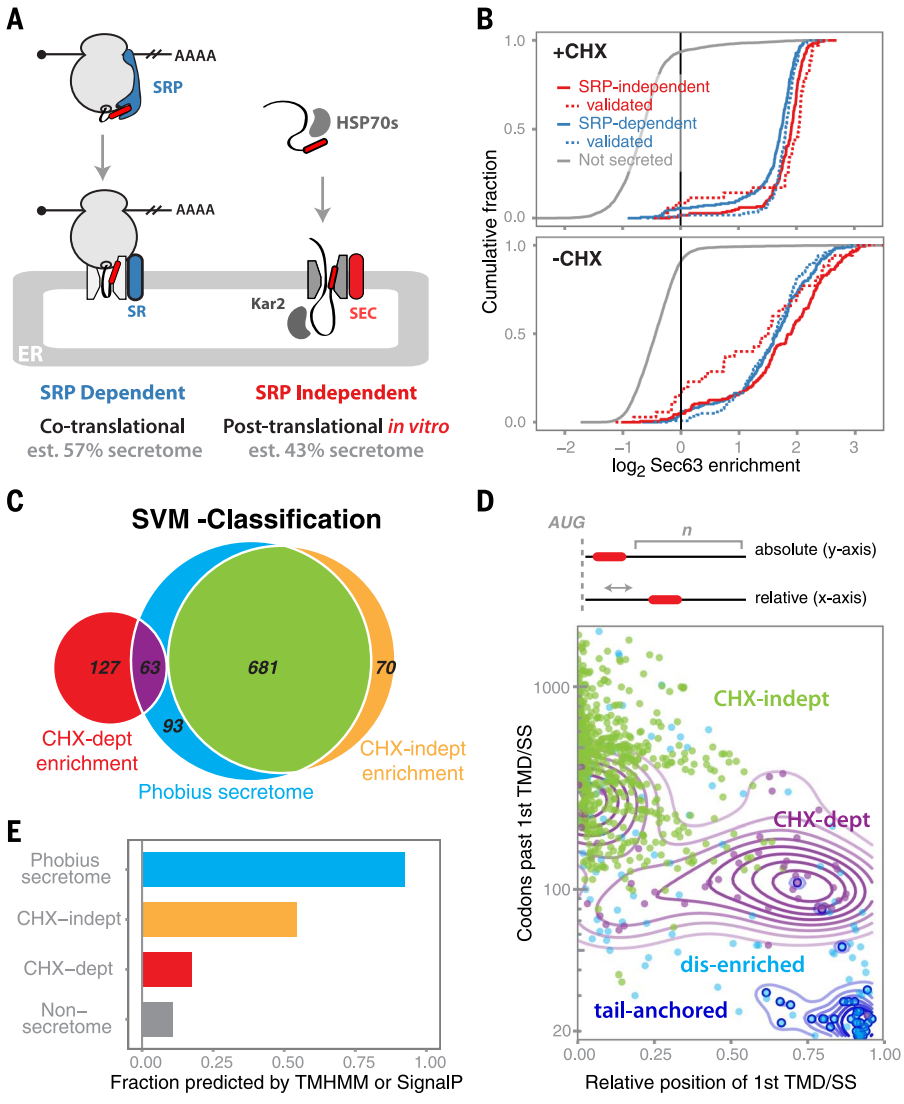


Fig. 3. Global characterization of co- versus posttranslational translocation in vivo. (**A**) Overview of current models for SRP-dependent and -independent targeting to and translocation into the ER. Predictions for the proportion of substrates that partition between pathways are taken from (*21*). (**B**) Cumulative distribution of the Sec63-BirA $\log_2$ enrichments for SRP-dependent (blue), SRP-independent (red), and nonsecreted (gray) genes with or without CHX. Biochemically validated genes (dashed lines) were consolidated from (*21*) and (*25*). (**C**) Venn diagram summarizing the SVM classifications for CHX dependence in the context of the Phobius-predicted secretome. The Sec63-BirA +CHX enrichment profile was fit as a mixture of two normal distributions, and all genes enriched above the 99th percentile of the dis-enriched distribution were classified by the SVM. (**D**) Number of codons downstream of the first hydrophobic domain of Phobius-secretome genes versus the position of this domain relative to overall gene length, plotted for genes in different SVM-classified enrichment categories. Contour lines are added for specific gene sets for visual clarity and represent Gaussian density fits of the corresponding points in that set. Colors match those in (C) with the tail-anchored genes (dark-blue) overlaid as open circles. (**E**) Proportion of genes for which a hydrophobic feature was predicted by either TMHMM or SignalP, for different gene categories. Colors and gene sets match those in (C) with the addition of nonsecretome genes (gray), as predicted by Phobius.

downstream regions suggests that ER retention mediated by polysomes promotes efficient translocon targeting.

Our SVM classification also revealed cotranslational, CHX-independent ER enrichment of 70 genes for which no hydrophobic domains were detected by Phobius (Fig. 3C). However, most of these were predicted to contain a hydrophobic domain by alternate hydrophobic prediction algorithms (TMHMM or SignalP) (*31*, *32*) (Fig. 3E). These genes thus likely represent genuine secretory proteins that were missed by Phobius, highlighting the value of our studies as an experimental complement to computational algorithms for globally identifying secreted and transmembrane proteins.

Timing and specificity of cotranslational targeting to the ER

We next asked when, during translation, RNCs are recruited to the ER, which is expected to depend upon the mechanism of recruitment. For example, SRP binds preferentially to short nascent chains containing cytosolically accessible hydrophobic sequences (*33*) and halts translation elongation until the RNC reaches the ER. By contrast, SRP-independent transport through the SEC complex relies on a poorly understood network of cytosolic chaperones, none of which are known to arrest translation.

In yeast, translocation occurs through two paralogous channels, Sec61 and Ssh1. The essential Sec61 translocon associates with several accessory factors, including both essential (Sec63 and Sec62) and nonessential (Sec66 and Sec72) peripheral components to form the SEC complex, or separately with the SRP receptor (SR). By contrast, the nonessential Ssh1 is a simpler translocon thought to interact peripherally only with SR (*16*). We reasoned that fusing BirA to specific complexes would allow us to globally monitor the timing and specificity of translocation of substrates through these distinct translocons (Fig. 4A).

Ssh1

Ssh1 is expected to receive RNCs from SRP and should therefore interact with the ribosomes after the hydrophobic sequence emerges from the ribosome peptide exit tunnel. Consistent with this model, for all secreted and TMD proteins, regardless of the location of their targeting sequence, BirA-Ssh1 enrichment began only after the hydrophobic domain was fully accessible (~60 amino acids from the start of targeting sequence) (*34*) (Fig. 4B and fig. S10A).

Type II signal anchors (SAs) and cleavable signal sequences (SSs) are oriented in a looped conformation with their N termini facing the cytosol (Fig. 4C). Models of how SSs and SAs achieve this topology within the translocon differ in the efficiency of RNC recruitment; i.e., the head-first model stipulates early RNC binding and subsequent

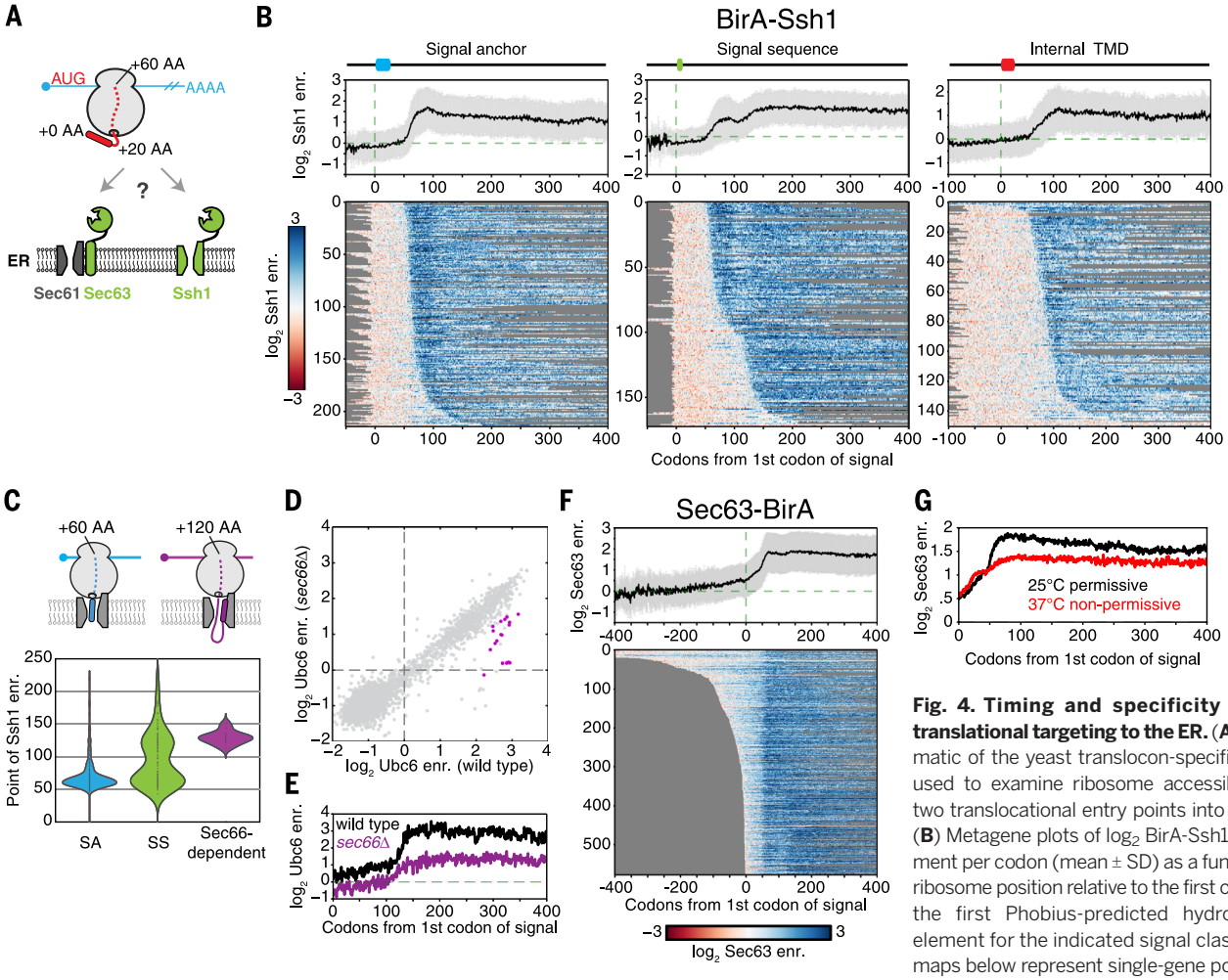


Fig. 4. Timing and specificity of cotranslational targeting to the ER. (**A**) Schematic of the yeast translocon-specific BirAs used to examine ribosome accessibility at two translocational entry points into the ER. (**B**) Metagene plots of $\log_2$ BirA-Ssh1 enrichment per codon (mean ± SD) as a function of ribosome position relative to the first codon of the first Phobius-predicted hydrophobic element for the indicated signal class. Heat maps below represent single-gene positional enrichments used to derive the corresponding averaged metagene plot, sorted by increasing distance to the point at which enrichment occurs. (**C**) Violin plot showing the distribution of the point of enrichment for BirA-Ssh1 relative to the first hydrophobic element, for different types of hydrophobic features and Sec66-dependent genes as defined in (D). Shown above are two RNC conformations consistent with nascent chain lengths. (**D**) Gene enrichments obtained with the general BirA-Ubc6 ER marker in yeast in wild-type versus *sec66*Δ backgrounds. Sec66-dependent genes are defined in fig. S11. (**E**) Metagene plot as in (B) of $\log_2$ BirA-Ubc6 enrichments for Sec66-dependent genes in wild-type (black) and *sec66*Δ (purple) backgrounds. (**F**) Metagene plot as in (B) of $\log_2$ Sec63-BirA enrichments. (**G**) Metagene plot of $\log_2$ enrichments as in (F) in a *sec65-1* SRP temperature-sensitive background at the permissive (25°C, black) and nonpermissive (37°C, red) temperatures.

signal inversion, whereas the looped-insertion model requires either delayed RNC binding in which the nascent chain is correctly oriented before binding (Fig. 4C) or delayed translocation following ribosome engagement. Studies of model SA substrates are consistent with the head-first model (*35*, *36*). Efficient targeting to Ssh1 immediately after translation of the hydrophobic sequence is also consistent with such a mechanism. Here, the timing of engagement was bimodally distributed: Most of the secretome was efficiently recruited to Ssh1 immediately after exit of the hydrophobic sequence from the ribosome; however, a prominent subset of proteins with cleavable SSs engaged only after enough synthesis (~120 amino acids) to allow the nascent chain to acquire a looped topology (Fig. 4, B and C). Thus, both head-first and looped insertion can occur in vivo, depending on the protein. Deletion of *SEC66*, a nonessential component of the SEC complex that mediates translocation of SRP-independent substrates, exclusively affected translocation of the looped-insertion substrates (Fig. 4, C to E, and fig. S11). Thus, proximity-specific ribosome profiling can decipher how distinct translocon components enable the efficient handling of diverse targeting sequences and topologies (*35*, *37*, *38*).

Sec63

Sec63 mediates both SRP-independent and -dependent translocation. Without a strict requirement for SRP-induced translational pausing in the cytosol, Sec63 translocation of SRP-independent substrates naïvely might have been expected to result in a delayed and more broadly distributed timing of ER targeting. Surprisingly, the opposite was observed: Sec63 began to interact with RNCs translating secretory proteins well before the emergence of the hydrophobic sequence from the ribosome (Fig. 4F), and maximal engagement occurred shortly after this element was fully solvent accessible. Thus, Sec63 interacts with ribosomes through two distinct modes: One depends on the presence of an accessible hydrophobic element, and the second reflects an interaction with ribosomes while the targeting sequence is in the exit tunnel. Consistent with this interpretation, acute loss of SRP function using a temperature-sensitive SRP allele (fig. S12) did not affect the early engagement, but did compromise the late (exposed targeting sequence) enrichment (Fig. 4G).

Dynamics of ER-associated ribosomes

Upon translation termination, ER-associated ribosomes can either immediately dissociate and return to the pool of cytosolic ribosomes or preferentially undergo multiple rounds of translation on ER-associated mRNAs. To investigate these dynamics in the context of living cells, we harvested samples for proximity-specific profiling after increasing lengths of biotinylation time in the absence of CHX. Enrichment for secretory messages is expected to decrease at a rate proportional to the time scale at which biotinylated ribosomes, originating from the ER, exchange into the cytosol and begin translating cytosolic messages (Fig. 5A). We observed rapid collapse of our bimodal enrichment distribution into a single population on the order of minutes, although secreted messages remain on the enriched side of the distribution at all time points tested, as expected from continual biotinylation of ER ribosomes (Fig. 5B). Based on a median gene length of ~425 codons and a translation rate of ~5.5 codons per second (*39*), translation of a single secretory protein is expected to take ~77 s. Thus, ribosomes at the yeast ER are highly dynamic, freely exchanging into the cytosol within at most a few rounds of translation.

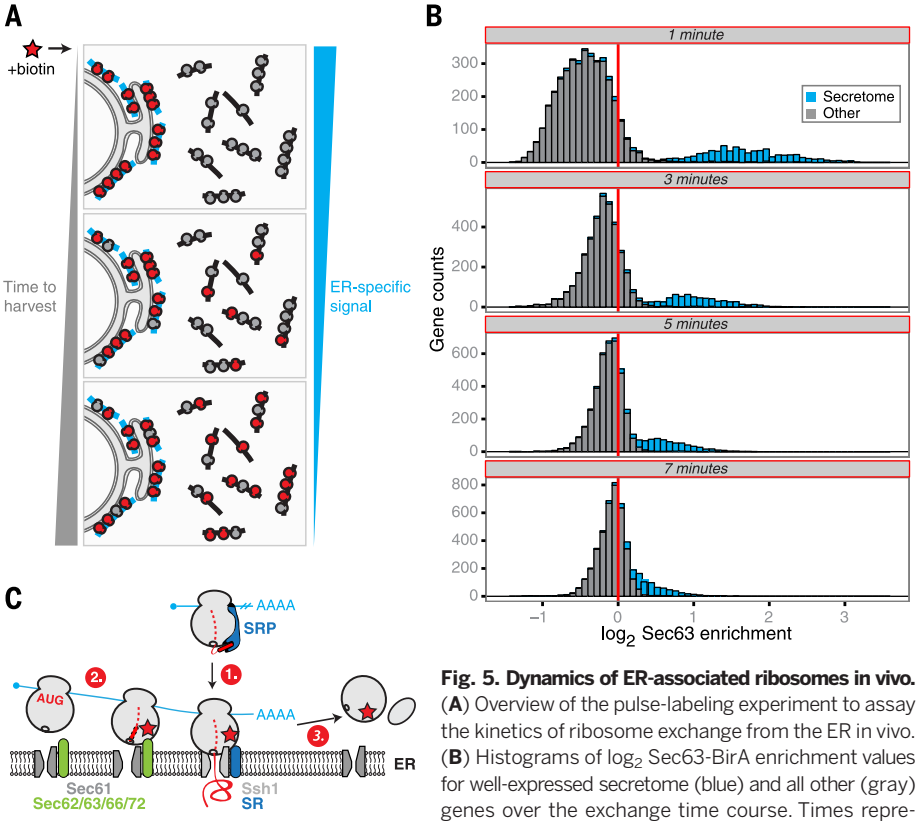


Fig. 5. Dynamics of ER-associated ribosomes in vivo. (**A**) Overview of the pulse-labeling experiment to assay the kinetics of ribosome exchange from the ER in vivo. (**B**) Histograms of $\log_2$ Sec63-BirA enrichment values for well-expressed secretome (blue) and all other (gray) genes over the exchange time course. Times represent the total time of ribosome biotinylation in the absence of CHX. (**C**) Working model consistent with the positional enrichments observed for the translocon-specific BirAs and ribosome recycling. (1) Initial recruitment to the ER depends on a fully accessible signal sequence. (2) Ribosomes translating ER-tethered mRNAs can interact with SEC early. (3) Upon termination, ribosomes recycle into the cytosolic pool.

Discussion

Here we present a proximity-based ribosome profiling strategy that can monitor translation for any location at which it is possible to target a BirA fusion protein. We applied this strategy to analyze modes of cotranslational translocation into the ER. Nearly one-quarter of the proteome is imported into the ER; accordingly, this process has been the focus of intense research. Much of this previous work, however, has explored the behavior of a small group of model substrates, often outside of a cellular context. Proximity-specific ribosome profiling allowed us to simultaneously probe the ER engagement of nascent chains across the full proteome in vivo, in the context of competing and redundant targeting pathways. This comprehensive characterization revealed several principles of how cells integrate distinct targeting pathways with the translocation machinery to allow for unexpectedly robust cotranslational ER import of a diverse set of substrates.

Foremost is the critical role of the timing of translation of the ER-targeting sequence relative to translation termination for determining the propensity of a protein to undergo import cotranslationally. This stands in contrast to the view that cotranslational import is dictated by the factors that mediate targeting (e.g., SRP). It had previously been appreciated that TA proteins must insert posttranslationally because the targeting sequence is obscured prior to translation termination. However, these represent a single point on a broader spectrum of signal positions. Proteins with targeting domains near the C terminus typically were targeted as RNCs only when the kinetics of translation were crippled. By contrast, the predominantly SRP-independent (*21*) set of substrates containing N-terminal SSs are robustly cotranslationally targeted. Indeed, the full range of cotranslational substrates could engage both the essential SEC and "alternate" Ssh1 translocons. Moreover, RNCs were able to interact with the SEC complex prior to exposure of a hydrophobic sequence, even though there are no known mechanisms for coordinating translation and recruitment to SEC.

The above findings suggest a model wherein a pioneering round of translation is responsible

for recruiting the RNC to the ER surface, after which the message remains tethered to the ER by ongoing translation by downstream ribosomes (Fig. 5C). As evidenced by the lack of enrichment for proteins with low (i.e., length-limited) ribosome occupancy downstream of the hydrophobic targeting sequence, the tethered state appears to be crucial for efficient cotranslational engagement.

Consistent with our understanding of SRP function, SRP likely plays a critical role in establishing specificity and ensuring translocation competency through its ability to halt translation. Subsequent rounds of ribosome initiation in the context of this ER-tethered mRNA would obviate the need for SRP to survey every translation event, particularly for messages with extensive downstream regions that can accommodate multiple ribosomes. Such a mechanism is consistent with the observed 1:50 stoichiometry of SRP to the ribosome (*40*), and would simplify the problem of cellular protein sorting while minimizing the toxicity associated with solvent-exposed hydrophobic domains. Although initial recruitment may direct an RNC to a specific translocon, once tethered to the ER the high effective concentration would enable upstream RNCs to engage any translocon. Alternatively, the apparent lack of translocon substrate specificity could be due to ribosome biotinylation in trans, though the observed differences in position and CHX-dependent enrichments argue against this. In either case, inhibition of translocation is known to induce a massive cytoplasmic stress response (*28*), underscoring the danger of having ER-targeted proteins in the cytosol even when they can be posttranslationally translocated.

Our studies also revealed a class of SSs that emphasize an intimate connection between the timing of import and protein topology, mediated by translocon accessory factors. The bimodal timing of targeting to Ssh1 suggests that insertion can occur in either a head-first or looped orientation. Our results implicate Sec66 in mediating the import of those proteins that undergo looped insertion. This functionality may be necessary for certain substrates whose insertion kinetics would preclude reorientation within the translocon. A clear future application of our method is probing the elusive roles of other translocon accessory factors, such as the translocating chain-associated membrane protein (TRAM) and translocon-associated protein (TRAP) in mammals (*37*, *38*).

A final principle that emerged from our studies is the dynamic nature of ER-associated ribosomes in yeast, which cycle readily between cellular compartments. This is in contrast to evidence from in vitro exchange experiments that showed stable association of the 60*S* ribosome subunit with the mammalian ER (*41*). It will be interesting to explore whether such a pattern holds in more specialized secretory cells, such as plasma cells, which rely on efficient translation at the ER. Indeed, electron micrographs have revealed the presence of circular polysomes (*42*) in these cells, consistent with a "closed-loop model" of translation (*43*) that is presumed to promote efficient translation reinitiation.

The principles uncovered here highlight the ability of proximity-specific ribosome profiling to synergize with prior mechanistic studies of ER-targeting pathways. Diverse biological systems localize mRNAs to generate cellular structure and function, yet compared to the ER, much less is known about how cotranslational protein targeting contributes to asymmetry at these sites. More generally, this approach enables the profiling of subpools of ribosomes that interact, even transiently, with cellular proteins of interest—e.g., those involved in protein folding, quality control, targeting, and posttranslational modification. As a flexible, precise, and global method, proximity-specific ribosome profiling provides a tool for exploring the interface between translation and cell biology.

REFERENCES AND NOTES

1. D. St Johnston, Moving messages: The intracellular localization of mRNAs. *Nat. Rev. Mol. Cell Biol.* **6**, 363–375 (2005). doi: 10.1038/nrm1643; pmid: 15852043
2. H. Jung, C. G. Gkogkas, N. Sonenberg, C. E. Holt, Remote control of gene function by local translation. *Cell* **157**, 26–40 (2014). doi: 10.1016/j.cell.2014.03.005; pmid: 24679524
3. J. H. Lee *et al*., Highly multiplexed subcellular RNA sequencing in situ. *Science* **343**, 1360–1363 (2014). doi: 10.1126/science.1250212; pmid: 24578530
4. A. David *et al*., Nuclear translation visualized by ribosome-bound nascent chain puromycylation. *J. Cell Biol.* **197**, 45–57 (2012). doi: 10.1083/jcb.201112145; pmid: 22472439
5. D. C. Dieterich *et al*., In situ visualization and dynamics of newly synthesized proteins in rat hippocampal neurons. *Nat. Neurosci.* **13**, 897–905 (2010). doi: 10.1038/nn.2580; pmid: 20543841
6. S. B. Stephens, C. V. Nicchitta, In vitro and tissue culture methods for analysis of translation initiation on the endoplasmic reticulum. *Methods Enzymol.* **431**, 47–60 (2007). doi: 10.1016/S0076-6879(07)31004-5; pmid: 17923230
7. M. Fernández-Suárez, T. S. Chen, A. Y. Ting, Protein-protein interaction detection in vitro and in cells by proximity biotinylation. *J. Am. Chem. Soc.* **130**, 9251–9253 (2008). doi: 10.1021/ja801445p; pmid: 18582056
8. N. T. Ingolia, S. Ghaemmaghami, J. R. S. Newman, J. S. Weissman, Genome-wide analysis in vivo of translation with nucleotide resolution using ribosome profiling. *Science* **324**, 218–223 (2009). doi: 10.1126/science.1168978; pmid: 19213877
9. T. Ast, M. Schuldiner, All roads lead to Rome (but some may be harder to travel): SRP-independent translocation into the endoplasmic reticulum. *Crit. Rev. Biochem. Mol. Biol.* **48**, 273–288 (2013). doi: 10.3109/10409238.2013.782999; pmid: 23530742
10. E. C. Mandon, S. F. Trueman, R. Gilmore, Protein translocation across the rough endoplasmic reticulum. *Cold Spring Harb. Perspect. Biol.* **5**, a013342 (2013). doi: 10.1101/cshperspect.a013342; pmid: 23251026
11. A. Ben-Shem *et al*., The structure of the eukaryotic ribosome at 3.0 Å resolution. *Science* **334**, 1524–1529 (2011). doi: 10.1126/science.1212642; pmid: 22096102
12. N. Ban *et al*., A new system for naming ribosomal proteins. *Curr. Opin. Struct. Biol.* **24**, 165–169 (2014). doi: 10.1016/j.sbi.2014.01.002; pmid: 24524803
13. M. Heiman *et al*., A translational profiling approach for the molecular characterization of CNS cell types. *Cell* **135**, 738–748 (2008). doi: 10.1016/j.cell.2008.10.028; pmid: 19013281
14. B. Kornmann *et al*., An ER-mitochondria tethering complex revealed by a synthetic biology screen. *Science* **325**, 477–481 (2009). doi: 10.1126/science.1175088; pmid: 19556461
15. K. Finke *et al*., A second trimeric complex containing homologs of the Sec61p complex functions in protein transport across the ER membrane of S. cerevisiae. *EMBO J.* **15**, 1482–1494 (1996). pmid: 8612571
16. Y. Jiang, Z. Cheng, E. C. Mandon, R. Gilmore, An interaction between the SRP receptor and the translocon is critical during cotranslational protein translocation. *J. Cell Biol.* **180**, 1149–1161 (2008). pmid: 18347066
17. Y. Shibata *et al*., The reticulon and DP1/Yop1p proteins form immobile oligomers in the tubular endoplasmic reticulum. *J. Biol. Chem.* **283**, 18892–18904 (2008). doi: 10.1074/jbc.M800986200; pmid: 18442980
18. Materials and methods are available as supplementary material on *Science* Online.
19. M. Elstner, C. Andreoli, T. Klopstock, T. Meitinger, H. Prokisch, The mitochondrial proteome database: MitoP2. *Methods Enzymol.* **457**, 3–20 (2009). doi: 10.1016/S0076-6879(09)05001-0; pmid: 19426859
20. C. C. Williams, C. H. Jan, J. S. Weissman, Targeting and plasticity of mitochondrial proteins revealed by proximity-specific ribosome profiling. *Science* **346**, 748–751 (2014).
21. T. Ast, G. Cohen, M. Schuldiner, A network of cytosolic factors targets SRP-independent proteins to the endoplasmic reticulum. *Cell* **152**, 1134–1145 (2013). doi: 10.1016/j.cell.2013.02.003; pmid: 23452858
22. L. Käll, A. Krogh, E. L. Sonnhammer, A combined transmembrane topology and signal peptide prediction method. *J. Mol. Biol.* **338**, 1027–1036 (2004). doi: 10.1016/j.jmb.2004.03.016; pmid: 15111065
23. J. J. Smith, J. D. Aitchison, Peroxisomes take shape. *Nat. Rev. Mol. Cell Biol.* **14**, 803–817 (2013). doi: 10.1038/nrm3700; pmid: 24263361
24. A. van der Zand, I. Braakman, H. F. Tabak, Peroxisomal membrane proteins insert into the endoplasmic reticulum. *Mol. Biol. Cell* **21**, 2057–2065 (2010). doi: 10.1091/mbc.E10-02-0082; pmid: 20427571
25. D. T. Ng, J. D. Brown, P. Walter, Signal sequences specify the targeting route to the endoplasmic reticulum membrane. *J. Cell Biol.* **134**, 269–278 (1996). doi: 10.1083/jcb.134.2.269; pmid: 8707814
26. B. P. Young, R. A. Craven, P. J. Reid, M. Willer, C. J. Stirling, Sec63p and Kar2p are required for the translocation of SRP-dependent precursors into the yeast endoplasmic reticulum in vivo. *EMBO J.* **20**, 262–271 (2001). doi: 10.1093/emboj/20.1.262; pmid: 11226176
27. S. Panzner, L. Dreier, E. Hartmann, S. Kostka, T. A. Rapoport, Posttranslational protein transport in yeast reconstituted with a purified complex of Sec proteins and Kar2p. *Cell* **81**, 561–570 (1995). doi: 10.1016/0092-8674(95)90077-2; pmid: 7758110
28. O. Brandman *et al*., A ribosome-bound quality control complex triggers degradation of nascent peptides and signals translation stress. *Cell* **151**, 1042–1054 (2012). doi: 10.1016/j.cell.2012.10.044; pmid: 23178123
29. M. Schuldiner *et al*., The GET complex mediates insertion of tail-anchored proteins into the ER membrane. *Cell* **134**, 634–645 (2008). doi: 10.1016/j.cell.2008.06.025; pmid: 18724936
30. S. Stefanovic, R. S. Hegde, Identification of a targeting factor for posttranslational membrane protein insertion into the ER. *Cell* **128**, 1147–1159 (2007). doi: 10.1016/j.cell.2007.01.036; pmid: 17382883
31. A. Krogh, B. Larsson, G. von Heijne, E. L. Sonnhammer, Predicting transmembrane protein topology with a hidden Markov model: Application to complete genomes. *J. Mol. Biol.* **305**, 567–580 (2001). doi: 10.1006/jmbi.2000.4315; pmid: 11152613
32. T. N. Petersen, S. Brunak, G. von Heijne, H. Nielsen, SignalP 4.0: Discriminating signal peptides from transmembrane regions. *Nat. Methods* **8**, 785–786 (2011). doi: 10.1038/nmeth.1701; pmid: 21959131
33. V. Siegel, P. Walter, The affinity of signal recognition particle for presecretory proteins is dependent on nascent chain length. *EMBO J.* **7**, 1769–1775 (1988). pmid: 3169004
34. M. Kowarik, S. Küng, B. Martoglio, A. Helenius, Protein folding during cotranslational translocation in the endoplasmic reticulum. *Mol. Cell* **10**, 769–778 (2002). doi: 10.1016/S1097-2765(02)00685-8; pmid: 12419221
35. P. K. Devaraneni *et al*., Stepwise insertion and inversion of a type II signal anchor sequence in the ribosome-Sec61 translocon complex. *Cell* **146**, 134–147 (2011). doi: 10.1016/j.cell.2011.06.004; pmid: 21729785
36. V. Goder, M. Spiess, Molecular mechanism of signal sequence orientation in the endoplasmic reticulum. *EMBO J.* **22**, 3645–3653 (2003). doi: 10.1093/emboj/cdg361; pmid: 12853479
37. D. Görlich, E. Hartmann, S. Prehn, T. A. Rapoport, A protein of the endoplasmic reticulum involved early in polypeptide translocation. *Nature* **357**, 47–52 (1992). doi: 10.1038/357047a0; pmid: 1315422
38. R. D. Fons, B. A. Bogert, R. S. Hegde, Substrate-specific function of the translocon-associated protein complex during translocation across the ER membrane. *J. Cell Biol.* **160**, 529–539 (2003). doi: 10.1083/jcb.200210095; pmid: 12578908

39. B. Bonven, K. Gulløv, Peptide chain elongation rate and ribosomal activity in Saccharomyces cerevisiae as a function of the growth rate. *Mol. Gen. Genet.* **170**, 225–230 (1979). doi: 10.1007/BF00337800; pmid: 372763
40. S. C. Ogg, P. Walter, SRP samples nascent chains for the presence of signal sequences by interacting with ribosomes at a discrete step during translation elongation. *Cell* **81**, 1075–1084 (1995). doi: 10.1016/S0092-8674(05)80012-1; pmid: 7600575
41. D. Borgese, G. Blobel, D. D. Sabatini, In vitro exchange of ribosomal subunits between free and membrane-bound ribosomes. *J. Mol. Biol.* **74**, 415–438 (1973). doi: 10.1016/0022-2836(73)90037-5; pmid: 4729519
42. A. K. Christensen, L. E. Kahn, C. M. Bourne, Circular polysomes predominate on the rough endoplasmic reticulum of somatotropes and mammotropes in the rat anterior pituitary. *Am. J. Anat.* **178**, 1–10 (1987). doi: 10.1002/aja.1001780102; pmid: 3825959
43. S. E. Wells, P. E. Hillner, R. D. Vale, A. B. Sachs, Circularization of mRNA by eukaryotic translation initiation factors. *Mol. Cell* **2**, 135–140 (1998). doi: 10.1016/S1097-2765(00)80122-7; pmid: 9702200

ACKNOWLEDGEMENTS

We thank members of the Weissman and P. Walter labs, as well as A. Ting, for discussion; and E. Costa, M. Kampmann, P. Kimmig, K. Kostova, and M. Smith for critical reading of the manuscript. Technical assistance was provided by the University of California, San Francisco, Center for Advanced Technology, Nikon Imaging Center, and the Consortium for Frontotemporal Dementia Research. This research was supported by the Center for RNA Systems Biology and the Howard Hughes Medical Institute. C.H.J. is the Rebecca Ridley Kry Fellow of the Damon Runyon Cancer Research Foundation (DRG-2085-11). C.C.W. is an NSF Graduate Research Fellow. Data are deposited in Gene Expression Omnibus under accession nos. GSE61011 and GSE61012.

SUPPLEMENTARY MATERIALS

www.sciencemag.org/content/346/6210/1257521/suppl/DC1
Materials and Methods
Figs. S1 to S12
Tables S1 to S4
References (*44*–*54*)

16 June 2014; accepted 12 September 2014
10.1126/science.1257521

RESEARCH ARTICLE SUMMARY

NANOMATERIALS

Casting inorganic structures with DNA molds

Wei Sun,[1,2] Etienne Boulais,[3] Yera Hakobyan,[3] Wei Li Wang,[1,2] Amy Guan,[1] Mark Bathe,[3*] Peng Yin[1,2*]

INTRODUCTION: The ability to manufacture inorganic nanoparticles (NPs) with arbitrarily prescribed three-dimensional (3D) shapes and positional surface modifications is essential to enabling diverse applications (e.g., in nano-optics and biosensing). However, it is challenging to achieve 3D arbitrary user-specified shapes with sub–5-nm resolution. Top-down lithography has limited resolution, particularly for 3D shapes; capping ligands can be used to tune the energy difference of selected crystallographic facets, but typically only for highly symmetric shapes with identical surface facets.

ON OUR WEB SITE

Read the full article at http://dx.doi.org/10.1126/science.1258361

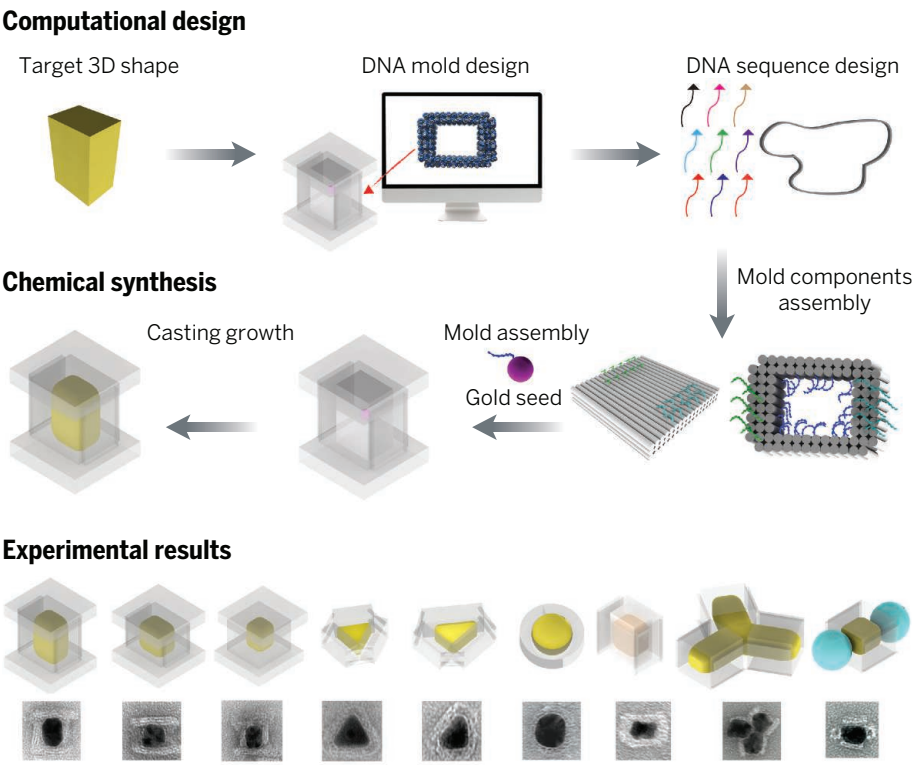
RATIONALE: We developed a framework to program arbitrary 3D inorganic NPs using DNA, which serves both as an informational "genome" to encode the 3D shape of a NP and as a physical "fabricator" to retrieve the information and execute the instruction to manufacture the NP. Specifically, our method uses a computationally designed, mechanically stiff synthetic DNA nanostructure with a user-specified cavity as a "mold" to cast the target inorganic NP. The mold encloses a small gold (Au) "seed." Under mild conditions, the Au seed grows into a larger metal NP that fills the entire cavity, thereby replicating its prescribed 3D shape. The remaining DNA mold additionally acts as a spatially programmable functionalization surface.

RESULTS: Using this DNA nanocasting method, we constructed three distinct sub–25-nm 3D cuboid silver (Ag) NPs with three independently tunable dimensions. The shape versatility of DNA-based nanocasting was further demonstrated via the synthesis of Ag NPs with equilateral triangular, right triangular, and circular cross sections. The material versatility was demonstrated via synthesis of a Au cuboid in addition to the Ag NPs. The DNA mold served as an addressable coating for the casted NP and thus enabled the construction of higher-order composite structures, including a Y-shaped Ag NP composite and a quantum dot (QD)–Ag-QD sandwiched structure through one-step casting growth.

We investigated the key design parameters for stiff DNA molds through mechanical simulations. Multilayered DNA molds provided higher mechanical stiffness for confining NP growth within the mold than single-layer DNA molds, as confirmed by experimental observation.

We additionally characterized plasmonic properties of the designer equilateral Ag triangle and Ag sphere through electron energy loss spectroscopy. Tuning of particle symmetry produced a shape-specific spectrum, which is consistent with the predictions of electromagnetism-based simulations.

CONCLUSION: DNA nanocasting represents a new framework for the programmable digital fabrication of 3D inorganic nanostructures with prescribed shapes, dimensions, and surface modifications at sub–5-nm resolution. The key design strategy is to encode linear sequences of DNA with the sophisticated user-specified 3D spatial and surface information of an inorganic NP, as well as to retrieve and execute the information to physically produce this structure via geometric confinement. Such a method may lead to computationally designed functional materials for the digital manufacture of optical nanocircuits, electronic nanocomputers, and perhaps even sophisticated inorganic nanorobots, each with their blueprints (or "genomes") encoded in the DNA molecules that constitute their "nanofabricators." ■



Casting metal particles with prescribed 3D shapes using programmable DNA nanostructure molds. (**Top**): Schematic of computational shape-by-design framework to encode the user-specified 3D shape of an inorganic particle in the linear sequences of DNA. (**Middle**): Assembly of the mold and casting growth of the metal particle. (**Bottom**): Experimental characterization of cast products (transmission electron micrographs; scale bars, 20 nm).

[1]Wyss Institute for Biologically Inspired Engineering, Harvard University, Boston, MA 02115, USA. [2]Department of Systems Biology, Harvard Medical School, Boston, MA 02115, USA. [3]Department of Biological Engineering, Massachusetts Institute of Technology, Cambridge, MA 02139, USA.
*Corresponding author. E-mail: py@hms.harvard.edu (P.Y.); mark.bathe@mit.edu (M.B.)
Cite this article as W. Sun *et al.*, *Science* **346**, 1258361 (2014). DOI: 10.1126/science.1258361

Published by AAAS

RESEARCH ARTICLE

NANOMATERIALS

Casting inorganic structures with DNA molds

Wei Sun,[1,2] Etienne Boulais,[3] Yera Hakobyan,[3] Wei Li Wang,[1,2] Amy Guan,[1] Mark Bathe,[3]* Peng Yin[1,2]*

We report a general strategy for designing and synthesizing inorganic nanostructures with arbitrarily prescribed three-dimensional shapes. Computationally designed DNA strands self-assemble into a stiff "nanomold" that contains a user-specified three-dimensional cavity and encloses a nucleating gold "seed." Under mild conditions, this seed grows into a larger cast structure that fills and thus replicates the cavity. We synthesized a variety of nanoparticles with 3-nanometer resolution: three distinct silver cuboids with three independently tunable dimensions, silver and gold nanoparticles with diverse cross sections, and composite structures with homo- and heterogeneous components. The designer equilateral silver triangular and spherical nanoparticles exhibited plasmonic properties consistent with electromagnetism-based simulations. Our framework is generalizable to more complex geometries and diverse inorganic materials, offering a range of applications in biosensing, photonics, and nanoelectronics.

Synthesis of shape-controlled inorganic structures underlies diverse applications in biosensing (*1*), light harvesting (*2*), and nanophotonics (*3*). Although a wide variety of synthetic nanostructures have been reported, the formation of nanoparticles (NPs) with arbitrarily prescribed three-dimensional (3D) shape and positional surface modification of sub–5-nm resolution has not been demonstrated with inorganic materials. Top-down lithography (e.g., electron beam lithography) has limited resolution, particularly for 3D shapes (*1*, *4*). In addition, it is a slow serial process and is therefore unsuitable for large-scale production. Capping ligands can be used to tune the energy difference of selected crystallographic facets, and hence NP growth dynamics, to produce diverse symmetric shapes (*5*–*11*). However, reliable dynamic growth simulation models are typically limited to highly symmetric shapes of identical surface facets (*11*–*14*), and it is challenging to predict irregular shapes or to control final NP dimensions.

Structural DNA nanotechnology (*15*) provides a promising route to overcoming these limitations. Using DNA molecules as construction materials, researchers have rationally designed and synthesized diverse shape-controlled nanostructures (*16*–*28*). Building on this success, we have developed a general framework to program 3D inorganic shapes (fig. S1) (*29*). Our approach uses computationally designed, chemically stable, and mechanically stiff DNA nanostructures as molds to cast metallic NPs of user-specified 3D shape, which can be asymmetric. A "nanomold" is self-assembled from DNA strands, contains the user-designed 3D cavity, and encloses a small nucleating gold (Au) seed. Under mild conditions, the Au seed grows into a larger metal cast NP that fills the entire cavity of the mold, thereby replicating its 3D shape.

Using this nanocasting method, we constructed three distinct sub–25-nm 3D cuboid silver (Ag) NPs with three independently tunable dimensions. The shape versatility of DNA-based nanocasting was further demonstrated via the synthesis of Ag NPs with equilateral triangular, right-triangular, and circular cross sections. Material versatility was demonstrated via synthesis of a Au cuboid in addition to the Ag NPs. The DNA mold served as an addressable coating for the cast NP and thus enabled the construction of higher-order composite structures, including a Y-shaped Ag NP composite and a quantum-dot (QD)–Ag-QD sandwiched structure. Finally, the designer equilateral Ag triangle and Ag sphere exhibited plasmonic properties that are consistent with electromagnetism-based simulations.

By serving both as an informational "genome" to carry the user-designed blueprint of the inorganic shape in a digitally precise fashion and as a physical "fabricator" for its accurate execution, DNA enables a new kind of shape-by-design framework for inorganic nanostructure fabrication and promises diverse transformative applications. For example, because the plasmonic properties of shape-controlled metal NPs can be predicted quantitatively in silico, the current shape-by-design framework can be further generalized to be a property-by-design framework for producing inorganic nanostructures with prescribed functional properties.

Ag cuboid casting

Figure 1A depicts the process of casting a cuboid-shaped Ag NP. First, we construct a DNA mold for the casting (steps 1 to 3). In steps 1a and 1b, an open-ended DNA nanostructure barrel and two DNA lids are respectively designed and assembled according to computed stiffness design. In step 2, a 5-nm Au NP is anchored to the interior surface of the barrel. In step 3, the attachment of the two lids to the barrel results in a box-like DNA mold with a cuboid cavity. At the end of step 3, we have constructed a DNA mold with a cuboid cavity and a Au seed inside. With this mold, in step 4 (the casting step), under suitable chemical conditions, the Au seed grows into a Ag NP confined by the mold. Using this strategy and its variants, we fabricated diverse shape-controlled NPs (Fig. 1B). We next describe the design and construction details for casting a Ag cuboid NP using the aforementioned strategy (Fig. 1A).

Computational design of the DNA mold

To design mechanically stiff molds for geometrically constrained metal growth in solution, we used scaffolded DNA origami (*22*), which enables the precise nanometer-scale design of complex 3D cavities of prescribed mechanical properties. The DNA sequences for the DNA mold were designed using caDNAno software (*30*), and its mechanical ground-state 3D solution structure and mechanical properties were then predicted by CanDo (*31*, *32*). Briefly, CanDo computes 3D solution structure by modeling B-form DNA as a continuous elastic rod with effective geometric and material properties. Crossovers are assumed to rigidly constrain adjacent helices on a square or honeycomb lattice. Effective mechanical properties of the molds, including their ground-state solution structures and their mechanical deformations in response to loading forces, are computed using the finite-element method (*29*).

We first designed a multilayer DNA mold with a cuboid cavity. The sidewalls of the DNA mold were designed to possess two or three layers of parallel DNA helices with 12 crossovers per helix on average (Fig. 1A). Two or three layers of sidewall thickness were selected to balance the competing needs to optimize structural stiffness and to increase the cavity dimensions; thicker sidewalls result in higher structural stiffness but smaller cavity size, owing to the length limit of the scaffold strand (8064 nucleotides). The x-y cross section of the central cavity was designed to be eight helices by six helices, with a z-dimensional height of nine helical turns. This provides a designed cuboid cavity (after the lid attachment in step 3) measuring 21 nm by 16 nm by 31 nm, assuming a hydrated helix width of 2.6 nm and a helical turn length of 3.4 nm (*33*). Simulation by CanDo verified that the ground-state solution structure of the DNA mold adopted the cuboid shape cavity (Fig. 2A and fig. S4A). We additionally examined the structural integrity of the mold using normal mode analysis (*29*).

To effectively confine metal growth, it is important that the DNA mold be sufficiently stiff. We therefore studied its response to different loading forces along the x and y directions (Fig. 2, B and C). The ground-state structure of the cuboid mold was used as the initial configuration

[1]Wyss Institute for Biologically Inspired Engineering, Harvard University, Boston, MA 02115, USA. [2]Department of Systems Biology, Harvard Medical School, Boston, MA 02115, USA. [3]Department of Biological Engineering, Massachusetts Institute of Technology, Cambridge, MA 02139, USA.
*Corresponding author. E-mail: py@hms.harvard.edu (P.Y.); mark.bathe@mit.edu (M.B.)

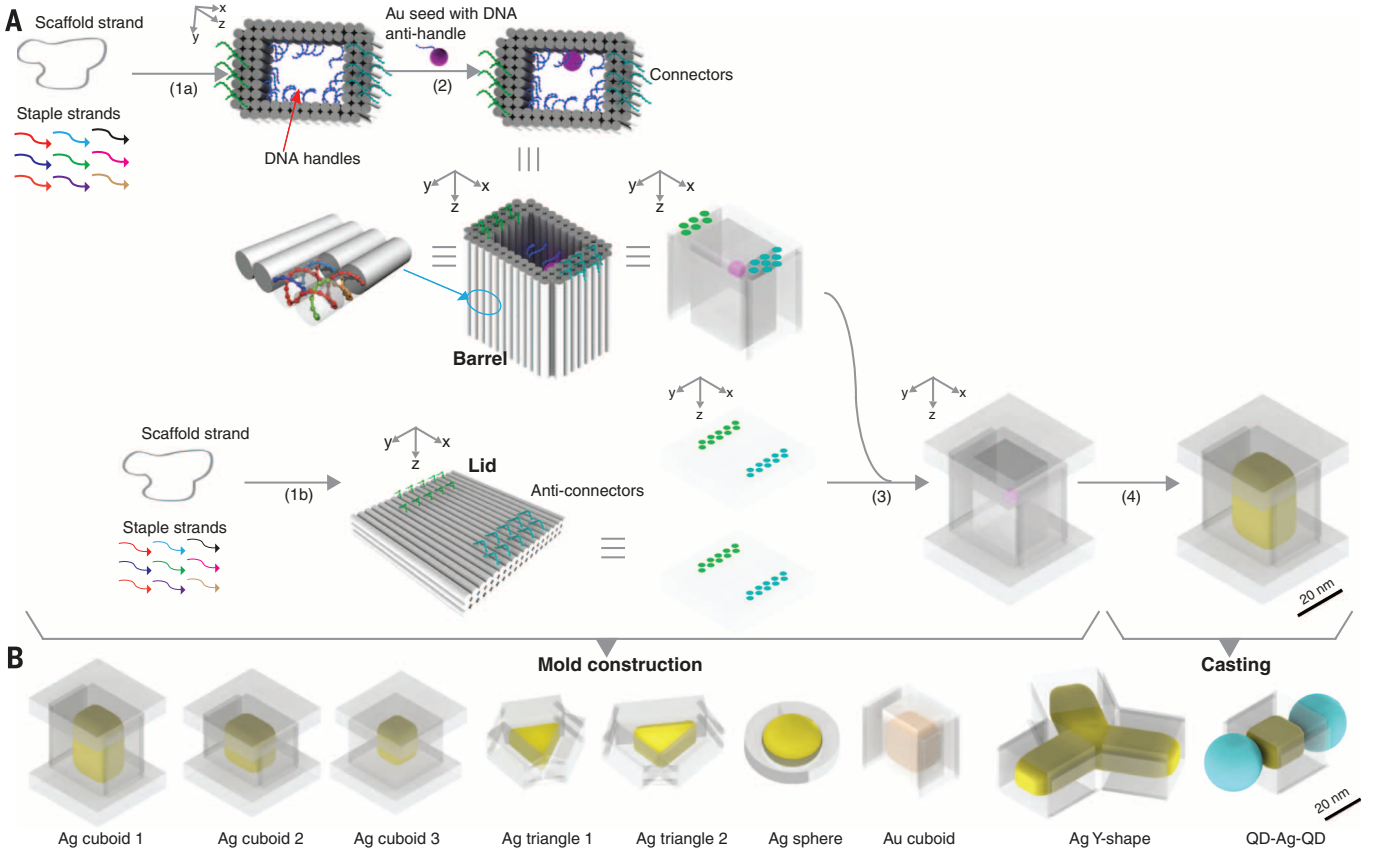


Fig. 1. Casting metal NPs with prescribed shapes using DNA nanostructure molds. (**A**) Design schematic for casting of Ag cuboid. Cyan and green dots denote (anti-)connectors. (**B**) Silver (yellow color) and gold (orange color) NPs cast within DNA molds (transparent layer). Ag, silver; Au, gold; QD, quantum dot (depicted as a cyan ball).

to which two types of loading were applied to model distinct types of mechanical inhibition from the mold onto a given growing NP, namely point contact (fig. S2) or distributed contact (fig. S3). In the point-contact model, a growing NP is assumed to contact a single pair of directly opposing points of the mold (Fig. 2B and table S1, top); equal and opposite point forces are applied to the mold and its deformation is computed. In the distributed-contact model, a growing NP is assumed to fully fill the mold cavity so that the NP applies a uniformly distributed force along opposing interior walls of the cavity (Fig. 2C and table S1, bottom). Under the point-contact scenario, the force response for the barrel was 17 pN/nm in the x direction, normal to the three-layer wall, and 10 pN/nm in the y direction, normal to the two-layer wall. In comparison, higher force-response values were found for the distributed-contact scenario, around 30 pN/nm in the x direction, normal to the three-layer wall, and 19 pN/nm in the y direction, normal to the two-layered wall.

The simulated mechanical properties of the DNA mold (i.e., threshold force and linear deformation range) were found to be comparable to those of viral capsids (*34*), which have been used to effectively confine inorganic nanomaterials grown within (*35*) [see (*29*) for calculation and comparison details]. This result suggests that the DNA mold is also sufficiently stiff to confine metal NP growth within, although growth expansion forces can produce slightly increased [up to 20% according to simulation (*29*)] mold dimensions through elastic deformation of double-stranded DNAs. Notably, mold stiffness was affected by the sidewall thickness. Mechanical simulation revealed that the force response value increased by a factor of 7 from one to three layers under the point-contact loading scenario (see tables S1, S4, and S5).

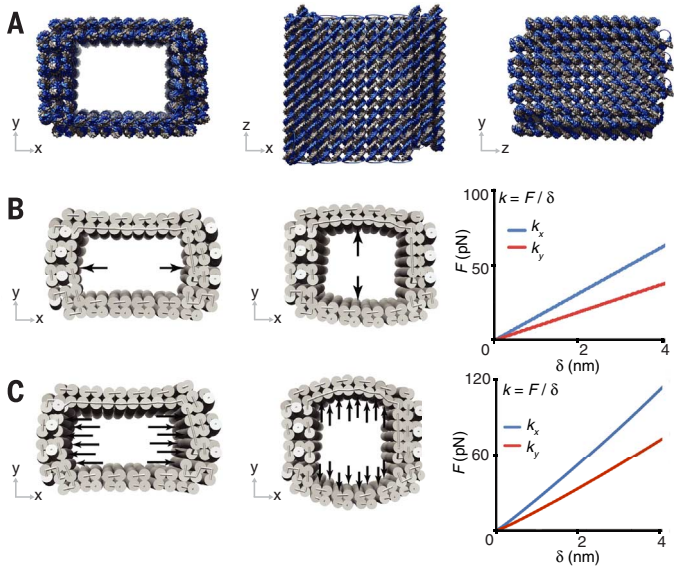


Fig. 2. Mechanical simulations of the rectangular DNA mold. (**A**) Ground-state solution conformation predicted for DNA mold with a cuboid cavity, 21 nm by 16 nm by 30 nm. (**B** and **C**) Under point-contact loading (B) and distributed-contact loading (C), the force-deformation (F-δ) response in the x and y directions for the DNA mold in (A); k is the predicted stiffness value along the direction specified.

Design details

The above computation suggests that our designed DNA mold (i) has the expected ground-state

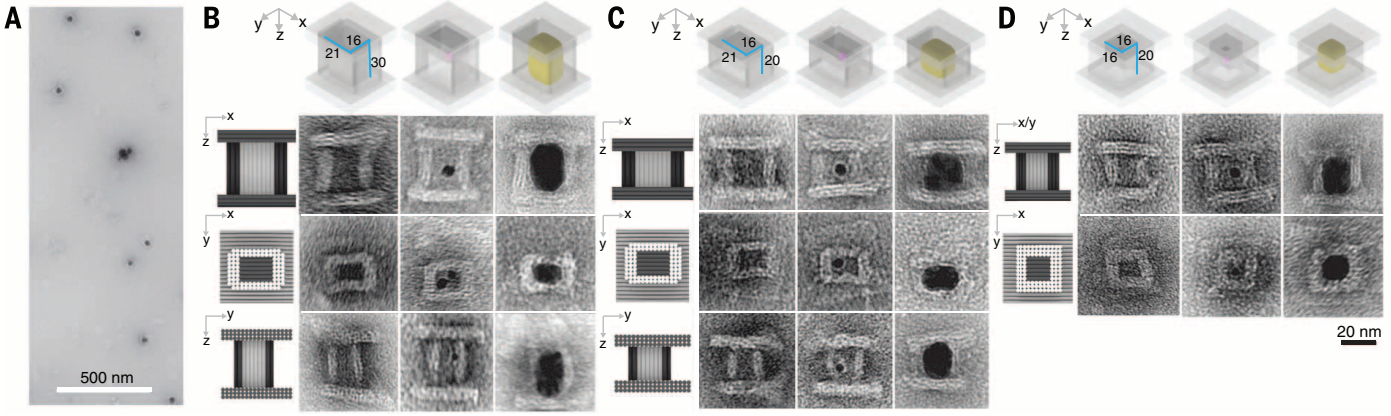


Fig. 3. Casting Ag cuboids with prescribed dimensions. (**A**) A large view TEM image for the Ag NP grown within the DNA mold with a 21 nm by 16 nm by 30 nm (or 21-16-30 nm) cuboid cavity [as shown in (B)]. (**B** to **D**) Design (top row) and TEM images (rows 2 to 4) of the Ag NPs grown in the DNA molds with dimensions of 21-16-30 nm (B), 21-16-20 nm (C), and 16-16-20 nm (D). In row 1 of each panel, small purple dot represents Au seed; cast Ag NP is shown in yellow. In rows 2 to 4 of each panel, a projection model is presented to the left of the TEM images. TEM images from left to right: empty DNA box, DNA box decorated with Au seed (small dark dots; see also figs. S47 to S49), and DNA box containing fully grown Ag NP (dark rectangles with rounded corners; see also figs. S52 to S54).

Table 1. Casting yield for different shaped NPs. Casting yield refers to NP growth yield in step 4 (Fig. 1) and was calculated as the ratio between the number of DNA molds with metal NPs of designed shapes and dimensions and the total number of seed-decorated DNA molds. See text and (*29*) for details. See table S6 for the yields of each step in constructing the seed-decorated molds, which are not accounted for in calculating the casting yield.

Shape	Casting yield (step 4)
Ag cuboid 1	40%
Ag cuboid 2	33%
Ag cuboid 3	39%
Ag triangle 1	10%
Ag triangle 2	14%
Ag sphere	18%
Au cuboid 1	6%
Ag Y-shape	10%
QD-Ag-QD	31%

solution conformation, and (ii) has sufficient mechanical stiffness to confine metal NP growth. Thus, we used this design for step 1a. In step 1b, a three-layered DNA lid was designed with 18 helices in the y direction, three helices in the z direction, and 13 helical turns in the x direction (Fig. 1A).

In step 2, for attachment of the Au "seed" to the DNA barrel (*36*), 27 single-stranded DNA (ssDNA) "handles," each 21 nucleotides (nt) in length, were immobilized in the interior surface of the barrel (Fig. 1A). A 21-nt "anti-handle" (an ssDNA with sequence complementary to the handle) was immobilized onto the Au seed surface. The stoichiometric ratio between the anti-handle and the Au seed was set at 1:1 to achieve approximately one anti-handle per seed, based on a previous report (*37*). The hybridization between the handle and the anti-handle anchored the Au seed to the interior of the barrel. Au was favored over Ag for the choice of seed because of the stability and nucleation versatility of Au (*38*–*41*).

To assemble the seed-decorated barrel and the lids in step 3, the barrel was designed to carry 14 and 16 ssDNA "connectors," each 16 nt in length, on both ends (fig. S28, left), and one side of the lid was designed to carry 20 complementary "anti-connectors." Connectors and anti-connectors were designed to be positioned in roughly matching patterns. Hybridization between them brought the barrel and the two lids together, completing the assembly of a box-like mold with a fully enclosed cuboid cavity. The ~0.5-nm gap between neighboring DNA helices (not depicted in the figure) that constituted the mold was expected to permit the diffusion of small ions or molecules, such as metal ions and ascorbic acid, into the enclosed box. In step 4, under suitable chemical conditions (see below), the Au seed would grow into a Ag cuboid that filled the cavity.

Experimental implementation

In a typical experiment, DNA barrels and lids were folded separately by slowly annealing the staple/scaffold mixtures from 80°C to 24°C over 72 hours. Crude products were subjected to 1.5% agarose gel electrophoresis with 0.5× TBE/10 mM $Mg(NO_3)_2$ as running buffer. Purified structures were extracted and subsequently recovered via centrifugation. Seed decoration was executed by incubating DNA barrels with 5-nm Au NPs (at a seed-to-barrel stoichiometry ratio of 2:1) at 35°C for 16 hours and then annealed to 24°C over 3 hours. Excess Au seeds were removed with a size-exclusion spin column. DNA lids were mixed with the seed-decorated DNA barrels (at lid-to-barrel stoichiometry ratio of 3:1) at 35°C for 16 hours and annealed to 24°C over 3 hours. Growth of Ag NPs in step 4 was triggered by the addition of silver nitrate (1.4 mM) and ascorbic acid (2 mM). After growth for 10 min at room temperature in dark conditions, Ag NPs grown within DNA boxes were imaged by transmission electron microscopy (TEM). See (*29*) for experimental details of mold assembly and purification, metal growth, and TEM sample preparations.

TEM characterization

TEM imaging confirmed successful formation of barrels in step 1a (fig. S23), formation of the lids in step 1b (fig. S30), attachment of Au seed to the barrel in step 2 (fig. S39), assembly of lids with the seed-decorated barrel in step 3 (Fig. 3B, middle, and fig. S47), and finally formation of Ag cuboids with expected dimensions in step 4 (Fig. 3A, Fig. 3B, right, and fig. S52). In a supporting experiment, lids also assembled successfully with a seed-free barrel (Fig. 3B, left).

From three projectional views of the TEM images (Fig. 3B, left column), the x-y, x-z, and y-z dimensions of the barrel cavity were measured respectively as 19.3 ± 1.5 nm by 13.3 ± 0.4 nm, 19.3 ± 1.5 nm by 30.5 ± 1.0 nm, and 13.3 ± 0.4 nm by 30.5 ± 1.0 nm (N = 20 for each projectional view), each approximately consistent with the designed 21 nm by 16 nm by 30 nm cuboid cavity enclosed in the box. From the x-y projection TEM image (Fig. 3B, middle row), the thicknesses of the top and bottom sidewalls of the barrel were measured to be 5.6 ± 0.2 nm (N = 20) and the left and right sidewalls were measured to be 7.8 ± 0.1 nm (N = 20; similar measurements were also obtained from x-z and y-z projections), which were in approximate agreement with two- or three-layered designs. However, because of partial dehydration and structural deformation during TEM sample preparation, small deviations of 2 to 3 nm were occasionally observed in some structures. The DNA lid exhibited the designed 39.5 ± 2.6 nm by 47.7 ± 0.7 nm (N = 20) dimensions under TEM (fig. S30). Because the barrel was designed to carry 27 handles, multiple seeds could in principle be attached to the barrel; here, we experimentally observed one to five seeds present in a single barrel (Fig. 3B, middle, and fig. S39).

After growth, the seed turned into a Ag cuboid, as revealed by the TEM images of dark rectangular projections in the x-z, x-y, and y-z planes, with an expected length of 21.2 ± 0.7 nm by 16.0 ± 0.4 nm by 32.1 ± 1.4 nm in x-y-z dimensions (N = 20 for each projectional view; Fig. 3A, Fig. 3B,

right, and figs. S51 and S52). Measured dimensions of the NP were slightly larger than the measured dimensions of the cavity, suggesting compression of the DNA mold sidewalls by the Ag NP growth. The presence of 4- to 8-nm-thick sidewalls (light-colored) around the NP (dark-colored) in the TEM images suggests that the DNA mold remained surrounding the NP after growth. Notably, all the Ag cuboids grown within the DNA molds exhibited round rather than sharp corners, in the absence of surface capping ligands. Such rounded corners are likely a consequence of surface energy minimization of Ag NPs by decreasing the number of dangling bonds at NP corners. In a supporting experiment, we removed one or two lids from the DNA box, and observed that some Ag NPs grew out of the DNA barrel (fig. S50). These unconfined Ag NPs exhibited much larger dimensions than those within the DNA barrels, further confirming the designed confinement effect of DNA molds. We observed NP growth only within the mold, not on its exterior surface, confirming the effectiveness of seed-nucleated growth.

Casting yield

Casting yield (40%, Table 1) from step 4 was defined as the ratio between the number of NPs with designed projectional shapes and the total number of seed-decorated boxes (with both lids well attached) in the TEM image (*29*) (fig. S51). Additionally, the reaction yields for each step in constructing a DNA mold in Fig. 1A are defined in (*29*) and listed in table S6. Specifically, the barrel formation yield (20%) from step 1a (Fig. 1) was determined from agarose gel (fig. S22) and was measured as the ratio between the molar quantity of the target structure (determined by comparing the SYBR Safe stained target band intensity and the intensity of a standard DNA marker with known molar quantity) and the molar quantity of the initial scaffold strand used in the experiment (*29*). Lid formation yield (12%) of step 1b was similarly defined and measured (fig. S29). Seed decoration yield (86%) from step 2 was determined as the ratio of the number of barrels with at least one seed attached to the interior surface and the total number of seed-decorated barrels in the TEM image (*29*). Box closure yield (31%) from step 3 was measured as the ratio of the number of seed-decorated barrels with both lids well attached and the total number of seed-decorated barrels in the TEM image (*29*).

Tuning the dimensions of the Ag cuboids

The dimensions of the Ag cuboid can be modified by changing the cavity size of the DNA mold. Using this strategy, we tested two additional barrels of different dimensions (figs. S5, S6, S25, and S27 and tables S2 and S3) and assembled DNA boxes accordingly. First, we reduced the *z*-direction length of the DNA box mold from 30 nm (nine DNA helical turns) to 20 nm (six DNA helical turns), and thus obtained a box with a 19.0 ± 1.4 nm by 13.9 ± 0.3 nm by 22.0 ± 0.9 nm cuboid cavity (N = 20 for each projectional view; Fig. 3C, left). After successful seed decoration (see fig. S40), box closure (Fig. 3C, middle, and fig. S48), and growth, a cuboid with measured dimensions of 20.6 ± 0.7 nm by 16.8 ± 0.7 nm by 21.6 ± 0.9 nm was formed (N = 20 for each projectional view; Fig. 3C, right, and fig. S53).

We next further reduced the x dimension from 21 nm (eight helices) to 16 nm (six helices) and obtained a box with a 13.6 ± 0.1 nm by 13.6 ± 0.1 nm by 22.2 ± 0.7 nm cuboid cavity (N = 20 for each projectional view; Fig. 3D, left). After seed decoration (fig. S41), box closure (Fig. 3D, middle, and fig. S49) and growth, the cuboid appeared under TEM with a 14.9 ± 1.5 nm by 14.9 ± 1.5 nm square in x-y projection (N = 20 for each projectional view; Fig. 3D, right and middle), and 14.9 ± 1.5 nm by 22.4 ± 0.7 nm rectangular shapes for x-z and y-z projections (N = 20 for each projectional view; Fig. 3D, right and top, and fig. S54). See Table 1 for casting yield (33 to 39%) and table S6 for yields of different steps in constructing the mold. For each DNA box design, the barrel formation yield (5 to 13%) (figs. S24 and S26), lid formation yield (12%), seed decoration yield (74 to 91%), box closure yield (13 to 21%), and casting yield (33 to 39%) (table S6) (*29*) were determined following the same definition described above.

NPs with prescribed cross sections

Using a simplified design strategy, we cast Ag NPs with prescribed cross section shapes (without height control). Here, we used open-ended barrel molds containing tunnels with designed shapes. The barrels were designed to have four-layered sidewalls and featured three distinct cross section cavities: an equilateral triangular channel (Fig. 4A and fig. S32), a right-triangular channel (Fig. 4B and fig. S34), and a circular shape channel (Fig. 4C and fig. S36). For capture of Au seeds, each barrel was designed to display three 21-nt ssDNA handles on its interior surface.

In the equilateral triangular barrel, the cross section of a fully confined Ag NP exhibited an equilateral triangular shape under TEM, with an expected edge length of 25.2 ± 1.9 nm (N = 20) and three rounded corners (Fig. 4A, right, and fig. S56). The DNA mold remained intact after Ag growth and wrapped around the Ag NP. No obvious bending or curvature of DNA sidewalls was observed. In the center of the Ag NP, a circular shade with 5-nm diameter was observed and was assigned to the Au seed in the DNA mold. TEM imaging of a tilted conformation further confirmed the 3D nature of the NP (fig. S57A). High-resolution TEM plus electron diffraction characterization (fig. S57, B and C) also revealed the highly crystalline nature of the Ag NP, which was consistent with its smooth surface morphology (absence of grain boundaries) and single seed-mediated growth pathway. In the right-triangular barrel with a measured 21.9 ± 1.1 nm by 30.2 ± 0.5 nm by 37.9 ± 0.5 nm cavity (N = 20), the fully grown Ag NP demonstrated a triangular cross section shape with dimensions of 21.7 ± 0.6 nm by 24.2 ± 0.7 nm by 28.2 ± 0.7 nm (N = 20; Fig. 4B, right, and fig. S58). Similar to the equilateral triangular NP, the right-triangular NP also exhibited rounded corners. In the circular-shaped channel, a Ag sphere

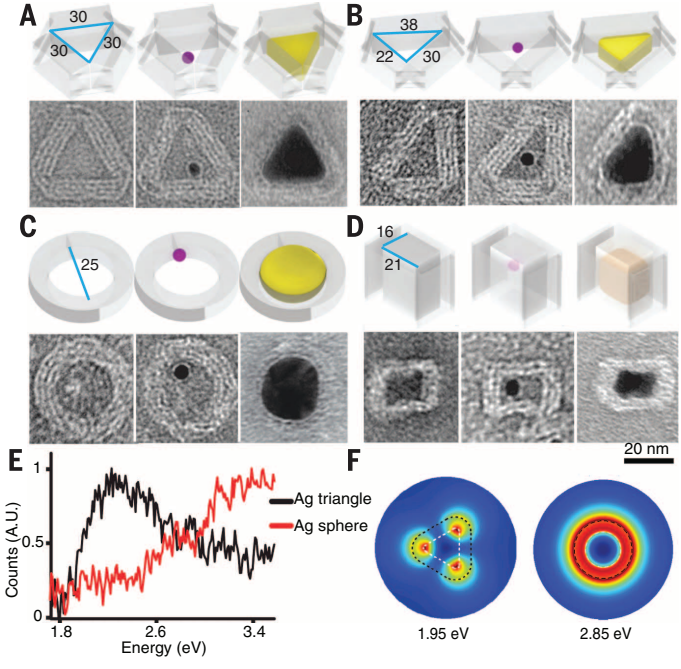


Fig. 4. Casting Ag and Au NPs with prescribed cross section shapes. In (A) to (D), the top row shows the design and the bottom row shows the TEM images of the empty barrel (left), the seed-decorated barrel (middle), and the fully grown NP (right). In the top row of each panel, the small purple dot represents a Au seed, cast Ag NP is shown in yellow, and Au NP is shown in orange. (**A**) Ag NP with 25-nm equilateral triangular cross section (see also figs. S32, S42, and S56). (**B**) Ag NP with 22-24-28 nm right-angle triangular cross section (see also figs. S34, S43, and S58). (**C**) Ag NP with 25-nm-diameter circular cross section (see also figs. S36, S44, and S59). (**D**) Au NP with 19 nm by 14 nm rectangular cross section (see also figs. S23, S39, and S61). (**E**) EELS measurement for Ag NP with 25-nm equilateral triangular cross section [black, as in (A)] and Ag sphere with 25-nm-diameter circular cross section [red, as in (C)]. (**F**) Simulated EELS amplitude map for dipolar resonant modes for Ag NP with 25-nm equilateral triangular cross section [as in (A), left] and Ag NP with 25-nm-diameter circular cross section [as in (C), right]. Colors represent simulated amplitude; white and black dashed lines show contours of NP and DNA mold, respectively.

NP was observed with a circular cross section diameter of 25.5 ± 1.6 nm (N = 20; Fig. 4C, right, and figs. S59 and S60), consistent with our design. In contrast to the capping ligand method, DNA-based nanocasting enabled one-pot parallel production of distinct prescribed shapes by mixing different molds in a single reaction solution (fig. S65).

In the open barrels, only NPs growing laterally rather than vertically were confined to form-specific shapes. This resulted in NP casting yields of 10 to 18% (Table 1), which is lower than that of the fully enclosed cavity. Most of the unconfined NPs exhibited spherical shapes, and did not fully occupy the channels (figs. S55, S56, S58, and S59; see Table 1 for casting yield and table S6 for yields of different steps in constructing the mold). For each design of open-ended DNA molds, the barrel formation yield (5 to 10%) (figs. S31, S33, and S35), seed decoration yield (60 to 75%), and casting yield (10 to 18%) (table S6) (*29*) were determined following the same definition described above.

Experimental characterization and simulation of plasmonic properties

Next, we used electron energy loss spectroscopy (EELS) (*42*) and electromagnetism-based simulations (*29*) to characterize NP plasmonic behavior, both experimentally and theoretically, of the equilateral Ag triangle in Fig. 4A and the Ag sphere in Fig. 4C.

For the equilateral Ag triangle, EELS measurement (Fig. 4E) showed an intense peak around 2.30 eV (corresponding to 540 nm) with a wide shoulder peak around 3.26 eV (corresponding to 380 nm). Simulation for the same equilateral Ag triangle (figs. S7 and S8) revealed, in the presence of the DNA mold and carbon film beneath, a strong dipolar mode around 1.95 eV from the plasmonic resonance near the corners (Fig. 4F), various resonance modes between 2.45 eV (corresponding to 506 nm) and 3.70 eV (corresponding to 336 nm) near the center and edges, and a bulk Ag plasmon mode at 3.80 eV (corresponding to 327 nm; fig. S9). The red-shifting of the simulated EELS spectra with respect to experiment may be due to variations in the carbon film thickness of the TEM grid, the dielectric function of the DNA mold, the NP thickness, and the radii of the rounded NP corners (figs. S10 and S11) (*29*). Simulation of optical properties of the NPs in an aqueous environment indicated plasmonic properties similar to those in vacuum (figs. S16 to S21) (*29*), suggesting the potential utility of the NPs for biosensing applications. Comparison with a previously published EELS result for a triangular Ag NP of similar dimensions (*43*) indicates a relative offset of ~0.1 eV for the predicted NP dipolar mode resonance, which may be due to the distinct substrate (mica) and surface coating used. In contrast, a larger energy offset of 0.4 eV is observed relative to a previously examined larger equilateral Ag triangle with edge length of 78 nm (*43*), indicating the importance of NP size on the resonance energy.

A highly distinct EELS response was measured for the Ag sphere (Fig. 4E), indicating shape-specific plasmonic properties. A single resonance band was observed near 3.26 eV (corresponding to 380 nm) experimentally, which was ascribed to the simulated (fig. S12) dipolar mode near 2.85 eV (corresponding to 435 nm; Fig. 4F) at the edge of the NP. Simulations also suggested several minor resonance modes between the 3.30 eV (corresponding to 376 nm) and 3.65 eV (corresponding to 340 nm) regions near the center of the NP (fig. S13). Similar environmentally sensitive resonance was also observed for the cast Ag sphere (figs. S14 and S15).

Further high-resolution EELS characterization or polarized light excitation using dark-field microscopy on the surface-immobilized metal NPs should reveal the spatial distribution of excited surface plasmons (*43*, *44*), which could enrich our fundamental understanding of nano-optics.

Au cuboid casting

To test the material versatility of our strategy, we cast a Au NP in a DNA barrel containing a 16 nm by 21 nm rectangular open tunnel. Relative to the Ag NP, the growth kinetics of the Au NP in 0.5× TBE/10 mM $Mg(NO_3)_2$ buffer was much slower. After 30 min of reaction time, no obvious size increase was observed for the NP, which was ascribed to the chelating effect of EDTA on gold precursors. Removing EDTA from the reaction buffer promoted the growth kinetics, where a reaction time of 30 min generated a Au NP with a 13.5 ± 0.7 nm by 19.0 ± 1.8 nm (N = 20) rectangular cross section within the barrel (Fig. 4D, right, and fig. S61). The casting yield (6%; table S6) was determined following the same definition described above. See (*29*) for yields of each step.

Composite structures

In addition to structural confinement and protection against undesired NP aggregation, the DNA mold provides a uniquely addressable 3D coating for the NP to be cast, which facilitates the composition of the DNA molds into higher-order complex structures. Here, we experimentally constructed a Y-shape Ag NP branched structure and a QD-Ag-QD composite structure.

A Y-shape DNA mold was assembled from three DNA barrels carrying complementary connector strands (fig. S37). Each barrel carried ssDNA handles to capture Au seeds. After seed decoration, TEM images revealed formation of the desired trimer (Fig. 5A, center, and fig. S45), as well as unintended by-products, such as incompletely assembled dimers and multimers (e.g., pentamers and hexamers). Ag growth within the Y-shape barrel complex generated individual NPs within each barrel, which together formed a Y-shape NP cluster (Fig. 5A, right, and fig. S62). The measured widths of Ag NP within each barrel were 22.7 ± 1.8 nm, 24.3 ± 1.4 nm, and 25.5 ± 0.9 nm (N = 20), slightly larger than the designed 21-nm width of the barrel mold. At the center of the Y-shape barrel complex, where the growth fronts of the Ag NPs met, narrow (<2 nm) interparticle gaps were observed. The casting yield (10%; table S6) was determined following the same definition described above. See (*29*) for yields of each step.

To build a composite structure where a Ag NP was sandwiched between two QDs, 5 or 6 biotin groups were introduced at both ends of a DNA barrel with a 21 nm by 16 nm by 30 nm cuboid

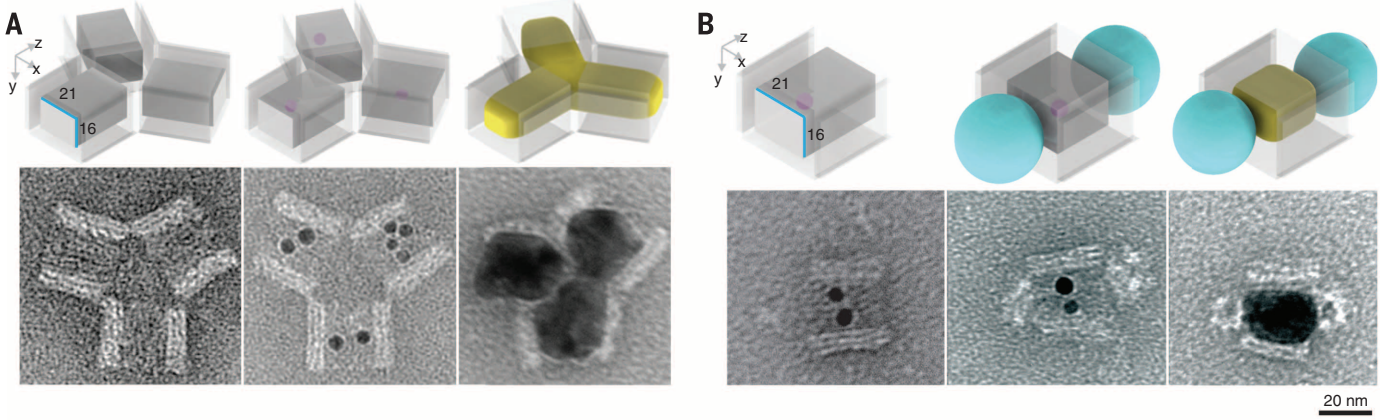


Fig. 5. Casting composite structures. (**A**) Y-shaped Ag NP junction. Top, schematics; bottom, TEM images of Y-shaped DNA barrel trimer (left), with seed decoration (middle), and Ag NP grown within (right) (see also figs. S45 and S62). (**B**) QD-Ag-QD composite structure. Top, schematics; bottom, TEM images of DNA barrel with seed decoration (left), QD attached (middle), and Ag NP grown within (right). Small purple dot represents Au seed; cast Ag NP is shown in yellow. The streptavidin-PEG layer of the QD is a depicted as a cyan ball (see also figs. S46 and S63).

tunnel (fig. S38). After attaching a Au seed inside the barrel, streptavidin-coated QDs were introduced and bound to both ends of the barrel. TEM imaging revealed the formation of the designed sandwiched structure between QDs and the seed-decorated barrels (Fig. 5B, middle, and fig. S46). After staining with uranium salt (*29*), the white sphere with 16- to 21-nm diameter at the ends of the barrel was attributed to the polyethylene glycol (PEG) and streptavidin coating layer around QD cores (CdSe@ZnS; see fig. S64 for control experiments with QD only). The conjugation yield of QDs to both ends of seed-decorated barrels was determined as 88% (table S6) (N = 129). Note that no QDs were found attached to side surfaces of DNA barrels, confirming that QD attachment was specifically mediated by biotins as designed. After Ag growth, TEM imaging revealed the formation of QD-Ag-QD composite structures (31% casting yield; table S6) (Fig. 5B, right, and fig. S63) (*29*). Ag NPs exhibited a 20.5 ± 0.5 nm by 28.4 ± 1.3 nm projection (N = 20), consistent with the designed size of DNA barrel mold. Thus, we demonstrated the assembly of QD at prescribed locations on selected faces of a nonspherical metal NP.

Optimization of the casting process

The stoichiometry between anti-handle and Au seed was set to 1:1 to minimize the undesirable effect of surface-immobilized ssDNA on NP growth. To increase the formation yield of box-like DNA molds, we optimized the number of connectors on the barrels. Increasing the connectors from 6 to 14 at each end of the barrel increased the yield from less than 10% to 31%, whereas changing the lid-to-barrel ratio from 2:1 to 6:1 slightly raised the yield from 28% to 33%.

The effectiveness of the stiffness-based design strategy was verified by the following failed mold designs: Single-layered DNA mold did not produce predesigned cross section shapes (fig. S67 and table S4); when the number of crossovers decreased to one or two, such as in the cases of DNA triangles that displayed sidewalls less than 16 nm thick, destructed DNA molds were observed during metal growth (figs. S69 and S71). We also note that although chemical inhibition between phosphate groups and the growing NP is also expected to occur (*45*, *46*), it was not optimized as a design parameter for programming the shape in the current study. Additionally, the structural integrity of DNA molds was affected by the buffer ionic condition. At 10 mM magnesium nitrate, DNA mold remained intact for 1 day at 1 to 2 mM reactant concentration but deteriorated when the reactant concentration was higher than 20 mM. See (*29*) and figs. S66 to S75 for more details on the optimization of nanocasting and various suboptimal or failed DNA molds used in the optimization experiments.

Discussion

Previous work on casting NPs at a scale below 25 nm had only limited success, largely because of the lack of shape-programmable molds with both mechanical rigidity and surface programmability to enable site-specific seed decoration followed by constrained growth. High-stiffness nanomolds such as viral capsids (*35*) and porous inorganic materials (*47*) are difficult to program into arbitrary geometric shapes, limiting their utility for nanoscale casting of diverse NP geometries and dimensions. Previous reports have shown the programming of 2D inorganic shapes with DNA templates. For example, the growth of metals mediated by randomly distributed nanocluster seeds (*48*–*52*) or strategically positioned NP seeds (*53*, *54*) on a DNA nanostructure surface has produced diverse 2D shapes. However, rough surface morphologies (*55*) and inhomogeneous width distributions along the DNA skeletons (*56*) are often observed for these unconfined metalized products. Our work differs by providing a general way to construct inorganic nanostructures with arbitrarily user-specified 3D shapes and precise prescribed dimensions, by using DNA nanostructures to spatially confine the growth of the final shape (rather than seeding the initial shape) of the inorganic NP. The cast NP retains the addressable coating, whereas traditional chemical synthesis of surface-modified NPs typically involves multiple-step low-yield conjugation and purification after NP formation.

Rapid progress in DNA self-assembly will help to further expand the complexity and diversity of the NP shapes. Recent advances in scaffold-free 3D construction with DNA bricks have already demonstrated highly complex cavities (e.g., toroidal shape cavity) and tunnels (e.g., crossed and branched tunnels) encoded in sub–25-nm DNA cuboids (*26*). It is conceivable that such complex cavity and tunnel shapes may be transferred to inorganic substrates via DNA nanocasting. Further, because of the length limitation of the M13 viral scaffold strand, current multilayered mold designs using scaffolded DNA origami are restricted to producing sub–25-nm cavities. However, by using scaffold-free construction with DNA bricks (*25*, *26*), DNA origami made from longer scaffolds (*57*), or hierarchical assembly of multiple origami (*28*, *58*) and brick structures, nanomolds with much larger and more complex cavities may be achieved. In addition to increasing the shape complexity of the cast NPs, further research will also focus on expanding the material diversity of the NPs. Aside from Ag and Au, the Au seed can also mediate the growth of other diverse inorganic materials [e.g., metals (*38*, *39*), oxides (*40*), and complex salts (*41*)] at mild conditions for potential casting with DNA molds. Replacing the Au seed with metal-binding peptides may further expand the cast diversity (e.g., metals, metal oxides, and chalcogenides) (*59*).

The casting yield (step 4) may be further optimized by using computer-aided design of DNA molds with high mechanical integrity to minimize mold distortion during growth. The formation of 3D enclosed, seed-decorated mold may be improved by optimizing self-assembly conditions [e.g., using isothermal folding (*60*)] or exploring alternative construction strategies [e.g., using DNA bricks (*26*)]. Additionally, replacing Au seeds (which tend to aggregate at DNA origami mold folding conditions) with more stable metal-binding peptides could simplify the current multistep assembly strategy and enable one-step, high-yield formation of DNA molds with enclosed peptide seeds.

The shape- and surface-controlled inorganic NPs fabricated herein may eventually enable novel applications in diverse fields including biosensors, photonics, and nanoelectronics. Near-term applications are likely those based on single-particle properties. For example, DNA nanocasting produces a prescribed metal shape with a uniquely addressable coating, which may display the binding site for a target molecule at the near-field maximum position and hence enable highly sensitive detection. Because optical simulations of the cast NPs in water suggest geometry-specific dipolar resonances and near-field distributions (*29*), highly multiplexed sensing may be achieved using diverse programmed metal shapes.

DNA-based nanocasting represents a general approach for synthesizing inorganic nanostructures with arbitrarily prescribed 3D shapes (*29*). Together with other strategies for transferring the geometric information of DNA nanostructures to diverse inorganic materials [e.g., coating DNA nanostructures with inorganic oxides (*61*) or etching graphene using metalized DNA nanostrucures as lithography masks (*52*)], it points to a new kind of manufacture framework: DNA-directed, digitally programmable fabrication of inorganic nanostructures and devices. Such DNA-based inorganic nanofabrication may eventually enable future production of sophisticated devices such as nanoscale optical circuits, electronic computers, and perhaps even inorganic molecular robots, each with their blueprints (or "genomes") encoded in the DNA molecules that constitute their "nanofabricators."

Materials and methods

DNA mold design

CaDNAno (*30*) was used to design the sequences and routing of staple strands using the scaffold strand (mutated P8064) derived from M13 bacteriophage.

Simulation of DNA mold mechanical properties

The mechanical properties of DNA molds were predicted using the finite-element method based on the ground-state 3D solution structure predicted by CanDo and standard geometric and mechanical properties of B-form DNA (*31*, *32*). Mechanical deformations of the molds were computed in response to internal point and distributed loading using the commercial finite-element software ADINA (ADINA R&D Inc., Watertown, MA). Normal mode analysis was performed to compute the lowest-energy modes of deformation of the molds (*29*, *62*, *63*).

DNA mold folding

Assembly of DNA-origami molds was accomplished following previous reported protocols (*22*, *23*). In a one-pot reaction, 50 nM scaffold was mixed with 250 nM staple strands (Bioneer Inc. or IDTDNA Inc.) in a buffer including 5 mM Tris,

1 mM EDTA, and 16 mM $MgCl_2$ (pH 8) and subjected to a thermal-annealing ramp that cooled from 80°C to 65°C over 75 min and then cooled from 64°C to 24°C over 70 hours.

Gel purification

We mixed 40 μl of folding products with 10 μl of glycerol, and the mixture was loaded into 1.5% agarose gel prestained with Sybr Safe containing 0.5× TBE and 10 mM $Mg(NO_3)_2$. The electrophoresis ran at 75 V for 3 hours in a gel box incubated in an ice-water bath. The monomer band was excised and origami was recovered by pestle crushing, followed by centrifugation for 3 min at 6000 rpm at room temperature using "Freeze 'N Squeeze" DNA Gel Extraction spin columns (Bio-Rad). Recovered DNA molds were stored at 4°C for further use.

DNA decoration onto 5-nm Au seeds

Conjugation of thiolated DNA onto 5-nm Au seeds was achieved following previous reported protocol (*64*). In a typical experiment, 20 μl of 2.5 μM phosphine-coated 5-nm Au seeds were mixed with 0.5 μl of 2 M $NaNO_3$ and 0.65 μl of 100 μM thiolated DNA in 0.25× TBE buffer. The reaction solution was incubated at room temperature for 36 hours in the dark. After that, the reaction solution was loaded into 1% agarose gel containing 0.5× TBE buffer. The electrophoresis was running at 95 V for 1 hour in a gel box on an ice-water bath. The purple band was recovered by pestle crushing, followed by centrifugation for 3 min at 10,000 rpm at room temperature using "Freeze 'N Squeeze" DNA Gel Extraction spin columns (Bio-Rad). Recovered DNA molds were stored at 4°C in dark for further use. The sequence for the thiolated DNA was TATGAGAAGTTAGGAATGTTATTTTT-Thiol. Note that thiol group was modified at the 3′ end of anti-handle sequence TATGAGAAGTTAGGAATGTTA via a TTTTT spacer.

Seed decoration of DNA mold

Purified DNA molds were mixed with 50 mM $NaNO_3$ and 10 nM purified 5-nm Au-DNA conjugates (at a seed-to-barrel stoichiometry ratio of 2:1) and incubated at 35°C for 16 hours, followed by slow annealing to 24°C over 3 hours. The reaction buffer was then purified using an S300 spin column (GE Healthcare) by centrifugation for 2 min at 750*g* at room temperature to remove excessive Au-DNA conjugates.

Lid attachment onto DNA mold

DNA lids were mixed with the seed-decorated DNA barrels (at lid-to-barrel stoichiometry ratio of 3:1) at 35°C for 16 hours and annealed to 24°C over 3 hours.

Metal growth

For Ag growth, we added 0.5 μl of 14 mM $AgNO_3$ and 0.5 μl of 20 mM ascorbic acid to 5 μl of purified seed-decorated DNA molds at room temperature, and pipetted 30 times for mixing. Then the reaction solution was kept in the dark at room temperature for 4 to 20 min. For Au growth, 0.5 μl of 14 mM $HAuCl_4$ and 0.5 μl of 20 mM ascorbic acid were added to 5 μl of purified seed-decorated DNA molds in 0.5× TB buffer at room temperature and pipetted 30 times for mixing. Then the reaction solution was kept in the dark at room temperature from 20 min to 2 hours.

TEM

NPs (3.5 μl) were adsorbed onto glow-discharged carbon-coated TEM grids for 2 min and then wiped away, followed by staining with 3.5 μl of 2% aqueous uranyl formate solution containing 25 mM NaOH for 45 s. Imaging was performed using an JEOL 1400 operated at 80 kV. High-resolution TEM and electron diffraction were performed using a JEOL 2010 with FEG operated at 200 kV for unstained NP sample deposited onto amorphous carbon film.

Yield analysis

Seed decoration yield from step 2, box closure yield from step 3, and casting yield from step 4 (*29*) in Fig. 1A were acquired through direct counting of NPs with prescribed shapes and dimensions from each of the three projection views. For each individual barrel and lid, the barrel and the lid formation yield from step 1a (Fig. 1A) were determined from agarose gel (*29*).

EELS experimental characterization

The low-loss EELS data were collected with TEAM I at the Lawrence Berkeley National Lab, a monochromated TEM operated at 80 kV. The EELS data were collected in the TEM mode under vacuum for the unstained NP sample deposited onto amorphous carbon film.

Simulation of NP plasmonic and optical properties

EELS results were simulated using MNPBEM (*65*, *66*), which is freely available as a MATLAB (MathWorks Inc., Natick, MA) toolbox (*29*). Optical property simulations were performed using the commercial finite element software COMSOL (COMSOL Inc., Burlington, MA) employing the full 3D continuum electromagnetic Helmholtz equation (*29*, *67*, *68*).

REFERENCES AND NOTES

1. P. P. Pompa *et al*., Metal-enhanced fluorescence of colloidal nanocrystals with nanoscale control. *Nat. Nanotechnol.* **1**, 126–130 (2006). doi: 10.1038/nnano.2006.93; pmid: 18654164
2. F. Wang *et al*., Plasmonic harvesting of light energy for Suzuki coupling reactions. *J. Am. Chem. Soc.* **135**, 5588–5601 (2013). doi: 10.1021/ja310501y; pmid: 23521598
3. A. V. Kildishev, A. Boltasseva, V. M. Shalaev, Planar photonics with metasurfaces. *Science* **339**, 1232009 (2013). doi: 10.1126/science.1232009; pmid: 23493714
4. A. L. Koh, A. I. Fernández-Domínguez, D. W. McComb, S. A. Maier, J. K. W. Yang, High-resolution mapping of electron-beam-excited plasmon modes in lithographically defined gold nanostructures. *Nano Lett.* **11**, 1323–1330 (2011). doi: 10.1021/nl104410t; pmid: 21344928
5. Y. Sun, Y. Xia, Shape-controlled synthesis of gold and silver nanoparticles. *Science* **298**, 2176–2179 (2002). doi: 10.1126/science.1077229; pmid: 12481134
6. Y. Xia, Y. Xiong, B. Lim, S. E. Skrabalak, Shape-controlled synthesis of metal nanocrystals: Simple chemistry meets complex physics? *Angew. Chem. Int. Ed.* **48**, 60–103 (2009). doi: 10.1002/anie.200802248; pmid: 19053095
7. T. Ming *et al*., Growth of tetrahexahedral gold nanocrystals with high-index facets. *J. Am. Chem. Soc.* **131**, 16350–16351 (2009). doi: 10.1021/ja907549n; pmid: 19856912
8. N. Ma, E. H. Sargent, S. O. Kelley, One-step DNA-programmed growth of luminescent and biofunctionalized nanocrystals. *Nat. Nanotechnol.* **4**, 121–125 (2009). doi: 10.1038/nnano.2008.373; pmid: 19197315
9. S. E. Lohse, C. J. Murphy, Applications of colloidal inorganic nanoparticles: From medicine to energy. *J. Am. Chem. Soc.* **134**, 15607–15620 (2012). doi: 10.1021/ja307589n; pmid: 22934680
10. Z. Wang, L. Tang, L. H. Tan, J. Li, Y. Lu, Discovery of the DNA "genetic code" for abiological gold nanoparticle morphologies. *Angew. Chem. Int. Ed.* **51**, 9078–9082 (2012). doi: 10.1002/anie.201203716; pmid: 22865657
11. L. Ruan *et al*., Tailoring molecular specificity toward a crystal facet: A lesson from biorecognition toward Pt{111}. *Nano Lett.* **13**, 840–846 (2013). doi: 10.1021/nl400022g; pmid: 23320831
12. A. Puzder *et al*., The effect of organic ligand binding on the growth of CdSe nanoparticles probed by ab initio calculations. *Nano Lett.* **4**, 2361–2365 (2004). doi: 10.1021/nl0485861
13. J. Yu, M. L. Becker, G. A. Carri, A molecular dynamics simulation of the stability-limited growth mechanism of peptide-mediated gold-nanoparticle synthesis. *Small* **6**, 2242–2245 (2010). doi: 10.1002/smll.201000889; pmid: 20853372
14. C. R. Bealing, W. J. Baumgardner, J. J. Choi, T. Hanrath, R. G. Hennig, Predicting nanocrystal shape through consideration of surface-ligand interactions. *ACS Nano* **6**, 2118–2127 (2012). doi: 10.1021/nn3000466 pmid: 22329695
15. N. C. Seeman, DNA in a material world. *Nature* **421**, 427–431 (2003). doi: 10.1038/nature01406; pmid: 12540916
16. J. H. Chen, N. C. Seeman, Synthesis from DNA of a molecule with the connectivity of a cube. *Nature* **350**, 631–633 (1991). doi: 10.1038/350631a0; pmid: 2017259
17. E. Winfree, F. Liu, L. A. Wenzler, N. C. Seeman, Design and self-assembly of two-dimensional DNA crystals. *Nature* **394**, 539–544 (1998). doi: 10.1038/28998; pmid: 9707114
18. W. M. Shih, J. D. Quispe, G. F. Joyce, A 1.7-kilobase single-stranded DNA that folds into a nanoscale octahedron. *Nature* **427**, 618–621 (2004). doi: 10.1038/nature02307; pmid: 14961116
19. P. W. K. Rothemund, Folding DNA to create nanoscale shapes and patterns. *Nature* **440**, 297–302 (2006). doi: 10.1038/nature04586; pmid: 16541064
20. P. Yin *et al*., Programming DNA tube circumferences. *Science* **321**, 824–826 (2008). doi: 10.1126/science.1157312; pmid: 18687961
21. Y. He *et al*., Hierarchical self-assembly of DNA into symmetric supramolecular polyhedra. *Nature* **452**, 198–201 (2008). doi: 10.1038/nature06597; pmid: 18337818
22. S. M. Douglas *et al*., Self-assembly of DNA into nanoscale three-dimensional shapes. *Nature* **459**, 414–418 (2009). doi: 10.1038/nature08016; pmid: 19458720
23. H. Dietz, S. M. Douglas, W. M. Shih, Folding DNA into twisted and curved nanoscale shapes. *Science* **325**, 725–730 (2009). doi: 10.1126/science.1174251; pmid: 19661424
24. D. Han *et al*., DNA origami with complex curvatures in three-dimensional space. *Science* **332**, 342–346 (2011). doi: 10.1126/science.1202998; pmid: 21493857
25. B. Wei, M. Dai, P. Yin, Complex shapes self-assembled from single-stranded DNA tiles. *Nature* **485**, 623–626 (2012). doi: 10.1038/nature11075; pmid: 22660323
26. Y. Ke, L. L. Ong, W. M. Shih, P. Yin, Three-dimensional structures self-assembled from DNA bricks. *Science* **338**, 1177–1183 (2012). doi: 10.1126/science.1227268; pmid: 23197527
27. D. Han *et al*., DNA gridiron nanostructures based on four-arm junctions. *Science* **339**, 1412–1415 (2013). doi: 10.1126/science.1232252; pmid: 23520107
28. R. Iinuma *et al*., Polyhedra self-assembled from DNA tripods and characterized with 3D DNA-PAINT. *Science* **344**, 65–69 (2014). doi: 10.1126/science.1250944 pmid: 24625926
29. See supplementary materials on *Science* Online.
30. S. M. Douglas *et al*., Rapid prototyping of three-dimensional DNA-origami shapes with caDNAno. *Nucleic Acids Res.* **37**, 5001–5006 (2009). doi: 10.1093/nar/gkp436; pmid: 19531737
31. C. E. Castro *et al*., A primer to scaffolded DNA origami. *Nat. Methods* **8**, 221–229 (2011). doi: 10.1038/nmeth.1570; pmid: 21358626
32. D. N. Kim, F. Kilchherr, H. Dietz, M. Bathe, Quantitative prediction of 3D solution shape and flexibility of nucleic acid nanostructures. *Nucleic Acids Res.* **40**, 2862–2868 (2012). doi: 10.1093/nar/gkr1173; pmid: 22156372
33. Y. Ke *et al*., Multilayer DNA origami packed on a square lattice. *J. Am. Chem. Soc.* **131**, 15903–15908 (2009). doi: 10.1021/ja906381y; pmid: 19807088

34. J. P. Michel *et al*., Nanoindentation studies of full and empty viral capsids and the effects of capsid protein mutations on elasticity and strength. *Proc. Natl. Acad. Sci. U.S.A.* **103**, 6184–6189 (2006). doi: 10.1073/pnas.0601744103; pmid: 16606825
35. M. B. Dickerson, K. H. Sandhage, R. R. Naik, Protein- and peptide-directed syntheses of inorganic materials. *Chem. Rev.* **108**, 4935–4978 (2008). doi: 10.1021/cr8002328; pmid: 18973389
36. Z. Zhao, E. L. Jacovetty, Y. Liu, H. Yan, Encapsulation of gold nanoparticles in a DNA origami cage. *Angew. Chem. Int. Ed.* **50**, 2041–2044 (2011). doi: 10.1002/anie.201006818; pmid: 21344547
37. D. Zanchet, C. M. Micheel, W. J. Parak, D. Gerion, A. P. Alivisatos, Electrophoretic isolation of discrete Au nanocrystal/DNA conjugates. *Nano Lett.* **1**, 32–35 (2001). doi: 10.1021/nl005508e
38. F. R. Fan *et al*., Epitaxial growth of heterogeneous metal nanocrystals: From gold nano-octahedra to palladium and silver nanocubes. *J. Am. Chem. Soc.* **130**, 6949–6951 (2008). doi: 10.1021/ja801566d; pmid: 18465860
39. F. Wang *et al*., Heteroepitaxial growth of high-index-faceted palladium nanoshells and their catalytic performance. *J. Am. Chem. Soc.* **133**, 1106–1111 (2011). doi: 10.1021/ja1095733; pmid: 21174411
40. R. G. Chaudhuri, S. Paria, Core/shell nanoparticles: Classes, properties, synthesis mechanisms, characterization, and applications. *Chem. Rev.* **112**, 2373–2433 (2012). doi: 10.1021/cr100449n; pmid: 22204603
41. G. Maurin-Pasturel *et al*., Nanosized heterostructures of Au@ Prussian blue analogues: Towards multifunctionality at the nanoscale. *Angew. Chem. Int. Ed.* **53**, 3872–3876 (2014). doi: 10.1002/anie.201310443; pmid: 24574155
42. J. A. Scholl, A. L. Koh, J. A. Dionne, Quantum plasmon resonances of individual metallic nanoparticles. *Nature* **483**, 421–427 (2012). doi: 10.1038/nature10904; pmid: 22437611
43. J. Nelayah *et al*., Mapping surface plasmons on a single metallic nanoparticle. *Nat. Phys.* **3**, 348–353 (2007). doi: 10.1038/nphys575
44. V. Myroshnychenko *et al*., Plasmon spectroscopy and imaging of individual gold nanodecahedra: A combined optical microscopy, cathodoluminescence, and electron energy-loss spectroscopy study. *Nano Lett.* **12**, 4172–4180 (2012). doi: 10.1021/nl301742h; pmid: 22746278
45. L. Berti, G. A. Burley, Nucleic acid and nucleotide-mediated synthesis of inorganic nanoparticles. *Nat. Nanotechnol.* **3**, 81–87 (2008). doi: 10.1038/nnano.2007.460; pmid: 18654466
46. S. J. Tan, M. J. Campolongo, D. Luo, W. Cheng, Building plasmonic nanostructures with DNA. *Nat. Nanotechnol.* **6**, 268–276 (2011). doi: 10.1038/nnano.2011.49 pmid: 21499251
47. C. Gao, Q. Zhang, Z. Lu, Y. Yin, Templated synthesis of metal nanorods in silica nanotubes. *J. Am. Chem. Soc.* **133**, 19706–19709 (2011). doi: 10.1021/ja209647d; pmid: 22085084
48. E. Braun, Y. Eichen, U. Sivan, G. Ben-Yoseph, DNA-templated assembly and electrode attachment of a conducting silver wire. *Nature* **391**, 775–778 (1998). doi: 10.1038/35826; pmid: 9486645
49. H. Yan, S. H. Park, G. Finkelstein, J. H. Reif, T. H. LaBean, DNA-templated self-assembly of protein arrays and highly conductive nanowires. *Science* **301**, 1882–1884 (2003). doi: 10.1126/science.1089389; pmid: 14512621
50. J. Liu *et al*., Metallization of branched DNA origami for nanoelectronic circuit fabrication. *ACS Nano* **5**, 2240–2247 (2011). doi: 10.1021/nn1035075; pmid: 21323323
51. R. Schreiber *et al*., DNA origami-templated growth of arbitrarily shaped metal nanoparticles. *Small* **7**, 1795–1799 (2011). doi: 10.1002/smll.201100465; pmid: 21608127
52. Z. Jin *et al*., Metallized DNA nanolithography for encoding and transferring spatial information for graphene patterning. *Nat. Commun.* **4**, 1663 (2013). doi: 10.1038/ncomms2690; pmid: 23575667
53. M. Pilo-Pais, S. Goldberg, E. Samano, T. H. Labean, G. Finkelstein, Connecting the nanodots: Programmable nanofabrication of fused metal shapes on DNA templates. *Nano Lett.* **11**, 3489–3492 (2011). doi: 10.1021/nl202066c; pmid: 21732612
54. A. Kuzyk *et al*., DNA-based self-assembly of chiral plasmonic nanostructures with tailored optical response. *Nature* **483**, 311–314 (2012). doi: 10.1038/nature10889; pmid: 22422265
55. E. C. Samano *et al*., Self-assembling DNA templates for programmed artificial biomineralization. *Soft Matter* **7**, 3240–3245 (2011). doi: 10.1039/c0sm01318h
56. M. Fischler *et al*., Formation of bimetallic Ag-Au nanowires by metallization of artificial DNA duplexes. *Small* **3**, 1049–1055 (2007). doi: 10.1002/smll.200600534 pmid: 17309092
57. H. Zhang *et al*., Folding super-sized DNA origami with scaffold strands from long-range PCR. *Chem. Commun.* **48**, 6405–6407 (2012). doi: 10.1039/c2cc32204h; pmid: 22618197
58. S. Woo, P. W. K. Rothemund, Programmable molecular recognition based on the geometry of DNA nanostructures. *Nat. Chem.* **3**, 620–627 (2011). doi: 10.1038/nchem.1070; pmid: 21778982
59. M. Sarikaya, C. Tamerler, A. K. Y. Jen, K. Schulten, F. Baneyx, Molecular biomimetics: Nanotechnology through biology. *Nat. Mater.* **2**, 577–585 (2003). doi: 10.1038/nmat964; pmid: 12951599
60. J.-P. J. Sobczak, T. G. Martin, T. Gerling, H. Dietz, Rapid folding of DNA into nanoscale shapes at constant temperature. *Science* **338**, 1458–1461 (2012). doi: 10.1126/science.1229919; pmid: 23239734
61. S. P. Surwade *et al*., Nanoscale growth and patterning of inorganic oxides using DNA nanostructure templates. *J. Am. Chem. Soc.* **135**, 6778–6781 (2013). doi: 10.1021/ja401785h; pmid: 23574340
62. M. Bathe, A finite element framework for computation of protein normal modes and mechanical response. *Proteins* **70**, 1595–1609 (2008). doi: 10.1002/prot.21708 pmid: 17975833
63. B. Brooks, D. Janežič, M. Karplus, Harmonic analysis of large systems. I. methodology. *J. Comput. Chem.* **16**, 1522–1542 (1995). doi: 10.1002/jcc.540161209
64. J. Sharma *et al*., Toward reliable gold nanoparticle patterning on self-assembled DNA nanoscaffold. *J. Am. Chem. Soc.* **130**, 7820–7821 (2008). doi: 10.1021/ja802853r; pmid: 18510317
65. U. Hohenester, A. Trügler, MNPBEM a matlab toolbox for the simulation of plasmonic nanoparticles. *Comput. Phys. Commun.* **183**, 370–381 (2012). doi: 10.1016/j.cpc.2011.09.009
66. U. Hohenester, Simulating electron energy loss spectroscopy with the MNPBEM toolbox. *Comput. Phys. Commun.* **185**, 1177–1187 (2014). doi: 10.1016/j.cpc.2013.12.010
67. E. Boulais, R. Lachaine, M. Meunier, Plasma mediated off-resonance plasmonic enhanced ultrafast laser-induced nanocavitation. *Nano Lett.* **12**, 4763–4769 (2012). doi: 10.1021/nl302200w pmid: 22845691
68. E. Boulais, R. Lachaine, M. Meunier, Plasma-mediated nanocavitation and photothermal effects in ultrafast laser irradiation of gold nanorods in water. *J. Phys. Chem. C* **117**, 9386–9396 (2013). doi: 10.1021/jp312475h

ACKNOWLEDGMENTS

We thank Y. Ke, J. Shen, and B. Wei for discussion, and E. Haney, D. Pastuszak and E. Chen for assistance in draft preparation. Supported by Defense Advanced Research Projects Agency Young Faculty Award N66001111413, Office of Naval Research (ONR) Young Investigator Program Award N000141110914, ONR grants N000141010827, N000141310593, and N000141410610, Army Research Office grant W911NF1210238, NIH Director's New Innovator Award 1DP2OD007292, NSF Faculty Early Career Development Award CCF1054898, NSF Expedition in Computing Award CCF1317291, NSF grants CCF1162459, CMMI1333215, CMMI1334109, and CMMI1344915 and Wyss Institute funds (P.Y.); ONR grants DURIP N000141310664 and N000141210621 and NSF-DMREF grant CMMI1334109 (M.B., E.B., and Y.H.); and the Natural Sciences and Engineering Research Council of Canada (E.B.). This work was performed in part at the Center for Nanoscale Systems (CNS), a member of the National Nanotechnology Infrastructure Network (NNIN), which is supported by NSF award ECS-0335765. CNS is part of Harvard University. The EELS of the Ag NPs was measured at National Center for Electron Microscopy, which is supported by the Office of Science, Office of Basic Energy Sciences, U.S. Department of Energy under contract DE-AC0205CH11231. Contributions: W.S. designed the system, conducted the experiments, and analyzed the data; E.B. designed and performed optical and EELS simulations, and analyzed the data; Y.H. designed and performed mechanical simulation, and analyzed the data; W.L.W. performed EELS experiments and analyzed the data; A.G. performed experiments and analyzed the data; M.B. designed and supervised the simulation study and interpreted the data; P.Y. conceived, designed, and supervised the study and interpreted the data; and all authors wrote the manuscript. All data described in this article are presented in the supplementary materials.

SUPPLEMENTARY MATERIALS

www.sciencemag.org/content/346/6210/1258361/suppl/DC1
Materials and Methods
Supplementary Text
Figs. S1 to S75
Tables S1 to S6
References (*69*–*84*)

7 July 2014; accepted 30 September 2014
Published online 9 October 2014;
10.1126/science.1258361

RESEARCH ARTICLE

THE RIBOSOME

Structure of the large ribosomal subunit from human mitochondria

Alan Brown,* Alexey Amunts,* Xiao-chen Bai, Yoichiro Sugimoto, Patricia C. Edwards, Garib Murshudov, Sjors H. W. Scheres, V. Ramakrishnan†

Human mitochondrial ribosomes are highly divergent from all other known ribosomes and are specialized to exclusively translate membrane proteins. They are linked with hereditary mitochondrial diseases and are often the unintended targets of various clinically useful antibiotics. Using single-particle cryogenic electron microscopy, we have determined the structure of its large subunit to 3.4 angstrom resolution, revealing 48 proteins, 21 of which are specific to mitochondria. The structure unveils an adaptation of the exit tunnel for hydrophobic nascent peptides, extensive remodeling of the central protuberance, including recruitment of mitochondrial valine transfer RNA (tRNA^{Val}) to play an integral structural role, and changes in the tRNA binding sites related to the unusual characteristics of mitochondrial tRNAs.

The human mitochondrial (mt) genome encodes 13 essential proteins of the oxidative phosphorylation (OXPHOS) complexes of the inner mitochondrial membrane. These proteins are translated by a dedicated set of ribosomes (mitoribosomes). The mitoribosome has a sedimentation coefficient of 55*S* and consists of a large subunit (LSU) (39*S*) and a small subunit (SSU) (28*S*). These subunits contain a 16*S* ribosomal RNA (rRNA) and a 12*S* rRNA, respectively, and no 5*S* rRNA (*1*). They differ from cytoplasmic and bacterial ribosomes in having a high protein-to-RNA ratio. All proteins synthesized by human mitoribosomes are hydrophobic, integral membrane proteins, and some require prosthetic groups for folding and functioning. Unlike their cytoplasmic counterparts, human mitoribosomes are permanently tethered to the mitochondrial inner membrane through the LSU (*2*). Mitochondrial diseases affect >1 in 7500 live births (*3*), with defects of mitochondrial translation responsible for a subgroup associated with decreased OXPHOS activity [reviewed in (*4*)]. Cancer cells have amplified OXPHOS capacity and elevated mitochondrial protein translation compared with adjacent stromal tissue (*5*). Specific inhibition of mitoribosomes has successfully induced selective cytotoxicity in leukemia cells (*6*), establishing mitoribosomes as drug targets for cancer. Furthermore, mitoribosomes are often the unintended targets of various clinically useful antibiotics that target protein synthesis by bacterial ribosomes (*7*).

The high-resolution structure of the yeast mt-LSU revealed a major remodeling of mitoribosomes compared with bacterial and cytoplasmic ribosomes (*8*). However, yeast mitoribosomes are themselves very distinct from mammalian mitoribosomes. Structural information for mammalian mitoribosomes is limited to a ~5 Å reconstruction of porcine LSU (*9*) and a ~7 Å structure of bovine 55*S* (*10*) that suggested substantial differences with the yeast mitoribosome. Here, we report a stereochemically refined, nearly complete model of human mt-LSU at 3.4 Å resolution, achieved by a combination of rapid biochemical purification in mild conditions (*11*), and recent developments in data processing (*12*) and model building (*8*). We identify 16 more proteins than in the previous porcine model (*9*) and reveal mt-tRNA^{Val} as a key structural component of the mitoribosome.

Overall structure of human mt-LSU

Intact human mitoribosomes were purified from human embryonic kidney (HEK293) cells within 28 hours of mitochondria disruption (*11*) and visualized using single-particle cryogenic electron microscopy (cryo-EM) (fig. S1). The data were processed, resulting in a reconstruction that extends to 3.8 Å (fig. S1). The SSU displays considerable conformational heterogeneity with respect to the LSU, so the SSU map could not be interpreted with an atomic model. The use of a soft mask over just the LSU improved its map quality and overall resolution to 3.4 Å (fig. S1D).

The model of the human mt-LSU contains two structural RNA molecules (16*S* mt-LSU rRNA and the newly identified mt-tRNA^{Val}), as well as a tRNA bound to the E site (fig. S3), and 48 proteins, of which 21 are specific to mitochondria (table S2, Fig. 1, and fig. S4). Five additional short protein elements remain unassigned but probably correspond to unbuilt protein extensions. The mt-LSU is highly protein-rich, with over two-thirds of the total mass of 1.7 MD consisting of proteins, of which 0.54 MD can be attributed to mitochondria-specific elements. This gives the human mt-LSU a distinct morphology from both bacterial ribosomes and yeast mitoribosomes (figs. S5 and S6). The connectivity between proteins has also expanded, with each protein making an average of 4.9 contacts (fig. S7). Both the average mass of the mitoribosomal proteins and the number of inter-protein contacts exceeds those of the mammalian cytoplasmic ribosome (*13*).

Although the protein composition has substantially increased, the length of mt-LSU rRNA (1559 nucleotides) has halved compared with bacterial 23*S* rRNA. Contraction has occurred in all domains (figs. S8 to S10). Using base-pair information extracted from the structure, we have constructed a revised secondary structure diagram of mt-LSU rRNA (fig. S7). In contrast to yeast mitoribosomes, where rRNA deletions are minor

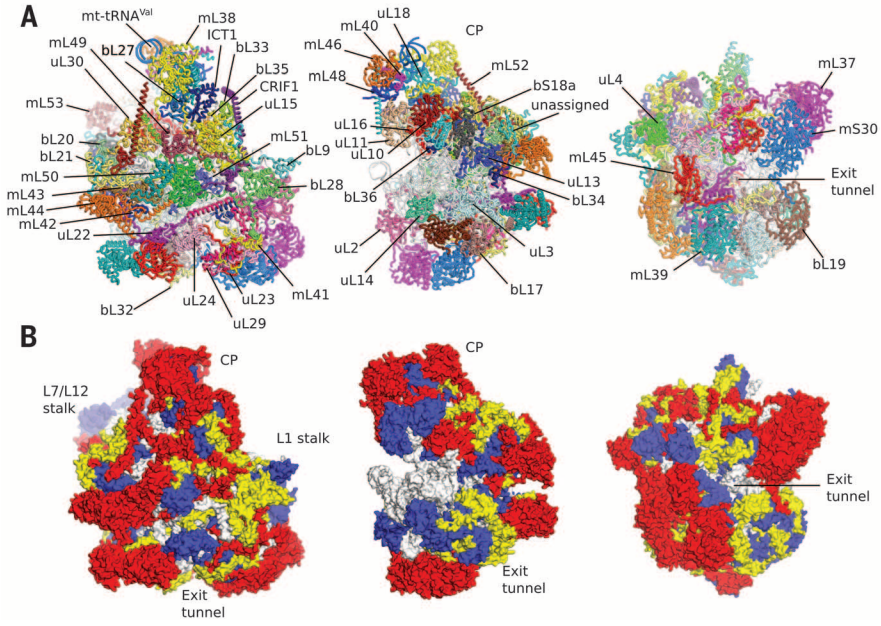


Fig. 1. Overview of human mt-LSU. (**A**) Location of proteins in the human mt-LSU, showing (from left to right) solvent-facing, side, and exit tunnel views. (**B**) Views as in A, proteins conserved with bacteria (blue), extensions of homologous proteins (yellow), and mitochondria-specific proteins (red). rRNA is shown in gray.

Medical Research Council, Laboratory of Molecular Biology, Francis Crick Avenue, Cambridge CB2 0QH, UK.
*These authors contributed equally to this work. †Corresponding author. E-mail: ramak@mrc-lmb.cam.ac.uk

and primarily occur at the tunnel exit (*8*), deletions of human mitoribosomal RNA are numerous and evenly distributed. The reduction is frequently a result of shortening surface-exposed helices. The extant regions are bridged by 37 short "bypass segments," often of just 2 to 4 nucleotides (fig. S9). When internal helices are excised, the location of downstream rRNA elements typically remains unaffected. For example, helices 95 to 97 (including the sarcin-ricin loop that is essential for guanosine triphosphate (GTP)–catalyzed steps of translation) have conserved locations despite the absence of connecting stem h94, due to partial stabilization by mitochondria-specific proteins (fig. S11). Truncation of rRNA and the absence of 5*S* rRNA have presumably contributed to the loss of uL5, and bL25 from the mt-LSU compared with bacterial ribosomes (fig. S8). However, uL6 is absent despite strong conservation of the rRNA to which it binds.

Mitochondria-specific protein elements

Proteins homologous to those in bacteria are, on average, ~60% larger in the human mt-LSU. The extensions are shorter and not conserved with those in the yeast mitoribosome (*8*) (fig. S4). Although some of the extensions fill voids left by rRNA deletions, the amount of rRNA replacement by protein extensions is small (fig. S12). Some extensions protrude into solvent, but predominantly they interact with mitochondria-specific protein elements (table S3).

Mitochondria-specific proteins are peripherally distributed over the solvent-accessible surface of the ribosome (Fig. 1), with clusters at the central protuberance, the L7/L12 stalk, and adjacent to the polypeptide exit site. They have generally adopted new positions rather than compensating for lost rRNA (Fig. 1 and fig. S12), although a large deletion in domain III (h53 to h59) is occupied by a ~100-kD heterodimer of mL37 and mS30 (fig. S12). Other mitochondria-specific proteins that compensate for lost rRNA (mL41, mL42, mL49, and mL51) are relatively small proteins that help stabilize bypass segments. The effect of not compensating all lost rRNA is an architecture less compact than cytoplasmic ribosomes. Despite the increased porosity, the rRNA accessible to solvent has reduced by 52% compared with bacterial ribosomes. This decrease can only partially be accounted for by reduced rRNA content (41%), with new protein elements contributing by burying 32,500 Å^2 of rRNA surface. This agrees with the hypothesis that accretion of mitochondria-specific elements shield the rRNA from reactive oxygen species (*14*) that are elevated in mitochondria as a by-product of OXPHOS and are a major source of RNA damage.

Two of the proteins (mS30 and bS18a) were previously classified as components of the mt-SSU (*10*, *15*). The presence of three sequence variants of bS18 had led to suggestions that differential incorporation of bS18 variants generates a heterogeneous population of mitoribosomes (*16*). However, the identification of bS18a in the mt-LSU suggests that bS18 variants may not promote structural diversity but represent a duplicated fold incorporated into distinct locations of the mitoribosome.

Mt-tRNA^{Val} is a part of the central protuberance

The map of human mt-LSU reveals a density corresponding to an L-shaped RNA molecule located at the top of the central protuberance in a position similar to that occupied by 5*S* rRNA in cytoplasmic ribosomes (fig. S13). The RNA component was also reported in the porcine mitoribosome (*9*). We biochemically extracted the RNA molecule from purified human mt-LSU (fig. S13A) and, using deep RNA-sequencing (*11*), identified it as mt-tRNA^{Val} (Fig. 2). A structural model of this tRNA agrees well with the density (fig. S13, B to D).

That mt-tRNA^{Val} becomes incorporated over other tRNAs may result from its location in the mtDNA chromosome (*17*). The mt-tRNA^{Val} gene is flanked by the two mt-rRNA genes, which are

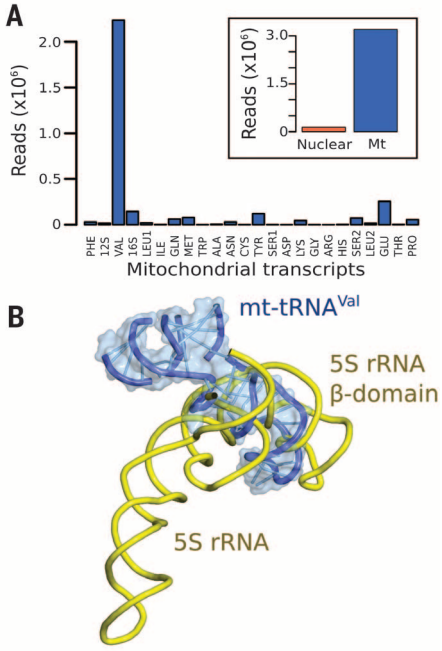


Fig. 2. Mt-tRNA^{Val} is part of the human mitoribosome. (**A**) Mapping of rRNA-sequencing reads to total human (inset) and mitochondrial transcripts. (**B**) The anticodon stem-loop of mt-tRNA^{Val} binds in a similar position to domain β of 5*S* rRNA.

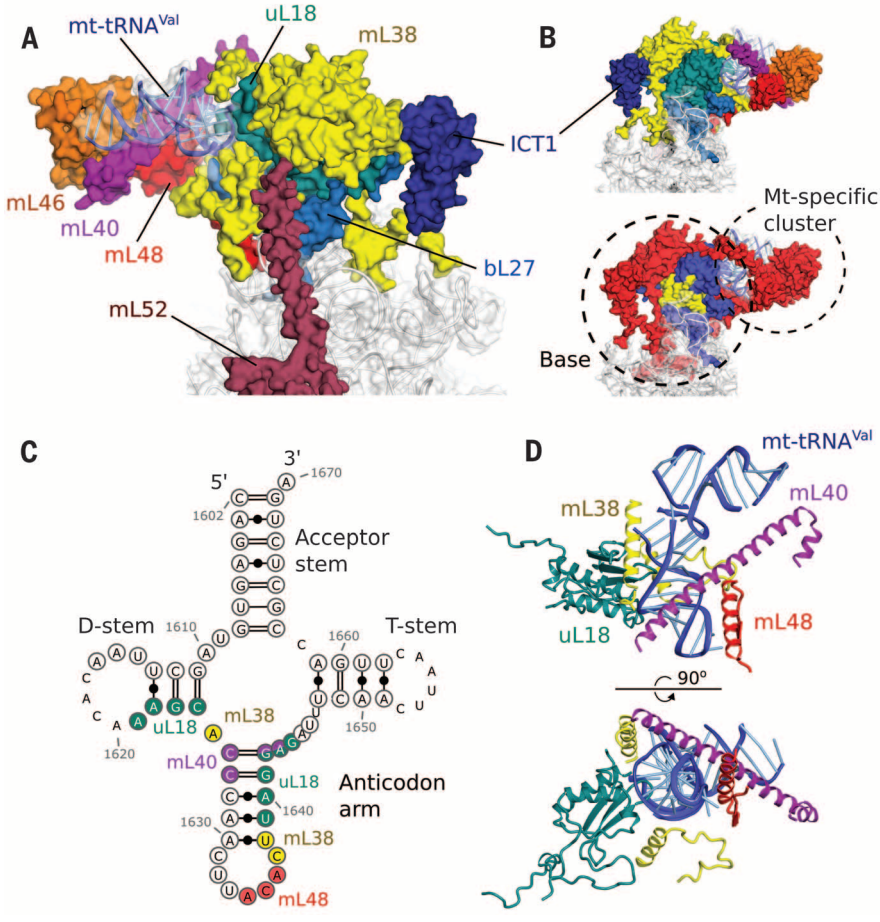


Fig. 3. The central protuberance containing mt-tRNA^{Val}. (**A**) Relative locations of proteins and mt-tRNA^{Val} in the central protuberance. (**B**) View of (A) rotated by 180°, colored by proteins (top) and conservation (bottom) in accordance with Fig. 1. (**C**) Secondary structure of mt-tRNA^{Val}. Modeled nucleotides are circled, and those interacting with surrounding proteins are colored. (**D**) The anticodon arm of mt-tRNA^{Val} (blue) interacts extensively with proteins, whereas the acceptor arm is solvent exposed.

transcribed together as a polycistronic transcript (*18*) (fig. S13E). In bacteria, it is the 5*S* rRNA gene that is located adjacent to the rRNA genes and cotranscribed with them as part of a polycistronic message (*19*). As with 5*S* rRNA in bacteria, mt-tRNA^{Val} would be present in stoichiometric amounts after processing and spatially coincident for incorporation into the LSU. The 12*S* rRNA-tRNA^{Val}-16*S* rRNA organization is almost invariant among vertebrates (*20*).

Remodeling of the central protuberance

The central protuberance of the human mt-LSU is substantially different from other ribosomes, including the yeast mitoribosome, as a result of the absence of 5*S* rRNA and its associated proteins (uL5 and bL25) coupled with the incorporation of mt-tRNA^{Val} and mitochondria-specific proteins (Fig. 3). Despite the remodeling, two functions of the central protuberance are maintained, through entirely mitochondria-specific elements—an interaction with the head of the small subunit and with tRNAs bound to the ribosome (fig. S14). This suggests that the interdependence between intersubunit communication and the fidelity of translation (*21*) is preserved in mitoribosomes. Due to functional flexibility at the interface, we could not assign the density mediating these functions to specific elements. It is coordinated by an entirely mitochondria-specific cluster (mL40, mL46, and mL48) that is bound to the base of the central protuberance (uL18, bL27, mL38, mL52, and ICT1) through mt-tRNA^{Val} (Fig. 3B) and by an unknown mitochondria-specific protein of the small subunit (fig. S14). This region is likely to undergo structural rearrangement during translation [reviewed in (*22*)], for which mt-tRNA^{Val} might provide the necessary plasticity. In the yeast mitoribosome, this function could be realized through specific rRNA expansion segments (*8*).

Mt-tRNA^{Val} is located at the top of the central protuberance, with the acceptor stem exposed to solvent and less well resolved than the anticodon arm, which is ordered due to contact with uL18, mL38, mL40, and mL48 (Fig. 3, C and D). mL40 binds through a 70 Å–long helix that stretches from the tip of the acceptor arm to the anticodon stem, where it makes base-specific interactions in the major groove. uL18, mL38, and mL40 primarily interact with the phosphate backbone. The core architecture of the central protuberance is maintained by mL38, which intertwines with the proteins of the base of the central protuberance and anchors the central protuberance to the rRNA core of the LSU body (Fig. 3), thereby performing a similar role to 5*S* rRNA in cytoplasmic ribosomes. ICT1 and a long helical element of mL52 (Fig. 3 and fig. S15) further connect the central protuberance to the main body, whereas CRIF1 approaches from the opposite side. A structurally similar feature of an α helix bridging the body and central protuberance is seen in the yeast mitoribosome (*8*).

Remodeling of tRNA binding sites

Conventional tRNAs have four-armed cloverleaf secondary structures and L-shaped tertiary structures. However, many human mt-tRNAs have absent or reduced D- and/or T-loops that form the tRNA elbow (Fig. 4A) (*23*). To accommodate these highly variable loops, the tRNA-binding sites have dispensed with elements, common to other ribosomes that interact with the tRNA elbow (Fig. 4B). In the A site, uL25 and the tip of h38 that are responsible for fixing the elbow of A-site tRNA in bacteria (*24*, *25*) have been lost. uL25 is also absent in the yeast mitoribosome (*8*). Similar deletions are observed in the P site, with the loss of the elbow-stabilizing uL5 and h84 (Fig. 4C). The L1 stalk, which controls the dynamics of tRNA ejection (*26*), also lacks the RNA

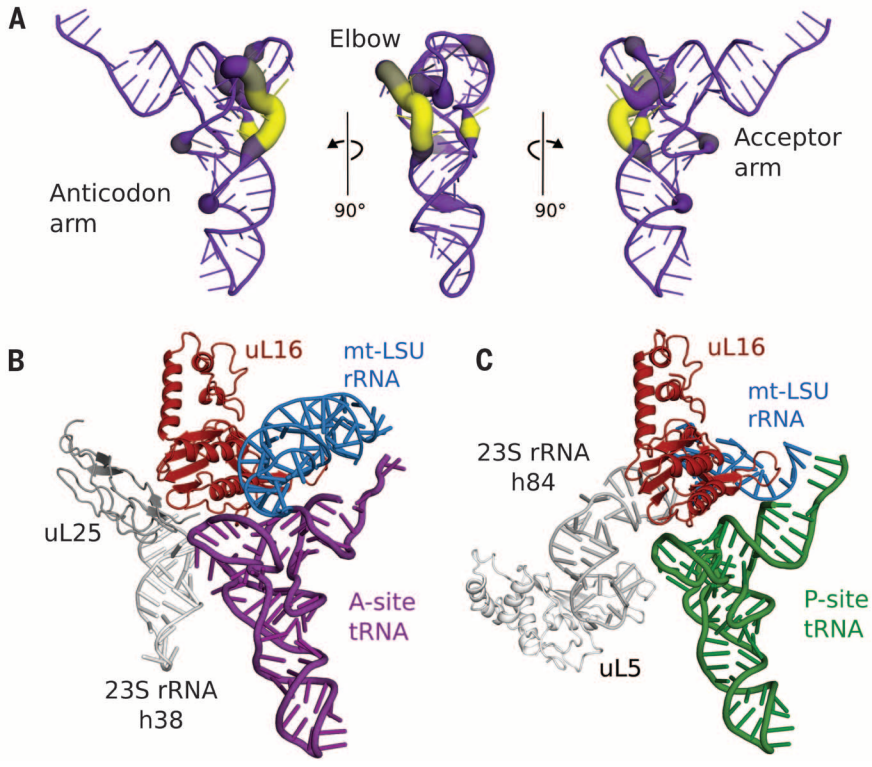


Fig. 4. Coevolution of mt-tRNAs and their binding sites. (**A**) Variability in the elbow region of human mt-tRNAs. The deletion of nucleotides relative to a bacterial tRNA (PDB ID: 2WDI) is shown by line color and thickness, with yellow and thick lines indicating most frequently deleted. (**B**) Modeling a bacterial A-site tRNA (purple) reveals that uL25 and 23S rRNA h38 (both gray) that stabilize the tRNA elbow region are deleted compared with bacterial ribosomes. (**C**) Similarly, uL5 and 23S rRNA h84 (both gray) that stabilize the elbow region of P-site tRNA (green) are deleted, but elements that bind the anticodon arm are conserved.

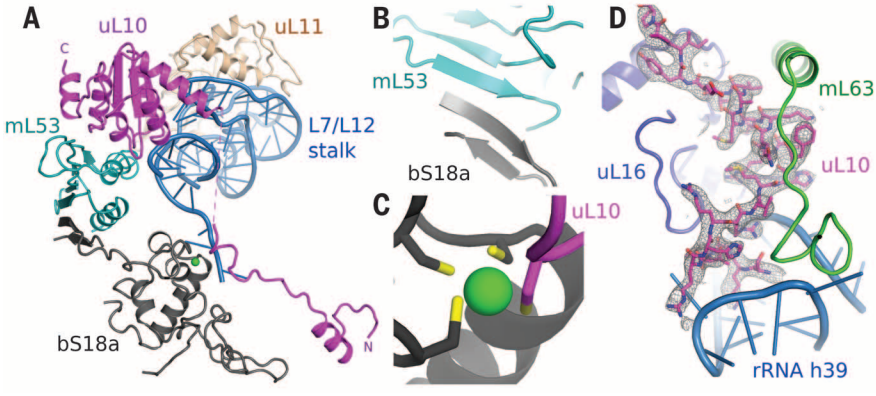


Fig. 5. Remodeling of the L7/L12 stalk. (**A**) Overview of new elements at the L7/L12 stalk. (**B**) bS18a forms a shared β sheet with mL53 to connect the stalk to the body of the mitoribosome. (**C**) The novel N-terminal extension of uL10 contributes a cysteine residue to a shared zinc-binding motif with bS18a. (**D**) Density for the N-terminal extension of uL10 that is highly coordinated to the body of the ribosome.

segments (h76 and h77) that bind the elbow of E-site tRNAs (*27*) (*28*) (figs. S8 and S9), although the remodeled stalk is not resolved in our structure. There do not appear to be additional stabilizing interactions at the acceptor stem, suggesting that human mt-tRNAs are less tightly bound to mitoribosomes.

The L7/L12 stalk

The L7/L12 stalk is a large ribosomal protrusion responsible for the recruitment of translation factors, as well as stimulation of factor-dependent GTP hydrolysis. In bacteria, it is formed by 23*S* rRNA (h42 to h44), uL10, uL11, and multiple copies of uL12 (*29*). In the absence of translational factors, the stalk is generally highly flexible and not well resolved in cryo-EM or crystal structures. In our reconstruction, the stalk is partially resolved (fig. S3B), allowing us to place homology models of uL10 and uL11. The stalk protein-binding platform (h43 and h44) is also resolved despite h42, which connects the platform to the main body of the ribosome, being remodeled and flexible.

The increased stability of the L7/L12 stalk is the product of an interprotein network not observed in other ribosomes (Fig. 5A). First, a mitochondria-specific stalk protein, mL*53*, bridges uL10 on the top of the stalk with bS18a in the body. The interaction between mL*53* and bS18a is mediated through a shared β sheet (Fig. 5B). Second, a mitochondria-specific N-terminal extension of uL10 forms a stable interaction with the main body of the mitoribosome, notably through a shared zinc-binding motif with S18a (Fig. 5C), and further coordinated by a C-terminal extension of uL16, mL*63*, and the loop of h39 (Fig. 5D). A linker region between the N-terminal extension and the conserved part of uL10 is not fully resolved in the maps, suggesting that some conformational flexibility is maintained. The differences in the L7/L12 stalk may explain why bacterial elongation factor G is incompatible with mammalian mitoribosomes (*30*). Additionally, uL*6*, which interacts with translational factors in bacteria, is not functionally replaced in the human mt-LSU (fig. S16).

The exit tunnel

The exit tunnel, through which nascent peptides pass before emerging from the ribosome, appears to be adapted for translating hydrophobic membrane proteins. Density for an endogenous polypeptide, or mixture of polypeptides, is seen throughout the exit tunnel and shows clear interactions with hydrophobic residues of the mitoribosomal tunnel wall, mainly from uL22 (Fig. 6A). These residues make the tunnel more hydrophobic than in cytoplasmic ribosomes (*13*). The hydrophobic nature of both the translated polypeptide and the exit tunnel may explain why a polypeptide remains trapped in the exit tunnel despite the lack of a P-site tRNA to tether it in the ribosome. Although the nascent peptide is better resolved in the upper part of the tunnel, broken density consistent with a helical structure is apparent closer to the exit. Thus, helices of mitochondrial OXPHOS proteins may start forming within the mitoribosomal tunnel similar to what has been seen in cytoplasmic ribosomes (*13*), and the hydrophobic nature of the wall may aid this by mimicking the hydrophobic environment of the membrane that is the eventual site of these proteins. In addition, the increased hydrophobic interactions could act to slow the rate of elongation, allowing more time for transmembrane domains to fold and for assembly of OXPHOS complexes.

The presence of a nascent polypeptide also unambiguously delineates the overall tunnel path, which is similar to that of bacterial and cytoplasmic ribosomes (Fig. 6B) and different from the yeast mitoribosome (*8*). The alternative exit tunnel observed in yeast results from deletion of rRNA h16 to 20 and h24 (fig. S17). Despite similar deletions in domain I of the human mitoribosome, a short segment that replaces h24 (nucleotides 1806 to 1813) seals this potential exit and precludes a yeast-like tunnel path being formed in human mitoribosomes (fig. S17). The peptidyl transfer center and upper tunnel of the human mt-LSU are architecturally similar to bacterial ribosomes and do not show the constriction observed in yeast (*8*).

The exit site of the mitoribosomal tunnel, where the nascent chain emerges, has two roles: forming a docking platform for maturation factors and tethering mitoribosomes to the inner mitochondrial membrane. In the human mt-LSU, this region is remodeled, with two rRNA deletions (h7 and h24) compensated by extensions and conformational changes of the conserved proteins that line the tunnel walls (Fig. 6, B to D). Deletion of h24 has caused a positional change of a β hairpin of uL24, which exposes uL22 to the

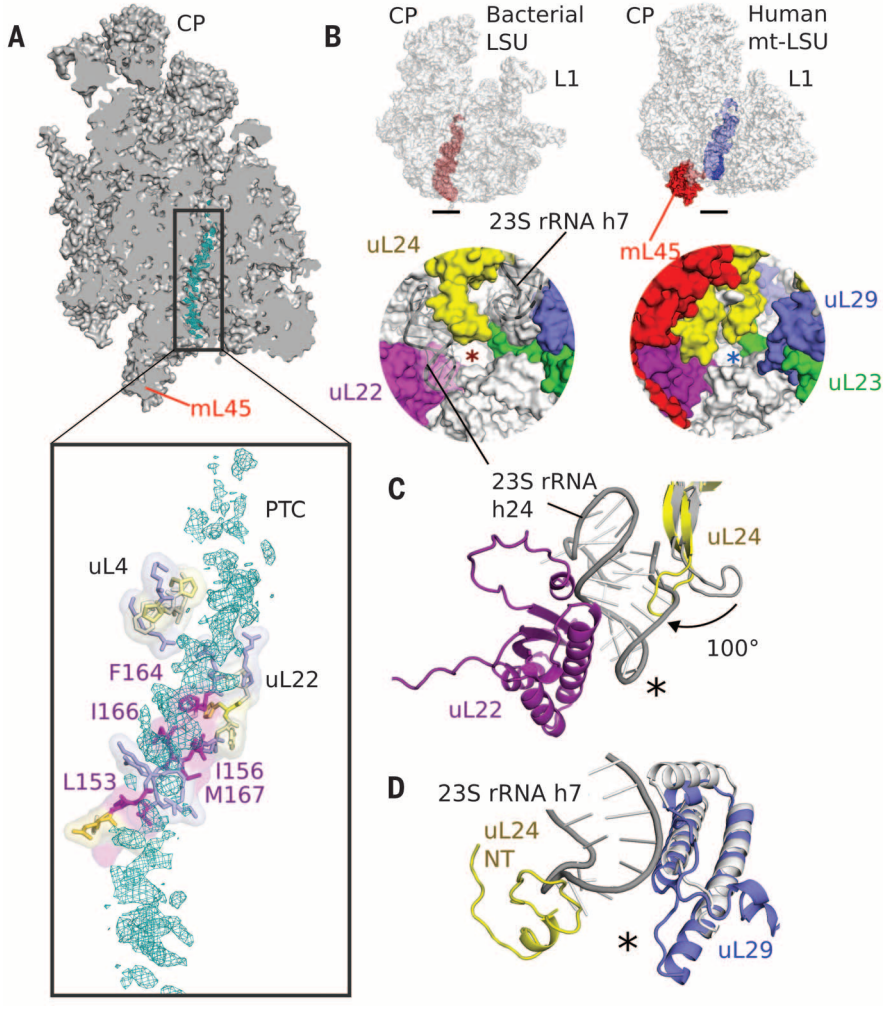


Fig. 6. The exit tunnel. (**A**) Slice through the mt-LSU showing nascent chain density (cyan) in the exit tunnel. The nascent polypeptide interacts with a β hairpin of uL22 enriched with hydrophobic residues. (**B**) The exit tunnel in bacteria (left, red) and human mitoribosomes (right, blue) showing a view of the polypeptide exit site below. The tunnel exit is marked with an asterisk. The polypeptide exit tunnel in mt-LSU is more proteinaceous than in bacteria as a result of two rRNA deletions. (**C**) Deletion of h7 in bacteria (gray) is compensated by changes to uL29 and an N-terminal extension of uL24. (**D**) Deletion of h24 (gray) results in the conserved β hairpin of uL24 rotating closer to the tunnel exit and exposes uL22 to the nascent polypeptide.

exit site, and h7 is partially replaced by uL29 and an N-terminal extension of uL24. Together these changes result in a more proteinaceous exit site than in other ribosomes and allows binding of mL45 that likely anchors the mitoribosome to the inner mitochondrial membrane in a way that would expose the translated nascent polypeptide to solvent (*9*), making it accessible to specific maturation factors and chaperones involved in the assembly of OXPHOS complexes.

Mitoribosomal mutations have been linked with hereditary mitochondrial diseases (*4*). These mutations and their potential effect on the structure are shown in tables S4 and S5 and fig. S18. Although all these mutations affect the mitoribosome, their effects are varied, suggesting that in each case they work in conjunction with other mutations to produce the disease. The structural information presented here can be used for the rational design of antibiotics with decreased autotoxicity. In addition, because mitoribosomes are involved in redirection of energy metabolism of tumorogenic cells (*31*), with many mitoribosomal proteins up-regulated in cancer (table S6), the structure might be useful for the development of novel cancer therapeutics.

REFERENCES AND NOTES

1. T. W. O'Brien, *IUBMB Life* **55**, 505–513 (2003).
2. M. Liu, L. Spremulli, *J. Biol. Chem.* **275**, 29400–29406 (2000).
3. D. Skladal, J. Halliday, D. R. Thorburn, *Brain* **126**, 1905–1912 (2003).
4. V. Boczonadi, R. Horvath, *Int. J. Biochem. Cell Biol.* **48**, 77–84 (2014).
5. F. Sotgia *et al.*, *Cell Cycle* **11**, 4390–4401 (2012).
6. M. Skrtić *et al.*, *Cancer Cell* **20**, 674–688 (2011).
7. R. Singh, L. Sripada, R. Singh, *Mitochondrion* **16**, 50–54 (2014).
8. A. Amunts *et al.*, *Science* **343**, 1485–1489 (2014).
9. B. J. Greber *et al.*, *Nature* **505**, 515–519 (2014).
10. P. S. Kaushal *et al.*, *Proc. Natl. Acad. Sci. U.S.A.* **111**, 7284–7289 (2014).
11. Materials and methods are available as supplementary materials on *Science* Online.
12. S. H. W. Scheres, *J. Struct. Biol.* **180**, 519–530 (2012).
13. R. M. Voorhees, I. S. Fernández, S. H. W. Scheres, R. S. Hegde, *Cell* **157**, 1632–1643 (2014).
14. R. N. Lightowlers, A. Rozanska, Z. M. Chrzanowska-Lightowlers, *FEBS Lett.* **588**, 2496–2503 (2014).
15. E. C. Koc *et al.*, *FEBS Lett.* **492**, 166–170 (2001).
16. E. C. Koc, W. Burkhart, K. Blackburn, A. Moseley, L. L. Spremulli, *J. Biol. Chem.* **276**, 19363–19374 (2001).
17. S. Anderson *et al.*, *Nature* **290**, 457–465 (1981).
18. J. Montoya, G. L. Gaines, G. Attardi, *Cell* **34**, 151–159 (1983).
19. D. Liao, *J. Mol. Evol.* **51**, 305–317 (2000).
20. P. D'Onorio de Meo *et al.*, *Nucleic Acids Res.* **40**, D1168–D1172 (2012).
21. M. H. Rhodin, R. Rakauskaitė, J. D. Dinman, *Mol. Genet. Genomics* **285**, 505–516 (2011).
22. J. Noeske, J. H. D. Cate, *Curr. Opin. Struct. Biol.* **22**, 743–749 (2012).
23. M. Helm *et al.*, *RNA* **6**, 1356–1379 (2000).
24. R. M. Voorhees, A. Weixlbaumer, D. Loakes, A. C. Kelley, V. Ramakrishnan, *Nat. Struct. Mol. Biol.* **16**, 528–533 (2009).
25. L. Jenner, N. Demeshkina, G. Yusupova, M. Yusupov, *Nat. Struct. Mol. Biol.* **17**, 1072–1078 (2010).
26. J. Fei *et al.*, *Proc. Natl. Acad. Sci. U.S.A.* **106**, 15702–15707 (2009).
27. M. R. Sharma *et al.*, *Cell* **115**, 97–108 (2003).
28. J. Lehmann, F. Jossinet, D. Gautheret, *Nucleic Acids Res.* **41**, 5494–5502 (2013).
29. J. M. Kavran, T. A. Steitz, *J. Mol. Biol.* **371**, 1047–1059 (2007).
30. H. K. Chung, L. L. Spremulli, *J. Biol. Chem.* **265**, 21000–21004 (1990).
31. D. Hanahan, R. A. Weinberg, *Cell* **144**, 646–674 (2011).

ACKNOWLEDGMENTS

We thank Y. Gordiyenko for help with rRNA purification; S. Peak-Chew and M. Skehel for mass spectrometry; G. McMullan, S. Chen, and C. Savva for help with data collection; J. Grimmett and T. Darling for help with computing; and I. S. Fernández and J. L. Llácer for stimulating discussions. This work was funded by grants from the UK Medical Research Council (MC_U105184332 to V.R. and MC_UP_A025_1013 to S.H.W.S.); a Wellcome Trust Senior Investigator award (WT096570), the Agouron Institute and the Jeantet Foundation (V.R.); fellowships from Human Frontiers Science Program (A.A.), and EU FP7 Marie Curie (X.B.). Cryo-EM density maps have been deposited with the Electron Microscopy Data Bank (accession number EMD-2762), and coordinates have been deposited with the Protein Data Bank (PDB) (entry code 3J7Y).

SUPPLEMENTARY MATERIALS

www.sciencemag.org/content/346/6210/718/suppl/DC1
Materials and Methods
Figs. S1 to S18
Tables S1 to S6
References (*32*–*120*)

30 June 2014; accepted 23 September 2014
Published online 2 October 2014;
10.1126/science.1258026

REPORTS

QUANTUM SPIN LIQUIDS

Coherent transmutation of electrons into fractionalized anyons

Maissam Barkeshli,[1] Erez Berg,[2]* Steven Kivelson[3]

Electrons have three quantized properties—charge, spin, and Fermi statistics—that are directly responsible for a vast array of phenomena. Here we show how these properties can be coherently and dynamically stripped from the electron as it enters a certain exotic state of matter known as a quantum spin liquid (QSL). In a QSL, electron spins collectively form a highly entangled quantum state that gives rise to the fractionalization of spin, charge, and statistics. We show that certain QSLs host distinct, topologically robust boundary types, some of which allow the electron to coherently enter the QSL as a fractionalized quasi-particle, leaving its spin, charge, or statistics behind. We use these ideas to propose a number of universal, conclusive experimental signatures that would establish fractionalization in QSLs.

A notable example of emergence in physics is fractionalization, where the long-wavelength, low-energy excitations of a many-body quantum phase of matter possess quantum numbers that are fractions of those of the microscopic constituents. In a fractional quantum Hall state, for example, the emergent quasiparticle excitations carry fractional electric charge and anyonic quantum statistics. In a quantum spin liquid (QSL), the electron fractionalizes at low energies into two quasi-particles—a spinon and a holon—that independently carry the spin and charge of the electron (*1*–*8*). When an electron is injected into such systems, it can decay into fractionalized components, but a direct quantum mechanical conversion of an electron to a single fractionalized quasi-particle has conventionally been thought to be impossible. Consequently, the question of how to experimentally detect fractionalization in a QSL, even in principle, has remained a major challenge. It is particularly timely to revisit this question, given the number of materials that have recently been shown to exhibit anomalous properties that may indicate that they are QSLs (*9*).

Here we show that some QSLs allow electrons to coherently enter through their boundary as a fractionalized quasi-particle, leaving behind their charge, spin, or even Fermi statistics. We show that this leads to universal experimental signatures that could provide incontrovertible evidence of fractionalization. Our considerations are based on recent theoretical breakthroughs regarding the physics of two-dimensional (2D) topologically ordered states with extrinsic line and point defects (*10*–*19*), of which robust boundary phenomena are a special case.

We focus primarily on explaining these phenomena in the context of the simplest gapped 2D QSL, the Z_2 short-ranged resonating valence bond (sRVB) state, and explaining how it can be distinguished from nonfractionalized magnetic insulators, or even from QSLs with different types of fractionalization. This type of QSL has been proposed (*20*) to explain recent neutron scattering experiments in $ZnCu_3(OH)_6Cl_2$ (herbertsmithite) (*21*) and also a number of experimental observations for the organic compound κ-$(ET)_2Cu_2(CN)_3$ (*22*). We build on recent results that demonstrate that gapped fractionalized phases support topologically distinct types of gapped boundaries

[1]Station Q, Microsoft Research, Santa Barbara, CA 93106, USA. [2]Department of Condensed Matter Physics, Weizmann Institute of Science, Rehovot, 76100, Israel. [3]Department of Physics, Stanford University, Stanford, CA 94305, USA.
*Corresponding author. E-mail: erez.berg@gmail.com

(*12*, *15*). These results imply that the Z_2 sRVB state necessarily supports exactly two topologically distinct types of gapped boundaries, referred to as the *e* edge and the *m* edge (*23*), that are separated by a topological quantum phase transition.

The Z_2 sRVB state is an insulating, spin-rotationally invariant gapped spin-liquid state. Its legitimacy as a state of matter has been proven by constructing model Hamiltonians with exact sRVB ground-states (*6*–*8*, *24*, *25*). At low energies, there are four topologically distinct types of elementary quasi-particle excitations: (i) topologically trivial excitations, which can be created with local operators, (ii) spinons and holons, which are topologically equivalent and carry spin 1/2 and charge 0, or spin 0 and charge 1, respectively, (iii) visons, which do not carry spin or charge and have mutually semionic statistics with respect to the spinons and holons, and (iv) the composite of a spinon or holon with a vison. Because electrons always carry both unit electric charge and spin 1/2, the spinons and holons cannot individually be created by any local combinations of electron operators and therefore must be topological excitations (*2*). That spinons and holons are topologically equivalent follows from the fact that one can be converted into the other by the local operation of adding or removing an electron. Moreover, the spinons and holons can be either bosonic or fermionic, depending on detailed energetics.

The Z_2 sRVB state can be understood at low energies in terms of a Z_2 lattice gauge theory. In this language, the spinons and holons carry the Z_2 gauge charge, whereas the visons are the Z_2 fluxes. As a result, the spinons and holons are sometimes referred to as the *e* particles and the visons as the *m* particles. This state can also be described at long wavelengths using Abelian Chern-Simons (CS) field theory (*26*, *27*)

$$\mathcal{L} = \frac{1}{4\pi} K^{IJ} \epsilon_{\mu\nu\lambda} a^I_\mu \partial_\nu a^J_\lambda + \mathcal{L}_{\text{matter}} \qquad (1)$$

where μ, ν, λ = 0, 1, 2 are 2 + 1D space-time indices; $\epsilon_{\mu\nu\lambda}$ is the Levi-Civita tensor, $K = \begin{pmatrix} 0 & 2 \\ 2 & 0 \end{pmatrix}$; $I, J = 1, 2$; and $\mathcal{L}_{\text{matter}}$ describes the fractionalized quasi-particles, which are minimally coupled to the $U(1)$ gauge fields a^I. The visons carry unit charge under a^1, whereas the spinons and holons both carry unit charge under a^2. The CS term binds charges to fluxes in such a way as to properly capture the nontrivial mutual statistics between spinons or holons and visons.

Clever numerical studies of spin-1/2 frustrated Heisenberg models (*28*–*31*) provided evidence for gapped spin-liquid ground states. However, it is not yet clear whether the ground state in those models is a Z_2 sRVB state or a certain competing QSL, the "doubled-semion" state, which is characterized instead by $K = \begin{pmatrix} 2 & 0 \\ 0 & -2 \end{pmatrix}$.

Each topologically ordered phase, characterized by a matrix *K*, can support topologically distinct types of gapped boundaries. A classification of such gapped edges (*12*, *15*), when applied to the Z_2 sRVB state, predicts exactly two topologically distinct types of gapped edges. As we explain below, these correspond to whether the *e* or the *m* particles are condensed along the boundaries. The doubled-semion state, in contrast, possesses only one type of gapped boundary (*32*).

The edge theory can be derived by starting with the Abelian CS theory (*1*). [For an alternative explanation, see (*32*).] It is well-known (*27*) that on a manifold with a boundary, Eq. 1 is only gauge-invariant if the gauge transformations are restricted to be zero on the boundary. This implies that on the boundary, the gauge fields correspond directly to physical degrees of freedom. One can derive an edge Lagrangian (*27*) in terms of scalar fields ϕ_I

$$\mathcal{L} = \frac{1}{4\pi} K_{IJ} \partial_x \phi_I \partial_t \phi_J - V_{IJ} \partial_x \phi_I \partial_x \phi_J \qquad (2)$$

where V_{IJ} is a positive-definite velocity matrix. The number of left (or right) movers is given by the number of positive (or negative) eigenvalues of the *K* matrix. In a Hamiltonian formulation, the first term on the right hand side of Eq. 2 implies that $[\phi_I(x), \phi_J(y)] = i\pi K^{-1}_{IJ} \text{sgn}(x-y)$. Quasi-particles that carry unit charge under a^I are created with the operators $e^{i\phi_I}$.

In the Z_2 sRVB state, the edge theory maps onto a single-channel Luttinger liquid, as there are two conjugate fields, $\phi \equiv \phi_1$ and $\theta \equiv \phi_2$, with $[\phi(x), \theta(y)] = i\frac{\pi}{2}\text{sgn}(x-y)$. A composite of two identical quasi-particles in the Z_2 sRVB state always corresponds to a topologically trivial excitation and therefore $e^{i2\phi_I}$ corresponds to a local operator on the edge. Thus, there are two basic types of local terms, $\delta\mathcal{L}_{Z_2} = \lambda_m \cos(2\phi) + \lambda_e \cos(2\theta)$ with coupling constants $\lambda_{e,m}$, that effectively backscatter counterpropagating modes and can induce an energy gap on the edge (*33*).

Because φ and θ are conjugate, the cosine terms cannot simultaneously pin their arguments, so there are two distinct phases. Where $|\lambda_m|$ is the dominant coupling, $\langle e^{i\phi} \rangle \neq 0$ and $\langle e^{i\theta} \rangle = 0$, implying that the *m* particles are condensed on the edge. Conversely, if $|\lambda_e|$ is dominant, the *e* particles are condensed on the edge: $\langle e^{i\theta} \rangle \neq 0$ and $\langle e^{i\phi} \rangle = 0$. The two phases, referred to as the *m* edge and *e* edge, respectively, are topologically distinct. In the absence of any additional global symmetries, there is a single quantum critical point between these two gapped phases in the Ising universality class. [See (*32*) for additional discussion.]

In the presence of spin rotation and charge conservation symmetries, the modes φ and θ must represent either low-energy spin or charge fluctuations (but not both), depending on the physical situation. If they describe charge fluctuations, then the charge density is given by $\rho_c = \frac{1}{\pi}\partial_x \phi$, and the operator $h = e^{i\theta + in\phi}$ creates a holon that is bosonic for even integer *n* and fermonic for odd *n*. The operator $e^{2i\theta}$ creates a topologically trivial excitation that carries charge 2 and no spin and is therefore physically equivalent to a Cooper pair. Alternatively, if the boson modes describe spin fluctuations, then the spin density is $S^z = \frac{1}{2\pi}\partial_x \phi$, and $S^{\pm} = e^{\pm i2\theta}$. The operator $e^{\pm i\theta + in\phi}$ creates a spin-1/2 spinon that is bosonic or fermionic for *n*, respectively, even or odd. In all cases, $e^{i\phi}$ creates a vison.

If charge and spin are conserved, any term proportional to cos(2θ) is prohibited, because this term changes either the charge or the spin of the edge. It follows that an *e* edge is incompatible with spin and charge conservation; the *m* edge is the generic gapped boundary of a Z_2 sRVB if charge and spin are conserved.

We will now explore how an *e* edge can be realized in a physically realistic system by bringing the edge into contact with another system with one or another pattern of symmetry breaking. Our results, explained below, are summarized in Table 1. Let us begin by considering a realization of a Z_2 sRVB state with easy-plane, or XXZ, spin-rotational symmetry. Again, this can be treated from the perspective of an Ising gauge theory or from the field theory perspective. In the bosonized edge theory, the bulk $U(1)$ spin rotational symmetry is associated with the global transformation $\theta \rightarrow \theta + f$ (where *f* is an arbitrary constant), and therefore, so long as this symmetry is not explicitly broken, terms that would pin θ, such as cos(2θ), are disallowed. However, a magnetic field applied at the edge in an in-plane direction leads to a term $-\mu_B B\cos(2\theta)$ (where μ_B is the Bohr magneton and *B* is the magnetic field), which for strong enough magnetic field can produce a phase transition to an *e* edge.

Now let us consider coupling a superconductor to the edge of a spin liquid. For simplicity we will consider a singlet superconductor, although the same results apply for the triplet superconductor. At low energies, the couplings between the superconductor and the spin liquid include Cooper pair tunneling of the form

$$\mathcal{H}_{\text{edge}} = t_{\text{pair}}(\Phi^\dagger_{\text{qsl}} \Phi_{\text{sc}} + H.c.) \qquad (3)$$

where Φ_{sc} is the Cooper pair operator on the edge of the superconductor, Φ_{qsl} is the Cooper

Table 1. Summary of conditions under which an *e* or *m* edge can be realized in the Z_2 sRVB. Aside from the XXZ case with an applied magnetic field *B*, the QSL is assumed to be *SO*(3) spin-rotationally invariant. The first two cases can, in principle, also be gapless, instead of realizing the gapped *m* edge. J_c, B_c, and t^c_{pair} are the critical Heisenberg exchange, magnetic field, and pair-tunneling strength needed to realize the *e* edge, respectively.

Edge physics	Edge type
Spin and charge conserved	*m*
Heisenberg exchange to colinear SDW	*m*
Heisenberg exchange $J > J_c$ to noncolinear SDW	*e*
Magnetic field $B > B_c$ at edge of XXZ system	*e*
Pair tunneling $t_{\text{pair}} > t^c_{\text{pair}}$ to superconductor	*e*

pair operator on the edge of the QSL, t_{pair} is the pair-tunneling amplitude, and *H.c.* stands for Hermitian conjugate. Φ_{sc} can be replaced by a c number because the Cooper pairs are condensed in the superconductor. The first term therefore prefers to condense pairs of holons, which are the Cooper pairs on the spin-liquid edge. In the bosonized field theory, this term corresponds to a perturbation $\delta\mathcal{L}_{pair} \propto t_{pair}\langle\Phi_{sc}\rangle\cos(2\theta)$, where the charge density is $\rho_c = \frac{1}{\pi}\partial_x\phi$. t_{pair} can drive a phase transition into the e edge, where single holons are also condensed: $\langle e^{i\theta}\rangle \neq 0$. The Cooper pair tunneling does not need to overcome the charge gap of the Z_2 spin liquid. By tuning the chemical potential in the superconductor using a gate voltage, the energy cost to adding holons to the edge can be made much smaller than the charge gap. In this situation, even a small pair-tunneling amplitude is sufficient to condense the holons.

A similar analysis shows that strong Heisenberg exchange coupling to a noncolinear spin density wave (SDW) can also realize the e edge. Coupling an $SO(3)$ spin rotationally invariant QSL to a colinear SDW (Néel state) is not by itself sufficient to realize the e edge, because the Néel state has a residual $U(1)$ spin rotation symmetry that precludes spinon condensation.

Now that we have investigated the physical conditions under which the distinct edge phases can be realized, we turn to describing their physical implications. In the Z_2 sRVB, the electron c_α can be thought of as a composite of a bosonic holon b and a fermionic spinon f_α: $c_\alpha = bf_\alpha$, where $\alpha = \uparrow,\downarrow$. When the e edge is created by strong Cooper pair tunneling from a superconductor, the bosonic holon is condensed on the edge. Consequently, any electron-tunneling term along the boundary between the QSL and the superconductor becomes

$$\delta\mathcal{H}_{edge} = tc^\dagger_{qsl}c_{sc} + H.c. \rightarrow t\langle b_{qsl}\rangle f^\dagger_{qsl}c_{sc} + H.c. \quad (4)$$

Thus, at an e edge with a superconductor, the electron can coherently tunnel into the spin liquid as a fermionic spinon, leaving its charge behind at the edge. This would not be allowed at an m edge, at which the electron would tunnel into the spin liquid as a whole. Then, depending on details of the energetics of the excitations in the QSL, the electron could subsequently decay into a holon and a spinon.

There is a useful analogy here with Tomasch oscillations observed long ago in the context of superconducting films (*34*). These oscillations reflect processes in which an electron with energy in excess of the superconducting gap tunnels coherently from a metal into a superconductor, where it becomes a Bogoliubov quasi-particle (*35*). There is a well-defined sense (*36*) in which the quasi-particles in a conventional superconductor are neutral spinons, although the broken gauge symmetry of the superconductor makes this analogy somewhat subtle.

The possibility of a direct coupling between electrons and fractionalized quasi-particles opens a new realm of possible probes of QSLs. Given the existence of a material with a Z_2 sRVB ground state and stable fermionic spinon quasi-particles, a direct experimental signature of such coherent fractionalization of the electron could be obtained by detecting a suitably generalized version of Tomasch oscillations: Consider the local electron tunneling density of states (LDOS), measured at the boundary of the superconductor, for a finite strip geometry (Fig. 1A). This will receive contributions from processes where superconducting quasi-particles coherently propagate into the spin liquid as fermionic spinons, reflect off the outer boundary, and propagate back. If the spinon inelastic mean free path is larger than the width d_{qsl} of the QSL, this leads to coherent oscillations of the LDOS as a function of the dimensionless ratio $eVd_{qsl}/\hbar v_{qsl}$ for voltages V larger than both the spinon and superconducting gaps, where v_{qsl} is the spinon velocity in the QSL and $\hbar$ is Planck's constant h divided by 2π. Moreover, incontrovertible evidence that the oscillations are associated with fractionalized excitations can be obtained by simultaneously monitoring the bulk current (I_b in the figure), which in this case will be parametrically small and free of signatures of coherent spinon interference. For an m edge, there would be no such coherent oscillations, as the electron must enter into the QSL as a whole and would subsequently decay into a spinon and holon.

Similar phenomena will occur when the e edge is created through magnetic effects, such as through a magnetic field applied at the edge, or through coupling to a noncolinear SDW. In these cases, the bosonic spinon is condensed at the edge. We can write the electron operator as $c_\alpha = hz_\alpha$, where z_α is a bosonic spinon, and h is a fermionic holon. Now the electron-tunneling Hamiltonian at the edge becomes $\delta\mathcal{H}_{edge} \propto t_{\alpha\beta}\langle z_\alpha\rangle h^\dagger_{qsl}c_{\beta;sdw} + H.c.$; here we have included a spin-dependent tunneling matrix element $t_{\alpha\beta}$. Thus, the electron in this case can propagate coherently into the spin liquid as a fermionic holon. If fermionic holons are stable fractionalized quasi-particles, we again expect to observe Tomasch oscillations in finite strip geometries (Fig. 1C).

Treating the case of gapless spin liquids in a theoretically controlled manner is more difficult than the case of gapped spin liquids. Nevertheless, we expect that in gapless systems such as Z_2 spin liquids with Dirac points in their spinon spectrum or Z_2 chiral spin liquids with stable spinon Fermi surfaces (*37*), generalized Tomasch oscillations of the sort envisaged here would occur as well. This is because (i) in such states, the Z_2 gauge field is gapped, and thus low-energy spinons can propagate coherently; and (ii) there is still a well-defined notion of whether the spinons or holons have condensed near the boundary.

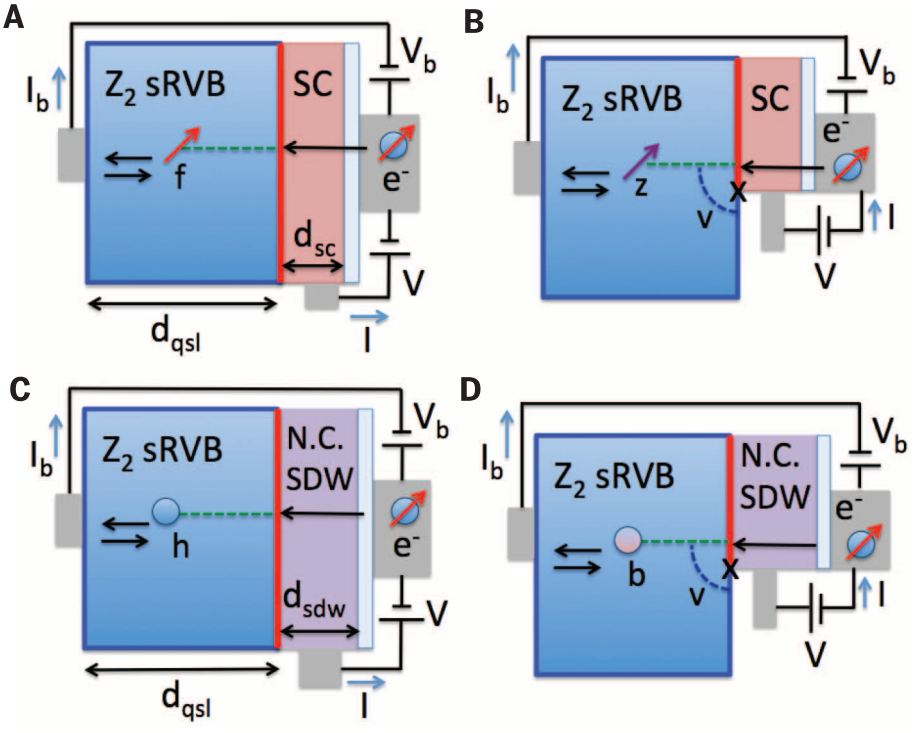


Fig. 1. Proposed geometries to observe geometric resonances (generalized Tomasch oscillations) in QSLs. d_{qsl} and d_{sc} are the widths of the QSL and superconducting regions, respectively. (**A**) An e edge is created by coupling to a superconductor (SC), in which case an electron can coherently enter the Z_2 sRVB as a fermionic spinon f. (**B**) At the domain wall between e and m edges, there is a Majorana fermion zero mode, allowing electrons to coherently pass into the QSL as a bosonic spinon z by emitting a vison v at the m edge. (**C**) An e edge is created by coupling a spin-rotationally invariant QSL to a noncolinear (N.C.) SDW, allowing an electron to coherently enter the QSL as a fermionic holon, h. (**D**) The Majorana fermion zero mode at the domain wall allows an electron to coherently enter the QSL as a bosonic holon, b. In (A) to (D), oscillations in $I(V)$ with a period determined by d_{qsl} [without oscillations in the bulk current $I_b(V_b)$] would provide a conclusive signature of fractionalization in the QSL.

At the boundary between two topologically distinct segments of edge, localized exotic topological zero modes arise that give rise to topologically protected degeneracies and projective non-Abelian statistics (*12*). In the case of the Z_2 sRVB state, the domain wall between e and m edges localizes a Majorana fermion zero mode, with the following physical consequences: Let us consider the case of the superconductivity-induced e edge, where an electron can coherently enter the QSL as a fermionic spinon. If this process occurs in the vicinity of the domain wall between an e and m edge, then the fermionic spinon can also emit or absorb a vison from the m edge, thus becoming a bosonic spinon. In other words, the Majorana fermion zero mode is a source or sink of fermion parity, allowing the electron to coherently enter into the spin liquid as a bosonic spinon. If the fermionic spinon in the bulk of the QSL can decay into a vison and a bosonic spinon, then this geometry (Fig. 1B) will allow the Tomasch oscillations to be observed in the tunneling conductance. Similar considerations show that when the e edge is induced by magnetism, the electron can enter into the spin liquid as a bosonic holon in the vicinity of the e-m domain wall (Fig. 1D).

The considerations outlined here suggest ways to tune through the topological phase transition that separates the e and m edges, such as by applying a magnetic field to the edge of an easy-plane QSL. This can be done by taking a thin sample and shielding the bulk of the QSL by sandwiching it between two superconductors. At the critical field for the edge quantum phase transition, there will be enhanced thermal transport through the edge, leading to a nonzero intercept at low temperatures in the thermal conductance: $\lim_{T\to 0}\kappa/T = N_{\mathrm{L}} c \frac{\pi^2}{3}\frac{k_{\mathrm{B}}^2}{h}$, where N_{L} is the number of layers in the QSL, $c = 1/2$ is the central charge of the edge at the critical point, and k_{B} is Boltzmann's constant. Because neither the trivial paramagnet nor the doubled-semion QSL have topologically distinct types of gapped boundaries, the observation of a topological quantum phase transition at the edge of a gapped insulating spin system would prove the existence of a fractionalized spin-liquid state and rule out the doubled-semion state. The present considerations are readily extended to other sorts of topologically ordered states, such as those that occur in fractional quantum Hall systems.

REFERENCES AND NOTES

1. P. W. Anderson, *Mater. Res. Bull.* **8**, 153–160 (1973).
2. S. A. Kivelson, D. S. Rokhsar, J. P. Sethna, *Phys. Rev. B* **35**, 8865–8868 (1987).
3. N. Read, S. Sachdev, *Phys. Rev. Lett.* **66**, 1773–1776 (1991).
4. X. G. Wen, *Phys. Rev. B* **44**, 2664–2672 (1991).
5. T. Senthil, M. P. A. Fisher, *Phys. Rev. B* **62**, 7850–7881 (2000).
6. R. Moessner, S. L. Sondhi, *Phys. Rev. Lett.* **86**, 1881–1884 (2001).
7. L. Balents, M. P. A. Fisher, S. M. Girvin, *Phys. Rev. B* **65**, 224412 (2002).
8. A. Seidel, *Phys. Rev. B* **80**, 165131 (2009).
9. L. Balents, *Nature* **464**, 199–208 (2010).
10. M. Barkeshli, X.-L. Qi, *Phys. Rev. X* **2**, 031013 (2012).
11. M. Barkeshli, C.-M. Jian, X.-L. Qi, *Phys. Rev. B* **87**, 045130 (2013).
12. M. Barkeshli, C.-M. Jian, X.-L. Qi, *Phys. Rev. B* **88**, 241103(R) (2013).
13. S. Beigi, P. W. Shor, D. Whalen, *Commun. Math. Phys.* **306**, 663–694 (2011).
14. A. Kitaev, L. Kong, *Commun. Math. Phys.* **313**, 351–373 (2012).
15. M. Levin, *Phys. Rev. X* **3**, 021009 (2013).
16. A. Kapustin, N. Saulina, *Nucl. Phys. B* **845**, 393–435 (2011).
17. N. H. Lindner, E. Berg, G. Refael, A. Stern, *Phys. Rev. X* **2**, 041002 (2012).
18. D. J. Clarke, J. Alicea, K. Shtengel, *Nat. Commun.* **4**, 1348 (2013).
19. M. Cheng, *Phys. Rev. B* **86**, 195126 (2012).
20. M. Punk, D. Chowdhury, S. Sachdev, *Nat. Phys.* **10**, 289–293 (2014).
21. T.-H. Han *et al.*, *Nature* **492**, 406–410 (2012).
22. Y. Qi, C. Xu, S. Sachdev, *Phys. Rev. Lett.* **102**, 176401 (2009).
23. These were identified long ago in the toric code model (*38*) in terms of rough versus smooth edges (*39*), although the generic necessity to realize one or the other in resonating valence bond states and their general independence of lattice structure has only recently been fully appreciated.
24. D. S. Rokhsar, S. A. Kivelson, *Phys. Rev. Lett.* **61**, 2376–2379 (1988).
25. T. Senthil, O. Motrunich, *Phys. Rev. B* **66**, 205104 (2002).
26. M. Freedman, C. Nayak, K. Shtengel, K. Walker, Z. Wang, *Ann. Phys.* **310**, 428–492 (2004).
27. X.-G. Wen, *Quantum Field Theory of Many-Body Systems* (Oxford Univ. Press, Oxford, 2004).
28. H.-C. Jiang, Z. Wang, L. Balents, *Nat. Phys.* **8**, 902–905 (2012).
29. H.-C. Jiang, H. Yao, L. Balents, *Phys. Rev. B* **86**, 024424 (2012).
30. S. Yan, D. A. Huse, S. R. White, *Science* **332**, 1173–1176 (2011).
31. S. Depenbrock, I. P. McCulloch, U. Schollwöck, *Phys. Rev. Lett.* **109**, 067201 (2012).
32. See the supplementary materials on *Science* Online.
33. If the resulting gaps are large, the field theory description of the edge is no longer controlled, but because the most important qualitative features of a gapped state do not depend on the magnitude of the gap, the field theory description of such phases should be adequate for present purposes: More formally, it gives a leading order description of the edge modes in the vicinity of an edge quantum critical point where the edge gaps, but not the bulk gaps, are vanishingly small.
34. W. J. Tomasch, *Phys. Rev. Lett.* **15**, 672–675 (1965).
35. W. L. McMillan, P. W. Anderson, *Phys. Rev. Lett.* **16**, 85–87 (1966).
36. S. Kivelson, D. Rokhsar, *Phys. Rev. B* **41**, 11693–11696 (1990).
37. M. Barkeshli, H. Yao, S. A. Kivelson, *Phys. Rev. B* **87**, 140402 (2013).
38. A. Kitaev, *Ann. Phys.* **303**, 2–30 (2003).
39. S. B. Bravyi, A. Y. Kitaev, http://arxiv.org/abs/quant-ph/9811052.

ACKNOWLEDGMENTS

This work was supported by NSF-DMR grant 1265593 (S.K.), the Israel Science Foundation, the Israel-U.S. Binational Foundation, the Minerva Foundation, and the German-Israeli Foundation (E.B.). M.B. thanks X.-L. Qi for recent collaborations on related topics. We thank E. Altman, C. Nayak, M. Freedman, Z. Wang, K. Walker, M. Hastings, M. P. A. Fisher, B. Bauer, and T. Grover for discussions.

SUPPLEMENTARY MATERIALS

www.sciencemag.org/content/346/6210/722/suppl/DC1
Supplementary Text
References (*40*–*45*)

12 March 2014; accepted 2 October 2014
10.1126/science.1253251

PHOTOCHEMISTRY

Reduction of aryl halides by consecutive visible light-induced electron transfer processes

Indrajit Ghosh,* Tamal Ghosh,* Javier I. Bardagi, Burkhard König†

Biological photosynthesis uses the energy of several visible light photons for the challenging oxidation of water, whereas chemical photocatalysis typically involves only single-photon excitation. Perylene bisimide is reduced by visible light photoinduced electron transfer (PET) to its stable and colored radical anion. We report here that subsequent excitation of the radical anion accumulates sufficient energy for the reduction of stable aryl chlorides giving aryl radicals, which were trapped by hydrogen atom donors or used in carbon-carbon bond formation. This consecutive PET (conPET) overcomes the current energetic limitation of visible light photoredox catalysis and allows the photocatalytic conversion of less reactive chemical bonds in organic synthesis.

Visible light provides sufficient energy to promote challenging chemical reactions. Biological photosynthesis as the omnipresent example uses a visible portion of the solar spectrum to separate charges by electron transfer, providing the energy for water oxidation. This transformation (water to oxygen, protons, and electrons) requires the cumulative absorption of four photons (*1*). In past decades, visible light–mediated chemical photoredox catalysis has emerged into a conceptually related valuable method for organic synthesis (*2*–*4*). Here, single-photon excitation of dye molecules, such as redox-active coordination compounds [e.g., $Ru(bpy)_3^{2+}$ or $Ir(ppy)_3$] (*3*, *5*), conjugated organics (e.g., eosin Y) (*6*), or inorganic semiconductors (e.g., CdS) (*7*) mediates photoinduced electron or energy transfer process to substrates.

A recent application is the generation of highly reactive aryl radicals, which are useful arylating reagents in synthesis, by photoinduced electron transfer (PET) from photoredox catalysts to suitable precursors followed by bond scission (*8*, *9*). However, the choice of aryl radical precursors is currently limited to electron-poor arenes, such as diazonium (*6*, *10*) or iodonium (*11*) salts, or in a few cases aryl iodides (*9*, *12*), with weakly bound leaving groups, due to the accessible reducing

Institute of Organic Chemistry, University of Regensburg, D-93040 Regensburg, Germany.
*These authors contributed equally to this work. **†Corresponding author. E-mail: burkhard.koenig@ur.de**

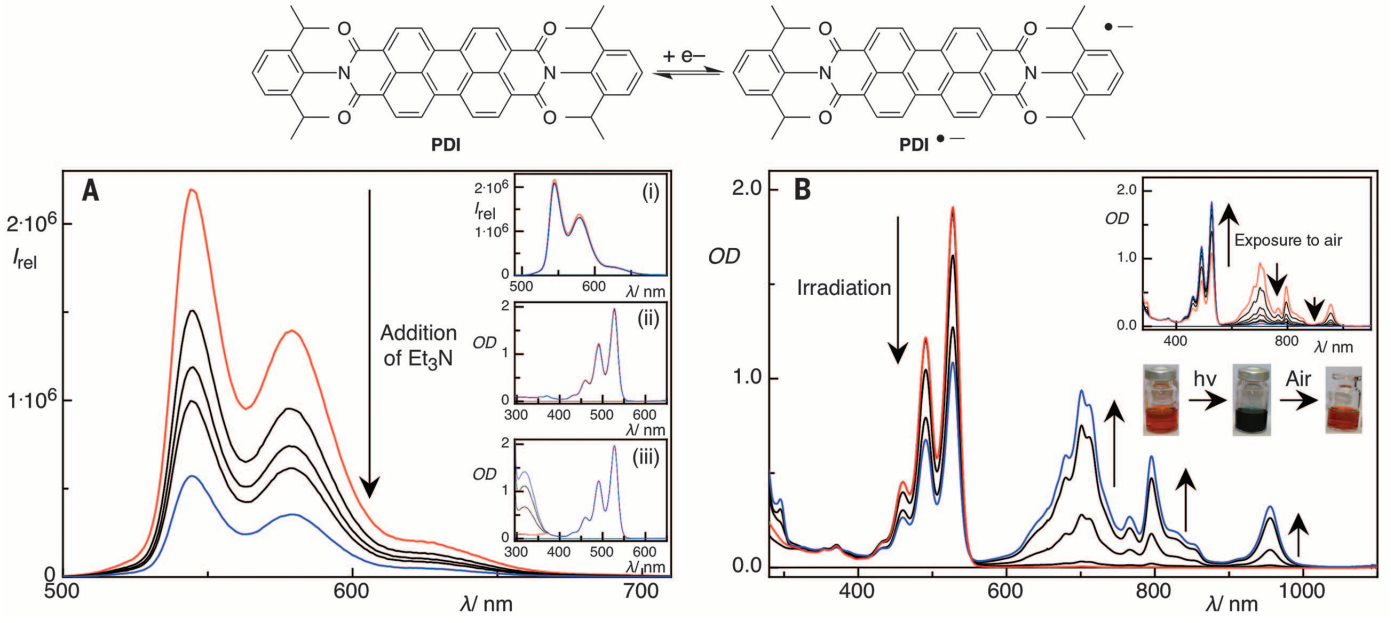
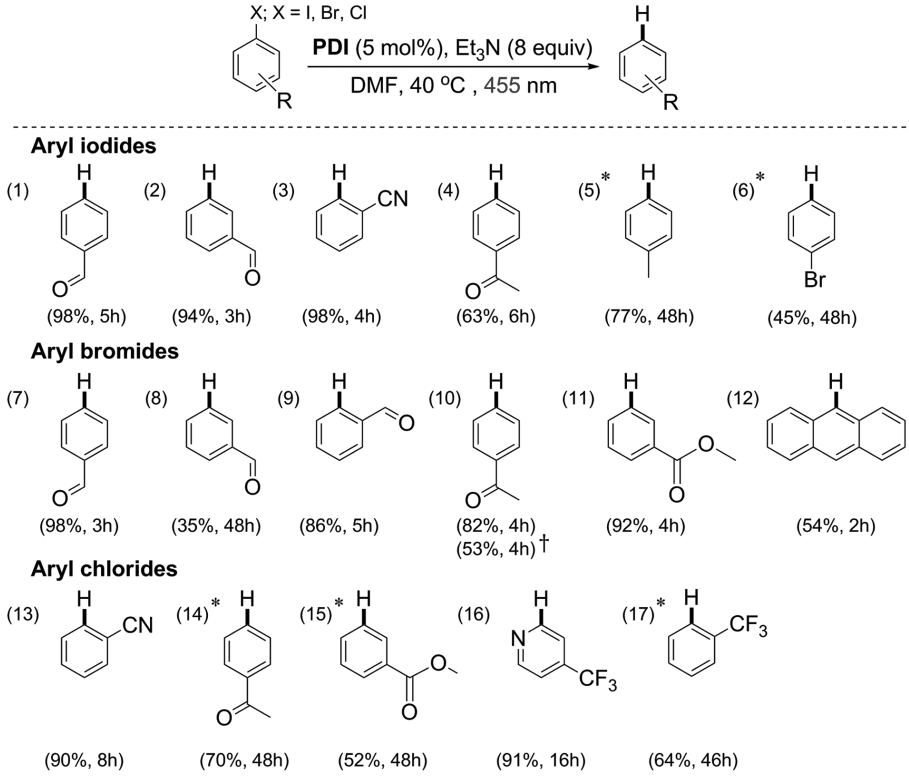


Fig. 1. Chemical structure of the photocatalyst PDI, one electron reduction of PDI to its radical anion, and effects of Et_3N and 4′-bromoacetophenone on its photophysical properties. (**A**) Changes in the fluorescence spectra (in this case, intensity; λ_{Ex} = 455 nm) of PDI upon successive addition of Et_3N in DMF. In the insets, changes in the fluorescence spectra of PDI upon addition of (i) 4′-bromoacetophenone, and changes in the absorption spectra of PDI upon addition of (ii) Et_3N, and (iii) 4′-bromoacetophenone are shown. (**B**) Formation of the PDI radical anion ($PDI^{\bullet-}$) upon photoexcitation (λ_{Ex} = 455 nm) of PDI in the presence of Et_3N. In the inset, regeneration of neutral PDI from $PDI^{\bullet-}$ upon exposure to air is shown (see also fig. S5).

power of typical visible light photoredox catalysts (*13*, *14*). Two mechanistic scenarios for the aryl radical generation can be considered: (i) oxidative quenching of the excited photoredox catalyst by the aryl radical precursor, which must be exergonic or, if the lifetime of the excited state is long and the subsequent bond cleavage fast and irreversible, at least thermo neutral (*15*); (ii) oxidation of the photoreduced catalyst in its ground state (fig. S1, left), which can be slightly endergonic. The energy conferred by visible light excitation for subsequent reduction chemistry is limited by the energy of a single absorbed photon. The energy of blue photons (440 nm) of 270 KJ/mol or 2.8 eV defines a maximum theoretical energy threshold between the donor (i.e., photocatalyst) and acceptor (i.e., substrate). In addition, part of the accessible energy is always lost due to intersystem crossing and reorganization of the excited states of the photocatalysts by nonradiative pathways. In the case of Ru complexes, this loss is ~0.6 eV (*3*). As a consequence, the available energy of typical photocatalysts just reaches the reduction potential (E^o) of aryl iodides (*9*), defining the current synthetic scope of photoredox catalysis.

Here, we report a practical approach to overcome the limitations of visible light–mediated chemical photocatalysis by using the energies of two photons in one catalytic cycle (*16*). Photocatalytic alkylation or arylation reactions as reported by MacMillan (*3*, *17*), Stephenson (*18*), Yoon (*2*), and others (*6*) employ a typical PET process (fig. S1, left). The excited dye becomes a stronger oxidant (and reductant) and is converted into its radical anion, which activates substituted benzyl



Yields (Error ca. 5 %) were calculated from GC measurements using internal standards.
*10 mol% catalyst and 16 equiv of Et_3N were employed.
†Photoreduction reaction was performed under sunlight.

Fig. 2. Photoreduction of aryl halides. Yields (%) and reaction times (hours) are given.

bromides (*3*, *19*), alpha bromo carbonyl compounds (*20*), aryl iodides (*9*, *12*), diazonium (*6*), and iodonium (*11*) salts. However, compounds that are less reactive (e.g., aryl bromides and chlorides) (*21*–*23*) due to a more negative reduction potential, higher carbon-halide bond dissociation energy, and a different, stepwise cleavage mechanism (*23*) are not accessible by this process using typical photocatalysts and, more importantly, visible light. Our approach is inspired by the Z scheme of biological photosynthesis, which has already been used in water photooxidation (*24*) but, surprisingly, has not yet been applied in organic synthesis. The energy of a second visible light excitation can be added to the process if the radical anion of the dye is reasonably stable in the ground state, colored, and thus can be excited again by visible light (fig. S1, right).

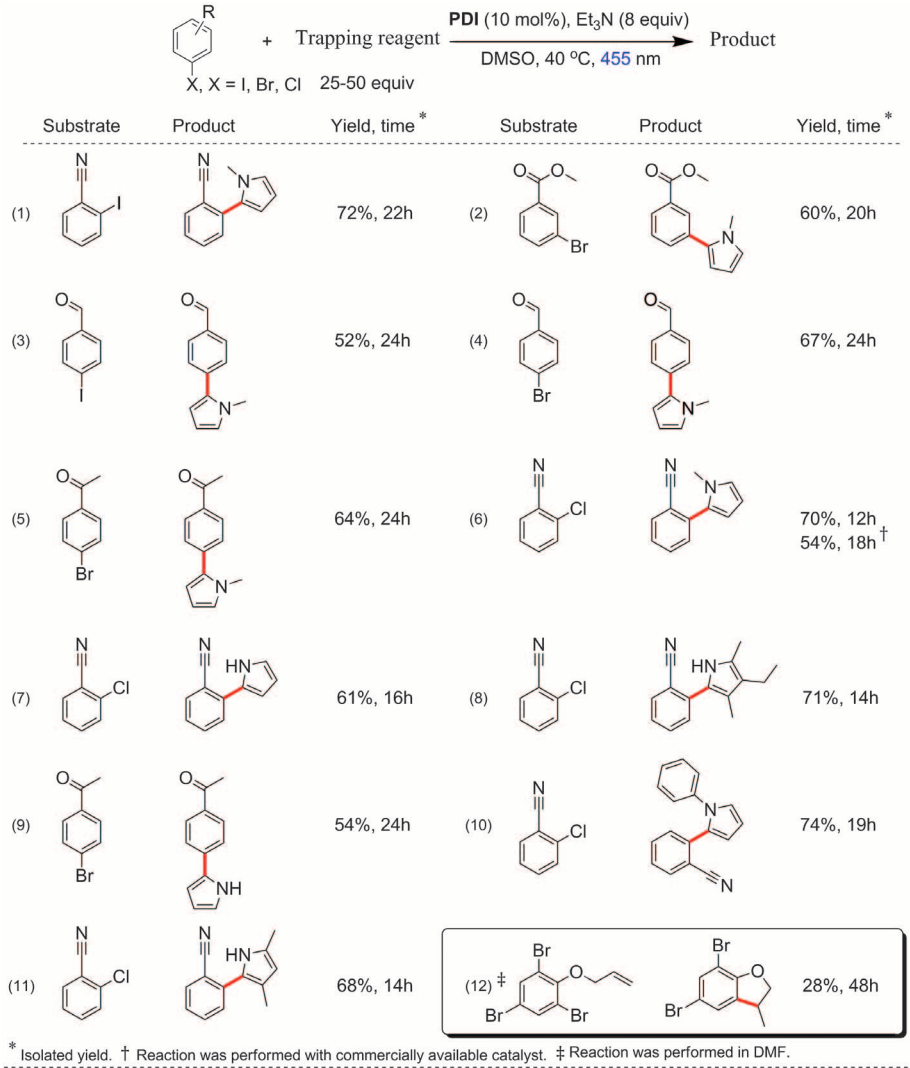
Perylene diimides—a class of fluorescent dye molecules that have been used as pigments, colorants, photoreceptors, and, more recently, as electronic materials because of their characteristic combination of thermal- and photostability and optical and redox properties (*25*)—fulfill the requirements of such a biomimetic organic dye–based catalytic system. Among different perylene diimides *N*,*N*-bis(2,6-diisopropylphenyl)perylene-3,4,9,10-bis(dicarboximide) (PDI) (see Fig. 1 for chemical structure) was selected due to its better solubility in *N*,*N*′-dimethylformamide (DMF) and dimethyl sulfoxide (DMSO) (solvents used in this study). Upon irradiation with blue light (455 nm) in the presence of triethylamine (Et_3N) as electron donor, PDI forms a colored radical anion $PDI^{\bullet-}$ (Fig. 1 and figs. S3 to S5) that can again be excited by visible light (*26*). In the absence of oxygen, the radical anion is very stable. Spectroscopic investigations confirmed that electron transfer from Et_3N to PDI requires photoexcitation (Fig. 1 and fig. S4) (*27*).

A synthetic application of this catalytic system is the photoreduction of aryl halides, including aryl chlorides, using visible light irradiation. The reaction conditions were optimized by irradiating a mixture of 4′-bromoacetophenone, PDI (5 mol%), and Et_3N with blue light (455 nm) (see table S1). In DMSO as solvent, the reduction product acetophenone was obtained in 4 hours with 47% photoreduction yield (entry 16, table S1). Continuous irradiation of the reaction mixture for 8 hours gave 69% yield. Use of DMF as solvent gave comparable or slightly better yields (see entry 10 in Fig. 2 and table S1) in a shorter reaction time of 4 hours. Control experiments confirmed that PDI, electron donor, and light irradiation are necessary for the photoreduction reaction to occur (entries 1 to 6 in table S1).

Using the optimized conditions, the reaction scope was explored with a range of substituted aryl bromides giving the corresponding reduction products in good to nearly quantitative yields (Fig. 2). The reduction potentials of NMe_2- and OMe-substituted aryl bromides are too high to be reached employing these photoreduction conditions, whereas *p*-nitro-substituted aryl bromides have such a low fragmentation rate (*22*) that back electron transfer becomes dominant. The photoreduction reactions could also be performed under sunlight (entry 10 in Fig. 2) or with 530-nm light-emitting diodes as the absorption spectrum of PDI spans a broad portion of the visible spectrum (fig. S3). Substituted aryl iodides having slightly lower reduction potentials than aryl bromides (*22*) gave comparable photoreduction yields (see entries 1 to 6 in Fig. 2). Notably, an aryl–iodine bond was chemoselectively reduced in the presence of a bromine substituent (entry 6 in Fig. 2).

A commercially available catalyst, *N*,*N*′-bis (3-pentyl)perylene-3,4,9,10-bis(dicarboximide) (for the chemical structure, see fig. S2), gave similar yields when the reaction mixtures were irradiated for 8 hours (see entries 14 and 15 in table S1). The slightly slower reaction rate is attributed to its poorer solubility.

Based on the reduction potential of $PDI/PDI^{\bullet-}$ [–0.37 V versus saturated calomel electrode (SCE)] and the $E_{0\text{–}0}$ transition energy of $PDI^{\bullet-}$, we estimated a reducing power of the excited state $PDI^{\bullet-*}$ according to the Rehm-Weller equation (*28*) that reaches or exceeds the reduction potentials of substituted aryl chlorides (*26*, *29*). This class of compounds, although easily accessible and relatively inexpensive, has not been considered in visible light photocatalysis because of their low reactivity due to high reduction potentials, high carbon-chlorine bond energies, and a stepwise fragmentation mechanism. To the best of our knowledge, the reduction of aryl chlorides has only been achieved using strong bases (*30*, *31*), such as potassium tert-butoxide, or nucleophiles under ultraviolet (UV) ($\lambda_{Ex} \leq$ 350 nm) irradiation ($S_{RN}1$) (*32*) and in the presence of an excess of highly reactive neutral organic reducing agents, such as N^2,N^2,N^{12},N^{12}-tetramethyl-7,8-dihydro-6H-dipyrido[1,4]diazepine-2,12-diamine (for the chemical structure, see fig. S2) and UV-A (365 nm) irradiation as introduced by Murphy (*21*). The consecutive PET (conPET) process generates the strong reducing $PDI^{\bullet-*}$ in situ by two subsequent visible light excitations starting from air-stable PDI. This avoids the use of highly air- and



* Isolated yield. † Reaction was performed with commercially available catalyst. ‡ Reaction was performed in DMF.

Fig. 3. C–H aromatic substitution reactions of aryl halides with substituted pyrroles and intramolecular addition to an alkene.

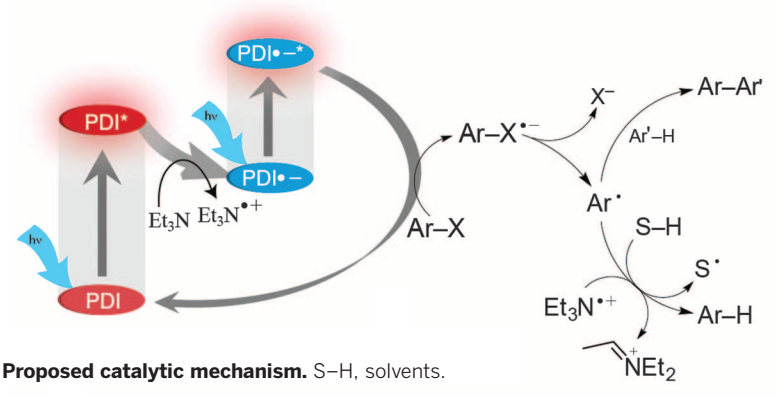


Fig. 4. Proposed catalytic mechanism. S–H, solvents.

moisture-sensitive donor molecules, which require strict inert reaction conditions, UV-A irradiation, and strongly basic conditions that are incompatible with many functional groups. Aryl chlorides bearing electron withdrawing groups gave the corresponding reduction products with good to excellent yields in photocatalytic conditions (entries 13 to 17 in Fig. 2) that require only mixing of substrates, PDI, Et_3N, and irradiation with visible light.

Next, we applied the aryl radical intermediates for C–C bond-forming arylation reactions. Challenge in this case is competition from fast hydrogen abstraction of the aryl radical from the solvent and the radical cation of Et_3N (*33*). We therefore selected as the reaction partner *N*-heterocyclic pyrroles, which were found to have high reaction rates in the addition of radicals. Substantial amounts of the expected arylation product were indeed obtained by irradiating aryl halides in the presence of *N*-methylpyrrole and catalytic amounts of PDI. The reduction product is a minor by-product but dominates when furan or thiophene are used as reaction partner. Changing the solvent from DMF, which favors the reduction product, to DMSO improved the yields greatly. Isolated yields of functionalized *N*-methylpyrrole derivatives obtained from different substituted aryl halides are depicted in Fig. 3. As in the photoreduction reaction, the C–H arylation reaction with *N*-methylpyrrole could also be performed with *N,N'*-bis(3-pentyl)perylene-3,4,9,10-bis(dicarboximide) (entry 6 in Fig. 3). The reaction scope was extended to other pyrrole derivatives affording arylated products in good to excellent yields (Fig. 3).

The photoreduction of aryl halides appears to proceed via a radical mechanism (*23*, *34*), as evidenced by the conversion of 2-(allyloxy)-1,3,5-tribromobenzene to the 5-*exo* cyclization product 5,7-dibromo-3-methyl-2,3-dihydrobenzofuran (entry 12, Fig. 3), which implies a radical intermediate (*12*, *34*). Furthermore, the reduction reaction of 4′-bromoacetophenone in the presence of 2,2,6,6-tetramethylpiperidinoxyl (TEMPO) gave the expected TEMPO adduct (see the supplementary materials). The formation of a PDI dianion, which could be formed via a two-electron reduction (*35*), was not detected under the reaction conditions (compare Fig. 1B and fig. S4 with fig. S3; fig. S3 shows the absorption spectrum of the electrochemically generated PDI dianion). The photoreduction of 4′-bromoacetophenone was minimal in air, preventing the formation of the PDI radical anion (entry 6 in table S1, Fig. 1B, and fig. S5). In the absence of light, no reduction product is obtained: 4′-bromoacetophenone added to a photochemically generated PDI radical anion (by photo-irradiating the mixture of PDI and Et_3N) and kept in the dark for 4 hours was not converted (entries 9 and 11 in table S1). When the reaction mixture was then illuminated with 455-nm light, acetophenone was obtained in yields comparable to the normal photoreduction protocol. Reduction of 4′-bromoacetophenone also did not occur when the substrate was added to a chemically generated [using $(Et_4N)_2S_2O_4$ as chemical reductant of PDI] radical anion (see entry 10 in table S1). Degradation products of the catalyst formed during the course of the reaction may still contribute to substrate conversion because only the perylene core is required (compare PDI and *N,N'*-bis(3-pentyl)perylene-3,4,9,10-bis(dicarboximide): The substituents in the amide nitrogens of perylene have almost no influence on the photophysical properties and are mainly introduced to increase the solubility of perylene diimides) (*25*).

All experiments support the proposed catalytic cycle shown in Fig. 4. Excited PDI* is reductively quenched by Et_3N to give $PDI^{\bullet-}$ and the radical cation of triethylamine ($Et_3N^{\bullet+}$) (*27*). Upon the second excitation, $PDI^{\bullet-*}$ reduces the substrate yielding the aryl radical precursor ($ArX^{\bullet-}$) and regenerating the neutral PDI. Fragmentation of $ArX^{\bullet-}$ yields the aryl radical, which abstracts a hydrogen atom from either $Et_3N^{\bullet+}$ or solvents to yield the reduction products, or reacts with unsaturated compounds yielding C–C coupling products. Gas chromatography–mass spectrometry (GC-MS) analysis of the crude product mixture confirmed the formation of diethylamine, and hydrogen atom abstraction reduction reactions in D_7-DMF gave deuterated products (see the supplementary materials).

Two conPET steps using perylene diimide dyes accumulate the energy from two visible light excitations. The process is a minimalistic chemical model of the Z scheme in biological photosynthesis and extends the scope of visible light photocatalysis to aryl chlorides. Highly reactive aryl radicals are obtained from stable, and in the case of aryl chlorides, inexpensive bulk chemicals, under very mild and metal-free reaction conditions.

REFERENCES AND NOTES

1. J. J. Concepcion, R. L. House, J. M. Papanikolas, T. J. Meyer, *Proc. Natl. Acad. Sci. U.S.A.* **109**, 15560–15564 (2012).
2. D. M. Schultz, T. P. Yoon, *Science* **343**, 1239176 (2014).
3. C. K. Prier, D. A. Rankic, D. W. C. MacMillan, *Chem. Rev.* **113**, 5322–5363 (2013).
4. J. Xuan, W. J. Xiao, *Angew. Chem. Int. Ed.* **51**, 6828–6838 (2012).
5. F. Teplý, *Collect. Czech. Chem. Commun.* **76**, 859–917 (2011).
6. D. P. Hari, P. Schroll, B. Koenig, *J. Am. Chem. Soc.* **134**, 2958–2961 (2012).
7. D. Ravelli, D. Dondi, M. Fagnoni, A. Albini, *Chem. Soc. Rev.* **38**, 1999–2011 (2009).
8. D. P. Hari, B. Koenig, *Angew. Chem. Int. Ed.* **52**, 4734–4743 (2013).
9. J. D. Nguyen, E. M. D'Amato, J. M. R. Narayanam, C. R. J. Stephenson, *Nat. Chem.* **4**, 854–859 (2012).
10. D. P. Hari, T. Hering, B. Koenig, *Angew. Chem. Int. Ed.* **53**, 725 (2014).
11. Y. X. Liu *et al.*, *Synlett* **24**, 507–513 (2013).
12. H. Kim, C. Lee, *Angew. Chem. Int. Ed.* **51**, 12303–12306 (2012).
13. The excited state redox potential of fac-Ir(ppy)3 is estimated to be −1.73 versus SCE (*9*). Some metal complexes with even stronger reducing power in the excited state have been reported but have not been applied to photoredox catalysis (*14*).
14. S. B. Harkins, J. C. Peters, *J. Am. Chem. Soc.* **127**, 2030–2031 (2005).
15. The Rehm-Weller equation estimates the reduction potential of a photoredox catalyst in its excited state from the ground-state redox potential and the $E_{0\text{-}0}$ transition energy (*28*).
16. For a recent example of two-step photoexcitation (Z scheme) of heterogeneous semiconductor in water splitting, see (*24*).
17. M. T. Pirnot, D. A. Rankic, D. B. C. Martin, D. W. C. MacMillan, *Science* **339**, 1593–1596 (2013).
18. L. Furst, B. S. Matsuura, J. M. R. Narayanam, J. W. Tucker, C. R. J. Stephenson, *Org. Lett.* **12**, 3104–3107 (2010).
19. J. M. R. Narayanam, J. W. Tucker, C. R. J. Stephenson, *J. Am. Chem. Soc.* **131**, 8756–8757 (2009).
20. D. A. Nicewicz, D. W. C. MacMillan, *Science* **322**, 77–80 (2008).
21. E. Cahard *et al.*, *Angew. Chem. Int. Ed.* **51**, 3673–3676 (2012).
22. C. Costentin, M. Robert, J. M. Savéant, *J. Am. Chem. Soc.* **126**, 16051–16057 (2004).
23. L. Pause, M. Robert, J. M. Saveant, *J. Am. Chem. Soc.* **121**, 7158–7159 (1999).
24. Y. Sasaki, H. Kato, A. Kudo, *J. Am. Chem. Soc.* **135**, 5441–5449 (2013).
25. F. Würthner, *Chem. Commun.* **2004** (14), 1564–1579 (2004).
26. D. Gosztola, M. P. Niemczyk, W. Svec, A. S. Lukas, M. R. Wasielewski, *J. Phys. Chem. A* **104**, 6545–6551 (2000).
27. M. J. Tauber, R. F. Kelley, J. M. Giaimo, B. Rybtchinski, M. R. Wasielewski, *J. Am. Chem. Soc.* **128**, 1782–1783 (2006).
28. D. Rehm, A. Weller, *Isr. J. Chem.* **8**, 259–271 (1970).
29. C. Ramanan, A. L. Smeigh, J. E. Anthony, T. J. Marks, M. R. Wasielewski, *J. Am. Chem. Soc.* **134**, 386–397 (2012).
30. M. E. Budén, J. F. Guastavino, R. A. Rossi, *Org. Lett.* **15**, 1174–1177 (2013).
31. Y. Cheng, X. Gu, P. Li, *Org. Lett.* **15**, 2664–2667 (2013).
32. R. A. Rossi, A. B. Pierini, A. B. Peñéñory, *Chem. Rev.* **103**, 71–168 (2003).
33. Z. Chami, M. Gareil, J. Pinson, J. M. Saveant, A. Thiebault, *J. Org. Chem.* **56**, 586–595 (1991).
34. M. Newcomb, in *Encyclopedia of Radicals in Chemistry, Biology and Materials*, C. S. Chatgilialoglu, A. Studer, Eds. (Wiley, Chichester, UK, 2012)pp. 107–124.
35. E. Shirman *et al.*, *J. Phys. Chem. B* **112**, 8855–8858 (2008).

ACKNOWLEDGMENTS

We thank the Deutsche Forschungsgemeinschaft (GRK 1626) for financial support. J.I.B. thanks the Alexander von Humboldt Foundation for a scholarship. We thank R. Vasold for his assistance in GC-MS measurements.

SUPPLEMENTARY MATERIALS

www.sciencemag.org/content/346/6210/725/suppl/DC1
Materials and Methods
Supplementary Text
Figs. S1 to S5
Table S1
References (*36*–*39*)

2 July 2014; accepted 1 October 2014
10.1126/science.1258232

PHASE TRANSFORMATION

Microscopic mechanisms of equilibrium melting of a solid

Amit Samanta,[1,2]* Mark E. Tuckerman,[3,4,5]* Tang-Qing Yu,[6] Weinan E[7,8]*

The melting of a solid, like other first-order phase transitions, exhibits an intrinsic time-scale disparity: The time spent by the system in metastable states is orders of magnitude longer than the transition times between the states. Using rare-event sampling techniques, we find that melting of representative solids—here, copper and aluminum—occurs via multiple, competing pathways involving the formation and migration of point defects or dislocations. Each path is characterized by multiple barrier-crossing events arising from multiple metastable states within the solid basin. At temperatures approaching superheating, melting becomes a single barrier-crossing process, and at the limit of superheating, the melting mechanism is driven by a vibrational instability. Our findings reveal the importance of nonlocal behavior, suggesting a revision of the perspective of classical nucleation theory.

Theoretical work on the melting of a solid dates back to Lindemann, who in 1910 envisioned the melting transition as a vibrational instability (*1*). In 1939, Born postulated the macroscopic instability criteria of a solid in terms of the elastic constants (*2*–*4*). Most other theoretical models are centered around the role of defects, including point defects such as vacancies and interstitials and line defects such as dislocations, that proliferate in the solid close to the melting point (*5*–*8*).

Contrary to these melting theories, classical notions of homogeneous melting envision the formation of an initial liquid nucleus that is aided by thermal fluctuations without any preferential nucleating sites (*9*, *10*). Within the framework of the classical nucleation theory (CNT), the radius r of the liquid nucleus serves as a reaction coordinate, and the Gibbs free energy $\Delta G(r)$ is a balance between the free energy gained in forming a liquid nucleus of volume $4\pi r^3/3$ and the work needed to create an interface between the solid and such a nucleus

$$\Delta G(r) = \frac{4}{3}\pi r^3 \rho \Delta\mu + 4\pi r^2 \gamma_s \qquad (1)$$

Here, $\Delta\mu = \mu_l - \mu_s < 0$ is the chemical potential difference between the liquid and solid phases, ρ is the liquid density, $4\pi r^2$ is the surface area of the nucleus, and γ_s is its surface tension. The critical nucleus size $r^* = -2\gamma_s/(\rho\Delta\mu)$ maximizes this free energy [$\Delta G(r^*) = 16\pi\gamma_s^3/3(\rho\Delta\mu)^2$] (*11*) and determines the length scale beyond which growth of the cluster becomes favorable. At the solid-liquid coexistence point, $\Delta\mu = 0$, and the theory predicts an infinite free-energy barrier and corresponding suppression of the nucleation rate. This picture involves numerous simplifying assumptions and fails to account for the potentially important role of defects, dislocations, and multiple barriers along potential melting paths (*11*).

Close to the coexistence point, the melting of a solid involves activation from a metastable local minimum. Consequently, a theoretical analysis of the melting mechanisms using standard atomistic simulation methods is not feasible because melting is a rare barrier-crossing event with mean first passage time many orders of magnitude greater than the vibrational frequency of atoms. State-of-the-art rare-event sampling techniques now render possible the computational study of equilibrium melting and the extraction of dominant pathways and free energetics. We used adiabatic free-energy dynamics (AFED) (*12*) together with the string method (*13*, *14*) in order to explore the multidimensional free-energy surface (FES) efficiently and to construct a microscopic picture of the melting process for two commonly studied prototypical systems: copper (Cu) and aluminum (Al) (*15*, *16*).

We began by analyzing the equilibrium melting process using as collective variables the volume (V) of the system and the two Steinhardt order parameters Q_4 and Q_6 (*17*); this combination captures the positional and orientational ordering. In Fig. 1, A and B, we show a projection of the Gibbs FES onto the V-Q_4 subspace for Cu at 1350 K, close to the melting point of 1358 K, and 1 atm pressure. Contrary to the simple picture from CNT of a smooth FES possessing metastable solid and liquid basins separated by an index-1 saddle point, the FES obtained here has multiple locally stable states characterized by different defects—primarily vacancy-interstitial pairs, dislocations, and interstitial clusters—and the free-energy barriers separating these states range over multiple energy scales. The FES for Al (fig. S1), close to the melting point of 933 K, exhibits a similar structure. How vacancy-interstitial pairs can form, diffuse, cluster, and annihilate is illustrated in Fig. 1C.

The existence of a multitude of metastable states suggests that there exists an ensemble of multiple competing transition pathways. One such melting channel and the associated free energy profile are shown in Fig. 2A. Along this path, as the system moves out of the solid basin, the volume of the solid and the number of vacancy and interstitial pairs increases. Thus, this particular melting pathway proceeds via the formation of point defects, which is entropically favorable but energetically costly. The competition between entropic and enthalpic contributions causes the free energy to reach a maximum value (Fig. 2A, "S2") at a certain defect concentration. After the saddle S2, the system lowers its free energy by forming defect clusters at the expense of isolated defects. Cluster formation is enabled via the defect kinetics. In both Cu and Al, diffusion barriers of interstitial defects are quite small (0.09 and 0.13 eV, respectively); barriers for vacancy diffusion are somewhat larger (0.70 and 0.65 eV, respectively). Previously, Couchman and Reynolds had conjectured that a relationship exists between the melting point and vacancy concentration, thus suggesting a direct role for vacancy diffusion in the melting process (*18*). At 1350 K in Cu, these defects are mobile and diffuse over long distances in the solid. Occasionally, some of these interstitial and vacancy migration paths meet, and defect clusters can form. Inside these defect clusters, there is a notable loss of crystalline order (the local Steinhardt parameter $q_6 \sim 0.1$), which coincides with an enhanced diffusivity of atoms inside the cluster. After S2, the system moves to a shallow metastable state, and the defect cluster evolves into a liquid nucleus, the existence of which during melting also constitutes a deviation from the CNT.

As the system moves out of the metastable state toward the saddle S1 (fig. S3), the size of the liquid nucleus increases. This process is sometimes observed to be aided by the coalescence of a few smaller liquid nuclei. A test of the system size scaling of the free-energy barrier (fig. S3E) reveals that the S1 barrier scales roughly as $N^{2/3}$. After the liquid nucleus attains a critical size, the free energy along the path decreases. This corresponds to the second important bottleneck, with a barrier of ~125 eV relative to the solid basin. From here, the liquid nucleus simply increases in size until the entire system transforms to the liquid state.

Our enhanced sampling calculations suggest the existence of a melting path along which dislocation activity aids the formation of an initial liquid nucleus. The corresponding free-energy profile and key saddle structures are shown in

[1]Condensed Matter and Materials Division, Lawrence Livermore National Laboratory, Livermore, CA 94550 USA. [2]Program in Applied and Computational Mathematics, Princeton University, Princeton, NJ 08544, USA. [3]Department of Chemistry, New York University (NYU), New York, NY 10003, USA. [4]Courant Institute of Mathematical Sciences, NYU, New York, NY 10012, USA. [5]NYU–East China Normal University Center for Computational Chemistry at NYU Shanghai, Shanghai 200062, China. [6]Courant Institute of Mathematical Sciences, NYU, New York, NY 10012, USA. [7]Beijing International Center for Mathematical Research and School of Mathematical Sciences, Peking University, Beijing, China. [8]Department of Mathematics and Program in Applied and Computational Mathematics, Princeton University, Princeton, NJ 08544, USA.
*Corresponding author. E-mail: asamanta@math.princeton.edu (A.S.); weinan@math.princeton.edu (W.E.); mark.tuckerman@nyu.edu (M.E.T.)

Fig. 2B. Along this path, we first observe the formation of defect clusters from point defects followed by the heterogeneous nucleation of dislocations from the defect clusters. The dislocation density increases as the system moves toward the saddle S1, and the first liquid embryo is formed heterogeneously from these dislocations. This process of initiating melting from dislocations is reminiscent of recent observations of heterogeneous nucleation in colloidal systems (*19*) and embedded lead (Pb) nanoparticles in an Al matrix (*20*) and differs considerably from the notion of proliferation of dislocations (*5*, *7*).

From our analysis of the escape pathways from the solid basin, we conclude that melting has a high probability of being coupled to defect activity. Nevertheless, motivated by recent reports of melting without the aid of defects (*21*), we were inspired to ask whether it is possible for melting to occur in this manner. By calculating Voronoi volumes associated with each of the atoms, we are able to show that close to the melting point, the free volume associated with vacancies is spatially delocalized, and it is difficult to identify individual defects. Previous experiments have shown that on-the-fly determination of defects at high temperatures is nontrivial (*22*). Furthermore, under equilibrium conditions, the possibility that Cu at 1350 K is defect-free seems remote because of the presence of nearly degenerate defect states, with transition barriers on the order of 1 to 4 eV. Nevertheless, we explored the possibility of a melting pathway connecting the defect-free solid minimum and the liquid basin that does not pass through the defect states. On the FES, a possible pathway for melting without the aid of defects has a notably higher free-energy barrier (~150 eV) than the barriers along the defect-mediated melting pathways. Along such a defect-free path, the formation of the initial liquid nucleus is correlated with thermal fluctuations and is not aided by any stable defects. However, if this path is allowed to relax in path space, it eventually converges to one of the two defect-mediated melting pathways.

Temperature plays an important role in determining the characteristics of the FES. Thus, we also sought to compare equilibrium melting to melting of a superheated solid. As the system is superheated beyond the melting point, the liquid basin engulfs larger portions of the FES, and the metastable state without defects vanishes (Fig. 2E). This change in the FES affects the melting mechanisms: Compared with the FES at 1350 K in Cu, at 1550 K (and at 1200 K for Al) there are fewer locally stable states present inside the solid basin, and there is only one important bottleneck for melting—namely, the barrier to escape the solid basin. This barrier has a substantial entropic contribution (fig. S4). The absence of a metastable state without defects indicates that melting at these superheated conditions always originates from a solid with preexisting point defects or defect clusters.

With further increase in temperature, the melting barrier along the minimum free-energy path vanishes at ~1600 K in Cu and ~1275 K in Al. Above these temperatures, atoms execute large-amplitude vibrations about their equilibrium positions, and the solid-to-liquid transition is a consequence of an instability (Fig. 2C, inset, and fig. S5). The crucial role of the vibrational amplitude in this process is realized only by separating the diffusive motions of the atoms from their vibrational motions. This mechanism is reminiscent of Lindemann's vibrational instability (*1*) and is in agreement with recent experimental observations of melting in superheated aluminum (*23*). The fact that Lindemann's criterion corresponds to an instability of the solid and not to equilibrium melting leads to an overestimation of the melting point. This is relevant because Lindemann's criterion is still commonly used to determine the melting point of a solid (*24*–*26*).

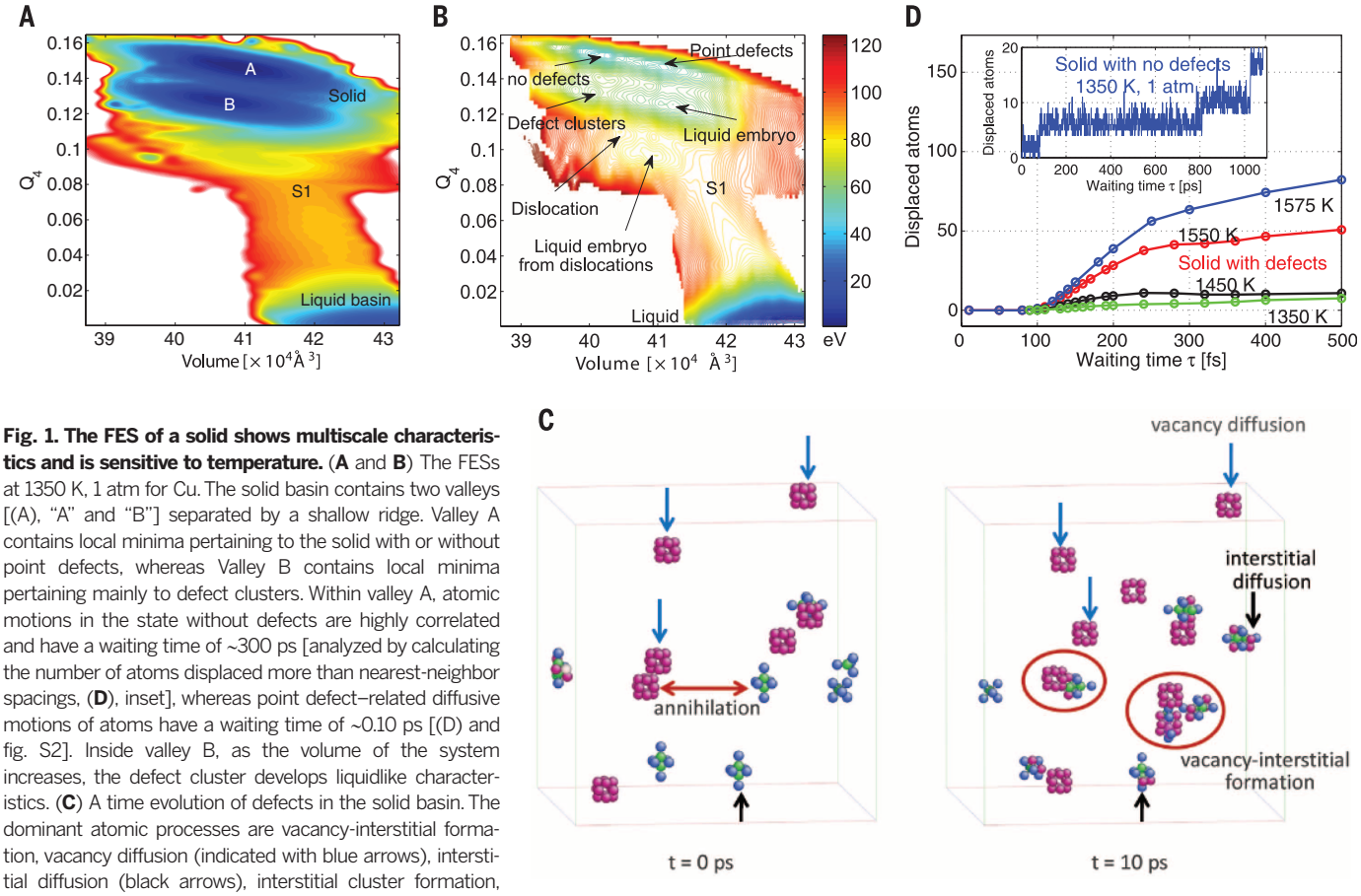


Fig. 1. The FES of a solid shows multiscale characteristics and is sensitive to temperature. (**A** and **B**) The FESs at 1350 K, 1 atm for Cu. The solid basin contains two valleys [(A), "A" and "B"] separated by a shallow ridge. Valley A contains local minima pertaining to the solid with or without point defects, whereas Valley B contains local minima pertaining mainly to defect clusters. Within valley A, atomic motions in the state without defects are highly correlated and have a waiting time of ~300 ps [analyzed by calculating the number of atoms displaced more than nearest-neighbor spacings, (**D**), inset], whereas point defect–related diffusive motions of atoms have a waiting time of ~0.10 ps [(D) and fig. S2]. Inside valley B, as the volume of the system increases, the defect cluster develops liquidlike characteristics. (**C**) A time evolution of defects in the solid basin. The dominant atomic processes are vacancy-interstitial formation, vacancy diffusion (indicated with blue arrows), interstitial diffusion (black arrows), interstitial cluster formation, and vacancy-interstitial annihilation (red double-ended arrow). Processes such as vacancy-interstitial pair formation and cluster formation are circled in red.

Theories such as CNT and that suggested by the present study address homogeneous melting in the bulk. The system-size scaling dependence of the associated free-energy barrier, however, indicates that as N grows, melting is more likely to be initiated from regions that break the translational and orientational order of the bulk solid. These include defect clusters, voids, grain boundaries, and dislocations, all of which increase the energy of a solid and lead to heterogeneous melting. We sought to investigate this case by initiating trajectories from preexisting dislocations and from grain boundaries obtained by rapidly cooling the liquid [(*17*), section XII, fig. S6]. In both cases, the resulting metastable states lie closer to the saddle S1 on the FES, resulting in a decrease in the melting barrier. As shown in Fig. 2D, melting in a solid with grain boundaries is initiated at these boundaries, and the barrier can be as low as 6 eV at the melting point (fig. S7). The atoms in the grain boundaries are fluid-like, and hence, melting occurs via gradual growth of these liquid-like regions. In a solid with multiple dislocations, the elastic interactions between the dislocations can decrease the melting barrier by as much as a factor of six below the barrier for melting of a Cu sample without preexisting defects.

The sensitivity of the free-energy surface to temperature is shown in Fig. 2C. There exist three different melting regimes: (i) Close to the melting point [temperature (T) < 1525 K for Cu, T < 1200 K for Al], the transition occurs via multiple barrier crossings, and elastic interactions play a dominant role in determining the melting mechanisms. (ii) At superheated temperatures (1525 to 1590 K for Cu, 1200 to 1265 K for Al), the solid-to-liquid transition is a single barrier-crossing event, and the barrier contains enthalpic as well as entropic contributions. (iii) At the limit of instability, melting is initiated by the propagation of large vibrations of the atoms in a short span of time across the crystal. This large variation in the underlying melting mechanisms suggests a strong coupling between the orientational order, density, and temperature: At a given temperature, how Q_6 and Q_4 change with V determines the structure of defects present in the solid, locations of the saddle points, and the basins of attraction.

Notwithstanding the above differences in the melting mechanisms, we find that melting is aided by mobile defects both at the thermodynamic melting point and at conditions of superheating. In both of these states, defects constitute less than 1/1000 of the total lattice sites. Consequently, melting and lattice instabilities are not triggered by the proliferation of defects (*6*, *27*, *28*), which contrasts with theories based on the assertion that "melting is correlated with the achievement of a critical vacancy concentration" (*29*). Further, our enhanced sampling calculations reveal that the size of a liquid nucleus does not change smoothly along the minimum free-energy pathway.

It is clear that multiple, competing pathways and multiple barrier-crossing events along each path are crucial for the formation of the initial liquid embryo and constitute a qualitative departure from the simplifying assumptions of CNT. An important element that is clearly missing in the ΔG of CNT is the contribution from the strain energy. Along the dislocation-mediated melting pathway (Fig. 2B), the liquid nucleus is formed preferentially on the dislocations via a decrease in the strain energy associated with the dislocations. The change in free energy can be expressed as $\Delta G(r) = -\alpha r \log r/r_o + \Delta\mu 4\pi r^3/3 + 4\pi r^2\gamma_s$, where $\alpha = Gb^2/4\pi(1-\nu)$, r_o is a constant, b is the Burgers vector, ν is Poisson's ratio, and $-\alpha r \log r/r_o$ is the decrease in the elastic energy of the dislocation owing to the formation of the liquid nucleus (*30*). At the melting point, $\Delta\mu = 0$; hence, the critical radius of the liquid nucleus is $r^* \sim Gb^2/32\pi^2\,\gamma_s(1-\nu)$. Similarly, formation of dislocations from point defects and defect clusters involves a competition between the elastic energy of dislocation and the interaction energy between the dislocation and the defects, likely requiring the addition of nonlocal energy terms in any mean-field type of description of melting. This physical interplay of processes with multiple length and time scales indicates that melting of a solid cannot be viewed through the simple lens of CNT but should be regarded as a complex "multiscale" phenomenon.

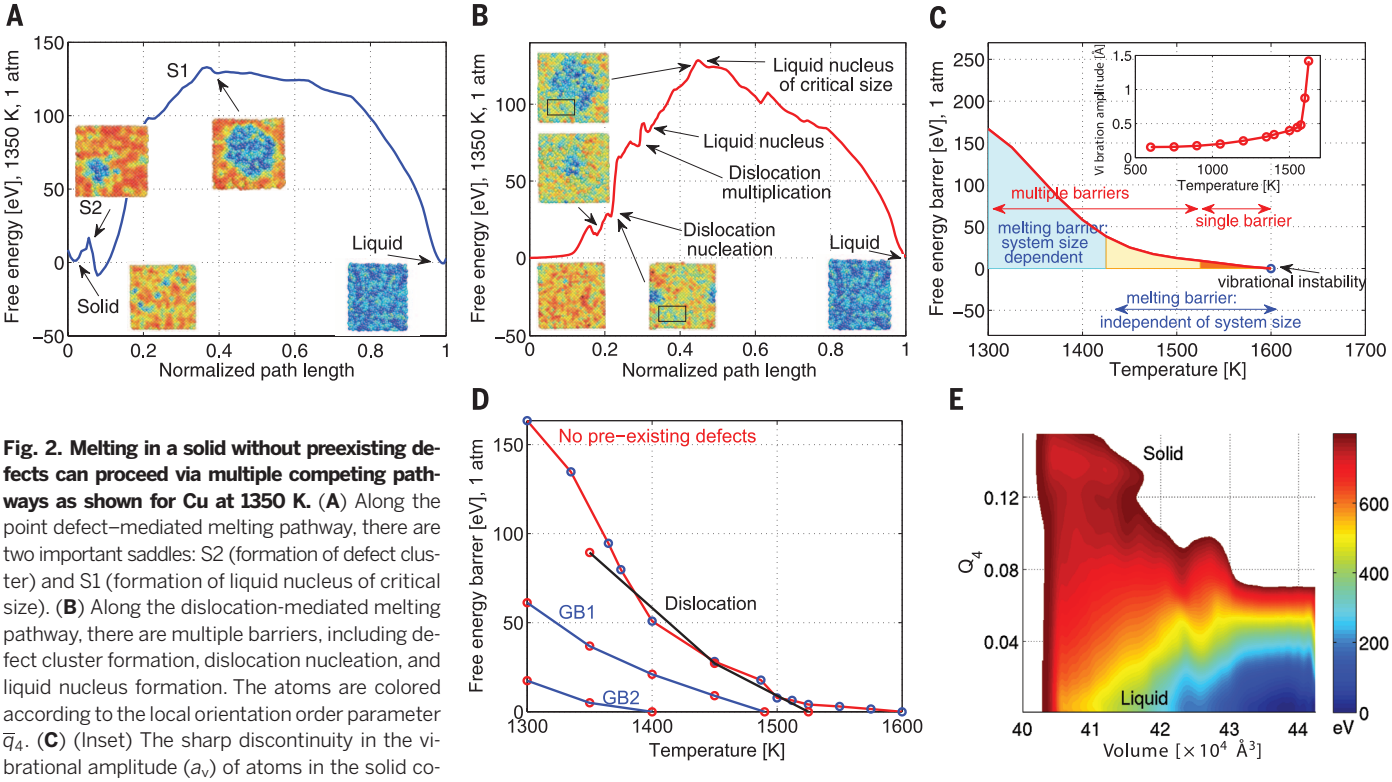


Fig. 2. Melting in a solid without preexisting defects can proceed via multiple competing pathways as shown for Cu at 1350 K. (**A**) Along the point defect–mediated melting pathway, there are two important saddles: S2 (formation of defect cluster) and S1 (formation of liquid nucleus of critical size). (**B**) Along the dislocation-mediated melting pathway, there are multiple barriers, including defect cluster formation, dislocation nucleation, and liquid nucleus formation. The atoms are colored according to the local orientation order parameter $\bar{q}_4$. (**C**) (Inset) The sharp discontinuity in the vibrational amplitude (a_v) of atoms in the solid coincides with the vanishing of the free-energy barrier. a_v is extracted from the root-mean-squared-displacement (RMSD) after subtracting the diffusion contributions, and hence, the sharp discontinuity observed in a_v is not observed in the usual RMSD profiles [for example, figure 2 in (*25*)]. (**D**) The effect of grain boundaries and dislocations on the melting barriers. The solid in GB1 has only two grains, whereas GB2 has about four grains. (**E**) FES at 1550 K for Cu, illustrating that melting is a single barrier-crossing event that involves enthalpic as well as entropic barriers at superheated conditions.

REFERENCES AND NOTES

1. F. A. Lindemann, *Phys. Z.* **11**, 609 (1910).
2. M. Born, *J. Chem. Phys.* **7**, 591 (1939).
3. N. F. Mott, *Nature* **145**, 801–802 (1940).
4. J. L. Tallon, *Nature* **299**, 188 (1982).
5. D. Kuhlmann-Wilsdorf, *Phys. Rev.* **140**, A1599–A1610 (1965).
6. T. Gorecki, *Z. Metallkunde Mat. Res. Adv. Tech.* **65**, 426 (1974).
7. L. Gómez, A. Dobry, Ch. Geuting, H. T. Diep, L. Burakovsky, *Phys. Rev. Lett.* **90**, 095701 (2003).
8. X. M. Bai, M. Li, *Phys. Rev. B* **77**, 134109 (2008).
9. M. Volmer, A. Weber, *Z. Phys. Chem.* **119**, 277 (1926).
10. R. Becker, W. Döring, *Ann. Phys.* **416**, 719–752 (1935).
11. R. P. Sear, *Int. Mater. Rev.* **57**, 328–356 (2012).
12. T. Q. Yu, M. E. Tuckerman, *Phys. Rev. Lett.* **107**, 015701 (2011).
13. W. E, W. Ren, E. Vanden-Eijnden, *J. Phys. Chem. B* **109**, 6688–6693 (2005).
14. L. Maragliano, A. Fischer, E. Vanden-Eijnden, G. Ciccotti, *J. Chem. Phys.* **125**, 024106 (2006).
15. R. Lynden-Bell, J. Van Duijneveldt, D. Frenkel, *Mol. Phys.* **80**, 801–814 (1993).
16. M. Forsblom, G. Grimvall, *Nat. Mater.* **4**, 388–390 (2005).
17. Materials and methods are available as supplementary materials on *Science* Online
18. P. R. Couchman, C. L. Reynolds Jr., *Philos. Mag.* **34**, 327–329 (1976).
19. A. M. Alsayed, M. F. Islam, J. Zhang, P. J. Collings, A. G. Yodh, *Science* **309**, 1207–1210 (2005).
20. H. Rösner, B. Freitag, G. Wilde, *Philos. Mag. Lett.* **87**, 341–347 (2007).
21. Z. Wang, F. Wang, Y. Peng, Z. Zheng, Y. Han, *Science* **338**, 87–90 (2012).
22. E. Fukushima, A. Ookawa, *J. Phys. Soc. Jpn.* **10**, 970–981 (1955).
23. B. J. Siwick, J. R. Dwyer, R. E. Jordan, R. J. D. Miller, *Science* **302**, 1382–1385 (2003).
24. J. J. Gilvarry, *Phys. Rev.* **102**, 308–316 (1956).
25. Z. H. Jin, P. Gumbsch, K. Lu, E. Ma, *Phys. Rev. Lett.* **87**, 055703 (2001).
26. K. Sokolowski-Tinten *et al.*, *Nature* **422**, 287–289 (2003).
27. R. M. J. Cotterill, J. U. Madsen, *Nature* **288**, 467–469 (1980).
28. H. J. Fecht, W. L. Johnson, *Nature* **334**, 50–51 (1988).
29. R. W. Cahn, *Nature* **334**, 17–18 (1988).
30. J. W. Cahn, *Acta Metall.* **5**, 169–172 (1957).

ACKNOWLEDGMENTS

Work by W.E and A.S. at Princeton was supported by the U.S. Department of Energy (DOE) (grant DE-SC0009248) and in Beijing by the National Natural Science Foundation of China (9130005). This work was partially performed under the auspices of DOE by Lawrence Livermore National Laboratory under contract DE-AC52-07NA27344. Work by M.E.T. was supported by NSF grant CHE-1301314.

SUPPLEMENTARY MATERIALS

www.sciencemag.org/content/346/6210/729/suppl/DC1
Materials and Methods
Figs. S1 to S7
References (*31*–*41*)

24 March 2014; accepted 10 October 2014
10.1126/science.1253810

EARLY UNIVERSE

On the origin of near-infrared extragalactic background light anisotropy

Michael Zemcov,[1,2] Joseph Smidt,[3,4] Toshiaki Arai,[5,6] James Bock,[1,2]* Asantha Cooray,[4] Yan Gong,[4] Min Gyu Kim,[7] Phillip Korngut,[2,1] Anson Lam,[8,1] Dae Hee Lee,[9] Toshio Matsumoto,[5,10] Shuji Matsuura,[5] Uk Won Nam,[9] Gael Roudier,[2] Kohji Tsumura,[11] Takehiko Wada[5]

Extragalactic background light (EBL) anisotropy traces variations in the total production of photons over cosmic history and may contain faint, extended components missed in galaxy point-source surveys. Infrared EBL fluctuations have been attributed to primordial galaxies and black holes at the epoch of reionization (EOR) or, alternately, intrahalo light (IHL) from stars tidally stripped from their parent galaxies at low redshift. We report new EBL anisotropy measurements from a specialized sounding rocket experiment at 1.1 and 1.6 micrometers. The observed fluctuations exceed the amplitude from known galaxy populations, are inconsistent with EOR galaxies and black holes, and are largely explained by IHL emission. The measured fluctuations are associated with an EBL intensity that is comparable to the background from known galaxies measured through number counts and therefore a substantial contribution to the energy contained in photons in the cosmos.

At near-infrared wavelengths, where the large zodiacal light foreground complicates absolute photometry measurements, the extragalactic background light (EBL) may be best accessed by anisotropy measurements. On large angular scales, fluctuations are produced by the clustering of galaxies, which is driven by the underlying distribution of dark matter. EBL anisotropy measurements can probe emission from epoch of reionization (EOR) galaxies (*1*–*3*) and direct-collapse black holes (*4*) that formed during the EOR before the universe was fully ionized by exploiting the distinctive Lyman cutoff feature in the rest-frame ultraviolet (UV), thus probing the UV luminosity density at high redshifts (*5*). However, large-scale fluctuations may also arise from the intrahalo light (IHL) created by stars stripped from their parent galaxies during tidal interactions (*6*) at redshift $z < 3$. A multiwavelength fluctuation analysis can distinguish among these scenarios and constrain the EOR star formation rate.

A search for such background components must carefully account for fluctuations produced by known galaxy populations. Linear galaxy clustering is an important contribution to fluctuations on scales much larger than galaxies themselves. On fine scales, the variation in the number of galaxies produces predominantly Poissonian fluctuations, with an amplitude that depends on the luminosity distribution. Anisotropy measurements suppress foreground galaxy fluctuations by masking known galaxies from an external catalog.

The first detections of infrared fluctuations in excess of the contribution from known galaxies with the Spitzer Space Telescope (*7*–*9*) were interpreted as arising from a population of faint first-light galaxies at $z > 7$. The Hubble Space Telescope was used at shorter wavelengths (*10*) to carry out a fluctuation study in a small deep field but did not report fluctuations in excess of known galaxy populations. Measurements with the AKARI satellite (*11*) show excess fluctuations with a blue spectrum rapidly rising from 4.1 μm to 2.4 μm. Fluctuation measurements in a large survey field (*6*) with Spitzer agreed with earlier measurements (*7*–*9*) but were instead interpreted as arising from tidally stripped stars at $z \sim 1$ to 3. Most recently, a partial correlation has been reported (*12*) between Spitzer and soft x-ray images, which Yue *et al.* (*4*) interpret as arising from direct-collapse black holes at $z > 12$.

We have developed and flown the specialized Cosmic Infrared Background Experiment [CIBER (*13*)], a rocket-borne instrument specifically designed to study the spatial and spectral properties of the EBL. The imaging instrument (*14*) measures fluctuations in $\Delta\lambda/\lambda = 0.5$ bands centered at 1.1 and 1.6 μm using two 11-cm telescopes each with a 2° by 2° field of view. Here, we report our analysis of data from two flights in 2010 and 2012.

The CIBER imager data are reduced from raw telemetered time streams, flat-field–corrected based

[1]Department of Physics, Mathematics, and Astronomy, California Institute of Technology, Pasadena, CA 91125, USA. [2]Jet Propulsion Laboratory (JPL), National Aeronautics and Space Administration (NASA), Pasadena, CA 91109, USA. [3]Theoretical Division, Los Alamos National Laboratory, Los Alamos, NM 87545, USA. [4]Department of Physics and Astronomy, University of California, Irvine, CA 92697, USA. [5]Department of Space Astronomy and Astrophysics, Institute of Space and Astronautical Science (ISAS), Japan Aerospace Exploration Agency (JAXA), Sagamihara, Kanagawa 252-5210, Japan. [6]Department of Physics, Graduate School of Science, The University of Tokyo, Tokyo 113-0033, Japan. [7]Department of Physics and Astronomy, Seoul National University, Seoul 151-742, Korea. [8]Department of Physics and Astronomy, University of California, Los Angeles, CA 90095, USA. [9]Korea Astronomy and Space Science Institute (KASI), Daejeon 305-348, Korea. [10]Institute of Astronomy and Astrophysics, Academia Sinica, Taipei 10617, Taiwan, Republic of China. [11]Frontier Research Institute for Interdisciplinary Science, Tohoku University, Sendai, Miyagi, 980-8578, Japan.
***Corresponding author. E-mail: jjb@astro.caltech.edu**

on a laboratory measurement, and masked for stars and galaxies using the Two Micron All Sky Survey (2MASS) *J*- and *H*-band catalogs (*15*). We analyze differences between fields to reduce the effect of flat-fielding errors. The auto- and cross-power spectra of the masked, differenced images, corrected for mode coupling from the mask using a correction matrix, are shown in Fig. 1. We also compute auto- and cross-spectra from a Spitzer infrared array camera (IRAC) 3.6-μm image that coincides with two of the five CIBER fields.

The CIBER auto- and cross-spectra show a significant excess over the predicted fluctuations from known galaxy populations (*16*) at $l < 5000$, where the multipole moment $l \cong \pi/\theta$, and θ is the angular separation of two points on the sky. The excess is also evident in the cross-power spectra with Spitzer, showing that the source of the fluctuations is largely common from 1.1 to 3.6 μm. The large-scale fluctuations measured with CIBER correlate between the two flights in all combinations of bands and are independent of the detector arrays; the data pass multiple internal consistency tests (see the supplementary materials).

We rule out the following sources for producing the large-scale fluctuations (Fig. 1): (i) sunlight scattered by interplanetary dust, (ii) starlight scattered by interstellar dust (known as diffuse Galactic light), and (ii) fluctuations from faint stars. Zodiacal light fluctuations are eliminated because we observed the same fields separated by 17 months and obtained consistent results, viewed through two independent lines of sight through the interplanetary dust cloud. Constraints on zodiacal light fluctuations from Spitzer at 8 μm (*8*), scaled by the zodiacal spectrum to near-infrared wavelengths (*17*), lie significantly below the detected fluctuations (Fig. 1). The zodiacal spectrum is scaled by a conservative upper limit to the fluctuation amplitude measured at 7 μm from AKARI (*17*, *18*) in Fig. 2.

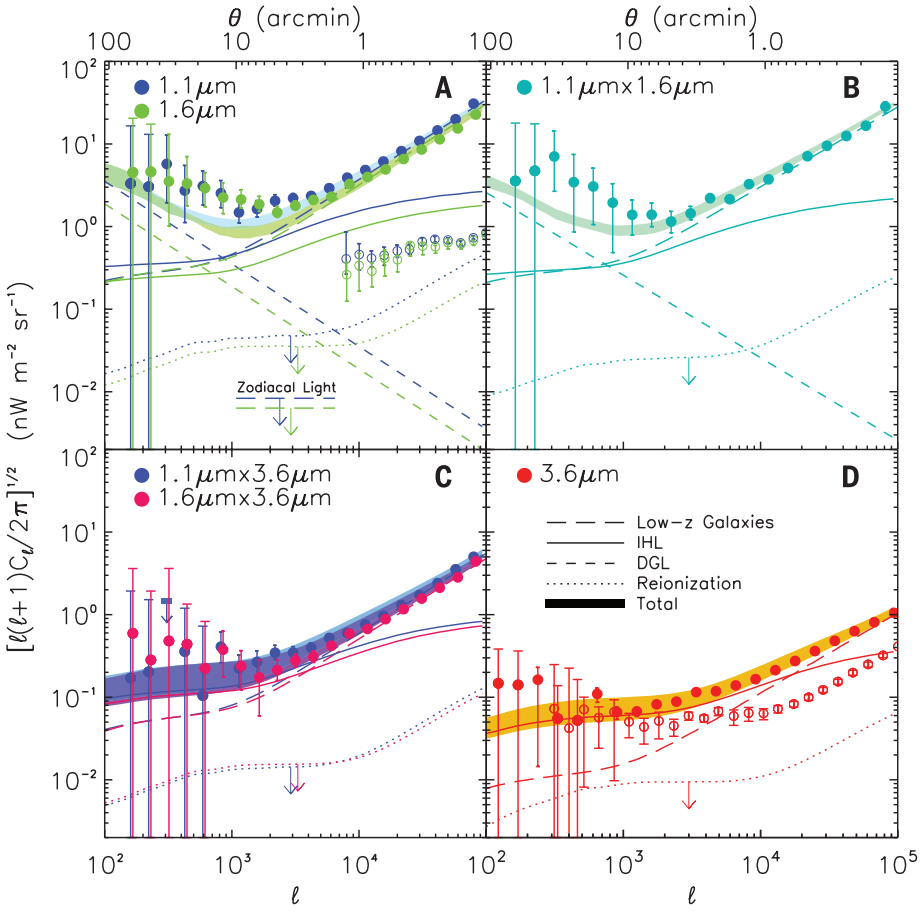


Fig. 1. CIBER and Spitzer auto- and cross-spectra at 1.1, 1.6 and 3.6 μm. We show the CIBER auto-spectra for 1.1 by 1.1 μm, and 1.6 by 1.6 μm (**A**), the CIBER 1.1 by 1.6 μm cross-spectrum (**B**), the CIBER-Spitzer 1.1 by 3.6 μm and 1.6 by 3.6 μm cross-spectra (**C**), and the Spitzer 3.6 by 3.6 μm auto-spectra (*6*) (**D**). At 1.1, 1.6, and 3.6 μm, we indicate previous measurements [open circles; (*6*, *10*); note that the Hubble measurements apply a much deeper flux cut at 1.1 and 1.6 μm for masking and that the Spitzer flux cut is somewhat deeper than the cut we are applying at 3.6 μm]. The 3.6-μm points use the same data set but are masked to a lower source flux for comparison to our spectrum, which is masked to $L < 16$. The increased depth reduces some of the mid-l power. We show constraints on astrophysical foregrounds, including unmasked stars and $z < 5$ galaxies (*16*), zodiacal light (*8*), and diffuse Galactic light. In all cases, we detect a significant excess power at $l < 5000$ (angular separations $\theta > 4.3'$). We model the data using components from IHL (*6*) and $z > 7$ first galaxies (*3*, *5*), obtaining a 95% confidence upper limit on the EOR contribution. The fitted total indicated by the filled band includes all of the astrophysical components plus a bounded systematic error for flat-field variations. The width of the band indicates the 68% uncertainty interval of the fit, including all of the modeling uncertainties. The correlation coefficients for 1.1 by 1.6 μm, 1.1 by 3.6 μm, and 1.6 by 3.6 μm are 0.76 ± 0.10, 0.55 ± 0.14 and 0.31 ± 0.14, respectively, with no statistically significant angular dependence in the correlations (see section 6.2 of the supplementary materials for a description of this calculation).

We estimate diffuse Galactic light fluctuations (Figs. 1 and 2) by scaling the Infrared Astronomical Satellite (IRAS) 100-μm intensity by a factor consistent with previous diffuse Galactic light measurements (*19*). We estimate the diffuse Galactic light component by calculating the CIBER–IRAS cross-spectra and fitting a single amplitude coefficient to a $C_l \propto l^{-3}$ spectrum with a fixed 1.1 μm / 1.6 μm color ratio, which is less than the detected CIBER power spectra at all spatial scales. Fluctuations from the extinction of the background light by galactic dust are also negligible.

We constrain fluctuations from unmasked stars using the UKIDSS-UDS stellar catalog (*20*), which is complete to $J = 24.9$, $H = 24.2$ (5 σ), accounting for > 99.9% of the integrated light from stars. We compute the autopower spectrum of residual stars below our cutoff flux and find that the amplitude is negligible on large scales and follows a Poisson spectrum.

The root mean square (RMS) fluctuation amplitude $\delta\lambda I_\lambda = \langle l(l+1)C_l/2\pi\rangle^{1/2}$ over $500 < l < 2000$ has a spectral energy distribution that is approximately Rayleigh-Jeans (Fig. 2). The 1.1-μm data point lies 2σ below the best-fitting λ^{-3} scaling, suggesting the possibility of a departure from the Rayleigh-Jeans spectrum at short wavelengths. To fit models to CIBER and Spitzer data, we mask Spitzer data to a depth $L < 16$ that is comparable to CIBER. The Spitzer power spectra give a non-Poissonian $l^{1.7}$ signal at high multipoles for the $L < 16$ flux cut (Fig. 1), which is evidence for nonlinear clustering that is not observed with a deeper flux cut (*6*) and is not predicted in linear galaxy clustering (*16*).

Having excluded explanations based on zodiacal light, diffuse Galactic light, and the clustering of known galaxies, we consider three possibilities to explain these measurements: EOR galaxies, EOR black holes, and IHL. For first-light galaxies, we use models for population II and population III stars (*21*) and combinations of the two. The direct-collapse black hole model at $z > 12$ is excluded both by amplitude and color, as it has no mechanism to generate substantial 1.1- and 1.6-μm power (*4*). For IHL, we use models based on the spectral energy distributions of old stellar populations in dark matter halos (*6*). We simultaneously fit the 1.1-, 1.6-, and 3.6-μm autopower spectra, taking into account galaxy clustering, diffuse Galactic light, and residual flat-field errors at low l. The IHL model, summarized in Fig. 1, generally fits the data but somewhat underpredicts the amplitude at 1.1 and 1.6 μm; neither the

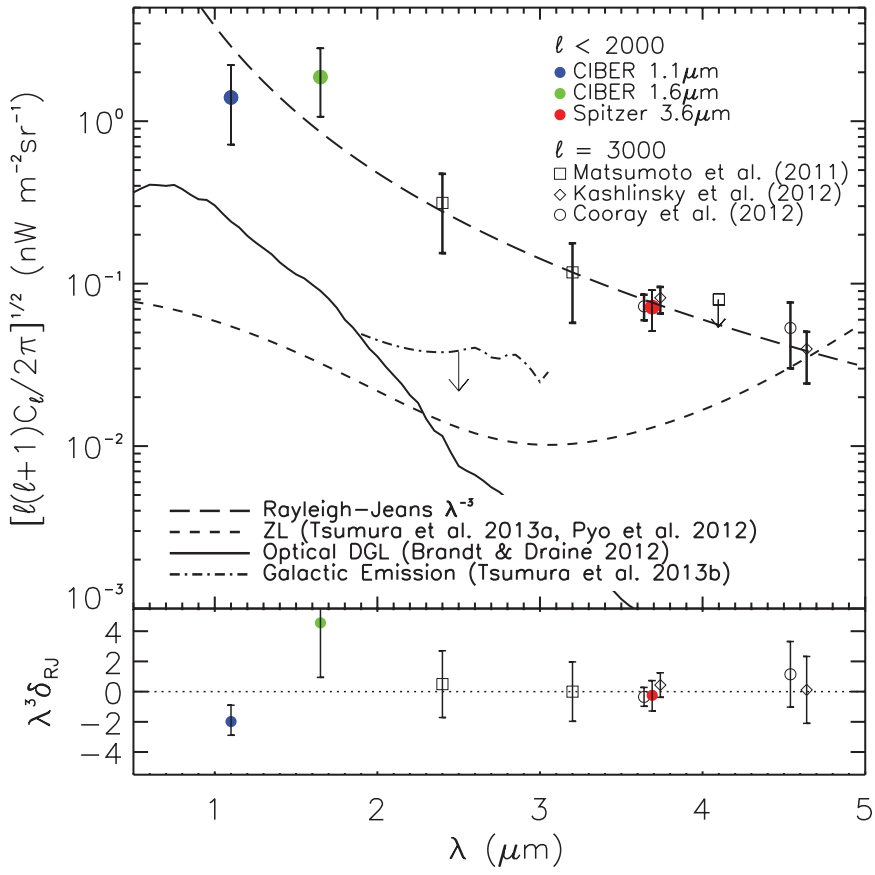


Fig. 2. The electromagnetic spectrum of the near-infrared fluctuations. We show measurements of the fluctuation power from CIBER and Spitzer averaged between 500 < ℓ < 2000 (solid points). Also indicated are previous measurements from AKARI (*11*) and Spitzer (*6*, *7*) at ℓ = 3000 that use deeper masking thresholds. In all cases, we subtract the contribution from the shot noise of unmasked galaxies (*16*). We indicate the best-fitting Rayleigh-Jeans spectrum to the points from this analysis, estimates for diffuse Galactic light fluctuations (*19*), a conservative constraint on zodiacal light fluctuations (*17*, *18*), and an upper limit on Galactic emission (*27*). The known foreground components have both smaller amplitudes and different spectra than the measurements. We show the residual from the best-fitting Rayleigh-Jeans spectrum δ_{RJ} in the bottom panel, scaled by λ^3 to reduce the range. The shortest wavelength measurement at 1.1 μm is 2.0 σ below the fit, indicating a possible short-wavelength departure from a Rayleigh-Jeans spectrum.

Table 1. Contributions to near-infrared EBL anisotropy and intensity. At each wavelength, we list the measured fluctuation amplitude at large angular scales; the model-dependent ratio of EBL intensity to EBL anisotropy; the IGL determined by previous measurements; the ratio of the IHL and IGL intensities; and finally, the inferred total background intensity from both components. We also list the background intensity that would arise assuming the measured fluctuations are entirely due to high-redshift EOR galaxies.

λ (μm)	Measured $\delta\lambda I_\lambda$* (nW m^{-2} sr^{-1})	$\frac{\lambda I_{\lambda,\mathrm{IHL}}}{\delta\lambda I_\lambda}$	$\lambda I_{\lambda,\mathrm{IHL}}$‡ (nW m^{-2} sr^{-1})	$\lambda I_{\lambda,\mathrm{IGL}}$§ (nW m^{-2} sr^{-1})	$\frac{\lambda I_{\lambda,\mathrm{IHL}}}{\lambda I_{\lambda,\mathrm{IGL}}}$	$\lambda I_{\lambda,\mathrm{IHL}} + \lambda I_{\lambda,\mathrm{IGL}}$ (nW m^{-2} sr^{-1})	$\lambda I_{\lambda,\mathrm{EOR}}$‖ (nW m^{-2} sr^{-1})
1.1	$1.4^{+0.8}_{-0.7}$	5	$7.0^{+4.0}_{-3.5}$	$9.7^{+3.0}_{-1.9}$	0.7	$16.7^{+5.0}_{-4.0}$	28
1.6	$1.9^{+0.9}_{-0.8}$	6	$11.4^{+5.4}_{-4.8}$	$9.0^{+2.6}_{-1.7}$	1.3	$20.4^{+6.0}_{-5.1}$	38
2.4	0.32 ± 0.05†	7	2.2 ± 0.4	$7.8^{+2.0}_{-1.2}$¶	0.3	$10.0^{+2.0}_{-1.3}$	6.4
3.6	$0.072^{+0.019}_{-0.021}$	9	$0.65^{+0.17}_{-0.19}$	5.2 ± 1.0	0.1	5.9 ± 1.0	1.4
3.6#	$0.049^{+0.021}_{-0.007}$	9	$0.44^{+0.19}_{-0.06}$	5.2 ± 1.0	0.1	5.6 ± 1.0	1.0
4.5	0.053 ± 0.023†	7	0.37 ± 0.16	3.9 ± 0.8	0.1	4.3 ± 0.8	1.0

*RMS fluctuation amplitude computed as averages of measured data over 500 < ℓ < 2000, except for those marked †, which are determined at ℓ = 3000 using fainter mask cuts due to restricted field size (see also note ||). ‡The IHL background from the product of columns 2 and 3. §The IGL background as compiled by (*28*). ||Computed EOR background assuming EOR fluctuations with $\lambda I_\lambda/\delta\lambda I_\lambda$ = 20. ¶Determined at *K* band corresponding to 2.2 μm. #Computed using the measurements of (*6*) averaged over 500 < ℓ < 5000.

IHL nor the EOR models quite match the high observed 1.6-/3.6-μm color ratio (see section 10 of the supplementary materials). This may indicate that additional components are reflected in the data. However, more theoretical work is required to determine whether adding nonlinear galaxy clustering and nonlinear IHL production to the model can improve the fit.

We estimate the EBL intensity associated with the fluctuations by taking the measured fluctuation amplitude between 500 < ℓ < 2000, obtained by subtracting estimated contributions from low-z galaxies and diffuse Galactic light, and multiplying by a model-dependent contrast factor $\lambda I_\lambda/\delta\lambda I_\lambda$, where λI_λ is the total intensity associated with a component. For the IHL model, which has a low contrast factor, we obtain an associated EBL of $7.0^{+4.0}_{-3.5}$ and $11.4^{+5.4}_{-4.8}$ nW m^{-2} sr^{-1} at 1.1 and 1.6 μm, respectively. As shown in Table 1, the IHL background is of a similar magnitude to the integrated galaxy light (IGL) background derived from galaxy counts. However, we note that the IHL background has a much bluer color than the IGL background. We similarly estimate the IHL background at longer wavelengths from AKARI and Spitzer. Nonlinear galaxy clustering appears to contribute to the Spitzer fluctuations, so we quote two values that depend on the choice of flux cut, the deeper flux cut being less sensitive to the nonlinear clustering contribution. The CIBER data do not appear to be as sensitive to the flux cut, perhaps due to the higher IHL to IGL ratio at these wavelengths.

The total EBL, the summation of the IHL and IGL backgrounds, is consistent with current EBL measurements. Near-infrared absolute photometric background measurements remain uncertain due to the bright zodiacal foreground, but the lowest such measurement (*22*) gives 21 ±15 nW m^{-2} sr^{-1} and 13.3 ± 2.8 nW m^{-2} sr^{-1} at 1.25 and 3.6 μm, respectively. The High Energy Stereoscopic System (HESS) measurement of the EBL using γ-ray

absorption spectra (*23*), 15 ± 2 (statistical) ± 3 (systematic) nW m^{-2} sr^{-1} at 1.4 μm, is independently consistent with the sum of the IHL and IGL backgrounds, within the uncertainties in all measurements.

An EOR interpretation of these measurements would result in a large background, as the contrast factor is larger than that of IHL, 10 to 100 for EOR models (*3*, *6*). The implied EOR background (see Table 1) originating from high redshifts is difficult to justify due to the overproduction of metals and x-ray background photons (*24*).

Our results indicate that a substantial fraction of the EBL at optical and near-infrared wavelengths originates from stars outside of galaxies (with boundaries as traditionally defined). This in turn adds to the cosmic energy budget and, depending on the mass characteristics and spectrum of the population responsible, could help alleviate the "photon underproduction crisis" (*25*) and the "missing baryon problem" (*26*). We see no evidence for a detected EOR background component in our data. Multiwavelength fluctuation measurements extending into the optical will help discriminate the EOR background component using the redshifted Lyman cutoff, and future spectroscopic measurements will enable tomographic measurements to determine the history of IHL production.

REFERENCES AND NOTES

1. A. Cooray, J. J. Bock, B. Keatin, A. E. Lange, T. Matsumoto, *Astrophys. J.* **606**, 611–624 (2004).
2. A. Kashlinsky, R. Arendt, J. P. Gardner, J. C. Mather, S. H. Moseley, *Astrophys. J.* **608**, 1–9 (2004).
3. E. R. Fernandez, E. Komatsu, I. T. Iliev, P. R. Shapiro, *Astrophys. J.* **710**, 1089–1110 (2010).
4. B. Yue, A. Ferrara, R. Salvaterra, Y. Xu, X. Chen, *Mon. Not. R. Astron. Soc.* **433**, 1556–1566 (2013).
5. A. Cooray, Y. Gong, J. Smidt, M. G. Santos, *Astrophys. J.* **756**, 92 (2012).
6. A. Cooray *et al.*, *Nature* **490**, 514–516 (2012).
7. A. Kashlinsky, R. G. Arendt, J. Mather, S. H. Moseley, *Nature* **438**, 45–50 (2005).
8. A. Kashlinsky, R. G. Arendt, J. Mather, S. H. Moseley, *Astrophys. J.* **654**, L5–L8 (2007).
9. A. Kashlinsky *et al.*, *Astrophys. J.* **753**, 63 (2012).
10. R. I. Thompson, D. Eisenstein, X. Fan, M. Rieke, R. C. Kennicutt, *Astrophys. J.* **666**, 658–662 (2007).
11. T. Matsumoto *et al.*, *Astrophys. J.* **742**, 124 (2011).
12. N. Cappelluti *et al.*, *Astrophys. J.* **769**, 68 (2013).
13. M. Zemcov *et al.*, *Astrophys. J. Suppl. Ser.* **207**, 31 (2013).
14. J. Bock *et al.*, *Astrophys. J. Suppl. Ser.* **207**, 32 (2013).
15. M. F. Skrutskie *et al.*, *Astron. J.* **131**, 1163–1183 (2006).
16. K. Helgason, M. Ricotti, A. Kashlinsky, *Astrophys. J.* **752**, 113 (2012).
17. K. Tsumura *et al.*, *Publ. Astron. Soc. Japan* **65**, 119 (2013).
18. J. Pyo, T. Matsumoto, W.-S. Jeong, S. Matsuura, *Astrophys. J.* **760**, 102 (2012).
19. T. D. Brandt, B. T. Draine, *Astrophys. J.* **744**, 129 (2012).
20. A. Lawrence *et al.*, *Mon. Not. R. Astron. Soc.* **379**, 1599–1617 (2007).
21. E. R. Fernandez, E. Komatsu, *Astrophys. J.* **646**, 703–718 (2006).
22. L. R. Levenson, E. L. Wright, B. D. Johnson, *Astrophys. J.* **666**, 34–44 (2007).
23. H.E.S.S. Collaboration., *Astron. Astrophys.* **550**, A4 (2013).
24. P. Madau, J. Silk, *Mon. Not. R. Astron. Soc.* **359**, L37–L41 (2005).
25. J. A. Kollmeier *et al.*, *Astrophys. J.* **789**, L32 (2014).
26. M. Fukugita, C. J. Hogan, P. J. E. Peebles, *Astrophys. J.* **503**, 518–530 (1998).
27. K. Tsumura *et al.*, *Proc. Astron. Soc. Japan* **65**, 120 (2003).
28. A. Franceschini, G. Rodighiero, M. Vaccari, *Astron. Astrophys.* **487**, 837–852 (2008).

ACKNOWLEDGMENTS

Our thanks to O. Doré, J. Filippini, and K. Ganga for useful conversations and comments throughout the course of this work and K. Helgason for kindly providing models of the statistics of the near-infrared CIB. The authors acknowledge the excellent support from the NASA sounding rockets program that was essential in developing, testing, qualifying, launching, and recovering our payloads. The CIBER auto- and cross-power spectra are available for public download at http://ciber.caltech.edu/zemcovetal. This work was supported by NASA APRA research grants NNX07AI54G, NNG05WC18G, NNX07AG43G, NNX07AJ24G, and NNX10AE12G. Initial support was provided by an award to J.B. from the Jet Propulsion Laboratory's Director's Research and Development Fund. Japanese participation in CIBER was supported by KAKENHI (20·34, 18204018, 19540250, 21340047, and 21111004) from Japan Society for the Promotion of Science (JSPS) and the Ministry of Education, Culture, Sports, Science and Technology (MEXT). Korean participation in CIBER was supported by the Pioneer Project from Korea Astronomy and Space Science Institute (KASI). M.Z. and P.K. acknowledge support from NASA Postdoctoral Program fellowships, A.C. acknowledges support from an NSF CAREER award AST-0645427 and NSF AST-1313319, and K.T. acknowledges support from the JSPS Research Fellowship for Young Scientists. This publication makes use of data products from the Two Micron All Sky Survey (2MASS), which is a joint project of the University of Massachusetts and the Infrared Processing and Analysis Center/California Institute of Technology, funded by the National Aeronautics and Space Administration and the National Science Foundation. This work made use of images and/or data products provided by the National Optical Astronomy Observatory (NOAO) Deep Wide-Field Survey (NDWFS), which is supported by NOAO, operated by AURA, Inc., under a cooperative agreement with the National Science Foundation.

SUPPLEMENTARY MATERIALS

www.sciencemag.org/content/346/6210/732/suppl/DC1
Materials and Methods
Supplementary Text
Figs. S1 to S27
Tables S1 to S2
References (*29*–*55*)

1 July 2014; accepted 3 October 2014
10.1126/science.1258168

EARLY EARTH

Sulfate was a trace constituent of Archean seawater

Sean A. Crowe,[1,2]*† Guillaume Paris,[3]* Sergei Katsev,[4] CarriAyne Jones,[1,2] Sang-Tae Kim,[5] Aubrey L. Zerkle,[6] Sulung Nomosatryo,[7] David A. Fowle,[8] Jess F. Adkins,[3] Alex L. Sessions,[3] James Farquhar,[9] Donald E. Canfield[2]

In the low-oxygen Archean world (>2400 million years ago), seawater sulfate concentrations were much lower than today, yet open questions frustrate the translation of modern measurements of sulfur isotope fractionations into estimates of Archean seawater sulfate concentrations. In the water column of Lake Matano, Indonesia, a low-sulfate analog for the Archean ocean, we find large (>20 per mil) sulfur isotope fractionations between sulfate and sulfide, but the underlying sediment sulfides preserve a muted range of $\delta^{34}S$ values. Using models informed by sulfur cycling in Lake Matano, we infer Archean seawater sulfate concentrations of less than 2.5 micromolar. At these low concentrations, marine sulfate residence times were likely 10^3 to 10^4 years, and sulfate scarcity would have shaped early global biogeochemical cycles, possibly restricting biological productivity in Archean oceans.

Sulfur interacts with carbon and oxygen in global biogeochemical cycles that regulate Earth's surface chemistry and biology (*1*). At 28 mM, sulfate is abundant in modern seawater, fueling extensive sedimentary microbial sulfate reduction (MSR) (*2*). At these concentrations, MSR typically imparts large sulfur isotope fractionations (*3*), allowing the use of sulfur isotopes to reconstruct past global change (*4*, *5*). Small sulfur isotope fractionations preserved in bulk pyrite from Archean (>2400 million years ago) rocks led to the original conclusion that the Archean oceans contained <200 μM sulfate, or ~1% of modern seawater (*5*). The distribution of mass-independent sulfur isotopes in Archean sediments (*4*, *6*–*8*) and box models of global sulfur cycling (*9*) imply even lower Archean seawater sulfate of <60 to 80 μM. Paradoxically, microscale sulfur isotope data from Archean pyrites (*10*–*12*) reveal large sulfur isotope fractionations of up to 40 per mil (‰) in the Archean—fractionations only seen at hundreds to thousands of micromolar sulfate in modern environments (*13*–*15*). Electron-donor availability (*3*, *16*) and MSR rate (*3*, *16*, *17*), however, also exert influence, with larger fractionation typically imparted when electron donors limit sulfate-reduction rates, allowing the

[1]Department of Microbiology and Immunology and Department of Earth, Ocean, and Atmospheric Sciences, University of British Columbia, Vancouver, British Columbia, Canada. [2]NordCEE and Department of Biology, University of Southern Denmark, Odense, Denmark. [3]Department of Geological and Planetary Sciences, California Institute of Technology, Pasadena, CA 91125, USA. [4]Large Lakes Observatory and Department of Physics, University of Minnesota, Minneapolis, MN 55812, USA. [5]School of Geography and Earth Sciences, McMaster University, Hamilton, Ontario, Canada. [6]Department of Earth and Environmental Sciences, University of St. Andrews, St. Andrews, UK. [7]Research Center for Limnology, Indonesian Institute of Sciences, Cibinong, West Java, Indonesia. [8]Department of Geology, University of Kansas, Lawrence, KS 66045, USA. [9]Department of Geology, University of Maryland, College Park, MD 20742, USA.
*These authors contributed equally to this work. **†Corresponding author. E-mail: sacrowe1@gmail.com**

unexplored possibility for large fractionations in low-sulfate (<100 μM) environments.

We explored sulfur isotope fractionation in Lake Matano, Indonesia, an extremely low-sulfate analog for the Archean oceans (*18*). Lake Matano is a persistently stratified ferruginous (Fe^{2+}-rich) lake, where dissolved ferrous iron (Fe^{2+}) accumulates below a chemocline located at ~115 m depth (Fig. 1A). The upper waters of Lake Matano have sulfate concentrations of less than 30 μM (Fig. 1B), far lower than that of the natural environments studied for sulfur isotope fractionation thus far (*13*, *14*) and lower than previous upper limits for Archean seawater (*5*, *8*, *9*). MSR is active within Lake Matano's water column, and peak rates of 30 to 40 nM day^{-1} are reached at sulfate concentrations of between 5 and 10 μM (*11*) (Fig. 1C).

We measured the $\delta^{34}S$ values of sulfate and sulfide in Lake Matano's water column (Fig. 1D) and in the underlying sediments (*19*, *20*). The $\delta^{34}S$ values of sulfate ranged from 8.1‰ within the surface waters to 39.1‰ in the lower reaches of the chemocline, where sulfate is present at barely detectable concentrations (Fig. 1D). Sulfate reduction in the chemocline thus leads to strong isotopic fractionation, despite extremely low sulfate concentrations, favoring the incorporation of ^{32}S into the sulfide produced. Measurements of water-column sulfides reveal $\delta^{34}S$ values from −13.2 to 5.4‰ (table S1), demonstrating that they record large fractionations with a range in $\delta^{34}S$ of up to 18.6‰. Depending on the depths considered, the $\delta^{34}S$ value of water-column sulfides translates to an appreciable isotopic difference ($\Delta^{34}S_{SO_4-H_2S}$) between water-column sulfide and the surface-water sulfate pool of up to 23‰.

We used both a Rayleigh distillation model and a one-dimensional (1D) reaction-diffusion model to calculate sulfur isotope fractionation factors. Rayleigh models underestimate fractionation in open systems (*21*, *22*) like Lake Matano and therefore provide minimum estimates of the true fractionation. Using the Rayleigh model, we obtain a fractionation factor ($\varepsilon_{SO_4-H_2S}$) of 21 ± 1‰ (*16*) (Fig. 2A). To further assess the true magnitude of fractionation during MSR, we constructed an open-system, reaction-diffusion model. As expected, applying the fractionation factor obtained from the Rayleigh model to the reaction-diffusion model underestimates the fractionation observed (Fig. 2B), whereas fractionations ranging between 20 and 70‰ encompass our entire sulfur isotope data set (Fig. 2B). The best fit with constant fractionation, independent of sulfate concentrations, comes from a fractionation factor of 35‰. As MSR proceeds, sulfate concentrations decrease (Fig. 1B), probably shifting MSR from organic matter limitation, which allows expression of large isotope fractionation, to sulfate limitation, which progressively mutes fractionation as sulfate concentrations decrease (*3*, *16*). We therefore also tested a model with fractionation of 70‰ at sulfate concentrations of >6 μM, with a linear decrease to 0‰ when sulfate is exhausted, obtaining an equally good fit. Regardless of the model used, these trends in the $\delta^{34}S$ values of sulfate illustrate large isotope fractionations down to sulfate concentrations below 6 μM (Fig. 2, A and B), confirming that MSR can produce large isotope fractionations at sulfate concentrations more than one order of magnitude lower than previously demonstrated (*5*, *14*, *15*).

Sediments under the chemocline record the integrated $\delta^{34}S$ values of sulfide exported from the water column and exhibit a range of $\delta^{34}S$ values from −4.2 to 6.6‰, with a mean of 2.5 ± 2.5‰ (Fig. 2C). These isotopic compositions are consistent with the range of $\delta^{34}S$ values observed in the water column and predicted by our fractionation models (Fig. 2, A and B) and are up to 14.9‰ lower than that of sulfate in the surface waters of the lake (table S1). Reaction-diffusion models with either a constant fractionation of 35‰ or a variable fractionation of 70‰ that decreases below 6 μM sulfate yield integrated sulfide export with $\delta^{34}S$ values of 3.8 and 2.7‰ (Fig. 2C), respectively. These $\delta^{34}S$ values are similar to the mean of measured sediment sulfides, in contrast to the model with a 20‰ fractionation, which yields a sulfide export flux at the far maximum range of the sediment $\delta^{34}S$ values (6.5‰) and outside of the standard deviation of the sediment mean.

The lack of a full expression of water-column sulfur isotope fractionation in bulk $\delta^{34}S$ measurements of sedimentary sulfides is due to the depletion of sulfate to low concentrations in the chemocline and the development of a strong water-column gradient in sulfate concentration and isotopic composition. As a result, $\delta^{34}S$ values of sulfate increase with decreasing sulfate concentrations (Fig. 1, B and C), leading to a reservoir effect and the production of correspondingly ^{34}S-enriched sulfide, despite the strong fractionation imparted during sulfate reduction. In the

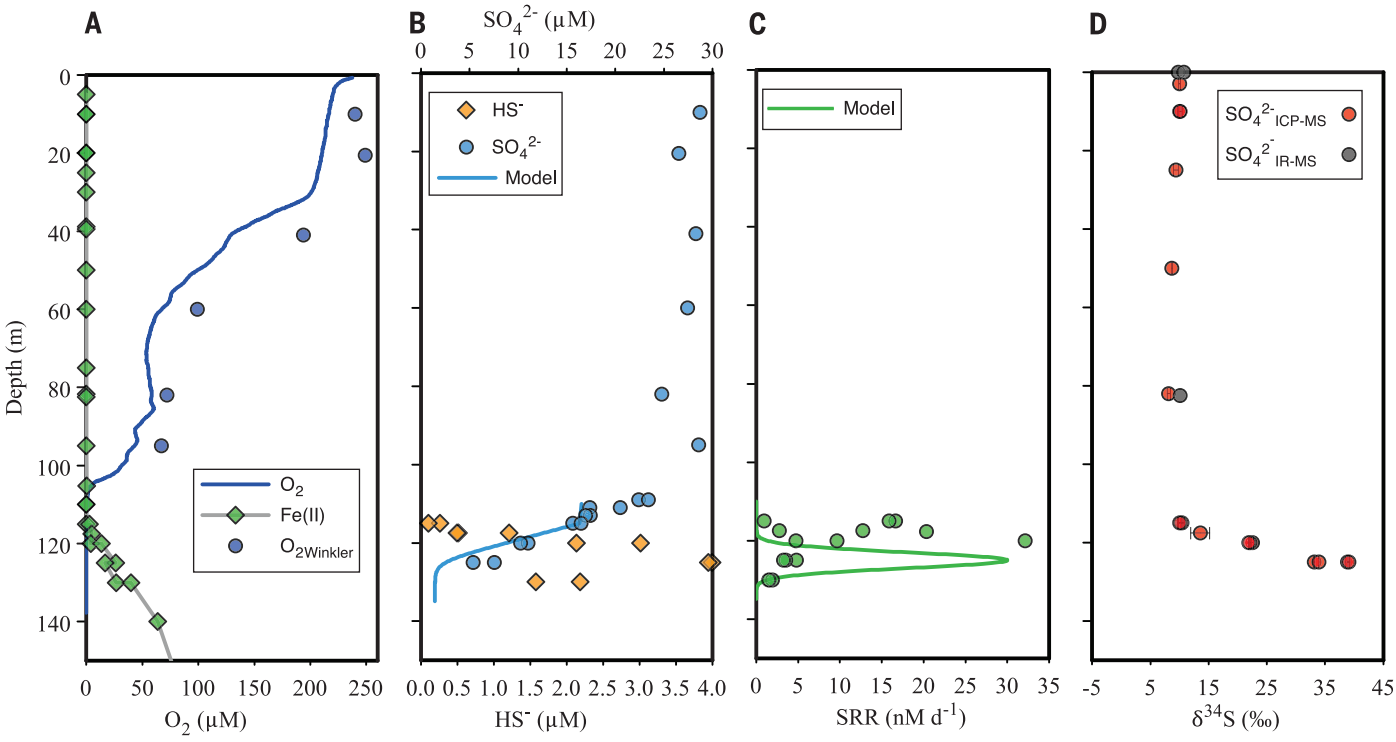


Fig. 1. Vertical chemical profiles in Lake Matano. (**A**) Dissolved O_2 and Fe^{2+}. (**B**) SO_4^{2-} and HS^- (solid line shows modeled SO_4^{2-} concentrations). (**C**) Sulfate-reduction rates (SRRs) (solid line depicts SRRs imposed in the 1D reaction-transport model). d, day. (**D**) $\delta^{34}S$ value of SO_4^{2-}. ICP-MS, inductively coupled plasma mass spectrometry; IR-MS, isotope-ratio mass spectrometry. Data in (A) to (C) come from (*32*), except model results.

end, the net isotopic fractionation between lake-surface sulfate and sedimentary sulfide is only ~7.5‰. A similar effect has been observed in other lakes, albeit at much higher sulfate concentrations (*14*, *15*).

Compilations of the S-isotope composition of Archean sulfides from bulk sediment analyses suggest that the expression of S-isotope fractionation in the Archean was typically less than ~10‰ (Fig. 3). Though most Archean sulfides display little fractionation at the scale of bulk sediment analyses, up to 30‰ (Fig. 3) variability can be observed in the $\delta^{34}S$ of some Archean bulk sediment analyses. Microscale analyses also reveal a broader range in $\delta^{34}S$ of more than 40‰, implying that much larger isotope fractionations were possible (*10*–*12*). The scatter of sulfur isotope data around the Archean MIF-S array (*23*) supports the idea that microbial sulfate reduction in the Archean was accompanied by large sulfur isotope fractionations, possibly more than 40‰, but that the expression of this isotope fractionation at the scale of bulk sedimentary sulfides was muted, similar to our observations in Lake Matano.

To test possible upper limits on Archean seawater sulfate concentrations, we have adapted our reaction-diffusion model to simulate a stratified Archean ocean water column. Like in Lake Matano, we expect that pelagic MSR would have ensued under the ferruginous ocean conditions dominating marine chemistry throughout much of the Archean eon (*24*). In an approach similar to previous models for sedimentary S-isotope fractionation (*5*), we varied seawater sulfate concentrations and computed the integrated $\delta^{34}S$ of sulfide exported from the water column to underlying sediments (Fig. 4). We also assume that MSR would take place in sediments, so we modeled the $\delta^{34}S$ of diagenetic sulfides formed under a range of overlying seawater sulfate concentrations.

Our water-column model shows that at modest MSR rates, comparable to those measured in the Chilean oxygen minimum zone (*25*), appreciable sulfate drawdown occurs with surface seawater sulfate concentrations in the low micromolar range (Fig. 4, A and B). Fractionation factors typical for marine environments (30‰), and justified as a conservative estimate based on microscale measurements of $\delta^{34}S$ in Archean pyrites, translate to a large range in the $\delta^{34}S$ of pelagic sulfate and sulfide (Fig. 4C), showing that reservoir effects similar to those in Lake Matano develop under conditions typical for stratified marine environments. Due to a combination of sulfate drawdown, reservoir effects, and decreased isotope fractionation at low sulfate concentrations, the integrated sulfide exported from the modeled Archean water column has $\delta^{34}S$ values closer to seawater sulfate than would be expected due to the isotope fractionation imparted. The imparted fractionation is best reflected by the sulfide produced in the upper regions of the water column.

Application of a constant fractionation factor of 30‰ in our models results in large differences between the $\delta^{34}S$ values of seawater sulfate and bulk pyrites of 15 to 23‰ (Fig. 4D). Comparing these modeled $\delta^{34}S$ values for sulfide with the distribution of $\delta^{34}S$ in bulk Archean sulfides (yellow diamond distribution plot in Fig. 4D) and assuming seawater $\delta^{34}S$ of 5‰ [the range reported is 3 to 8‰ (*26*–*28*)] shows that these large differences are not supported by the bulk pyrite record. It therefore implies that other processes, such as sulfate limitation of MSR, were at play in the Archean. Conservatively applying a fractionation factor that decreases below 6 μM sulfate, a sulfate concentration that imparts large fractionation in Lake Matano, brings modeled differences between the $\delta^{34}S$ of seawater sulfate and bulk pyrites into a range supported by the Archean bulk pyrite record (Fig. 4D). Under this scenario, both water-column and sediment models predict that MSR would impart bulk sediment sulfide $\delta^{34}S$ values of more than 10‰ lighter than seawater sulfate at sulfate concentrations more than ~5 μM (Fig. 4D). Comparison under this scenario suggests that more than half of the measured sulfide $\delta^{34}S$ values could be described by deposition at seawater sulfate concentrations between 1 and 2.5 μM, and more than 90% deposited at seawater sulfate concentrations <5 μM (Fig. 4D). Taking into consideration that the $\delta^{34}S$ value of seawater sulfate may have reached up to 15‰ in the Neoarchean, and that $\delta^{34}S$ values in pyrite may also include contributions from ^{34}S-enriched photochemical sources (*29*), the concentration window may have extended as high as 10 to 15 μM. Higher seawater sulfate concentrations would have left bulk sulfide $\delta^{34}S$ values much lighter and are therefore not supported by the sedimentary $\delta^{34}S$ sulfide record. The ~30‰ variability observed at the scale of some bulk sediments could be imparted by dynamic processes that cause changes in the concentration of sulfate, the rate of sulfate transport into the sulfate-reduction zone, the rate of MSR (*17*), electron-donor availability (*16*), or the $\delta^{34}S$ of seawater sulfate. These could include variability in depositional depth of sediments analyzed, fluctuations in the depth of mixing, shifting organic matter availability, or variable contributions of atmospheric versus riverine sulfur fluxes to the oceans. Overall, both the limited sulfur isotope fractionation measured at the bulk sediment

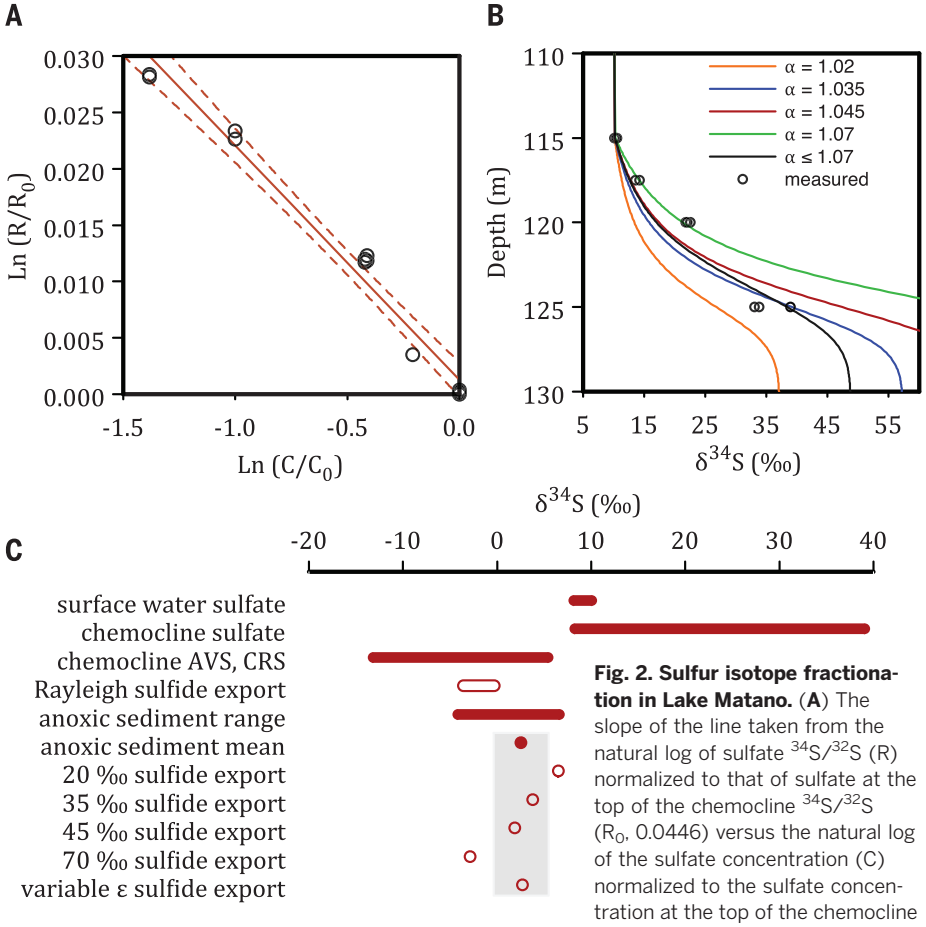


Fig. 2. Sulfur isotope fractionation in Lake Matano. (**A**) The slope of the line taken from the natural log of sulfate $^{34}S/^{32}S$ (R) normalized to that of sulfate at the top of the chemocline $^{34}S/^{32}S$ (R_0, 0.0446) versus the natural log of the sulfate concentration (C) normalized to the sulfate concentration at the top of the chemocline (C_0, 16 μM). The slope of this relation (m = −0.2075) is used to calculate the Rayleigh fractionation factor [$\alpha = (m + 1)^{-1} = 1.0211$]. (**B**) Results from our 1D reaction-diffusion modeling with constant fractionation factors (α) of 1.020, 1.035, 1.045, and 1.070, in addition to a variable fractionation factor with α of 1.070 at sulfate concentrations >6 μM and a linear decrease of α from 1.070 to 1.000 below 6 μM. (**C**) Ranges in $\delta^{34}S$ observed (solid lines and circles) or computed (hollow lines and circles) for different sulfur pools in Lake Matano. The shaded box outlines 1 SD from the anoxic sediment mean. AVS, acid volatile sulfide; CRS, chromium reducible sulfide.

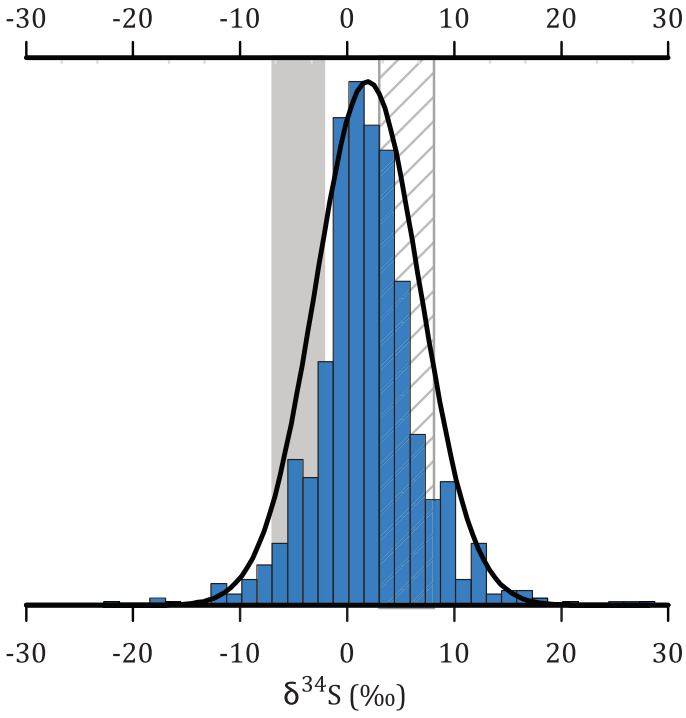


Fig. 3. Compilation of nearly 3000 individual measurements of the $\delta^{34}S$ values of bulk Archean sedimentary sulfides. The black line shows the normal distribution, and the general agreement between the data and the normal distribution suggests a single population. The vertical hatched band delineates the likely range of $\delta^{34}S$ for surface ocean seawater sulfate (*26*–*28*). The vertical gray band shows a 10‰ difference from seawater sulfate. Very few measurements extend beyond this 10‰ difference.

scale and the large isotopic fractionations at the microscale point strongly to sulfate concentrations less than 2.5 μM.

Our results suggest that Archean ocean sulfate concentrations were <0.01% modern seawater, implying very different global sulfur dynamics. With surface seawater sulfate concentrations in the low micromolar range, sulfate residence times (*16*) would have been on the order of 10^3 to 10^4 years, and sulfate could have been poorly mixed in the Archean oceans. Though homogeneity of S isotopes in some Archean barites has been taken as evidence for conservative sulfate behavior (*29*), such conservative behavior at these low seawater sulfate concentrations would imply smaller-than-estimated volcanic and weathering sulfate fluxes to the Archean oceans (*30*). Regardless, the short residence times would have rendered seawater sulfate and its isotopic composition extremely sensitive to perturbations in the global sulfur cycle.

At seawater sulfate concentrations up to 2.5 μM, sediment sulfate reduction would have contributed less than ~10% to sedimentary organic carbon degradation (*16*), leaving the balance to fuel other microbial processes. Organisms also require sulfur as a nutrient, using it for protein synthesis at a typical cellular ratio of 48C:1S:0.45P (*31*); cellular sulfur quotas are thus

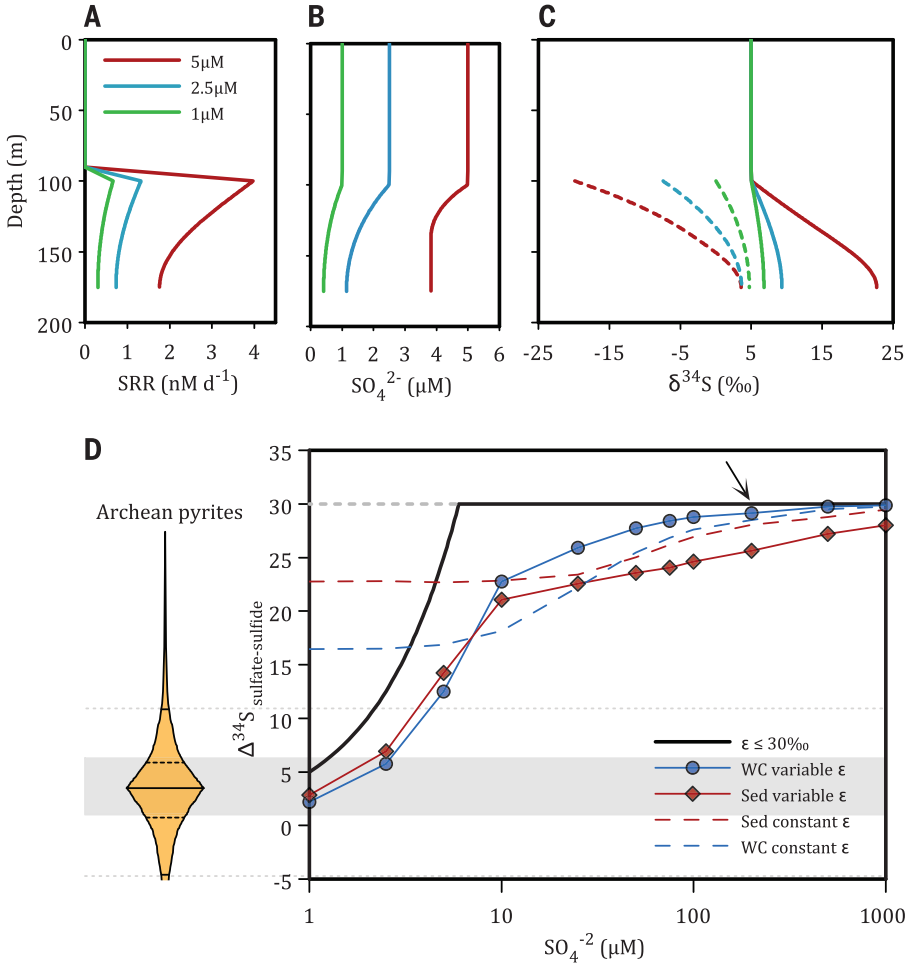


Fig. 4. Models of marine sulfur cycling and isotope fractionation in the Archean eon. (**A**) Modeled rates of microbial sulfate reduction in a stratified Archean ocean water column with different surface seawater sulfate concentrations. (**B**) Resulting sulfate concentration profiles. (**C**) Sulfate (solid lines) and sulfide (dashed lines) $\delta^{34}S$ profiles generated using a variable ε of 30‰ at sulfate concentrations >6 μM that decreases to 0‰ when sulfate is exhausted. (**D**) Mean integrated $\delta^{34}S$ for sulfide produced and exported from the water column to sediments (blue) and diagenetic sulfide (red) at various surface seawater sulfate concentrations. The solid black line indicates the imposed sulfur isotope fractionation factor at different sulfate concentrations (ε ≤ 30‰, justified from microscale analyses of Archean pyrites), and the gray dashed line symbolizes a constant fractionation factor (ε = 30‰). The golden diamond distribution plot at left illustrates sedimentary $\Delta^{34}S_{sulfate\text{-}sulfide}$ calculated from bulk Archean sulfides (from Fig. 3) and using 5‰ as a conservative value for $\delta^{34}S$ of seawater sulfate. The horizontal gray band delineates values between the 25th and 75th percentiles, whereas the horizontal dashed lines delineate the 5th and 95th percentiles, encompassing 90% of the Archean data. The arrow demarcates the previous 200 μM threshold for the full expression of sulfur isotope fractionation (*5*).

higher than those of phosphorus. At low concentrations, nutrients such as phosphorus tend to limit biological production, and by analogy, sulfur may have played a more important role as a biologically scarce nutrient.

REFERENCES AND NOTES

1. S. T. Petsch, R. A. Berner, *Am. J. Sci.* **298**, 246–262 (1998).
2. B. B. Jørgensen, *Nature* **296**, 643–645 (1982).
3. D. E. Canfield, *Geochim. Cosmochim. Acta* **65**, 1117–1124 (2001).
4. R. A. Berner, S. T. Petsch, *Science* **282**, 1426–1427 (1998).
5. K. S. Habicht, M. Gade, B. Thamdrup, P. Berg, D. E. Canfield, *Science* **298**, 2372–2374 (2002).
6. Q. J. Guo *et al.*, *Geology* **37**, 399–402 (2009).
7. I. Halevy, D. T. Johnston, D. P. Schrag, *Science* **329**, 204–207 (2010).
8. J. W. Jamieson, B. A. Wing, J. Farquhar, M. D. Hannington, *Nat. Geosci.* **6**, 61 (2013).
9. I. Halevy, *Proc. Natl. Acad. Sci. U.S.A.* **110**, 17644–17649 (2013).
10. J. Farquhar *et al.*, *Proc. Natl. Acad. Sci. U.S.A.* **110**, 17638–17643 (2013).
11. W. W. Fischer *et al.*, *Proc. Natl. Acad. Sci. U.S.A.* **111**, 5468–5473 (2014).
12. B. S. Kamber, M. J. Whitehouse, *Geobiology* **5**, 5–17 (2007).
13. D. E. Canfield, J. Farquhar, A. L. Zerkle, *Geology* **38**, 415–418 (2010).
14. M. L. Gomes, M. T. Hurtgen, *Geology* **41**, 663–666 (2013).
15. M. Nakagawa *et al.*, *Limnol. Oceanogr.* **57**, 974–988 (2012).
16. M. S. Sim, S. Ono, K. Donovan, S. P. Templer, T. Bosak, *Geochim. Cosmochim. Acta* **75**, 4244–4259 (2011).
17. W. D. Leavitt, I. Halevy, A. S. Bradley, D. T. Johnston, *Proc. Natl. Acad. Sci. U.S.A.* **110**, 11244–11249 (2013).
18. S. A. Crowe *et al.*, *Proc. Natl. Acad. Sci. U.S.A.* **105**, 15938–15943 (2008).
19. Materials and methods are available as supplementary materials on *Science* Online.
20. G. Paris, A. L. Sessions, A. V. Subhas, J. F. Adkins, *Chem. Geol.* **345**, 50–61 (2013).
21. M. B. Goldhaber, I. R. Kaplan, *Mar. Chem.* **9**, 95–143 (1980).
22. B. B. Jorgensen, *Geochim. Cosmochim. Acta* **43**, 363–374 (1979).
23. S. Ono *et al.*, *Earth Planet. Sci. Lett.* **213**, 15–30 (2003).
24. S. W. Poulton, D. E. Canfield, *Elements* **7**, 107–112 (2011).
25. D. E. Canfield *et al.*, *Science* **330**, 1375–1378 (2010).
26. E. M. Cameron, K. Hattori, *Chem. Geol.* **65**, 341 (1987).
27. D. E. Canfield, J. Farquhar, *Proc. Natl. Acad. Sci. U.S.A.* **106**, 8123–8127 (2009).
28. I. B. Lambert, T. H. Donnelly, J. S. R. Dunlop, D. I. Groves, *Nature* **276**, 808–811 (1978).
29. D. L. Roerdink, P. R. D. Mason, J. Farquhar, T. Reimer, *Earth Planet. Sci. Lett.* **331–332**, 177–186 (2012).
30. E. E. Stüeken, D. C. Catling, R. Buick, *Nat. Geosci.* **5**, 722–725 (2012).
31. C. T. A. Chen, C. M. Lin, B. T. Huang, L. F. Chang, *Mar. Chem.* **54**, 179–190 (1996).
32. S. A. Crowe *et al.*, *Geobiology* **12**, 322–339 (2014).

ACKNOWLEDGMENTS

We thank A. Sturm and C. Henny for help with fieldwork. S. Poulton provided sediment $\delta^{34}S$ data. A. Hefford helped compile Archean S-isotope data. Funding to S.A.C. was provided by an Agouron Institute Geobiology Fellowship and a *Natural Sciences and Engineering Research Council* of Canada Postdoctoral Fellowship. Additional funding was provided by the Danish National Research Foundation (grant no. DNRF53) and the European Research Council. All data are available in the supplementary materials.

SUPPLEMENTARY MATERIALS

www.sciencemag.org/content/346/6210/735/suppl/DC1
Materials and Methods
Supplementary Text
Figs. S1 and S2
Tables S1 to S5
References (*33*–*68*)
Data S1

21 July 2014; accepted 10 October 2014
10.1126/science.1258966

EARLY EARTH

Neoarchean carbonate-associated sulfate records positive $\Delta^{33}S$ anomalies

G. Paris,[1]* J. F. Adkins,[1] A. L. Sessions,[1] S. M. Webb,[2] W. W. Fischer[1]

Mass-independent fractionation of sulfur isotopes (reported as $\Delta^{33}S$) recorded in Archean sedimentary rocks helps to constrain the composition of Earth's early atmosphere and the timing of the rise of oxygen ~2.4 billion years ago. Although current hypotheses predict uniformly negative $\Delta^{33}S$ for Archean seawater sulfate, this remains untested through the vast majority of Archean time. We applied x-ray absorption spectroscopy to investigate the low sulfate content of particularly well-preserved Neoarchean carbonates and mass spectrometry to measure their $\Delta^{33}S$ signatures. We report unexpected, large, widespread positive $\Delta^{33}S$ values from stratigraphic sections capturing over 70 million years and diverse depositional environments. Combined with the pyrite record, these results show that sulfate does not carry the expected negative $\Delta^{33}S$ from sulfur mass-independent fractionation in the Neoarchean atmosphere.

The sulfur isotopic composition of Archean [3.8 to 2.4 billion years ago (Ga)] sedimentary rocks provides critical evidence that Earth's atmosphere contained very little, if any, free O_2 before the rise of oxygen ~2.4 Ga (*1*–*6*). Most processes on Earth fractionate sulfur isotopes proportionally to their relative mass differences [$\Delta^{33}S = 0$ (*7*)], yet Archean pyrite (FeS_2) commonly deviates from this relationship, skewed toward positive $\Delta^{33}S$ values (*1*, *8*). This mass-independent fractionation (MIF) pattern is widely attributed to photodissociation of SO_2 by ultraviolet (UV) light allowed by the extremely low levels of O_2 and O_3 in Earth's atmosphere at that time (*1*, *6*). In this scenario, coeval sulfate aerosols ultimately deposited in the ocean as dissolved sulfate carry the complementary negative $\Delta^{33}S$ anomalies required by isotopic mass balance (*1*, *2*, *5*, *8*, *9*). Recent experiments (*10*–*12*) and models of the Archean atmosphere (*2*) show a much wider range of MIF patterns, including positive $\Delta^{33}S$ anomalies in sulfate instead of lower-valent S species. Sulfate minerals that would provide a test of the distribution of MIF signal are absent from Archean evaporite sequences—bedded sulfate deposits occur only after the rise of oxygen (*13*). Paleoarchean barites (3.5 to 3.2 Ga) are a notable exception. They carry small, negative $\Delta^{33}S$ values [0 to −1.5‰ (*1*, *14*–*16*)] but have an enigmatic petrogenesis (*17*). No such sulfate record exists for the billion-year interval from Mesoarchean time through the Paleoproterozoic rise of oxygen. Consequently, the notion of an Archean marine sulfate pool with negative $\Delta^{33}S$ values remains largely untested.

Sulfate minerals are not the only portal into the past marine sulfate pool. Small quantities of carbonate-associated sulfate (CAS) have become an important archive for studying marine sulfate in younger successions (*18*). However, the very low sulfate concentrations of Archean carbonates have kept this archive largely out of reach for conventional analytical methods. Two studies measuring Archean CAS suggested that Archean sulfate carried positive $\Delta^{33}S$ (*4*, *19*). However, both studies used large sample sizes (>100 g of $CaCO_3$), raising the risks of lower preservation as well as contamination by pyrite. We recently developed a technique using inductively coupled plasma mass spectrometry to measure both $\Delta^{33}S$ and $\delta^{34}S$ using a few tens of milligrams of low-CAS carbonate (*20*). Greater sensitivity allows the measurement of sulfur isotopes from specific petrographic and sedimentary fabrics with different diagenetic histories, coupled with light and electron microscopy (Fig. 1 and fig. S4), to directly assess sample quality based on the presence of additional S-bearing phases (e.g., organic sulfur, pyrite). In parallel, we applied synchrotron x-ray absorption spectroscopy (XAS) to measure sulfur speciation in these samples. We examined three sedimentary sections from a range of marine paleoenvironments across the Neoarchean Campbellrand carbonate platform (*21*). Section W1 (aragonite sea-floor fans, precipitated laminae, preserved as early diagenetic fabric-retentive dolomite) captures shallow subtidal environments, whereas sections GKP01 and W2 [herringbone, an early marine calcitic cement (*22*), microbial laminae, dolomite, and calcite spar] capture deep subtidal and slope environments (*21*).

The CAS data preserve positive $\delta^{34}S$ values and unambiguously positive $\Delta^{33}S$ values and display significant variability, sometimes at very small scales (Fig. 2 and additional data table S1). The carbonate fabrics contain 5 to 70 parts per million (ppm) sulfate—two orders of magnitude lower than typical Phanerozoic carbonates. Because of such low levels, we consider the potential impacts of contamination and/or sulfide oxidation

[1]Division of Geological and Planetary Sciences, California Institute of Technology, Pasadena, CA 91125, USA. [2]Stanford Synchrotron Radiation Lightsource, Menlo Park, CA 94025, USA.
*Corresponding author. E-mail: gparis@caltech.edu

on these measurements. Contamination by post-Archean sulfur of any form, in the laboratory or field, can be confidently ruled out because it would not carry a substantial MIF signal. Modern oxidation of indigenous pyrite or organic sulfur would carry such a signal, although our sample-cleaning protocol is designed to extract only the sulfate bound into the carbonate lattice (*21*). Late, void-filling calcite spar is notable for having extremely low sulfate concentrations (≤4.3 ppm) and so provides an important negative control. XAS analyses of samples prepared under strictly anaerobic conditions indicate an average of 22 (±14%) sulfate S, 67 (±13%) pyrite S, and 12 (±7%) organic S [(*21*); table S3 and fig. S5] and show that there is an appreciable amount of sulfate present. At worst, our analyses represent a mixture of CAS and oxidized pyrite, yet plots of either $\delta^{34}S$ or $\Delta^{33}S$ versus concentration show no correlation (fig. S8), as would be expected for such a mixture. Moreover, the mean $\Delta^{33}S$ value for CAS is higher than that for coeval disseminated pyrite (*4*, *23*–*30*), averaging 6.39 and 4.48‰, respectively (fig. S9). Although we cannot rule out a heterogeneous distribution of pyrite grains, with smaller, easier-to-oxidize grains carrying larger-than-average $\Delta^{33}S$ values, this should still lead to a correlation between sulfate concentration and $\Delta^{33}S$.

A possibility that is more difficult to rule out is the existence of an ancient fluid-flow event that oxidized pyrite while simultaneously recrystallizing carbonate minerals. The absence of measurable sulfate in void-filling sparry cements argues against this possibility, as do variable sulfate concentrations between closely colocated carbonate fabrics. Carbon and oxygen isotopic compositions are consistent with previously reported values and are inconsistent with extensive interaction with hydrothermal fluids (*31*). There is no correlation between $\delta^{34}S$ or $\Delta^{33}S$ and either carbon or oxygen isotope ratios (fig. S10), as might be expected of a diagenetic origin for sulfate. Lastly, the carbonates contain substantially more reduced iron (0.5 to 1%) than reduced sulfur (<0.1%), yet no detectable oxidized iron (*32*). Such a pattern is inconsistent with any diagenetic event that locally oxidized pyrite. We conclude that the measured CAS represents Neoarchean marine sulfate with a strong positive $\Delta^{33}S$ anomaly.

Our data challenge the canonical view of the Archean sulfur cycle in which S_8 compounds with positive $\Delta^{33}S$ values and SO_4^{2-} with negative $\Delta^{33}S$ values derived from SO_2 photolysis to form the reduced and oxidized pools of sulfur, respectively. In Fig. 3A, we compare the sulfur isotopic compositions as normalized ratios $\delta'^{33}S$ and $\delta'^{34}S$ (*7*) of CAS against an extensive set of published values from Campbellrand platform pyrites. If sulfate originated from pyrite oxidation, CAS should overlap pyrites and show both negative and positive $\Delta^{33}S$ values. Instead, we observe that the $\delta'^{34}S$ values of CAS and disseminated pyrite complement each other, which provides a simple framework to interpret previously published data. Microbial sulfate reduction produces pyrite

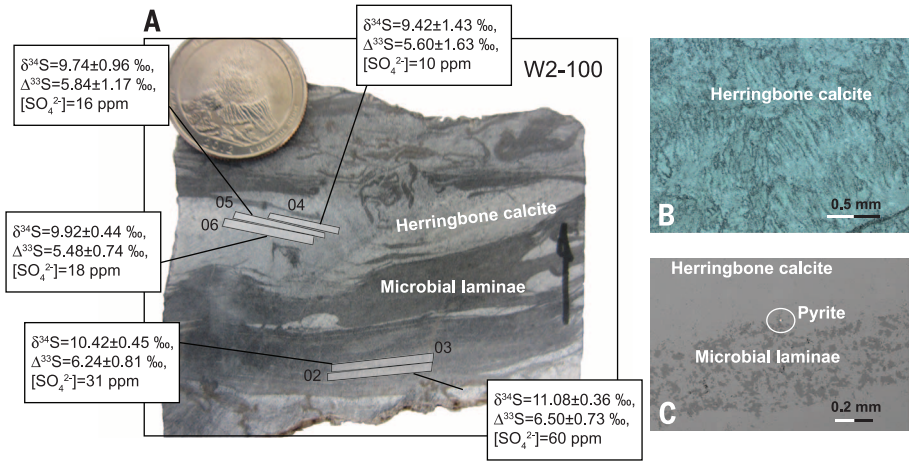


Fig. 1. Measurement of multiple sulfur isotope ratios from specific petrographic textures within a sample. (**A**) Cut face of hand sample W2-100 contains several different calcite fabrics, dark microbial laminae, and marine herringbone calcite cements. Sample locations are shown as numbered light gray areas. U.S. quarter is shown for scale. (**B**) Transmitted light and (**C**) backscatter electron photomicrographs of a thin section facing the location of samples 4 to 6. Herringbone calcite generally lacks reflective (or high backscatter) sulfide-bearing minerals, whereas microbial laminae textures may contain rare small (~2 μm) pyrite grains.

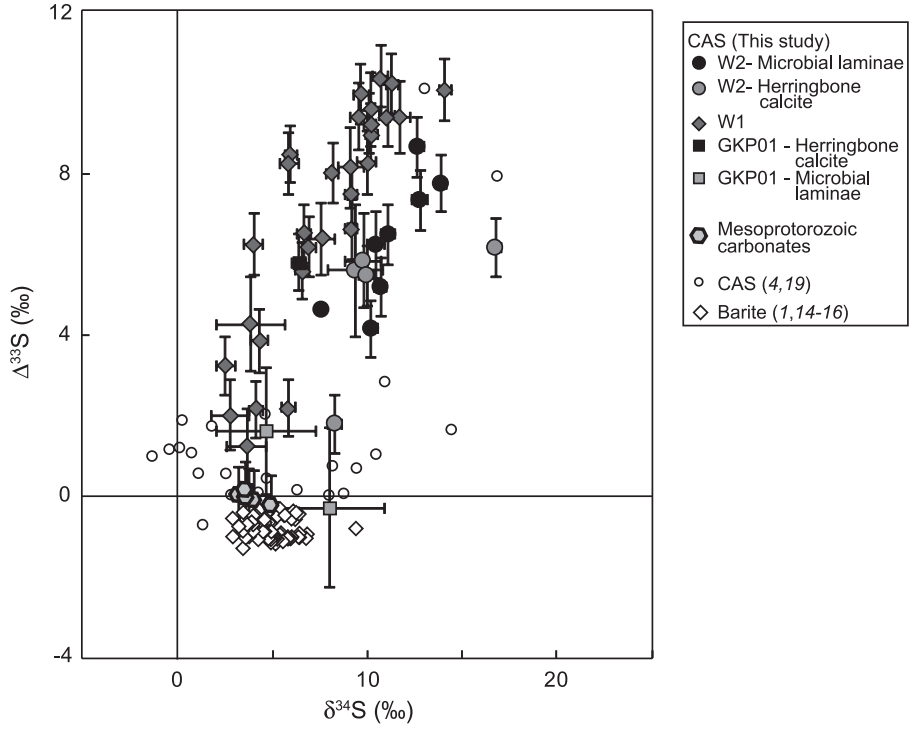


Fig. 2. Crossplot of $\delta^{34}S$ versus $\Delta^{33}S$ values for all Archean sulfate measured to date. CAS [Campbellrand carbonate platform, 2.6 to 2.5 Ga, this study, mean ± 2 SD (*4*, *21*), and various locations, 3.0 to 2.6 Ga (*19*)] and the Paleoarchean barite record (*1*, *14*–*16*). For comparison, CAS data from the Mesoproterozoic-age Helena Formation measured in this study are shown; note the lack of MIF in these samples (after the rise of oxygen).

with the same $\Delta^{33}S$ as, and lower $\delta^{34}S$ than, sulfate. In Fig. 3A, this MIF is expressed as vectors parallel to the dashed line toward the left, which explains most of the disseminated pyrite. To explain the few ^{34}S-enriched pyrites, either porewater sulfate must have become enriched in ^{34}S over the course of sulfate reduction [as in modern anoxic pore waters (*33*)], or additional mass-dependent processes were involved. The overall fractionation leaves the remaining dissolved sulfate pool slightly enriched in heavy isotopes within the Campbellrand basin, moving the $\delta^{34}S$-intercept of the fractionation line above the origin of the $\delta^{34}S$-$\Delta^{33}S$ crossplot (Fig. 2).

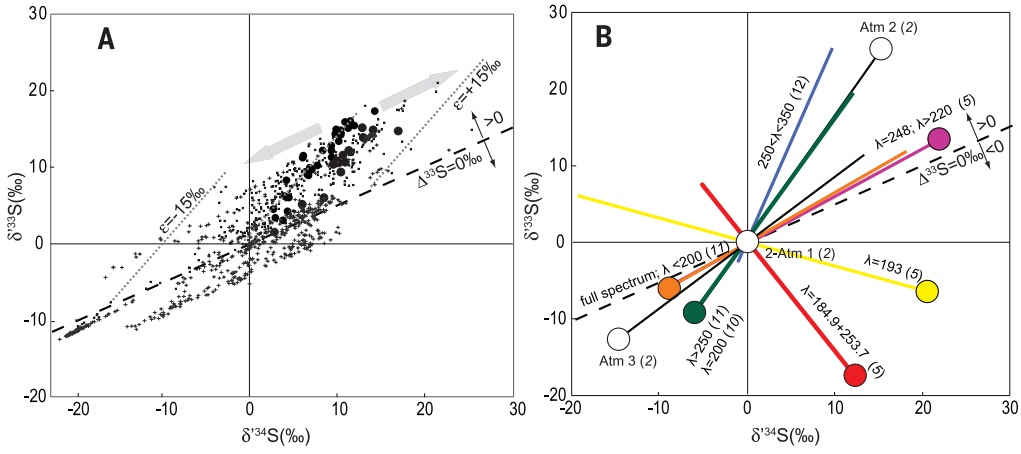


Fig. 3. Comparison between sulfur isotopic compositions in data and laboratory and numerical experiments. (**A**) Comparison of sulfur isotope composition for CAS (this study, circles) and pyrite [disseminated, dots; nodule and layers, crosses (*4*, *23*–*30*, *33*)] from the Campbellrand platform. The CAS data define a narrow range, departing from bulk Earth sulfur (the origin on this plot) by MIF processes. Dashed line is the mass-dependent (MD) fractionation law. Disseminated pyrite isotopic compositions depart from the CAS trend via MD processes (gray arrows). Dotted lines indicate the MIF law for section W1 with no fractionation and with MD fractionations (ε) of –15 and +15‰. The Neoarchean pyrite record from South Africa also includes pyrites, mostly nodular, with negative $\Delta^{33}S$ values. (**B**) Mass fractionation laws for published photochemistry experiments at different wavelengths λ (nm) or atmospheric compositions. The slope of each line is the average mass law centered on the origin for a given data set. The circles indicate the oxidized sulfur endmember, close to which are reported the wavelengths used for each experiment. Atm 1, 2, and 3 are Archean theoretical atmospheres 1, 2, and 3 (*2*).

Nodular pyrites (*25*–*27*, *29*, *33*) commonly display a negative $\Delta^{33}S$ signature, shown below the dashed line in Fig. 3A. Rather than marine sulfate, these pyrites could be representative of a sulfur pool mass-balancing the Archean sulfur cycle (*1*, *2*, *8*, *14*, *29*).

The small-scale variation observed in $\Delta^{33}S$ values within samples may reflect the atmospheric processes that create MIF. In the modern world, the $\Delta^{33}S$ of sulfate aerosols produced after volcanic injections of SO_2 into the stratosphere changes within a few years (*34*). Therefore, atmospheric fractionations, but also output fluxes, can vary on time scales much shorter than the temporal resolution of the stratigraphic record. Because atmospheric processes create MIF that follow a linear trend in the $\delta'^{33}S$-$\delta'^{34}S$ space, the observation of a slope between $\Delta^{33}S$ and $\delta^{34}S$ values supports this notion. The small-scale variation could also reflect differing extents of sulfur cycling between different coeval pools (elemental sulfur, sulfide, etc.) (*33*, *35*). Regardless, these possibilities each point to relatively low concentrations, a short residence time of seawater sulfate in this marine basin, and limited exchange between sulfur pools to prevent $\Delta^{33}S$ homogenization (*35*).

Existing models of Archean sulfur cycling were influenced by early experimental results for SO_2 interaction with UV light that produced oxidized species with negative $\Delta^{33}S$ values (*5*). In Fig. 3B, we compile all the results from experimental work (*5*, *8*–*12*) and atmospheric modeling (*2*) exploring sulfur isotope MIF trends. We derive mass fractionation laws, defined as the slope between the normalized ratios $\delta'^{33}S$ and $\delta'^{34}S$ (*7*) for the products of atmospheric processes either in the laboratory or in simulations of the Archean atmosphere. The oxidized sulfur products are marked at the ends of the mass fractionation lines with circles. The mass laws for these different experiments display a broad range of slopes, and different signs of $\Delta^{33}S$ for SO_4^{2-}. Recent studies (*2*, *10*–*12*) show more scenarios in which the oxidized sulfur pool resulting from SO_2 photochemistry bears positive $\Delta^{33}S$ values (Fig. 3B). More broadly, time series of records of sulfur isotopes in Archean carbonates can now provide a key test for hypotheses derived from experiments and theory regarding the composition and evolution of Earth's early atmosphere.

REFERENCES AND NOTES

1. J. Farquhar, H. Bao, M. Thiemens, *Science* **289**, 756–758 (2000).
2. Y. Ueno *et al.*, *Proc. Natl. Acad. Sci. U.S.A.* **106**, 14784–14789 (2009).
3. A. Bekker *et al.*, *Science* **326**, 1086–1089 (2009).
4. Q. Guo *et al.*, *Geology* **37**, 399–402 (2009).
5. J. Farquhar, J. Savarino, S. Airieau, M. H. Thiemens, *J. Geophys. Res. Planets* **106**, 32829 (2001).
6. A. A. Pavlov, J. F. Kasting, *Astrobiology* **2**, 27–41 (2002).
7. Isotopic ratios are usually reported as $\delta^{3x}S$ (3*x* being either 33, 34, or 36) values where $\delta^{3x}S = 1000 \times [(^{3x}S/^{32}S)_{sample}/(^{3x}S/^{32}S_{VCDT}) - 1] \times 1000$. The terrestrial mass fractionation law is conventionally defined as $\delta'^{33}S = 0.515 \times \delta'^{34}S$, where $\delta'^{3x}S = 1000 \times \ln[(^{3x}S/^{32}S)_{sample}/(^{3x}S/^{32}S_{VCDT})]$ with VCDT the Vienna Canyon Diablo Troilite reference standard. Deviations from this relationship are commonly termed "mass-independent fractionation" and are quantified as $\Delta^{33}S = \delta'^{33}S - 0.515 \times \delta'^{34}S$.
8. I. Halevy, D. T. Johnston, D. P. Schrag, *Science* **329**, 204–207 (2010).
9. J. R. Lyons, *Geophys. Res. Lett.* **34**, L22811 (2007).
10. A. L. Masterson, J. Farquhar, B. A. Wing, *Earth Planet. Sci. Lett.* **306**, 253–260 (2011).
11. A. R. Whitehill, S. Ono, *Geochim. Cosmochim. Acta* **94**, 238–253 (2012).
12. A. R. Whitehill *et al.*, *Proc. Natl. Acad. Sci. U.S.A.* **110**, 17697–17702 (2013).
13. J. P. Grotzinger, J. F. Kasting, *J. Geol.* **101**, 235–243 (1993).
14. H. Bao, D. Rumble III, D. R. Lowe, *Geochim. Cosmochim. Acta* **71**, 4868–4879 (2007).
15. Y. Ueno, S. Ono, D. Rumble, S. Maruyama, *Geochim. Cosmochim. Acta* **72**, 5675–5691 (2008).
16. D. L. Roerdink, P. R. D. Mason, J. Farquhar, T. Reimer, *Earth Planet. Sci. Lett.* **331–332**, 177–186 (2012).
17. M. J. Van Kranendonk, *Earth Sci. Rev.* **74**, 197–240 (2006).
18. L. C. Kah, T. W. Lyons, J. T. Chesley, *Precambrian Res.* **111**, 203–234 (2001).
19. S. D. Domagal-Goldman, J. F. Kasting, D. T. Johnston, J. Farquhar, *Earth Planet. Sci. Lett.* **269**, 29–40 (2008).
20. G. Paris, A. L. Sessions, A. V. Subhas, J. F. Adkins, *Chem. Geol.* **345**, 50–61 (2013).
21. Materials and methods are available on *Science* Online.
22. D. Y. Sumner, J. P. Grotzinger, *J. Sediment. Res.* **66**, 419 (1996).
23. G. Hu, D. Rumble, P.-L. Wang, *Geochim. Cosmochim. Acta* **67**, 3101–3118 (2003).
24. A. J. Kaufman *et al.*, *Science* **317**, 1900–1903 (2007).
25. S. Ono, N. J. Beukes, D. Rumble, *Precambrian Res.* **169**, 48–57 (2009).
26. B. S. Kamber, M. J. Whitehouse, *Geobiology* **5**, 5–17 (2007).
27. S. Ono, A. J. Kaufman, J. Farquhar, D. Y. Sumner, N. J. Beukes, *Precambrian Res.* **169**, 58–67 (2009).
28. D. Papineau, S. J. Mojzsis, *Geobiology* **4**, 227–238 (2006).
29. J. Farquhar *et al.*, *Proc. Natl. Acad. Sci. U.S.A.* **110**, 17638–17643 (2013).
30. A. L. Zerkle, M. W. Claire, S. D. Domagal-Goldman, J. Farquhar, S. W. Poulton, *Nat. Geosci.* **5**, 359–363 (2012).
31. W. W. Fischer *et al.*, *Precambrian Res.* **169**, 15–27 (2009).
32. N. J. Beukes, *Sediment. Geol.* **54**, 1–46 (1987).
33. W. W. Fischer *et al.*, *Proc. Natl. Acad. Sci. U.S.A.* **111**, 5468–5473 (2014).
34. M. Baroni, M. H. Thiemens, R. J. Delmas, J. Savarino, *Science* **315**, 84–87 (2007).
35. I. Halevy, *Proc. Natl. Acad. Sci. U.S.A.* **110**, 11244–11249 (2013).

ACKNOWLEDGMENTS

We thank J. Johnson for help with stratigraphic sample collection and fruitful comments; N. Beukes and I. Halevy for helpful discussions; K. Bergmann for assistance with C and O analyses; and C. Ma, T. Present, and J. Johnson for assistance with scanning electron microscopy. We acknowledge support from NSF Division of Earth Sciences award no. EAR-1349858. Assistance from N. Dalleska and use of IC instrumentation in the Environmental Analysis Center at the California Institute of Technology is gratefully acknowledged. G.P. was funded by the Henry and Camille Dreyfus Postdoctoral Program in Environmental Chemistry. W.W.F. acknowledges support from the David and Lucile Packard Foundation. Drill core GKP01 was sampled with support from the Agouron Institute. Use of the Stanford Synchrotron Radiation Lightsource, SLAC National Accelerator Laboratory, is supported by the U.S. Department of Energy, Office of Science, Office of Basic Energy Sciences under Contract No. DE-AC02-76SF00515. The SSRL Structural Molecular Biology Program is supported by the DOE Office of Biological and Environmental Research and by the National Institutes of Health, National Institute of General Medical Sciences (including P41GM103393).

SUPPLEMENTARY MATERIALS

www.sciencemag.org/content/346/6210/739/suppl/DC1
Materials and Methods
Figs. S1 to S10
Tables S1 to S3
References (*36*–*54*)
Additional Data Table S1

2 July 2014; accepted 22 September 2014
10.1126/science.1258211

EARLY EARTH

Large sulfur isotope fractionations associated with Neoarchean microbial sulfate reduction

Iadviga Zhelezinskaia,[1]* Alan J. Kaufman,[1] James Farquhar,[1] John Cliff[2]

The minor extent of sulfur isotope fractionation preserved in many Neoarchean sedimentary successions suggests that sulfate-reducing microorganisms played an insignificant role in ancient marine environments, despite evidence that these organisms evolved much earlier. We present bulk, microdrilled, and ion probe sulfur isotope data from carbonate-associated pyrite in the ~2.5-billion-year-old Batatal Formation of Brazil, revealing large mass-dependent fractionations (approaching 50 per mil) associated with microbial sulfate reduction, as well as consistently negative $\Delta^{33}S$ values (~ −2 per mil) indicative of atmospheric photochemical reactions. Persistent ^{33}S depletion through ~60 meters of shallow marine carbonate implies long-term stability of seawater sulfate abundance and isotope composition. In contrast, a negative $\Delta^{33}S$ excursion in lower Batatal strata indicates a response time of ~40,000 to 150,000 years, suggesting Neoarchean sulfate concentrations between ~1 and 10 μM.

The Archean Eon [4.0 to 2.5 billion years ago (Ga)] is generally characterized as a time in Earth history when oxygen was a trace constituent in the atmosphere (*1*) and oceanic sulfate abundance was lower than its present-day concentration by as much as a factor of 150 (*2*, *3*). Although sulfur isotope signatures in marine sedimentary rocks suggest that microbial sulfate reduction (MSR) was used as a metabolic strategy as far back as 3.5 Ga (*4*), overwhelming evidence for mass-independent sulfur isotope fractionations derived from atmospheric reactions (*5*) and preserved in Archean records argues against the prominence of contemporaneous MSR in the oceans (*6*–*9*). Iron speciation and trace metal abundances indicate a Neoarchean (2.5 to 2.8 Ga) role for MSR and sulfide production, implying euxinic (lacking oxygen but containing free hydrogen sulfide) conditions in some basins (*10*). Moreover, recent high-precision secondary ion mass spectrometry (SIMS) analyses of pyrite (*11*–*13*) and organic matter (*14*) in Archean successions reveal evidence of micrometer-scale mass-dependent sulfur isotope fractionation (MDF-S).

To further investigate the extent of MSR and the magnitude of MDF-S, we used multiple isotopic techniques to constrain temporal and spatial changes in sulfur and carbon cycling in a Neoarchean sedimentary succession from Brazil (*15*). We focused on samples from the ~2.5 Ga Batatal Formation (fig. S1) collected from an exploration drill core (GDR-117 provided by AngloGold Ashanti) intersecting ~180 m of strata (Fig. 1). The shallow marine Batatal platform, which is composed of two shale-rich intervals above and below a stromatolitic carbonate, is considered to be a time equivalent of once-contiguous deep-water slope successions in the Hamersley basin of Western Australia and the Transvaal basin of South Africa (*16*) (fig. S2). This geographically and spatially discrete sedimentary unit thus provides a unique opportunity to examine similarities and differences in sediment geochemistry across the terminal Neoarchean world.

Distal shale and proximal carbonate facies of the Batatal Formation reveal large sulfur isotope variations (Fig. 1). Pyrite in carbonate (and to a lesser degree in carbonaceous shale) is depleted in ^{34}S and ^{33}S relative to black shale facies. In microdrilled and bulk carbonate-associated pyrite (CAP), $\delta^{34}S$ values (*17*) were as low as −30 per mil (‰) and −14‰, respectively, and both phases were found to have consistently negative $\Delta^{33}S$ values (*18*). In contrast, samples from shale-rich facies are relatively more enriched in both ^{34}S and ^{33}S, depending on carbonate content (fig. S4). SIMS pyrite analyses in a subset of five carbonate samples were conducted to examine the extent of micrometer-scale sulfur isotopic variation within grains and across textural boundaries (fig. S6). Although the $\Delta^{33}S$ values determined by SIMS mirror those of bulk and microdrilled samples, the ion probe $\delta^{34}S$ measurements reveal even greater degrees of ^{34}S depletion, with pyrite $\delta^{34}S$ values as low as −38‰. Notably, SIMS analyses yielding the most negative $\delta^{34}S$ values also have constant $\Delta^{33}S$ (Fig. 2A). Although some macroscopic pyrite samples drilled in the upper Batatal carbonaceous shale have negative $\Delta^{33}S$ values and $\delta^{34}S$ signatures as low as −13.6‰, we did not study these samples by the SIMS technique and thus do not know whether these pyrite grains preserve the fine-scale variability and extreme ^{33}S and ^{34}S depletions seen in the carbonate samples. The SIMS pyrite data from carbonate samples in the interval between 1261 and 1272 m form arrays indicating similar levels of ^{33}S depletion (~ −2‰), whereas the array of measurements from the sample 36 m lower in the core (1308 m) defines a $\Delta^{33}S$ floor at −3‰.

The SIMS determinations of $\Delta^{36}S/\Delta^{33}S$ for the Batatal CAP grains are consistent with those of bulk and microdrilled analyses (Fig. 2B), and most fall in the range of previously published Neoarchean data (*5*, *12*) characterized by a $\Delta^{36}S/\Delta^{33}S$ slope of ~ −1. In some cases (e.g., samples 1308.08, 1266.72, and 1261.90), however, coupled values lie below the reference array, indicating greater depletion in ^{36}S abundances (fig. S8). We attribute the additional ^{36}S depletion in CAP to a metabolic response of MSR at the time the Batatal carbonates were deposited (see fig. S8). Experiments on modern sulfate reducers (*19*) show that variations within and relationships between multiple sulfur isotopes are produced by bacteria grown under different conditions, likely reflecting the differential transport of sulfate into and out of the cells. On the other hand, Rayleigh distillation (*20*) is also known to produce variations in $\Delta^{36}S$, but this process also generates large variability in $\delta^{34}S$ that is not observed in the data from this study (*15*) (fig. S9).

Carbon isotope measurements of shale and carbonate in the Batatal Formation reveal a pronounced difference between deep- and shallow-water facies. The magnitude of carbon isotope fractionation between carbonate carbon and organic carbon ($\Delta^{13}C_{carb-org}$) in shale and carbonate facies is remarkably constant, with values generally ranging between 15 and 20‰ (Fig. 1). This range of fractionation is much smaller than that measured in the broadly equivalent units from Western Australia and South Africa [~30‰ (*21*, *22*)] (Fig. 1 and fig. S10). Reduced fractionation is unlikely the result of metamorphism but may be biologically mediated in the deep ocean environment. Sedimentological and petrographic observations coupled with a comparison of modern shallow marine environments suggest that the reduced fractionation may be the result of carbon limitation in an evaporitic setting (*15*) where oceanic sulfate was potentially concentrated.

Sulfur isotope compositions of CAP also differ between this study and prior research on temporally equivalent Neoarchean successions in Western Australia (*21*) and South Africa (*23*). In those reports, $\delta^{34}S$ values in mixed shale and carbonate facies that accumulated in continental slope settings fell to a nadir of −10‰ in bulk rock measurements and down to −21‰ for SIMS analysis (*12*). New SIMS results from the Batatal Formation reveal even more negative $\delta^{34}S$ pyrite values as low as −38‰ (Fig. 2). Coupled with the estimated range of terminal Neoarchean seawater sulfate compositions (+6 to +15‰) [compare with (*3*, *24*)], this observation suggests that MDF-S values were as much as 40 to 50‰. The magnitude of this fractionation is considerable, even in comparison with those recorded in modern environments (*6*).

[1]Department of Geology and Earth System Science Interdisciplinary Center, University of Maryland, College Park, MD 20742, USA. [2]Centre for Microscopy Characterization and Analysis, ARC Centre of Excellence for Core to Crust Fluid Systems, University of Western Australia, Crawley, WA 6009, Australia.
*Corresponding author. E-mail: zhelezka@umd.edu

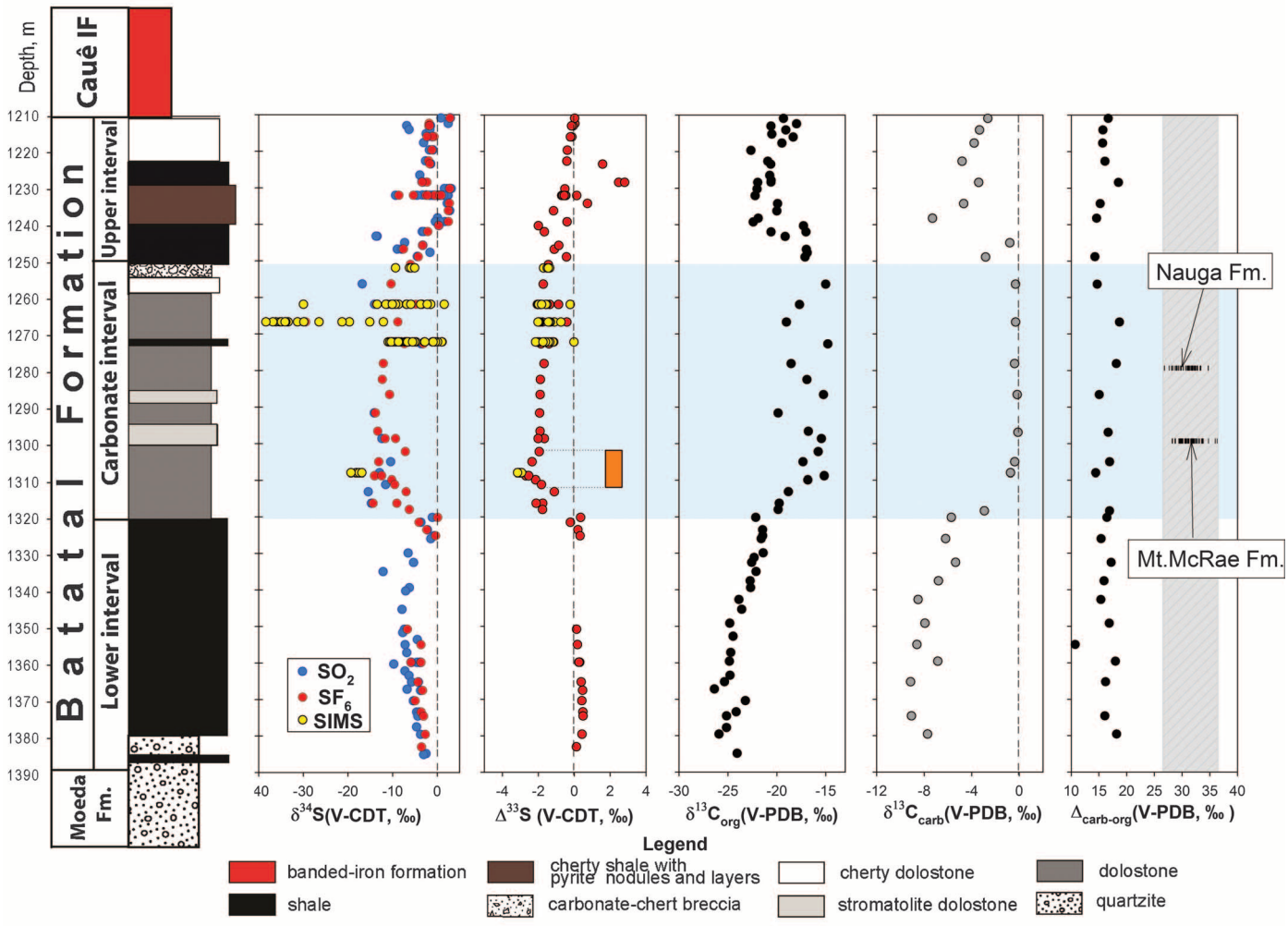


Fig. 1. High-resolution time-series sulfur and carbon isotopic data from ~2.5 Ga Batatal Formation in Brazil. The most negative $\delta^{34}S$ and $\Delta^{33}S$ values are recorded exclusively in the carbonate interval. Although the carbonates record shows large variations in $\delta^{13}C$ between shallow- and deep-water facies, the magnitude of carbon isotope fractionation between coexisting organic and inorganic phases ($\Delta_{carb-org}$) is relatively constant and unusually small. Shaded area represents extent of carbon isotope fractionation in Neoarchean formations from Western Australia [Mt. McRae Shale Formation, from (*21*)] and South Africa [Nauga Formation, from (*22*)].

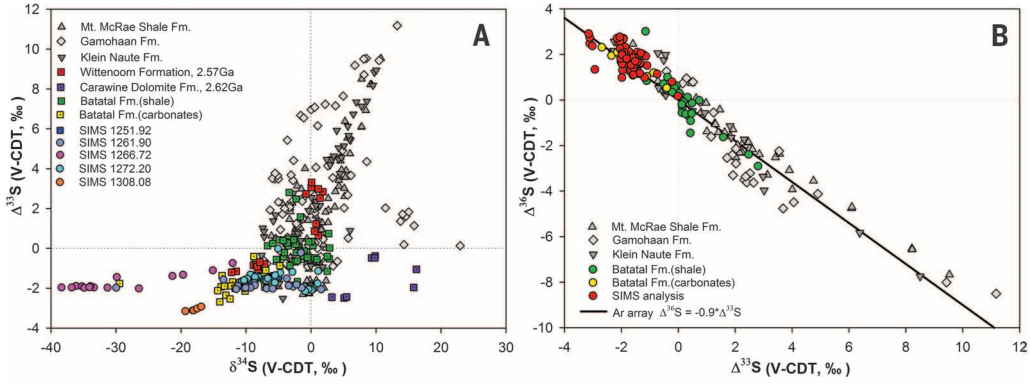


Fig. 2. Sulfur isotope data for the Batatal Formation in the context of published Neoarchean measurements. (**A**) Cross-plot of $\Delta^{33}S$ versus $\delta^{34}S$ values of pyrites from Neoarchean successions from South Africa (*20*, *22*) and Western Australia (*20*, *23*, *31*) as well as bulk and SIMS measurements from Batatal shale and carbonate samples. The bulk Batatal data show large sulfur isotope fractionation in CAP attributed to microbial sulfate reduction; the SIMS analyses reveal two different floors of $\Delta^{33}S$ values at negative $\delta^{34}S$. (**B**) Cross-plot of $\Delta^{36}S$ versus $\Delta^{33}S$ values of various Neoarchean successions (*20*, *22*); note that Batatal carbonates have consistently negative $\Delta^{33}S$ and consistently positive $\Delta^{36}S$ values, likely defining end-member compositions on the Archean array.

Habicht *et al.* (*2*) argued that large fractionations would not be preserved in typical shale facies unless pore water sulfate concentrations were higher than 200 μM (for comparison, modern seawater SO_4^{2-} is 28 mM). This threshold now appears to be an upper limit, as recent observations of modern meromictic lakes (*25*, *26*) with SO_4^{2-} as low as 25 to 100 μM indicate that isotopic fractionation of more than 20‰ is

possible. The discrepancy between microscale sulfur isotope measurements that reveal evidence for strongly negative $\delta^{34}S$ values [e.g., (*13, 14*)] and bulk measurements that fail to yield a clear indication of strongly negative $\delta^{34}S$ signatures may reflect SO_4^{2-} transport limitation (closed or partially closed) in Archean sediments. The strongly negative and variable $\delta^{34}S$ with constant $\Delta^{33}S$ and variable $\Delta^{36}S$ at the micrometer scale supports this interpretation applied to the Batatal depositional environment; this further provides a link between Batatal sediment pore fluids and overlying seawater sulfate. The greater ^{34}S depletion in the microscale analyses relative to bulk measurements also implies mass-dependent redistribution of sulfur isotopes by MSR within the sediments. However, the average negative $\delta^{34}S$ pyrite values (~ −10‰) preserved in bulk samples relative to the inferred positive $\delta^{34}S$ composition of coeval seawater SO_4^{2-} imply that the system was not completely closed [the proportional fraction of sulfate reduced would be ~0.5 to 0.7, assuming a starting sulfate composition of 15‰ and a fractionation of 50‰ (*15*)].

The large sulfur isotope fractionations observed here imply that MSR did not deplete and fractionate residual pore water sulfate to a large enough extent that transport limitation controlled the expression of isotopic compositions. Following recent suggestions (*27*) that the availability of electron donors, cell-specific growth rates, and sulfur isotope fractionation are interdependent, we interpret the production and preservation of sulfide with strongly negative $\delta^{34}S$ values to reflect a lower proportion of electron donors (i.e., organic matter or H_2) relative to sulfate ([e^- donor]/[SO_4^{2-}]) in the Batatal shallow marine carbonate-rich environment relative to those found in typical Archean shales. Indeed, organic carbon contents in the Brazilian sediments are much lower than contemporary deep-water facies from Western Australia and South Africa. We further suggest that Batatal CAPs derive their sulfur predominantly from sulfate reduction, rather than from an atmospherically derived source carrying positive $\delta^{34}S$ and $\Delta^{33}S$ compositions. Our observations of the shallow and potentially evaporitic Batatal carbonate are in agreement with model predictions (*28*) suggesting greater contributions of atmospherically derived elemental sulfur (with positive $\Delta^{33}S$) to distal environments, whereas sulfate sourced from the atmosphere (with negative $\Delta^{33}S$) and from continental weathering was concentrated in proximal settings.

A notable feature of the SIMS analyses of samples at 1266.72, 1261.90, and 1272.20 m depth is the almost constant $\Delta^{33}S$ [average −1.7 ± 1.02‰ (2σ)] for the most highly fractionated (most negative $\delta^{34}S$ values) pyrite grains (Fig. 2). This array suggests variations in MDF-S associated with MSR from a starting sulfate pool with a constant negative $\Delta^{33}S$. The relatively constant $\Delta^{33}S$ over nearly 60 m of the Batatal Formation carbonate is interpreted to reflect a long-term stability [~0.4 to 1.5 million years, based on a carbonate accumulation rate of 40 to 150 m per million years (*29*)] in the $\Delta^{33}S$ composition of sulfate supplied to the shallow marine environment (i.e., the proportion of atmospheric and nonatmospheric sulfate was stable over the depositional interval).

The negative shift in $\Delta^{33}S$ values of samples between core depths of 1302 to 1308 m, however, suggests a secular change in the isotopic composition of oceanic sulfate. The amount of time necessary for shallow marine carbonate accumulation of ~6 m is relatively short (40,000 to 150,000 years) but is still sufficiently long to suggest that $\Delta^{33}S$ was well mixed in the oceans. According to our calculations, the residence time of sulfate was lower than the response time by a factor of 2. Thus, order-of-magnitude constraints can be placed on oceanic sulfate concentrations of 10^{-5} to 10^{-6} mol/liter assuming only volcanic fluxes (~10^{11} mol/year), or higher if weathering fluxes are also included (*15*). Our Neoarchean sulfate concentration estimate is consistent with previous assessments (*2*, *3*).

The connection between pyrite with negative $\Delta^{33}S$ and oceanic sulfate implies that at the time the Batatal Formation was deposited, the source of oceanic sulfate had a predominantly negative $\Delta^{33}S$ composition. If correct, the negative oceanic $\Delta^{33}S$ signature indicates that the atmospheric source of sulfate dominated over that of elemental sulfur, and that sources of sulfate from the oxidation of sedimentary sulfides with positive $\Delta^{33}S$ (*10*) were negligible. This conclusion implies either that late Neoarchean oxidative weathering occurred at low levels, or that weathering fluxes of sulfate were episodic and somehow were not captured by the Batatal CAPs.

Evaluated in the context of the long-term Archean bias toward positive pyrite $\Delta^{33}S$ compositions (*30*) (fig. S11), our analyses suggest that MSR was an important sink for sulfate with negative $\Delta^{33}S$ in the Neoarchean ocean. Support for this view comes from analyses of CAP with negative $\Delta^{33}S$ in slightly older carbonate-rich Neoarchean strata of Western Australia (Fig. 2A) (*24*, *31*), including the Carawine Dolomite, which contains textural evidence for shallow marine evaporitic conditions (*32*), as inferred from the sedimentology of the Batatal carbonates. Given the low concentration of CAP in Batatal bulk samples and relative abundances of carbonate and shale in Neoarchean successions (*33*), however, we estimate that carbonates could represent only about 1% of the negative $\Delta^{33}S$ sink necessary to balance the sulfur cycle (*15*). Other chemical inventories in the oceans, including basinal banded iron formations (*30*) and abyssal hydrothermal volcanogenic massive sulfide deposits (*3*), must therefore have been the dominant sinks for atmospherically derived sulfate with negative $\Delta^{33}S$ compositions.

REFERENCES AND NOTES

1. A. A. Pavlov, J. F. Kasting, *Astrobiology* **2**, 27–41 (2002).
2. K. S. Habicht, M. Gade, B. Thamdrup, P. Berg, D. E. Canfield, *Science* **298**, 2372–2374 (2002).
3. J. W. Jamieson, B. A. Wing, J. Farquhar, M. D. Hannington, *Nat. Geosci.* **6**, 61–64 (2013).
4. Y. Shen, J. Farquhar, A. Masterson, A. J. Kaufman, R. Buick, *Earth Planet. Sci. Lett.* **279**, 383–391 (2009).
5. J. Farquhar, J. Savarino, S. Airieau, M. H. Thiemens, *J. Geophys. Res.* **106**, 32829–32839 (2001).
6. D. E. Canfield, *Am. J. Sci.* **304**, 839–861 (2004).
7. D. T. Johnston, *Earth Sci. Rev.* **106**, 161–183 (2011).
8. I. Halevy, D. T. Johnston, D. P. Schrag, *Science* **329**, 204–207 (2010).
9. C. T. Reinhard, N. J. Planavsky, T. W. Lyons, *Nature* **497**, 100–103 (2013).
10. C. T. Reinhard, R. Raiswell, C. Scott, A. D. Anbar, T. W. Lyons, *Science* **326**, 713–716 (2009).
11. B. S. Kamber, M. J. Whitehouse, *Geobiology* **5**, 5–17 (2007).
12. J. Farquhar *et al.*, *Proc. Natl. Acad. Sci. U.S.A.* **110**, 17638–17643 (2013).
13. D. Wacey, M. R. Kilburn, M. Saunders, J. Cliff, M. D. Brasier, *Nat. Geosci.* **4**, 698–702 (2011).
14. T. R. Bontognali *et al.*, *Proc. Natl. Acad. Sci. U.S.A.* **109**, 15146–15151 (2012).
15. See supplementary materials on *Science* Online.
16. E. S. Cheney, *Precambrian Res.* **79**, 3–24 (1996).
17. Sulfur has four stable isotopes: two more abundant (^{32}S and ^{34}S) and two rare (^{33}S and ^{36}S) isotopes. Sulfur isotope composition of materials is reported as $\delta^xS = 1000 \times [(^xS/^{32}S)_{sample}/(^xS/^{32}S)_{standard} - 1]$, where x is 33, 34, or 36.
18. The deviation from the mass-dependent relationships is calculated by the following equations: $\Delta^{33}S = \delta^{33}S - 1000 \times [(\delta^{34}S/1000 + 1)^{0.515} - 1]$ and $\Delta^{36}S = \delta^{36}S - 1000 \times [(\delta^{34}S/1000 + 1)^{1.90} - 1]$.
19. D. T. Johnston, J. Farquhar, D. E. Canfield, *Geochim. Cosmochim. Acta* **71**, 3929–3947 (2007).
20. S. Ono, B. Wing, D. Johnston, J. Farquhar, D. Rumble, *Geochim. Cosmochim. Acta* **70**, 2238–2252 (2006).
21. A. J. Kaufman *et al.*, *Science* **317**, 1900–1903 (2007).
22. W. W. Fischer *et al.*, *Precambrian Res.* **169**, 15–27 (2009).
23. S. Ono, A. J. Kaufman, J. Farquhar, D. Y. Sumner, N. J. Beukes, *Precambrian Res.* **169**, 58–67 (2009).
24. S. Ono *et al.*, *Earth Planet. Sci. Lett.* **213**, 15–30 (2003).
25. G. Paris *et al.*, *Mineral. Mag.* **76**, 2204 (2012).
26. M. L. Gomes, M. T. Hurtgen, *Geology* **41**, 663–666 (2013).
27. W. D. Leavitt, I. Halevy, A. S. Bradley, D. T. Johnston, *Proc. Natl. Acad. Sci. U.S.A.* **110**, 11244–11249 (2013).
28. I. Halevy, *Proc. Natl. Acad. Sci. U.S.A.* **110**, 17644–17649 (2013).
29. W. Altermann, D. R. Nelson, *Sediment. Geol.* **120**, 225–256 (1998).
30. J. Farquhar, B. A. Wing, *Earth Planet. Sci. Lett.* **213**, 1–13 (2003).
31. M. A. Partridge, S. D. Golding, K. A. Baublys, E. Young, *Earth Planet. Sci. Lett.* **272**, 41–49 (2008).
32. B. M. Simonson, K. A. Schubel, S. W. Hassler, *Precambrian Res.* **60**, 287–335 (1993).
33. K. C. Condie, D. J. Des Marais, D. Abbott, *Precambrian Res.* **106**, 239–260 (2001).

ACKNOWLEDGMENTS

We thank C. Noce, N. Geboy, and A. Shrestha, as well as the facilities and the scientific and technical assistance of the Australian Microscopy and Microanalysis Research Facility at the Centre for Microscopy, Characterization and Analysis at the University of Western Australia, a facility funded by the University, State, and Commonwealth governments. Supported by the Fulbright Program (grantee ID 15110620, I.Z.), NASA Astrobiology Institute grant NNA09DA81A (J.F.), and NSF Frontiers of Earth Surface Dynamics program grant 432129 (A.J.K.). All data are provided in the supplementary materials.

SUPPLEMENTARY MATERIALS

www.sciencemag.org/content/346/6210/742/suppl/DC1
Materials and Methods
Supplementary Text
Figs. S1 to S12
Tables S1 and S2
References (*34*–*72*)

19 May 2014; accepted 12 September 2014
10.1126/science.1256211

ANIMAL BEHAVIOR

Bats jamming bats: Food competition through sonar interference

Aaron J. Corcoran[1,2]* and William E. Conner[1]

Communication signals are susceptible to interference ("jamming") from conspecifics and other sources. Many active sensing animals, including bats and electric fish, alter the frequency of their emissions to avoid inadvertent jamming from conspecifics. We demonstrated that echolocating bats adaptively jam conspecifics during competitions for food. Three-dimensional flight path reconstructions and audio-video field recordings of foraging bats (*Tadarida brasiliensis*) revealed extended interactions in which bats emitted sinusoidal frequency-modulated ultrasonic signals that interfered with the echolocation of conspecifics attacking insect prey. Playbacks of the jamming call, but not of control sounds, caused bats to miss insect targets. This study demonstrates intraspecific food competition through active disruption of a competitor's sensing during food acquisition.

Active sensory systems such as echolocation and electrolocation allow animals to exploit habitats where vision is ineffective (*1*) but are also susceptible to "jamming" (i.e., signal interference) from conspecifics. Electric fish and bats alter the frequency of electric and acoustic emissions, respectively, to avoid jamming from conspecifics [the "jamming avoidance response" (*2*–*5*)]. Although some insects adaptively jam their bat predators as a defense (*6*, *7*), jamming among echolocating animals appears to occur only inadvertently (*2*–*4*).

Mexican free-tailed bats (*Tadarida brasiliensis*) form the largest known colonies of any active sensing animal, with some caves housing more than one million individuals (*8*). Studies of captive, roosting *T. brasiliensis* have revealed a complex social system mediated by a vocal repertoire of at least 15 communication, or "social," calls (*9*). Echolocation signals also mediate social interactions outside the roost, as *T. brasiliensis* exhibit jamming avoidance responses (*2*, *3*) and are attracted to conspecific feeding buzzes, presumably to find insect prey (*10*).

Here we report results of field observations and playback experiments (Fig. 1) that demonstrated the jamming function of a previously unstudied social call from *T. brasiliensis* (Fig. 2, A to C), which we term the sinusoidal frequency-modulated (sinFM) call after its spectral-temporal pattern. Initial field observations showed that sinFM calls are produced only when another bat is rapidly emitting echolocation calls ("feeding buzz") in the late stages of insect pursuit—a time when bats are particularly susceptible to jamming (*6*, *7*). We hypothesized that sinFM calls are used for jamming conspecifics while competing for insect prey. The proposed function of sinFM calls contrasts starkly with reports of bat jamming avoidance (*2*–*4*) and proposed functions of social calls recorded in a foraging context, namely cooperative foraging and food patch defense (*11*–*13*). Alternatively, sinFM calls could startle bats without disrupting echolocation (*14*).

We determined the function of sinFM calls by quantifying natural social interactions between bats at two foraging sites in Arizona and New Mexico. We collected data using low-light videography, visual observations with a spotlight, and three-dimensional (3D) reconstruction of bat flight paths, using time-of-arrival-differences of sounds recorded on two microphone arrays (Fig. 1A) (*15*). In a second field experiment, we broadcast synthesized sinFM calls or controls [(i) no playback, (ii) 40-kHz tones played during the feeding buzz, (iii) noise bursts also played during the buzz, and (iv) sinFM calls played before the buzz; Fig. 1C] to *T. brasiliensis* attacking moths tethered to a monofilament line approximately 5 m above the ground (Fig. 1B). Stimulus parameters were selected to replicate the natural situation (*15*).

Acoustically, sinFM calls appear well adapted for jamming conspecifics. In all sinFM field recordings with good signal-to-noise ratio [n = 68 interactions from ≥ 7 individuals (*15*)], the calls overlapped temporally and spectrally with a conspecific's feeding buzz (Fig. 2, A to D, and Table 1), with 187 ± 118 ms (mean ± SD) of delay between the onset of the buzz and the onset of the sinFM call. SinFM calls had one to five repeated units (syllables) separated by short silent intervals (Table 1). Total sinFM call duration and the number of sinFM syllables were both highly correlated with the duration of the competitor bat's feeding buzz after the start of the sinFM call (Fig. 2, E and F). Mean feeding buzz duration was independent of the presence of sinFM

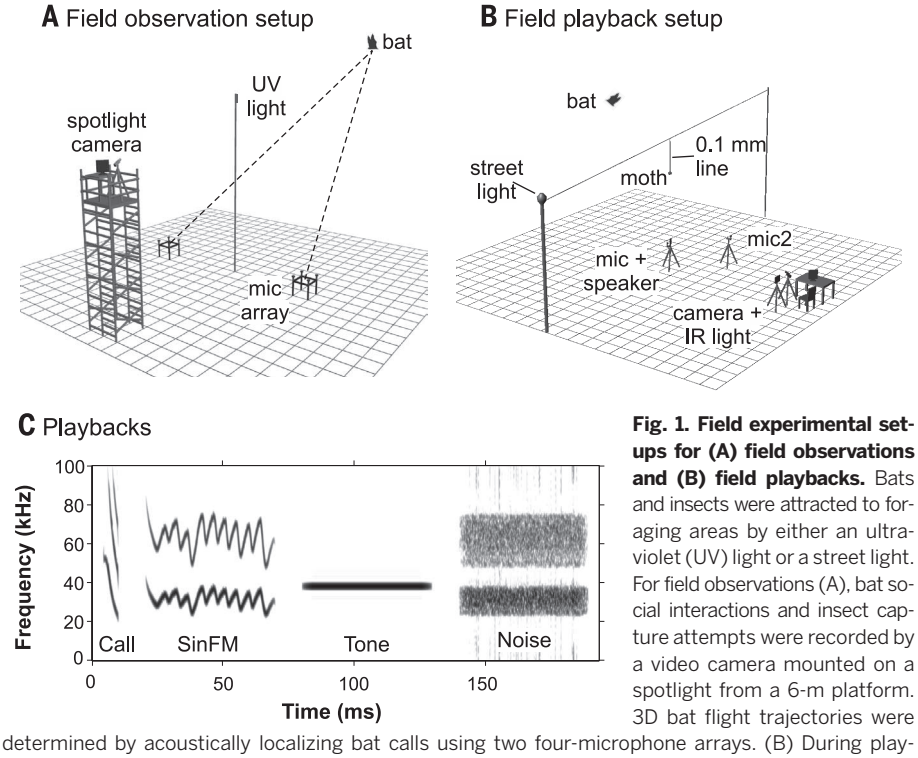


Fig. 1. Field experimental setups for (A) field observations and (B) field playbacks. Bats and insects were attracted to foraging areas by either an ultraviolet (UV) light or a street light. For field observations (A), bat social interactions and insect capture attempts were recorded by a video camera mounted on a spotlight from a 6-m platform. 3D bat flight trajectories were determined by acoustically localizing bat calls using two four-microphone arrays. (B) During playbacks, bats attacked moths tethered to a 0.1-mm monofilament line. Attacks were recorded on two microphones and an infrared (IR) video camera. Ultrasound was broadcast from a speaker placed directly below the tethered moth. (**C**) Spectrograms of the three acoustic playbacks that were used—sinFM, tone, and noise—and a buzz-phase echolocation call for reference. Detailed methods are available (*15*). Gridlines are spaced at 1-m intervals.

[1]Department of Biology, Wake Forest University, 030 Winston Hall, Winston Salem, NC 27106, USA. [2]Department of Biology, University of Maryland, Biology-Psychology Building, College Park, MD 20742, USA.
*Corresponding author. E-mail: aaron.j.corcoran@gmail.com

calls (Fig. 2G). Therefore, in real time bats appear to dynamically modulate the number of sinFM syllables and the total sinFM call duration, depending on the duration of the conspecific competitor's feeding buzz.

The sinFM call's rapid frequency modulations occur at a rate that ensures that at least one full FM cycle occurs in the listening window between the successive calls of the other bat's feeding buzz (Fig. 2C and Table 1). The maximum downward FM rate of sinFM calls is close to that found in feeding buzz calls (Table 1) and may stimulate the same FM-rate–sensitive auditory neurons that encode prey location information (*16*). FM signals that temporally overlap echoes are known to interfere with the estimation of target distance (*17*).

Bats were 85.9 and 77.3% less likely to capture insects in the presence of conspecific-produced sinFM calls at the Arizona[Southwestern Research Station (SWRS)] and New Mexico (Animas) field sites, respectively (Fig. 2H; see the figure legend for sample sizes and statistics). Playbacks of sinFM calls to individual bats attacking tethered moths caused capture success to decrease by 73.5% as compared to no playback (Fig. 2I).

Audio and video recordings show bats continuing attacks on prey after hearing sinFM calls from conspecifics (Fig. 2, A and B, and movie S1) and from the ultrasonic speaker (fig. S2 and movies S2 and S3). In natural interactions, bats continued buzzes for 213 ± 145 ms after sinFM calls began, and buzz durations were not abbreviated as compared to attacks lacking sinFM calls (Fig. 2G). In the playback experiment, bats continued attacks both when sinFM calls were broadcast during the feeding buzz (sinFM) and when sinFM calls were broadcast before the feeding buzz (sinFM early; fig. S2). SinFM playbacks only prevented capture when they overlapped the feeding buzz and not when they preceded the buzz (Fig. 2I). These results contradict the primary prediction of the food defense hypothesis: that bats abort attacks on prey after hearing the call (*12*, *13*). In contrast, these results support the predictions of the jamming hypothesis that capture success decreases only when sinFM calls temporally overlap with the feeding buzz and that bats miss prey despite persistent attacking behavior. SinFM calls appear to interfere with the bat's ability to determine prey position and to successfully coordinate capture.

We used quantitative criteria to examine 3D flight trajectories of bat interactions involving sinFM calls (fig. S1). Sixteen sequences lasting 3 to 10 s had sufficient quality for 3D flight trajectory reconstruction. An example sequence (Fig. 3A) and a summary of all interactions (fig. S1C) show multiple bat competitors alternately and repeatedly attempting to capture insects (indicated by buzz calls) in a central foraging area while another bat makes a sinFM call. SinFM calls do not cause bats to leave the foraging area or move away from prey, as has been shown for food defense social calls in other species (*12*, *13*). Instead, bats frequently circle back to the foraging area after missing prey while a competitor makes sinFM calls. The bats making sinFM calls appear intent on capturing prey rather than chasing away their competitors, as shown by a detailed analysis of bat flight trajectories (Fig. 3B, C).

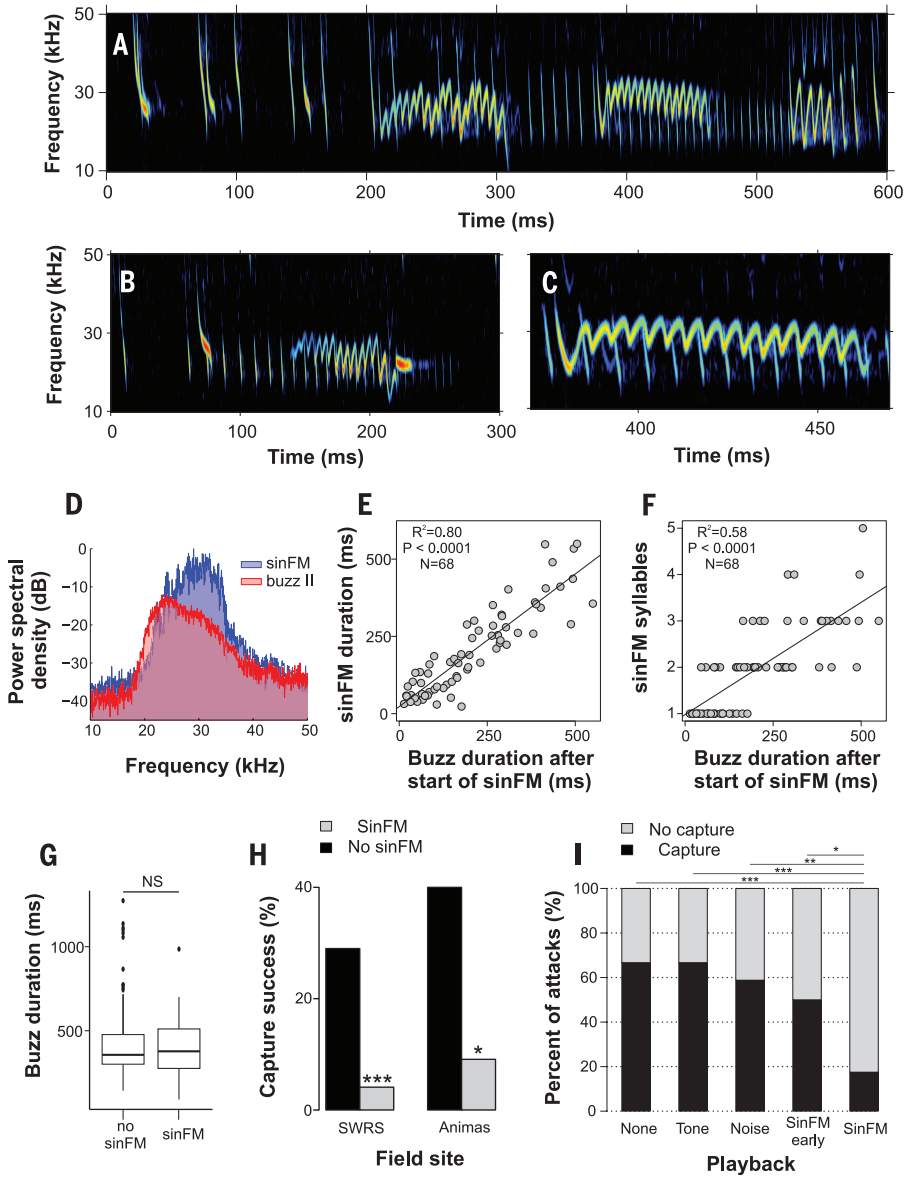


Fig. 2. Acoustics and results of *T. brasiliensis* sinFM interactions and playback experiments. Spectrograms show examples of (**A**) three-syllable and (**B**) one-syllable sinFM calls overlapping another bat's feeding buzz. (**C**) Close-up of a sinFM syllable from (A). (**D**) Representative power spectra of sinFM and buzz 2 calls [for buzz 2 definition, see (*15*)]. Scatter plots show correlation between the duration of the competitor bat's buzz after start of sinFM and (**E**) sinFM duration or (**F**) number of sinFM syllables. Solid lines depict linear regression. (**G**) Box plots of feeding buzz durations when conspecific sinFM calls were present (n = 68) or absent (n = 185; t test). (**H**) Capture success at two field sites with and without a competitor bat producing sinFM calls. (**I**) Capture success as a function of playback type for individual bats attacking tethered moths. All playbacks overlapped the feeding buzz, except sinFM early, which preceded the feeding buzz. *P < 0.05, **P < 0.01, ***P < 0.001 for Fisher's exact test. n = 185 attacks and n = 145 for no sinFM at SWRS and Animas; n = 74 and n = 12 for sinFM at SWRS and Animas in (H). For the playback experiment (I), n = 57, no playback; n = 18, tone; n = 17, noise; n = 18, sinFM early; and n = 40, sinFM. See Fig. 1C and text for playback descriptions.

Two acoustic playbacks (tones and noise bursts) further tested the predictions of the jamming hypothesis and competing hypotheses. Tone playbacks had the same spectral level and pulse durations as sinFM calls but were at a single frequency (40 kHz) not likely to jam bat echolocation. Tone playbacks had no effect on capture success (Fig. 2I), indicating that the effect of sinFM calls is not an acoustic startle reaction. Noise playbacks had the same duration and spectral distribution of acoustic energy as sinFM calls (*15*), and like

Table 1. Acoustic properties of *T. brasiliensis* sinFM and buzz calls. Syll dur, syllable duration; syll interval, syllable interval; total dur, total duration (including silent intervals) for sinFM, buzz 1, and buzz 2; peak freq, peak frequency; max freq, maximum frequency; min freq, minimum frequency; sweep, sweep rate; sin period, sinusoid period. NA, not applicable.

Call type	*n*	Syll dur (ms)	Syll interval (ms)	Total dur (ms)	*n* calls/ syllables	Peak freq (kHz)	Max freq (kHz)	Min freq (kHz)	Sweep (kHz/ms)	Sin period (ms)
sinFM	29	64.8 ± 19.4	82.4 ± 39	201 ± 139	2 ± 0.9	28.5 ± 5.4	35.4 ± 4.1	21.8 ± 4.3	−5.5 ± 1.2	6.0 ± 0.8
Buzz 1*	20	4.7 ± 1.5	36.0 ± 21.7	205 ± 100	7.7 ± 5.1	27.6 ± 3.8	42.1 ± 7.8	20.7 ± 2.4	−3.6 ± 1.1	NA
Buzz 2*	20	2.0 ± 0.2	6.5 ± 1.1	200 ± 85	24.7 ± 9.1	23.6 ± 2.7	35.3 ± 5.5	17.3 ± 1.0	−5.3 ± 0.9	NA

*See materials and methods (*15*) for definitions.

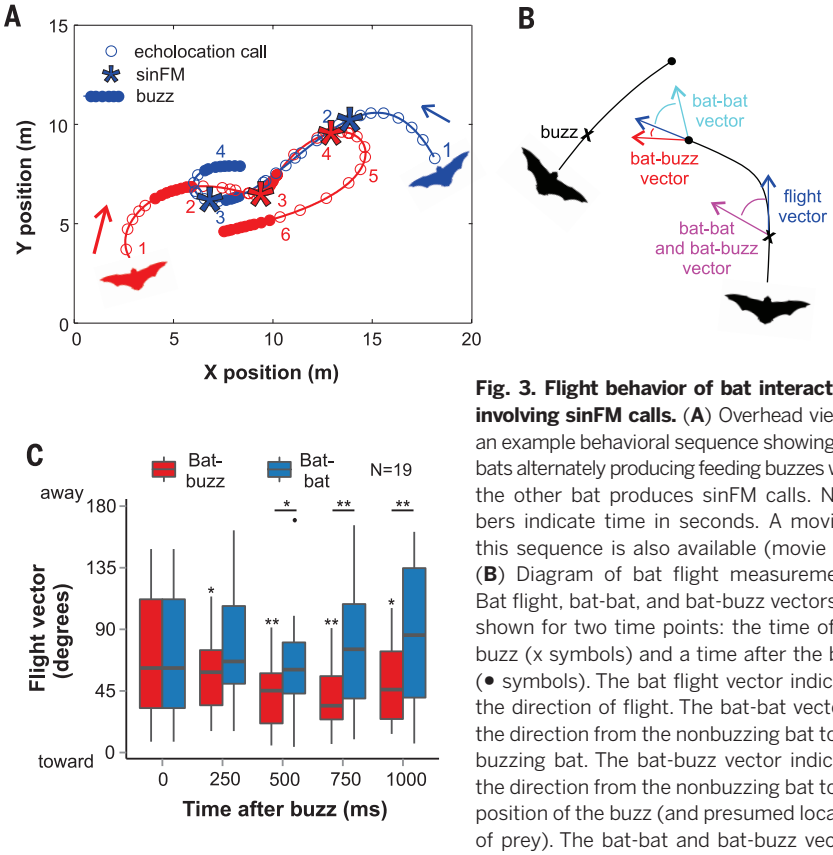


Fig. 3. Flight behavior of bat interactions involving sinFM calls. (**A**) Overhead view of an example behavioral sequence showing two bats alternately producing feeding buzzes while the other bat produces sinFM calls. Numbers indicate time in seconds. A movie of this sequence is also available (movie S4). (**B**) Diagram of bat flight measurements. Bat flight, bat-bat, and bat-buzz vectors are shown for two time points: the time of the buzz (x symbols) and a time after the buzz (• symbols). The bat flight vector indicates the direction of flight. The bat-bat vector is the direction from the nonbuzzing bat to the buzzing bat. The bat-buzz vector indicates the direction from the nonbuzzing bat to the position of the buzz (and presumed location of prey). The bat-bat and bat-buzz vectors are identical at the time of the buzz and diverge after that time. (**C**) Flight direction of bats producing sinFM calls relative to the position of the conspecific buzz (red box plots) and the competing bat (blue box plots) at 250-ms time intervals after the beginning of the buzz. Note that bats fly toward the position of the conspecific buzz (prey) and not of the bat competitor. * $P < 0.05$ and ** $P < 0.01$ for paired *t* tests comparing values to the 0-ms time point and for comparisons between buzz and bat conditions at each time.

tones, also did not affect capture success (Fig. 2I). This indicates that the specific spectral-temporal structure of sinFM calls may be important to their jamming function.

The favorable conditions of our playback experiment allowed us to acquire high-quality audio recordings to test whether bats exhibited jamming avoidance in response to playbacks. Bats did not alter the timing of echolocation emissions (fig. S2) or pulse intervals or call durations in response to playbacks (fig. S3). However, bats increased the frequency of multiple acoustic parameters in response to sinFM, sinFM early, and tone playbacks (fig. S3). This behavior is similar to how *T. brasiliensis* avoid jamming from conspecific echolocation (*2*, *3*); however, it does not allow bats to avoid jamming from sinFM calls, as evidenced by decreased capture success (Fig. 2I).

Acoustic data, capture rates, and 3D flight behavior from naturally occurring interactions and playback experiments provide compelling evidence supporting the hypothesized jamming function of sinFM calls. These results provide an extraordinary example of interference competition through disruption of a competitor's senses, a phenomenon never before documented in animals. Although echolocation allows bats to be the dominant nocturnal predator of night skies, it also makes them susceptible to jamming, a vulnerability now known to be exploited by bat competitors.

REFERENCES AND NOTES

1. M. E. Nelson, M. A. MacIver, *J. Comp. Physiol. A Neuroethol. Sens. Neural Behav. Physiol.* **192**, 573–586 (2006).
2. E. H. Gillam, N. Ulanovsky, G. F. McCracken, *Proc. Biol. Sci.* **274**, 651–660 (2007).
3. J. Ratcliffe *et al.*, *Can. J. Zool.* **82**, 966–971 (2004).
4. N. Ulanovsky, M. B. Fenton, A. Tsoar, C. Korine, *Proc. Biol. Sci.* **271**, 1467–1475 (2004).
5. W. Heiligenberg, *Neural Nets in Electric Fish* (MIT Press, Cambridge, MA, 1991)
6. A. J. Corcoran, J. R. Barber, W. E. Conner, *Science* **325**, 325–327 (2009).
7. A. J. Corcoran, J. R. Barber, N. I. Hristov, W. E. Conner, *J. Exp. Biol.* **214**, 2416–2425 (2011).
8. M. Betke *et al.*, *J. Mammal.* **89**, 18–24 (2008).
9. K. M. Bohn, B. Schmidt-French, S. T. Ma, G. D. Pollak, *J. Acoust. Soc. Am.* **124**, 1838–1848 (2008).
10. E. H. Gillam, *Can. J. Zool.* **85**, 795–801 (2007).
11. G. S. Wilkinson, J. W. Boughman, *Anim. Behav.* **55**, 337–350 (1998).
12. K. E. Barlow, G. Jones, *Anim. Behav.* **53**, 991–999 (1997).
13. G. S. Wright, C. Chiu, W. Xian, G. S. Wilkinson, C. F. Moss, *Curr. Biol.* **24**, 885–889 (2014).
14. D. L. Bates, M. B. Fenton, *Can. J. Zool.* **68**, 49–52 (1990).
15. Materials and methods are available as supplementary materials on *Science* Online.
16. Z. M. Fuzessery, M. D. Richardson, M. S. Coburn, *J. Neurophysiol.* **96**, 1320–1336 (2006).
17. W. M. Masters, K. A. S. Raver, *J. Comp. Physiol. A Neuroethol. Sens. Neural Behav. Physiol.* **179**, 703–713 (1996).

ACKNOWLEDGMENTS

We thank Z. Walker, K. Roman, D. Margius, N. Dowdy, and K. Irvin for field assistance; the Southwestern Research Station staff for coordination of activities; and C. Moss for thoughtful review of the manuscript. Funding was provided by the Wake Forest University Summer Fellowship Program, the American Museum of Natural History (Theodore Roosevelt Grant), an institutional training grant (UMD T32 DC-00046) from the National Institute of Deafness and Communicative Disorders of the National Institutes of Health, and the National Science Foundation (grant number IOS-1257248). Data are available in the supplementary materials.

SUPPLEMENTARY MATERIALS

www.sciencemag.org/content/346/6210/745/suppl/DC1
Materials and Methods
Supplementary Text
Figs. S1 to S3
References (*18*–*22*)
Movies S1 to S4

1 August 2014; accepted 9 October 2014
10.1126/science.1259512

LOCAL TRANSLATION

Targeting and plasticity of mitochondrial proteins revealed by proximity-specific ribosome profiling

Christopher C. Williams,* Calvin H. Jan,* Jonathan S. Weissman†

Nearly all mitochondrial proteins are nuclear-encoded and are targeted to their mitochondrial destination from the cytosol. Here, we used proximity-specific ribosome profiling to comprehensively measure translation at the mitochondrial surface in yeast. Most inner-membrane proteins were cotranslationally targeted to mitochondria, reminiscent of proteins entering the endoplasmic reticulum (ER). Comparison between mitochondrial and ER localization demonstrated that the vast majority of proteins were targeted to a specific organelle. A prominent exception was the fumarate reductase Osm1, known to reside in mitochondria. We identified a conserved ER isoform of Osm1, which contributes to the oxidative protein-folding capacity of the organelle. This dual localization was enabled by alternative translation initiation sites encoding distinct targeting signals. These findings highlight the exquisite in vivo specificity of organellar targeting mechanisms.

The vast majority of mitochondrial proteins (~99% in *Saccharomyces cerevisiae*) are encoded in the nuclear genome (*1*). These proteins are translated in the cytosol and must be sorted into the matrix, inner membrane (IM), intermembrane space (IMS), and outer membrane (OM) of the mitochondrion by a network of channels and chaperones. While the predominant view is that protein import into mitochondria occurs posttranslationally on unfolded polypeptides, cotranslational translocation has been demonstrated for some substrates (*2*). Moreover, ribosomes have been observed on the OM by electron microscopy (*3*), and numerous mRNAs associate closely with mitochondria (*4*–*6*), consistent with a broader role for cotranslational protein insertion.

To directly evaluate which proteins are translated on the surface of mitochondria in an unperturbed context, we applied the proximity-specific ribosome profiling technique (*7*). This approach involves in vivo biotinylation of Avi-tagged ribosomes that are in contact with a spatially localized biotin ligase (BirA), followed by affinity purification of biotinylated ribosomes and readout of translational activity by deep sequencing of ribosome-protected fragments. To mark ribosomes selectively on the mitochondrial surface, we fused BirA to the C terminus of *OM45*, a major component of the OM (Fig. 1A). Whereas a cytosolic BirA efficiently labeled both Avi-tagged large (Rpl16/uL13) and small (Rps2/uS5) subunits (*7*), Om45-BirA only biotinylated the large subunit, indicating that labeled ribosomes were constrained at the mitochondria with their peptide exit tunnels facing the OM (Fig. 1B). This pattern was observed for cotranslational import at the ER (*7*), arguing that ribosomes marked by Om45-BirA are engaged in protein translocation.

Proximity-specific profiling experiments were performedwith a brief (2-min) pulse of biotin in the absence of any translation inhibitors, to preserve the in vivo rates of translation and targeting. Of the enriched genes (fig. S1A), 87% were annotated as mitochondrial, and a clear subset of expressed mitop2 (*1*) mitochondrial reference genes (156 out of 551) were cotranslationally targeted (Fig. 1C and table S1). Each mitochondrial sublocalization was significantly enriched in cotranslationally targeted proteins ($P < 0.05$, Fisher's exact test). The IM proteins were distinct among sublocalizations (Fig. 1D); most IM proteins were cotranslationally targeted, whereas smaller subsets of OM, IMS, and matrix proteins were enriched (fig. S2A). By virtue of their transmembrane domains (TMDs), the IM proteins must simultaneously avoid aggregation in the cytosol and errant integration into other membranes. Cotranslational insertion may minimize the potential for toxicity associated with the accumulation of membrane proteins in the cytosol (*8*).

Omission of translation elongation inhibitors in the above experiments allowed us to define the proteins that were unambiguously translated at the mitochondrial surface. However, these were only a subset of the mRNAs that purify with mitochondria in the presence of the translation elongation inhibitor cycloheximide (CHX) (table S1) (*5*). We reasoned that by providing a prolonged time for ribosome–nascent chains (RNCs) to engage mitochondria, CHX pretreatment would yield a more comprehensive view of the mitochondrial proteome. Indeed, when we included CHX, we maintained mitochondrial specificity (fig. S1, B and C) but observed a large increase in the number of enriched proteins (Fig. 2A). For example, 68% (131 out of 191) of the mitop2-annotated matrix proteins were enriched compared to 27% (51 out of 187) without CHX (Figs. 2B and 1D).

We focused on the subset of genes that had a high probability of containing N-terminal mitochondrial matrix and IM protein-targeting sequences (MTSs), as predicted by MitoProt (*9*). The bimodal distribution of enrichments for this group raised the question of why some RNCs were translocation incompetent. We observed a clear difference in protein size between the enriched and depleted matrix proteins; the large majority of RNCs observed at the mitochondria were more than ~180 codons in length (Fig. 2C and fig. S3).

Mitochondrial proteins were selectively enriched across a wide range of expression levels (fig. S1C). This sensitivity allowed for the identification of 39 candidate mitochondrial proteins translated at the OM with no prior mitochondrial annotation in mitop2, Gene Ontology (GO), or Yeast GFP Fusion Localization databases (*1*, *10*, *11*) (Fig. 2A and table S1). These genes were more likely to contain MTSs, as predicted by Mitoprot (*9*), than nonenriched genes ($P = 0.002$, Mann-Whitney U test) (fig. S1D), supporting their candidacy as mitochondrial. Among this set was Hap1, a heme-responsive transcription factor (*12*). A Hap1-GFP (green fluorescence protein) fusion expressed from the endogenous locus was found both in the nucleus, as expected, and in the mitochondria, as predicted by our translational enrichments (Fig. 2D). Heme biosynthesis occurs in the mitochondria and is regulated by Hap1. Because MTS-mediated import requires an energized IM, Hap1 localization may allow for direct sensing of mitochondrial integrity. Hap1 sequestration in mitochondria could allow the cell to tune nuclear transcriptional activity through Hap1 localization (*13*).

We next investigated the evolution of mitochondrial protein localization among paralogs. *S. cerevisiae* underwent a whole-genome duplication (WGD) ~100 million years ago, making it well suited for exploring changes in protein localization between duplicate paralogs (termed ohnologs) (*14*). With the exception of the IM proteins, we found notable fluidity in the targeting of ohnologs to mitochondria that was not due to disparity in expression levels (Fig. 3A). By contrast, targeting of ohnologs to the ER rarely showed discrepancies between paralog pairs (Fig. 3B), emphasizing the relative plasticity of the mitochondrial proteome. In contrast to proteins residing in the ER or mitochondrial IM, matrix and cytosolic proteins have similar environments, which would allow proteins to function in either location.

We further exploited our mitochondrial and ER protein localization data sets to explore the extent to which individual proteins show dual localization between the two intracellular sites. The close physical association of these organelles makes the biochemical isolation of pure mitochondria

Department of Cellular and Molecular Pharmacology, Howard Hughes Medical Institute, California Institute for Quantitative Biosciences, Center for RNA Systems Biology, University of California, San Francisco, San Francisco, CA 94158, USA.
*These authors contributed equally to this work.
†Corresponding author. E-mail: jonathan.weissman@ucsf.edu

and microsomes challenging, confounding searches for dual localization in such preparations. For example, the ERMES complex, which tethers the ER and mitochondria (*15*), was originally thought to be exclusively mitochondrial. Proximity-specific ribosome profiling of the mitochondria and ER resolved components of the ERMES complex to their respective compartments and provided highly specific catalogs of

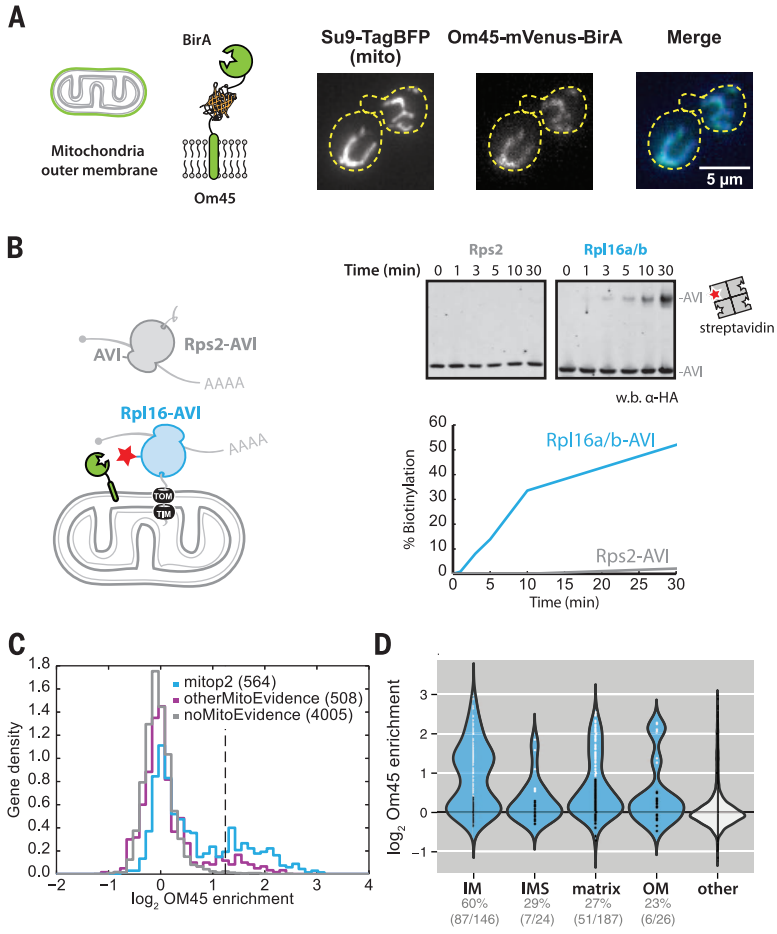


Fig. 1. Cotranslational mitochondrial protein targeting as revealed by proximity-specific ribosome profiling. (**A**) Localization of biotin ligase to the outer membrane. Schematic of the Om45 fusion protein and confocal fluorescence images of Om45-mVenus-BirA and Su9-TagBFP are shown. (**B**) Assessment of ribosome orientation at the mitochondrial outer membrane. The kinetics of Avi-tagged Rps2 (gray) and Rpl16a/b (blue) biotinylation by Om45-mVenus-BirA were determined by Western blot analysis of streptavidin-shift gels. (**C**) Histogram of $\log_2$ ratios for biotinylated footprints/input footprints in the absence of CHX. Genes annotated in the mitop2 reference set are shown in blue and enrichment threshold is shown as a dashed vertical line. Genes with mitochondrial GO cellular component terms not in mitop2 are shown in magenta. (**D**) Violin plot showing $\log_2$ gene enrichments for proteins grouped by their annotated location within mitochondria in the absence of CHX arrest. Gene enrichments are overlaid as points, with white and black colors indicating enrichment or disenrichment, respectively, as determined by subcompartment-specific Gaussian mixture modeling (fig. S2A) and quantified below the plot.

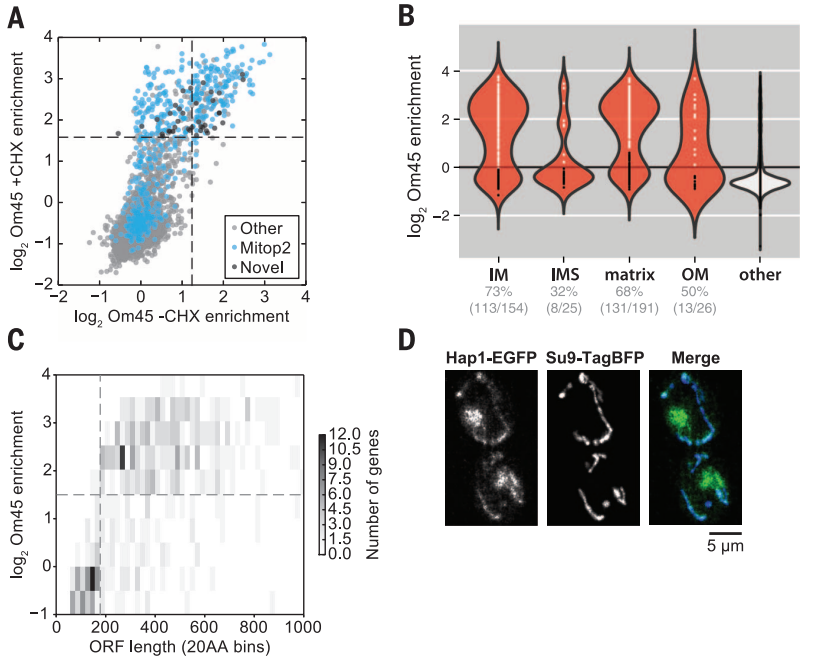


Fig. 2. Comprehensive characterization of RNC targeting to the mitochondria. (**A**) Scatter plot of $\log_2$ gene enrichments for footprints from ribosomes biotinylated by Om45-mVenus-BirA in the presence or absence of CHX. Novel genes represent those that were significantly enriched but had no known mitochondrial annotations. (**B**) Violin plot showing $\log_2$ gene enrichments for proteins grouped by their location within mitochondria in the presence of CHX arrest (as in Fig. 1D). Gene enrichments were determined by subcompartment-specific Gaussian mixture modeling (fig. S2B). (**C**) Two-dimensional histogram of genes binned by open reading frame length compared to their $\log_2$ gene enrichment in the presence of CHX. (**D**) Epifluorescence microscopy of Hap1-EGFP and Su9-TagBFP.

proteins at each organelle (Fig. 4, A and B, and fig. S4).

Very few proteins exhibited dual localization. Most proteins with both secretory and mitochondrial annotations (*10*) were cotranslationally inserted exclusively to the ER (Fig. 4B). Among the few counterexamples was the fumarate reductase *OSM1*. Although several studies suggest that Osm1 localizes exclusively to the mitochondria (*11*, *16*, *17*), high-throughput studies hint at a possible ER function. Specifically, a genetic-interaction data set indicated that *osm1*Δ shows a synthetic sick phenotype with a hypomorphic temperature-sensitive allele of *ERO1* (*18*) (fig. S5), the protein responsible for driving disulfide bond formation in the ER. Additionally, Osm1 is included in the N-glycoproteome, consistent with its entry into the secretory pathway (*19*). Our analysis of the glycosylation pattern of Osm1 and fluorescence microscopy of an endogenously expressed Osm1-GFP fusion protein demonstrated that Osm1 is localized to both the ER and mitochondria (Fig. 4, C and E).

Given the exquisite specificity of the vast majority of ER signal sequences (SSs) and MTSs, how is Osm1 efficiently targeted to both organelles? Ribosome profiling experiments using lactimidomycin (LTM), which leads to the accumulation of ribosomes at translation start sites (*20*), revealed that *OSM1* possesses two functional in-frame start codons predicted to encode either an ER (Met^{1}) or MTS (Met^{32}) signal (Fig. 4D). Mutation of the upstream methionine to alanine (Met1Ala) resulted in strict mitochondrial localization, whereas the Met32Ala mutant localized exclusively to the ER (Fig. 4E).

Osm1 homologs, including those of non-WGD yeast species, are predicted to contain SSs (*21*) (fig. S6), emphasizing the conserved ER localization of this class of fumarate reductases. Given the genetic interaction between *ERO1* and *OSM1*, an appealing function for this ER-localized form is to drive oxidative protein folding. Ero1 is a flavoprotein, and its reoxidation, following disulfide bond catalysis, can be driven by oxidized FAD (*22*, *23*). Furthermore, studies of oxidative folding under anaerobic conditions suggest that fumarate is the terminal electron acceptor and Osm1 generates free oxidized FAD via the reduction of fumarate (*24*). Consistent with this model, we found that the ER-form of Osm1 (Met32Ala), but not the mitochondrial-form (Met1Ala), supported growth under anaerobic conditions (Fig. 4F).

Proximity-specific ribosome profiling allowed us to elucidate several fundamental aspects of mitochondrial biogenesis. First, we discovered a major role for cotranslational targeting, but one that is most prominent for IM proteins. Second, we found that ohnologs encoding soluble proteins exhibit a high degree of fluidity in their mitochondrial localization, facilitating the exchange of function between the mitochondrial matrix and

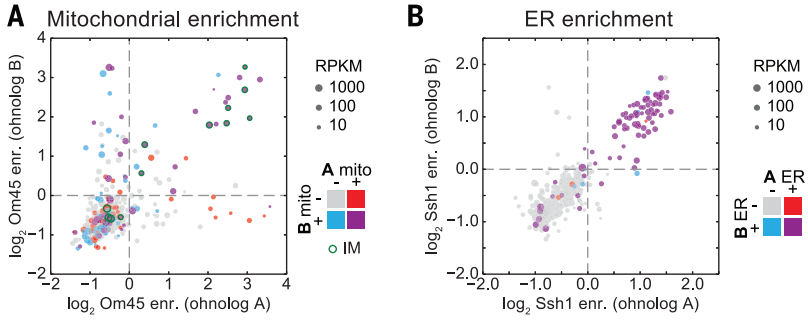


Fig. 3. Conservation of paralogous protein localization. (**A**) Scatter plot of mitochondrial $\log_2$ gene enrichments for ohnolog pairs, whose *x*- and *y*-axis assignment is arbitrary. Color codes indicate the expected ohnolog localizations based on existing evidence consolidated from mitop2, GO, and GFP annotations. Point size represents minimum expression level between paralogs. (**B**) As in (A), for ER enrichments.

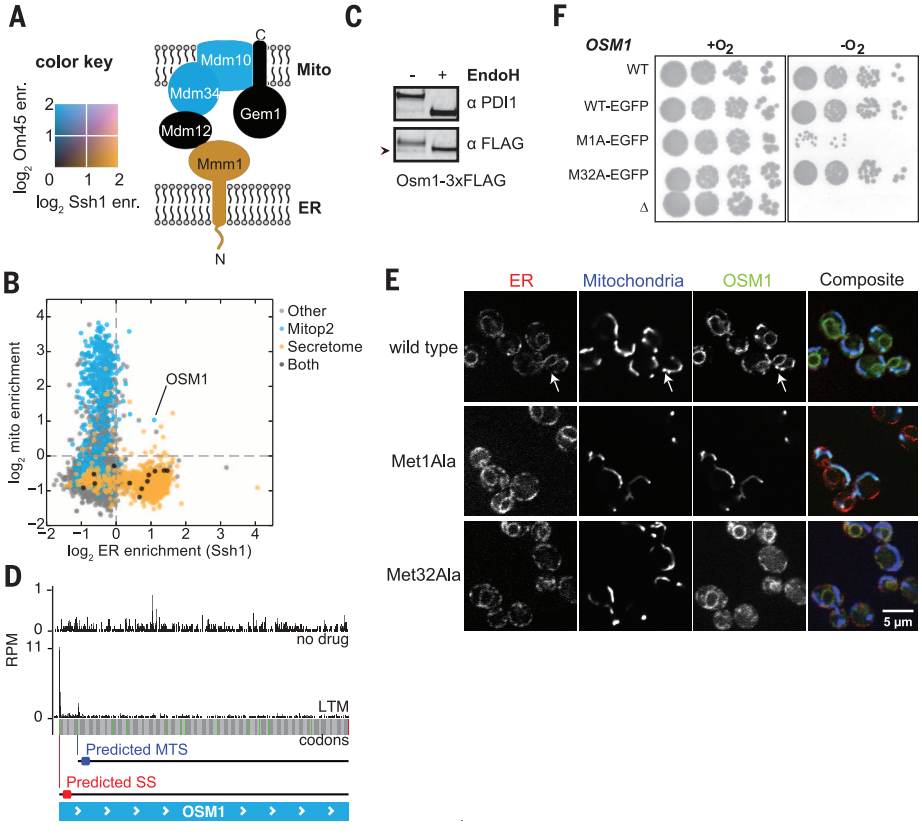


Fig. 4. Dual localization of proteins to the mitochondria and ER. (**A**) The color-mapped $\log_2$ enrichments for ribosome labeling by Om45 (blue) and Ssh1 (orange) are overlaid for members of the ERMES complex. (**B**) Scatter plot of ER enrichments compared to mitochondrial enrichments in the presence of CHX. Points are colored by their annotated localization. (**C**) Western blot analysis of N-linked glycans. Extracts from cells expressing Osm1-3xFLAG were blotted for PDI1 or FLAG with or without EndoH treatment. Arrowhead indicates an Osm1 band migrating below the size of the deglycosylated protein. (**D**) Ribosome occupancy of Osm1 with or without LTM treatment. In-frame AUG codons are shown in green; predicted localization of proteins made from the indicated start codon are shown. (**E**) Confocal fluorescence microscopy of Osm1-EGFP localization compared to ER (Sec63-mCherry) or mitochondria (Su9-BFP). Wild-type, Met1Ala, and Met32Ala variants of Osm1 are shown. (**F**) Analysis of signal requirements for Osm1 to support anaerobic growth as the sole fumarate reductase gene.

the cytosol. This plasticity may have facilitated or have been driven by the metabolic changes associated with a switch toward preferring fermentation over respiration that occurred after the WGD in budding yeast (the Crabtree effect) (*25*). Third, we demonstrated the exquisite specificity of protein targeting to the ER versus mitochondria in vivo. How targeting factors, such as SRP (*26*) and NAC (*27*), act on diverse RNCs to create this specificity in vivo remains an open question.

REFERENCES AND NOTES

1. M. Elstner, C. Andreoli, T. Klopstock, T. Meitinger, H. Prokisch, *Methods Enzymol.* **457**, 3–20 (2009).
2. T. D. Fox, *Genetics* **192**, 1203–1234 (2012).
3. R. E. Kellems, V. F. Allison, R. A. Butow, *J. Cell Biol.* **65**, 1–14 (1975).
4. M. Suissa, G. Schatz, *J. Biol. Chem.* **257**, 13048–13055 (1982).
5. P. Marc *et al.*, *EMBO Rep.* **3**, 159–164 (2002).
6. Y. Saint-Georges *et al.*, *PLOS ONE* **3**, e2293 (2008).
7. C. H. Jan, C. C. Williams, J. S. Weissman, *Science* **346**, 1257521 (2014).
8. O. Brandman *et al.*, *Cell* **151**, 1042–1054 (2012).
9. M. G. Claros, P. Vincens, *Eur. J. Biochem.* **241**, 779–786 (1996).
10. J. M. Cherry *et al.*, *Nucleic Acids Res.* **40**, D700–D705 (2012).
11. W.-K. Huh *et al.*, *Nature* **425**, 686–691 (2003).
12. L. Guarente, B. Lalonde, P. Gifford, E. Alani, *Cell* **36**, 503–511 (1984).
13. A. M. Nargund, M. W. Pellegrino, C. J. Fiorese, B. M. Baker, C. M. Haynes, *Science* **337**, 587–590 (2012).
14. K. Wolfe, *Nat. Genet.* **25**, 3–4 (2000).
15. B. Kornmann *et al.*, *Science* **325**, 477–481 (2009).
16. H. Muratsubaki, K. Enomoto, *Arch. Biochem. Biophys.* **352**, 175–181 (1998).
17. K. Enomoto, Y. Arikawa, H. Muratsubaki, *FEMS Microbiol. Lett.* **215**, 103–108 (2002).
18. M. Costanzo *et al.*, *Science* **327**, 425–431 (2010).
19. D. F. Zielinska, F. Gnad, K. Schropp, J. R. Wiśniewski, M. Mann, *Mol. Cell* **46**, 542–548 (2012).
20. N. Stern-Ginossar *et al.*, *Science* **338**, 1088–1093 (2012).
21. K. P. Byrne, K. H. Wolfe, *Genome Res.* **15**, 1456–1461 (2005).
22. E. Gross *et al.*, *Proc. Natl. Acad. Sci. U.S.A.* **103**, 299–304 (2006).
23. B. P. Tu, J. S. Weissman, *Mol. Cell* **10**, 983–994 (2002).
24. Z. Liu, T. Österlund, J. Hou, D. Petranovic, J. Nielsen, *Appl. Environ. Microbiol.* **79**, 2962–2967 (2013).
25. J. M. Thomson *et al.*, *Nat. Genet.* **37**, 630–635 (2005).
26. D. Akopian, K. Shen, X. Zhang, S. O. Shan, *Annu. Rev. Biochem.* **82**, 693–721 (2013).
27. M. del Alamo *et al.*, *PLOS Biol.* **9**, e1001100 (2011).

ACKNOWLEDGEMENTS

We thank members of the Weissman and P. Walter labs for discussion and E. Costa and V. Okreglak for critical reading of the manuscript. The University of California, San Francisco, Center for Advanced Technology and Nikon Imaging Center provided technical support. We thank C. Policarpi for assistance in strain construction and pilot ribosome profiling experiments, G. Brar for sharing unpublished ribosome profiling data, P. Walter for use of the Su9-TagBFP plasmid, and J. Horst for assistance with anaerobic growth conditions and equipment. This research was supported by the Center for RNA Systems Biology and the Howard Hughes Medical Institute. C.C.W. is an NSF Graduate Research Fellow. C.H.J. is the Rebecca Ridley Kry Fellow of the Damon Runyon Cancer Research Foundation (DRG-2085-11). Data are deposited in Gene Expression Omnibus under accession nos. GSE61011 and GSE61012.

SUPPLEMENTARY MATERIALS

www.sciencemag.org/content/346/6210/748/suppl/DC1
Materials and Methods
Figs. S1 to S6
Tables S1 to S5
References (*28*–*31*)

16 June 2014; accepted 12 September 2014
10.1126/science.1257522

QUALITY CONTROL

Quality control of inner nuclear membrane proteins by the Asi complex

Ombretta Foresti,[1,2] Victoria Rodriguez-Vaello,[1,2] Charlotta Funaya,[3] Pedro Carvalho[1,2]*

Misfolded proteins in the endoplasmic reticulum (ER) are eliminated by a quality control system called ER-associated protein degradation (ERAD). However, it is unknown how misfolded proteins in the inner nuclear membrane (INM), a specialized ER subdomain, are degraded. We used a quantitative proteomics approach to reveal an ERAD branch required for INM protein quality control in yeast. This branch involved the integral membrane proteins Asi1, Asi2, and Asi3, which assembled into an Asi complex. Besides INM misfolded proteins, the Asi complex promoted the degradation of functional regulators of sterol biosynthesis. Asi-mediated ERAD was required for ER homeostasis, which suggests that spatial segregation of protein quality control systems contributes to ER function.

Misfolded proteins in the membrane and lumen of the endoplasmic reticulum (ER) are eliminated by ER-associated protein degradation (ERAD) (*1*, *2*). In *Saccharomyces cerevisiae*, two ubiquitin ligase complexes, Hrd1 and Doa10, are involved in ERAD and show different specificity for misfolded proteins (*1*–*5*). Proteins with a misfolded domain in the cytosol (ERAD-C substrates) are targeted to degradation by the Doa10 complex, whereas proteins with misfolded domains in the membrane (ERAD-M) or lumen (ERAD-L) of the ER are ubiquitinated by the Hrd1 complex. The ubiquitin-conjugating (E2) enzyme Ubc7 is part of both complexes, and consequently *ubc7*Δ cells are defective in all ERAD branches. Besides misfolded proteins, ERAD is involved in the degradation of specific folded proteins, such as the sterol biosynthetic enzyme HMG-CoA reductase, in response to certain physiological stimuli (*2*).

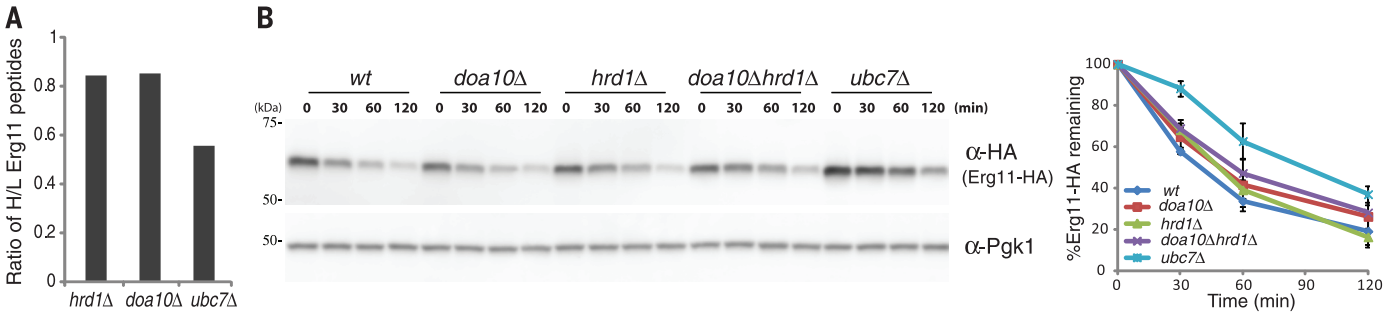
To identify endogenous substrates of the different ERAD branches in *S. cerevisiae*, we compared the proteomes of *doa10*Δ, *hrd1*Δ, and *ubc7*Δ cells with the use of SILAC (stable isotope labeling by amino acids in culture) followed by quantitative proteomics (*6*) (table S1). This analysis revealed a set of proteins whose steady-state levels in *doa10*Δ or *hrd1*Δ were comparable to those in wild-type (*wt*) cells but were higher in *ubc7*Δ mutants relative to *wt* cells (table S2). Among these proteins were Erg11 (lanosterol 14-α-demethylase) and Nsg1, both involved in ergosterol synthesis (Fig. 1A and table S2). Given that Erg11 is an ER membrane protein and that sterol biosynthesis is regulated by ERAD (*2*), we tested whether Erg11 was an ERAD substrate. In *wt* cells, a plasmid-borne, functional Erg11 fused to hemagglutinin (Erg11-HA) was degraded with a half-life of ~60 min (Fig. 1B and fig. S1A). We observed similar kinetics of degradation in *doa10*Δ, *hrd1*Δ, or even *doa10*Δ *hrd1*Δ double mutant cells (Fig. 1B and fig. S1B). In agreement with the SILAC analysis, the degradation of Erg11-HA was delayed in *ubc7*Δ, indicating that this E2 works with an uncharacterized ubiquitin ligase (E3). The degradation of Erg11 was further reduced by simultaneous mutation of *UBC7* and *UBC4*, indicating that these E2s have redundant roles in Erg11 ERAD (fig. S3).

The ERAD of all known membrane-bound substrates requires the Cdc48 adenosine triphosphatase (ATPase). Inactivation of Cdc48 function in cells bearing the temperature-sensitive *cdc48-3* allele showed impaired degradation of Erg11-HA (Fig. 1C). These findings suggest the existence of an ERAD branch independent of the known E3s Hrd1 and Doa10 but requiring Ubc7 and Cdc48.

Besides the canonical ERAD E3s, there is a third ER integral membrane E3. This is composed of two paralog proteins, Asi1 and Asi3, localized to the inner nuclear membrane (INM) (*7*, *8*). The INM is connected to the rest of the ER membrane at nuclear pores, which restrict the exchange of proteins between the nucleus and cytoplasm and between the INM and the rest of the ER (*9*). Consequently, the INM defines a specialized ER subdomain enriched in proteins with nuclear functions. Indeed, *ASI1*, *ASI3*, and several *ASI* (amino acid signaling–independent) mutants were originally identified as defective in transcriptional repression of amino acid permeases (AAPs) (*10*). The effect of Asi1 and Asi3 on AAP expression appears to be achieved by controlling the binding of the transcription factors Stp1 and Stp2 to the promoter of AAP genes without affecting their localization or stability (*7*, *8*). This repression of AAPs requires Asi2, another INM protein (*8*).

Deletion of *ASI1*, *ASI2*, or *ASI3* (but not of other *ASI* genes) blocked the degradation of Erg11

[1]Cell and Developmental Biology Programme, Centre for Genomic Regulation (CRG), Carrer del doctor Aiguader 88, 08003 Barcelona, Spain. [2]Universitat Pompeu Fabra, Carrer del doctor Aiguader 88, 08003 Barcelona, Spain. [3]Electron Microscopy Core Facility, European Molecular Biology Laboratory, 69117 Heidelberg, Germany.
***Corresponding author. E-mail: pedro.carvalho@crg.eu**



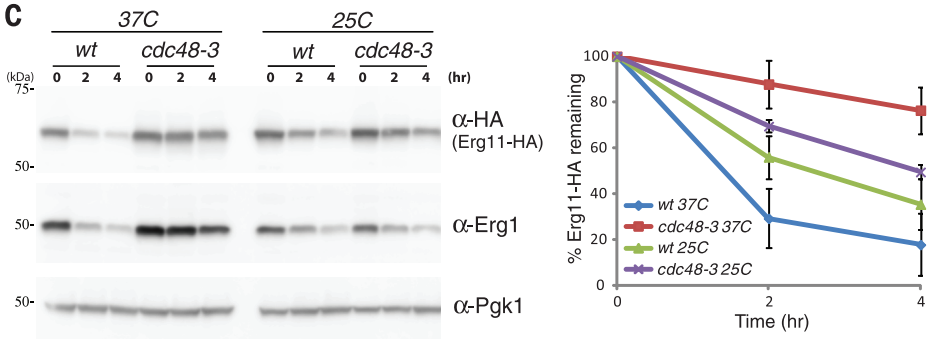


Fig. 1. Erg11 is degraded by a novel ERAD branch. (**A**) Erg11 abundance in the indicated mutants relative to *wt* cells, as detected by mass spectrometry upon SILAC labeling. Cells were grown in the presence of either heavy (*wt*) or light (mutants) L-lysine. Note that high steady-state levels of Erg11 result in low heavy/light ratios. (**B**) Degradation of Erg11-HA after inhibition of protein synthesis by cycloheximide in *wt* cells or in cells with the indicated deletions. Cell extracts were analyzed by SDS–polyacrylamide gel electrophoresis and blotting. The graph shows the average of at least three experiments; error bars represent the standard deviation of the mean. (**C**) Degradation of Erg11-HA and Erg1 in *wt* or temperature-sensitive *cdc48-3* cells either at the permissive temperature (25°C) or after a 2-hour shift to the restrictive temperature (37°C). Samples were analyzed as in (B).

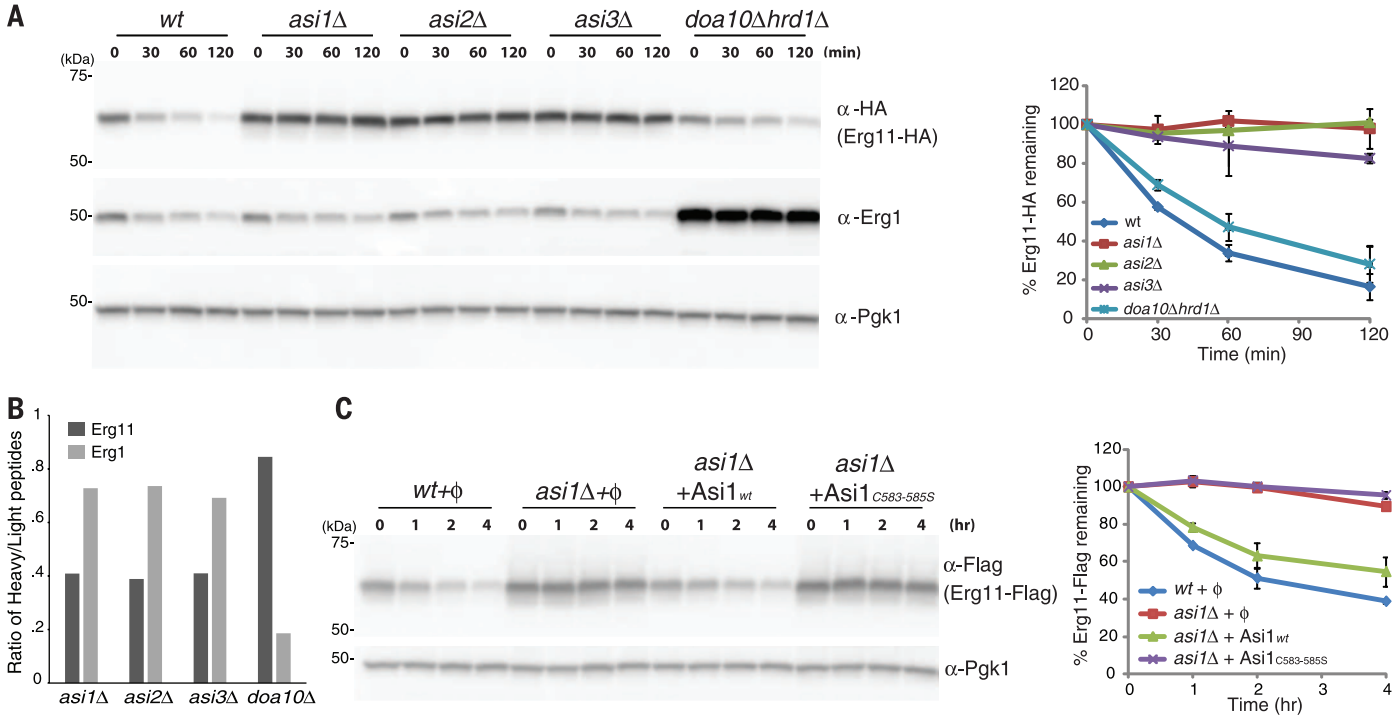


Fig. 2. The INM proteins Asi1, Asi2, and Asi3 define a novel ERAD branch required for Erg11 degradation. (**A**) Degradation of Erg11-HA and Erg1 in cells with the indicated genotype were analyzed as in Fig. 1B. (**B**) Erg11 and Erg1 abundance in the indicated mutants relative to *wt* cells, as detected by mass spectrometry upon SILAC labeling. (**C**) The degradation of endogenous Erg11-Flag in *wt* or *asi1*Δ cells bearing an empty plasmid (ϕ), a plasmid-borne $Asi1_{wt}$, or a plasmid-borne $Asi1_{C583\text{-}585S}$ mutant. Samples were analyzed as in Fig. 1B.

and Nsg1 (Fig. 2A and figs. S1B, S2, and S4). Moreover, SILAC analysis showed higher levels of Erg11 in *asi1*Δ, *asi2*Δ, and *asi3*Δ (Fig. 2B). This effect was specific for Erg11, as the degradation (Fig. 2A) and steady-state levels (Fig. 2B) of Erg1, a Doa10 substrate (*11*), were mostly unaffected. Thus, the Asi and Doa10 branches of ERAD independently affect different steps in sterol biosynthesis.

The ubiquitin ligase activity of Asi1 is required for ERAD because a RING domain mutant, *asi1(C583,585S)*, while expressed at *wt* levels (*7*), was defective in Erg11 degradation (Fig. 2C). Thus, Asi1, Asi2, and Asi3, together with the E2 Ubc7 and the Cdc48 ATPase, define a branch of ERAD involved in the degradation of Erg11 and Nsg1.

To characterize the mechanism of Erg11 ERAD, we evaluated its interaction with Asi1, Asi2, and Asi3, which were expressed as functional Flag-tagged proteins (fig. S5). Erg11-HA coprecipitated with Asi1, Asi2, and Asi3, whereas the Doa10 substrate Erg1 did not (Fig. 3A). Asi1, Asi2, and Asi3 comigrate upon sucrose gradient centrifugation (*8*). Moreover, Asi1 coprecipitates with Asi3 (*8*). We tested whether Asi2 was part of this complex. Affinity isolation of tagged Asi1, Asi2, or Asi3 led to coprecipitation of the other two proteins (Fig. 3B and table S3). Thus, Asi1, Asi2, and Asi3 assemble into the Asi complex. However, Asi2 was dispensable for the interaction between Asi1 and Asi3, which form the core of the Asi complex (Fig. 3C).

All three ERAD E3s in yeast control the turnover of sterol biosynthetic enzymes, which suggests that sterol regulation is an ancient function of ERAD (*2*). The degradation of Hmg2 and Erg1 by Hrd1 and Doa10, respectively, is regulated by the levels of specific sterol metabolites as part of homeostatic feedback mechanisms (*3*, *11*). However, manipulation of sterol intermediates did not have a major effect on Erg11 degradation (fig. S6). We then tested whether Asi-mediated ERAD was important to exclude Erg11 from the INM, where the Asi complex resides (*7*, *8*). In *wt* cells, endogenous Erg11 fused to green fluorescent protein (GFP) was all over the ER (fig. S7A). In *asi1*Δ cells, Erg11 levels were higher, as expected, with the protein concentrated at the nuclear ER including both the inner and outer nuclear membranes (fig. S7, A to C). Furthermore, Erg11 overexpression was toxic to *asi1*Δ cells (fig. S7D). Thus, ERAD is involved in restricting sterol synthesis to specific ER subdomains.

Because the INM is not involved in protein biogenesis and consequently not prone to accumulate misfolded proteins, we wondered whether the Asi complex plays any role in protein quality control. Asi complex mutations did not affect the degradation of several ERAD substrates (fig. S8). Multiple E3s can contribute to the degradation of some ERAD substrates (*12*); therefore, we tested whether *ASI1* mutations, when combined with *hrd1*Δ or *doa10*Δ, would further stabilize several substrates (table S4). Only Sec61-2, a translocon subunit with a G213D mutation, was further stabilized. The misfolding of this ERAD-M substrate is induced by high temperature (37°C) and consequently can be spatially and temporally uncoupled from Sec61-2 biogenesis. Whereas in *hrd1*Δ the degradation of Sec61-2 was slowed down as expected (*4*), in *hrd1*Δ*asi1*Δ or *hrd1*Δ*asi3*Δ mutants it was severely impaired (Fig. 4A and fig. S9). This is consistent with the observation that Sec61 can normally travel through the INM (*13*), although it functions only in ER membranes

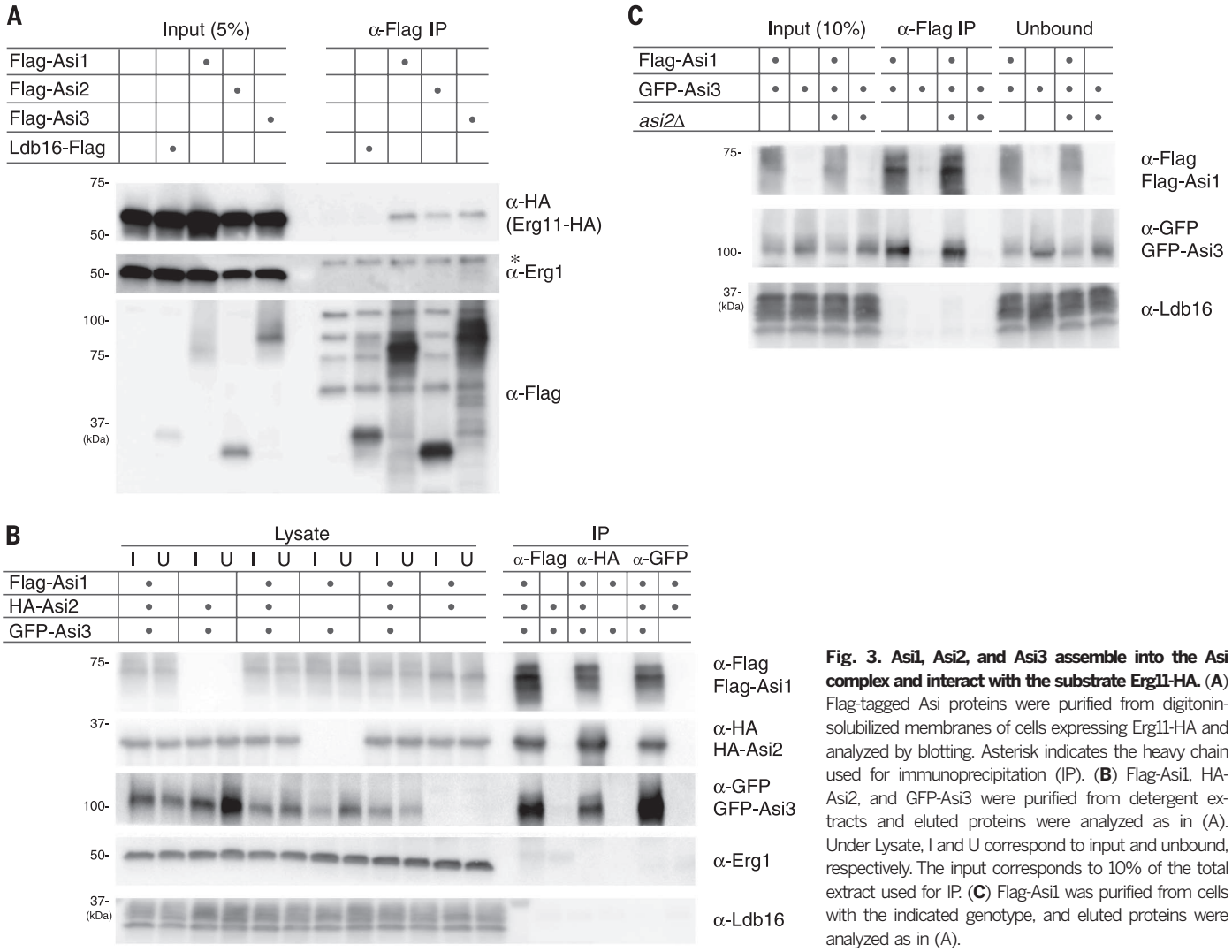


Fig. 3. Asi1, Asi2, and Asi3 assemble into the Asi complex and interact with the substrate Erg11-HA. (**A**) Flag-tagged Asi proteins were purified from digitonin-solubilized membranes of cells expressing Erg11-HA and analyzed by blotting. Asterisk indicates the heavy chain used for immunoprecipitation (IP). (**B**) Flag-Asi1, HA-Asi2, and GFP-Asi3 were purified from detergent extracts and eluted proteins were analyzed as in (A). Under Lysate, I and U correspond to input and unbound, respectively. The input corresponds to 10% of the total extract used for IP. (**C**) Flag-Asi1 was purified from cells with the indicated genotype, and eluted proteins were analyzed as in (A).

exposed to the cytoplasm (*14*). Compared to *hrd1Δ* single mutants, *hrd1Δasi2Δ* cells showed only a slight delay in Sec61-2 degradation (fig. S9B). In contrast, mutations in *ASI1*, *ASI2*, or *ASI3* had indistinguishable effects on Erg11 and Nsg1 degradation (Fig. 2A and fig. S4). This different requirement for Asi components suggests that the complex can operate in distinct modes, perhaps according to the folding state of the substrate. Thus, the Asi complex contributes to the degradation of certain ERAD-M substrates, likely as they travel through the INM.

To directly test the role of the Asi complex in INM quality control, we manipulated the relative distribution of Sec61-2 between the INM and the rest of the ER. A long unstructured polypeptide segment appended to a high-affinity nuclear localization signal (NLS) targets several proteins to

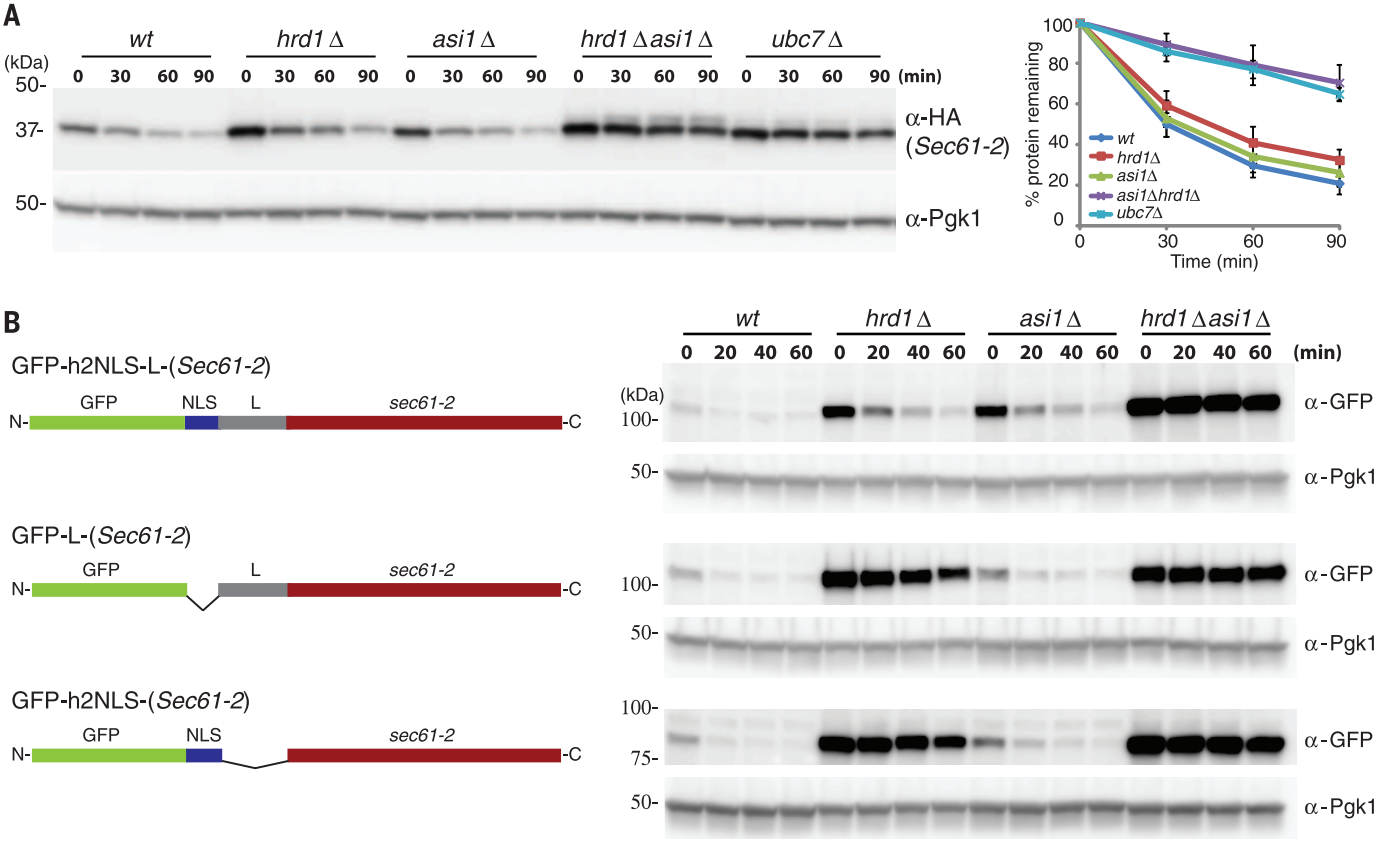


Fig. 4. Quality control of INM by the Asi complex is required for ER homeostasis. (**A**) The degradation of sec61-2-HA analyzed in cells with the indicated genotype. Misfolding of Sec61-2 was induced by shifting the cells to 37°C for 40 min before cycloheximide addition. Samples were analyzed as in Fig. 1B. (**B**) The degradation of GFP-h2NLS-L-(Sec61-2) and derivatives was analyzed as in (A) but using antibodies to GFP. (**C**) Quantification of cycloheximide shut-off experiments performed as in (B). The average of at least three experiments was used; error bars represent SD of the mean. (**D**) Cells with the indicated genotype were grown for 3 days at 30°C either in synthetic complete (SC) media or SC supplemented with 5-fluoroorotic acid (5-FOA), which generates a toxic compound in *URA3*-expressing cells. Note that the triple mutant *asi1Δire1Δhrd1Δ* cannot grow on plates containing 5-FOA, indicating that loss of a functional Asi1 copy is incompatible with survival in this genetic background.

the INM (*15*) and can relocalize certain ER membrane proteins to the INM, such as Sec61 (*15*). We generated GFP-h2NLS-L-(Sec61-2), a Sec61-2 derivative fused at the N terminus to a high-affinity NLS, a long unstructured domain (L), and GFP. In *wt* cells, GFP-h2NLS-L-(Sec61-2) displayed an extremely short half-life, whereas in *hrd1Δasi1Δ* mutants it was strongly stabilized (Fig. 4B) and accumulated at the nuclear envelope (fig. S10A). Preventing GFP-h2NLS-L-(Sec61-2) from targeting the INM, either by removing the NLS or by shortening the linker (*15*), increased the dependency of its degradation on Hrd1 while decreasing the requirement for Asi1 (Fig. 4, B and C, and fig. S10A). The degradation of all chimeric constructs was due to the Sec61-2 mutation, as equivalent chimeras to *wt* Sec61 were stable (fig. S10B). Thus, the quality control of misfolded ER membrane proteins is spatially segregated, with the Asi complex acting on substrates localized to the INM.

To assess how general this role of the Asi complex in quality control is, we took advantage of the genetic interaction between ERAD and the unfolded protein response (UPR), a rectifying transcriptional program triggered by an increased ER load of misfolded proteins (*16*, *17*). UPR mutants, such as *ire1Δ*, depend on ERAD to survive, particularly under stress conditions such as high temperature (*16*, *17*). Asi complex mutations in UPR-deficient cells did not affect cell fitness (Fig. 4D), consistent with the observation that single Asi complex mutants efficiently degrade all tested ERAD substrates (fig. S8). In contrast, cells lacking Ire1, Hrd1, and an Asi complex core component were not viable (Fig. 4D and fig. S11). In agreement with the less prominent role of Asi2 in the degradation of misfolded Sec61-2 (fig. S9B), *hrd1Δire1Δasi2Δ* mutants had a milder growth defect (fig. S11). Thus, the Asi complex plays an important function in protein quality control and contributes to ER homeostasis.

Our results identify an ERAD branch defined by the Asi complex. Like the other branches, Asi mediates the degradation of both misfolded proteins and regulators of sterol biosynthesis. A distinctive feature of the Asi complex is its INM localization (fig. S12). Doa10 localizes both to the INM and the rest of the ER, and can target substrates in the nucleoplasm as well as in the cytoplasm (*13*). Because the ER encloses a continuous luminal space, the Hrd1 complex can target all misfolded luminal proteins. In contrast, INM misfolded proteins are not accessible to Hrd1, because it is excluded from this ER subdomain (*13*). Sequence analysis reveals obvious Asi complex homologs only in fungi. If a functional homolog of the Asi complex exists in higher eukaryotes, it might become critical in postmitotic cells that do not undergo frequent nuclear envelope disassembly and reassembly events, known to "refresh" the pool of INM proteins (*9*).

Asi1, Asi2, and Asi3 control AAP gene expression in response to amino acid availability, a process mediated by the transcription factors Stp1 and Stp2 (*7*, *8*, *10*). Even if the turnover of Stp1 or Stp2 is not affected by Asi complex mutations, Asi1 ubiquitin ligase activity is essential to control the response to amino acids (*7*). Intriguingly, the Cdc48 ATPase complex inhibits transcription in a proteolysis-independent manner by preventing ubiquitinated transcription factors from binding to their target sequences (*18*). Whether these functions of Cdc48 and Asi complexes in gene regulation are linked is unclear. However, an appealing possibility is that the ERAD machinery at the INM has been co-opted to perform additional functions, such as controlling transcription factor activity.

REFERENCES AND NOTES

1. J. L. Brodsky, *Cell* **151**, 1163–1167 (2012).
2. A. Ruggiano, O. Foresti, P. Carvalho, *J. Cell Biol.* **204**, 869–879 (2014).
3. R. Y. Hampton, R. G. Gardner, J. Rine, *Mol. Biol. Cell* **7**, 2029–2044 (1996).
4. J. Bordallo, R. K. Plemper, A. Finger, D. H. Wolf, *Mol. Biol. Cell* **9**, 209–222 (1998).
5. R. Swanson, M. Locher, M. Hochstrasser, *Genes Dev.* **15**, 2660–2674 (2001).
6. L. M. de Godoy *et al.*, *Nature* **455**, 1251–1254 (2008).
7. M. Boban *et al.*, *J. Cell Biol.* **173**, 695–707 (2006).
8. A. Zargari *et al.*, *J. Biol. Chem.* **282**, 594–605 (2007).
9. S. S. Katta, C. J. Smoyer, S. L. Jaspersen, *Trends Cell Biol.* **24**, 221–229 (2014).
10. H. Forsberg, M. Hammar, C. Andréasson, A. Molinér, P. O. Ljungdahl, *Genetics* **158**, 973–988 (2001).
11. O. Foresti, A. Ruggiano, H. K. Hannibal-Bach, C. S. Ejsing, P. Carvalho, *eLife* **2**, e00953 (2013).
12. A. Stolz, S. Besser, H. Hottmann, D. H. Wolf, *Proc. Natl. Acad. Sci. U.S.A.* **110**, 15271–15276 (2013).
13. M. Deng, M. Hochstrasser, *Nature* **443**, 827–831 (2006).
14. T. A. Rapoport, *Nature* **450**, 663–669 (2007).
15. A. C. Meinema *et al.*, *Science* **333**, 90–93 (2011).
16. R. Friedlander, E. Jarosch, J. Urban, C. Volkwein, T. Sommer, *Nat. Cell Biol.* **2**, 379–384 (2000).
17. K. J. Travers *et al.*, *Cell* **101**, 249–258 (2000).
18. A. Ndoja, R. E. Cohen, T. Yao, *Mol. Cell* **53**, 893–903 (2014).

ACKNOWLEDGMENTS

Mass spectrometric measurements and data analysis were performed in the CRG/UPF Proteomics Unit (part of the ProteoRed, Instituto de Salud Carlos III). We thank M. Hochstrasser, M. Mendoza, and L. Veenhoff for reagents; C. Chiva and E. Sabido for help with the SILAC; R. Oliete for Erg11 and Nsg1 plasmids; and V. Goder, A. Ruggiano, and J. Valcarcel for critical reading of the manuscript. This work was supported by CRG, an International Early Career Award from the HHMI, the EMBO Young Investigator Program, grants from the Spanish MCCIN and ERC (P.C.), and a fellowship from the Spanish MCCIN (V.R.-V.).

SUPPLEMENTARY MATERIALS

www.sciencemag.org/content/346/6210/751/suppl/DC1
Materials and Methods
Figs. S1 to S12
Tables S1 to S7
References (*19*–*25*)

5 May 2014; accepted 9 September 2014
Published online 18 September 2014;
10.1126/science.1255638

NOROVIRUS

Enteric bacteria promote human and mouse norovirus infection of B cells

Melissa K. Jones,[1]* Makiko Watanabe,[1]* Shu Zhu,[1] Christina L. Graves,[2,3] Lisa R. Keyes,[1] Katrina R. Grau,[1] Mariam B. Gonzalez-Hernandez,[4] Nicole M. Iovine,[5] Christiane E. Wobus,[4] Jan Vinjé,[6] Scott A. Tibbetts,[1] Shannon M. Wallet,[2,3] Stephanie M. Karst[1]†

The cell tropism of human noroviruses and the development of an in vitro infection model remain elusive. Although susceptibility to individual human norovirus strains correlates with an individual's histo-blood group antigen (HBGA) profile, the biological basis of this restriction is unknown. We demonstrate that human and mouse noroviruses infected B cells in vitro and likely in vivo. Human norovirus infection of B cells required the presence of HBGA-expressing enteric bacteria. Furthermore, mouse norovirus replication was reduced in vivo when the intestinal microbiota was depleted by means of oral antibiotic administration. Thus, we have identified B cells as a cellular target of noroviruses and enteric bacteria as a stimulatory factor for norovirus infection, leading to the development of an in vitro infection model for human noroviruses.

Noroviruses (NoVs) are nonenveloped plus-strand RNA viruses that are the leading cause of epidemic and sporadic gastroenteritis (*1*–*5*). The cellular tropism of human NoVs (HuNoVs), and thus the development of a cultivation system for their in vitro propagation, has long eluded the NoV research community (*6*–*11*). Several pieces of data led us to ask whether NoVs can infect B cells. First, interferon-deficient and interleukin 10–deficient mice infected with a mouse NoV (MuNoV) contained virus-positive cells in the B cell zones of Peyer's patches (*12*, *13*). Second, MuNoV-infected *Rag1*$^{-/-}$ mice (which lack B and T cells) and B cell–deficient mice had reduced virus titers compared with those of wild-type mice, suggesting the absence of a target cell (*14*). Last, chimpanzees infected

[1]Department of Molecular Genetics and Microbiology, Emerging Pathogens Institute, College of Medicine, University of Florida, Gainesville, FL, USA. [2]Department of Oral Biology, College of Dentistry, University of Florida, Gainesville, FL, USA. [3]Department of Periodontology, College of Dentistry, University of Florida, Gainesville, FL, USA. [4]Department of Microbiology and Immunology, University of Michigan, Ann Arbor, MI, USA. [5]Department of Medicine, Division of Infectious Diseases, University of Florida, Gainesville, FL, USA. [6]Division of Viral Diseases, Centers for Disease Control and Prevention, Atlanta, GA, USA.
*These authors contributed equally to this work. **†Corresponding author. E-mail: skarst@ufl.edu**

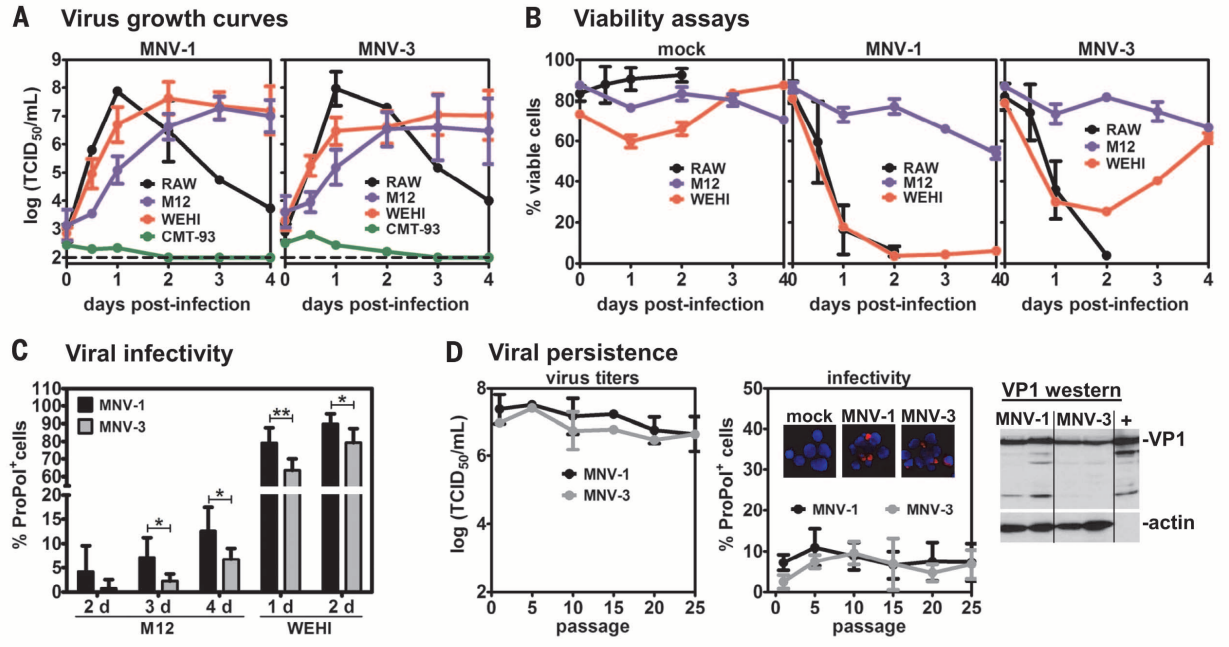
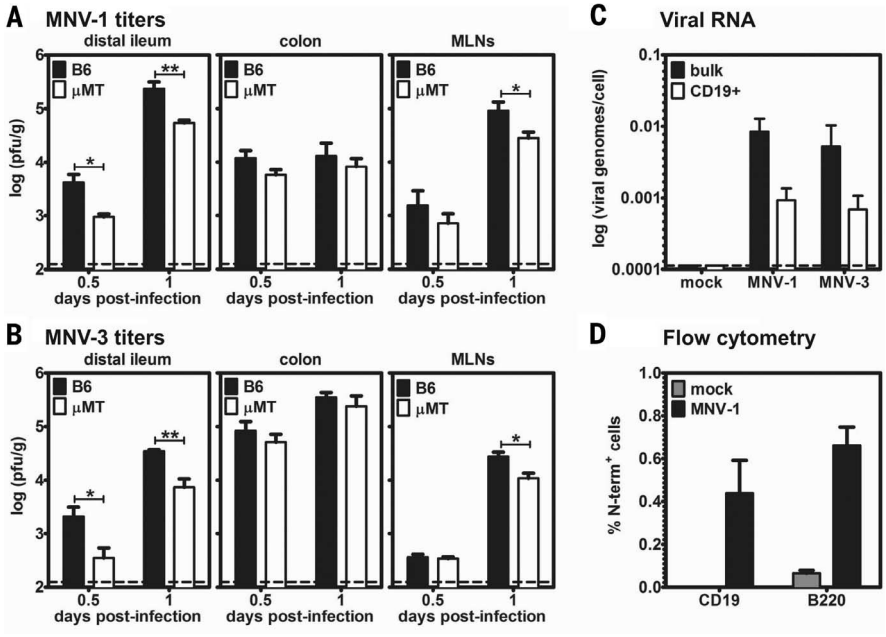


Fig. 1. MuNoVs infect B cells in culture. (**A**) The indicated mouse cell lines were infected with MNV-1 (left) or MNV-3 (right) at multiplicity of infection (MOI) 5 and virus growth curves determined by using standard $TCID_{50}$ assay. The limit of detection is indicated by a dashed line. (**B**) The indicated cell lines were mock-inoculated (left) or infected with MNV-1 (middle) or MNV-3 (right) at MOI 5, and cell viability was determined at various times after infection by using propidium iodide staining. (**C**) M12 or WEHI-231 cells were infected with MNV-1 (black bars) or MNV-3 (gray bars) at MOI 20 for M12 cells or MOI 5 for WEHI-231 cells. At the indicated dpi on the *x* axis, cells were stained with antibody to ProPol and 4′,6-diamidino-2-phenylindole (DAPI) and imaged on a fluorescent microscope. The percentage of virally infected cells in each cell line was then quantified as the average ratio of $ProPol^+$ cells per total cells. (**D**) Duplicate wells of M12 cells were infected with MNV-1 (black line) or MNV-3 (gray line) at MOI 5 and passaged every 2 days. At the first passage and every fifth passage, the virus titers in the supernatants were determined by using a standard $TCID_{50}$ assay (left). A portion of these cultures were analyzed by means of immunofluorescence assay for infectivity rates (middle). (Inset) Representative images merging the viral ProPol signal (red) and the DAPI staining of nuclei (blue) are shown from passage 10 (P10) cultures. A representative Western blot of cell lysates from persistently MNV-1– or MNV-3–infected M12 cultures (two independent cultures per virus strain) generated at passage 23 (P23) is shown. The MNV-1 virus stock used for initial infections was also tested (labeled as "+"). The blot was probed with antibody to VP1 and reprobed for actin as a loading control. For all, $n = 3$ to 5 experimental repeats. Error bars denote mean ± SD; Student's *t* test in (C), $*P < 0.05$, $**P < 0.01$, $***P < 0.001$.

Fig. 2. MuNoVs target Peyer's patch B cells. (**A** and **B**) Groups ($n = 5$ mice) of B6 mice (black bars) and μMT mice (white bars) were infected with 10^7 $TCID_{50}$ units (A) MNV-1 or (B) MNV-3 and harvested at 0.5 or 1 dpi. Virus titers were determined by performing plaque assay on homogenates of the indicated tissues. The data are presented as plaque-forming units (PFU) per gram of tissue on a logarithmic scale, and data for all mice in each group were averaged ($n = 2$ experiments). Limits of detection are indicated by dashed lines. Error bars denote mean ± SD; Student's *t* test, $*P < 0.05$, $**P < 0.01$, $***P < 0.001$. (**C**) Groups of B6 mice ($n = 8$ mice) were inoculated with either mock inoculum or 10^7 $TCID_{50}$ units MNV-1 or MNV-3. At 1 dpi, Peyer's patches were harvested, and quantitative reverse transcription polymerase chain reaction (RT-PCR) was performed on bulk cells (black bars) and purified $CD19^+$ cells (white bars) by using virus ORF1-specific primers ($n = 5$ experiments). Data are reported as viral genomes per cell on a logarithmic scale. The limit of detection is indicated by a dashed line. (**D**) *Stat1*$^{-/-}$ mice ($n = 2$ mice) were inoculated with mock inoculum (gray bars) or 10^7 $TCID_{50}$ units MNV-1 (black bars). Intracellular staining for the MNV-1 nonstructural N-term protein was performed on B cells isolated from Peyer's patches. CD19 or B220 are markers of B cells. Portions of cells were stained with preimmune sera in place of antibody to N-term as a background control. Data are presented as the percentage of B cells stained by N-term subtracted by the percentage of B cells stained by preimmune sera ($n = 3$ experiments).

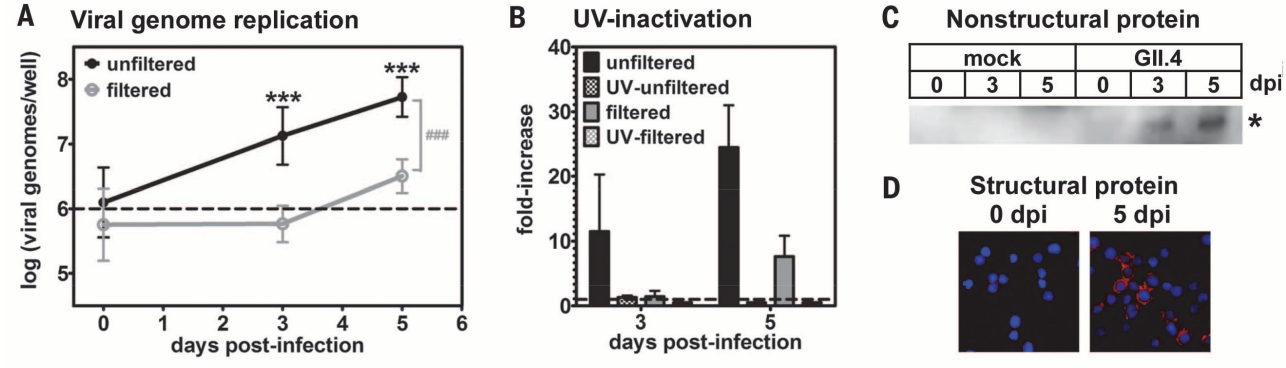


with a HuNoV contained capsid protein–positive duodenal B cells (*15*). Thus, in this study we probed whether NoVs infect B cells.

To investigate whether MuNoVs infect B cells in culture, M12 and WEHI-231 mouse B cell lines were infected with either MNV-1 or MNV-3. These two MuNoV strains were selected because they display numerous pathogenic distinctions. Specifically, MNV-1 establishes an acute infection, whereas MNV-3 establishes persistence (*16*–*18*); MNV-3 is attenuated compared with MNV-1 (*19*); and MNV-3 elicits more robust protective immunity than does MNV-1 (*14*). Both MuNoV strains replicated efficiently in the B cell lines, although peak titers were reached ~1 day later than in mouse RAW264.7 macrophages, a cell line known to be permissive to MuNoVs (Fig. 1A) (*20*). The mouse intestinal epithelial CMT-93 cell line was nonpermissive. Synthesis of viral proteins—as measured by means of Western blot analysis of the viral RNA-dependent RNA polymerase (RdRp), the VP1 capsid protein, and the VP2 minor structural protein—also reflected the slower replication of MuNoVs in B cells as compared with macrophages (fig. S1). MuNoV infection of M12 cells did not result in visible cytopathic effect (CPE), a finding that was confirmed by using propidium iodide staining (Fig. 1B) and trypan blue exclusion. In contrast, MuNoV infection of WEHI-231 cells resulted in visible CPE and loss of cell viability. This difference in infection outcome may relate to the distinct nature of the B cell lines considering that WEHI-231 cells are immature B cells, whereas M12 cells are mature B cells. Whereas MNV-1 infection resulted in complete loss of viability in WEHI-231 cells, MNV-3 infection resulted in a transient loss of ~60% of cells followed by recovery of the culture. Consistent with this, at 2 to 4 days post infection (dpi) actin was undetectable in MNV-1–infected, but not MNV-3–infected, WEHI-231 cells (fig. S1).

To determine percent infectivity, cells were stained for the MuNoV protease-RdRp (ProPol) nonstructural proteins. Although 80 to 90% of RAW264.7 and WEHI-231 cells were productively infected, only 5 to 15% of M12 cells were productively infected (Fig. 1C and fig. S2). To determine whether M12 cultures cleared this low-level infection or instead became persistently infected, we measured virus titers in supernatant fluid after repeated passaging of infected cultures. We consistently detected 10^6 to 10^7 median tissure culture infectious dose ($TCID_{50}$)/mL of each virus in the supernatant through 25 culture passages, which correlated with consistent low infection frequency and positive staining for the viral VP1 protein (Fig. 1D). Similarly, MNV-3 established persistent infection in WEHI-231 cells after the initial drop in cell viability. Thus, MuNoVs can persistently infect B cells in culture.

We used several complementary approaches to confirm that B cells are bona fide NoV targets in vivo. First, MNV-1 and MNV-3 titers were significantly reduced in the distal ileum and mesenteric



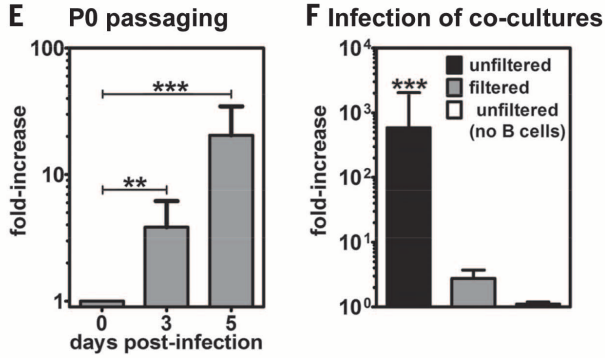


Fig. 3. HuNoVs productively infect B cells in culture. (**A**) A GII.4-Sydney HuNoV-positive stool sample was inoculated onto human BJAB B cells (black line) or filtered through a 0.2-μm filter before application (gray line). The inoculum contained 1×10^6 genome copy numbers, indicated by a dashed line. Viral genome copy numbers per well were determined by means of genogroup II-specific quantitative RT-PCR ($n = 12$ experiments). The 3- and 5-dpi genome copy numbers were compared with 0 dpi under each condition for statistical purposes, indicated by asterisks. The unfiltered and filtered data sets were statistically different from each other at 3 and 5 dpi, as indicated by the gray pound sign, but not at 0 dpi. (**B**) 1×10^6 genome copy numbers of unfiltered (black bars) or filtered (gray bars) stool inoculum was untreated (solid bars) or UV-treated (hatched bars) before inoculation onto B cells. Samples were analyzed as described above, and data were reported as the fold-increase in viral genome copy numbers from 0 to 3 or 5 dpi ($n = 3$ experiments). (**C** and **D**) Mock inoculum or 5×10^5 genome copy numbers of unfiltered GII.4-Sydney HuNoV-positive stool was applied to BJAB cells, and the cells were washed after 2 hours. (C) Cell lysates were tested in Western blotting by using a polyclonal antibody to NS6. The asterisk indicates a band of the expected size for the HuNoV NS5-NS6 processing intermediate (35 kD) that was only observed in infected cells at 3 to 5 dpi. No mature NS6 protein was detected, which is consistent with a report demonstrating that the NS5-NS6 cleavage site of a HuNoV is processed very inefficiently by the viral protease (*33*). (D) Cells were stained with antibody to VP1 (red) and DAPI (blue) and imaged on a fluorescent microscope. No VP1 signal was detected in mock-inoculated cells at 5 dpi, nor infected cells stained with an isotype control antibody. (**E**) 5×10^5 genome copy numbers of a P0 inoculum was passaged onto naïve BJABs. At 0, 3, and 5 dpi, wells were collected and analyzed by means of genogroup II-specific quantitative RT-PCR ($n = 4$ experiments). The data are presented as the fold-increase in genomes from 0 to 3 or 5 dpi. The genome copy numbers detected at each time point were compared with 0 dpi for statistical purposes, indicated by black asterisks. (**F**) 1×10^6 genome equivalents of the unfiltered (black bars) or filtered (gray bars) GII.4-Sydney HuNoV-positive stool sample were applied to the apical side of a transwell with polarized HT-29 IECs grown on the membrane and BJAB B cells cultured in the basal compartment. At 0 and 3 dpi, the basal compartment was collected for viral genome analysis by means of quantitative RT-PCR ($n = 5$ experiments). The data are presented as the fold-increase in genomes from 0 to 3 dpi. In two experiments, unfiltered stool was applied to a coculture with no cells in the basal chamber as a control (white bars). The 3-dpi genome copy numbers were compared with 0 dpi under each condition for statistical purposes, indicated by black asterisks. Similar coculture results were obtained by using another GII.4-Sydney HuNoV-positive stool sample. For all, error bars denote mean ± SD; Student's *t* test, $*P < 0.05$, $**P < 0.01$, $***P < 0.001$.

lymph nodes (MLNs) of B cell–deficient mice (μMT mice) as compared with B6 mice (Fig. 2, A and B). To test whether the reduced virus titers in μMT mice reflected decreased viral replication or increased clearance of input virus, we infected mice with light-sensitive MNV-1 to allow differentiation between input and newly replicated virus [this assay, along with complete methods, are described in (*21*)]. No significant differences in the ratio of light-insensitive (newly replicated) to total virus titers were observed between B6 and μMT mice (fig. S3A), demonstrating that B cells are required for optimal viral replication in vivo. Further supporting in vivo B cell infection, B cells purified from Peyer's patches of wild-type B6 mice contained viral genomes (Fig. 2C). Although MuNoV nonstructural protein expression has not been demonstrable in any cell type from in vivo samples of wild-type animals, we did observe viral nonstructural protein in B cells from Peyer's patches of *Stat1*$^{-/-}$ mice, in which MuNoVs achieve higher titers (Fig. 2D). Together, these findings suggest that B cells are infected in vivo during NoV infections.

On the basis of our observations with MuNoVs, we asked whether HuNoVs infect B cells. The currently dominant HuNoV strain circulating worldwide is a genogroup II, genotype 4 (GII.4) strain called GII.4-Sydney (*22*, *23*). When a GII.4-Sydney HuNoV-positive stool sample was inoculated onto the BJAB human B cell line, there was a significant 10-fold and 25-fold increase in viral genome copy number at 3 and 5 dpi, respectively, compared with input levels (Fig. 3, A and B, and fig. S4). Genome replication was not observed when the stool sample was ultraviolet (UV)–inactivated before inoculation. Filtration of the HuNoV-positive stool sample over a 0.2-μm membrane decreased genome replication, suggesting the presence of a filterable cofactor (Fig. 3, A and B). Viral nonstructural and structural proteins were detected in cells inoculated with unfiltered stool inoculum by using Western blotting and immunofluorescence assay, respectively (Fig. 3, C and D), although BJAB cultures were not persistently infected (figs. S5 and S6). To determine whether viral genome replication and protein synthesis in BJAB cells were indicative of productive infection, lysates from BJAB cultures at 3 dpi were passaged onto naïve BJAB cells (fig. S5). HuNoV genomes increased fourfold and 20-fold at 3 and 5 dpi, respectively, after inoculation with passage 0 (P0) virus (Fig. 3E), indicating that primary BJAB infection results in the production of new infectious virus particles.

Because NoVs must breach the intestinal epithelium in order to access target B cells, we also tested HuNoV infection in a coculture system with polarized HT-29 intestinal epithelial cells (IECs). GII.4-Sydney HuNoV-positive stool was applied into the apical supernatant fluid of HT-29 IECs grown on a transwell with BJAB B cells in the basal chamber. A nearly 600-fold increase in viral genome copy number was detected in the B cell fraction of infected cultures at 3 dpi when unfiltered inoculum was tested (Fig. 3F). No increase was detected in the basal chamber in the absence of B cells. Moreover, filtration of the stool sample ablated B cell–associated viral genome replication, which is consistent with results in direct B cell infections.

On the basis of the reduced B cell infectivity we observed in filtered stool samples, we tested whether enteric bacteria could serve as a cofactor to facilitate HuNoV infection of B cells. HuNoVs are well known to bind histo-blood group antigens (HBGAs) (*24*, *25*), which are expressed by the host as well as by certain bacteria (*26*–*28*). We first tested *Enterobacter cloacae* because it expresses H type HBGA (Fig. 4A) that the GII.4-Sydney HuNoV strain can bind (*29*). Filtered stool containing GII.4-Sydney virus displayed a dose-dependent restoration of infectivity when incubated with *E. cloacae* before inoculation of BJAB B cells (Fig. 4B). Neither *Escherichia coli* (which did not express H antigen) nor lipopolysaccharide (LPS, a component of the outer membrane of Gram-negative bacteria) rescued infectivity, whereas synthetic H antigen restored infectivity of filtered stool comparably with *E. cloacae*. Antibody to VP1 neutralized infectivity of the unfiltered stool, as expected. Providing insight into the mechanism of H antigen–mediated stimulation, filtration of GII.4-Sydney HuNoV-positive stool inoculum ablated virus attachment to B cells, and synthetic H antigen was sufficient to restore attachment (Fig. 4C). Overall, these results demonstrate that HuNoV interactions with enteric bacteria, likely

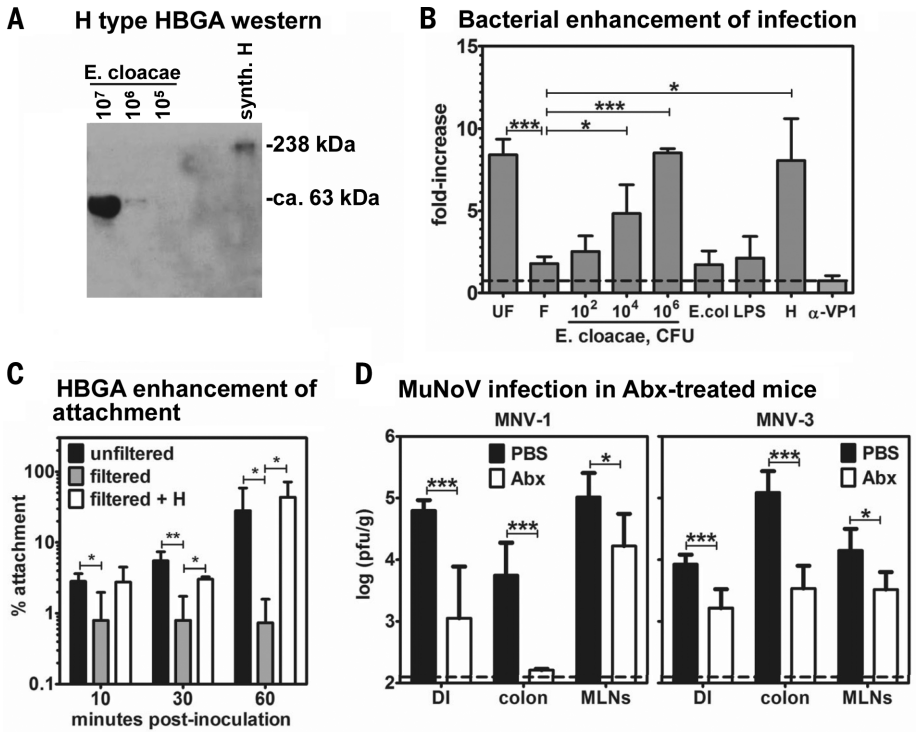


Fig. 4. Intestinal bacteria facilitate NoV infections. (**A**) Lysates were prepared from the indicated colony-forming units (CFU) of heat-killed *E. cloacae* for the purpose of Western blotting. Membranes were probed with antibody to H antigen. Synthetic H-type HBGA (synth. H) was tested as a positive control. No H-type HBGA was detected in *E. coli* lysates or BJAB cell lysates. (**B**) Filtered GII.4-Sydney HuNoV-positive stool inoculum was incubated with the indicated dose of heat-killed *E. cloacae*, 10^6 CFU heat-killed *E. coli*, 1 mg/mL *E. coli* LPS, or 500 ng/mL synthetic H-type HBGA before inoculation onto B cells. To test for antibody-mediated neutralization of virus infectivity, unfiltered stool inoculum was incubated with 10 μg/mL antibody to VP1 before B cell inoculation. Viral genome copy numbers were determined at 0 and 3 dpi under each condition (n = 3 to 4 experiments). Data are reported as the fold-increase in copy numbers over time. Each condition was compared with the untreated filtered inoculum data set for statistical purposes. (**C**) Unfiltered stool (black bars), filtered stool (gray bars), or filtered stool preincubated with 500 ng/mL H antigen (white bars) was inoculated onto BJAB cells for the indicated times at 4°C (n = 4 experiments). Viral genome copy numbers were quantified from unwashed cells to determine the amount of input virus and from washed cells to determine the amount of cell-attached virus. Data are reported as the percent of viral genomes remaining cell-associated compared with input. (**D**) Groups of phosphate-buffered saline (PBS)–treated (black bars) and Abx-treated (white bars) B6 mice (n = 3 to 4 mice) were infected with 10^7 $TCID_{50}$ units MNV-1 (left) or MNV-3 (right). At 1 dpi, virus was titered from the distal ileum (DI), colon, and mesenteric lymph nodes (MLNs) by using a standard virus plaque assay (n = 3 experiments). PBS-treated and Abx-treated groups under each condition were compared for statistical purposes. For all, error bars denote mean ± SD; Student's t test, *P < 0.05, **P < 0.01, ***P < 0.001.

through binding to bacterially expressed HBGAs, facilitate productive attachment to, and infection of, B cells.

To examine whether intestinal bacteria contribute to NoV infection in vivo, we depleted the intestinal microbiota of wild-type B6 mice before MuNoV infection (fig. S7). Indeed, antibiotic depletion of normal intestinal flora resulted in a significant reduction in MuNoV titers (Fig. 4D), demonstrating a biologically substantial role for enteric bacteria during NoV infection. These reduced titers reflected decreased viral replication because the ratio of replicated to input virus was similar between antibiotic-treated and control mice (fig. S3B). These collective data are consistent with recent studies of other viruses that have been shown to exploit commensal bacteria for optimal infection, and in particular with the ability of bacterial LPS to stimulate poliovirus attachment to permissive cells (*30*–*32*).

We have developed a cell culture system for a HuNoV by revealing that the current globally dominant GII.4-Sydney HuNoV strain infects human B cells. This infection is substantially enhanced by free HBGA or by HBGA-expressing bacteria. It is thus likely that previous attempts to culture HuNoVs failed because of the nature of the cell type tested and the absence of stimulatory carbohydrate molecules. Animal studies of the related MuNoVs validate that intestinal B cells are in vivo targets of NoVs and that enteric bacteria are required for efficient infection of susceptible hosts.

REFERENCE AND NOTES

1. D. C. Payne *et al*., *N. Engl. J. Med.* **368**, 1121–1130 (2013).
2. H. L. Koo, N. Ajami, R. L. Atmar, H. L. DuPont, *Discov. Med.* **10**, 61–70 (2010).
3. M. M. Patel *et al*., *Emerg. Infect. Dis.* **14**, 1224–1231 (2008).
4. R. I. Glass, U. D. Parashar, M. K. Estes, *N. Engl. J. Med.* **361**, 1776–1785 (2009).
5. J. J. Siebenga *et al*., *J. Infect. Dis.* **200**, 802–812 (2009).
6. E. Duizer *et al*., *J. Gen. Virol.* **85**, 79–87 (2004).
7. M. K. Lay *et al*., *Virology* **406**, 1–11 (2010).
8. E. Papafragkou, J. Hewitt, G. W. Park, G. Greening, J. Vinjé, *PLOS ONE* **8**, e63485 (2013).
9. M. M. Herbst-Kralovetz *et al*., *Emerg. Infect. Dis.* **19**, 431–438 (2013).
10. T. M. Straub *et al*., *Emerg. Infect. Dis.* **13**, 396–403 (2007).
11. S. Takanashi *et al*., *Arch. Virol.* **159**, 257–266 (2014).
12. S. M. Mumphrey *et al*., *J. Virol.* **81**, 3251–3263 (2007).
13. M. Basic *et al*., *Inflamm. Bowel Dis.* **20**, 431–443 (2014).
14. S. Zhu *et al*., *PLOS Pathog.* **9**, e1003592 (2013).
15. K. Bok *et al*., *Proc. Natl. Acad. Sci. U.S.A.* **108**, 325–330 (2011).
16. L. B. Thackray *et al*., *J. Virol.* **81**, 10460–10473 (2007).
17. A. Arias, D. Bailey, Y. Chaudhry, I. Goodfellow, *J. Gen. Virol.* **93**, 1432–1441 (2012).
18. C. C. Hsu, L. K. Riley, H. M. Wills, R. S. Livingston, *Comp. Med.* **56**, 247–251 (2006).
19. S. M. Kahan *et al*., *Virology* **421**, 202–210 (2011).
20. C. E. Wobus *et al*., *PLOS Biol.* **2**, e432 (2004).
21. Materials and methods are available as supplementary materials on *Science* Online.
22. J. van Beek *et al*., *Eurosurveillance* (2013); available at www.eurosurveillance.org/ViewArticle.aspx?ArticleId=20345.
23. J.-S. Eden, M. M. Tanaka, M. F. Boni, W. D. Rawlinson, P. A. White, *J. Virol.* **87**, 6270–6282 (2013).
24. S. Marionneau *et al*., *Gastroenterology* **122**, 1967–1977 (2002).
25. P. Huang *et al*., *J. Infect. Dis.* **188**, 19–31 (2003).
26. G. F. Springer, P. Williamson, W. C. Brandes, *J. Exp. Med.* **113**, 1077–1093 (1961).
27. D. A. Rasko, G. Wang, M. A. Monteiro, M. M. Palcic, D. E. Taylor, *Eur. J. Biochem.* **267**, 6059–6066 (2000).
28. W. Yi *et al*., *J. Am. Chem. Soc.* **127**, 2040–2041 (2005).
29. T. Miura *et al*., *J. Virol.* 10.1128/JVI.01060-13 (2013).
30. S. K. Kuss *et al*., *Science* **334**, 249–252 (2011).
31. M. Kane *et al*., *Science* **334**, 245–249 (2011).
32. C. M. Robinson, P. R. Jesudhasan, J. K. Pfeiffer, *Cell Host Microbe* **15**, 36–46 (2014).
33. J. May, B. Korba, A. Medvedev, P. Viswanathan, *Virology* **444**, 218–224 (2013).

ACKNOWLEDGMENTS

We thank R. Condit, G. McFadden, and H. Virgin for critical discussions and reading of the manuscript. We thank R. Renne and F. Zhu for providing cell lines and J. Pfeiffer for mouse antibiotic depletion protocols. The data presented in this manuscript are tabulated in the main paper and in the supplementary materials. The findings and conclusions in this article are those of the authors and do not necessarily represent the official position of the Centers for Disease Control and Prevention. This work was funded by NIH R01 AI080611 and R21 AI103961 for C.E.W; and National Institute of Food and Agriculture 2011-68003-30395 for J.V. C.L.G. was supported in part by NIH/National Institute of Dental and Craniofacial Research T90 DE021990-02 (Burne). A patent application pertinent to this work has been filed (U.S. patent application no. 61/992,040: Methods and Compositions for Caliciviridae, M.J. and S.K. as inventors).

SUPPLEMENTARY MATERIALS

www.sciencemag.org/content/346/6210/755/suppl/DC1
Materials and Methods
Figs. S1 to S7
References (*34*–*44*)

9 June 2014; accepted 16 September 2014
10.1126/science.1257147

HIV ENTRY

Conformational dynamics of single HIV-1 envelope trimers on the surface of native virions

James B. Munro,[1]*‡ Jason Gorman,[2] Xiaochu Ma,[1] Zhou Zhou,[3] James Arthos,[4] Dennis R. Burton,[5,6] Wayne C. Koff,[7] Joel R. Courter,[8]† Amos B. Smith III,[8] Peter D. Kwong,[2] Scott C. Blanchard,[3]‡ Walther Mothes[1]‡

The HIV-1 envelope (Env) mediates viral entry into host cells. To enable the direct imaging of conformational dynamics within Env, we introduced fluorophores into variable regions of the glycoprotein gp120 subunit and measured single-molecule fluorescence resonance energy transfer within the context of native trimers on the surface of HIV-1 virions. Our observations revealed unliganded HIV-1 Env to be intrinsically dynamic, transitioning between three distinct prefusion conformations, whose relative occupancies were remodeled by receptor CD4 and antibody binding. The distinct properties of neutralization-sensitive and neutralization-resistant HIV-1 isolates support a dynamics-based mechanism of immune evasion and ligand recognition.

The HIV-1 envelope (Env) spike is a membrane-fusion machine that mediates viral entry into cells (*1*). HIV-1 Env, composed of three gp120 glycoproteins and three gp41 subunits, evades recognition by antibodies by favoring a neutralization-resistant ground-state conformation in which N-linked glycans cover most of the surface (*2*–*5*). Interaction with the CD4 receptor causes structural rearrangements in gp120, which lead to formation of a co-receptor–binding site (*1*, *2*, *6*, *7*). These rearrangements include movement of the variable loops 1 and 2 (V1/V2) from their apical position in the unliganded trimer, to the trimer periphery (*8*–*10*). Subsequent interactions with the co-receptor trigger additional Env remodeling, with gp41 rearranging into a stable six-helix bundle that facilitates fusion between viral and cellular membranes. Although static images of HIV-1 Env in various conformations have been obtained (*6*–*9*, *11*–*17*), direct measurement of the dynamic features of the Env trimer has been lacking.

To enable real-time observations of conformational transitions in the native HIV-1 Env spike on the surface of virions, we used single-molecule fluorescence resonance energy transfer (smFRET) (*18*). Short peptides were introduced that permit enzymatically targeted incorporation of fluorophores (*19*, *20*) into the V1 loop and one of the following: the V4 loop, the E loop, or the V5 loop of gp120. The attachment of donor and acceptor fluorophores at these sites provided

[1]Department of Microbial Pathogenesis, Yale University School of Medicine, New Haven, CT 06536, USA. [2]Vaccine Research Center, National Institute of Allergy and Infectious Diseases, National Institutes of Health, Bethesda, MD 20892, USA. [3]Department of Physiology and Biophysics, Weill Cornell Medical College of Cornell University, New York, NY 10021, USA. [4]Laboratory of Immunoregulation, National Institute of Allergy and Infectious Diseases, National Institutes of Health, Bethesda, MD 20892, USA. [5]Department of Immunology and Microbial Science, and IAVI Neutralizing Antibody Center, The Scripps Research Institute, La Jolla, CA 92037, USA. [6]Ragon Institute of MGH, MIT, and Harvard, Cambridge, MA 02129, USA. [7]International AIDS Vaccine Initiative (IAVI), New York, NY 10004, USA. [8]Department of Chemistry, University of Pennsylvania, Philadelphia, PA 19104, USA.
*Present address: Department of Molecular Biology and Microbiology, Tufts University School of Medicine, Boston, MA 02111, USA. †Present address: Incyte Corporation, Experimental Station, Wilmington, DE 19880, USA. **‡Corresponding author. E-mail: walther.mothes@yale.edu (W.M.); scb2005@med.cornell.edu (S.C.B.); james.munro@tufts.edu (J.B.M.)**

distinct reference points for observing movements of the V1 loop via time-dependent changes in FRET efficiency (Fig. 1). Dually tagged viruses were engineered for the neutralization-sensitive HIV-1_{NL4-3} laboratory-adapted strain and the neutralization-resistant tier-2 primary isolate HIV-1_{JR-FL}. Dually tagged HIV-1_{NL4-3} viruses were isolated that met a series of functional criteria (*21*) (figs. S1 to S3). Insertions were then made in homologous positions in the HIV-1_{JR-FL} Env that had little effect on infectivity (fig. S1B). Both HIV-1_{NL4-3} and HIV-1_{JR-FL} tolerated the Q*3* peptide (*20*, *22*) (GQQQLG) in the V1 loop and the A1 peptide (*19*) (GDSLDMLEWSLM) in the V4 loop (V1-Q*3*/V4-A1) (fig. S4). HIV-1_{NL4-3} also tolerated the Q*3* peptide in the V1 loop and the A1 peptide in the V5 loop (V1-Q*3*/V5-A1).

To ensure that only a single fluorescently labeled gp120 molecule was present on the surface of the HIV-1 virus, plasmid encoding wild-type Env was cotransfected at a ratio of 40:1 over the dually tagged Env. Viruses were harvested and enzymatically labeled with donor (e.g., Cy3B or Cy*3*) and acceptor [e.g., Cy*5*(4S)COT or Alexa Fluor 647] fluorophores (fig. S5) (*21*, *23*). A biotin-lipid incorporated into the viral membrane, which had negligible effects on virus infectivity (fig. S7), facilitated surface immobilization on streptavidin-coated quartz microscope slides and single-molecule imaging (*24*).

HIV-1_{NL4-3} and HIV-1_{JR-FL} virions containing a fluorescently labeled gp120 domain within the context of a native Env trimer were imaged at a time resolution of 25 frames per second (40-ms integration time) by using a prism-based total internal reflection fluorescence (TIRF) microscope (Fig. 1A). Donor and acceptor fluorescence were collected, optically separated, and recorded on electron-multiplying charge-coupled device arrays. FRET efficiencies were calculated from donor and acceptor fluorescence intensities and compiled into population histograms (Fig. 2, A and B) (*21*). Consistent with the probability of tagged gp120 monomer incorporation into the Env trimer (1:40 ratio to wild-type gp120) and with labeling efficiencies of 40% and 55% for the Q*3* and A1 tags, respectively, ~12% of all surface-bound virions displayed FRET, equating to 23% of all visible molecules (*21*) (fig. S6).

The unliganded V1-Q*3*/V4-A1–labeled HIV-1_{NL4-3} Env exhibited evidence of spontaneous reversible

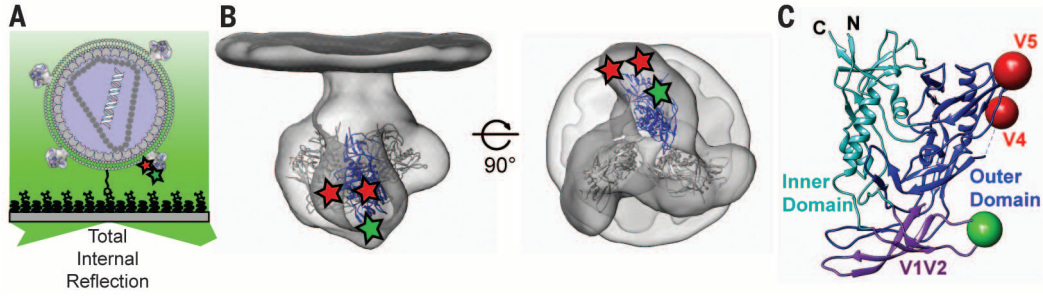


Fig. 1. Single-molecule FRET imaging indicates conformational dynamics of HIV-1 Env. (**A**) Experimental design. Native HIV-1 virions containing a single dually labeled Env molecule among native trimers were immobilized on the surface of passivated quartz microscope slides and imaged via TIRF microscopy. (**B**) Approximate position of the organic dyes in the variable loops V1 (green; Cy3B or Cy3) and V4 or V5 (red; Cy5(4S)COT or Alexa Fluor 647) of gp120 of HIV-1 Env. The Env structure, with the ribbon structure of the gp120 trimer, is adapted from PDB accession code 4NCO (*6*–*8*, *11*, *45*). (**C**) Ribbon structures of the gp120 inner domain (cyan), outer domain (blue), and V1/V2 region (purple) are highlighted.

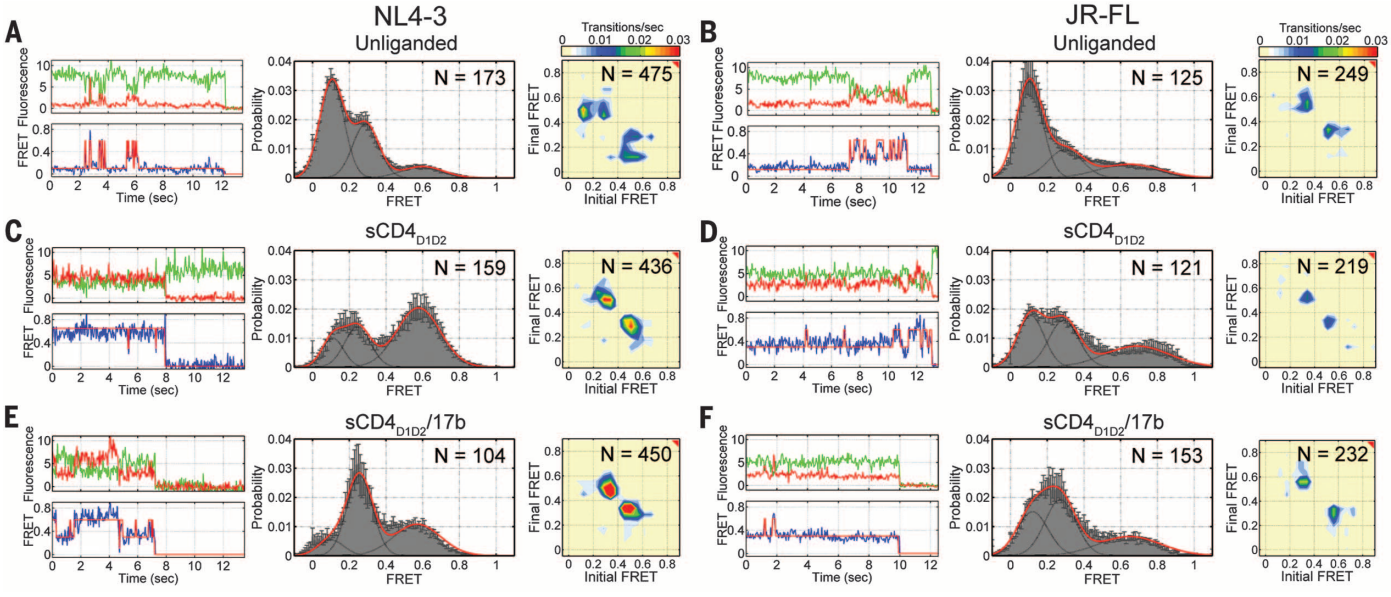


Fig. 2. Ligands remodel the conformational landscape of HIV-1 Env. (**A**) (Top left) Representative fluorescence (Cy3B, donor, green; Cy5(4S)COT, acceptor, red) and (bottom left) FRET (blue) trajectories obtained from a single HIV-1_{NL4-3} Env on the surface of an intact virion. Idealization of FRET trajectories (red) was achieved by fitting each trace to a three-state Markov model (*28*). (Center) FRET trajectories from individual unliganded HIV-1_{NL4-3} Env proteins were compiled into a population FRET histogram and fit to the sum of three Gaussian distributions (red) with means 0.1, 0.3, and 0.6 (black). (Right) TDPs displaying the relative frequencies of observed transitions were generated from the idealization of individual FRET trajectories. (**B**) (Left) Fluorescence and FRET trajectories for the unliganded HIV-1_{JR-FL} Env. (Center) FRET histogram fit to the sum of three Gaussian distributions with means 0.1, 0.3, and 0.65, and TDP. (**C** and **D**) Fluorescence and FRET trajectories, FRET histograms, and TDPs for (C) HIV-1_{NL4-3} Env and (D) HIV-1_{JR-FL} Env in the presence of $sCD4_{D1D2}$ (5 μM). (**E** and **F**) The same data for (E) HIV-1_{NL4-3} Env and (F) HIV-1_{JR-FL} Env in the presence of $sCD4_{D1D2}$ (5 μM) and 17b Fab (2 μM). The number of FRET trajectories and the number of FRET transitions are indicated on the histograms and TDPs, respectively. Histograms represent the means ± SEM determined from three independent populations of smFRET traces.

fluctuations between at least three conformations, each identified by a distinct FRET value: low (~0.10), intermediate (~0.30), and high FRET (~0.60) (Fig. 2A). The unliganded V1-Q3/V4-A1–labeled HIV-1_{JR-FL} Env and a HIV-1_{NL4-3} Env protein dually labeled in the V1 and V5 loops (V1-Q3/V5-A1) exhibited similar behavior (Fig. 2B and fig. S8). These findings, together with evidence of isotropic fluorophore tumbling (table S1), suggest that the time-dependent changes in FRET efficiency observed in each system reflect changes in interfluorophore distance. The observed transitions in the milliseconds-to-seconds time scale indicated that the HIV-1 Env trimer of both strains exhibits the intrinsic capacity to undergo large-scale conformational changes (*25*), which reposition the V1/V2 loop closer to the gp120 outer domain, where V4 and V5 reside.

The most populated conformation for both unliganded Env proteins exhibited low FRET (Fig. 2, A and B). This finding is consistent with prefusion HIV-1 Env predominantly occupying a closed, ground-state configuration that is conformationally masked (*6*, *7*, *26*), where the V1/V2 loops are proximal to the apex of the trimer and distal to the Env periphery (Fig. 1, B and C, and table S2). Consistent with this interpretation, mutations D368R and E370R (*22*) in the CD4-binding site of gp120 of HIV-1_{NL4-3}, which inhibit formation of the bridging sheet necessary for CD4 binding (*11*, *27*), stabilize the low-FRET state (fig. S9).

We next investigated the sequence of conformational transitions of the unliganded HIV-1 Env through the application of hidden Markov modeling (*28*). The smFRET trajectories from the V1-Q3/V4-A1–labeled HIV-1_{NL4-3} and HIV-1_{JR-FL} Envs were fit to a three-state model containing low-, intermediate-, and high-FRET states. The well-defined peaks arranged symmetrically with respect to the diagonal axis in transition-density plots (TDPs) (Fig. 2, A and B) reflect the quality of the idealization and indicate that the system is in equilibrium. These data revealed that the neutralization-sensitive HIV-1_{NL4-3} Env frequently transitioned out of the low-FRET ground-state configuration into the high-FRET state, which had preferential access to the intermediate-FRET state. Direct transitions between low and intermediate FRET were seldom observed (Fig. 2A). The D368R/E370R mutant displayed a dramatic reduction in transitions out of the low-FRET state (fig. S9). This finding further verified our assignment of the low-FRET state as a ground-state conformation. In contrast, the neutralization-resistant HIV-1_{JR-FL} Env exhibited reduced dynamics compared with HIV-1_{NL4-3} (Fig. 2B and table S3). This finding was most notably reflected in a substantial reduction in occupancy of the intermediate-FRET state. When transitions out of the low-FRET ground state were observed, however, HIV-1_{JR-FL} Env, like HIV-1_{NL4-3}, appeared to rapidly interconvert between the high- and intermediate-FRET states. Again, direct transitions between low- and intermediate-FRET states were seldom observed. These findings indicate that both HIV-1 isolates preferentially achieve the intermediate-FRET configuration via the high-FRET state. Moreover, they reveal dynamic distinctions between the neutralization-sensitive laboratory-adapted HIV-1_{NL4-3} and the neutralization-resistant clinical isolate HIV-1_{JR-FL}.

We next sought to investigate how the conformational landscape of the Env trimer responds to ligands. To measure the effects of CD4 and the co-receptor binding to Env, we used saturating concentrations of soluble CD4 ($sCD4_{D1D2}$) (5 μM) (fig. S10); the CD4 mimetic small molecule JRC-II-191 (100 μM) (*29*); and the antigen-binding fragment (Fab) of antibody 17b (2 μM), a surrogate for the co-receptor. Antibody 17b binds Env at the co-receptor–binding site, which promotes a conformation of Env resembling the co-receptor–bound conformation (*8*, *11*, *30*). Whereas HIV-1_{NL4-3} and HIV-1_{JR-FL} Env use distinct co-receptors (CXCR4 and CCR5, respectively), 17b binds to an epitope conserved in both strains. For HIV-1_{NL4-3} Env, the addition of $sCD4_{D1D2}$ stabilized the high-FRET state (Fig. 2C). The combination of $sCD4_{D1D2}$ and 17b Fab stabilized the intermediate-FRET state (Fig. 2E). Likewise, the CD4-mimetic JRC-II-191 stabilized the intermediate-FRET state (fig. S11). Although saturating ligand concentrations were used (figs. S10A and S11C), TDPs indicate that the ligand-bound Env remains dynamic. In each of the ligand-saturated conditions examined, conformational sampling between high- and intermediate-FRET states predominated, whereas transitions between low and intermediate FRET were again rarely observed. For HIV-1_{JR-FL} Env, $sCD4_{D1D2}$ and $sCD4_{D1D2}$/17b stabilized intermediate- and high-FRET states to similar extents (Fig. 2, D and F, and table S2). To test if this was due to incomplete $sCD4_{D1D2}$ binding, the conformational equilibrium of HIV-1_{JR-FL} Env was tested in the presence of the potent HIV-1 inhibitor, dodecameric $sCD4_{D1D2}$ ($sCD4_{D1D2}$-Igαtp, 0.1 mg/ml) (*31*). Here again, intermediate- and high-FRET states were stabilized to similar extents, and Env exhibited transitions between both states, despite the presence of a saturating ligand concentration (fig. S12).

Collectively, these observations reveal that the unliganded Env proteins of both HIV-1 isolates

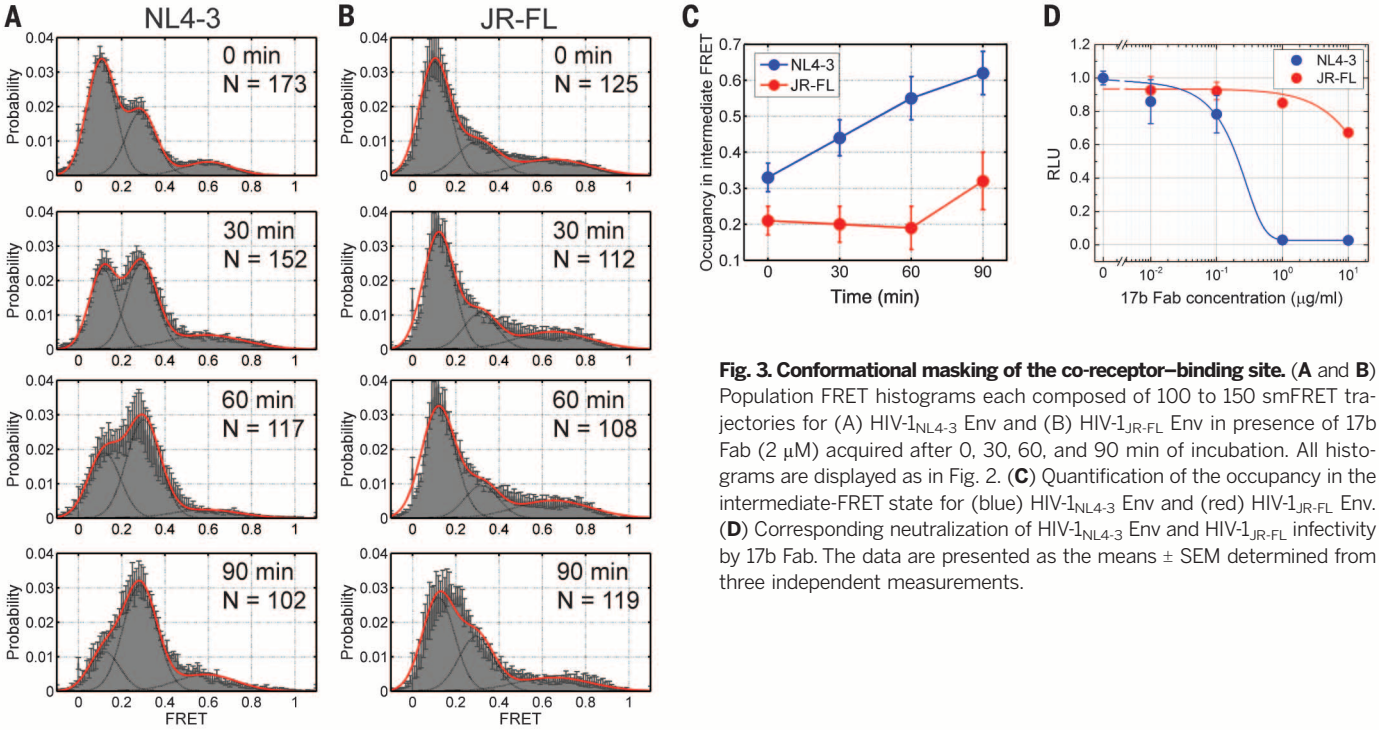


Fig. 3. Conformational masking of the co-receptor–binding site. (**A** and **B**) Population FRET histograms each composed of 100 to 150 smFRET trajectories for (A) HIV-1_{NL4-3} Env and (B) HIV-1_{JR-FL} Env in presence of 17b Fab (2 μM) acquired after 0, 30, 60, and 90 min of incubation. All histograms are displayed as in Fig. 2. (**C**) Quantification of the occupancy in the intermediate-FRET state for (blue) HIV-1_{NL4-3} Env and (red) HIV-1_{JR-FL} Env. (**D**) Corresponding neutralization of HIV-1_{NL4-3} Env and HIV-1_{JR-FL} infectivity by 17b Fab. The data are presented as the means ± SEM determined from three independent measurements.

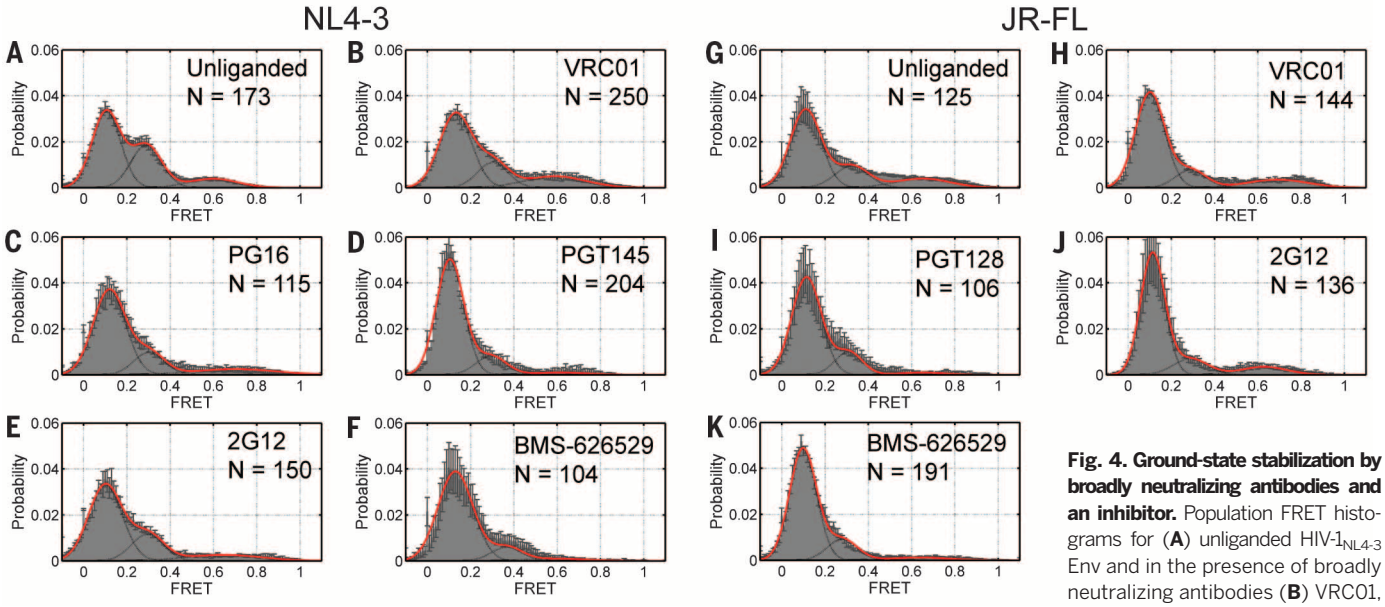


Fig. 4. Ground-state stabilization by broadly neutralizing antibodies and an inhibitor. Population FRET histograms for (**A**) unliganded HIV-1_{NL4-3} Env and in the presence of broadly neutralizing antibodies (**B**) VRC01, (**C**) PG16, (**D**) PGT145, (**E**) 2G12 (all at 0.7 μM), and (**F**) the small molecule BMS-626529 (100 μM). The same data for (**G**) unliganded HIV-1_{JR-FL} Env and in the presence of (**H**) VRC01, (**I**) PGT128, (**J**) 2G12, and (**K**) BMS-626529. Histograms are displayed as in Fig. 2.

predominantly occupy ground-state configurations but are inherently competent to access conformations stabilized by $sCD4_{D1D2}$ and $sCD4_{D1D2}$/17b. These data indicate that spontaneously sampled Env conformations may serve a functional role in infectivity. For instance, this finding suggests, as has been previously speculated (*32*), that CD4 and 17b may facilitate the capture of preexisting Env conformations that are spontaneously sampled in the unliganded spike, rather than triggering a trimer-opening event. These observations also have implications for antibody neutralization strategies, as HIV-1_{NL4-3} can be readily stabilized in a single conformation by activating ligands, whereas the neutralization-resistant HIV-1_{JR-FL} Env persistently exhibits relatively unstable, isoenergetic intermediate- and high-FRET states.

To examine directly the correlation between the occupancy of intermediate-FRET Env configurations and sensitivity to neutralization, we probed the response of both strains to 17b Fab alone (2 μM) as a function of time (Fig. 3, A and B). As expected, the neutralization-sensitive HIV-1_{NL4-3} Env showed a marked increase in occupancy of the intermediate-FRET state over time, whereas the neutralization-resistant HIV-1_{JR-FL} Env showed no increase even after 60 min of incubation and only a slight increase after 90 min (Fig. 3, A to C). These experiments highlight functional distinctions of the two Env proteins and confirm that the intermediate-FRET state, which these data reveal is directly associated with co-receptor binding, is masked to a greater extent in the clinically isolated HIV-1_{JR-FL} Env, which explains the increased resistance to 17b neutralization (Fig. 3D).

The observed changes in the conformational landscape of HIV-1 Env in response to sCD4 and 17b allow us to assign the low- and intermediate-FRET configurations to ground-state and the CD4/17b-bound Env conformations, respectively (*8*, *13*). The assignment of the high-FRET states is less clear because the HIV-1_{NL4-3} and HIV-1_{JR-FL} Env isolates differ in their responses to sCD4. Based on our observations of HIV-1_{NL4-3}, the high-FRET state may correspond to a CD4-bound conformation. Alternatively, it may represent a previously uncharacterized structural state that is a necessary intermediate during the activation of Env by CD4.

A model of binding through capture of preexisting conformations implies that intrinsic access to activated states is required for Env function. We therefore asked if broadly neutralizing antibodies that can neutralize up to 90% of all HIV-1 isolates (*33*–*37*), some of which bind to the ground-state Env conformation (*13*, *37*, *38*), remodel the conformational landscape by stabilizing HIV-1 Env in the ground state. Surface-bound viruses from both strains were incubated with neutralizing concentrations of antibodies VRC01, PG16, PGT128, PGT145, or 2G12 (figs. S3 and S13), which recognize different HIV-1 Env epitopes (*39*). smFRET measurements indicated that all broadly neutralizing antibodies tested exhibited a tendency to stabilize the low-FRET ground-state conformation of both HIV-1_{NL4-3} and HIV-1_{JR-FL} Env (Fig. 4). Each antibody, however, differentially affected the intermediate- and high-FRET configurations (fig. S14 and table S2). The potent small-molecule inhibitor of HIV-1 entry, BMS-626529 (*40*), also stabilized the low-FRET ground-state conformation for both HIV-1_{JR-FL} and HIV-1_{NL4-3} to an extent comparable to the broadly neutralizing antibodies tested (Fig. 4, F and K). In contrast, the small-molecule CD4-mimetic, JRC-II-191, stabilized activated FRET states of HIV-1_{NL4-3} Env (fig. S11). These findings suggest that stabilization of the ground-state Env conformation is both a general and effective means of inhibiting HIV-1 entry.

The data presented here demonstrate that smFRET imaging can be applied to biomolecular systems as complex as HIV-1 Env on the surface of intact virions. These findings serve as an important step toward achieving smFRET imaging in living cells. HIV-1 Env from both laboratory-adapted and clinically isolated strains can spontaneously transition from a stable ground-state configuration to transient, CD4- and co-receptor–stabilized states. Thus, gp120 exhibits physical properties that typify dynamic enzymes, whose functions are regulated through the modulation of intrinsically accessible conformations (*25*, *41*). Moreover, the smFRET methodologies developed here allow for the precise delineation of conformations induced by antibodies and ligands in functional virions (*42*). Our analysis also directly reveals molecular and temporal events in gp120 that underlie the two-step activation of HIV-1 Env by CD4 and co-receptor. The reduced dynamics of HIV-1_{JR-FL} Env out of the ground state, as well as the resistance to stabilization in a single conformation, reveals the mechanism of the masking of functional centers by neutralization-resistant HIV-1 isolates. Furthermore, this work suggests that stabilizing the ground state represents an effective strategy to antagonize viral fusion machines.

REFERENCES AND NOTES

1. S. C. Harrison, *Nat. Struct. Mol. Biol.* **15**, 690–698 (2008).
2. R. Wyatt, J. Sodroski, *Science* **280**, 1884–1888 (1998).
3. R. Pantophlet, D. R. Burton, *Annu. Rev. Immunol.* **24**, 739–769 (2006).
4. X. Wei *et al.*, *Nature* **422**, 307–312 (2003).
5. R. Wyatt *et al.*, *Nature* **393**, 705–711 (1998).
6. J.-P. Julien *et al.*, *Science* **342**, 1477–1483 (2013).
7. D. Lyumkis *et al.*, *Science* **342**, 1484–1490 (2013).
8. J. Liu, A. Bartesaghi, M. J. Borgnia, G. Sapiro, S. Subramaniam, *Nature* **455**, 109–113 (2008).

9. T. A. White *et al.*, *PLOS Pathog.* **6**, e1001249 (2010).
10. G. Hu, J. Liu, K. A. Taylor, K. H. Roux, *J. Virol.* **85**, 2741–2750 (2011).
11. P. D. Kwong *et al.*, *Nature* **393**, 648–659 (1998).
12. M. Pancera *et al.*, *Proc. Natl. Acad. Sci. U.S.A.* **107**, 1166–1171 (2010).
13. E. E. Tran *et al.*, *PLOS Pathog.* **8**, e1002797 (2012).
14. Y. Mao *et al.*, *Nat. Struct. Mol. Biol.* **19**, 893–899 (2012).
15. A. Harris *et al.*, *Proc. Natl. Acad. Sci. U.S.A.* **108**, 11440–11445 (2011).
16. C. G. Moscoso *et al.*, *Proc. Natl. Acad. Sci. U.S.A.* **108**, 6091–6096 (2011).
17. S. R. Wu *et al.*, *Proc. Natl. Acad. Sci. U.S.A.* **107**, 18844–18849 (2010).
18. R. Roy, S. Hohng, T. Ha, *Nat. Methods* **5**, 507–516 (2008).
19. Z. Zhou *et al.*, *ACS Chem. Biol.* **2**, 337–346 (2007).
20. C. W. Lin, A. Y. Ting, *J. Am. Chem. Soc.* **128**, 4542–4543 (2006).
21. Materials and Methods are available as supplementary materials on *Science* Online.
22. Single-letter abbreviations for the amino acid residues are as follows: A, Ala; C, Cys; D, Asp; E, Glu; F, Phe; G, Gly; H, His; I, Ile; K, Lys; L, Leu; M, Met; N, Asn; P, Pro; Q, Gln; R, Arg; S, Ser; T, Thr; V, Val; W, Trp; and Y, Tyr.
23. Q. Zheng *et al.*, *Chem. Soc. Rev.* **43**, 1044–1056 (2014).
24. N. G. Mukherjee, L. A. Lyon, J. M. Le Doux, *Nanotechnology* **20**, 065103 (2009).
25. K. Henzler-Wildman, D. Kern, *Nature* **450**, 964–972 (2007).
26. P. D. Kwong *et al.*, *Nature* **420**, 678–682 (2002).
27. U. Olshevsky *et al.*, *J. Virol.* **64**, 5701–5707 (1990).
28. F. Qin, *Biophys. J.* **86**, 1488–1501 (2004).
29. H. Haim *et al.*, *PLOS Pathog.* **5**, e1000360 (2009).
30. N. Sullivan *et al.*, *J. Virol.* **72**, 4694–4703 (1998).
31. J. Arthos *et al.*, *J. Biol. Chem.* **277**, 11456–11464 (2002).
32. A. L. DeVico, *Curr. HIV Res.* **5**, 561–571 (2007).
33. T. Zhou *et al.*, *Science* **329**, 811–817 (2010).
34. L. M. Walker *et al.*, *Science* **326**, 285–289 (2009).
35. L. M. Walker *et al.*, *Nature* **477**, 466–470 (2011).
36. M. Pancera *et al.*, *Nat. Struct. Mol. Biol.* **20**, 804–813 (2013).
37. J.-P. Julien *et al.*, *Proc. Natl. Acad. Sci. U.S.A.* **110**, 4351–4356 (2013).
38. J.-P. Julien *et al.*, *PLOS Pathog.* **9**, e1003342 (2013).
39. P. D. Kwong, J. R. Mascola, G. J. Nabel, *Nat. Rev. Immunol.* **13**, 693–701 (2013).
40. Z. Li *et al.*, *Antimicrob. Agents Chemother.* **57**, 4172–4180 (2013).
41. J. B. Munro, K. Y. Sanbonmatsu, C. M. Spahn, S. C. Blanchard, *Trends Biochem. Sci.* **34**, 390–400 (2009).
42. Subsequent to the submission of this manuscript, the structure of a trimeric prefusion HIV-1 Env (*43*) was determined in complex with broadly neutralizing antibodies PGT122 (*35*) and 35O22 (*44*). To determine the conformational state these antibodies captured in the crystal lattice, we measured smFRET on labeled JR-FL virions in the presence of either PGT122 or 35O22 or both. These data indicated that PGT122 strongly stabilized the ground state. In contrast, 35O22 had little effect on Env conformation. HIV-1 Env complexed with both antibodies exhibited slight ground state stabilization.
43. M. Pancera *et al.*, *Nature* **514**, 455–461 (2014).
44. J. Huang *et al.*, *Nature* 10.1038/nature13601 (2014).
45. J. S. McLellan *et al.*, *Nature* **480**, 336–343 (2011).

ACKNOWLEDGMENTS

We thank J. Jin, L. Agosto, T. Wang, R. B. Altman, and M. R. Wasserman for assistance; C. Walsh, J. Binely, A. Trkola, and M. Krystal for reagents; and members of the Structural Biology Section, Vaccine Research Center, for critically reading the manuscript. We thank I. Wilson and J. Sodroski for encouraging us to extend our approach to a R5-tropic Env. The data presented in this paper are tabulated in the main paper and in the supplementary materials. This work was supported by NIH grants R21 AI100696 to W.M. and S.C.B; P01 56550 to W.M., S.C.B., and A.B.S.; and R01 GM098859 to S.C.B.; by the Irvington Fellows Program of the Cancer Research Institute to J.B.M; by a fellowship from the China Scholarship Council-Yale World Scholars to X.M.; by grants from the International AIDS Vaccine Initiative's (IAVI) Neutralizing Antibody Consortium to D.R.B., W.C.K., and P.D.K.; and by funding from the NIH Intramural Research Program (Vaccine Research Center) to P.D.K. IAVI's work is made possible by generous support from many donors including: the Bill & Melinda Gates Foundation and the U.S. Agency for International Development (USAID). This study is made possible by the generous support of the American people through USAID. The contents are the responsibility of the authors and do not necessarily reflect the views of USAID or the U.S. government. Reagents from the NIH are subject to nonrestrictive material transfer agreements. Patent applications pertaining to this work are the U.S. and World Application US2009/006049 and WO/2010/053583, Synthesis of JRC-II-191 (A.B.S., J.R.C.), U.S. Patent Application 13/202,351, Methods and Compositions for Altering Photopysical Properties of Fluorophores via Proximal Quenching (S.C.B., Z.Z.); U.S. Patent Application 14/373,402 Dye Compositions, Methods of Preparation, Conjugates Thereof, and Methods of Use (S.C.B., Z.Z.); and International and US Patent Application PCT/US13/42249 Reagents and Methods for Identifying Anti-HIV Compounds (S.C.B., J.B.M., W.M.). S.C.B. is a co-founder of Lumidyne Corporation.

SUPPLEMENTARY MATERIALS

www.sciencemag.org/content/346/6210/759/suppl/DC1
Materials and Methods
Figs. S1 to S15
Tables S1 to S3
References (*46*–*56*)

4 April 2014; accepted 15 September 2014
Published online 8 October 2014;
10.1126/science.1254426

INSECT PHYLOGENOMICS

Phylogenomics resolves the timing and pattern of insect evolution

Bernhard Misof,[1]*† Shanlin Liu,[2,3]* Karen Meusemann,[1,4]* Ralph S. Peters,[5]* Alexander Donath,[1]* Christoph Mayer,[1]* Paul B. Frandsen,[6]* Jessica Ware,[7]* Tomáš Flouri,[8]* Rolf G. Beutel,[9]* Oliver Niehuis,[1]* Malte Petersen,[1]* Fernando Izquierdo-Carrasco,[8]* Torsten Wappler,[10]* Jes Rust,[10]* Andre J. Aberer,[8] Ulrike Aspöck,[11,12] Horst Aspöck,[13] Daniela Bartel,[12] Alexander Blanke,[1,18] Simon Berger,[8] Alexander Böhm,[12] Thomas R. Buckley,[14] Brett Calcott,[15] Junqing Chen,[3] Frank Friedrich,[16] Makiko Fukui,[17] Mari Fujita,[18] Carola Greve,[1] Peter Grobe,[1] Shengchang Gu,[3] Ying Huang,[2,3] Lars S. Jermiin,[19] Akito Y. Kawahara,[20] Lars Krogmann,[21] Martin Kubiak,[16] Robert Lanfear,[22,23,24] Harald Letsch,[25] Yiyuan Li,[2,3] Zhenyu Li,[3] Jiguang Li,[3] Haorong Lu,[3] Ryuichiro Machida,[18] Yuta Mashimo,[18] Pashalia Kapli,[8,26] Duane D. McKenna,[27] Guanliang Meng,[2,3] Yasutaka Nakagaki,[18] José Luis Navarrete-Heredia,[28] Michael Ott,[29] Yanxiang Ou,[3] Günther Pass,[12] Lars Podsiadlowski,[30] Hans Pohl,[9] Björn M. von Reumont,[31] Kai Schütte,[32] Kaoru Sekiya,[18] Shota Shimizu,[18] Adam Slipinski,[4] Alexandros Stamatakis,[8,33] Wenhui Song,[2,3] Xu Su,[2,3] Nikolaus U. Szucsich,[12] Meihua Tan,[2,3] Xuemei Tan,[3] Min Tang,[2,3] Jingbo Tang,[3] Gerald Timelthaler,[12] Shigekazu Tomizuka,[18] Michelle Trautwein,[34] Xiaoli Tong,[35] Toshiki Uchifune,[18,36] Manfred G. Walzl,[12] Brian M. Wiegmann,[37] Jeanne Wilbrandt,[1] Benjamin Wipfler,[9] Thomas K. F. Wong,[19] Qiong Wu,[2,3] Gengxiong Wu,[3] Yinlong Xie,[3] Shenzhou Yang,[2,3] Qing Yang,[2,3] David K. Yeates,[4] Kazunori Yoshizawa,[38] Qing Zhang,[2,3] Rui Zhang,[2,3] Wenwei Zhang,[3] Yunhui Zhang,[3] Jing Zhao,[2,3] Chengran Zhou,[2,3] Lili Zhou,[2,3] Tanja Ziesmann,[1] Shijie Zou,[3] Yingrui Li,[3] Xun Xu,[3] Yong Zhang,[2,3] Huanming Yang,[3] Jian Wang,[3] Jun Wang,[3,39,40,41,42]*† Karl M. Kjer,[43]*† Xin Zhou[2,3]*†

Insects are the most speciose group of animals, but the phylogenetic relationships of many major lineages remain unresolved. We inferred the phylogeny of insects from 1478 protein-coding genes. Phylogenomic analyses of nucleotide and amino acid sequences, with site-specific nucleotide or domain-specific amino acid substitution models, produced statistically robust and congruent results resolving previously controversial phylogenetic relationships. We dated the origin of insects to the Early Ordovician [~479 million years ago (Ma)], of insect flight to the Early Devonian (~406 Ma), of major extant lineages to the Mississippian (~345 Ma), and the major diversification of holometabolous insects to the Early Cretaceous. Our phylogenomic study provides a comprehensive reliable scaffold for future comparative analyses of evolutionary innovations among insects.

Insects (*1*) were among the first animals to colonize and exploit terrestrial and freshwater ecosystems. They have shaped Earth's biota, exhibiting coevolved relationships with many groups, from flowering plants to humans. They were the first to master flight and establish social societies. However, many aspects of insect evolution are still poorly understood (*2*). The oldest known fossil insects are from the Early Devonian [~412 million years ago (Ma)], which has led to the hypothesis that insects originated in the Late Silurian with the earliest terrestrial ecosystems (*3*). Molecular data, however, point to a Cambrian or at least Early Ordovician origin (*4*), which implies that early diversification of insects occurred in marine or coastal environments. Because of the absence of insect fossils from the Cambrian to the Silurian, these conclusions remain highly controversial. Furthermore, the phylogenetic relationships among major clades of polyneopteran insect orders—including grasshoppers and crickets (Orthoptera), cockroaches (Blattodea), and termites (Isoptera)—have remained elusive, as has the phylogenetic position of the enigmatic Zoraptera. Even the closest extant relatives of Holometabola (e.g.,

beetles, moths and butterflies, flies, sawflies, wasps, ants, and bees) are unknown. Thus, in order to understand the origins of physiological and morphological innovations in insects (e.g., wings and metamorphosis), it is important to reliably reconstruct the tempo and mode of insect diversification. We therefore conducted a phylogenomic study on 1478 single-copy nuclear genes obtained from genomes and transcriptomes representing key taxa from all extant insect orders and other arthropods (144 taxa) and estimated divergence dates with a validated set of 37 fossils (*5*).

Phylogenomic analyses of transcriptome and genome sequence data (*6*) can be compromised by sparsely populated data matrices, gene paralogy, sequence misalignment, and deviations from the underlying assumptions of applied evolutionary models, which may result in biased statistical confidence in phylogenetic relationships and temporal inferences. We addressed these obstacles by removing confounding factors in our analysis (*5*) (fig. S2).

We sequenced more than 2.5 gigabases (Gb) of cDNA from each of 103 insect species, which represented all extant insect orders (*5*). Additionally, we included published transcript sequence data that met our standards (table S2) and official gene sets of 14 arthropods with sequenced draft genomes (*5*), of which 12 served as references during orthology prediction of transcripts (tables S2 and S4). Comparative analysis of the reference species' official gene sets identified 1478 single-copy nuclear genes present in all these species (tables S3 and S4). Functional annotation of these genes revealed that many serve basic cellular functions (tables S14 and S15 and figs. S4 to S6). A graph-based approach using the best reciprocal genome- and transcriptome-wide hit criterion identified, on average, 98% of these genes in the 103 de novo sequenced transcriptomes, but only 79% and 62% in the previously published transcriptomes of in- and out-group taxa, respectively (tables S12 and S13).

After transcripts had been assigned and aligned to the 1478 single-copy nuclear-encoded genes, we checked for highly divergent, putatively misaligned transcripts. Of the 196,027 aligned transcripts, 2033 (1%) were classified as highly divergent. Of these, 716 were satisfactorily realigned with an automated refinement. However, alignments of 1317 transcripts could not be improved, and these transcripts were excluded from our analyses (supplementary data file S5, http://dx.doi.org/10.5061/dryad.3c0f1).

Nonrandom distribution of missing data among taxa can inflate statistical support for incorrect tree topologies (*7*). Because we detected a nonrandom distribution of missing data, we only considered data blocks if they contained information from at least one representative of each of the 39 predefined taxonomic groups of undisputed monophyly (table S6). In this representative data set, the extent of missing data was still between 5 and 97.7% in pairwise sequence comparisons, with high percentages primarily because of the data scarcity in some previously published out-group taxa (table S19 and figs. S7 to S10).

We inferred maximum-likelihood phylogenetic trees (Fig. 1) with both nucleotide (second-codon positions only and applying a site-specific rate model) and amino acid–sequence data (applying a protein domain–based partitioning scheme to improve the biological realism of the applied evolutionary models) from the representative data set (*5*) (figs. S21, S22, and S23, A and D). Trees from both data sets were fully congruent. The absence of taxa that cannot be robustly placed on the tree (rogue taxa) in the amino acid–sequence data set and the presence of a few rogue taxa that did not bias tree inference in the nucleotide sequence data set (*5*) indicated a sufficiently representative taxonomic sampling.

To detect confounding signal derived from nonrandom data coverage, we randomized amino acids within taxa, while preserving the distribution of data coverage in the representative data set (*5*). This approach revealed no evidence of biased node support that could be attributed to nonrandom data coverage (*5*) (figs. S11 and S12 and table S20). Phylogenomic data may violate the assumption of time-reversible evolutionary processes, irrespective of what partition scheme one applies, which could lead to incorrect tree estimates and biased node support. Because sections in the amino acid–sequence alignments of the representative data set violating these assumptions were present, we tested whether the observed compositional heterogeneity across taxa biased node support but found no evidence for this (*5*) (fig. S20). We next discarded data strongly violating the assumption of time-reversible evolutionary processes (tables S21 and S22, data files S6 to S8, and figs. S13 to S19). Results from phylogenetic analysis of this filtered data set (*5*) were fully congruent with those obtained from analyzing the unfiltered representative data set. The nucleotide sequence data of the representative data set containing also first and third codon positions strongly violated the assumption of time-reversible evolutionary processes, but still supported largely congruent topologies (fig. S23, B to D). In summary, our phylogenetic inferences are unlikely to be biased by any of the above-mentioned confounding factors.

Our phylogenomic study suggests an Early Ordovician origin of insects (Hexapoda) at ~479 Ma [confidence interval (CI), 509 to 452 Ma] and a radiation of ectognathous insects in the Early Silurian ~441 Ma (CI 465 to 421 Ma) (Figs. 1 and 2). These estimates imply that insects colonized land at roughly the same time as plants (*8*), in agreement with divergence date estimates on the basis of other molecular data (*4*).

The early diversification pattern of insects has remained unclear (*2*, *7*, *9*). We received support for a monophyly of insects, including Collembola and Protura as closest relatives (*10*), and Diplura as closest extant relatives of bristletails (Archaeognatha), silverfish (Zygentoma), and winged insects (Pterygota) (Fig. 1). Furthermore, our analyses corroborate Remipedia, cave-dwelling crustaceans, as the closest extant relatives of insects (*11*, *12*).

A close phylogenetic relationship of bristletails to a clade uniting silverfish and winged insects (Dicondylia) is generally accepted. However, the monophyly of silverfish has been questioned, with the relict *Tricholepidion gertschi* considered more distantly related to winged insects than

[1]Zoologisches Forschungsmuseum Alexander Koenig (ZFMK)/Zentrum für Molekulare Biodiversitätsforschung (ZMB), Bonn, Germany. [2]China National GeneBank, BGI-Shenzhen, China. [3]BGI-Shenzhen, China. [4]Australian National Insect Collection, Commonwealth Scientific and Industrial Research Organization (Australia) (CSIRO), National Research Collections Australia, Canberra, ACT, Australia. [5]Abteilung Arthropoda, Zoologisches Forschungsmuseum Alexander Koenig (ZFMK), Bonn, Germany. [6]Department of Entomology, Rutgers University, New Brunswick, NJ 08854, USA. [7]Department of Biological Sciences, Rutgers University, Newark, NJ 08854, USA. [8]Scientific Computing, Heidelberg Institute for Theoretical Studies (HITS), Heidelberg, Germany. [9]Institut für Spezielle Zoologie und Evolutionsbiologie mit Phyletischem Museum Jena, FSU Jena, Germany. [10]Steinmann-Institut, Bereich Paläontologie, Universität Bonn, Germany. [11]2. Zoologische Abteilung (Insekten), Naturhistorisches Museum Wien, Vienna, Austria. [12]Department of Integrative Zoology, Universität Wien, Vienna, Austria. [13]Institut für Spezifische Prophylaxe und Tropenmedizin, Medizinische Parasitologie, Medizinische Universität Wien (MUW), Vienna, Austria. [14]Manaaki Whenua Landcare Research, Auckland, New Zealand. [15]Center for Advanced Modeling, Emergency Medicine Department, Johns Hopkins University, Baltimore, MD 21209, USA. [16]Biozentrum Grindel und Zoologisches Museum, Universität Hamburg, Hamburg, Germany. [17]Evolutionary Morphology Laboratory, Graduate School of Science and Engineering, Ehime University, Japan. [18]Sugadaira Montane Research Center/Hexapod Comparative Embryology Laboratory, University of Tsukuba, Japan. [19]Land and Water Flagship, CSIRO, Canberra, ACT, Australia. [20]Florida Museum of Natural History, University of Florida, Gainesville, FL 32611, USA. [21]Entomology, Staatliches Museum für Naturkunde Stuttgart (SMNS), Germany. [22]Ecology Evolution and Genetics, Research School of Biology, Australian National University, Canberra, ACT, Australia. [23]National Evolutionary Synthesis Center, Durham, NC 27705, USA. [24]Department of Biological Sciences, Macquarie University, Sydney, Australia. [25]Department für Botanik und Biodiversitätsforschung, Universität Wien, Vienna, Austria. [26]Natural History Museum of Crete, University of Crete, Post Office Box 2208, Gr-71409, Iraklio, and Biology Department, University of Crete, Iraklio, Crete, Greece. [27]Department of Biological Sciences and Feinstone Center for Genomic Research, University of Memphis, Memphis, TN 38152, USA. [28]Centro Universitario de Ciencias Biólogicas y Agropecuarias, Centro de Estudios en Zoología, Universidad de Guadalajara, Zapopan, Jalisco, México. [29]Leibniz Supercomputing Centre of the Bavarian Academy of Sciences and Humanities, Garching, Germany. [30]Institute of Evolutionary Biology and Ecology, Zoology and Evolutionary Biology, University of Bonn, Bonn, Germany. [31]Department of Life Sciences, The Natural History Museum London, London, UK. [32]Abteilung Entomologie, Biozentrum Grindel und Zoologisches Museum, Universität Hamburg, Hamburg, Germany. [33]Fakultät für Informatik, Karlsruher Institut für Technologie, Karlsruhe, Germany. [34]California Academy of Sciences, San Francisco, CA 94118, USA. [35]Department of Entomology, College of Natural Resources and Environment, South China Agricultural University, China. [36]Yokosuka City Museum, Yokosuka, Kanagawa, Japan. [37]Department of Entomology, North Carolina State University, Raleigh, NC 27695, USA. [38]Systematic Entomology, Hokkaido University, Sapporo, Japan. [39]Department of Biology, University of Copenhagen, Copenhagen, Denmark. [40]Princess Al Jawhara Center of Excellence in the Research of Hereditary Disorders, King Abdulaziz University, Jeddah, Saudi Arabia. [41]Macau University of Science and Technology, Avenida Wai Long, Taipa, Macau, China. [42]Department of Medicine, University of Hong Kong, Hong Kong. [43]Department of Ecology, Evolution, and Natural Resources, Rutgers University, New Brunswick, NJ 08854, USA.

*Major contributors.

†Corresponding author. E-mail: xinzhou@genomics.cn (X.Z.), b.misof.zfmk@uni-bonn.de (B.M.), kjer@aesop.rutgers.edu (K.M.K), wangj@genomics.cn (J.W.)

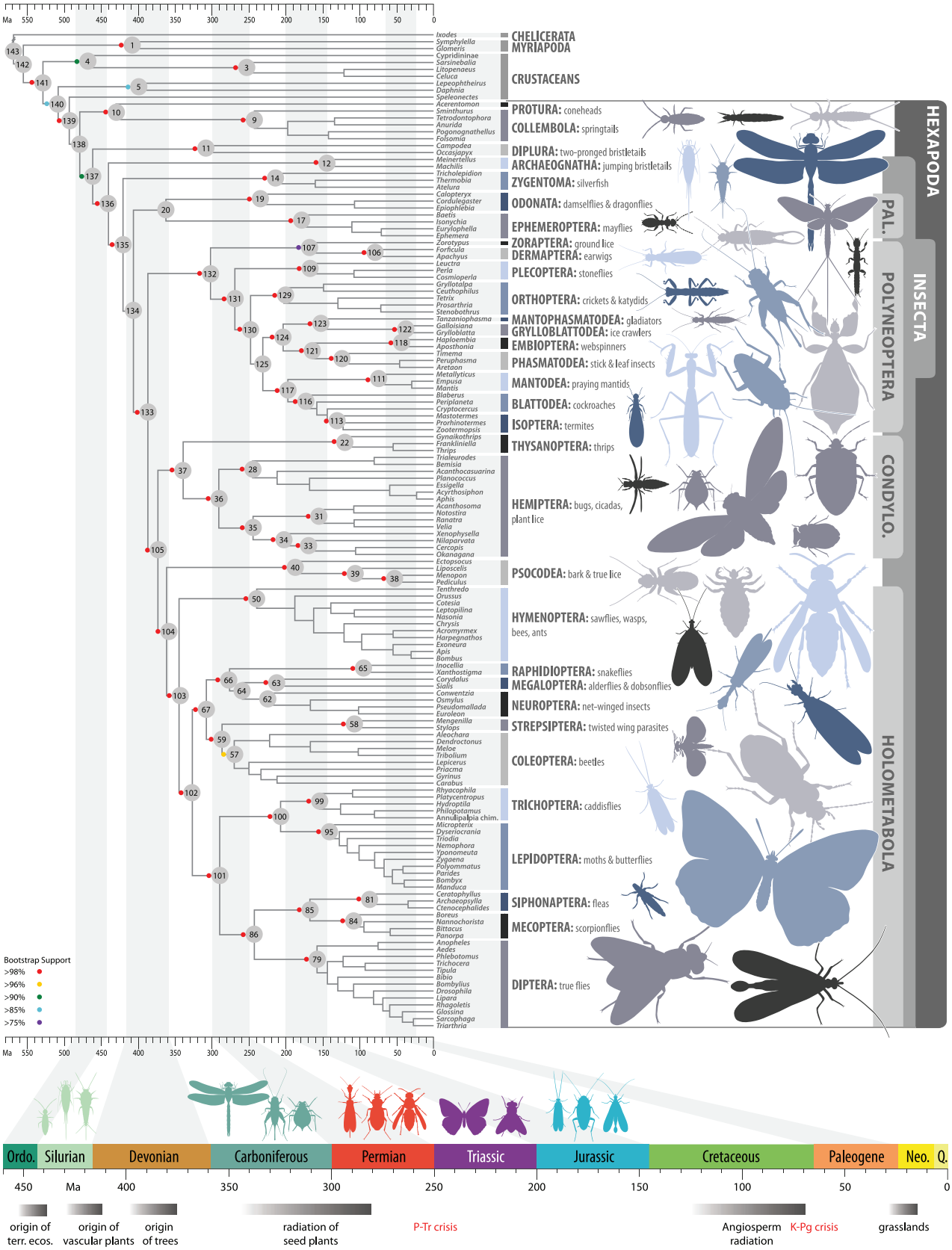


Fig. 1. Dated phylogenetic tree of insect relationships. The tree was inferred through a maximum-likelihood analysis of 413,459 amino acid sites divided into 479 metapartitions. Branch lengths were optimized and node ages estimated from 1,050,000 trees sampled from trees separately generated for 105 partitions that included all taxa (5). All nodes up to orders are labeled with numbers (gray circles). Colored circles indicate bootstrap support (5) (left key). The time line at the bottom of the tree relates the geological origin of insect clades to major geological and biological events. CONDYLO, Condylognatha; PAL, Palaeoptera.

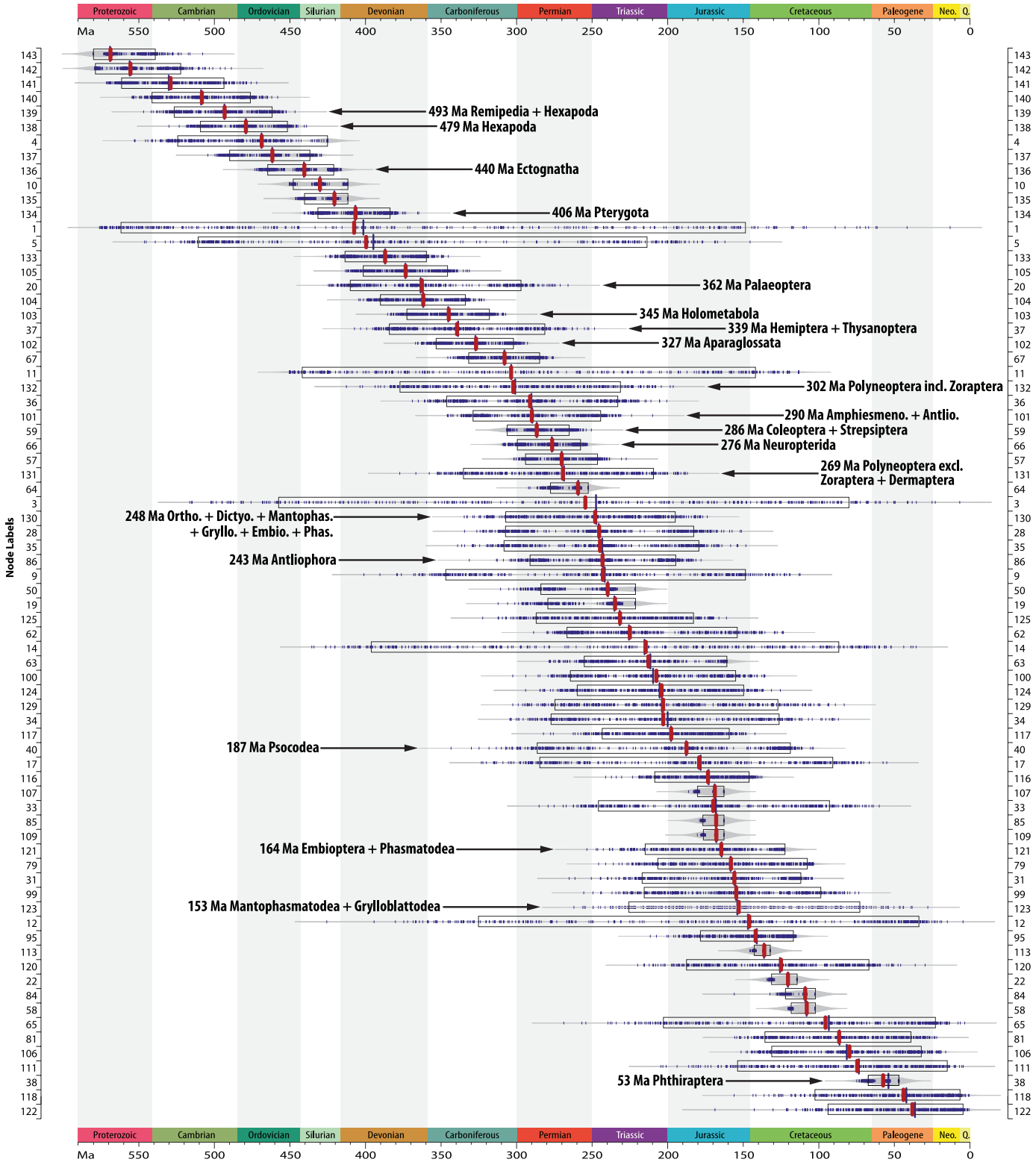


Fig. 2. Sorted ordinal and interordinal node age estimates. For each labeled node (numbers on the left and right of the figure correspond to the node labels in the tree of Fig. 1), the median (red bar), and the range of the upper and lower confidence interval (black rectangle) of age estimates are illustrated. These medians and upper and lower confidence intervals are derived from uniformly sampled trees over all 105 metapartitions (*5*). Additionally, we present medians of age estimates separately derived from each metapartition. Within the bean plot (gray scale), blue bars indicate the distribution of median age estimates, large blue bars indicate the inferred median of medians. All node age estimates refer to the estimated common origin of included species. Stem-lineage representatives can, of course, be older. The maximum root age of the tree was set to 580 Ma to coincide with the oldest Ediacaran fossils (*5*).

other silverfish (*13*). We find that silverfish are monophyletic, consistent with recently published morphological studies (*14*), and estimate that *Tricholepidion* diverged from other silverfish in the Late Triassic (~214 Ma) (Figs. 1 and 2). This result implies parallel and independent loss of the ligamentous head endoskeleton, abdominal styli, and coxal vesicles in winged insects and silverfish (*5*).

The diversification of insects is undoubtedly related to the evolution of flight. Fossil winged insects exist from the Late Mississippian (~324 Ma) (*15*), which implies a pre-Carboniferous origin of insect flight. The description of †*Rhyniognatha* (~412 Ma) from a mandible, potentially indicative of a winged insect, suggested an Early Devonian to Late Silurian origin of winged insects (*3*). Our results corroborate an origin of winged insect lineages during this time period (*16*) (Figs. 1 and 2), which implies that the ability to fly emerged after the establishment of complex terrestrial ecosystems.

Ephemeroptera and Odonata are, according to our analyses, derived from a common ancestor. However, node support is low for Palaeoptera (Ephemeroptera + Odonata) and for a sister group relationship of Palaeoptera to modern winged insects (Neoptera), which indicates that additional evidence, including extensive taxon sampling and the analysis of genomic meta-characters (*17*), will be necessary to corroborate these relationships.

We find strong support for the monophyly of Polyneoptera, a group that comprises earwigs, stoneflies, grasshoppers, crickets, katydids (Orthoptera), Embioptera, Phasmatodea, Mantophasmatodea, Grylloblattodea, cockroaches, mantids, termites, and Zoraptera (*18*–*20*). We estimated the origin of the polyneopteran lineages at ~302 Ma (CI 377 to 231 Ma) in the Pennsylvanian (Figs. 1 and 2), consistent with the idea that at least part of the rich Carboniferous neopteran insect fauna was of polyneopteran origin. Finally, our analyses suggest that the major diversity within living cockroaches, mantids, termites, and stick insects evolved after the Permian mass extinction.

Given that the oldest known fossil hemipterans date to the Middle Pennsylvanian (~310 Ma) (*21*), it had been thought that the stylet marks on liverworts from the Late Devonian (~380 Ma) (*22*) could not have been of hemipteran origin. Our study indicates that true bugs (Hemiptera) and their sister lineage, thrips (Thysanoptera), all of which possess piercing-sucking mouthparts, originated ~373 Ma (CI 401 to 346 Ma), which gives support to the possibility of a hemipteroid origin of Early Paleozoic stylet marks.

True bugs, thrips, bark lice (Psocoptera), and true lice (Phthiraptera) (together called Acercaria) were thought to be the closest extant relatives of Holometabola (Acercaria + Holometabola = Eumetabola) (*10*). However, convincing morphological features and fossil intermediates supporting a monophyly of Acercaria are lacking (*13*). We recovered bark and true lice (Psocodea) as likely closest extant relatives of Holometabola (*5*), which suggests that both groups started to diverge in the Devonian-Mississippian ~362 Ma (CI 390 to 334 Ma) (Figs. 1 and 2). However, this result did not receive support in all statistical tests and, therefore, should be further investigated in future studies that embrace additional types of characters (*17*).

We estimated that the radiation of parasitic lice occurred ~53 Ma (CI 67 to 46 Ma), which implies that they diversified well after the emergence of their avian and mammalian hosts in the Late Cretaceous–Early Eocene and contradicts the hypothesis that parasitic lice originated on feathered theropod dinosaurs ~130 Ma (*23*).

Within Holometabola, our study recovered phylogenetic relationships fully congruent with those suggested in recent studies (*2*, *24*, *25*). Although we estimated the origin of stem lineages of many holometabolous insect orders in the Late Carboniferous, we dated the spectacular diversifications within Hymenoptera, Diptera, and Lepidoptera to the Early Cretaceous, contemporary with the radiation of flowering plants (*21*, *26*). The almost linear increase in interordinal insect diversity suggests that the process of diversification of extant insects may not have been severely affected by the Permian and Cretaceous biodiversity crises (Fig. 2).

With this study, we have provided a robust phylogenetic backbone tree and reliable time estimates of insect evolution. These data and analyses establish a framework for future comparative analyses on insects, their genomes, and their morphology.

REFERENCES AND NOTES

1. The term "insects" is used here in a broad sense and synonymous to Hexapoda (including the ancestrally wingless Protura, Collembola, and Diplura).
2. M. D. Trautwein, B. M. Wiegmann, R. Beutel, K. M. Kjer, D. K. Yeates, *Annu. Rev. Entomol.* **57**, 449–468 (2012).
3. M. S. Engel, D. A. Grimaldi, *Nature* **427**, 627–630 (2004).
4. O. Rota-Stabelli *et al.*, *Curr. Biol.* **23**, 392–398 (2013).
5. Materials and methods are available as supplementary material on *Science* Online.
6. Transcriptome refers to the sequencing of all of the mRNAs of an individual or many individuals present at the time of preservation.
7. E. Dell'Ampio *et al.*, *Mol. Biol. Evol.* **31**, 239–249 (2014).
8. C. C. Labandeira, *Arthro Syst. Phylo.* **64**, 53–94 (2006).
9. K. Meusemann *et al.*, *Mol. Biol. Evol.* **27**, 2451–2464 (2010).
10. W. Hennig, *Die Stammesgeschichte der Insekten* (Kramer, Frankfurt am Main, 1969).
11. With the notable exception of Cephalocarida, for which RNA-sequencing data were unavailable to us.
12. B. M. von Reumont *et al.*, *Mol. Biol. Evol.* **29**, 1031–1045 (2012).
13. N. P. Kristensen, *Annu. Rev. Entomol.* **26**, 135–157 (1981).
14. A. Blanke, M. Koch, B. Wipfler, F. Wilde, B. Misof, *Front. Zool.* **11**, 16 (2014).
15. J. Prokop, A. Nel, I. Hoch, *Geobios* **38**, 383–387 (2005).
16. These estimates are robust whether or not †*Rhyniognatha* (Pragian stage, ~ 412 Ma) is used as a calibration point.
17. O. Niehuis *et al.*, *Curr. Biol.* **22**, 1309–1313 (2012).
18. H. Letsch, S. Simon, *Syst. Entomol.* **38**, 783–793 (2013).
19. K. Ishiwata, G. Sasaki, J. Ogawa, T. Miyata, Z.-H. Su, *Mol. Phylogenet. Evol.* **58**, 169–180 (2011).
20. K. Yoshizawa, *Syst. Entomol.* **36**, 377–394 (2011).
21. A. Nel *et al.*, *Nature* **503**, 257–261 (2013).
22. C. C. Labandeira, S. L. Tremblay, K. E. Bartowski, L. VanAller Hernick, *New Phytol.* **202**, 247–258 (2014).
23. V. S. Smith *et al.*, *Biol. Lett.* **7**, 782–785 (2011).
24. R. G. Beutel *et al.*, *Cladistics* **27**, 341–355 (2011).
25. B. M. Wiegmann *et al.*, *BMC Biol.* **7**, 34 (2009).
26. J. A. Doyle, *Annu. Rev. Earth Planet. Sci.* **40**, 301–326 (2012).

ACKNOWLEDGMENTS

The data reported in this paper are tabulated in the supplementary materials and archived at National Center for Biotechnology Information, NIH, under the Umbrella BioProject ID PRJNA183205 ("The 1KITE project: evolution of insects"). Supplementary files are archived at the Dryad Digital Repository http://dx.doi.org/10.5061/dryad.3c0f1. Funding support: China National GeneBank and BGI-Shenzhen, China; German Research Foundation (NI 1387/1-1; MI 649/6, MI 649/10, RE 345/1-2, BE1789/8-1, BE 1789/10-1, STA 860/4, Heisenberg grant WA 1496/8-1); Austria Science Fund FWF; NSF (DEB 0816865); Ministry of Education, Culture, Sports, Science and Technology of Japan Grant-in-Aid for Young Scientists (B 22770090); Japan Society for the Promotion of Science (P14071); Deutsches Elektronen-Synchrotron (I-20120065); Paul Scherrer Institute (20110069); Schlinger Endowment to CSIRO Ecosystem Sciences; Heidelberg Institute for Theoretical Studies; University of Memphis-FedEx Institute of Technology; and Rutgers University. The authors declare no conflicts of interest.

SUPPLEMENTARY MATERIALS

www.sciencemag.org/content/346/6210/763/suppl/DC1
Materials and Methods
Supplementary Text
Figs. S1 to S27
Tables S1 to S26
Data File Captions S1 to S14
References (*27*–*187*)

17 June 2014; accepted 23 September 2014
10.1126/science.1257570

Multilabel Slide Scanner

The Lamina multilabel slide scanner is a high throughput imaging system designed to help research pathologists to more easily study protein expression and the relationships between disease markers in formalin-fixed, paraffin-embedded tissue sections. This allows research pathologists to gain a deeper understanding of diseases for the development of more effective therapies and treatments. Configured to meet the needs of a larger research facility, the Lamina scanner includes high-speed brightfield and fluorescence imaging modalities along with the proprietary Autofluorescence Reduction Technology. It is designed to reduce interference from autofluorescence—an unwanted byproduct of tissue fixation—and fluorophore cross-talk, in which the signal from one fluorophore bleeds into multiple channels. Both of these effects obscure real signals, which can result in an incorrect assessment of a slide. The Lamina scanner delivers these improvements in real-time during whole-slide scanning, enabling clearer visualization of protein biomarker expression in fluorescently labeled tissues.

PerkinElmer
For info: 877-754-6973
www.perkinelmer.com

Multipurpose X-Ray Diffractometer

SmartLab 3 system is a highly versatile multipurpose X-ray diffractometer with built-in intelligent guidance. Award-winning guidance software recognizes installed components and seamlessly integrates them into data collection and data analysis methods. The cross beam optics module offers permanently mounted, permanently aligned, and user selectable optical geometries for various diffraction experiments. As an example, one can choose a Bragg-Brentano and parallel beam combination for measurements of both powders and thin films without the need for instrument reconfiguration. One could also choose a Bragg-Brentano and focusing transmission combination to measure organic materials in both transmission and reflection modes. The fifth, or in-plane, axis of the SmartLab 3 diffractometer allows the measurement of structures that are in the surface plane of the sample. This enables the measurement of extremely thin films and depth profiling in coatings. The SmartLab 3 system further extends application capability with the next generation HyPix-400 2-D detector.

Rigaku
For info: 610-294-8091
www.rigaku.com



pH/mV Measurement Instruments

While the TruLab 1110 is ideal for routine pH/mV lab measurements where a robust workhorse meter is required, the TruLab 1310 and 1310P (with printer) provides precise lab measurements and automatic Good Laboratory Practice (GLP) documentation, plus a USB interface for data transfer and backup. All TruLab instruments offer autobuffer recognition plus recalibration prompts. The TruLab 1320 and 1320P (with printer) are two-channel instruments with simultaneous measurement of pH, ISE, or Redox. The 1320 series logs calibration information for GLP compliance and has a USB interface for data transfer and backup. In addition, YSI is also introducing the TruLine, IoLine, and Science suite of electrodes for its TruLab product line. The variety of pH and ORP TruLine sensors are compact in design, available as glass or plastic probe bodies, can be ordered with or without temperature and with a refillable option.
YSI Science pH electrodes are proven, highly versatile laboratory electrodes.

Xylem Analytics
For info: 978-778-1010
www.xylemanalytics.com

Mass Spectrometer

The TripleTOF 6600 high-resolution, accurate-mass system brings new power to scientists developing biotherapeutics. Delivering the broad mass and dynamic range required for these compounds, the new instrument offers the unique ability to address biomolecules and their complexities quickly and easily. Together, the TripleTOF 6600 system and BioPharmaView software deliver accurate assay information for protein digests, in a simplified view. The software is designed with a deconvolution feature that allows for comparisons of end results to "gold standard" spectra to determine product quality, making it smarter and more efficient. SWATH Acquisition 2.0 allows researchers to develop simple, universal assays that ensure complete information coverage of their analytes in a fast and automated workflow. Combined with the increased dynamic range of the TripleTOF 6600 System, SWATH 2.0 enables researchers to achieve deeper insight into complex samples.

AB Sciex
For info: 877-740-2129
www.absciex.com

Vapor Sorption Analyzer

The Vstar vapor sorption analyzer includes the Autosorb iQ for micropore analysis and cutting-edge research, the Autosorb 6iSA for high throughput surface area and pore analysis, the Nova for low-cost routine analysis, and the Aquadyne DVS for gravimetric water sorption measurements. The Vstar provides a fast, accurate, and reliable means of obtaining water sorption isotherms on a wide variety of materials, but it doesn't stop there. The Vstar also can measure adsorption isotherms of a variety of organic vapors, providing insight into the materials' resistance to organic vapors, viability as an adsorbent for these vapors in storage or sequestration applications, and information on the chemical properties of these materials. The Vstar is available in one-, two-, three-, or four-station models, each of which is available with a variety of options. The ability to analyze up to four samples simultaneously (on the Vstar 4) provides unprecedented throughput.

Quantachrome Instruments
For info: 800-989-2476
www.quantachrome.com

Electronically submit your new product description or product literature information! Go to www.sciencemag.org/products/newproducts.dtl for more information.

Newly offered instrumentation, apparatus, and laboratory materials of interest to researchers in all disciplines in academic, industrial, and governmental organizations are featured in this space. Emphasis is given to purpose, chief characteristics, and availability of products and materials. Endorsement by *Science* or AAAS of any products or materials mentioned is not implied. Additional information may be obtained from the manufacturer or supplier.

Downloaded from www.sciencemag.org on November 6, 2014

cell sciences®
cytokine center



www.cellsciences.com

Buy one, get one free

Stock up now on select cytokines, growth factors and chemokines.

Order any two vials from this list for just $235
Enter promo code CYT241 when you place your order on-line or mention the promo code to get your discount when calling our toll-free number 888-769-1246.

These recombinant proteins are low endotoxin, carrier-free, highly pure, biologically active and suitable for cell culture and animal studies. Get two of the same item or pick any two different items from the list.* See our web site for complete product specifications.

Browse our web site of recombinant proteins, including hundreds more cytokines, growth factors, chemokines and neurotrophins. Bulk quantities of these proteins are available at competitive pricing. Call or visit our web site for details. Cell Sciences also carries corresponding antibodies and ELISA kits.

Catalog No:	Item:	Size:
CRB100B	Recombinant Human BMP-2	10 µg
CRC400B	Recombinant Human CNTF	20 µg
CRF000B	Recombinant Human FGF-acidic/FGF1	50 µg
CRF001B	Recombinant Human FGF-basic/FGF2	50 µg
CRK300B	Recombinant Human FGF-7/KGF	10 µg
CRG300B	Recombinant Human G-CSF/CSF3	10 µg
CRG100B	Recombinant Human GM-CSF/CSF2	20 µg
CRG101B	Recombinant Mouse GM-CSF/CSF2	20 µg
CRG500B	Recombinant Human GRO-alpha/CXCL1	25 µg
CRG502B	Recombinant Rat GRO-alpha/KC/CXCL1	25 µg
CRI004B	Recombinant Human IFN-alpha 2b	100 µg
CRI000B	Recombinant Human IFN-gamma	100 µg
CRI001B	Recombinant Mouse IFN-gamma	100 µg
CRI002B	Recombinant Rat IFN-gamma	100 µg
CRI500B	Recombinant Human IGF-1	100 µg
CRI100B	Recombinant Human IL-2	50 µg
CRI153B	Recombinant Human IL-10	10 µg
CRI137B	Recombinant Human IL-15	10 µg
CRI162B	Recombinant Human IL-17	25 µg
CRI172B	Recombinant Human IL-21	10 µg
CRI225B	Recombinant Human IL-33	10 µg
CRM151B	Recombinant Human M-CSF/CSF1	10 µg
CRR000B	Recombinant Human RANTES/CCL5	20 µg
CRS000B	Recombinant Human SDF-1 alpha	10 µg
CRS002B	Recombinant Human SDF-1 beta	10 µg
CRT100B	Recombinant Human TNF-alpha	50 µg
CRT192B	Recombinant Mouse TNF-alpha	20 µg
CRV000B	Recombinant Human VEGF 165	10 µg
CRV014B	Recombinant Mouse VEGF 165	10 µg

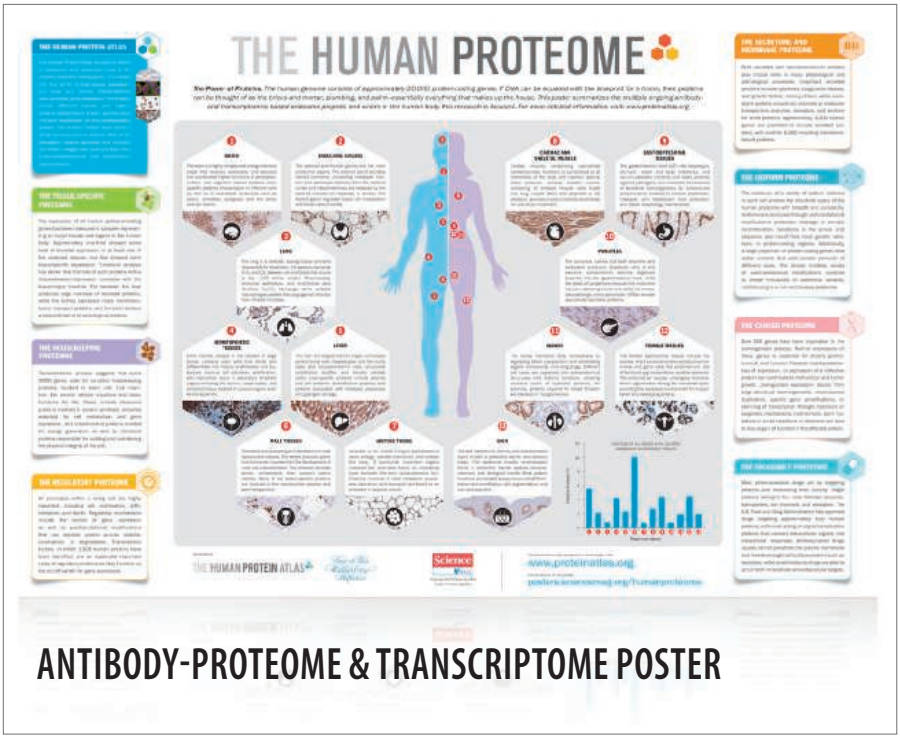
* Good on orders in US and Canada only. This offer may not be combined with other offers or discounts. All products for research use only.

CELL SCIENCES INC • 480 NEPONSET STREET, BUILDING 12A, CANTON, MA 02021 • INFO@CELLSCIENCES.COM
TOLL FREE: (888) 769-1246 • TEL: (781) 828-0610 • FAX: (781) 828-0542 • WEB WWW.CELLSCIENCES.COM

THE HUMAN PROTEOME

presented by the

Human Protein Atlas Project



ANTIBODY-PROTEOME & TRANSCRIPTOME POSTER

THE POWER OF PROTEINS

The human genome consists of approximately 20,000 protein-coding genes. If DNA can be equated with the blueprint for a home, then proteins can be thought of as the bricks and mortar, plumbing, and paint–essentially everything that makes up the house. This poster summarizes the multiple ongoing antibody and transcriptomics-based proteome projects and where in the human body this research is focused.

- Protein Profiling established in a multitude of tissues and cells
- Systematic exploration of human proteome using

Prestige Antibodies®
Powered by ATLAS ANTIBODIES

Learn more and request your free poster copy at:
sigma-aldrich.com/poster

©2014 Sigma-Aldrich Co. LLC. All rights reserved. SIGMA-ALDRICH is a trademark of Sigma-Aldrich Co. LLC, registered in the US and other countries.
Prestige Antibodies is a registered trademark of Sigma-Aldrich Co. LLC.

SIGMA-ALDRICH®

This person is made up of 20,000 unique proteins.

Want to take a closer look?

For the first time a comprehensive database of 13,000,000 annotated images, mapping the human proteins in all major organs and tissues, all in one place. The Human Protein Atlas (HPA) is a fully searchable database that has taken a team of scientists and IT engineers over 1,000 man years to compile. 20,000 protein coding-genes analyzed with transcriptomics and antibody-based profiling down to the single cell level.

A truly unique resource that is completely free with unrestricted access.

Want to take a closer look yourself?
Then why not search for your favourite protein.
Visit **www.proteinatlas.org**.



THE HUMAN PROTEIN ATLAS

Panasonic

Life Science

TwinGuard®

EXPERIENCE TWICE THE SECURITY

30% more

ENERGY SAVINGS

2x Protection

DUAL COMPRESSOR SYSTEMS

VIP® Insulation

UNIFORMITY



Simply **secure.**

Give your samples the ultimate protection of patented Twin Guard® technology –two independent systems can individually sustain ultra-low temperatures in the event of a failure, so you can rest easy knowing your valuable work is in good hands.

Learn more at **us.panasonic-healthcare.com/twinguard**

Discovery powered by precision™

SOLVING THE WORLD'S TOUGHEST HEALTH CHALLENGES TAKES ALL OF US.

It takes the will to find a new way forward. And no one gets there alone.

That's why AbbVie teams with peers, academics, clinical experts and others to take on the most complex health challenges.

Uniting the best of pharma with the boldness of biotech, together we're going beyond conventional thinking to innovate end-to-end approaches that make a real difference.

Starting with science, we arrive at solutions that help millions of patients around the world live better.

abbvie.com/allofus





PEOPLE. PASSION.
POSSIBILITIES.

abbvie

CM-0140-01-0814

AAAS *Travels*

AEGEAN ODYSSEY



April 27–May 11, 2015

Athens • Delphi • Mykonos • Santorini • Knossos • Crete

Explore the cultural heritage of ancient Greece and pay homage to the great Parthenon Temple on the Acropolis. Visit the Oracle at Delphi, against the backdrop of Mt. Parnassos. On Santorini, we'll explore the ancient Akrotiri archaeological site and on Crete we'll unravel the mysteries of the Minoans. Sparkling new museums with dazzling collections from ancient Greece and evening light on the harbors at Mykonos and Chania will enchant us! $4,295 pp + air

For a detailed brochure, call (800) 252-4910
All prices are per person twin share + air

BETCHART EXPEDITIONS Inc.
17050 Montebello Rd, Cupertino, CA 95014
Email: AAASInfo@betchartexpeditions.com
www.betchartexpeditions.com

Join the Conversation!

Twitter is a great way to connect with AAAS members and staff about the issues that matter to you most. Be a part of the discussion while staying up-to-date on the latest news and information about your personal member benefits.

Follow us @AAASmember and join the conversation with #AAAS

AAAS MEMBERCENTRAL
MemberCentral.aaas.org

SCIENCE & DIPLOMACY

A quarterly publication from the AAAS Center for Science Diplomacy

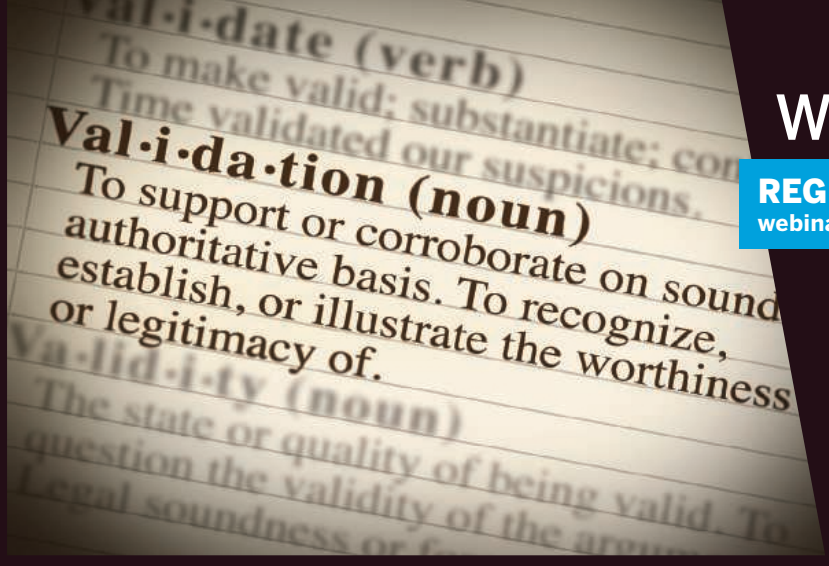
SCIENCE & DIPLOMACY

provides an open access forum for rigorous thought, analysis, and insight to serve stakeholders who develop, implement, or teach all aspects of science and diplomacy. Learn more about the latest ideas in science diplomacy and receive regular updates by following @SciDip on Twitter, liking the quarterly's page on Facebook (www.facebook.com/sciencediplomacy), and registering for free at **www.sciencediplomacy.org/user/register**.



WWW.SCIENCEDIPLOMACY.ORG

AAAS
ADVANCING SCIENCE, SERVING SOCIETY



Webinar

REGISTER NOW!
webinar.sciencemag.org

Antibody validation roundtable

specificity + sensitivity + reproducibility = validation

Wednesday, December 3, 2014

12 noon Eastern, 9 a.m. Pacific, 5 p.m. UK, 6 p.m. Central Europe

Concerns about incorrectly or insufficiently characterized antibodies employed in biomedical research have been raised by recent reports of nonreproducible research studies. Reproducibility issues have resulted in loss of time, resources, and scientific reputation, with publication retractions occurring in certain cases. This webinar will highlight the challenges surrounding how antibody specificity affects reproducibility in biomedical research and introduce viewers to the key requirements for proper antibody validation. Panelists, including a journal editor, an academic researcher, a pharmaceutical company investigator, and an antibody supplier will share their views and unique perspectives. This forum is intended to serve as one step along an ongoing path toward building consensus on best practices for antibody validation and possible guidelines for reporting of antibody-based data in research manuscripts.

By registering in advance for this webinar you can pose your specific questions for consideration by the panelists.

During the webinar, the panelists will:

- Describe how antibody data reproducibility issues impact academia, industry, and publishing
- Explain key requirements for proper antibody validation
- Discuss who is responsible, with potential impacts on research resources.

Speakers



Marcia McNutt, Ph.D.
Science/AAAS
Washington, DC



David Rimm, M.D., Ph.D.
Yale University School of Medicine
New Haven, CT



Christopher Kerfoot, Ph.D.
Mosaic Laboratories
Lake Forest, CA



Craig Thompson, Ph.D.
Cell Signaling Technology
Danvers, MA

Webinar sponsored by

Cell Signaling TECHNOLOGY®

Brought to you by the *Science*/AAAS Custom Publishing Office

Science AAAS

@SciMagWebinars

Multilabel Slide Scanner

The Lamina multilabel slide scanner is a high throughput imaging system designed to help research pathologists to more easily study protein expression and the relationships between disease markers in formalin-fixed, paraffin-embedded tissue sections. This allows research pathologists to gain a deeper understanding of diseases for the development of more effective therapies and treatments. Configured to meet the needs of a larger research facility, the Lamina scanner includes high-speed brightfield and fluorescence imaging modalities along with the proprietary Autofluorescence Reduction Technology. It is designed to reduce interference from autofluorescence—an unwanted byproduct of tissue fixation—and fluorophore cross-talk, in which the signal from one fluorophore bleeds into multiple channels. Both of these effects obscure real signals, which can result in an incorrect assessment of a slide. The Lamina scanner delivers these improvements in real-time during whole-slide scanning, enabling clearer visualization of protein biomarker expression in fluorescently labeled tissues.

PerkinElmer
For info: 877-754-6973
www.perkinelmer.com

Multipurpose X-Ray Diffractometer

SmartLab 3 system is a highly versatile multipurpose X-ray diffractometer with built-in intelligent guidance. Award-winning guidance software recognizes installed components and seamlessly integrates them into data collection and data analysis methods. The cross beam optics module offers permanently mounted, permanently aligned, and user selectable optical geometries for various diffraction experiments. As an example, one can choose a Bragg-Brentano and parallel beam combination for measurements of both powders and thin films without the need for instrument reconfiguration. One could also choose a Bragg-Brentano and focusing transmission combination to measure organic materials in both transmission and reflection modes. The fifth, or in-plane, axis of the SmartLab 3 diffractometer allows the measurement of structures that are in the surface plane of the sample. This enables the measurement of extremely thin films and depth profiling in coatings. The SmartLab 3 system further extends application capability with the next generation HyPix-400 2-D detector.

Rigaku
For info: 610-294-8091
www.rigaku.com



pH/mV Measurement Instruments

While the TruLab 1110 is ideal for routine pH/mV lab measurements where a robust workhorse meter is required, the TruLab 1310 and 1310P (with printer) provides precise lab measurements and automatic Good Laboratory Practice (GLP) documentation, plus a USB interface for data transfer and backup. All TruLab instruments offer autobuffer recognition plus recalibration prompts. The TruLab 1320 and 1320P (with printer) are two-channel instruments with simultaneous measurement of pH, ISE, or Redox. The 1320 series logs calibration information for GLP compliance and has a USB interface for data transfer and backup. In addition, YSI is also introducing the TruLine, IoLine, and Science suite of electrodes for its TruLab product line. The variety of pH and ORP TruLine sensors are compact in design, available as glass or plastic probe bodies, can be ordered with or without temperature and with a refillable option.
YSI Science pH electrodes are proven, highly versatile laboratory electrodes.

Xylem Analytics
For info: 978-778-1010
www.xylemanalytics.com

Mass Spectrometer

The TripleTOF 6600 high-resolution, accurate-mass system brings new power to scientists developing biotherapeutics. Delivering the broad mass and dynamic range required for these compounds, the new instrument offers the unique ability to address biomolecules and their complexities quickly and easily. Together, the TripleTOF 6600 system and BioPharmaView software deliver accurate assay information for protein digests, in a simplified view. The software is designed with a deconvolution feature that allows for comparisons of end results to "gold standard" spectra to determine product quality, making it smarter and more efficient. SWATH Acquisition 2.0 allows researchers to develop simple, universal assays that ensure complete information coverage of their analytes in a fast and automated workflow. Combined with the increased dynamic range of the TripleTOF 6600 System, SWATH 2.0 enables researchers to achieve deeper insight into complex samples.

AB Sciex
For info: 877-740-2129
www.absciex.com

Vapor Sorption Analyzer

The Vstar vapor sorption analyzer includes the Autosorb iQ for micropore analysis and cutting-edge research, the Autosorb 6iSA for high throughput surface area and pore analysis, the Nova for low-cost routine analysis, and the Aquadyne DVS for gravimetric water sorption measurements. The Vstar provides a fast, accurate, and reliable means of obtaining water sorption isotherms on a wide variety of materials, but it doesn't stop there. The Vstar also can measure adsorption isotherms of a variety of organic vapors, providing insight into the materials' resistance to organic vapors, viability as an adsorbent for these vapors in storage or sequestration applications, and information on the chemical properties of these materials. The Vstar is available in one-, two-, three-, or four-station models, each of which is available with a variety of options. The ability to analyze up to four samples simultaneously (on the Vstar 4) provides unprecedented throughput.

Quantachrome Instruments
For info: 800-989-2476
www.quantachrome.com

Electronically submit your new product description or product literature information! Go to www.sciencemag.org/products/newproducts.dtl for more information.

Newly offered instrumentation, apparatus, and laboratory materials of interest to researchers in all disciplines in academic, industrial, and governmental organizations are featured in this space. Emphasis is given to purpose, chief characteristics, and availability of products and materials. Endorsement by *Science* or AAAS of any products or materials mentioned is not implied. Additional information may be obtained from the manufacturer or supplier.



This is the start of something big.

Science Advances | AAAS

SIGNIFICANT RESEARCH, GLOBAL IMPACT

Introducing *Science Advances* – the new, online-only, open-access journal from *Science* and AAAS. Find out how you can be among the first authors published at **scienceadvances.org.**

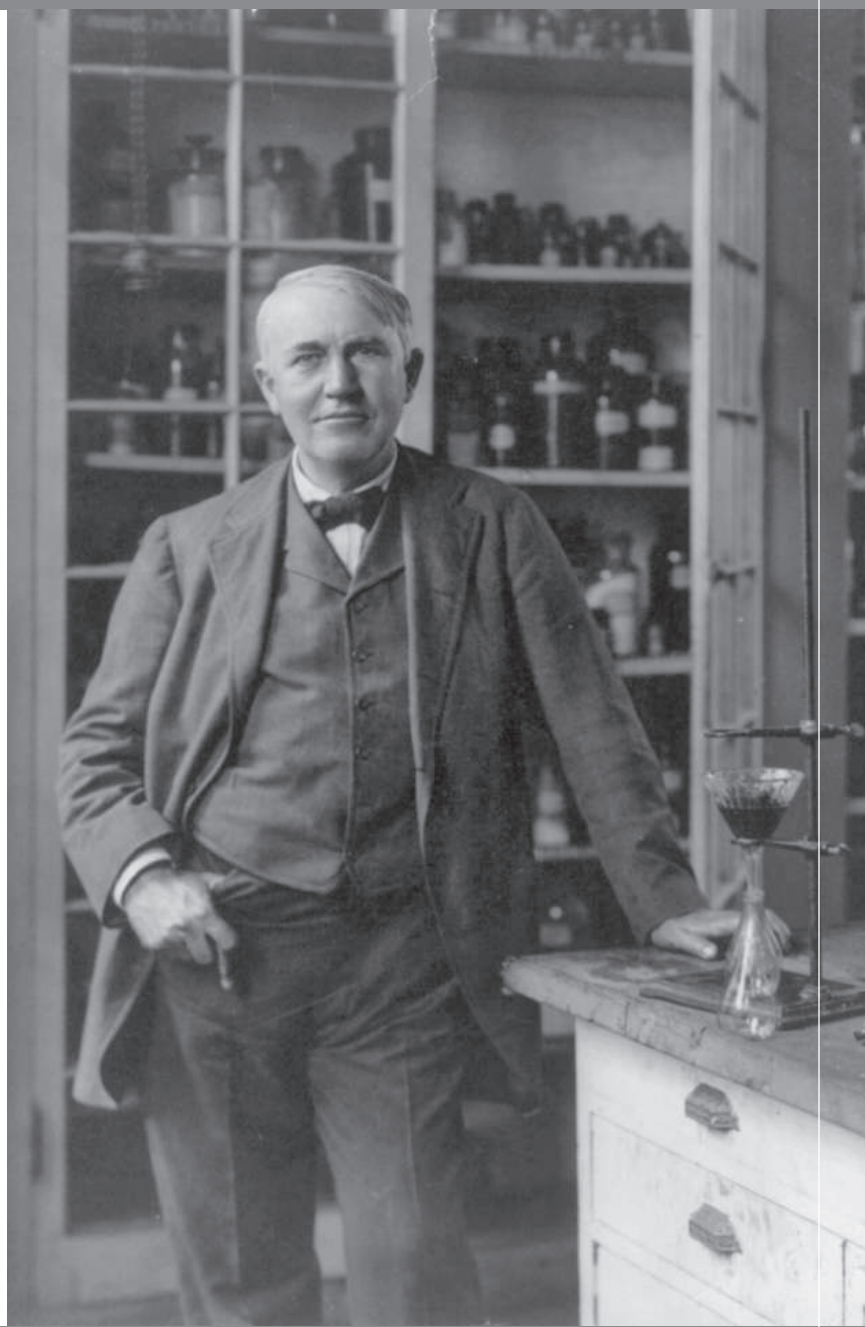
WHAT DO YOU AND THOMAS EDISON HAVE IN COMMON?

AAAS.

By investing in AAAS you join Thomas Edison and the many distinguished individuals whose vision led to the creation of AAAS and our world-renowned journal, *Science,* more than 150 years ago.

Like Edison, you can create a legacy that will last well into the future through planned giving to AAAS. By making AAAS a beneficiary of your will, trust, retirement plan, or life insurance policy, you make a strong investment in our ability to advance science in the service of society for years to come.

To discuss your legacy planning, contact Juli Staiano, Director of Development, at (202) 326-6636, or jstaiano@aaas.org, or visit www.aaas.org/1848 for more information.



1848 SOCIETY
AAAS

"I feel great knowing that I will leave behind a legacy that will be channeled through the AAAS. It also means a lot to me to be able to honor my late parents, too."

–PETER ECKEL
Member, 1848 Society and AAAS Member since 1988



Have your cake and eat it too
R&D Systems Luminex® Assays

Get the **most plexible analytes** and enjoy
the **accuracy and precision you expect**
from R&D Systems products.

Find out how to win a cake for your lab.
rndsystems.com/LabCake

R&D systems™
a bio-techne brand

Luminex is a registered trademark of Luminex

ScienceCareers online @sciencecareers.org



Science Careers Advertising

For full advertising details, go to ScienceCareers.org and click For Employers, or call one of our representatives.

Tracy Holmes
Worldwide Associate Director
Science Careers
Phone: +44 (0) 1223 326525

THE AMERICAS

E-mail: advertise@sciencecareers.org
Fax: 202 289 6742

Tina Burks
Phone: 202 326 6577

Nancy Toema
Phone: 202 326 6578

Marci Gallun
Sales Administrator
Phone: 202 326 6582

Online Job Posting Questions
Phone: 202 312 6375

EUROPE / INDIA / AUSTRALIA / NEW ZEALAND / REST OF WORLD

E-mail: ads@science-int.co.uk
Fax: +44 (0) 1223 326532

Axel Gesatzki
Phone: +44 (0) 1223 326529

Sarah Lelarge
Phone: +44 (0) 1223 326527

Kelly Grace
Phone: +44 (0) 1223 326528

JAPAN

Katsuyoshi Fukamizu (Tokyo)
E-mail: kfukamizu@aaas.org
Phone: +81 3 3219 5777

Hiroyuki Mashiki (Kyoto)
E-mail: hmashiki@aaas.org
Phone: +81 75 823 1109

CHINA / KOREA / SINGAPORE / TAIWAN / THAILAND

Ruolei Wu
Phone: +86 186 0082 9345
E-mail: rwu@aaas.org

All ads submitted for publication must comply with applicable U.S. and non-U.S. laws. *Science* reserves the right to refuse any advertisement at its sole discretion for any reason, including without limitation for offensive language or inappropriate content, and all advertising is subject to publisher approval. *Science* encourages our readers to alert us to any ads that they feel may be discriminatory or offensive.

ScienceCareers
FROM THE JOURNAL SCIENCE AAAS

ScienceCareers.org

Science Careers

Cernet

"《科学》职业" 已经与Cernet/赛尔互联开展合作。中国大陆的高校可以直接联系Cernet/赛尔互联进行国际人才招聘。



请访问 Sciencecareers.org/CER 点得联系信息。

招募学术精英，《科学》是您的不二之选 Science



AAAS is here – helping scientists achieve career success.

Every month, over 400,000 students and scientists visit ScienceCareers.org in search of the information, advice, and opportunities they need to take the next step in their careers.

A complete career resource, free to the public, *Science* Careers offers a suite of tools and services developed specifically for scientists. With hundreds of career development articles, webinars and downloadable booklets filled with practical advice, a community forum providing answers to career questions, and thousands of job listings in academia, government, and industry, *Science* Careers has helped countless individuals prepare themselves for successful careers.

As a AAAS member, your dues help AAAS make this service freely available to the scientific community. If you're not a member, join us. Together we can make a difference.

To learn more, visit
aaas.org/plusyou/sciencecareers

AAAS + U = Δ

ACCEPT THE NAVY CHALLENGE

Become a member of an elite research and development community involved in basic and applied scientific research and advanced technological development for tomorrow's Navy.

NAVAL RESEARCH LABORATORY

Listed below are career opportunities at the Naval Research Laboratory (NRL) for Senior Scientists to perform a variety of theoretical research, technology development, analytical studies, and consultative services.

Senior Scientist for Advanced EO Imaging Sensors
ST-0850/0855
Washington, DC
VA#: NW408XX-00-1201614K9924794S

Serves as the technical expert in the fields of large area focal plane arrays, advanced multi-and hyperspectral sensors, large format reconnaissance sensors, data acquisition and processing for multi-spectral sensors, real time signal processing for non-uniformity correction and image optimization, multi-spectral infrared visualization of composite imagery, and super-resolution techniques for image sequences. Conducts and leads a broad-based, multidisciplinary research program pushing the frontiers of advanced EO Imaging Sensors with particular emphasis on the development of Infrared Focal Plane Arrays (IRFPA) and their use in Navy and DoD reconnaissance, surveillance, and threat detection sensors. As a distinguished scientist and recognized leader in his/her field the incumbent will be called upon to brief DoD senior officials regarding Laboratory research efforts in the above areas, to serve as liaison between NRL, the Navy and other national and international organizations, and to consult on important scientific and programmatic issues.

Senior Scientist for Biosensors and Biomaterials
ST-0401
Washington, DC
VA#: NW40401-00-1201603K9924613S

Conducts independent research and leads teams of scientist in the area of biosensors and biomaterials. Suggests, influences, and directs the research and development efforts of these teams. Advises on problem exploration and definition, plans experimental strategies, interprets data, and formulates new thrusts. Understands the state-of-the-art in biosensors research and incorporates the exploration of the most critical R&D questions into in-house research initiatives. Identifies how new biosensors and biomaterials can be used for the Navy, Department of Defense, and the Nation. Independent research is expected to focus on controlling the function of biological recognition molecules (natural or genetically engineered) on surfaces and using advanced optical techniques for signal transduction. Results of research are expected to lead to the discovery of a variety of biosensor approaches pertinent to a wide range of applications. As principal investigator for several biosensors projects, the incumbent is responsible for development of important new scientific areas and maintaining high quality scientific performance. Active technical consultant on government committees. Responsible for the scientific and technical oversight of a variety of university and industry collaborations, both formal and informal, in the US and abroad.

Applicants should be recognized as national/international authorities in the above areas of research, and should have demonstrated the scientific vision and organizational skills necessary to bring long term, multi-faceted research programs to successful completion. Salaries range from $120,749 to $181,500 per year. To apply, go to **www.usajobs.gov,** log in and enter the vacancy announcement number. Contact Annemarie Mycka, **Annemarie.mycka@nrl.navy.mil** or Ginger Kisamore, **ginger.kisamore@nrl.navy.mil** if additional information is needed. **Emailed application material CANNOT be accepted**. Vacancy announcements close on **November 28, 2014.**

NAVAL RESEARCH LABORATORY
WASHINGTON, DC

NAVY IS AN EQUAL OPPORTUNITY EMPLOYER

ScienceCareers online @sciencecareers.org

Director, Fudan University Institute of Genetics

Fudan University has initiated a search for the Director of Fudan University Institute of Genetics (FUIG). The successful candidate will also be appointed as an endowed professor in the School of Life Sciences (SLS). The FUIG was founded by the late Professor C.C. Tan (Tan Jiazhen) in 1961 and is recognized as a leading institute of genetic studies in China and function to promote academic research and interactions in genetics and molecular biology. Since the founding of the SLS in 1986, the members of the FUIG have also been members of the SLS, which has six departments, including the Department of Genetics and Genetic Engineering. Current research areas at SLS include human genetics, molecular analysis of human diseases, animal and plant developmental genetics, microbial and population genetics, statistical and evolutionary genetics, genomics and bioinformatics.

Applicants should be geneticists who are full professors or holders of equivalent positions in the general area of genetics, and have demonstrated excellence in research and training in the analysis of genetic mechanisms and/or the use of genetic methods to study one or more of the following topics: human genetics and diseases, cell and developmental biology, epigenetic regulation, protein modifications, and other molecular/cellular regulatory mechanisms. Candidates who also have excellent communication skills and administrative experiences are preferred.

In addition to continuing active research, the Director of FUIG will help to strength the FUID as a forum for promoting scientific exchange and interactions, as a platform for building collaboration and developing joint grants, and as a training base for young geneticists. The Director of FUID will be a member of a core group of faculty members who will help to shape the future development of genetics, as well as life sciences in general, at Fudan. The successful candidate will receive generous start-up funds, competitive compensation, and housing subsidy. In addition, the Director of FUID will also be a member of the State Key Laboratory of Genetic Engineering at Fudan, with state-of-art core facilities, and will have the opportunity to participate in the recently established Collaborative Innovation Center for Genetics and Development, which supports collaborations that address major questions in genetics regarding complex relationships between genomes and phenomes.

Review of applicants will begin on December 1, 2014, and the position remains open until filled. For more information, please contact Ms. Xiaohua Liang (liangxh@fudan.edu.cn). Interested candidates should send a CV with educational history, work positions, research experiences and expertise, and a list of publications, a statement of further development in genetics at Fudan, and a statement of research interests.

Faculty Positions in Experimental Biophysics

華東師範大學 EAST CHINA NORMAL UNIVERSITY

The State Key Laboratory of Precision Spectroscopy East China Normal University, Shanghai, China

The State Key Laboratory of Precision Spectroscopy at East China Normal University (Shanghai, China) was established in 2007, and has significantly developed various optical techniques on the development of high precision, high sensitivity, and high resolution in atomic and molecular physics. The Laboratory is significantly expanding the current research scope and we recently established a Center for Laser and Computational Biophysics, a new initiative to build an internationally visible research center in modern biophysics with integration of both experimental and theoretical efforts. The Center is currently at the initial stage and invites applications for a number of faculty positions to begin in the fall of 2015 (or earlier) at the Associate or Full Professor level in experimental biophysics. Applicants should have a Ph.D. degree, preferably with postdoctoral experience in a closely related field, and a clear record of research accomplishments. The successful candidates will be expected to develop world-class research programs and teach classes at both undergraduate and graduate levels. The University will provide attractive annual salary, start-up fund, housing allowance and other benefits.

All applicants should send a cover letter, a curriculum vitae with a publication list, a research proposal (3-5 pages) and a statement of teaching interest in a single pdf file by Dec. 1, 2014 to Ms. Ling Wang, the State Key Laboratory of Precision Spectroscopy, East China Normal University, Shanghai 200062, China through e-mail to: wangling@admin.ecnu.edu.cn. Please also arrange three reference letters directly to the above e-mail address. Applications after the deadline could be reviewed until the positions are filled.

For more infomation, please visit http://www.lps.ecnu.edu.cn/

西南交通大学 Southwest Jiaotong University

Southwest Jiaotong University, P.R.China Anticipates Your Working Application

Southwest Jiaotong University (SWJTU), founded in 1896, situates itself in Chengdu, the provincial capital of Sichuan. It is a national key multidisciplinary "211" and "985 Feature" Projects university directly under the jurisdiction of the Ministry of Education, featuring engineering and a comprehensive range of study programs and research disciplines spreading across more than 20 faculties and institutes/centers. Boasting a complete Bachelor-Master-Doctor education system with more than 2,500 members of academic staff, our school also owns 2 first-level national key disciplines, 2 supplementary first-level national key disciplines (in their establishment), 15 first-level doctoral programs, 43 first-level master programs, 75 key undergraduate programs, 10 post-doctoral stations and more than 40 key laboratories at national and provincial levels.

Our university is currently implementing the strategy of "developing and strengthening the university by introducing and cultivating talents". Therefore, we sincerely look forward to your working application.

More information available at http://www.swjtu.edu.cn/

I. Positions and Requirements

A.High-level Leading Talents

It is required that candidates be listed in national top talents programs such as ***Program of Global Experts, Top Talents of National Special Support Program, "Chang Jiang Scholars", China National Funds for Distinguished Young Scientists and National Award for Distinguished Teacher.***

Candidates are supposed to be no more than 50 years old. The limitation could be extended in the most-needed areas of disciplinary development.

Candidates who work in high-level universities/institutes and reach the above requirements are supposed to be no more than 45 years old.

B. Young Leading Scholars

Candidates are supposed to be listed in or qualified to apply for the following programs:

•National Thousand Young Talents Program

•The Top Young Talents of National Special Support Program(Program for Supporting Top Young Talents)

•Science Foundation for the Excellent Youth Scholars

Candidates should have good team spirit and leadership, outstanding academic achievements, broad academic vision and international cooperation experience and have the potential of being a leading academic researcher.

C. Excellent Young Academic Backbones

Candidates under 40 years old are expected to graduate from high-level universities/institutes either in China or other countries. Those who are professors, associate professors and other equal talents from high-level universities/institutes overseas could be employed as professors and associate professors as well.

D. Excellent Doctors and Post Doctoral Fellows

Candidates under 35 years old are supposed to be excellent academic researchers from high-level universities either in China or other countries.

II. Treatments

The candidates will be provided with competitive salaries and welfares that include settling-in allowance, subsidy of rental residence, start-up funds of scientific research, assistance in establishing scientific platform and research group as well as international-level training and promotion . As for outstanding returnees, we can offer further or specific treatments that can be discussed personally.

III . Contact us:

Contacts: Ye ZENG & Yinchuan LI Telephone number: 86-28-66366202 Email: *talent@swjtu.edu.cn*

Address: Human Resources Department of SWJTU, the western park of high-tech zone, Chengdu, Sichuan, P.R.China, 611756

http://www.swjtu.edu.cn/











Hiring Professors at All Ranks at South University of Science and Technology (SUSTC)Shenzhen, China

The South University of Science and Technology (SUSTC) invites applications and nominations for all ranks of tenured and tenure-track faculty members in the Division of Science, Division of Engineering and Division of Management & Finance.

SUSTC, officially established in April 2012, is a public institution funded by the municipal of Shenzhen, a special economic zone city in southern China. The University is accredited by the Ministry of Education, China and is a pioneer in higher education reform in China. Set on five hundred acres of wooded landscape in the picturesque Nanshan (South Mountain) area, the new campus offers an idyllic environment suitable for learning and scholarship. SUSTC engages in basic and problem-solving research of lasting impact to benefit society and mankind.

The Division of Science, Division of Engineering, and the Division of Management & Finance wish to hire faculty members at all ranks. Key areas include but not limited to: *Neural and Cognitive Sciences, Biology and Gene Engineering, Modern Physics, Control and Modification of Materials, Nanoscience and Nanotechnology, Mathematics and Applied Mathematics, Molecular Chemistry and Catalysis, Large-Scale Computational Research, Robotics and Artificial Intelligence, Information Systems and Electronic Engineering, Modern Cities and Future Developments, Energy Sciences and Technology, Environmental Sciences, Financial Mathematics and Management Sciences.* The Divisions especially encourage research that requires a multi-disciplinary approach. Experienced researchers whose interests do not fall within the above areas are invited to suggest new areas of research. **Cluster hiring is possible, with senior members accompanied by junior members in a group.**

The teaching language at SUSTC is English or Putonghua. The choice is made by the instructor. As we expect an international faculty, the majority of teaching materials and reference books will be in English and many classes will be conducted in English. With a very high faculty-to-student ratio, SUSTC is committed to delivering a student-centered education and encourages students to develop their innovative spirits. Students at junior and senior years are expected to participate in research in the Research Centers.

The University offers competitive salaries, fringe benefits including medical insurance, retirement and housing subsidy. Leading Professors, Chair Professors and Professors will be appointed with tenure. Associate Professors and Assistant Professors will be offered tenure-track contracts.

Please visit our website to apply: http://talent.sustc.edu.cn/en/. All applications should include a CV and a detailed list of publications with Research ID. **Those interested in cluster hiring should send CVs and publication lists with Research ID as a group.** Evaluations will commence immediately and appointments will be made on a continuous basis. Additional information on SUSTC is available on the University homepage **http://www.sustc.edu.cn.**

Qualified applicants are also encouraged to apply for the Recruitment Program of Global Expert ("Thousand Talents Program") through SUSTC. Successful applicants will get extra research fund and living allowance from the government. Additional information is available through email inquiry or **http://talent.sustc.edu.cn/.**

If you have any questions, please feel free to contact us at **hiring@sustc.edu.cn.**



ScienceCareers online @sciencecareers.org
OPPORTUNITIES IN CHINA

WASHINGTON STATE UNIVERSITY

Faculty Positions Available
Position 1: Antimicrobial Resistance: Ecology, Epidemiology, and Evolution
Position 2: Antimicrobial Resistance: Surveillance and Epidemiology

These are permanent full-time faculty positions in the Paul G. Allen School for Global Animal Health (www.globalhealth.wsu.edu) at Washington State University. Rank is at the level of Assistant, Associate or full Professor; position may be tenured, tenure-track, or clinical track depending on qualifications and scholarly focus. Residency in the U.S. is not a requirement for these positions.

Position 1: Antimicrobial Resistance: Ecology, Epidemiology, and Evolution
Required Qualifications: • A doctoral degree (PhD, DrPH, DVM, MD or equivalent). • 2 years post-doctoral research experience in epidemiological modeling. • Evidence of research publication in high impact international journals.
Preferred Qualifications: • Record of modeling and testing interventions. • Collaboration with state, national, and/or international health organizations. • Record of work with and travel in low- and middle-income countries. • Successful record of teaching at the graduate and/or professional medical levels.
• Success in working in multidisciplinary collaborative programs is strongly desired.

Position 2: Antimicrobial Resistance: Surveillance and Epidemiology
Required Qualifications: • Doctoral degree (PhD, DrPH, DVM, MD or equivalent). • 2 years post-doctoral research experience in epidemiological modeling. • Evidence of research publication in high impact international journals.
Preferred Qualifications: • Record of applying active surveillance approaches to resistance determinants and/or pathogens. • Collaboration with state, national, and/or international health organizations. • Record of work with and travel in low- and middle-income countries. • Successful record of teaching at the graduate and/or professional medical levels. • Success in working in multidisciplinary collaborative programs is strongly desired.

To apply for this position, please visit **https://www.wsujobs.com**, you are required to submit a letter of application, curriculum vitae, research statement, and the names and addresses of three references.

WSU is an Affirmative Action/Equal Opportunity Educator & Employer and supports diversity in the workplace. WSU employs only US citizens and lawfully authorized non-US citizens. WSU is committed to providing access and reasonable accommodation for individuals with disabilities.

Memorial Sloan-Kettering Cancer Center

2015 Position
Postdoctoral Fellow/Faculty in Germline Cancer Genomics

The Clinical Genetics Service in the Department of Medicine at Memorial Sloan Kettering Cancer Center has an opening for a post-doctoral fellow or laboratory track faculty level applicant. The focus of the laboratory is on use of next generation genomic tools to discover novel cancer predisposition genes/alleles (see e.g. PMID: 24013638; PMID: 23544012). Studies will be conducted using computational analysis of primary exome- or genome- level germline data in cancer-affected kindreds/cohorts using family based, linkage, population based analytical strategies. Prior bench experience in molecular biology is desirable.

A curriculum vitae should be sent to **Kenneth Offit, M.D., MPH, Chief, Clinical Genetics Service, Memorial Sloan-Kettering Cancer Center, 1275 York Avenue, Box 192, New York, NY 10065**; e-mail: **offitk@mskcc.org**.

Memorial Sloan-Kettering Cancer Center is an Equal Opportunity Employer with a strong commitment to enhancing the diversity of its faculty and staff. Women and applicants from diverse racial, ethnic and cultural backgrounds are encouraged to apply.

GRU GEORGIA REGENTS UNIVERSITY | Medical College of Georgia

Assistant, Associate, or Full Professor of Neuroscience
Department of Neuroscience and Regenerative Medicine

Georgia Regents University (GRU) is accepting applications for an Assistant, Associate, or Full Professor position (tenure-track or tenured) in the Department of Neuroscience and Regenerative Medicine. Candidates should have a PhD or MD; postdoctoral experience; interests in neural development, synaptic plasticity, or disorders of the central or peripheral nervous systems; and a strong record of research accomplishments. Faculty members are expected to establish or have cutting edge research programs and participate in teaching medical and graduate students. Appointment to an endowed chair may be possible for senior, highly qualified individuals. GRU is a state supported academic medical center located in a historic city with outstanding recreational and lifestyle opportunities.

Apply online at **http://www.gru.edu/jobs/university/**. Reference job opening **ID: 00004987**. Submit a CV, statement of current/future research interests, and contact information for three references to: **Dr. Darrell Brann, c/o Deenie Cerasuolo (dcerasuo@gru.edu)**. Applications will be received until the position is filled.

GRU is an EEO/AA/Equal Access Employer.



AAAS is here – promoting universal science literacy.

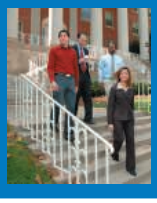
In 1985, AAAS founded Project 2061 with the goal of helping all Americans become literate in science, mathematics, and technology. With its landmark publications *Science for All Americans* and *Benchmarks for Science Literacy*, Project 2061 set out recommendations for what all students should know and be able to do in science, mathematics, and technology by the time they graduate from high school. Today, many of the state standards in the United States have drawn their content from Project 2061.

As a AAAS member, your dues help support Project 2061 as it works to improve science education. If you are not yet a member, join us. Together we can make a difference.

To learn more, visit
aaas.org/plusyou/project2061

AAAS + U = Δ

Director, National Institute of Neurological Disorders and Stroke, National Institutes of Health





The NIH is the center of medical and behavioral research for the Nation ----making essential medical discoveries that improve health and save lives.

Are you an exceptional candidate who can provide leadership to one of the preeminent institutes for Neuroscience research in the world?? Are you at that point in your career where you're ready to "give back"? This position offers a unique opportunity to serve as the chief visionary for the Institute, actively engaging others to create a shared vision for the purpose and direction of the organization in its dedication to conduct, foster, and support research, and research training, on hundreds of individually identified neurological and muscle disorders, which in the aggregate afflict more than 50 million citizens. The Director, NINDS, develops Institute goals, priorities, policies, and program activities, and keeps the Director, NIH abreast of NINDS developments, accomplishments, and needs as they relate to the overall mission of the NIH. S/he is responsible for managing a high-level complex organization and demonstrates integrity and fairness, adhering in work and behavior to the highest ethical and scientific research standards. The mission of NINDS is to support research that increases understanding of life processes and lays the foundation for advances in disease diagnosis, treatment, and prevention.

We are looking for applicants with a Ph.D., M.D., or comparable doctorate degree in a health sciences field plus senior-level scientific experience and knowledge of research programs in one or more scientific areas related to the biomedical research enterprise who have a commitment to excellence and the energy, enthusiasm, and innovative thinking necessary to lead a dynamic and diverse organization. Applicants should be known and respected within their profession, both nationally and internationally, as individuals of outstanding scientific competence.

The successful candidate for this position will be appointed at a salary commensurate with his/her qualifications. Full Federal benefits will be provided including leave, health and life insurance, long-term care insurance, retirement, and savings plan (401k equivalent).

If you are ready for an exciting leadership opportunity, please see the detailed vacancy announcement at http://www.jobs.nih.gov (under Executive Jobs).
Applications must be received by 11:59p.m. ET, December 8, 2014.

NINDS, NIH, AND DHHS ARE EQUAL OPPORTUNITY EMPLOYERS.

PRINCETON Neuroscience INSTITUTE

C V Starr Fellowships in Neuroscience

The Princeton Neuroscience Institute aims to recruit several exceptional individuals for our CV Starr Fellowships in Neuroscience. These are individuals who are expecting or have recently obtained a PhD degree in neuroscience or areas relevant to neuroscience (molecular biology, psychology, computer science, engineering, physics, or mathematics). Please note that previous experience in neuroscience is not required.

The PNI focuses on interdisciplinary research in neuroscience, spanning from molecular, cellular and genetic approaches to systems and human cognitive neuroscience. PNI houses state of the art facilities for experimental research in all of these areas, as well as advanced computational resources that support theoretical and quantitative approaches to neuroscience.



The CV Starr Fellowship program provides a generous salary and a modest annual research budget. Fellows are encouraged to pursue independent research with the guidance and mentorship of one or more core faculty members in the Institute. We are particularly interested in projects that bridge the research programs of multiple laboratories. Fellows also have the opportunity to teach in our Institute programs.

For more information about the Institute, see http://www.princeton.edu/pni/.

Applications should be submitted online at **https://jobs.princeton.edu/** (requisition **#1400754**). Candidates must submit a CV, a list of publications, a statement of research interests and goals, and the contact information for three references. Finalists will be invited to Princeton to present a talk concerning their current research. This position is subject to the University's background check policy.

Princeton University is an Equal Opportunity Employer and all qualified applicants will receive consideration for employment without regard to race, color, religion, sex, national origin, disability status, protected veteran status, or any other characteristic protected by law.



ScienceCareers online @sciencecareers.org

UNIVERSITY OF CALIFORNIA
UCRIVERSIDE

COMPUTATIONAL SYSTEMS BIOLOGIST

The Department of Botany and Plant Sciences at the University of California, Riverside seeks outstanding candidates for an open Computational Systems Biologist position at the rank of Assistant Professor. We are interested in candidates involved in research in systems biology, using computational approaches or a combination of both experimental and computational approaches. A Ph.D. in a relevant discipline is required including several years of postdoctoral research. The successful candidate will hold an academic appointment in the Department of Botany and Plant Sciences with the option of a secondary cooperating faculty appointment in a quantitative department such as statistics, computer science, engineering or related. The candidate will also join the innovative and multidisciplinary Institute for Integrative Genome Biology (IIGB) which connects theoretical and experimental researchers from different departments in Life, Physical and Mathematical Sciences, Medicine, Engineering and various campus based Centers. The IIGB is organized around a 10,000 sq. ft. suite of Instrumentation Facilities that serve as a centralized, shared-use resource for faculty, staff and students, offering advanced tools in bioinformatics, microscopy, proteomics and genomics. Its bioinformatic component is equipped with a modern high-performance compute (HPC) infrastructure. This position will include an appointment in the Agricultural Experiment Station, which includes the opportunities to conduct research and outreach relevant to the mission of the California Agricultural Experiment Station (http://cnas.ucr.edu/about/anr/).

Qualified candidates are expected to have excellent publication and research records in computational systems biology or related areas, such as bioinformatics or computational genome biology. The research program should be heavily focused on involving modern high-throughput data, especially from next generation sequencing technologies. An additional requirement is a strong commitment to teaching in computational systems biology. Review of applications will begin **November 7, 2014** and continue until the position is filled. Interested individuals should: (1) submit a *curriculum vitae*, (2) provide a statement of research, and (3) three letters of reference. A teaching statement is strongly recommended. Please submit your applications through the AP Recruit job link: **https://aprecruit.ucr.edu/apply/JPF00230**

The University of California is an Equal Opportunity/Affirmative Action/ Disability/Veterans Employer.

STANFORD UNIVERSITY DEPARTMENT OF CHEMICAL AND SYSTEMS BIOLOGY

The Department of Chemical and Systems Biology at Stanford University School of Medicine invites applications for a tenure-track position at the **ASSISTANT PROFESSOR** level. We are particularly interested in candidates with a strong interdisciplinary record in the broad areas of chemical biology, systems biology, and/or cellular and molecular biology in normal and disease states. Stanford offers an outstanding environment for creative interdisciplinary biomedical research. The main criterion for appointment in the University Tenure Line is a major commitment to research and teaching. For more information on our department, please visit: **http://chemsysbio.stanford.edu/**.

Candidates should have a Ph.D. and/or M.D. degree and postdoctoral research experience. Applications should include a cover letter addressed to Tobias Meyer, Ph.D., Search Committee Chair; a curriculum vitae, publication list, description of future research plans, and at least 3 letters of reference. All materials should be submitted online to Academic Jobs Online at **https://academicjobsonline.org/ajo/jobs/4602**.

To ensure full consideration, please submit your applications by **December 1, 2014**. Late applications may be considered. Questions should be addressed to **Kathy Johnson, FAA,** at **csbsearch@stanford.edu**.

Stanford University in an Equal Opportunity Employer and is committed to increasing the diversity of its faculty. It welcomes nominations of and applications from women, members of minority groups, protected veterans and individuals with disabilities, as well as from others who would bring additional dimensions to the university's research, teaching and clinical missions.

Berkeley
University of California

ASSISTANT or ASSOCIATE PROFESSOR OF METABOLIC BIOLOGY

The Department of Nutritional Sciences and Toxicology, at the University of California, Berkeley, seeks an assistant or associate professor (nine-month tenure-track, or tenured) with an expected start of July 1, 2015.

We expect the appointee to develop/have developed a vigorous, independent research program investigating metabolic biology, metabolic regulation, disorders and/or functions of nutrients, phytochemicals, and/or toxicants, related to disease. Applicants should have a bioscience Ph.D. or M.D., or equivalent degree, strong productivity and a record of excellence in experimental biology at the time of application. The appointee will have access to Ph.D. students in multiple interdepartmental programs. The appointee also will contribute to educating undergraduates studying metabolic and nutritional biology, and/or molecular toxicology. Numerous opportunities exist for interactions with colleagues at UCB and in the Bay Area.

For more information and to apply, visit **http://apptrkr.com/534076**

The closing date for this search is: December 4, 2014. The application deadline has been extended from its original date; please do not re-apply if an application has already been submitted. Send questions to nstsearch@berkeley.edu. For additional information about the Department, the graduate programs and the campus visit http://nst.berkeley.edu, and http://berkeley.edu.

EOE

JOHNS HOPKINS
KRIEGER SCHOOL of ARTS & SCIENCES

Johns Hopkins Bloomberg Distinguished Professorship in Evolutionary Genomics

The Johns Hopkins University is searching for an outstanding senior scientist in the area of Evolutionary Genomics for an endowed chair as a Bloomberg Distinguished Professor. This position will be held jointly between the Department of Biology (Kreiger School of Arts and Sciences) and the Institute for Genetic Medicine (JHU School of Medicine).

Applicants should currently be at the level of senior Associate Professor or Full Professor, and should have a documented track record of accomplishment and creativity using modern Genomic, Genetic, and/or Computational approaches to study questions of Evolutionary Biology. Areas of interest include, but are not limited to: evolution of developmental regulatory mechanisms, organ systems and traits; evolution of chromosomes, genome organization and epigenetic mechanisms; microbial or viral evolution and host/parasite interactions; human origins; origins of multicellularity; the evolution of behavior; evolutionary and population genetic theory.

Candidates should submit a detailed CV along with a one-page statement of past accomplishments and a one-page statement of current and future interests to apply.interfolio.com/27067. All applications will be kept strictly confidential until later stages of the review, when we will specifically ask to be allowed to seek outside recommendations. Review of applications will begin December 1st and the search will remain open until the appropriate candidate is identified.

Applications from women and minority candidates are especially encouraged. Johns Hopkins University is an equal opportunity employer and does not discriminate on the basis of race, color, gender, religion, age, sexual orientation, national or ethnic origin, disability, marital status, veteran status, or any other occupationally irrelevant criteria. The university promotes affirmative action for minorities, women, disabled persons, and veterans.

COLUMBIA UNIVERSITY
IN THE CITY OF NEW YORK

The 2015 Louisa Gross Horwitz Prize for Biology or Biochemistry

The Louisa Gross Horwitz Prize was established under the will of the late S. Gross Horwitz through a bequest to Columbia University and is named to honor the donor's mother. Louisa Gross Horwitz was the daughter of Dr. Samuel David Gross (1805-1889), a prominent surgeon of Philadelphia and author of the outstanding *Systems of Surgery* who served as President of the American Medical Association.

Each year since its inception in 1967, the Louisa Gross Horwitz Prize has been awarded by Columbia University for outstanding basic research in the fields of biology or biochemistry. The purpose of this award is to honor a scientific investigator or group of investigators whose contributions to knowledge in either of these fields are deemed worthy of special recognition.

The Prize consists of an honorarium and a citation which are awarded at a special presentation event. Unless otherwise recommended by the Prize Committee, the Prize is awarded annually. Dr. James P. Allison, University of Texas MD Anderson Cancer Center was the 2014 awardee.

QUALIFICATIONS FOR THE AWARD

The Prize Committee recognizes no geographical limitations. The Prize may be awarded to an individual or a group. When the Prize is awarded to a group, the honorarium will be divided among the recipients, but each member will receive a citation. Preference will be given to work done in the recent past.

Nominations must be submitted electronically at: **http://www.cumc.columbia.edu/research/horwitz-prize**

All communications and materials must be written in the English language.

Re-nomination(s) are by invitation only.

Self-nominations are not permitted.

Nominations should include:

1) A summary, no more than 500 words long, of the research on which this nomination is based.
2) A summary, no more than 500 words long, of the significance of this research in the fields of biology or biochemistry.
3) A brief biographical sketch of the nominee, including positions held and awards received by the nominee.
4) A listing of up to ten of the nominee's most significant publications relating to the research noted under item 1.
5) A copy of the nominee's curriculum vitae.

Deadline date: January 30, 2015

THE UNIVERSITY OF ARIZONA CANCER CENTER

Postdoctoral Research Associate

The position is in the laboratory of Dr. Andrew Kraft, Director of the University of Arizona Cancer Center. This NCI funded project is dedicated to understanding the role of Pim protein kinase in regulating transformation. The research will focus on identifying the protein kinase pathway interacting partners, signal transduction pathway, and potential substrates using protein biochemistry and mass spectrometry. Validation will be done using knock-out and knock-in mice, cell culture and a novel tissue recombination assay (*Can Res* **72:**294, 2012; *PNAS* **108:**528, 2011) . Model systems to be analyzed include T-cell acute leukemia (T-ALL) and prostate cancer. The applicant should have a very strong background in protein chemistry, molecular and cellular biology, experience with transgenic animals, and strong interest in translational research.

This position is available immediately and salary is commensurate with experience. Please submit a letter of interest, curriculum vitae, and the names of three references.

Applicants can apply on-line at
www.uacareers.com/56768

Andrew S. Kraft, M.D.
Director,
University of Arizona Cancer Center

The University of Arizona is an EEO/AA - M/W/D/V Employer.

Robert S. Langer Family and Friends Professorship
Dept. of Biomedical Engineering – Cornell University

Cornell is a community of scholars, known for intellectual rigor and engaged in deep and broad research, teaching tomorrow's thought leaders to think otherwise, care for others, and create and disseminate knowledge with a public purpose.

The Department of Biomedical Engineering at Cornell University invites applications for the Robert S. Langer Family and Friends Professorship. The department seeks exceptional full professor candidates who will dramatically enhance research and teaching in the department, develop synergies with current areas of departmental strength, and embrace the department's vision of a quantitative, multi-scale approach to applying engineering solutions to problems in human health.

Candidates are expected to currently have an internationally recognized program of research and teaching in biomedical engineering. The department has five areas of research emphasis: biomaterials and drug delivery; biomedical mechanics; nanobiotechnology; imaging and instrumentation; and cellular and tissue engineering. Exceptional candidates who add to or complement these areas will be given serious consideration. Considerable institutional resources are available for the support of the successful applicant's research program and a competitive start-up package can be expected.

Cornell BME bridges between engineering and physical sciences and the biological and medical sciences. It values interdisciplinary projects and actively promotes interactions with Weill Cornell Medical College, College of Veterinary Medicine, and basic engineering and biological sciences. Cornell hosts numerous centers, including Physical Sciences-Oncology Center on the Microenvironment & Metastasis, Weill Institute for Cell & Molecular Biology, Nanobiotechnology Center, Cornell Nanofabrication Facility, and Cornell Center for Materials Research.

Submit applications to: **https://academicjobsonline.org/ajo/jobs/4890**. Questions may be sent to: **cornellbmesearch@cornell.edu, Larry Bonassar, Chair, Search Committee, 607-255-938**1.

Cornell University is an innovative Ivy League university and a great place to work. Our inclusive community of scholars, students and staff impart an uncommon sense of larger purpose and contribute creative ideas to further the university's mission of teaching, discovery and engagement. Located in Ithaca, NY, Cornell's far-flung global presence includes the medical college's campuses on the Upper East Side of Manhattan and in Doha, Qatar, as well as the new CornellNYC Tech campus to be built on Roosevelt Island in the heart of New York City.

Diversity and Inclusion are a part of Cornell University's heritage. We're an employer and educator recognized for valuing AA/EEO, Protected Veterans, and Individuals with Disabilities.

ScienceCareers online @sciencecareers.org

ScienceCareers online @sciencecareers.org

WESTERN MICHIGAN UNIVERSITY

Tenure Track Faculty Position
Fish Biologist

The Department of Biological Sciences and the Environmental and Sustainability Studies Program at Western Michigan University seek applications for a jointly-appointed tenure-track position with specialization in Fish Biology at the rank of Assistant/Associate Professor beginning in Fall 2015, pending budgetary approval. A Ph.D. and relevant post-doctoral experience are required. Candidates with expertise in any area of fish ecology, evolutionary biology, ecophysiology, and ecotoxicology are encouraged to apply. The successful candidate will participate in a new interdisciplinary undergraduate Freshwater Science and Sustainability major, establish an extramurally funded research program, participate in the training of Master's and Ph.D. students, and serve on departmental and university committees. As part of regular teaching duties (2-3 courses per year), some teaching in an online or hybrid format will be required in collaboration with the Great Lakes Water Studies Institute at Northwestern Michigan College in Traverse City, MI (https://www.nmc.edu/resources/water-studies/). The Institute has excellent research facilities on Lake Michigan available to the candidate.

Information concerning the Biological Sciences Department's and the Environmental and Sustainability Studies Program's faculty and programs can be obtained at www.wmich.edu/biology/ and http://www.wmich.edu/environment, respectively. Western Michigan University is a learner centered, discovery driven university with high research activity, provides Master's and Ph.D. degrees, and offers a unique opportunity for individuals seeking a balanced research and teaching career. Applicants should visit **www.wmich.edu/hr/jobs** to apply. To apply please send letter of application, curriculum vitae, statements of research interests and teaching philosophy, and have three letters of reference sent to **Maarten Vonhof, Ph.D., Fish Biologist Search Committee, Department of Biological Sciences, Room 3441 Wood Hall, Western Michigan University, Kalamazoo, MI 49008-5410**. Applications are due **December 31, 2014**, but will be considered until position is filled.

WMU is an Equal Opportunity/Affirmative Action Employer. Minorities, women, veterans, individuals with disabilities and all other qualified individuals are encouraged to apply.

Faculty Position in Neuroscience
Department of Physiology Northwestern University
Feinberg School of Medicine

A tenure-track position is open for full-time faculty in neuroscience, from the assistant to full professor rank. Candidates performing interdisciplinary neuroscience research, utilizing innovative techniques to investigate fundamental issues of neural function ranging from cellular/molecular to systems/behavioral levels should apply. The scientific excellence of the candidate is more important than the particular area of research. Applicants should have an outstanding record of research that adds to existing departmental strengths in sensorimotor function, learning and memory, and pain perception. Candidates seeking appointment at the associate or full professor level should have substantial research productivity and a history of grant support and academic service. Northwestern has a large neuroscience community consisting of over 150 faculty members, located not only in the Physiology department but in a variety of departments on both our Chicago and Evanston campuses, providing many opportunities for collaboration. The successful applicants will also have the opportunity to participate in graduate and medical education.

Applicants should send (as a single PDF) a cover letter, curriculum vitae, a two-page description of research accomplishments and plans, and the names and contact information for three references by email to **neuroscience@northwestern.edu**

Northwestern University is an Affirmative Action, Equal Opportunity Employer. Women and diversity candidates are encouraged to apply. Hiring is contingent upon eligibility to work in the United States.

Worcester Polytechnic Institute

Associate or Full Professor, Biophysical Chemistry

The Department of Chemistry and Biochemistry (CBC) at Worcester Polytechnic Institute (WPI, Worcester, MA) invites applications for a faculty position at the Associate or Full Professor level in Biophysical Chemistry beginning Fall 2015. The department offers undergraduate and graduate (MS and PhD) degrees in Chemistry and Biochemistry. CBC is integral to WPI's ongoing major life science research initiative and seven new faculty at the assistant, associate and full professor level were recently hired.

The candidate will be a dynamic scholar and teacher, with a strong track record of creativity and an internationally highly visible research program studying the physical properties of biosensors, biomaterials or biological systems. The successful candidate will have a strong record of continued funding, high impact publications, and a solid presence in the scientific community.

Interested candidates should submit a cover letter, a curriculum vitae, statement of research and teaching interests, achievements and plans, and a list of three references. Applicants are asked to apply electronically by visiting Careers at WPI: **http://apptrkr.com/538652** Review of applications will be conducted on a rolling basis and continue until the position is filled. For additional information, please contact Dr. Arne Gericke (agericke@wpi.edu)

WPI

To enrich education through diversity,
WPI is an affirmative action, equal opportunity employer.

Join the Conversation!

Twitter is a great way to connect with AAAS members and staff about the issues that matter to you most. Be a part of the discussion while staying up-to-date on the latest news and information about your personal member benefits.

Follow us @AAASmember and join the conversation with #AAAS

AAAS MEMBERCENTRAL
MemberCentral.aaas.org

HelmholtzZentrum münchen
German Research Center for Environmental Health

DZIF

Helmholtz Zentrum München invites applications for the position of a

Research Group Leader
Host control of viral latency and reactivation

We are looking for an individual with an established, successful research program on the immune response of viral infection in the human host. The successful candidate is expected to conduct research on the cellular immune control of latent and active viral infection in humans, translating the results into novel approaches for virus-specific immunotherapy and immunodiagnostics. Topics of particular interest will be investigations on the diversity and efficiency of antiviral T cell responses, viral immunomodulatory mechanisms and their influence on T cell function and diversity, and the integration of adaptive and innate cellular responses in control of human infection. The development of a collaborative, translational research program together with local clinical institutions is strongly encouraged.

The successful candidate is expected to strengthen the core research area Infection and Immunity of the Helmholtz Zentrum München and the Munich branch of the German Center for Infection Research (DZIF). The position will be part of the Research Unit Gene Vectors and located at the Großhadern campus of Helmholtz Zentrum München.

The position is initially limited to December 31, 2015 and can be extended subject to financing by DZIF.

Applications should include detailed documentation in English (CV, certificates, credentials, list of publications, selected reprints and a short statement describing the impact of the candidate's research profile and research strategy, and current third-party funding). Applications should be submitted by November 14, 2014 to: Prof. Dr. Wolfgang Hammerschmidt, E-mail: hammerschmidt@helmholtz-muenchen.de, Helmholtz Zentrum München Deutsches Forschungszentrum füt Gesundheit und Umwelt (GmbH), Department of gene vectors, Marchioninistr. 25, D-81377 München Großhadern.

BOSTON UNIVERSITY

Junior & Senior Faculty Positions in Biomedical Engineering

The Boston University Department of Biomedical Engineering (BU BME) invites applications for a **senior faculty position** and a **tenure-track junior faculty** position in the areas of Synthetic Biology, Cellular Engineering and/or Neuroengineering. BU BME is one of the nation's top-ranked departments, attracting exceptional graduate and undergraduate students. We have strengths in numerous research areas, boast a wealth of research resources and facilities, with strong ties to the BU School of Medicine, as well as other top medical research centers in the Boston area. As a Coulter Translational Partnership school, faculty can translate research advances into new applications that impact society.

The senior position will hold a tenured appointment in BME, must hold a PhD in an appropriate area, must have a strong history of external funding and be internationally recognized for distinguished contributions related to synthetic biology and/or cellular engineering. The successful candidate will be expected to maintain a robust, extramurally funded research program building on existing strengths in synthetic biology and cellular engineering. The junior position will hold a tenure-track appointment in BME, must hold a PhD in an appropriate area, have postdoctoral experience and show potential for leading an independent and vibrant research program. BU also places high value on quality teaching.
For more information, please visit:
www.bu.edu/eng; www.bu.edu/bme

Applicants should submit a brief letter of interest, statement of accomplishments and plans, a current CV and contact information of three references to:

Senior: https://academicjobsonline.org/ajo/jobs/4644
Junior: https://academicjobsonline.org/ajo/jobs/4645

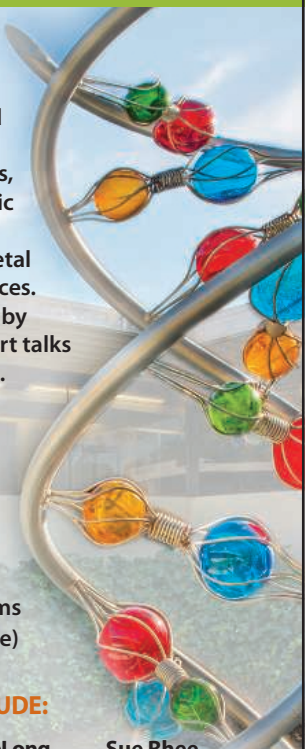
Boston University is an equal opportunity employer and all qualified applicants will receive consideration for employment without regard to race, color, religion, sex, national origin, disability status, protected veteran status, or any other characteristic protected by law. We are a VEVRAA Federal Contractor.

WE INVITE YOU TO JOIN LEADERS IN ENERGY AND ENVIRONMENTAL GENOMICS AT:

THE 10TH ANNUAL
DOE Joint Genome Institute Genomics of Energy & Environment Meeting

March 24 - 26, 2015 in Walnut Creek, CA

REGISTER HERE, NOW:
http://bit.ly/JGI-UMX



TOPICS INCLUDE:

Microbial genomics, fungal genomics, metagenomics, and plant genomics; genome editing, secondary metabolites, pathway engineering, synthetic biology, high-throughput functional genomics, and societal impact of technological advances. State-of-the-art presentations by invited speakers as well as short talks selected from poster abstracts.

WORKSHOPS INCLUDE:

Fungal Genomics • Genomic Technologies • Phytozome for Comparative Plant Genomics • Sample QC Workshop • Synthetic Biology • DOE Systems Biology Knowledgebase (KBase)

CONFIRMED SPEAKERS INCLUDE:

Leif Andersson *Uppsala University*
Joan Bennett *Rutgers University*
Steve Briggs *UC San Diego*
Tom Brutnell *Danforth Center*
Mark Burk *Genomatica*
Atul Butte *Stanford University*
Rick Cavicchioli *University of New South Wales*
Michelle Chang *UC Berkeley*
Edward DeLong *University of Hawaii*
Jack Gilbert *Argonne National Laboratory*
Barbara Jasny *Science Magazine*
Shawn Kaeppler *Great Lakes Bioenergy Research Center*
Sophien Kamoun *Sainsbury Lab*
Susan Lynch *UC San Francisco*
Francis Martin *INRA*
Sue Rhee *Carnegie Institution for Science*
Antonis Rokas *Vanderbilt University*
Blake Simmons *Joint BioEnergy Institute*
Rotem Sorek *Weizmann Institute*
Jerry Tuskan *BioEnergy Science Center*
Stephen Wright *University of Toronto*

JGI JOINT GENOME INSTITUTE
UNITED STATES DEPARTMENT OF ENERGY

ScienceCareers online @sciencecareers.org

POSITIONS OPEN

UC San Diego

FACULTY POSITIONS
UC San Diego Department of Bioengineering

The Department of Bioengineering in the Jacobs School of Engineering at the University of California, San Diego (UCSD) is inviting applications for one or more positions at the **ASSISTANT PROFESSOR, ASSOCIATE PROFESSOR,** or **FULL PROFESSOR** levels (tenure-track or tenured faculty positions).

A Ph.D. or advancement to candidacy in bioengineering or related engineering disciplines is required for these positions. Successful applicants will be expected to teach undergraduate courses in UCSD's Bioengineering, Biotech, and/or BioSystems Engineering Major tracks and graduate courses in Bioengineering and establish a vigorous program of high-quality federally funded bioengineering research.

To obtain more information or submit your application materials, go to **website: https://apol-recruit.ucsd.edu/apply** and apply to **position number 10-852.**

STAFF ASSOCIATE
Columbia University

Position is immediately available for a full-time Senior Staff Associate in the Department of Anesthesiology, College of Physicians and Surgeons of Columbia University. Our research focuses on the effect of carbon monoxide and other environmental agents on the developing mouse brain. The candidate will be expected to have proficiency with breeding mice and caring for rodent colonies, and experience working with live animals in a wet laboratory environment. The position requires working with newborn mouse pups, exposing them to a range of different gases in a controlled setting. Experience with brain perfusion and tissue collection, mitochondrial isolation, enzyme activity assays, immunohistochemistry, western blotting, light and fluorescence microscopy is desired.

Bachelor's degree in chemistry, biology, or physics is required or equivalent in education, training, and experience. An advanced degree, such as a Master's, is also desired. A minimum of eight years of related experience is required. Knowledge of various related laboratory procedures and techniques is preferred.

Ability to work with minimal supervision is expected. Applicants must be able to develop and learn new techniques as required for these studies. Qualified applicants will also be expected to coordinate day-to-day laboratory operations and supervise and teach other laboratory personnel such as technicians, fellows, residents, and students on an as-needed basis.

Please visit our online application site at **website: https://academicjobs.columbia.edu/applicants/Central?quickFind=60043** to submit your application and for further information about this position.

Columbia University is an Equal Opportunity/Affirmative Action Employer.

Stop searching for a job; start your career.

ScienceCareers
FROM THE JOURNAL SCIENCE AAAS

ScienceCareers.org

Download your free copy today.

ScienceCareers.org/booklets



From technology specialists to patent attorneys to policy advisers, learn more about the types of careers that scientists can pursue and the skills needed in order to succeed in nonresearch careers.

ScienceCareers
FROM THE JOURNAL SCIENCE AAAS

Online Career Fairs

December 10, 2014



For careers in science, there's only one Science

Meet recruiters without leaving your lab or desk!

Science Careers is excited to bring you an easy, efficient and powerful way to connect with employers from all over... all in one place. This virtual event allows you to queue up to visit with representatives from any companies you are interested in during the event hours.

Features and Benefits of Attending this Event

- No travel required—you can login from anywhere
- Queues tell you how many people are in line ahead of you and how long you will be waiting so you can better manage your time
- Login before the event to learn more about participating employers
- Employers can see your resume while you are talking to them



ScienceCareers
FROM THE JOURNAL SCIENCE AAAS

For more information, visit:
ScienceCareers.org/onlinecareerfair

By **Vijaysree Venkatraman**

Reflections of a woman pioneer

In her career as a physicist at the Massachusetts Institute of Technology (MIT) in Cambridge, Mildred "Millie" Dresselhaus, who is now 83, has researched the electronic structure of carbon in its myriad forms. Dresselhaus was in Oslo for the Kavli awards ceremony this year. *Science* Careers caught up with her for a chat. This interview has been edited for brevity and clarity.

Q: Tell us about your early years at MIT.
A: I earned my Ph.D. from the University of Chicago in 1958 and married a fellow physicist that year. We both joined the research staff of MIT's Lincoln Laboratory in 1960. In 1967, I became a visiting professor at MIT. Thanks to a fund established by Abby Rockefeller Mauzé, the eldest of the six Rockefeller siblings, I was soon hired full time.

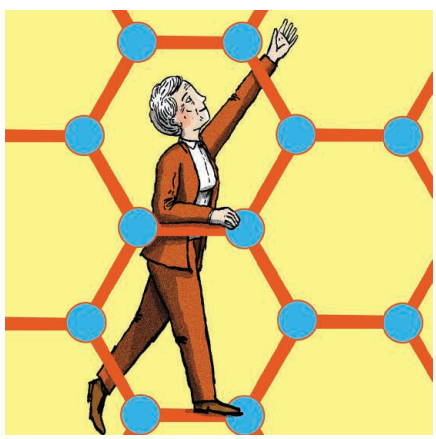
We had very few women professors, particularly in the sciences, and for the most part, they didn't have children. My daughter was born before I joined the institute. I took a total of 5 days off for the birth of my three sons.

Q: Were there many women students on campus?
A: Only 4% of all undergraduates were female, a large fraction in biology—far fewer in physics, chemistry, or engineering. Academically, women were doing well. But one thing they mentioned was how isolated they felt. There would be empty seats next to them in class, so they wondered if they belonged there. Male professors didn't know how to interact with their female research students.

Q: How have things changed?
A: Now, close to 50% of undergraduates are women. They are no longer concentrated in biology. Attitudes are changing, too. Today, students have their own support groups. They take hold of the situation and try to arrive at solutions.

Q: Is it just a matter of time until women achieve equal (or near-equal) representation on faculties?
A: No. That will take much longer. At graduation, the average academic performance of women at the institute is better than that of men. But some women choose to have less demanding jobs if they start a family or for some other reason. If you take time off, you are no longer considered competitive; your publication record isn't as convincing. Even in biology, where the number of men and women students has been roughly equal for a while now, women are still not equally represented at the faculty level.

Q: Are there hidden barriers to advancement?
A: Yes. I was a great believer in the idea of a critical mass of female students. With a minimum of 15% in each class, I thought the lack of isolation would be enough. In the 1980s, we were coasting toward these numbers. At the faculty level, men and women seemed to have equal chance of attaining tenure. A decade later, Nancy Hopkins initiated her eye-opening study on the status of women at MIT. The data on pay scales, lab space, and other resources allotted to women showed how wrong I was. Nancy said that we'd have to beat on these guys to change things.



"Men's careers wind down when they reach their 70s. Women don't retire so quickly."

Q: All those inbuilt prejudices! What made you stay on?
A: The same reason we all stay on: because we love the work. Here's the interesting thing about women researchers: Once they hit their stride, they don't want to stop. For many of them, this happens after they are done with the child rearing. Men's careers wind down when they reach their 70s. Women don't retire so quickly. I continue to work. So does Brenda Milner, the winner of the 2014 Kavli Prize for neuroscience. She is 96 now.

Q: What would your message be to those women who aspire to be in academia?
A: Don't give up. There are equal opportunity laws in this country. There are processes to check if women have been interviewed for the job. Where the selection process is equal, some of you will get the jobs you aspire to get. Once you are on the faculty, you should advance at the same speed. Develop connections with the women who are already in such positions. Be confident. Apply. ■

Vijaysree Venkatraman is a Boston-based science journalist. For more on life and careers, visit www.sciencecareers.org.

ILLUSTRATION: ROBERT NEUBECKER

Downloaded from www.sciencemag.org on November 6, 2014

Published by AAAS